3DXRD – a new probe for materials science

Poulsen, Henning Friis

Publication date:
2004

Document Version
Publisher's PDF, also known as Version of record

3DXRD –
a new probe for materials science

3DXRD –
a new probe for materials science

by

Henning Friis Poulsen

Centre for Fundamental Research: Metal Structures in Four Dimensions,
Materials Research Department,
Risø National Laboratory, Roskilde, Denmark.

Denne afhandling er af Danmarks Tekniske Universitet antaget til forsvar for den tekniske doktorgrad. Antagelsen er sket efter bedømmelse af den foreliggende afhandling.

Kgs. Lyngby, den 5. februar 2004

Lars Pallesen
Rektor

/Kristian Stubkjær
Forskningsdekan

This dissertation has been accepted by the Technical University of Denmark for public defence in fulfilment of the requirements for the degree of Doctor Technices. The acceptance is based on the present dissertation.

Kgs. Lyngby, 5 February 2004

Lars Pallesen
Rector

/Kristian Stubkjær
Dean of Research

Contents:

Preface

3-Dimensional X-Ray Diffraction (3DXRD) is a novel experimental method for structural characterisation of polycrystalline materials. It is based on two principles: the use of highly penetrating hard x-rays from a synchrotron source and a "tomographic" approach to the acquisition of diffraction data. Uniquely, the method enables a fast and non-destructive characterization of the individual microstructural elements (grains and sub-grains) within mm-cm sized specimens. The position, morphology, phase, and crystallographic orientation can be derived for hundreds of elements simultaneously as well as their elastic and plastic strains. Furthermore, the dynamics of the individual elements can be monitored during typical processes such as deformation or annealing. Hence, for the first time information on the interaction between elements can be obtained directly. The provision of such data is vital in order to extend beyond state-of-art models in metal and ceramic science.

The 3DXRD methodology has developed over a period of 7 years, as the result of work by a group at Risø National Laboratory, with the author of this thesis as project leader. The work has lead to the establishment of a dedicated instrument, the so-called 3DXRD microscope. The microscope was installed at the European Synchrotron Facility (ESRF) in Grenoble at the end of 1999.

The aim of this thesis is to give a comprehensive account of 3DXRD microscopy, with focus both on methodology and applications. At the time of writing, the technique has reached a natural 1st stage in its development. A geometric formalism has been established, and implemented in terms of a set of experimental routines and analysis programs. Likewise, a number of prime applications have been identified, from which major results have emerged. The work is presented partly in this thesis itself, partly in 15 selected publications, which are attached.

The thesis is written for a general reader who has a background in the natural sciences and a basic understanding of diffraction. To ease the presentation the methodology is introduced without the use of equations and with a minimum of materials science specific conventions. For a mathematical treatment and details of the algorithms please refer to the attached publications. Likewise, the main applications are introduced by a short preamble, written in a popular way. These are mainly intended to motivate the use of 3DXRD. For a thorough introduction to the relevant scientific fields references to textbooks and recent seminal work is included. To underline the prospects of 3DXRD, a number of untested suggestions for methodological improvements and alternative applications are included.

The 15 attached publications contain most of the technical details. They were mainly selected to represent the prime results obtained, but serve also to illustrate the history behind the development of 3DXRD microscopy. These publications are summarised in this thesis itself.

Most of the work presented is the result of a larger cross-disciplinary, collaborative effort. A team of instrumentalists has been required to build the microscope, operate it, and to develop the associated software. Furthermore, to optimise the use of beam time, the synchrotron experiments are performed in shifts. Likewise, most of the

applications have been pursued in collaboration with experts within various fields of materials science.

The list of references is split into two. The first part contains publications being authored or co-authored by the author of this thesis. These references are numbered A1-A15 (the attached publications) and A16-A50. The second part contains works of other authors. These are referred to by numbers.

1. Introduction

Hard polycrystalline materials such as metals, alloys and ceramics form the basis of much of modern industry. The physical, chemical and mechanical properties of these materials are to a large extent governed by their structure. Hence, a comprehensive description of structural evolution during processing is at the heart of materials science.

Describing the structural dynamics is complicated by the inherent complexity of the processes. Typically, the structure is organized on a number of length scales, ranging from the atomic to the macroscopic. Interactions between the various elements of the structure occur simultaneously. Generally speaking, models that bridge all of the relevant length scales do not exist. Arguably, our understanding is best at the atomic and macroscopic scales where models can be based on simulations using molecular dynamics and continuum mechanics, respectively. At the intermediate scale, the meso-scale, a description is typically phenomenological in nature. Furthermore, most models aim at predicting average properties, and in doing so neglect effects caused by the pronounced heterogeneities often present.

As an example, consider the processes involved with plastically deforming a coarse-grained metal. These are illustrated by electron micrographs in Fig 1.1. When applying an external load, individual dislocations (line defects) appear on the atomic scale. To reduce their associated strain fields, these will tend to screen each other by forming dislocation structures. Simultaneously, as a collaborative effect of the movement of millions of dislocations, each of the grains will change its shape. The combined result of these local morphological changes is that the shape of the sample is altered in accordance with the external force applied.

Despite a wealth of experimental studies, it is an open question to what extent the plastic response of each grain is governed by its initial orientation, its interaction with neighbouring grains or by the emerging dislocation structures. Existing approaches to modelling all neglect at least one of these aspects. Another typical aspect is that the models include certain materials parameters, *in casu* hardening laws, which are more or less unknown and which only can be derived from first principles by modelling on a different (atomic) length scale.

Historically, advances in understanding have often been linked with the introduction of new and more powerful structural characterization tools. Hence, the introduction of optical microscopy by Sörby [1] is generally seen as the birth of modern metallurgy. Likewise, numerous fields were revolutionized by the advent of electron microscopy [2].

In a similar way, in the view of the author the present difficulty in establishing a comprehensive description for the meso-scale behaviour is at least partly due to a lack of appropriate experimental tools. As discussed below, characterisation on the relevant scale is almost exclusively performed by application of surface-sensitive probes. Due to effects such as stress relaxation, migration of dislocations and atypical diffusion, samples must be sectioned before investigation to get results representative

of bulk behaviour. This destructive procedure prohibits studies of the dynamics of the individual elements of the structure.

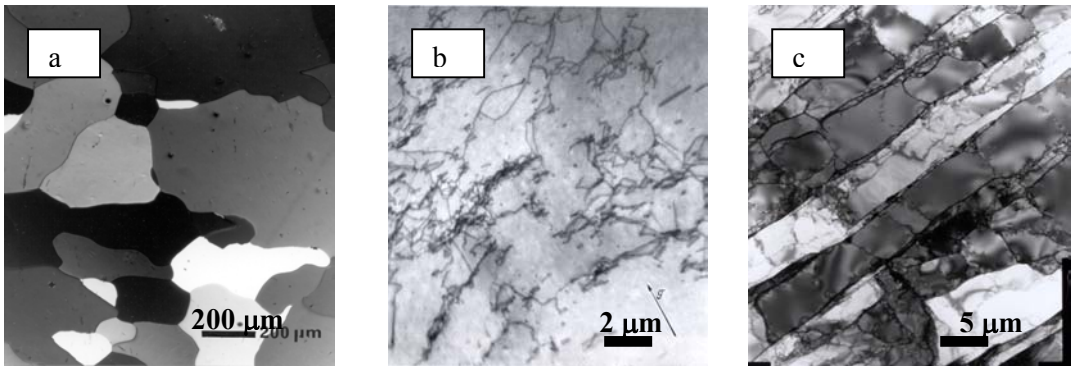

Figure 1.1.
Evolution of typical metal structures during deformation, as observed by various electron microscopes. In the undeformed state the structure is characterised by grain boundaries (a). After some deformation tangled dislocations appear (b). These form into dislocations structures with more deformation (c). Note the difference in scales.

Hence, a given process can only be studied *post mortem* by comparing a set of specimens produced by interrupting the process at different stages. While such studies have been - and will continue to be - indispensable in many areas, it is clear that they provide no direct information of the local interactions and, therefore, on the governing mechanisms. More generally, it is difficult to characterise the effect of heterogeneities.

It appears that what is required is an experimental technique with the following properties:

- Sufficient penetration power and flux for non-destructive 3D characterisation of the material within the bulk and on a micrometre scale.
- Contrast mechanisms by which the individual elements of the structure can be completely characterised with respect to their position, morphology, phase, crystallographic orientation, elastic and plastic strain.
- A probing volume large enough that results from many individual elements are derived, thereby ensuring that results are representative in a statistical sense.
- Sufficient time resolution to follow typical processes *in-situ*.

The aim of this thesis is to present a method, 3-Dimensional X-Ray Diffraction (3DXRD), which within some limits on resolution and degree of deformation, exhibits exactly these properties. The method is based on two inventions. Firstly, a beam of high energy x-rays, with an energy in the 50-100 keV range, is used for diffraction. When produced by a synchrotron source and focused by suitable optics such a beam exhibits a unique combination of penetration power and flux. Secondly, the conventional approach for providing spatially resolved information with diffraction is to scan the sample with respect to the beam. With x-rays this approach is, in general, much too slow for dynamic studies. Hence, it has been replaced by a "tomographic" approach to diffraction, providing information on many parts of the

material simultaneously. In practice the tomographic approach is realized by abundant and exclusive use of two-dimensional detectors.

The method has been implemented in a dedicated instrument, the 3DXRD microscope. Placed at the Materials Science Beamline at the European Synchrotron Radiation Facility (ESRF) in Grenoble, the instrument is the result of a collaborative effort between Risø and ESRF. At the moment of writing the microscope at ESRF is unique.

The author has been responsible for the 3DXRD project from the first feasibility studies in 1995-97 [A1,A16-19]. During this period the project has developed along several lines

- *Hardware developments*. The group was the first to apply two-dimensional detectors for diffraction with hard x-rays [A1,A16] and to implement schemes for focusing such beams to the micrometre scale [A20]. Furthermore specialized slits [A21], furnaces, rotation stages and a tensile device had to be developed. The x-ray optics design was devised in 1997-98, the 3DXRD microscope itself commissioned in autumn 1999, and a major up-grade implemented in January 2003.
- *Software*. Prior to the work presented here, programs for quantitative analysis of polycrystalline data sets did not exist. Hence, concepts have been developed for image analysis, x-ray tracing, indexing, and statistical analysis of such data. Work has been initiated on visualization in the relevant multi-dimensional spaces.
- *Geometric analysis*. To provide a unified structural characterization, concepts had to be merged from a number of fields. These include single crystal diffraction, powder diffraction, tomography, texture analysis, and stress characterization. Recently focus has been on reconstruction methods, from which it appears that further advances are likely to require theoretical work within applied mathematics.
- *Verification*. Methods have been proven by comparison to results from electron microscopy, by checks of internal consistency in the data and by developing several independent procedures for the same task. In addition, software is verified by simulations.
- *Prototype applications*. In close collaboration with colleagues at Risø, research programs have been pursued for a set of applications. These address fundamental issues within the fields of deformation, recovery and recrystallization of commercial purity metals. In general the work has progressed from feasibility studies of a few grains/sub-grains to statistically-based analysis on data from several hundred individual elements. Focus has been on identification of the relative importance of various interactions.
- *External user applications*. Subject to peer-review, the 3DXRD microscope is available to the public. Risø and ESRF has joined forces in establishing and diversifying a user program, which at the time of writing had lead to experiments by more than 20 groups from Europe and the US.
- Supplementary to the 3DXRD program, a unique method for characterising *plastic strain fields* by means of x-ray tomography has been developed at the HASYLAB synchrotron in Hamburg. Similarly, at the Advanced Photon Source (APS) in Chicago a program has been initiated on characterisation of dislocation dynamics. This is based on the extraction and analysis of *peak-shapes* from individual diffraction spots.

The scope of this thesis is defined by these methodological developments as well as by the applications that the author has been a (co-) driving force behind.

The presentation will somewhat arbitrarily distinguish between three length-scales, a nano-scale, a meso-scale and a macroscopic (or engineering) scale. The nano-scale refers to studies of individual defects and structures so small that quantification effects are important. Characterisation on the meso-scale implies identification, but not necessarily mapping, of individual structural elements, comprising a large number of defects. Examples here are grains, dislocation structures, inclusions and cracks. Characterisation on the macroscopic scale implies averaging over all elements, such that the structure can be described as a continuum. Typical examples are (local) texture and stress measurements, and structural refinement using powder diffraction. In compliance with normal usage the word microstructure will refer to the structure as observed by microscopic techniques, covering both the nano- and meso-scale categories.

The outline of the thesis is as follows:

In chapter 2 a summary is given of the characteristics of the structural probes conventionally used for meso-scale studies. This survey is followed by an account of the properties of hard x-rays, in general, and the utilization of these at hard x-ray synchrotron beamlines.

In chapter 3 the geometric principles underlying the 3DXRD method are presented. The basic set-up is sketched and various approaches to de-convolute the information concerning spatial, orientation and strain co-ordinates are discussed. A major simplification is shown to occur if the individual elements of the microstructure give rise to distinct and non-overlapping diffraction spots on the detector. For this case, a polycrystalline-indexing scheme has been developed, which enables a complete characterisation of the average properties (position, volume, orientation and elastic strain) of each element. The main limitation of this method is found to be a restriction to relatively low strains. Furthermore, for undeformed and coarse-grained materials the method can be extended in a simple way to generation of 3D grain maps. Details of the program developed (*GRAINDEX*), equations for the associated co-ordinate transforms and experimental verifications can be found in the attached publications [A2] and [A3].

Chapter 4 gives a presentation and discussion of two reconstruction formalisms. These are intended partly to extend the 3DXRD methodology past the restriction of negligible spot overlap and partly to enable superior grain maps to be generated even in the case where *GRAINDEX* can be applied. The original publications are attached: [A4], [A5] and [A6].

In chapter 5 the 3DXRD microscope is presented with respect to the hardware and software specifications at the time of writing.

In chapter 6 the case is stated for combined 3DXRD and absorption contrast tomographic studies. In association with this, a summary is given of the tomographic method for plastic strain mapping, with the original publication attached: [A7].

Chapter 7 describes the applications. For each topic the case for use of 3DXRD is stated and possible implementations are discussed. Experimental results are summarised and strategies for data analysis outlined. Publications [A8] and [A9] relate to studies of polycrystalline deformation *via* a determination of the rotation of individual embedded grains as a function of load. They give the first results on 4 grains and a statistically representative study on 95 grains, respectively. Similarly, publications [A10] and [A11] present growth data on 6 and 240 emerging nuclei during recrystallization, respectively. Publication [A12] contains the first results of microstructural dynamics during an early stage of annealing of deformed polycrystals. The potential for studies of phase transformations is illustrated by 2 publications, [A13] and [A14], on steel and high T_c superconducting tapes, respectively. The former is an example of work performed in collaboration with external users: in this case Offerman and co-workers from the Technical University of Delft. The latter is an extension of R&D work on tape optimisation performed in collaboration with the Danish manufacturer, NST.

The 3DXRD concept may be seen as an alternative crystallographic approach, complementary to traditional single crystal and powder diffraction techniques. The prospect for applications within other fields such as (bio-) chemistry, high pressure physics and environmental science is outlined at the end of chapter 7. In particular it is demonstrated how polycrystalline indexing enables structural refinements of the individual grains. A verification study is attached as [A15].

In chapter 8 an outlook is provided. Hardware improvements are suggested to improve the spatial and time resolutions. The prospect of transferring the 3DXRD methodology to neutron-, electron-, or laboratory-based x-ray diffraction is discussed. Furthermore the specifications of 3DXRD are compared to those of two alternative x-ray diffraction methods for 3D mapping, developed by other groups [3,4]. To the knowledge of the author these methods were developed after the initial work by the Risø group and none of them are based on the use of hard x-rays or on tomographic principles.

Finally, conclusions are drawn in chapter 9.

2. Methods for structural characterisation in materials science

As a motivation for introducing the 3DXRD method, this chapter contains a survey of the experimental methods conventionally used for structural characterisation in materials science. The options and limitations for studies on the meso-scale are discussed. The list of methods is not complete, but intended to reflect the common use.

This survey is followed by an account of the properties of hard x-rays – defined as x-rays with an energy at or above 50 keV - and the utilisation of these at hard x-ray synchrotron beamlines. To put the development of the 3DXRD microscope into perspective, a brief account is given of the historical development in the use of such beamlines, with the prime focus initially on problems in condensed matter physics.

2.1 Electron and optical microscopy

The predominant set of tools for structural characterisation today are the families of electron microscopies (EM). Thanks to its atomic scale resolution, transmission electron microscopy (TEM) is an indispensable tool for studies of dislocation structures, precipitates, interfaces and nano-scale structures in general [5]. Scanning electron microscopy (SEM) on the other hand offers relatively easy sample preparation, larger inspection areas and very user-friendly measurements, but at the expense of a spatial resolution of 5-50 nm [6].

Within the last decade, SEM studies in combination with the automatic electron back-scattering pattern (EBSP) method [7-10] have become the workhorse for many metallurgical studies. The EBSP method – also known as EBSD - enables determination of the crystallographic orientation of selected local areas and reveals the microstructure by orientation contrast. Used in conventional SEMs, the spatial resolution is about 0.5 – 1 μm, whereas field emission gun SEMs may give resolutions as high as 50 nm [11]. A limitation for certain studies may be the angular resolution of the orientation determination, which presently is 0.5^{o}-1^{o}.

Despite the enormous impact of EM, it is well recognised that using electrons as a probe is associated with a set of inherent disadvantages. Firstly, probing the elastic and plastic strain by EM is notoriously difficult. Secondly, the dynamical scattering processes involved complicate structural refinement from diffraction data. Thirdly, the electrons penetrate ≤ 1 μm into materials such that only the surface region is probed. This fact implies a number of limitations, which are central to this thesis. They are discussed in detail below.

- *2D characterisation*: Structural objects of interest: grains, dislocation structures, cracks etc. are in general truly three-dimensional in nature. Based on observations from a single section it is only possible to provide a 3D description by subjecting the objects to a statistical treatment. The discipline of stereology [12] was invented to facilitate such a description. However, it

turns out that a number of parameters of interest simply cannot be inferred from a single 2D section without additional assumptions. These include grain shapes, size distributions, nucleation frequencies, and characterisation of clustering phenomena. Also the large data sets needed for statistical analysis are often an issue.

Three-dimensional characterisation can be obtained by so-called serial sectioning (for a recent study see [13]). First one section is characterized by EM, then the sample is polished or etched to remove a certain layer of material and the new surface section is characterized. This procedure is repeated until sufficient 3D data are obtained. This method is tedious and technologically it is not trivial to align the different sections with respect to each other. In practice the method is therefore fairly seldom used in Materials Science.

- *Representability and quantification:* Specimens of interest tend to be heterogeneous on several length scales. Traditionally, the areas investigated by EM have very often been too small to ensure that the observed effects were representative of the full volume. Furthermore, this limitation has severely hindered the use of EM for quantitative work. As an example, as a rule of thumb a few thousand grains are needed to represent a size or orientation distribution properly. With the recent introduction of automatic EBSP measuring schemes these limitations to some extent have been overcome.

  A related problem has to do with characterization of structural elements with a small volume fraction. A prime example are the nuclei in nucleation-and-growth events, where the fraction may be at the parts-per-million level. The probability of finding such objects by surface probes is very small.

- *Dynamic studies:* In general surface dynamics cannot be considered to be representative of the bulk. The geometry of structural elements on the surface is different from those in the bulk. The size and shape of elements is altered by the sectioning, the number of neighbours is reduced and an additional free surface is introduced. Furthermore, the stress component normal to the surface relaxes. As a result, driving forces as well as boundary conditions will in general be atypical. As examples, dislocations may migrate to the surface, grain boundaries may be pinned on surface grooves prohibiting growth, grain interaction effects are reduced and reaction rates may be altered.

  For metals a guiding principle may be that the topology connected with grains 5 layers below the surface can be considered to be representative of the bulk [14]. Processing requirements may raise more severe limits. Deformations may for instance give rise to large-scale gradients (bands, dead-zones) through the sample. Moreover, to mimic standard/industrial deformation processes a specimen thickness of 1-2 mm or more is often required.

  The situation for ceramics and (compacted) powders, in general, is similar. The processes to be investigated are controlled by diffusion. The diffusion will involve solid state, liquid or gas phases. When one of the latter two are involved, surface dynamics are clearly not representative due to effects such as evaporation and free surface area. However, even in those cases where the

diffusion is purely solid-state, differences in grain size distributions, porosity and effective surface area may influence reaction rates. The relevant penetration depth is in this case the largest of the diffusion path lengths for the components involved.

- *Specimen preparation and geometry.* The specimen preparation needed for EM characterisation implies that contamination of the surface, whether chemical or mechanical, is an issue. Likewise, for high temperature studies the quenching process involved often requires consideration. For TEM studies in particular the thin foil geometry accentuates the surface/bulk issues discussed above. In addition the wedge shaped specimen geometry normally used introduces an additional driving force.

Optical microscopy is universally used for routine investigations. It is associated with the same limitations as described above for EM with the possible exception of representability, as larger inspection areas can be used.

2.2 X-ray diffraction with low energy x-rays.

Up to the 1960's x-ray diffraction was the method of choice for structural characterisation. (For a textbook on x-ray metallography from that period, see *e.g.* Taylor [15]). These studies were based on the use of photographic films and laboratory sources, typically equipped with metal targets ranging from Cu to Mo in the periodic system, and therefore producing x-ray lines at 8 – 17 keV. The penetration power of x-rays at these energies is limited, of the order of micrometres. Using a reflection geometry the penetration is further reduced. Hence, the methodologies developed are subject to the same limitations as discussed for the case of EM.

Nevertheless, it is remarkable that routines were at hand not only for bulk stress, texture and chemical analysis but that x-rays also were widely used for estimates of grain sizes. The average grain size was derived by counting the number of diffraction spots in a single image or alternatively by measuring the sizes of a set of diffraction spots. As shown by Hirsch and Kellar grains as small as 1 μm could be observed in this way, by focusing the beam [16-18]. However, the diffraction patterns were never really quantified – *e.g.* in terms of a grain size distribution - and in general no information was extracted on the position, shape, orientation or strain state of individual grains.

Seen from a modern perspective it is evident that this lack of quantification can be overcome by the use of computers and two-dimensional detectors. Furthermore, superior optical elements have become available for focusing the x-ray beam. However, with the invention of EM, the development of x-ray metallography essentially came to a complete stop. As a consequence, today laboratory x-ray sources are mainly used for characterisation of average structural properties.

Within the last 30 years x-ray instrumentation in general has been revolutionised by the construction of ever more powerful synchrotron sources. Thanks to groundbreaking work in accelerator physics the electrons or positrons orbiting in the

synchrotron ring have been confined to smaller and smaller cross-sections. Consequently, today the x-ray beam produced by the charged particles can be focused to very small focal spots by suitable optics. Hence, a number of so-called micro-focus beamlines have been build, using a variety of focusing elements. As examples, focusing multi-layers [19], zone-plates [20,21], refractive lenses [22,23] and waveguides [24] have been reported to provide x-ray beams with a size in the range of 0.1 – 1 μm. However, it is characteristic of these focusing elements that the efficiency decreases substantially with increasing energy. Hence, the existing micro-focus beamlines are all dedicated to x-rays with energies around or below 20 keV.

For materials science purposes, micro-focus beamlines have been used in a way similar to the EBSP method. By so-called micro-diffraction techniques, the grains and sub-grains on the surface are mapped by scanning the specimen with respect to the beam. At each position the orientation and lattice strain is measured. An example of such work is reported by Biermann and co-workers [25].

However, with the clear exception of the measurements of lattice strains it appears that similar results can be obtained with EM. Furthermore, it is not clear how to interpret a map of lattice strains in terms of plastic deformation when only *post-mortem* information on a sectioned surface is available. Also, the scanning procedure is relatively slow. For these reasons, an alternative approach is sought in the present thesis.

2.3 Conventional bulk-sensitive methods

In terms of penetration power, neutron diffraction is the superior probe: in most cases centimetres-thick specimens can be studied. Furthermore, systematic errors such as absorption and extinction are small and the method is applicable to set-ups involving complex sample surroundings. However, the neutron flux is low – in practice single crystals have to have a size of ~100 μm or larger to be used for diffraction. Applications to characterisation of meso-scale structures have therefore been limited to integral methods, mainly Small Angle Neutron Scattering (SANS) [26]. With SANS the fluctuations of the scattering cross section for neutrons are probed. For hard materials SANS is mainly used for characterisation of voids and precipitates in the size range of 1 – 100 nm. The defect concentration and the mean and width of the size-distributions can be found.

Prior to 3DXRD, the only bulk-sensitive method that was able to generate 3D maps of the microstructure was x-ray tomography. Computerised tomography (CT) was developed in the late 1970's primarily for medical use, but it can be applied equally well to materials. It is based on measuring the attenuation through the specimen while rotating the sample around an axis perpendicular to the beam direction. The tomographic reconstruction yields a three-dimensional representation of the density distribution within the sample [27,28]. As such it does not provide any information on crystallographic orientation or strain and it cannot distinguish features such as grains and dislocation structures within a mono-phase system. It is, however, indispensable for studies of multiphase systems, whether crystalline or amorphous, and in particular for characterisation of voids and cracks.

While x-ray tomography is well suited for use with laboratory sources, superior results are obtained with synchrotron radiation. The combination of a high flux, negligible beam divergence and monochromatic radiation reduces artefacts in the reconstructions substantially. As a result, synchrotron-radiation-based micro-tomography routinely generates maps with a spatial resolution of 1-2 μm [29,30].

2.4 Hard x-rays: properties

Hard x-rays exhibit a number of properties that are very advantageous for diffraction studies of bulk materials:

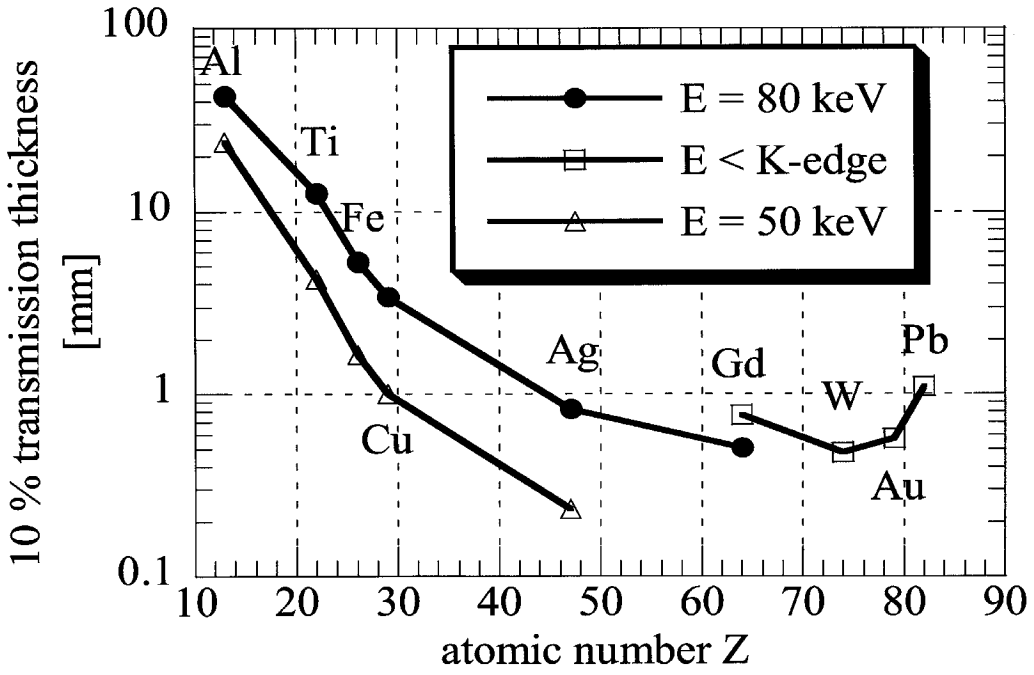

Figure 2.1
The penetration of x-rays through matter at 50 keV and 80 keV for selected elements. The penetration data for elements symbolized by ❑ refer to the use of an x-ray energy just below the absorption K-edge of the element.

1. The *attenuation* of x-rays decreases rapidly with energy, E, above the K-edge of the material under investigation, asymptotically approaching a minimum in the 500 – 1000 keV range. Simultaneously, the diffracted intensity from a given object decreases in proportion to E^{-2}, due to the Lorentz factor [31]. As a compromise between penetration power and the number of diffracted photons, the 50-100 keV range is found to be ideal. The penetration of hard x-rays for a transmission set-up in this range is illustrated in Fig 2.1. For light elements such as Al, a penetration of 4 cm is possible. For steel the number is 5 mm. For materials with high atomic numbers, 0.5-1 mm is obtainable. For the latter case, a significant gain in penetration can be obtained by going to 200-500 keV.

2. It is well known from single crystal diffraction that *extinction* effects diminish rapidly with increasing energy, with decreasing crystal size and with

increasing degree of disorder within the crystal [32]. For the polycrystalline case of interest here, each grain is a small crystal and in general far from perfect due to impurities, inclusions and dislocations. Hence, the intra-grain extinction will be small, in particular in deformed specimens.

For polycrystals, an additional extinction term arises from the possible attenuation of the diffracted beam from a grain of interest by further diffraction by other grains. This effect will be referred to as *inter-grain extinction*. To estimate the importance of this effect, it is illustrative first to discuss the limiting case of an ideal powder with infinitely many, infinitely small, randomly oriented grains. In this case the extinction is simply equal to the total cross section for coherent scattering times the thickness of the specimen. The resulting extinction is shown in Fig 2.2(a) as function of energy for Al and a fixed specimen thickness of 1 mm. Evidently, the effect decreases approximately with E^{-2}. However, if one wishes to take advantage of the higher penetration power at higher energies and sets the thickness equal to the penetration depth at all energies a different result appears. In that case, the inter-grain extinction exhibits a global maximum in the energy range 50-100 keV at ~ 10% attenuation, cf. Fig 2.2(a).

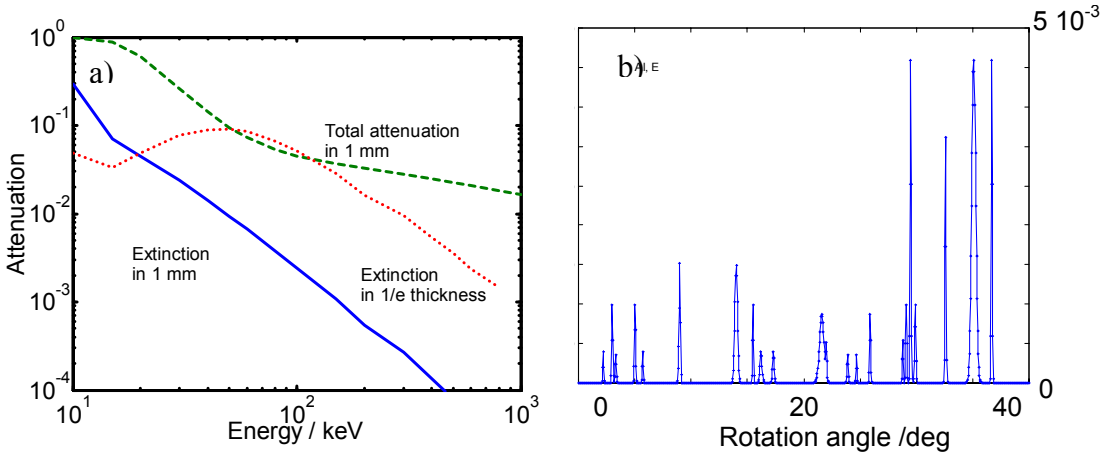

Figure 2.2
Simulations of extinction in Al. a) Results for the ideal powder case. The inter-grain extinction (full line) and the total attenuation (dashed line) are shown for a specimen with 1 mm thickness. Also shown is the extinction in a specimen with variable thickness but fixed attenuation of 1/e (dotted line). b) A simulation of the extinction within one plate-like Al grain with a thickness of 100 μm at 50 keV. The resulting attenuation is shown as function of rotating the grain around one axis perpendicular to the beam. The reflections are represented as Gaussian profiles with a width of $\sigma = 0.1^{o}$. The orientation of the grain is picked at random.[1]

For the case of main interest here – a textured sample with 10-100 grains along the beam path – there is no simple way to calculate, and thereby correct, the inter-grain extinction effects. To estimate the magnitude of the effect, a simulation of the attenuation through one 100 μm thick Al grain is shown in Fig 2.2(b). The inter-grain extinction arising for a diffraction path through N of such grains will correspond to summing N of such profiles. Unless the

[1] The attenuation due to thermal diffuse scattering is included in a) but not in b).

orientations of the grains share some common axis, *e.g.* are twins, the profiles will add in an incoherent way. If the grains are nearly perfect – the case displayed - the spikes will be sharp, and the chance of overlapping spikes small. If the grains are associated with a larger orientation spread, the spikes will be smaller and the chance of overlap larger. In both cases, it is seen that the extinction is limited to a few percent for $N < 100$. For the applications presented in this thesis extinction effects are estimated to be negligible.

Related to extinction is the issue of *Multiple Bragg scattering*, the so-called Renninger peaks [31]. The Renninger peaks appear as additional diffraction spots on the detector, when the diffracted beam from one element of the microstructure is diffracted once more within another element. Application of hard x-rays is here advantageous, as the ratio between the flux of the twice diffracted beam and that of the one time diffracted beam falls off with E^{-2}.

3. *Small Bragg angles*. It follows from Braggs law that the scattering angle 2θ is inversely proportional to x-ray energy. Hence, the diffracted x-rays from the accessible reflections get condensed more and more in the forward direction with increasing energy. This has the practical advantage that a complete characterisation of the diffraction pattern can be obtained with conventional two-dimensional detectors, such as Charged-Couple Devices (CCDs) and Image Plate systems, which have a flat screen.

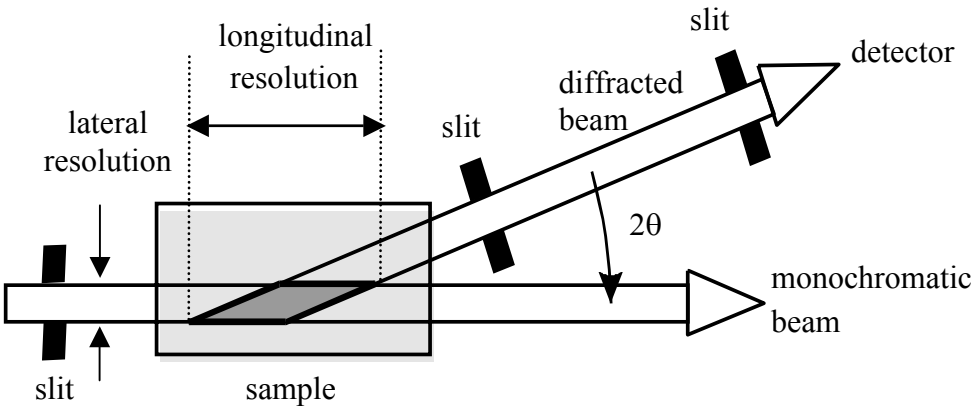

Figure 2.3
Sketch of the elongated gauge volume associated with a primitive hard x-ray diffraction set-up. Courtesy of S.F. Nielsen.

For completeness, the two main disadvantages of using hard x-rays for diffraction should also be mentioned. The first is the E^{-2} dependency on the integrated intensity of a given object. The second is the elongated gauge volume associated with 3D work, caused by the small 2θ angle. This effect is illustrated in Fig 2.3. In the 50-100 keV range, typically the gauge volumes will have aspect ratios of 1:10. This ratio implies a deterioration in the spatial resolution of 2D or 3D maps, which however to a large extent can be removed by applying suitable reconstruction principles.

2.5 Hard x-ray work using synchrotron sources

Prior to the use of synchrotron sources, the only sources for the generation of hard x-rays were radioactive sources and x-ray tubes. As discovered by Röntgen, these exhibit a flux that is sufficient for radiography and tomography. As such the hard x-rays are utilised extensively in society at large, at hospitals, airports and for industrial inspection. By contrast, the photon flux from these sources is barely sufficient to perform diffraction experiments. Thus work on so-called γ-diffractometers has focused on macroscopic studies of large single crystals [33-35].

Synchrotrons generate electromagnetic radiation in a continuous spectrum, ranging from the ultra-violet into the x-ray region. There is a rather sharp cut-off to this spectrum at the high energy end, proportional to the energy of the particles in the ring to the second power. During the last 15 years, a number of synchrotrons have been commissioned with very high energies - in the 4-12 GeV range - the range where x-ray studies in the 50-300 keV region become feasible. The properties of these synchrotrons are summarised in Table 2.1.

Synchrotron	Location	Ring energy (GeV)	Use	Hard x-ray beamlines	Source size (μm^2)
DORIS-III	Hamburg	4.5	Dedicated	BW5	7400 x 800
PETRA-II	Hamburg	7-12	Parasitic	PETRA-II	2600 x 280
ESRF	Grenoble	6	Dedicated	ID11	138 x 20
				ID15	138 x 20
APS	Chicago	7	Dedicated	11-ID	563 x 36
				1-ID	563 x 36
Spring-8	Himeji	8	Dedicated	BL04B2	-
KEK	Tsukuba	6.5	Parasitic	-	-

Table 2.1
Principal parameters for synchrotrons of relevance for hard x-ray diffraction. The numbers listed under source size refer to the FWHM of the distribution. Parasitic use implies that the beam is only available when the ring is not used to serve the particle physics community. Several other beamlines at SPRING-8 can be used for hard x-ray diffraction, but are not dedicated for that purpose.

In addition to the tuneable energy, synchrotrons offer two main advantages with respect to laboratory sources. The first one is an increase in flux by many orders of magnitude. Shown in Fig 2.4 is the number of photons available for experiments at the ID11 beamline at ESRF. The second is the small source sizes associated with the so-called third-generation sources: ESRF, APS and Spring-8, see Table 2.1. As discussed in chapter 5, such source sizes enable focusing of the x-ray beam from 1 mm down to ~1 μm with only a small loss in intensity.

Historically, the first synchrotron study using hard x-rays was reported by Hastings and co-workers in 1989 [36]. Following this feasibility study the first dedicated instrument for high energy diffraction was commissioned by Schneider at HASYLAB in 1993 [A22,A23]. Within the areas of condensed-matter physics and crystallography this has been used for a series of pioneering applications on amorphous scattering [A24], diffuse scattering [A25,37], phase transformations [38,A26], non-resonant

magnetic studies [39], and charge density studies [40,A27]. Studies within these fields have been continued at other hard x-ray beamlines, emerging through the 1990s, cf. Table 2.1. For examples of recent work see [41-46]. Furthermore, Reichert and co-workers have directed hard x-ray work into new fields involving studies of solid/solid and solid/liquid interphases and diffuse scattering from binary systems [47-48].

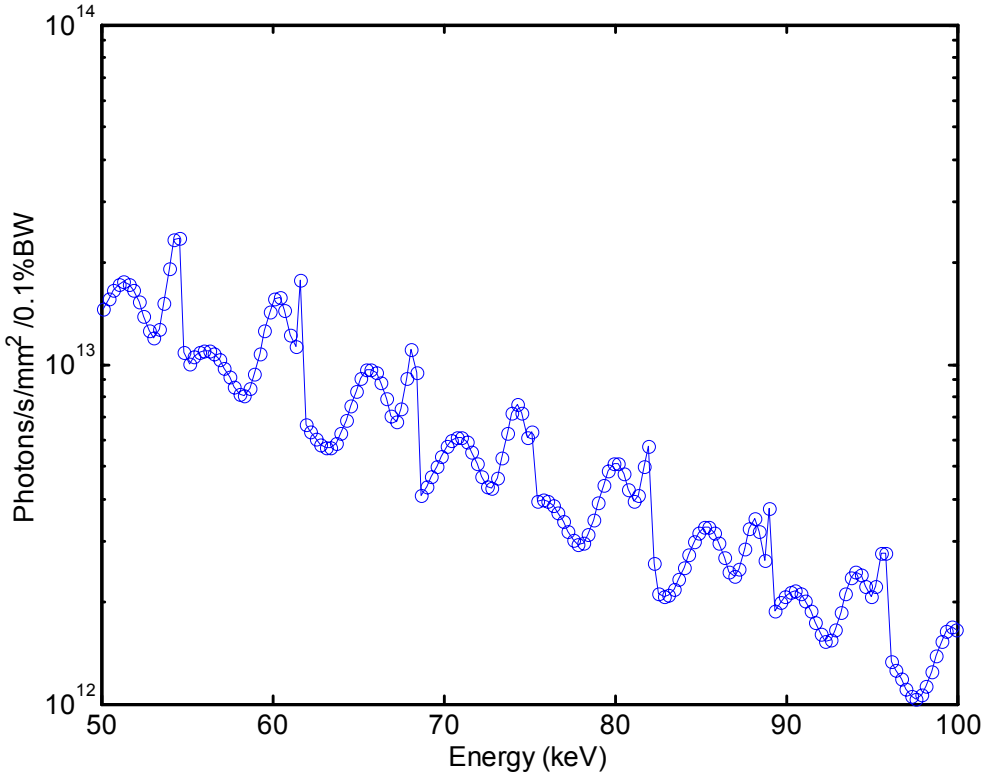

Figure 2.4
A simulation of the flux available at the second experimental hutch at the ID11 beamline at ESRF as function of x-ray energy. (This is where the 3DXRD microscope is situated, see chapter 5). The number of photons entering the hutch through a 1 mm^2 pinhole within an energy band of 0.1% is shown. The "wiggles" on the curve are due to the undulator [32] installed at the beamline. The positions of the wiggles can be changed by varying the gap of the undulator – the results shown are for a gap of 5 mm. Courtesy of L. Margulies.

Work within the field of macroscopical characterisation for materials science and engineering has developed along 3 independent routes. Powder diffraction work, averaging over a full specimen, have been reported by a number of groups, *e.g.* [A15, A28,46,49,50]. Macroscopic and local texture characterisation with hard x-rays were initiated at HASYLAB by the Risø group [A28,A29] and later developed into a dedicated set-up by Wcislak, Bunge and co-workers [51]. Characterisation of the local stress and strain within bulk materials has been performed by numerous groups, using energy dispersive settings as well as monochromatic set-ups [52-58,A30,59,60].

The use of hard x-ray diffraction for structural characterisation on the meso-scale is the topic of this thesis.

3. 3DXRD: geometric principles

The aim of 3DXRD is to characterise the crystallographic lattice as function of position within the bulk of a specimen. Locally, the lattice is uniquely determined by its 6 lattice parameters and its orientation in space. In most of this thesis it will be assumed that the structural phase is known, but that the lattice can be subject to stress. The associated elastic strain causes a perturbation of the lattice parameters from the strain-free reference values.

Crystallographic orientations can be expressed in numerous ways, as described in detail in the literature on texture [61]. In this thesis and the attached publications three representations are used for the crystallographic orientation. For algebra the natural choice is a 3x3 orthogonal matrix **U.** For visualisation and sampling a representation by three parameters is preferable. Traditionally, a set of Euler angles (ϕ, φ_1, φ_2), expressing subsequent rotations around three axes, are used [62]. Alternatively, any rotation can be represented in a unique way by a rotation axis $\underline{n}$ and a rotation angle ϕ. In the Rodrigues parameterisation these are coupled in the definition of the Rodrigues vector $\underline{r} = \tan(\phi/2)\underline{n}$ [63]. The Rodrigues representation is in several ways the natural representation with superior geometrical properties. Its key features are summarized in [A6].

The elastic strain is represented by a symmetric 3x3 matrix, the strain tensor, $\boldsymbol{\varepsilon}$ [64]. The relation between $\boldsymbol{\varepsilon}$ and the lattice parameters can be expressed algebraically, see [A3]. The strain tensor is linearly related to the stress tensor $\boldsymbol{\sigma}$ by Hooke's law.

At first sight, it appears that the task at hand is a determination of the spatial variation of $\underline{r}$ and $\boldsymbol{\varepsilon}$. However, in general the situation is more complex. Due to limitations in instrumentation – a finite spatial resolution – and local defects, each point in space must be associated with a distribution of orientations and a distribution of strains. Hence, one must operate in what will be termed the *12-dimensional lattice space*.

Diffraction from single crystals is conventionally described in terms of scattering vectors and the reciprocal space. These concepts can be extended in a simple way to include spatial variations. Hence, each local diffraction event is characterised by the position in space where the event takes place and by the associated scattering vector, **G**. Likewise the *6-dimensional diffraction space* may be introduced as the product of direct space and reciprocal space.

Finally, in terms of an actual diffraction experiment with a monochromatic beam, what is measured is the intensity of the diffracted beam incident on a set of detectors, each at a given position in space. This information may be acquired while the specimen is rotated and translated.

Hence, from a mathematical point-of-view, the task at hand is the reconstruction of the 12D lattice space by operations in the 6D diffraction space and based on projections onto a 3D space (direct space). Furthermore, the aim is to make such reconstructions sufficiently fast that dynamic information can be obtained.

It is clear from the outset that in the most general case this task cannot be performed completely. Fortunately, the typical organisation of the microstructure into a (hierarchical) set of elements, such as grains, dislocation structures etc. alleviates the problem tremendously. Moreover, the geometry can be simplified by choice of experimental set-up.

The first 3DXRD studies related to idealised specimens (undeformed, coarse-grained specimens) and simplified set-ups. With time the methodology has advanced allowing progressively more ambitious studies. Simultaneously, the mathematical rigour has increased.

In this chapter first the basic experimental set-up is presented. In the remainder of the chapter focus is on a particular but very important case, where complete structural characterisation is obtainable. It is the case where the various structural elements produce distinct (non-overlapping) diffraction spots. In this case, the diffraction spots can be sorted with respect to element of origin by means of a polycrystalline indexing scheme. The structure of the elements can then be characterised independently. A large number of problems within polycrystal and powder research can be tailored to apply to this situation. In the following chapter, the presentation returns to the general case.

3.1 The basic 3DXRD set-up

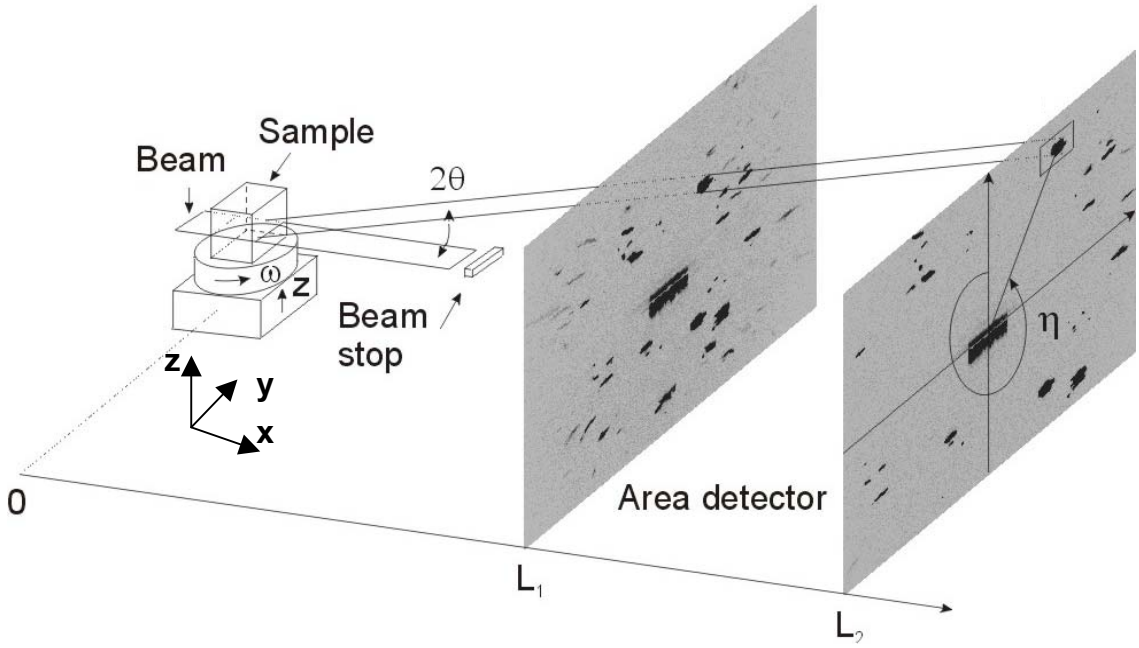

Figure 3.1
Sketch of the 3DXRD principle for the case of the incoming monochromatic beam being focused in one dimension. The Bragg angle 2θ, the rotation angle ω and the azimuthal angle η are indicated for the diffracted beam arising from one grain of a coarse-grained specimen, and for two settings of the area detector. The axes for the laboratory co-ordinate system are also shown.

The 3DXRD method is an extension of the "rotation method" known from single crystal crystallography [31]. The basic set-up is sketched in Fig 3.1. A

monochromatic x-ray beam is constrained to a suitable cross-section by means of focusing and/or the use of absorbing slits. This beam impinges on the sample as a uniform field. The sample is mounted on an ω rotation stage, where ω is the rotation around an axis perpendicular to the incoming beam. As an option x-, y-, and z-translations may be added as well as additional rotations.

Any part of the illuminated structure, which fulfils the Bragg condition, will generate a diffracted beam. This beam is transmitted through the sample and probed by one or more 2D detectors. Essential to 3DXRD is the idea to use such detectors to mimic a 3D detector, similar to the ones used in particle physics. This can be done in two ways. Firstly, by positioning several 2D detectors at different distances to the centre-of-rotation, L, and exposing these either simultaneously (many detectors are semi-transparent to hard x-rays) or subsequently. Secondly, by acquiring images with one 2D detector positioned at several distances to the rotation axis, as illustrated in Fig 3.1.

To probe the complete structure, and not just the part that happens to fulfil the Bragg condition, the sample is rotated. Hence, exposures are made for equi-angular settings of ω with a step of $\Delta\omega$. To provide a uniform sampling the sample is oscillated by $\Delta\omega$ during each exposure.

With the detectors available, experience has proven three complementary detector configurations to be of particular use. Depending on the issue at hand, they may be used on a stand-alone basis or they can be combined. Below are listed the three configurations including typical numbers for the present use of the 3DXRD microscope in brackets.

Configuration A. A detector with a high spatial resolution (6 μm) positioned close to the specimen. Data acquisition is repeated at several distances (3 settings of L in the range of 4-8 mm). The angular resolution is relatively low, of the order of 10^{-3} rad. This implies that the diffraction patterns are not influenced by any elastic strain, as the associated angular perturbations are too small to be observed. Hence, only spatial and orientation degrees of freedom are probed.

Configuration B. A detector with a low spatial resolution (300 μm) positioned at a fixed medium distance to the specimen. The distance is optimised such that the full diffraction pattern appears in the images (L = 400 mm at 50 keV). The diffraction spots now appear on a set of rings – the Debye-Scherrer rings well known from powder diffraction. In this case the spatial degrees of freedom are to a large extent integrated out, whilst the angular resolution is medium, of the order of 3×10^{-4} rad.

Configuration C. A detector with a medium spatial resolution (50 μm) positioned far from the detector (2500 mm). With this detector only a small fragment of the diffraction pattern is observed, typically one or a few diffraction spots. However, the angular resolution is very high, and in practice determined by the choice of monochromator. (For a flat perfect crystal monochromator the resolution is of the order of 10^{-5} rad.)

Typical exposures for each of the 3 configurations are shown in Fig 3.2, for the case of an undeformed, coarse-grained specimen.

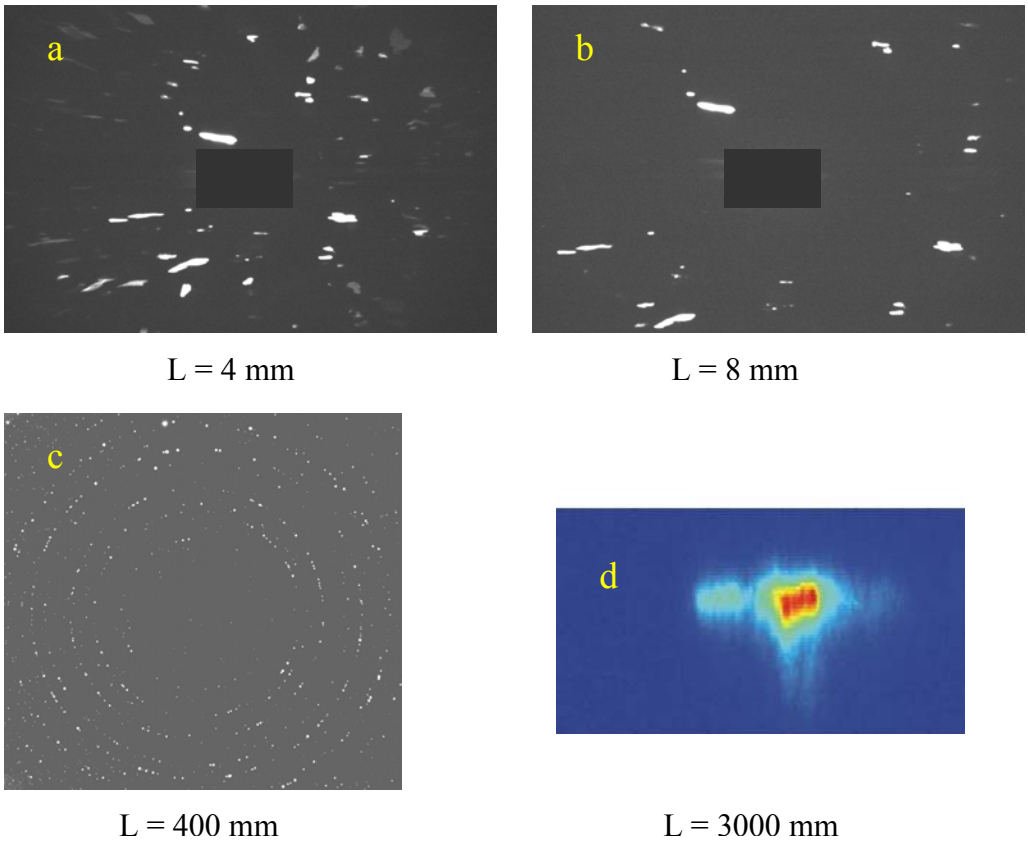

Figure 3.2
Typical exposures of coarse-grained undeformed polycrystals using detector configurations A (a,b), B (c) and C (d). L is the distance from the detector plane to the ω-axis of rotation, see Fig 3.1. The dimensions of the images are 3.5 x 2.3 mm^2, 230 x 230 mm^2, and 20 x 2 mm^2, for configuration A, B, and C, respectively. The background is shown black in a) - c) and dark blue in d). Images a and b are from [A3] and d from [A32].

To further tailor the experimental geometry to the problem at hand, the cross section of the incident beam may be varied. Again experience has demonstrated that three configurations are of particular use. Below these are listed with typical numbers for the 3DXRD microscope in brackets.

Box beam A square cross-section with dimensions much larger than the size of the structural elements (from 5 x 5 μm^2 to 1 x 1 mm^2). In this case, an ω-scan provides a full characterisation of the entire specimen, or a sub-volume, depending on specimen size.

Line beam The beam is confined as much as technically possible in the direction perpendicular to the ω-axis (1 μm x 1 mm). In this case, an ω-scan provides a full characterisation of the illuminated layer. For 3D characterisation the procedure is repeated at a set of layers by translating the specimen in *z*.

Pencil beam The beam is confined in both directions to dimensions smaller than the size of the structural elements (2 x 5 μm^2). For each ω-position a line through the specimen is probed. In this case, to provide full three-dimensional information, a three dimensional scan is required, over y, z and ω.

The set-ups presented above are in several ways ideal. They are conceptually simple, resulting in robustness and versatility. A complete description is provided and, most importantly, measurements are fast. For the line beam configuration shown in Fig 3.1 the 6D diffraction space is sampled by scanning over one rotation (ω) and one translation (z). For the case of a box beam, measurements are even faster. In this case, sampling is provided by a single ω-scan.

3.2 *GRAINDEX*: Indexing distinct diffraction spots

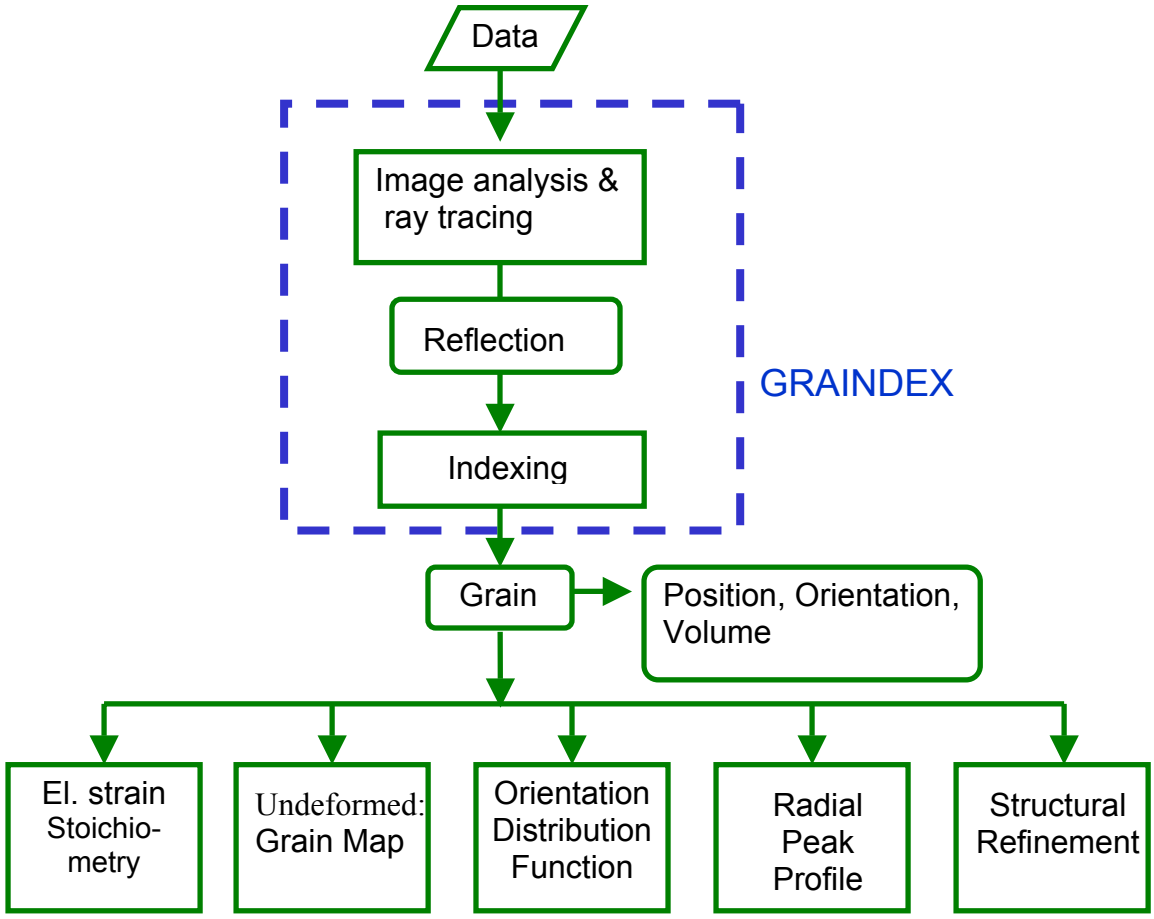

Figure 3.3:
A flow-chart for the *GRAINDEX* algorithm (marked by the hatched box) and associated further analysis on the individual grains.

A general-purpose indexing routine has been developed for polycrystalline data. The routine is implemented as the program *GRAINDEX*. Details of the routine and the

program are given in [A2]. The routine will be presented below for the case for which it originally was developed: the set-up sketched in Fig 3.1 – with a line beam and detector configuration A [A2]. Other configurations of detectors and beam profiles will be considered afterwards.

Formally, the application of *GRAINDEX* is subject to the following assumptions:

- Kinematical scattering theory (absence of absorption and extinction).
- The energy bandwidth and the divergence of the incoming monochromatic beam are negligible. The beam impinging on the sample is a uniform field. The set-up is perfectly aligned and the detector characteristics are ideal.
- The crystallographic space groups of the phases are known either from the literature or from powder diffraction work on the same specimen.

Furthermore, in the following it is assumed that the specimen comprises only one crystalline phase. Multi-phase systems are handled by applying *GRAINDEX* successively for each phase.

The flow of the algorithm is illustrated in Fig 3.3. Initially image analysis is performed for each image. Diffraction spots are identified by setting an intensity threshold and searching for connected regions with intensities above the threshold. Once found, the spots are associated with a center-of-mass (CMS) position, an ω setting, and an integrated intensity.

Next, x-ray tracing is performed (illustrated in Fig 3.1). Spots generated by the same reflection, but appearing in images acquired at different detector positions, are identified. A best fit is determined to a line through the CMS positions of these spots. This determines the scattering vector, **G**. Extrapolating the fitted line to its intersection with the incident beam defines the CMS position (x, y) of the illuminated section of the grain of origin. By analogy to particle physics this procedure is called tracking. Most notably, the tracking concept works also for imperfect grains, where the rays associated with one reflection may cross each other and diverge as a function of L. As long as the diffraction spots are distinct, their CMS positions will be positioned on a straight line.

The key part of the routine is the indexing algorithm, which sorts the reflections with respect to grain of origin. In the limit, where the accuracy on the extrapolated CMS positions is much better than the average grain size, the sorting can be based on the extrapolated (x,y) positions. In the opposite limit, the sorting must rely on crystallographic criteria. This situation is handled by scanning over 3D orientation space. For each grid-point, the scattering vectors arising from a grain of that orientation are simulated. If the simulated and observed reflections match within tolerance a grain is identified. For intermediate cases, a combination of the spatial and the crystallographic criteria is used.

To discriminate against spots caused by stray radiation, overlapping spots, and other artefacts, validity tests are incorporated in the algorithm on all types of objects: spots, reflections and grains. For details see [A2]. This publication also includes a verification of the code and the principle by a simulation of 100 grains and 2500

reflections. All grains were identified and 99.8% of the reflections were indexed correctly.

GRAINDEX has been implemented as an on-line program, complete with an interactive interface and batch processing. It has the intriguing feature that the speed of the algorithm is nearly independent of the number of reflections. Hence, when run on a fast PC an indexing of a few hundred grains is performed in 10 minutes. The program has formed the backbone of much of the research performed so far with the 3DXRD microscope. As such it has proven to be very robust. Artefacts related to intensity fluctuations or minor deviations from kinematical scattering theory are not a concern, as the sorting is not based on intensities. Likewise, stray reflections are generally filtered out as the probability of N reflections by chance forming a coherent diffraction pattern falls off rapidly with N.

3.2.1 Alternative configurations

With modifications, *GRAINDEX* also applies to the case of a box beam. In this case the extrapolation line through the set of spot CMS's does not provide a point of origin, but a line through the specimen. The CMS of the grain of origin will be positioned on this line. The criterion on position is therefore replaced by the condition that the extrapolated lines of the reflections shall intersect in a point within the specimen.

GRAINDEX has been applied extensively to detector configuration B as well. In this case there is little or no spatial information in the diffraction patterns, and all illuminated grains can therefore to a good approximation be considered as positioned at the origin. The tracking procedure is then replaced by simply drawing a line between the CMS position of each diffraction spot and the origin. The indexing is in this case based solely on the crystallographic criterion.

3.2.2 Spot overlap

N	*w = 0.1 deg*	*w = 1 deg*
10	*0.00033*	*0.032*
100	*0.0036*	*0.319*
1000	*0.036*	*0.995*
10000	*0.36*	*1*

Table 3.1.
Probability of a diffraction spot overlapping with any other spots arising from a set of N randomly oriented grains. The numbers refer to a detector configuration B setting and to reflections belonging to an {hkl}-family with a multiplicity of 12. The total width of the orientation spread within the diffraction spots is 2w. The detector point-spread-function is assumed negligible.

The main limitation to the use of *GRAINDEX* is the restriction that spots must be distinct. The program can tolerate a minor fraction of the spots overlapping with other spots, as such spots are filtered out, but it fails when overlap becomes a dominant feature. A formula for the probability of spot overlap is derived in [A15] for

detector configuration B. The spot overlap is a steep function of the mosaic spread (the degree of orientation spread within one diffraction spot). To illustrate the magnitude some numbers are listed in Table 3.1. Evidently, ~5000 grains can be indexed simultaneously for relatively perfect grains with a mosaic spread of less than 0.1 degree. At a 1 degree spread, the number is ~50, and above 10 degrees polycrystalline indexing with *GRAINDEX* is no longer feasible. Hence, the use of *GRAINDEX* is restricted to moderate degrees of deformation.

The problem can be alleviated to a certain extent in two ways

- by basing the indexing only on spots appearing in rings associated with a low multiplicity
- by using a detector configuration intermediate to A and B. Notably, in configuration B the diffraction spots are confined to the Debye-Scherrer rings, that is most of the detector area is not used (see Fig 3.2c). When simultaneously moving the detector closer to the specimen and improving the spatial resolution of the detector, spots originally confined to a ring become distributed radially within an annulus. Tests have proven that for high symmetry spacegroups such as fcc, *GRAINDEX* can handle at least 5 times as many grains in this mode as in configuration B.

The fact that the grains vary in size can also be helpful. The integrated intensities are proportional to the grain volumes. Hence, the diffraction spots from the largest grains may be discernible as bright spots on a fluctuating background composed of a sea of fainter spots from the smaller grains. As an example, an analysis of the 57 largest grains within an ensemble of 1500 is reported in [A15].

3.3 Analysis of single grains based on *GRAINDEX*

The output of *GRAINDEX* is a list of grains and their associated reflections. Furthermore, the orientation and the CMS position of each grain are determined from best fits to the set of scattering vectors and to the *(x, y, z)* positions associated with the reflections, respectively. These fits are optimised so as to be obtained quickly and should be seen as first approximations. If needed, further iterations can be performed, as discussed below.

The output from *GRAINDEX* can be used to estimate the volume of each grain (or in the case of the line beam configuration, the illuminated area). Kinematical scattering implies that the integrated intensity of any diffraction spot is proportional to the volume. Hence, all that is required is a suitable intensity calibration. Such calibrations are discussed in [A10].

The list of grains may be used as input for further analysis, as sketched in Fig 3.3. These add-on routines will be presented below, with the exception of the options for determinations of radial peak profiles and for structural refinement, which are discussed in sections 7.4 and 7.7, respectively.

3.3.1 Grain Maps

The sketch in Fig 3.1 suggests a simple way to produce a 2D map of the grain boundaries when using a line beam and detector configuration A. This method does not even necessarily involve indexing. Assume that the grains are substantially larger than the detector resolution. Assume further that they are associated with a mosaic spread sufficiently small that the diffracted x-rays are approximately parallel. In this case the periphery of any illuminated grain section will be projected directly onto the detector screen. Hence, it appears that grain-shapes can be determined by back-projecting the peripheries of the diffraction spots along the directions determined by the fits to the CMS positions. 3D maps are then obtained by stacking layers.

Two details are worth mentioning. Firstly, the contour of the grain boundary is demagnified in the longitudinal direction by a factor of $\sin(2\theta)\cos(\eta)$. Hence, at $\eta = 90^0$ and $\eta = 270^0$ the diffraction spots collapse into lines from which the grain contours cannot be retrieved. In practice, spots within a certain η-interval around these numbers must be discarded. Secondly, in practice the detector is associated with a point-spread-function with relatively long tails. For best results the point-spread-function must be de-convoluted.

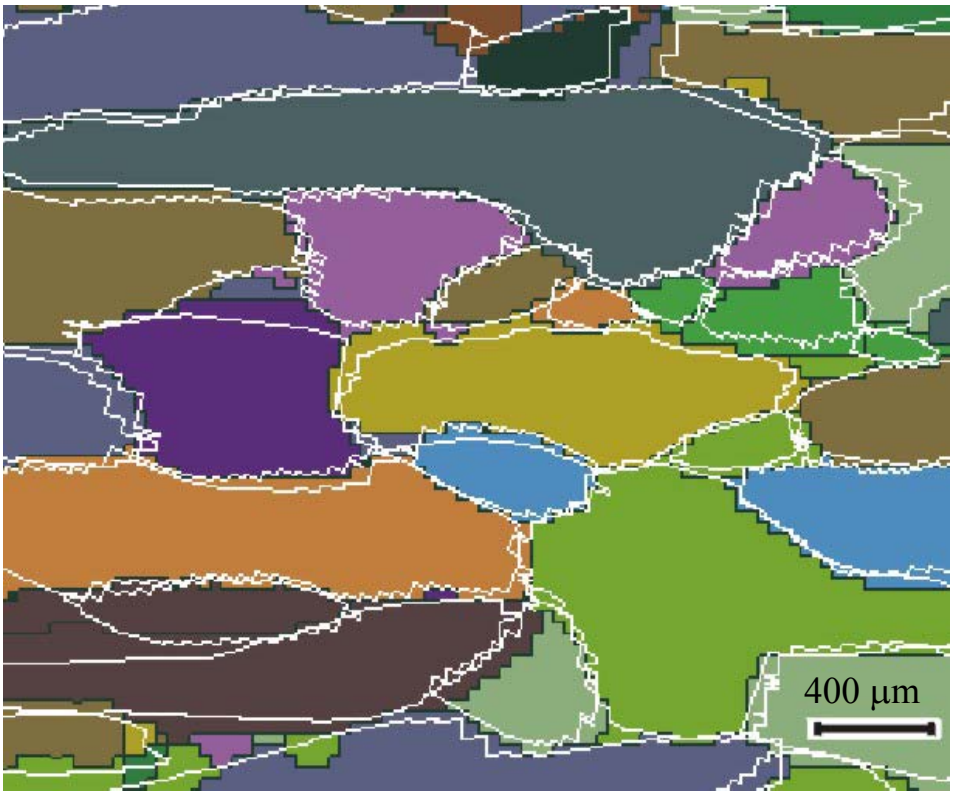

Figure 3.4
Validation of the simple back-projection algorithm for generation of grain maps. Colours and black outlines mark the grain and grain boundaries on the surface of an aluminium polycrystal as determined by electron microscopy (EBSP). Superposed as white lines are the grain boundaries resulting from the synchrotron experiment. From [A3].

The simple back-projection method is described in [A3], which also includes verification by means of comparison to an EBSP map. This comparison is reproduced here as Fig 3.4. The average deviation between the boundary positions in the 3DXRD and the EBSP maps is 24 μm, comparable to the point-spread-function of the detector available at that time. The total data acquisition time for one layer was less than 2 minutes.

Unfortunately, this method is associated with two disadvantages:

1. The projection implies that the spatial resolution along the direction of the incident beam is one order of magnitude worse than in the transverse direction. The solution to this problem is to combine information from several diffraction spots obtained at ω-settings ~90^0 from each other. However, interpolation based on contours is not a robust tool.
2. There is no straightforward way to extend the simple back-projection method to a box beam or to samples with a small but not negligible mosaic spread.

In chapter 4 reconstruction methods are discussed, aimed at overcoming these shortcomings as well as the overall constraint of non-overlapping diffraction spots.

3.3.2 The Single Grain Orientation, Elastic Strain and Stoichiometry

With detector configuration B, the CMS of each diffraction spot can be determined to a high accuracy with respect to the angles 2θ, η and – depending on Δω - also ω. From *GRAINDEX*, a list of such CMS angles can be generated for all the diffraction spots associated with a given grain. This list can then be used as input for a simultaneous 12-dimensional fit to the position, average orientation and average elastic strain tensor for the grain.

While conceptually elegant, this approach has some disadvantages. The 12-parameter fit is non-trivial, as discussed in [A3]. Furthermore, the spatial distortions in the detector may render the derivation of an absolute metric impossible.

As an alternative, the orientation and strain contributions are separated. For determination of orientations, the diffraction spots are integrated over 2θ. Experimentally, the accuracy on orientations found in this way is ~ 0.2 degrees. Similarly, the components of $\boldsymbol{\varepsilon}$ are determined solely from the 2θ positions of the diffraction spots. The shifts of the 2θ positions are measured with respect to strain free reference values, as determined from a reference powder. Such shifts are not influenced by grain rotations. Provided a sufficient number of reflections are measured (≥ 10), the strain components can be derived by a least-square fit. The algorithm is similar to the one used for macroscopic stress and strain determination with neutron diffraction [65].

This approach, where the orientation and strain components are separated, is presented and verified in [A3]. The strain components of a single embedded Cu grain are determined as function of tensile deformation [A3,A31]. The uncertainty in the strain determination is found to be $1x10^{-4}$. Recently, Martins has reported on an extended study of this type involving tensile deformation of Al up to 2.1% elongation. In this case, the positions, orientations and all strain components were characterised *in-situ* for a large number of grains simultaneously [66].

The only error sources associated with this procedure are the experimental inaccuracy in 2θ and the provision of a strain-free reference material. The accuracy can be increased substantially by using detector configuration C instead. This has been done in an experiment at APS, where lattice strains were measured with an accuracy of 1 x 10^{-5} [A32].

In materials science phases are often *non-stoichiometric*. This is true for instance for perovskites, steel, and various non-equilibrium phases *e.g.* as in quenched samples. Non-stoichiometric phases tend to be heterogeneous exhibiting intra-granular variations. In many cases there is also a distribution in the average stoichiometry of the individual particles. In such cases, the average lattice parameters will be perturbed. Hence, it appears that the methodology introduced for characterisation of the strain tensor for each grain applies equally well to characterisation of the composition. In general both types of perturbation may occur simultaneously. The first 3DXRD study with both contributions appearing have been performed by Kruijver and co-workers [A33].

3.3.3 The orientation spread within one grain

It is of interest to characterise the distribution of orientations within the grains, *e.g.* as in connection with studies of polycrystalline deformation [A8,A9,A32]. Following conventions from macroscopic texture analysis [61], this implies the generation of an orientation distribution function (ODF) for each grain. These can be extracted in a relatively straightforward manner by use of detector configuration B, provided the detector resolution is larger than the average grain size.

Single grain ODFs will tend to be sharp and "spiky". This implies that the traditional approach to ODF generation by expansion of spherical harmonics [62] is troublesome, due to truncation errors and the inherent singularity at the origin. These problems can be avoided by the use of an algebraic formulation and a Rodrigues space representation. A MATLAB program based on these principles has been developed [A6]. (Similar programs for generation of macroscopic ODFs have been reported by Barton *et al*. [67] and Weiland *et al*. [68]).

3.4 The conical slit

The conical slit is a novel x-ray optics element developed at Risø [A1,A21]. It is used as a supplement to the basic set-up introduced in section 3.1. The device is placed between the specimen and the 2D detector, as sketched in Fig 3.5(a). It comprises a set of conical openings positioned in accordance with the Debye-Scherrer rings of the phase to be investigated. It appears that diffracted rays will be transmitted through the slit if and only if they originate from a 3D gauge volume, defined by the slit.

Historically, the intention was to generate 3D grain maps by scanning the slit or the sample in x, y, and z [A1]. In fact, the first partial grain map presented in 1996 [A17] was generated in this way. Notably, such scanning procedures do not rely on separation of diffraction spots and they can therefore be extended to arbitrary degrees of deformation. However, as stated in the introduction, scanning procedures are much

slower than “tomographic” routines. As such no further work has been done in this direction.

In the more recent meso-scale applications the conical slit has been fixed and used together with detector configuration B. This has served to define an intrinsic ”volume of interest”, see Fig 3.5(b). Referring to the figure, without the slit the diffraction spots would arise from the entire illuminated volume. By comparison with the slit in place, the number of diffraction spots appearing in the images is reduced by factor of 4 to 40, while retaining all the relevant information from the vicinity of a structural element of choice.[2]

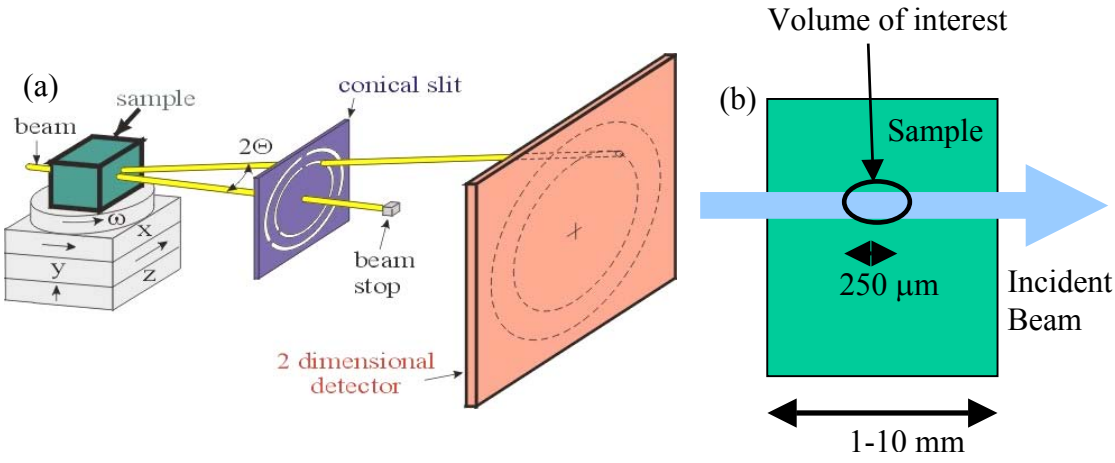

Figure 3.5
(a) Sketch of the conical slit set-up. From [A34]. (b) Illustration of the primary use of the slit: to define an intrinsic volume-of-interest. Typical numbers for the 3DXRD microscope are given.

Details of the manufacture, alignment strategies and validation tests of this set-up are described in [A21]. The device is used routinely with the 3DXRD microscope, for applications see [A9,A30,A35,A36,59,60]. It is associated with three limitations:

1. A conical slit is designed for a specific combination of lattice parameters, x-ray energy and slit-to-specimen distance. However, all samples belonging to the same symmetry group, *e.g.* fcc, can be studied using the same slit by varying the x-ray energy.
2. Manufacturing is an issue. The existing slits have been constructed by wire electro-discharge machining [A21]. They comprise 6-7 openings with gaps of 20 μm. Due to the projection factor, see Fig 2.3, this implies a resolution along the beam of 250-350 μm.
3. For strained specimens the conical slit may cut the reflections such that only the low or high 2θ part from a given point in the specimen is transmitted through the slit. To circumvent this problem, and provide an un-biased and complete sampling, a reconstruction method has been established [A36]. It requires the acquisition of a series of exposures while translating the specimen along the direction of the incoming beam. This procedure has been used for strain scanning in a number of macroscopic applications [A36,59,60].

[2] Notably, extinction and absorption effects are not reduced.

For macro-scale applications, primarily strain scanning, Honkimäki has further developed the conical slit concept [69]. Substituting openings in the shape of annuli with spiral shaped openings, limitation 1 is overcome. That is one device can be applied universally, independent of x-ray energy and space group.

3.5 Characterisation of large volumes

Characterisation of large sample volumes is complicated by the spot overlap issue as well as by the fact that it may not be possible to condition the monochromatic beam to illuminate the whole volume at once. For such cases an approach has been developed, where the volume of interest is divided into a set of sub-volumes, to be characterised successively [A37].

The basic principle is sketched in Fig 3.6 for characterisation of one layer in the specimen. By means of 2D scan over ω and y, information is obtained for a sequence of channels through the specimen. For each of these channels, diffraction spots are identified and the associated reflections are determined by ray tracing, as described in section 3.2. For indexing, reflections from different stripes have to be combined. Presently, this is done *ad-hoc*, using derivatives of *GRAINDEX*. Following indexing, the analysis can proceed as described in sections 3.2 and 3.3.

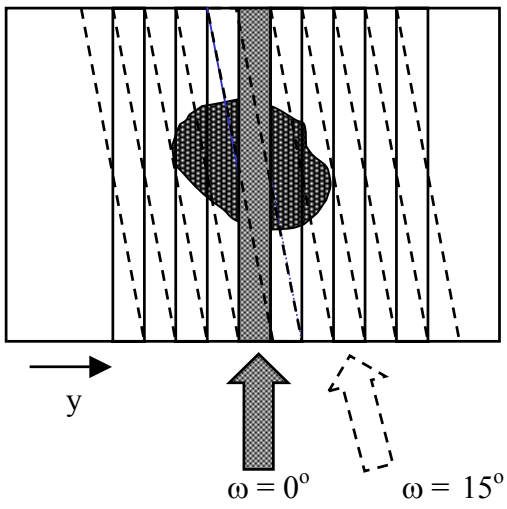

Figure 3.6
Strategy for sampling an extended layer of a polycrystal by means of a 2D scan over y and ω. At an angular setting of ω = 0° the incident beam illuminates a narrow channel through the thickness of the sample (hatched area). Images are acquired while scanning the sample in the y direction with a step size identical to the size of the beam. This procedure is repeated at a number of ω-settings, illustrated here by ω = 15°. It is seen that in the central part the layer is probed homogenously both spatially and with respect to angle. From [A37].

This scheme is easily generalised to a characterisation of a large 3D volume, by use of a box beam and by extending the scanning procedure to ω, y and z (for a first application see [A12]). Furthermore, it may be combined with use of the conical slit, in which case a 4D scan (over ω, x, y and z) is required. Adding dimensions necessarily makes the characterisation slower, eventually prohibiting dynamic studies.

However, the multi-dimensional scans may serve to survey a larger volume prior to dynamic studies, in order to identify regions of specific interest.

A special case of such generalised scans is the so-called *super-scans*. These are one-dimensional scans in the x, y or z direction, where for each point in the scan an acquisition is made while oscillating the specimen around a nominal ω value. The super-scans are used for aligning specific structural elements. By monitoring the integrated intensity of an associated diffraction spot as function of position, the projected CMS position of the element in the direction of the scan is found. By combining y and z scans on two diffraction spots arising from the same structural element, the (x,y,z) CMS position of the element can be found using trigonometry. Notably, the accuracy on the CMS position determined in this way can be substantially better than the spatial resolution of the set-up.

3.6 Dynamic experiments

Dynamic studies are performed simply by repetition of any of the measuring schemes presented above.

In addition to the constraints set by the required time resolution, two complications occur

1. *Stability.* Positional drifts are unavoidable during *in-situ* processing studies due to various relaxation phenomena. To correct for these, internal and external markers are used. The internal markers are parts of the microstructure, such as grains or inclusions, which for various reasons are assumed to be fixed and rigid. The external markers presently used are 300 nm thick Au markers, which have been deposited onto specimens prior to 3DXRD studies by a lithographic technique. Their position can be monitored with an accuracy of 1 μm by the characteristic x-ray fluorescence signal.

2. *Validation of integrated intensities.* To ensure that the integrated intensity of a given diffraction spot is proportional to grain volume one must verify that the grain is fully contained within the illuminated part of the specimen and that the intrinsic orientation spread is fully covered by the angular oscillation range. In connection with dynamic experiments it may happen that these conditions are fulfilled for some periods of time and for others not, as the grain may grow outside the illuminated volume or it may rotate outside the oscillation range. To discriminate against such events so-called validation tests are made.

   The use of such a validation test is illustrated in Fig 3.7. The integrated intensity of a diffraction spot is monitored continuously during annealing using a box beam with fixed slit positions and a fixed oscillation range. At regular intervals the slit is opened in both directions and the oscillation range is increased while maintaining the same speed of rotation. In this figure, initially the intensity is seen to be the same for the regular and extended settings. After ~100 minutes the intensity for the extended settings are larger than those for the regular. From this point onwards the grain is no longer a

valid grain. The same procedure also prevents grains growing into the illuminated channel from neighbouring volumes to be incorrectly treated as new nucleation events.

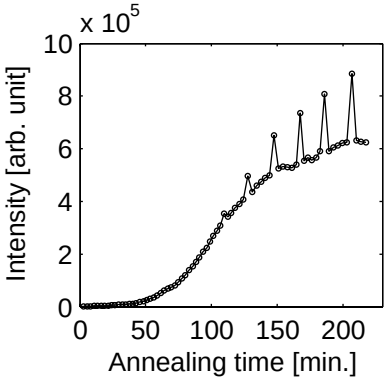

Figure 3.7
Illustration of the validation procedure. Shown is a growth curve for a single grain obtained during annealing. The integrated intensity of a diffraction spot is repeatedly measured. At regular intervals the dimensions of the incident beam is enlarged in both directions by opening a slit. Simultaneously, the oscillation range is extended. For the latter half of the period shown the grain is no longer valid. From [A11].

3.7 Conclusions and outlook

- A general-purpose indexing program for polycrystals and powders has been developed. The main limitation to the use of *GRAINDEX* is the requirement that diffraction spots do not overlap. For undeformed specimens several thousand grains can be indexed simultaneously.
- When *GRAINDEX* is applicable, the individual microstructural elements can be characterised with respect to their position, volume, average orientation and the average values of the components of the elastic strain tensor. Furthermore, when relevant the orientation distribution function can be derived.
- For the case of undeformed grains and the use of a line beam, 2D grain maps can be generated by back-projecting the outlines of the diffraction spots. By stacking such maps, the grain boundary topology is visualised in 3D.
- Large sample volumes can be investigated by characterising a set of sub-volumes. The results are stored in a database. Tools are under development for on-line search in the database for objects of specific interest, such as structural elements with a particular combination of size, orientation and neighbourhood conditions.
- A conical slit is introduced as a novel optical element for diffraction work. In connection with 3DXRD this slit is mainly used to define an internal volume of interest to reduce the number of diffraction spots. In addition the conical slit is used for strain scanning on engineering components.

4. Reconstruction

The methodology presented in sections 3.2-3.6 is associated with two limitations. Firstly, *GRAINDEX* cannot handle spot overlap, which therefore precludes certain studies *e.g.* work on medium to heavily deformed specimens. Secondly, grain maps can only be deduced for the case of undeformed grains illuminated by a line beam.

In this chapter, a reconstruction formalism is sought that overcomes both limitations. The only restriction is that the lattice strain is assumed to be negligible. This restriction is fulfilled when using detector configuration A.

The aim of the reconstruction is to determine which orientations are present and where in the specimen. A distinction can be made between a reconstruction where each sample position is associated with one orientation (as is typical of many scanning methods such as EBSP) and one where each position is associated with an orientation distribution. Focus here will be on the second type, for a number of reasons. Firstly, this is the more general case. Secondly, at present for many applications, the smallest element in the microstructure is substantially smaller than the spatial resolution of 3DXRD. Thirdly, an experimental compromise between resolution, inspection volume and data acquisition speed is generally needed. Hence, even if the microscope can be operated with a spatial resolution better than the size of the typical element such a setting may not be relevant.

From a mathematical point-of-view the reconstruction task is an "inverse problem". Such problems have been investigated in great detail, driven by applications such as computerized tomography (CT) and positron emission tomography (PET). The resulting reconstruction principles can broadly be categorized as belonging to one of two categories: transform methods and algebraic methods [27,28]. In the transform methods the projection involved is treated as an operator: a generalized Radon transform [70]. Solutions are based on theorems that couple Radon and Fourier transforms. In the algebraic methods the geometry is formulated as a constrained set of linear equations [71]. With both types of method, routinely the density in a grid with 10^9 volume-elements (voxels) is reconstructed with an accuracy in the 1% range.

In the case of 3DXRD, the reconstruction space is the 6D lattice space. The voxels might for instance be 6D cubes. (A superior choice is presented in [A6].)

By experimental design or choice of material, the topology of the reconstruction space can be simplified, increasing the chance of a successful reconstruction substantially. As examples:

1. The diffraction spots are not overlapping. In this case, by initial use of *GRAINDEX*, the reconstruction of the grains can be performed independently.
2. The grains are "undeformed", that is the orientation spread within each grain is negligible. Then the space and angular degrees of freedom separate.
3. A line beam is used. 3D maps can then be generated by stacking independent reconstructions from a set of layers.

To investigate the feasibility of 3DXRD reconstructions, three studies have been made. Initially, an algebraic and a transform method were developed and applied to two simplifying cases. The results are reported in [A4] and [A5], respectively. The general 6D case is treated mathematically in [A6]. The three publications are summarised below, followed by a conclusion on the feasibility of 3DXRD reconstructions.

4.1 The *ART* routine for undeformed grains and a line beam

The case of undeformed grains and a line beam was already treated in section 3.3. Here it was demonstrated that 2D grain maps can be generated by back-projecting the contour of one diffraction spot for each grain (see Fig 3.4). However, as described earlier this method has a number of drawbacks, which will tend to worsen the spatial resolution.

The aim of the work in [A4] is to develop and test an algebraic routine for reconstruction of the 2D grain maps. The result should be better maps, as all the information from all the diffraction spots associated with a given grain is combined.

The routine developed works as follows: the illuminated plane in the sample is tessellated into a set of squares (pixels) on a regular 2D grid. The aim of the reconstruction for a given grain section is to determine the density of these pixels. For pixels fully outside the grain the density should be 0, and for pixels fully inside it should be equal to a materials' constant ρ_0. Pixels at the boundary may be partly inside the grain, and should therefore have intermediate values.

The problem is formulated in terms of a set of linear equations: $\mathbf{A}\underline{x} = \underline{b}$, where the unknown $\underline{x}$ comprises the pixel densities and $\underline{b}$ is a list of the observables: the intensities in the individual detector pixels at various ω settings. The information on the experimental set-up and diffraction geometry is stored in **A**. The solution is constrained by the requirement stated above: $0 \leq x_i \leq \rho_0$.

Once a density map has been determined for one grain, the grain boundary is defined by setting a threshold say at $\rho_0/2$. If required, a space-filling map - free of overlaps and voids between the individual reconstructed grain boundaries - can be generated by interpolation.

In general **A** will be large and the set of equations may be under-determined as well as over-determined. These facts in combination with the need for handling the constraint on density make an iterative solution attractive. *ART* is a simple and versatile iterative routine, which have been used extensively for CT and PET applications [28,71].

The routine was optimised for 3DXRD use by simulations. These demonstrate that the added constraint on the density is crucial to obtain good reconstructions. This is illustrated in Fig 4.1. Left to right, what is shown in this tableau is the reconstruction of one grain segment with a ρ_0 that is set too low, one that is set optimally and one that is set too high (or not set at all). The one in the middle fits the input to the simulation on the sub-pixel level. The simulations also show that 1 reflection gives a poor reconstruction, as already indicated by the work on the simple back-projection

method in 3.3.1. On the other hand, the use of 4-5 reflections per grain is found to be sufficient to provide a high-quality map.

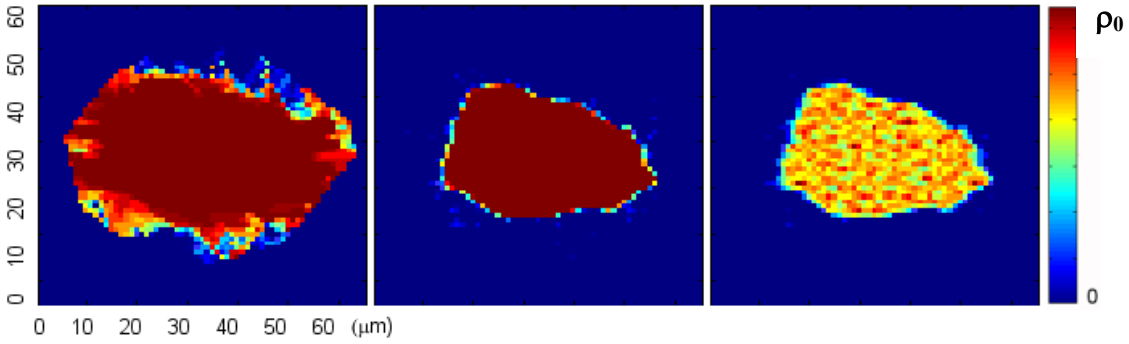

a) $\rho_0 = ¼\ \rho_{theory}$ b) $\rho_0 = \rho_{theory}$ c) $\rho_0 = 5\ \rho_{theory}$

Figure 4.1
Reconstructed density maps for simulated data representing a 2D section of one grain. The upper limit on density ρ_0 is varied with respect to the optimal setting, $\rho_{theory.}$ The linear colour code is shown on the right. The interpretation is as follows: for $\rho_0 > \rho_{theory}$ pixelation errors leads to pronounced "salt-and-pepper-noise" (c). Lowering ρ_0 to ρ_{theory} a uniform density distribution is enforced in the grain interior (b). Lowering ρ_0 further a missing density in the grain interior is added to the grain boundary areas, implying a larger apparent grain size (a). From [A4].

The *ART* method is verified in [A4] by experimental data on an annealed Al polycrystal with an average grain size of 150 μm. The cylindrical specimen had a height of 3 mm and a radius of 0.4 mm. A high-resolution detector with a point spread function of ~6 μm was used.

Results for 4 neighbouring grains in one layer are shown in Fig 4.2. Based on 5 reflections each, the CMS positions of these grains were determined to within 1-2 μm. From the overlaps and voids in the 3 boundary regions in Fig 4.2, the spatial resolution is estimated to be 5 μm.

3D maps of grains are generated by stacking the individual segments. An example of such a reconstructed, embedded grain – from the same sample - is shown in Figure 4.3 [A38]. To the knowledge of the author this is the first reported result of its kind.

4.2 The FBP routine for undeformed grains and a box beam

The filtered back-projection algorithm (FBP) is the most commonly used transform method algorithm [27]. This algorithm is summarised in publication [A5], where it is demonstrated that it can be applied to 3DXRD data. The case chosen is that of undeformed grains fully illuminated by a uniform box beam – the simplest case involving a real projection. (Transform methods cannot be applied to the case discussed in section 4.1.)

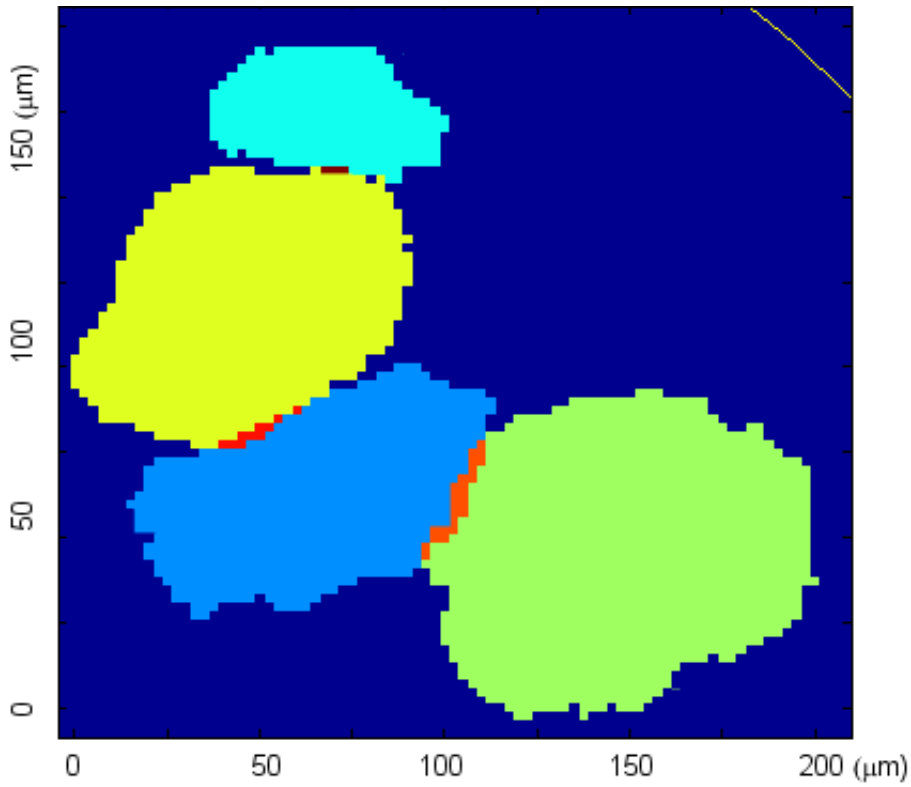

Figure 4.2
Independent reconstruction of 4 neighbouring grain sections, based on 3DXRD data for an interior layer of an Al polycrystal. The grains are marked by different colours. Regions of overlap between the grains are marked in red. The surface of the polycrystal is indicated by a solid yellow curve. From [A4].

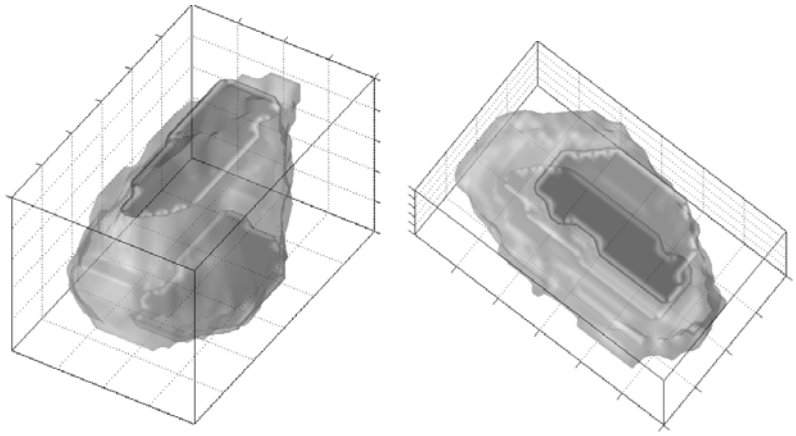

Figure 4.3
Two viewpoints of a 3D grain map generated by serially stacking 11 layers. Each voxel displayed is 10x10x10 μm^3. The spatial resolution is 5 µm in all directions. From [A38].

It is shown in [A5] that the geometry underlying diffraction in this case is equivalent to the geometry of parallel-beam CT, provided one angle is substituted by another. Furthermore, it is shown that to a reasonable approximation, reconstructions can be performed not only grain-by-grain but also z-layer by z-layer. The 3D grain maps are

then obtained by stacking the reconstructions for the layers. The full reconstruction algorithm comprises four steps:

A. The sample volume of interest is tessellated into a set of cubes (voxels) on a regular 3D grid.
B. The diffraction spots are indexed by *GRAINDEX* and the CMS positions of the grains are found to a high precision.
C. For each grain and each z-layer, the routine identifies one line in each of the associated diffraction spots. The intensity distributions along these lines are used as the input – in CT language: the sinogram – for the FBP algorithm. The output is the reconstructed density distribution in the z-layer.
D. The grain boundaries can either be derived for each grain independently or interpolation can be used to obtain a space-filling map. In the first case, the boundaries are defined by setting a density threshold at a fraction of the average density in the interior of the reconstructed density distributions. In the second case, each voxel is associated with the grain that has the highest reconstructed density at that position.

It appears that the bulk of the computation can be performed with two existing algorithms: *GRAINDEX* and FBP.

The routine developed was verified by a 3D simulation of a polycrystal with 10 grains. Using 64 reflections for each grain, a sub-pixel accuracy is obtained. A comparison between the original and the simulated map is shown in Fig 4.4.

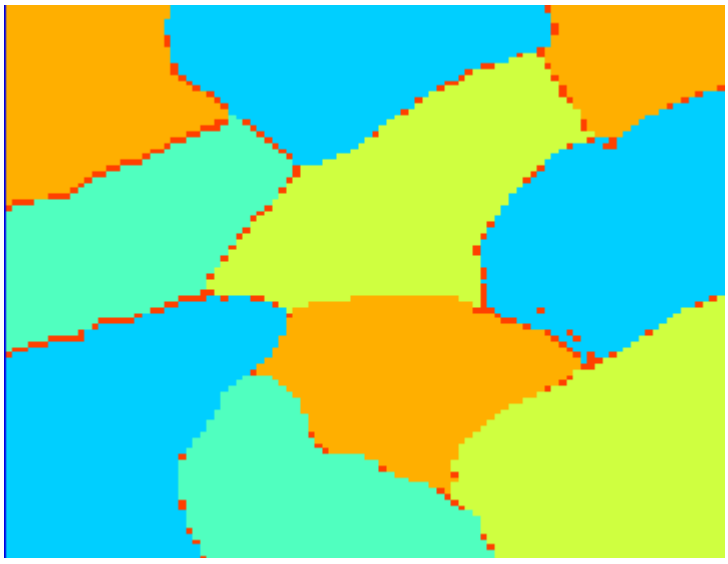

Figure 4.4
Validation of the filtered back-projection algorithm. The grain segments in one layer of the original map – the input to the simulation – are shown in arbitrary colours. The simulated map was based on interpolation: each voxel was associated with the grain exhibiting the highest reconstructed density at that position. The red points are those where there is a difference between the original and the interpolated map. From [A5].

In addition, the influence of the number of reflections is investigated. It is found that ~30 reflections are needed to avoid deterioration of the map. It is interesting to compare this number to the corresponding number of 5 found in section 4.1 for the

ART case. The difference is likely to be related to the fact that FBP cannot take the additional density constraint into account, cf. also the discussion in connection with Fig 4.1.

The FBP algorithm has yet to be tested on 3DXRD experimental data.

4.3 The general 6D case

To facilitate reconstructions for the general case, it was necessary first to develop a suitable mathematical framework. This is done in [A6], where the 6D lattice space is represented as the product of direct space and orientation space, parameterised by Rodrigues' vectors. The geometry of the lattice space and the corresponding 3DXRD projection surfaces are deduced. The projection surface comprises all the points in the 6D space that can give rise to diffracted intensity impinging on a given pixel in the detector at given sample and detector settings.

The geometric analysis shows that the task of reconstructing the 6D lattice space from 3DXRD data is considerably more complex than traditional reconstructions, as used in medical applications. There are several reasons for this:

- Conventionally, reconstruction space is often identical to direct space, which obviously is 3D. Introducing a 6D space makes discretization an issue. To represent orientation elements of a size of $(0.5 \text{ deg})^3$ over 100x100x10 positions in a sample requires a set of $\sim 10^{11}$ 6D-voxels. Fortunately, the vast majority of this space will in most cases be empty, a fact which should be used in the analysis. The problem is then how to represent and incorporate such topological information.
- The dimension of the projection surface is also higher than usual: 3.
- Both the lattice space and the projection surfaces are curved.
- In conventional reconstructions the number of projections through a given voxel can be determined at will by adjusting the angular step. In CT typically 360-1800 projections are used. By contrast, in diffraction, the number and directions of the projections giving rise to non-zero intensities is given by the crystallography of the system. In practice only 10-50 projections may be of sufficient quality.

Based on this geometric analysis, the applicability of the two major classes of reconstruction algorithms is discussed in [A6].

The use of transform methods is found to be troublesome. The formalism can be generalized to some extent to curved and higher dimensional spaces [72,73], but the solutions are much less adaptable to numerical work. Perhaps more importantly, there is no straightforward way to incorporate additional constraints, on density, topology etc.

By contrast, it is straightforward to incorporate the geometrical complexity and the constraints into algebraic methods. Moreover, these can be extended to handle detector point-spread functions, conical slits or to incorporate absorption corrections. A specific routine, based on the *ART*-algorithm, has been developed. This includes a

strategy for how to find the vast parts of the lattice space that are void. The reconstruction is then restricted to the remaining part.

For reference, the publication [A6] includes a derivation of the geometry for a number of simplifying cases. Some of these may be solved also by transform methods, cf. section 4.2.

In passing it is noted, that the 6D lattice space introduced may be of relevance also for modelling. When simulating macroscopic dynamics, the spatial resolution in the simulation will typically not be sufficient to characterize the smallest individual elements in the microstructure. In such cases, each discretization element in the simulation, whether a voxel, nodal point or similar, will be associated with an orientation distribution.

4.4 Conclusions and outlook.

- Reconstructions are clearly feasible in simplified geometries.
- Reconstructions of the full 6D lattice space – with or without overlap of diffraction spots - is mathematically more complex than CT and PET reconstructions. In the most general case it is currently un-solvable. However, the structural organisation inherent in typical microstructures implies that the information content in 3DXRD and CT data to a rough approximation are similar. In view of the success of CT, this is reassuring. A conclusion on this prospect must await the outcome of experimental tests.
- The iterative *ART* routine is an ideal reconstruction tool for 3DXRD. It can handle the complex geometry and full use can be made of simplifications in the set-up or other additional constraints. Hence, plans are presently pursued to generate an *ART*-based program for general-purpose 3DXRD type reconstructions. The program will be developed in collaboration with the group of Herman, who established the *ART* routine and has produced much of the methodology behind medical scanners.
- The spatial resolution is presently limited by the detector's characteristics. For best results, the point-spread function and the heterogeneity in the response of the detector must be known to a high accuracy.
- Further progress is likely to require work in applied mathematics. In particular for the general case, additional topological criteria may be required to enable any solutions to be achieved. A suitable criterion could be that the microstructural elements were as few and as perfect as possible, given the constraint by data. Relevant tools might arise from the emerging discipline of "discrete tomography" [74].

5. The 3DXRD Microscope

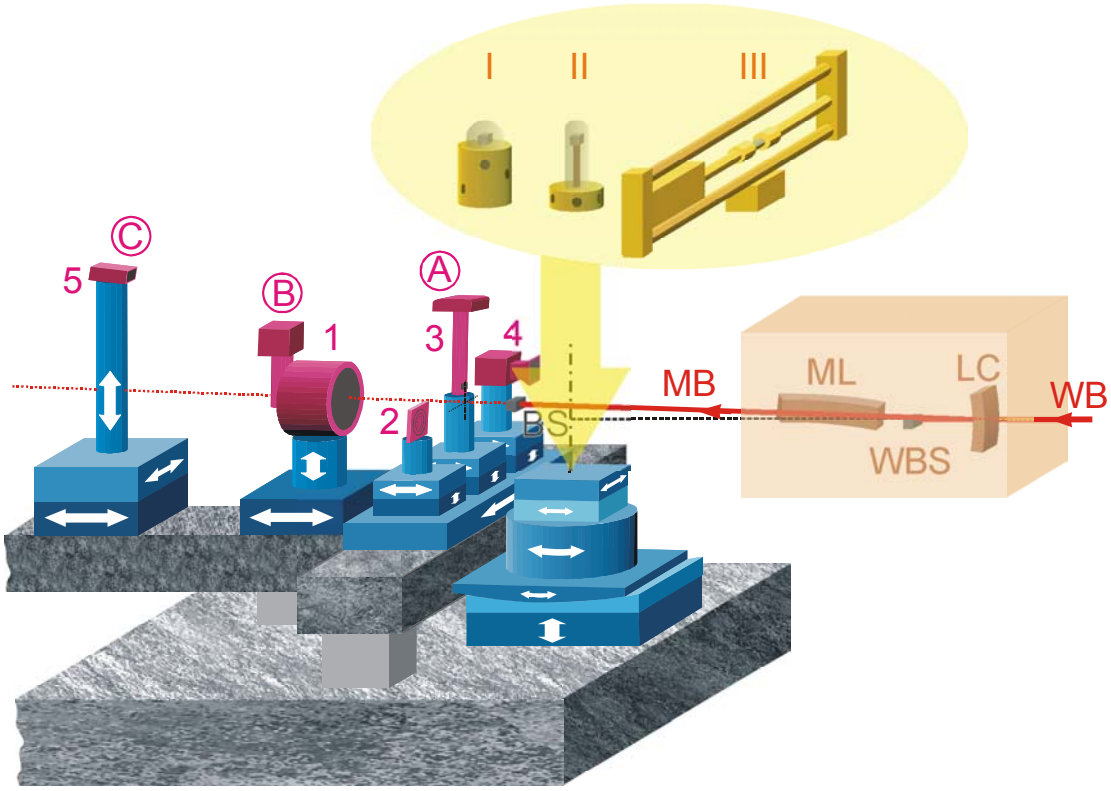

Figure 5.1
Layout of the 3DXRD microscope, comprising the x-ray optics within the Pb box (orange) and the diffractometer (blue) mounted on granite blocks. The beam path for a Laue-ML optics configuration is marked in red. Abbreviations: WB: white beam, LC: Laue crystal, ML: multi-layer, WBS: white beam stop, MB: focused monochromatic beam, and BS: monochromatic beam stop. There are 3 area detectors (purple) available: a high resolution one (3) in configuration A, a low resolution, large area one (1) in configuration B and a medium resolution one (5) in configuration C. The installation of a further detector (4) with a 2 μm resolution is planned. In addition a conical slit (2) can be positioned close to the specimen. Sample auxiliaries (yellow) include a cryostat (I), two furnaces (II) and a 25 kN stress rig (III). Courtesy of R.V. Martins.

The 3DXRD microscope at ESRF is installed in a separate laboratory, the 2nd experimental hutch at beamline ID11 [75,76]. The beamline is a so-called insertion device beamline equipped with an in-vacuum undulator with a minimum gap of 5 mm. The beam enters the experimental hutch through a pinhole of a fixed dimension of 1x1 mm^2. The photon flux at the point of entry is shown as a function of x-ray energy in Fig 2.4. The design of the microscope is sketched in Fig 5.1. It comprises the x-ray optics, contained within Pb shielding, and a diffractometer. Adjacent to the experimental hutch, there is a control room.

The 3DXRD microscope is dedicated to spatially-resolved studies of hard polycrystalline materials, on the meso-scopic and macroscopic scales. At this point in time it is used only for diffraction, but it is clear that complementary studies with absorption contrast tomography could be performed with a small effort (to be

discussed in chapter 6). Below an overview of the set-up is given including the main specifications. For further technical details see [A20,A37,75,76].

5.1 Optics

The design criteria for the x-ray optics have been (listed according to priority)

1. Maximum flux within a beam size, that is variable from 1 mm to as small as possible.
2. A variable energy bandpass from 0.1% to 1% and a variable divergence of the monochromatic beam, from 10^{-4} to 10^{-3} rad.
3. A long focal length, enabling the use of spacious sample environments. In practice, the distance between the monochromator and sample is chosen to be 2 m.
4. A uniform intensity profile of the beam, or at least a known and stable profile.
5. Energy-tuneable optics, such that the energy can be chosen at will.
6. Fixed exit optics, such that the sample stage and detectors do not have to be translated whenever the energy or mode of focusing is changed.

These specifications are different from those of relevance say for condensed matter physics. In particular, the angular resolution often can be relatively relaxed. Hence, by focusing in two dimensions and enhancing the band pass to 1% a flux increase of the order of 10^6 is obtained with respect to "standard optics", where the beam is monochromated by a flat, perfect Si crystal.

Based on these considerations, two types of optical elements have been constructed and optimised for hard x-ray purposes. The first is an asymmetrically cut and bent crystal of perfect Si, used in transmission mode (a Laue crystal) [77]. The second is an elliptically shaped and laterally graded multilayer (ML), used in reflection mode at a glancing angle [A20]. The ML is made of W/B_4C. Both elements provide focusing in one dimension. The optical elements and associated benders were all manufactured at ESRF.

	Energy (keV)	Focal Length	Energy bandwidth	Focal area (μm^2)	Total flux (ph/s)	Peak flux (ph/s)
Laue	50 or 80	2 m	0.06-1%	1.2 x 1000	$3\ 10^{11}$	$2\ 10^{8}$
Laue-ML	50 or 80	2; 1.4 m	0.06-1%	2 x 5	$1.5\ 10^{11}$	$1.5\ 10^{10}$
ML-ML	50-100	2; 1.4 m	1%	5 x 5	$1.5\ 10^{12}$ *	$6\ 10^{10}$ *
Double mono	< 100	∞	0.01%	-	$1.7\ 10^{11}$ **	$2\ 10^{5}$

Table 5.1
Pertinent features of the 4 optical configurations in use with the 3DXRD microscope. The focal area is defined by the product of the FWHM of the intensity distribution of the beam in the vertical and horizontal directions at the focal point. The numbers for flux are for 50 keV. The peak flux is defined here as the number of photons per second that impinges on the central 1x1 μm^2 area within the focal spot - it is equal to the total flux divided by the area of the focal spot. (*) These numbers are estimates. (**) For the maximum area of 1000 x 1000 μm^2.

To adhere to the wish for 3 types of incident beam (see section 3.1) the Laue crystal and ML devices are combined into 3 standard optic configurations. The main specifications of the three are listed in Table 5.1. For a *line beam*, the Laue crystal is used alone. For a *pencil beam* there are two options. Either two MLs are combined in the so-called Kirkpatrick-Baez configuration [78] or one Laue crystal is combined with one ML. In both cases the two devices focus in orthogonal directions (vertical vs. horizontal). The minimal focal spot size obtainable is approximately the same, but the flux is higher in the ML-ML mode. However, so far the Laue-ML combination has been used almost exclusively, due to its flexibility in terms of energy bandwidth and beam divergence. For a *box beam* the same configurations are used as for the pencil beam, but the sample is placed off the focal point and the devices are slightly defocused in order to obtain an incident beam on the sample of the required dimensions.

Unfortunately, the 3 optics configurations all fail to some extent with respect to the 3 design criteria at the bottom of the list. The Laue crystal is only energy tuneable within ~10%. Hence, to cover most of the relevant energy range, the configurations have been duplicated for set-ups with nominal energies of 50 keV and 80 keV. Moreover, none of the configurations provides a fixed-exit beam. Hence, shifts in the optics configuration or x-ray energy are time-demanding procedures, requiring several hours of beamtime for alignment. Another issue is the profile of the resulting monochromatic beam, which exhibits Lorentzian-type tails. These must be cut off by absorbing slits to avoid “ghost peaks” arising from parts of the specimen considered outside the volume-of-interest.

Experience has shown that the list of priorities is not universal. In some cases photon flux is not the limiting factor, while uniformity or speed of operation is. Therefore, as a supplement, in January 2003 a fourth configuration was implemented, also listed in Table 5.1. In this case none of the broadband elements are used. Instead the monochromatic beam is generated by a conventional double bounce monochromator comprising two flat, perfect Si crystals. The flux is orders of magnitude lower, but this fourth configuration is fully energy tuneable and it provides a fixed-exit beam with a very uniform and easily adjustable profile together with very little set-up time.

Two schemes for providing a *broadband,* fixed exit, energy-tuneable monochromatic beam have been demonstrated by Lienert and co-workers [A20,A40]. The first is based on combining meridionally bent Laue and Bragg crystals [79,A20]. The second is based on a non-dispersive setting with either two bent Laue crystals or two SiGe gradient crystals [A40]. While of considerable interest these schemes have yet to be implemented on the 3DXRD instrument.

Work along similar lines has been implemented at APS by Shastri *et al.* [80]. As an alternative it has been suggested to use refractive lenses for focusing [22,23]. However, so far the flux obtained with these lenses with hard x-rays have been insufficient. A detailed comparison of the various focusing schemes is beyond the scope of this thesis.

5.2 Diffractometer

The diffractometer comprises a sample stage and two arms for the positioning of conical slits and 2D detectors. The two arms are placed transverse and parallel to the monochromatic beam, see Fig 5.1. In addition a variable slit and a shutter for the 2D detectors are placed between the Pb box and the specimen.

The sample stage is designed to carry weights up to 200 kg. From the bottom to the top it contains an x-y translation system - used only for alignment and not shown in Fig 5.1 - a z-translation, a tilt, the ω rotation table and an x-y table, upon which the specimen is fixed. The tilt serves to position the rotation axis perpendicular to the monochromatic beam, which is offset from the horizontal plane by $2\theta_m$, the Bragg angle of the monochromator. To avoid the wobble of the rotation axis associated with conventional rotation stages, a friction-less stage from the company PRECITECH, previously used in metrology, has been converted for use on the 3DXRD microscope. As a result the positioning accuracy and reproducibility of the entire set-up from the z-translation and up is 1-2 μm.

To ensure a fast and uniform sampling of diffraction space, two oscillation routines have been developed. They both serve to clock the opening and closing of a shutter, such that exposures are made during exactly the period, where the specimen is rotated from $\omega_0 - \Delta\omega/2$ to $\omega_0 + \Delta\omega/2$, where ω_0 is some nominal setting of ω. The routines differ in the way an ω-scan is performed. In the "step-scan" mode ω_0 is incremented in steps, and for each nominal value the rotation table is first rotated backwards past $\omega_0 - \Delta\omega/2$, then rotated through the interval of $\Delta\omega$ by the requested rotation velocity. In the "sweep-scan" mode, a set of exposures is made while ω is continuously rotated through the full range of interest. This leaves some "holes", corresponding to the periods where images are read out. These are "filled out" during a second sweep. The frequency of exposure obtainable in the two modes is 1 image per 3 second and 4 images per second, respectively.

The transverse arm is used for positioning items that need to be close to the specimen. A conical slit, a high-resolution detector and beam diagnostics tools are permanently mounted on three independent (x, y, z)-stages. The three stages are fixed on a translation table, moving along the arm, allowing fast swaps between the set-ups. Furthermore, tracking is facilitated by a combined movement of the x- and z-stages mounted below the high-resolution detector. (The z-movement is needed to match the $2\theta_m$ offset of the monochromatic beam.)

The parallel arm is used to position items at a distance of 0.4 –3 m to the specimen, such as 2D detectors in configurations B and C. The arm can be rotated around the ω rotation axis, up to an angle of 10 degrees from the direction of the incident beam (not shown in Fig 5.1).

The conical slit predominantly used is made of WC and is 2 mm thick. It contains 6 conically shaped openings, placed in accordance with the {111}, {200}, {220}, {222}, {331} and {422} reflections of an fcc lattice. The gaps are all 20 μm, while the maximum deviations from the ideal geometry – due to manufacturing and alignment errors - are estimated to be 5 μm. The slit system is to be placed 100 mm

from the rotation axis, and is specified for use at 55.00 keV and 62.62 keV for pure Al and pure Cu, respectively.

The specifications for the three area detectors available are summarised in Table 5.2. The detectors are all CCDs coupled to fluorescence screens by either lenses (Quantix and Medoptics detectors) [81] or an image intensifier (FRELON) [82].

	Detector confi-guration	Chip (nr of pixels)	Width of psf (μm)	Active area (mm^2)	Dyn. range (bits)	Readout time (sec)
Quantix	A	1536 x 1024	6	3.5 x 2.4	12	2.5
FRELON	B	1024 x 1024	200-300	128 x 128 - 230 x 230	14	0.2
Medoptics	C	954 x 932	~ 50	45.8 x 44.7	14	0.5

Table 5.2
Pertinent features of the three area detectors in use with the 3DXRD microscope. Numbers for the point-spread-function (psf) of the detectors refer to the FWHM. The FRELON detector can be zoomed in and out within the range listed. This detector also exists in a 2048x2048 pixel configuration.

Sample auxiliaries include a regular furnace and a purpose-build μ-furnace, which can operate up to 1300 ^{o}C and 700 ^{o}C, respectively. In the μ-furnace only an evacuated glass capillary surrounds the specimen. Hence, depending on specimen size, the distance from the rotation axis to a high-resolution detector can be kept below or at 5 mm. Both furnaces can be operated in a controlled atmosphere. For studies of deformation, a specially designed 25 kN Instron tensile machine is available. For cryogenic studies a displex cryostat is available.

The temperature in the experimental hutch is controlled within 0.1 degree, to avoid drifts due to thermal expansion. With this regulation, the typical drift of beam position versus sample position is measured to be less than 5 μm over 24 hours.

The motors, detectors and auxiliaries are all controlled *via* device-servers. Presently these device servers are being incorporated into a general software framework, FABLE. Once completed, FABLE will enable automatic data acquisition, calibration, reduction and initial analysis, including indexing by *GRAINDEX*. This will speed up the data analysis phase substantially and will enable on-line feedback on the quality of data and data-taking strategies.

6. Combining 3DXRD and absorption contrast tomography

The 3DXRD set-up sketched in Fig 3.1 is very similar to the set-up typically used for absorption contrast x-ray tomography at synchrotrons. Furthermore it appears that the specifications of the two methods in terms of space and time resolution are not that different, see Table 6.1. Hence, combined studies can be envisioned. With suitable detector combinations one may even probe the same specimen with both techniques simultaneously.

	Tomography	3DXRD
Spatial resolution	1[a] - 3[b] μm	5 μm
Resolving power	0.5[a] - 3[b] μm	0.2 μm
Time resolution	3 min[b] – 30 min[a]	1 sec – 1 h

Table 6.1
Comparison of state-of-the-art specifications for x-ray tomography and 3DXRD, assuming favourable conditions in both cases. For tomography, numbers are given for 20 keV at the ID19 beamline at ESRF (a) as well as for 100 keV x-rays at the ID15 beamline at ESRF (b).

This combination is most interesting as diffraction and tomography utilise different contrast mechanisms. While 3DXRD is sensitive to variations in phase, orientation and elastic strain of crystalline materials, tomography is sensitive to density variations, independent of whether the material is crystalline or not.

On the macroscopic scale, several synchrotron experiments have been performed which combine tomography and diffraction. These have typically required the subsequent use of two different set-ups. Prominent examples are the work by Preuss and co-workers on fragmentation of SiC fibres in a Ti-6Al-4V matrix [83], and by Stock on a range of topics including sea urchin teeth [84,85].

To the knowledge of the author the only combined study on the grain level is the work on wetting of Al by Ga [A41]. This work, which was performed in collaboration with W. Ludwig and D. Bellet, is summarised in section 6.1 below.

Next, in section 6.2, a unique method is presented for characterising the three-dimensional *plastic* strain field within mm^3-sized specimens. Developed in collaboration with F. Beckmann at HASYLAB, the basic idea is to determine the positions of dispersed marker particles by absorption contrast tomography. Doing this *in-situ* as a function of the external strain the displacement of the individual markers are determined. The method is applicable to a broad range of materials and deformation modes. The main use of the method is likely to be in connection with characterisation on the macroscopic scale for studies of crack propagation. However, it also serves as a very valuable additional tool to the 3D "toolbox" for meso-scopic x-ray studies.

In section 6.3 potential applications of a combined analysis are outlined.

6.1 A study of wetting

When an Al polycrystal is brought into contact with liquid Ga, the Ga will penetrate the specimen along the grain boundaries [86,87]. This is a precursor process triggering liquid metal embrittlement and is a relatively poorly understood phenomena, because of the complex interplay between the capillary forces driving the penetration, the grain boundary characteristics and the induced strain (the thickness of the Ga layer is of order 1 μm). Due to embrittlement and the true 3D nature of the process it is difficult to characterise by electron microscopy.

A combined 3DXRD and x-ray tomography study was performed using the beamlines ID11 and ID19 at ESRF, respectively [A41]. The cylindrical specimen had a diameter of 800 μm and a height of 1 mm. It was mapped at 41 equidistant layers by 3DXRD and reconstructed by the simple back-projection method outlined in section 3.3.1.

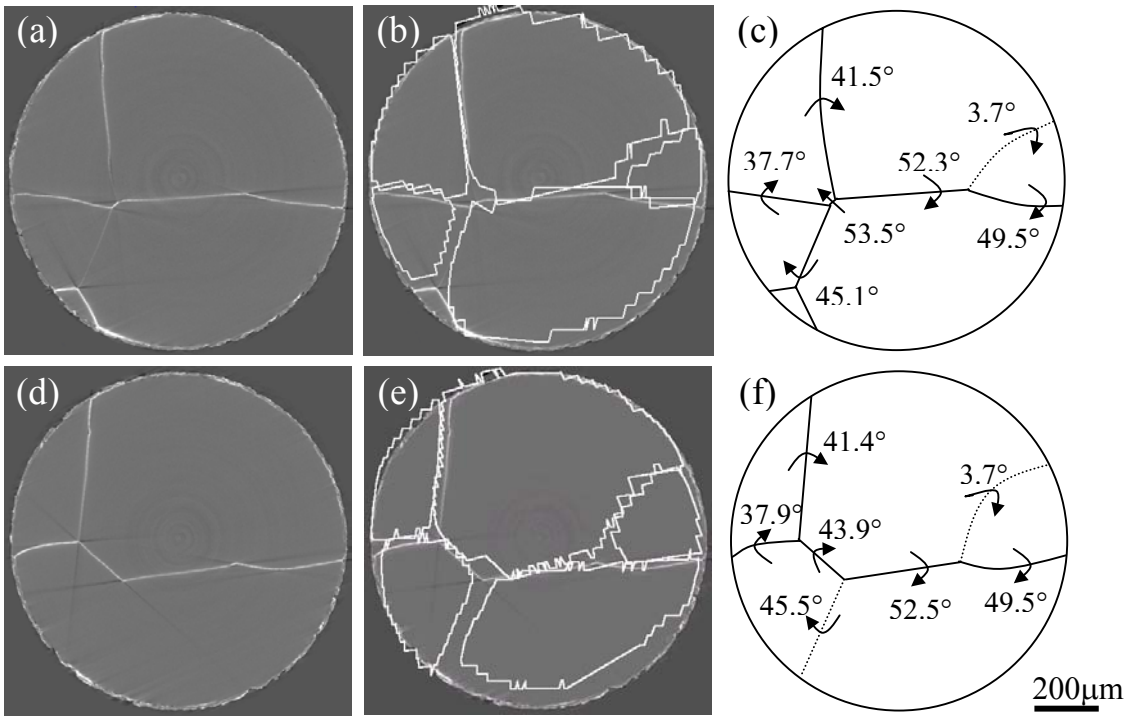

Figure 6.1.
Two layers 100 μm apart through a cylindrical Al sample, which had been wetted by liquid Ga. The two layers are reconstructed tomographically in (a) and (d) where the grey lines correspond to the position of the Ga. The white superimposed lines in (b) and (e) correspond to the grain boundaries determined with 3DXRD. (c) and (f) are schematic illustrations of the grain boundaries determined by both techniques (full lines) and only by 3DXRD (dotted lines). The calculated misorientations between neighbouring grains are written on the boundaries. From [A41].

Images of two layers perpendicular to the cylindrical axis and near the centre in terms of height are presented in Fig. 6.1. The 3DXRD technique detects all the grain boundaries while the tomographic images only shows those boundaries decorated with Ga. Furthermore the 3DXRD data enables the misorientations between neighbouring grains to be calculated. These are listed in the schematic representations

of the grain boundaries determined for the two layers in Figs. 6.1(c) and 6.1(f). Likewise grain boundary planes may be determined. Hence, thanks to the combination of methods the wetting behaviour can be directly correlated to the grain boundary characteristics. (As an example, in the layers shown in Fig 6.1 there are two non-decorated boundaries. One of them is the only low-angle boundary, the other is wetted in one layer but not in the other.)

It has been suggested that tomography and decoration with Ga is used as a general tool for mapping grain boundaries in Al [88]. Evidently the spatial resolution is better with tomography than with 3DXRD – this is particularly true for the example of early work reproduced in Fig 6.1. However, decoration has the drawback of being a destructive process and also the penetration is not complete. Hence, at Risø work has focused on improving the spatial resolution of the diffraction method.

6.2 Plastic strain

As metals predominantly deform plastically, and the local deformation in most cases is heterogeneous, it is of obvious interest to characterise the spatial variations of the plastic strain as function of external strain. This is true on the macroscopic scale, where the heterogeneity is a function of the geometry of the specimen and the mode of deformation. It is also true on the meso-scale, where grain orientations, inclusions and cracks may influence the field.

The most relevant object to characterise is the field of the displacement gradient tensor, $\mathbf{e}$. This tensor is typically seen as the sum of two tensors, a symmetric, $\boldsymbol{\varepsilon}$, and an anti-symmetric one, $\boldsymbol{\omega}$. $\boldsymbol{\omega}$ is the rigid body rotation tensor, characterising the local rotation of the crystallographic lattice. $\boldsymbol{\varepsilon}$ is the plastic strain tensor, comprising 6 independent elements, 3 axial strains and 3 shear strains, corresponding to the diagonal and off-diagonal elements of the tensor, respectively. It should be emphasised that both $\boldsymbol{\omega}$ and $\boldsymbol{\varepsilon}$ are of interest for modelling.

To measure the field of the displacement gradient, it is sufficient to monitor the positions of a (large) set of approximately homogeneously dispersed reference points as a function of external strain. This has been done rather extensively in two dimensions using *e.g.* scratches, etched patterns or grids deposited on the surface as the reference points [89-91]. In three dimensions relatively little has been done. Wire or grid markers have in some cases been inserted as markers, but the scale of the markers was rather coarse – upwards of 100 μm – and the inspection destructive [92].

In [A7] a rather universal method is presented for characterising the displacement gradient in 3D by means of embedded markers and absorption contrast tomography. The CMS positions of the markers serve as the reference points. The markers are small rigid objects with sufficient density contrast to be observable with x-ray tomography. These may already be present in the material of interest as inclusions. Alternatively, marker particles may be added to the material during processing. In the latter case the size, dispersion and hardness of the markers can be optimised as a compromise between the spatial resolution of the method and the wish for a negligible interference from the markers on the plastic properties of the matrix.

The suggested analysis procedure is as follows: at each strain level the density distribution is reconstructed by existing programs, based *e.g.* on the FBP algorithm [27]. Markers are identified from the reconstruction by setting a density threshold and applying additional criteria on connectivity. Next, the identified markers in reconstructions, taken at subsequent strain levels, are paired based on their relative position and size. Repeating this procedure through all strain levels, the particle displacements are found as function of external strain. The local displacement gradient tensor is then obtained at the position of each particle by a least square fit using the relative displacements of the 8 nearest neighbours as input to the fit. Finally, for visualisation, each **e**-component is interpolated on a regular 3D grid. The result is nine 3D maps, one for each of the components.

This methodology is demonstrated in [A7] on a model system of Al with W particles. The experiment was performed at beamline BW2 at HASYLAB using 24 keV x-rays. The particle trajectories for ~2500 markers were determined while the specimen was uni-axially compressed by 9.5%. For illustration, data for the central part of the specimen is reproduced in Fig 6.2.

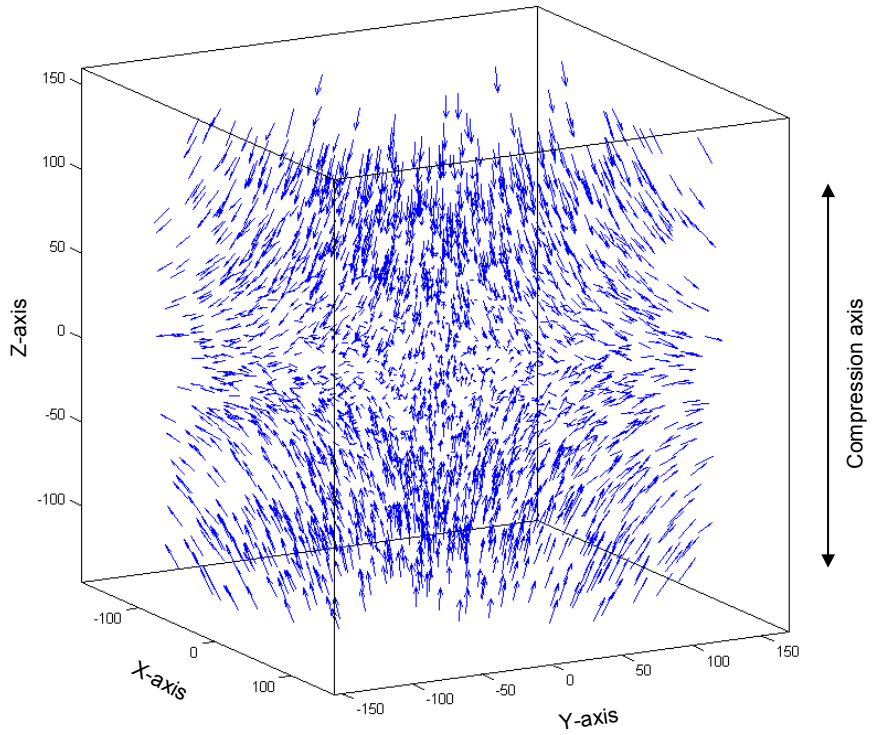

Figure 6.2
Map of particle displacements for compressive deformation from 0% to 9.5%. The axes refer to pixel units, with a pixel size of 1.5 μm. From [A7].

The results are encouraging. Firstly, it is found that the accuracy on determining the shifts in the particle positions is 0.3 μm, to be contrasted with a detector pixel size of 1.5 μm and a spatial resolution of 2.8 μm. (These numbers reflect the fact that the centre position of a distribution often can be determined to an accuracy that is much

better than the width of the distribution.) With a grid size of 30 μm in the final 3D maps of the components of **e**, this implies a strain resolution of 1%, which generally speaking is sufficient. Secondly, the volume fraction of the particles is 1%. As discussed at length in the article, this is sufficient that the Al/W alloy for many applications can be viewed as a good model system for characterisation of Al.

The method is broadly applicable. It may be used with non-crystalline as well as crystalline specimens. It is compatible with large strains, as long as the specimen is characterised at a sufficient number of intermediate steps and the morphology of each marker is fixed. Further, it can be applied to most conventional deformation processes, including rolling, drawing and extrusion, by placing the deformation tool either on or close to the instrument.

The main limitation is the need for identification of a suitable type of marker and for optimisation of the associated processing route. However, with a new generation of detectors it seems realistic to obtain a resolution power of the order of 500 nm. This is in the range where the precipitates found in many commercial-purity metals could be used directly as internal markers.

Hence, in the view of the author the method could find broad applications in engineering. The results are directly comparable to Finite Element Model simulations and may as such be used for tests of these as well as for optimisation of various materials' parameters in the code.

Potential applications on the meso-scale and the prospect of combining such studies with 3DXRD will be dealt with in section 7.1.

6.3 Outlook

The idea of a combined analysis can be taken one step further, namely to a simultaneous reconstruction. As a first step this may involve the 3DXRD reconstruction being used to constrain the tomographic analysis or *vice versa*. However, ultimately the vision must be to refine the structure once and for all based on all available experimental data. From the discussion in chapter 4, it appears that such reconstruction programs can be made, as the 3DXRD and absorption contrast tomography reconstruction algorithms are rooted in the same mathematical formalism.

The possible applications of a combined analysis – with or without simultaneous reconstruction - are numerous. To list some of the prospects:

- Fundamental issues within fatigue and damage control could be addressed directly for the first time by *in-situ* studies. In particular, it would be possible to study the interaction between propagating voids or cracks, the associated elastic strain fields and the grain or dislocation structures in the material.

- Tomography provides information exclusively on the density. In some cases it is not possible to infer the phase from the density alone, in particular if the density variations are small. By contrast, 3DXRD allows for the structural

refinement of the individual constituents, cf. section 7.7, but may not have the spatial resolution to separate these. With a combined analysis, both the position and phase can be derived. This seems particularly interesting for studies of phase transformations.

- As shown in Table 6.1, the time resolution obtainable with 3DXRD can be much better than what is possible with tomography. At first glance this may seem counter-intuitive, as the flux available for tomography is several orders of magnitude higher. However, in general tomography does require the acquisition of a full tomogram with say 360-720 ω positions. By contrast, 3DXRD growth curves of the type introduced in section 3.6 rely on a single ω position. Hence, the following strategy may be optimal for *in-situ* growth studies. Prior to the processing, the specimen is studied by tomography and 3DXRD for mapping and for identifying objects of particular interest. The dynamics of these objects are then followed by 3DXRD methods.

- With a combined method, absorption and extinction corrections are facilitated to a degree that is impossible with only one of the techniques at hand. The relevant absorption data is a direct output of the tomographic part, while the 3DXRD maps can be used to generate a model of the extinction.

- Specimen alignment of the 3DXRD microscope is not a trivial issue as diffraction space is 6-dimensional. By contrast, tomography only probes a 3D space, and allows for alignment errors to be corrected in the course of analysis. Hence, tomography can be used for alignment of the 3DXRD microscope.

7. Applications

7.1 Polycrystalline deformation

An understanding of polycrystalline deformation is essential for science and industry, in order to predict texture and flow-stress development in metals and alloys [61,93]. In geo-science models are used reversably to determine which geological processes gave rise to the observed textures in minerals and rocks.

During plastic deformation a polycrystal changes its shape. The external force produces line defects in the lattice - dislocations. The dislocations move in certain directions (slip directions) within certain planes (slip planes), causing the two sides of the plane to slide with respect to each other. As a result of the movement of millions of dislocations each grain changes its shape. The dynamics of the grains are coupled, as the two sides of any grain boundary at all times must adjoin and be in stress equilibrium. To facilitate this, the grains have to change shapes in different ways and their average crystallographic orientations must rotate with respect to each other.

The relevant combinations of directions and planes – the slip systems – are normally the closest packed ones. In fcc systems there are 12 of these. The aim of polycrystalline deformation models is to predict the activity on each of these as a function of external strain and based on that to derive macroscopic properties such as texture. However, despite 70 years of effort, there is no consensus on how to approach the modelling. This is a reflection of the fact that the task is a many-body problem, which furthermore involves several length scales. In particular, it is debated to what extent the deformation behaviour is determined by:

- the initial orientation of the grain
- the interaction with the neighbours
- the emerging dislocation structures, cf. Fig 1.1

In the early, “classical”, models by Sachs and Taylor each grain is modelled as an entity with no internal structure. Furthermore, the specific stress and strain boundary conditions at the grain boundaries are not taken into account. Specifically, in the Taylor model [94] the grains are all subject to the same strain, while in the Sachs model [95] only one slip system is active. In the later self-consistent models the grains are still entities but are now treated as inclusions in a homogeneous – but possibly anisotropic - matrix, where the properties of the matrix are those of the grain assembly on average [96,97].

Within the last decade, computers have become sufficiently powerful that the problem can be tackled by Finite Element Modelling (FEM) [98]. With such simulations the interaction of neighbouring grains is taken into account and one can simulate the possible “break-up” of a grain into a number of sub-grains. However, the computer power is not sufficient to include the effect of the emerging dislocation structures.

Within the last two decades the dislocation structures have been characterised in detail by TEM [99-101] revealing a rich variety of structures. The occurrences of these are correlated to the orientation of the grain [102-103]. Hence, models for the relationship

between assumed active slip systems and dislocation structures have been derived [104]. Such models neglect possible effects from grain interaction.

7.1.1 The 3D toolbox

The 3D methods presented in chapters 3, 4 and 6 can be used in numerous ways to explore plastic deformation on the grain and sub-grain scale. The slip operations cannot be probed directly, but they can be inferred from the displacement gradient tensor, **e**. One may differentiate between methods, where results are obtained for the average properties of each grain, and methods where the grains are discretized into sub-volumes. Initially the average methods are explored.

The most direct way to derive the average displacement gradient tensor, $\langle \mathbf{e} \rangle$, for a given grain is to measure the shape change by 3D mapping before and after deformation. The shape change can be seen as composed of the effect of $\langle \mathbf{e} \rangle$, acting homogenously on all parts of the grain, together with effects from local fluctuations. A general-purpose routine can be based on simulation. For a given trial $\langle \mathbf{e} \rangle$ the resulting 3D grain shape is calculated based on the grain map for the initial state. Run iteratively the correspondence between the simulated and the measured shapes is optimised by a least-square fit. Unfortunately, to obtain a strain resolution of say 1% in this way, the present spatial resolution of the 3DXRD microscope is at the limit.

As an alternative, the grain volume can be projected along various directions in direct space by super-scans in y and z on a set of associated reflections (super-scans were introduced in section 3.5). For each of the resulting 1D intensity profiles the width is determined by the second moment. Then the components of the plastic strain tensor are derived from a fit to the shifts in the moments, similar to the procedure suggested in section 3.3.2 for fitting the elastic strains from the shifts of diffraction spots in the direction of 2θ. If the intensity profiles are sufficiently robust such a procedure would have the necessary resolution. However, so far no attempts have been made to measure the shape change during deformation by this technique.

As an indirect way to determine $\langle \mathbf{e} \rangle$, the average lattice strain for a number of reflections associated with the given grain may be characterised. In this way the elastic strain tensor can be derived, cf section 3.3.2 and [A3]. However, a model is required for the elastic-plastic interaction in order to extract the active slip systems from the lattice strains [105,106]. Another disadvantage is that the lattice strain saturates with increasing external load, implying that the method is primarily of interest at low strains, close to the onset of plastic deformation. First results for total strains up to 2% [A32] are summarised below.

The third and so-far most used approach is to measure the grain rotations [A8, A33, A9]. Evidently only a sub-set of the full displacement gradient tensor is determined in this way. This is not sufficient to determine the set of slip-systems directly, but theoretical prediction can of course be compared to the observations. Within the constraint of spot overlap the measurements are straightforward, as the grain rotation manifests itself in relatively large displacements of the diffraction spots in the images acquired (see Fig 2 in [A8]). Furthermore, as demonstrated below, fundamental issues can be tackled based on rotation data alone.

Turning next to methods that provide a discretization, the marker technique introduced in section 6.2 seems ideal. As demonstrated in [A7] the displacement gradient tensor is determined in an unambiguous and essentially load-independent way over mm^3-sized volumes. As a supplement the grain boundary positions and the (sub-)grain orientations need to be determined at one stage during the process. This can be done either by 3DXRD mapping in the undeformed stage or *post-mortem* by EM and serial sectioning.

As an alternative the local rotation field within grains may be determined by means of the 6D reconstruction formalism introduced in chapter 4. The spatial resolution ought to be better than for the marker method, but it is as yet unknown to what total strains such a method is applicable.

For completeness, it is noted that complementary data on the 3D distribution of lattice strain within each grain cannot be obtained by the methods of chapters 3,4 and 6. For this purpose a scanning approach is needed. Larson and co-workers have demonstrated the feasibility of such measurements by applying a knife-edge procedure [3]. However, independent of instrumental method, the extent to which such data can be understood in terms of existing deformation models remains uncertain.

7.1.2 Summary of experiments

The experiments performed so far have focused on the effect of grain interaction and the degree of correlation between deformation behaviour and initial orientation. As discussed above, it is necessary to settle these issues in order to clarify what class of models are relevant. At this stage three publications have appeared with relation to grain rotation [A8, A35, A9], and one with relation to elastic strains [A32].

In the rotation publications, the rotation path of a number of deeply embedded grains have been characterised during tensile deformation up to 6-11% total strains using the 3DXRD microscope. The essential experimental parameters of the three studies are summarised in Table 7.1.

Material	Sample thickness	Grain size	# grains studied	Max strain
99.996% pure Al [A8]	3 mm	300 µm	4	11%
99 % pure Cu [A35]	2 mm	35 µm	8	6%
99.6% pure Al [A9]	4 mm	75 µm	95	6%

Table 7.1.
Comparison of parameters for the three 3DXRD experiments published so far with relation to grain rotation.

Technically, the main difference between the three studies is that a conical slit was added to the set-up for the latter two experiments on Cu and 99.6% pure Al. This reduced the problem of spot overlap, but introduced the new potential problem that the grains characterised are not fully illuminated by the beam any more. A number of experimentally-supported arguments on the point that the sub-volume actually probed is representative of the full grain are given in [A9].

First results are reported in [A8]. The rotation paths of 4 grains were followed during loading. None of these followed the predictions from the classical models. Furthermore, the spread of the emerging orientation distribution within a grain was found to be substantially smaller than the grain rotation on average. However, this result was based on analysis of a single grain, so it may be questioned as to what extent this represents the typical behaviour.

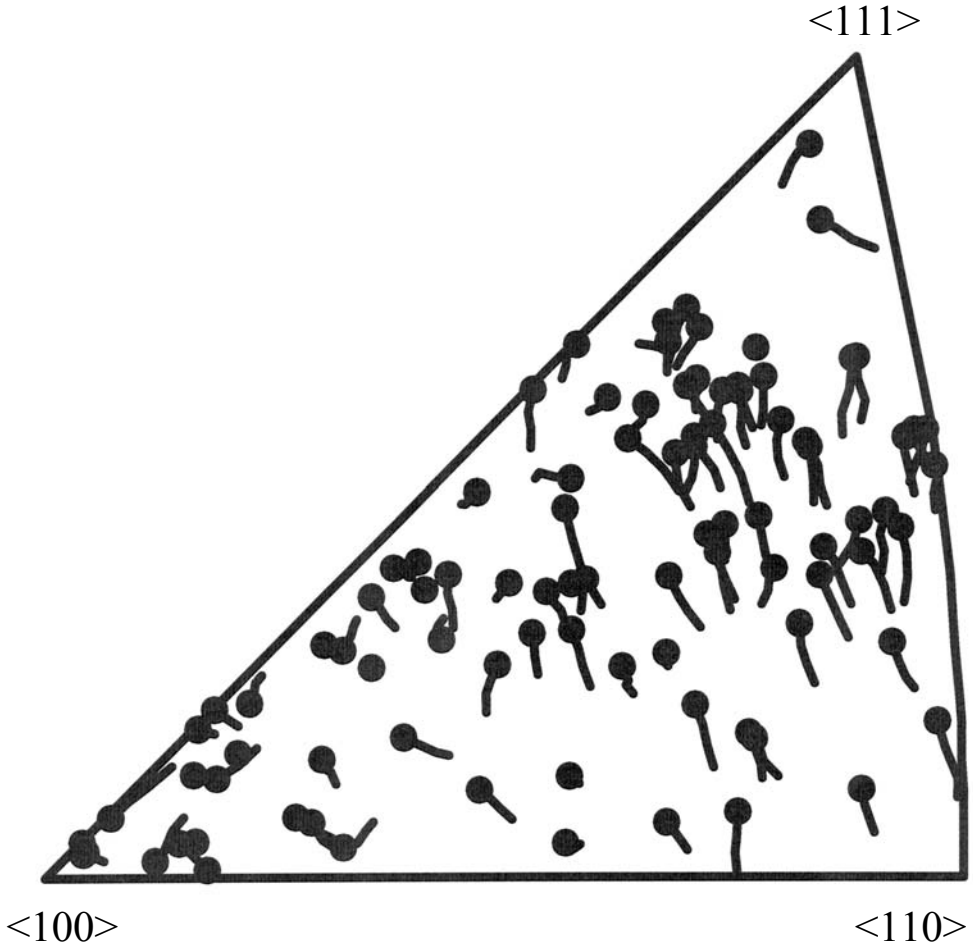

Figure 7.1
The rotation of the tensile axis of each of the 95 embedded grains expressed in a stereographic triangle. The curves are the observed paths for the average orientation of each grain during tensile deformation from 0% to 6%. The final orientation of the axis is marked with a filled circle. From [A9].

Next, the results for [A9] are summarised. In this study, the rotation paths for 95 grains were determined. The resulting rotations of the tensile axis are plotted in the standard stereographic triangle in Fig 7.1. (This so-called inverse pole figure shows for each grain where the tensile axis is oriented with respect to the <100>, <110> and <111> axes of the grain [61].) From this figure and a similar plot of the rotation around the tensile axis (Fig 5 in [A9]), the following observations are made:

- In the right hand part of the triangle, grains with almost identical initial orientation display in most cases nearly parallel rotation paths. As the grains in such a set will have different neighbour configurations, this indicates that the

effect of grain interaction is relatively small. However, there are also a few examples of grains with similar initial orientation exhibiting distinctly different rotation paths. In the left part of Fig 7.1 the rotations are more stochastic in nature.

- There is a clear correlation between rotation path and initial orientation. In a following article, based primarily on work by G. Winther, this observation is elaborated further [A42]. It is demonstrated that the triangle can be divided into 4 regions, exhibiting distinctly different rotation behaviour. It is further shown that neither the classical nor the self-consistent models make a satisfying prediction of the rotation field over the whole triangle.

The orientation spread is also characterised. Unfortunately, the use of a conical slit implies that a given grain is illuminated in different parts at different ω settings. This prohibits the generation of a grain ODF. Instead the characterisation is based on an analysis of the individual spots. It is found that:

- All grains rotate and exhibit broadened diffraction spots. Hence, all grains are subject to plastic deformation.
- Averaged over many grains, the rotation of the tensile axis and the FWHM of the internal orientation spread are 2.0 degrees and 0.8 degrees, respectively, at 6% strain. These numbers confirm the observation from [A8] that the orientation spread is not dominating in comparison to the average rotation of a grain.

To test whether these conclusions also apply at higher strains, the experiment has been repeated recently, applying external strains of up to 20%. The analysis is in progress.

The first application of lattice strains for studies of polycrystalline deformation was performed on Cu [A32]. This experiment focused specifically on the effect of grain interaction. Advantage was made of the inherent axial symmetry around the tensile axis during tensile deformation. Lattice strains were determined for a set of individual reflections, which all happen to have had the scattering vector parallel to the axis. The advantage of this geometry is that the classical and self-consistent models will predict all grains to exhibit the same lattice strain while FEM simulations will not.

As reported in [A32], measurements of 20 {440} reflections were repeated at 4 loads through the elastic-plastic transition up to a total strain of 2%. The results are shown in Fig 7.2. The standard deviation on the spread in lattice strain is found to be $\Delta\varepsilon$ = 24, 34, 36 and 33 μ-strain at the 4 load levels of 0.012%, 0.2%, 0.73% and 2%, respectively. These numbers constitute upper limits on the spread induced by grain interaction, as potential experimental errors all will tend to increase the spread.

FEM simulations of the same material are not available. However, based on comparison with simulations on a number of other materials [107,108] it is inferred that the experimental data is at odds with simulations in two ways. Firstly, the spread is substantially smaller than predicted. Secondly, within experimental uncertainty $\Delta\varepsilon$ is constant above the plastic transition. By contrast the spread is monotonically increasing in the FEM simulations [109].

The preliminary conclusion is that FEM simulations of lattice strains over-emphasise the effect of grain interaction on the average deformation behaviour of the individual grains. Two explanations are suggested for this disagreement:

1. In the FEM calculations cited the grains are box-shaped with six neighbours whereas real grains are closer to the shape of tetrakaidecahedrons with 14 neighbours. It is obvious that an increased number of neighbours would reduce the calculated variations. However, this effect does neither explain the full amount of the discrepancy nor why $\Delta\varepsilon$ is constant.

2. FEM calculations do not consider the formation of deformation-induced local discontinuities like dislocation walls, which may screen the elastic strain fields associated with the interaction with the neighbours.

The results on rotation paths and elastic strain development are seen to corroborate each other and lead to the conclusion that the plastic response is not dominated by grain interaction effects, at least for small tensile strains and in the <110> corner of the triangle.

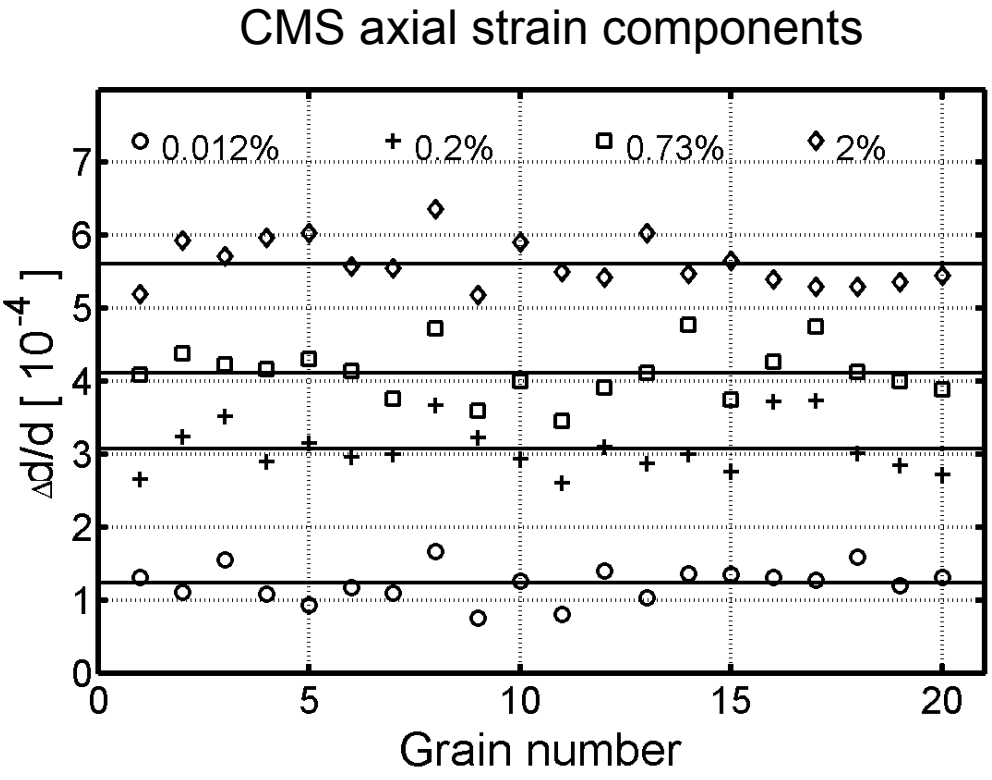

Figure 7.2
The development of elastic axial strain components of 20 individual grains within a Cu polycrystal during tensile deformation. The strains are determined based on the CMS positions of the 2θ peak profiles. The total strain loads are given in the legend. The mean elastic strains at each load are indicated by solid lines. From [A32].

7.1.3 Outlook

With the set of tools outlined in section 7.1.1 a number of outstanding issues in the field of plastic deformation and texture development can be addressed. Two examples are:

- The set of active slip systems can be deduced from the displacement gradient tensor. Hence, one can envisage *e.g.* measuring the active slip systems in a set of 100 grains. Such data would clearly enable tests of polycrystalline models in a unique and very fundamental way. Furthermore, the measurement of active slip systems as a function of load will provide the first direct experimental data on work hardening laws at the grain scale.
- A complete characterisation of the local behaviour can be obtained by applying all the tools to the same specimen. By integrating 3D grain boundary maps and plastic strain fields as determined by tomography with data sets on the lattice rotations and elastic strain developments of each grain within a volume of interest, the first truly complete reference data set would be collected on the dynamics of plastic deformation.

7.2 Recrystallization

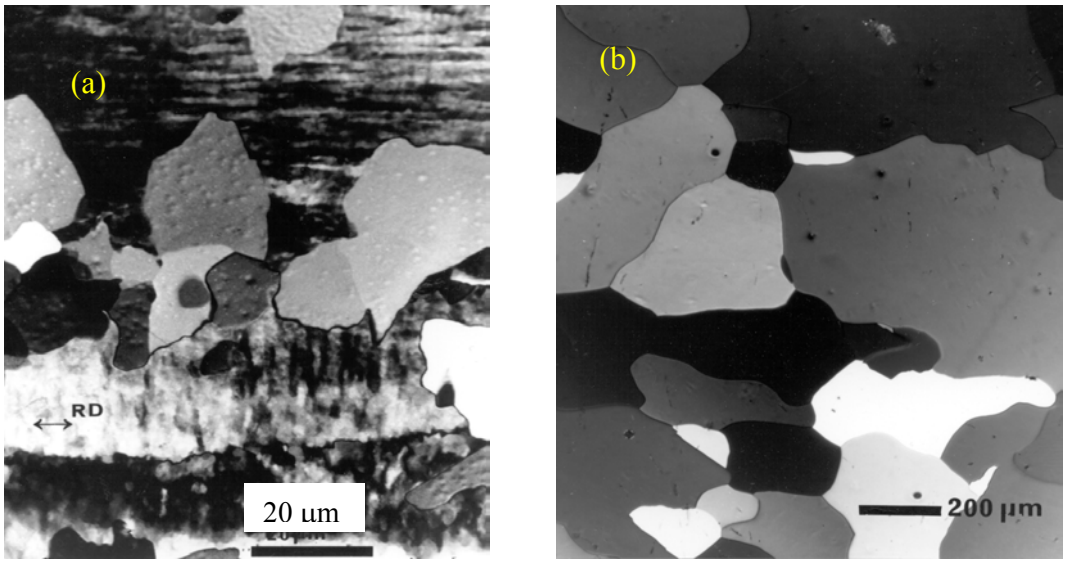

Figure 7.3
Typical metal structures appearing during recrystallization (a) and grain growth (b), as observed by traditional microscopes. In (a) the nuclei grow at the expense of the deformed material, which has a stripy appearance. In (b) there is no deformed material left. Grains coarsen by consuming each other. (The two micrographs refer to different samples).

During annealing of deformed metals and alloys the stored energy is reduced by three processes: static recovery, primary recrystallization and grain growth [110]. During recovery the dislocation structures coarsen, to be discussed in section 7.3. During

recrystallization new dislocation-free grains emerge – nucleate – and grow into the deformed microstructure by an activated migration process. The growth continues until the boundaries of the new grains – the nuclei – impinge. The third process: grain growth relates to the migration of the interface between the impinged nuclei. The driving force for the latter process is the reduction of grain boundary area. Typical microstructures appearing during recrystallization and grain growth are shown in Fig 7.3 (a) and (b), respectively.

As annealing is an integral part of most processing routes, a detailed and quantitative description of recrystallization is of much interest technologically. However, similar to deformation, the process is inherently complex. Some of the main complications are:

1. The nucleation is typically heterogeneous. This will be seen as clustering. (As an example most of the nuclei in 7.3(a) form a band across the middle of the figure. These nuclei are likely to have formed along a grain boundary in the deformed microstructure.) Furthermore there may be several competing nucleation processes with different activation energies and the nucleation events can be retarded in time due to the need for an initial rearrangement of the dislocation structure.
2. The probability of impingement of the nuclei increases with time, implying a decrease in the fraction of the grain boundary area that is free to grow into the deformed matrix. This fraction will depend on the degree of clustering and on the shape of the nuclei.
3. From single-crystal studies it is known that the mobility of the interface between the nuclei and the deformed structure depends strongly on the misorientation [111]. A similar *local* dependence may be expected also for polycrystals, implying that the boundary of a nucleus will grow in a non-uniform and anisotropic way, reflecting the heterogeneity of the deformed microstructure.
4. Concurrent with recrystallization, recovery can take place in deformed regions. As a result the driving force for growth may decrease with time.
5. Concurrent with recrystallization, grain growth can take place in regions where the nuclei have impinged. Initially, the main effect will be that the impinged grain boundaries are smoothed out, at later stages small grains may start to disappear.

This complexity has implied that no single experimental tool or model at present is able to provide a complete description.

For ease of presentation in the following a distinction is made between two principal approaches to recrystallization studies:

- A statistical approach, where both nucleation and growth are parameterised by probabilities. Examples of analytical models based on this approach are the Johnson-Mehl-Avrami-Kolmogorov (JMAK) model [112-116] and the micostructural path model [117]. Examples of numerical models are the so-called component models [118,119]. Typically these models do not take heterogeneities into account. In particular, prior to impingement all grains (of a given orientation) are assumed to grow according to the same universal curve.

Experimental input to such models is today typically provided by EBSP. The observables include L, the mean chord length, S_v, the un-impinged grain boundary area density as well as V_v, the volume fraction of recrystallised material. The latter two parameters are deduced from the maps by applying a stereological principle: the Cahn-Hagel method [120,121].

- A first-principles approach based on elucidating the dynamics of the interface between a nucleus and the deformed matrix.

  Typical examples of models are here the cellular automata [122] and the node displacement models [123]. Using a specific deformed microstructure to initiate the process, local growth rules are applied to simulate the dynamics. The experimental verification of such models has been hampered by the lack of an appropriate tool for studies of the microstructural dynamics in polycrystals.

3DXRD has the potential to overcome the limitations involved with both approaches. From an instrumental point-of-view, the statistical approach is much simpler though. In section 7.2.1 results for two "statistical" studies on recrystallization of the Aluminium AA1050 alloy are summarised. For historical reasons, these have been performed with a rather simple set-up. Nevertheless, a unique data set is obtained for a large number of grains, clearly demonstrating the gross simplification made by any model not taking heterogeneity into account. Next in section 7.2.2 an instrumental "road map" is provided to what is argued to be a complete statistical description. Finally, in section 7.2.3 the prospect for work at the first principles level is outlined.

7.2.1 Summary of experiments

Two 3DXRD studies have been performed on the recrystallization of 99.6% pure Al, annealed at 270 ^{o}C. For the first time growth curves of the individual embedded grains are determined. The first study mainly proves the principles by an analysis of growth curves from 6 grains [A10], while the second comprises a statistically-relevant analysis of 244 grains [A11].

The aims of the studies were two-fold:

1. To determine how prominent the heterogeneity is. In particular to determine the fluctuations in growth velocity between grains.

2. To determine the cause of the emergence of the so-called cube texture in the final recrystallization texture. (In metallurgy orientation space is divided into a small number of orientation classes, known by archaic names such as cube, brass, S, gosh etc.) From EM it is known that the volume fraction of the cube orientation class changes from virtually nothing to approximately 15% after annealing at 270 ^{o}C. Furthermore it is known that the cube grains on average are larger than those of other orientations. This larger mean grain size can be due to one of the following three mechanisms or a combination of them: a) earlier nucleation of the cube grains, b) higher growth rate, or c) less impingement of the cube grains. Information on b) is readily available using

the Cahn-Hagel method and EBSP, while it has proven difficult to detect the possible influence of mechanisms a) and c) with EM.

The second aim may at first sight appear rather specific. However, for a range of Al alloys, controlling the cube texture component is essential.

The set-up for the two experiments involved a 100 x 100 μm^2 box-beam and detector configuration B. With these settings, the diffracted signal consists of continuous broad arc-segments originating from the deformed matrix and sharp diffraction spots originating from the emerging new grains. The continuous arc segments were treated as a background and subtracted [124]. Apart from this additional complication, growth curves were derived as described in section 3.6; that is with periodic validation tests on whether grains grew out of or into the illuminated volume.

The ω–range was 1-2 degrees, too narrow for indexing purposes, and therefore for a complete determination of the orientations of the diffracting grains. However, restricted information on the orientation of a grain can be deduced from the position of one diffraction spot. The position fixes one axis, such that the grain orientation is known apart from a rotation around that axis. With some approximations this information was sufficient to group the diffraction spots into 3 orientation classes, namely cube, rolling and "other" [A11].

Bulk behaviour was ensured by the fact that the thickness of the sample was much larger than the grain size, and the fraction of surface grains therefore negligible.

The main result from the first study, [A10], is shown in Fig 7.4. The growth curves for the 6 grains analysed are seen to be very different. Two of the nuclei form instantaneously, while the other 4 exhibit retarded nucleation. (The nucleation time is defined here as the time at which the radius of the grains has just exceeded the detection limit, in this case 1.3 μm.) Furthermore, by differentiating the curves it is found that the growth velocities for the 6 grains at any given point in time vary by an order of magnitude. To put this in perspective, previous models for this material assumed all grains to nucleate at the beginning of the process and grains with the same orientation to grow with the same rate [125,126].

In the second study, 244 growth curves were derived of which 14, 124 and 106 related to grains belonging to the cube, rolling and other classes, respectively. These numbers are sufficient to correlate the growth behaviour with orientation. This was done statistically, by means of histograms and Kolmogorov-Smirnof tests [127].

As extracts from the results, the frequencies of nucleation times and initial growth velocities are shown in Figs 7.5 and 7.6, respectively. (The initial growth is assumed to a good approximation to represent un-impinged growth.) Similar curves are reported for grain size distributions at different times.

The main findings are:

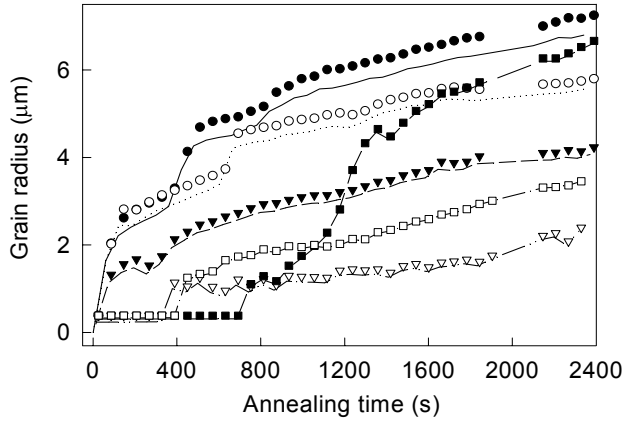

Figure 7.4
The evolution of the equivalent spherical radius for 6 grains during annealing at 270 °C. From the first study on recrystallization in AA1050 [A10].

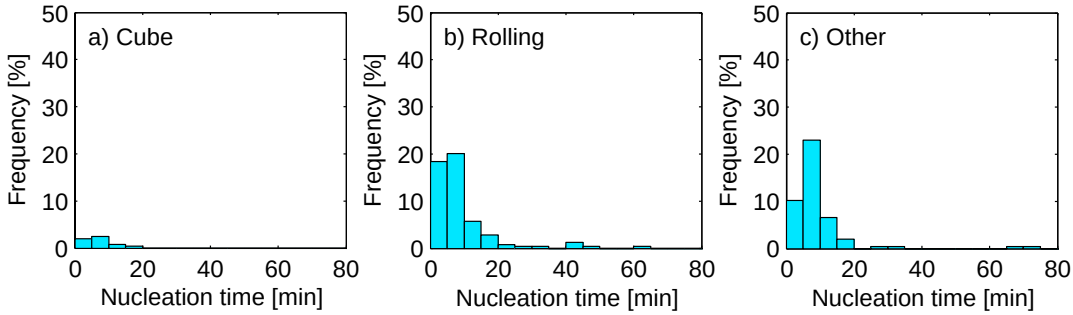

Figure 7.5
Frequency of nucleation times for each of the three orientation classes: a) cube, b) rolling, and c) other grains. The frequency is referring to the total number of grains, *i.e.* 244. From the second study on recrystallization in AA1050 [A11].

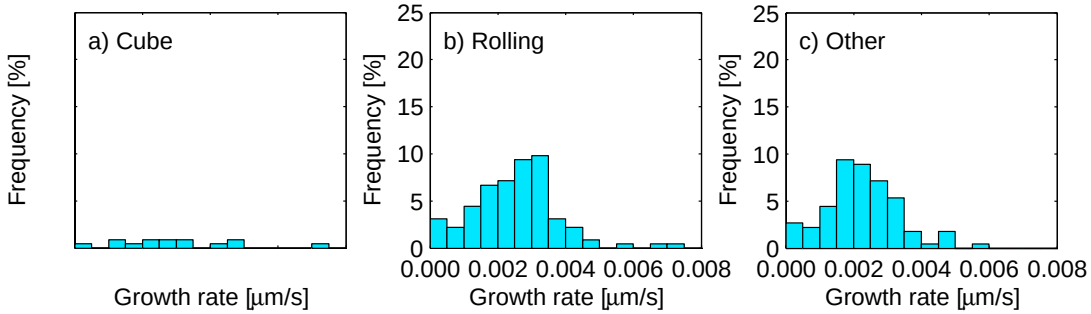

Figure 7.6
Frequency of the growth rate after 10 minutes of annealing for the three orientation classes: a) cube, b) rolling, and c) other grains. The frequency is referring to the total number of grains, *i.e.* 244. From the second study on recrystallization in AA1050 [A11].

1. The growth rates vary substantially between grains (also within the same orientation class) and with time. Notably, these variations are larger than those

caused by impingement. These variations are related to the heterogeneities in the deformed microstructure.

2. The nucleation behaviour of the 3 orientation classes is found to be statistically identical, cf. Fig 7.5, while the cube grains on average have a higher growth rate than other grains, cf. Fig 7.6. With subsequent analysis indicating that the impingement conditions are the same for all 3 classes, it is concluded that the size advantage of the cube grains is predominantly due to preferential growth.

The experimental and analytical procedures outlined above have been applied to studies of recrystallization for a number of other Al alloys [128,129]. In these studies, which were parts of the external user program, issues of direct relevance for the Aluminium industry were pursued.

7.2.2 Outlook on the statistical approach

The methodology introduced above has three shortcomings:

1. The grouping into orientation classes is for some of the spots not unambiguous. This raises the issue of a possible biasing in the statistics, as discussed in [A11].

2. No direct information is obtained on possible clustering of nuclei, one of the key parameters.

3. The growth curves represent the combined effects of recrystallization, impingement and grain growth. To separate the contributions it is necessary to know which fraction of the grain boundary is adjacent to another nuclei, and which fraction is "free to grow" into the deformed matrix. This information is not available.

The suggested remedies to these shortcomings are:

1. Characterisation of the full orientation can be obtained by indexing. This requires the ω-range to be extended to ~ 20 degrees. In some cases, even with the fast sweep-scan procedure such a range may be prohibitive for dynamic studies. However, the indexing needs only to be performed once, at the end of the annealing experiment for the fully-recrystallised material.

2. Determination of the CMS positions of the nuclei can be done in two ways, by a full grain mapping with detector configuration A and by a series of super-scan alignments using detector configuration B. Performing either the super-scans or a full map once in the initial stage of annealing will provide the positions of most of the nuclei.

3. The impinged volume fraction for a given grain at a given time can be deduced directly from a full map with detector configuration A. There are two requirements to exploiting such maps for establishment of impingement-corrected growth curves. The first is that the distance between nuclei must be substantially larger than the spatial resolution. The second is that the time

resolution is sufficient to allow maps to be generated with an appropriate frequency during the annealing.

A less demanding procedure is suggested for the case, where any of the two requirements are not fulfilled. This procedure is based on determining the positions for the nucleation sites only. This can be done at one point in time, as discussed above - case 2). Some assumption on the growth is then introduced, such as the grains growing isotropically, but with varying and unknown growth rates. Based on the observed growth rates and a geometric analysis, it is estimated when and where impingement takes place. This analysis scheme may be run iteratively, thereby optimising model parameters.

Evidently, the main limitation is the need for a compromise between resolution in time and space. The time required for a full 3D map depends crucially on whether a line- or box beam is used. In the latter case it is estimated to be 1-5 minutes. Depending on activation energies and annealing temperatures, such a time resolution may or may not be adequate.

A possible remedy to the time/space problem is suggested by Nielsen and co-workers [130]. They report on an interrupted 3DXRD annealing experiment of the type introduced in 7.2.1. Individual growth curves are determined at the operation temperature before and after on-line cooling to room temperature. Based on inspection of 63 growth curves it is concluded that the growth kinetics of the individual grains were not affected by this interruption. Hence, maps or super-scans may be generated at room temperature, where the driving force for growth is negligible. (This conclusion is not trivial. In general it is conceivable that the deformed material recovers to a certain extent during the temperature ramps. Hence, the validity of the approach using interrupted annealing needs verification in each case.)

7.2.3 First principles studies

Local studies of the dynamics of the interface between a nucleus and the deformed matrix require mapping. One may distinguish between three levels of ambition:

1. The nucleus is continuously mapped while it grows, using detector configuration A. The structure of the surrounding deformed matrix is not probed, but may be known *a priori* to some extent *e.g.* in connection with studies of deformed single crystals.
2. The nucleus is continuously mapped while it grows. In addition the deformed structure is characterised prior to annealing by 3DXRD orientation contrast methods. (This may be done either by resolving the elements in the deformed microstructure – see the following section - or less ambitiously by acquisitions of macroscopic pole figures. The conical slit may serve to define a volume close to an interface of interest.) The growth of the nucleus is then correlated with the disappearance of certain orientations.
3. Both the nucleus and the deformed microstructure are continuously mapped during annealing. A direct correlation is now feasible. The feasibility of mapping the deformed microstructure is discussed in section 7.3.

Very recently, Schmidt and co-workers have succeeded in performing a first experiment on ambition level 1 [131]. A "video" was made showing the change in the 3D shape of a single embedded nucleus during annealing. The spatial resolution was 5 μm and the time resolution was 10 minutes.

7.3 Recovery and nucleation

During plastic deformation and subsequent annealing of a metal a range of metastable structures develop [100,110]. The associated processes occurring during annealing are collectively known as static recovery.

The deformation-induced microstructure is arranged hierarchically. Typical examples of the structures appearing are shown in Fig 1.1 (b) and (c) for a cell-forming material. Tangled dislocations initially gather into dislocation cells. With time the remaining dislocations annihilate within the cells, such that these become near-perfect small crystals. The cells simultaneously organise into larger structures such as cell-blocks, separated mainly by low angle boundaries. The cell-blocks in turn are separated by near parallel boundaries, associated with higher misorientations. In the later stages of recovery, the entire structure coarsens.

The recovery influences recrystallization behaviour. In particular, some of the structures that eventually nucleate are generated by the recovery processes. Likewise, the annihilation of dislocations diminishes the driving force for the growth of nuclei.

Recovery is studied in several ways. Bulk probes are used, typically calorimetry, electrical resistivity and hardness measurements. The results represent an average over all processes and over the heterogeneity of the specimen. Within the last two decades deformation-induced microstructures have been characterised in much detail by TEM and EBSP, both prior to annealing [99-101,132] and after *ex-situ* annealing [110,133]. Such studies have provided much insight into structural arrangements, but it has proven more difficult to quantify the structural evolution. Most importantly, due to the limitations of EM, the dynamics of cell and cell-block formation, the coarsening and the nucleation events have never been observed directly in an unambiguous way. (*In-situ* TEM observations have been reported by a number of groups, but generally these are considered questionable for the reasons detailed in section 2.1.)

A number of models have been proposed for both recovery and nucleation, but there is no consensus on their relative importance [110,134-138]. Nor is it clear that the proposed mechanisms can explain all experimental results.

It appears that 3DXRD studies of the dynamics of the individual elements in the deformation-induced microstructure could constitute a break-through. In this context it is noteworthy that after annealing for some time, the cells are considered to be nearly perfect. The associated diffraction spots will therefore exhibit no or only a little intrinsic orientation spread. Hence, in principle the formalism derived in chapter 3 for grains can be applied directly to the dislocation structures.

However, the dimensions of the cells make such studies technically challenging. In particular, a full 3D mapping of the structure is not feasible. The required spatial resolution is in the range of 100 nm – 1 μm, depending on material and degree of deformation. By contrast, the spatial resolution available with 3DXRD is currently 5 μm [A4].

Instead one may attempt to identify the individual cells by orientation contrast. In this case, the limitation is spot overlap. The fact that the individual diffraction spots are point-like is favourable, but this is countered by two other factors:

- *Texture*. For small-to-moderate degrees of deformation, the orientations of the dislocation structures emerging within an "old grain" will be perturbations of the average orientation of the grain.
- *Conical slit*. The minimum gauge volume of the conical slit presently available is 5x5x250 μm^3. Assume the cells have a size of 1 μm, then there would be ~6000 cells within the gauge volume. From Table 3.1 this is seen to be at the limit, even if the cells have random orientations.

The conclusion is that in general the individual dislocation structures within a millimetre thick specimen cannot be resolved by orientation contrast today.

Nevertheless, many problems can be pursued. The spot overlap problem can be countered by studies of thin specimens. If there are 10-20 cells across the thickness, the middle ones will be representing, in a restricted sense, bulk behaviour. A feasibility study has been performed with this approach. The deformed microstructure was characterised in two materials, subject to very different deformation conditions, and the recovery processes were followed on-line during annealing. Preliminary results from this study are summarised in section 7.3.1.

Likewise, individual cells with *rare* orientations will give rise to isolated spots even when the majority of diffraction spots cannot be resolved. Such cells are clearly not "characteristic" ones, but they are nevertheless of much interest, as they are surrounded by high angle boundaries, and therefore may be associated with a large driving force for growth. In section 7.3.2 it is demonstrated how dislocation structures with such rare orientations can be identified despite being embedded within a 2 mm thick specimen. Based on this the prospect for *in-situ* nucleation studies is discussed. Furthermore, a summary is given of article [A12] where such a method is applied to an outstanding problem in recovery/ recrystallization studies: do new orientations emerge during annealing of deformed metals or do all the recovered cells and nuclei develop by growth of specific cells already present in the deformed microstructure?

7.3.1 Static Recovery

The microstructural development during annealing has been studied for two foils, made of commercially- pure Al materials. The two materials, I and II, were subjected to very different deformation conditions. Material I was rolled to a medium degree of deformation, corresponding to a 40% reduction in thickness. Material II was deformed by the Equal Channel Angular Extrusion (ECAE) process [139] to very high strains, corresponding to a total reduction of 99.995% (ε_{vm} = 10) [140]. From

EM the average cell sizes for the two materials in the as-deformed state were found to be 2 x 2 x 2 μm^3 and 0.5 x 0.5 x 1 μm^3, respectively.

The 3DXRD set-up involved detector configuration B in combination with a 50 keV box beam, focused to a size of 7 x 7 μm^2. This set-up is similar to the one used for obtaining growth curves in connection with recrystallization (section 7.2 and [A10-A11]) with the exception that the incident beam is not uniform, but has a Lorentzian shape. The routines described in chapter 3 for sampling integrated intensities evenly and for validating growth curves do not conform to such a beam. These routines were therefore modified in the following way: instead of performing an ω-scan at one (y,z) position, 9 ω-scans were performed in a 3x3 (y,z)-grid, with a distance between the nodes in the grid of 5 μm. The position and the integrated intensity of a given cell were then determined from a least-squares fit to the intensities in each of the grid points.

Following a characterisation at room temperature, foils I and II were annealed isothermally on-line at 300 ^oC and 175 ^oC, respectively.

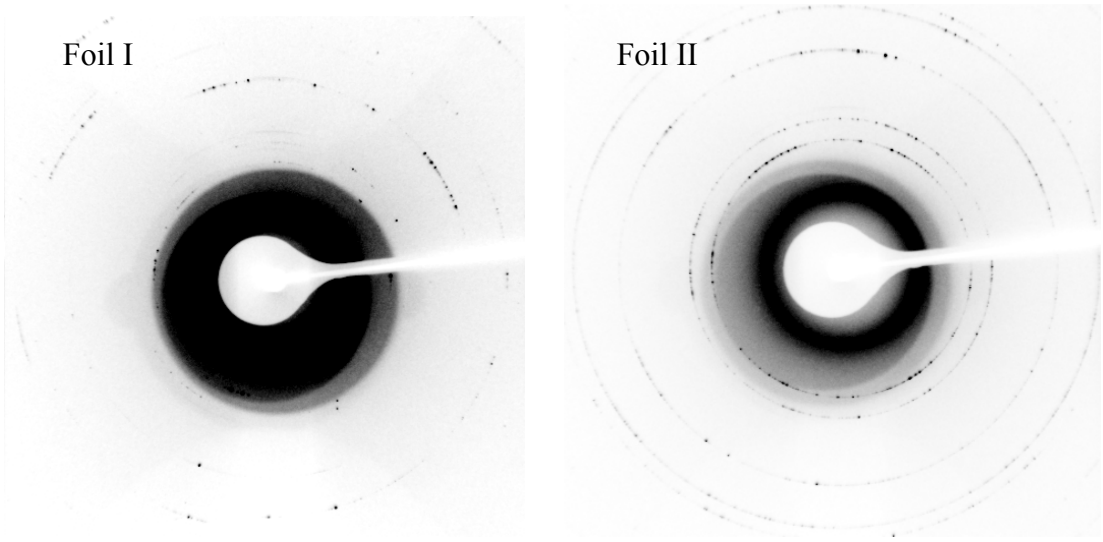

Figure 7.7
Raw data from foil I (left) and foil II (right), representing deformation of Al to medium and very high strains, respectively. The continuous rings near the centre arise from background scattering due to insufficient shielding. Distinct diffraction spots are observed as black dots. Courtesy of C. Gundlach and J.R. Bowen, respectively.

Raw data for the foils are shown in Fig 7.7. Distinct diffraction spots are observed in both cases. For foil I, the spots are clustered within some segments of the Debye-Scherrer rings, scattered around the average orientation of the old grain. For foil II, the orientations are nearly random, reflecting high angle boundaries between the individual elements of the microstructure [140].

These type of data are directly amenable to the type of analysis presented in sections 3.3-3.6 and to derivation of growth curves of the type shown in Fig 7.4. Resulting growth curves for a few individual dislocation structures are shown in Fig 7.8. These curves represent the first results emerging from an ongoing data analysis. Most

notably, the curve for foil II demonstrates that the growth and shrinkage of grains as small as 200 nm can be followed *in-situ*.

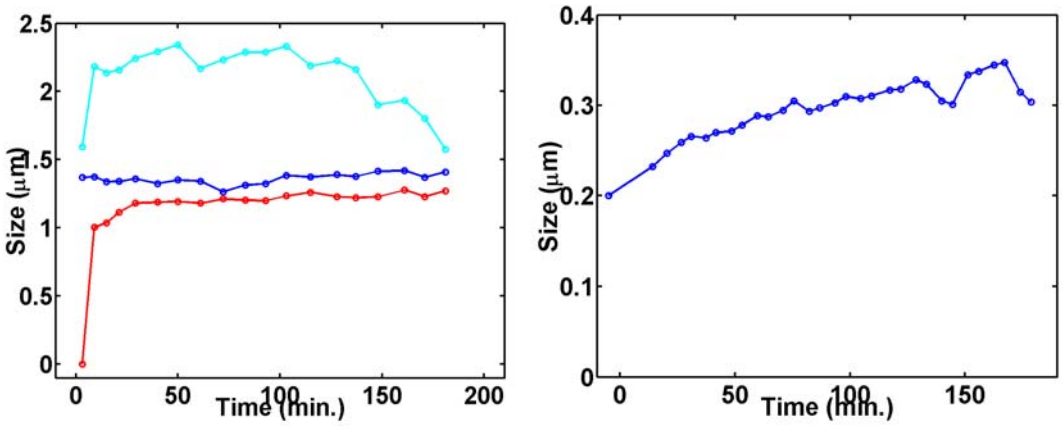

Figure 7.8
Growth curves for cells during recovery of foil I (left) and foil II (right). The equivalent spherical radius is shown as a function of annealing time. The detection threshold was ~150 nm. Courtesy of C. Gundlach and J.R. Bowen, respectively.

In addition to volume, the individual cells may be characterised with respect to orientation, elastic strain etc., in accordance with the scheme presented in section 3.3. This enables some fundamental issues in recovery to be addressed:

- Hu suggested in 1962 a possible coarsening mechanism. In this, two neighbouring structures rotate until they obtain the same orientation, at which point they coalesce [134]. This mechanism has been much debated. If it occurs, the rotations would be easily observable with 3DXRD, cf. the work on grain rotations [A8, A9].
- Initially the cells may contain many intrinsic dislocations. These will deform the lattice and give rise to a broadening of the diffraction spots. (Such a broadening is apparent for foil I but not for foil II.) From an analysis of such a broadening an estimate could be made of the concentration of dislocations within individual cells and the time dependence of their removal.

Extrapolating from the progress in recrystallization, where growth curves were first determined for 6 grains [A10], then for 240 grains [A11], it is foreseeable that analysis of a larger ensemble of dislocation structures will be feasible in the future. The statistical analysis described in section 7.2 could then be copied. As a result it may be feasible to:

- Determine possible “nucleation times” for various recovery processes and estimate the degree of heterogeneity involved.
- Correlate the coarsening behaviour to the initial lattice strain, initial orientation, initial size or position within the specimen.
- Correlate the emerging growth curves with models for coarsening.
- Determine activation energies.

The limitations of the thin foil procedure are found to be:

1. The flux limitation on size implies that microstructural elements smaller than a given threshold value will not be visible. This raises the issue of biasing statistical data.

2. To avoid surface elements it is required to determine the position of the elements with a precision of around 1 μm. This should be possible with appropriate use of super-scans, cf. section 3.5, but the procedure needs verification.

3. The grains initially embedded within the foil may grow to a size comparable to the thickness. From this point onwards the dynamics is clearly not representative of bulk behaviour anymore.

7.3.2 Nucleation and the emergence of new orientations

In-situ studies of the nucleation process itself pose a formidable challenge. Such studies require the identification of the "embryo", the element in the deformation-induced microstructure that eventually nucleates. In addition to the embryos being small they are in general also rare. In the extreme, the aim might be to identify and characterise a single embryo with a size of 1 μm within 1 mm^3 of material, and to observe this starting to grow. It is almost impossible to find objects occurring at such small volume fractions by scanning methods. As an example, even with the fastest EBSP techniques, where up to 60 images can be acquired per second, it would on average take 200 days of un-interrupted measurements to scan a sufficient volume. Moreover, by EBSP there would be no representative way to determine which site actually becomes a nucleus.

Notably, 3DXRD is not a scanning method, but based on a tomographic principle. In [A37] a possible 3DXRD solution is outlined if the embryo for some reason can be assumed to have an unusual orientation, such that it will give rise to a distinct diffraction spot. Using a box-shaped beam and detector configuration B, a single element of the microstructure can be found and characterized by means of one ω−scan. Provided there is no spot-overlap, volume fractions as low as 10^{-7} can be identified in this way. Furthermore, such measurements can be repeated within an (y,z,ω)-grid, as discussed in section 3.5. For each of the (y,z) points one may answer the question: is there a embryo of this particular orientation within this part of the specimen or not? It follows that the sensitivity is proportional to the number of grid points in the (y,z)-grid. Consequently, a single 1 μm embryo appearing within 1 mm^3 of material can be found and characterised with respect to position, volume and orientation within some hours of synchrotron beam time.

This scheme is applied in [A12] to the currently-debated issue of possible "new orientations". Existing recovery/ nucleation models all predict that orientation should be conserved, while a number of recent EM investigations suggest that some fraction of the nuclei do appear with new orientations (*e.g.* [141-143]). However, due to the limitations of EM, the experimental studies can be questioned on the basis that the deformed microstructure was not mapped over a sufficient volume.

The specimen studied in [A12] is an Al single crystal of a specific orientation, the so-called S-orientation, which had been subjected to channel die deformation. Previous TEM investigations had indicated that new orientations may arise during heat treatment of such crystals [133]. By 3DXRD the same volume of 0.08 mm^3 was investigated in the as-deformed state and after 5 minutes of annealing at 300 ^oC. At this point, no nucleation events had taken place, but the microstructure had recovered. Data were acquired within a (y,z,ω)-grid with 21 x 19 (y,z)-grid-points and 10 steps in ω.

Shown in Fig 7.9 are {200} pole figures for a single (y,z) grid point in the as-deformed state (b-c) and the annealed state (d). (An {hkl} pole figure is a stereographic projection of a set of {hkl} reflections. The directions of the reflections are determined with respect to a set of axes fixed to the sample, plotted on a unit sphere and projected onto the equatorial plane [61]. Pole figures can be generated directly from raw diffraction data without the need for indexing. In the present case the observed {200} diffraction spots are plotted with respect to the conventional set of axes: RD, ND and TD: direction of deformation, normal direction and transverse direction, respectively.) Furthermore, for comparison EBSP data for the as-deformed state is included: Fig 7.9 (a). From these figures and additional figures in the publication it is observed that:

- the pole figures for both the as-deformed and the annealed specimens exhibit distinct diffraction maxima, poles, characteristic of the single crystal. These are spread out to some extent, due to the deformation. The vast majority of the microstructure is associated with these poles and cannot be resolved with 3DXRD.
- the sensitivity of 3DXRD to weak components is superior to EBSP (compare the size of the tails of the 3 poles in a) and b)).
- upon annealing the poles become sharper, such that orientation components such as the one marked B disappears.
- upon annealing new distinct spots appear with orientations far from the poles. The positions of these exhibit little correlation with the position of the spots in the as-deformed state (compare c) and d)).

By comparing pole figures from all the grid-points, it is found that some of the emerging spots are associated with orientations that are not present in any of the 19x21 pole figures for the as-deformed state. This rules out the possibility of an erroneous identification of a “new orientation” due to a minor drift in position between the measurements for the as-deformed and for the annealed state.

Principally there are two ways the new minority orientation components can be generated. Either they have emerged from very rare parts of the deformed structure, associated with a very small volume fraction (in [A12] the relationship is found to be $V_v < 9 \cdot 10^{-7}$). In addition, their size must be at the very tail of the distribution of cell sizes, as well as substantially below the classical nucleation threshold. Or they have emerged by rotation.

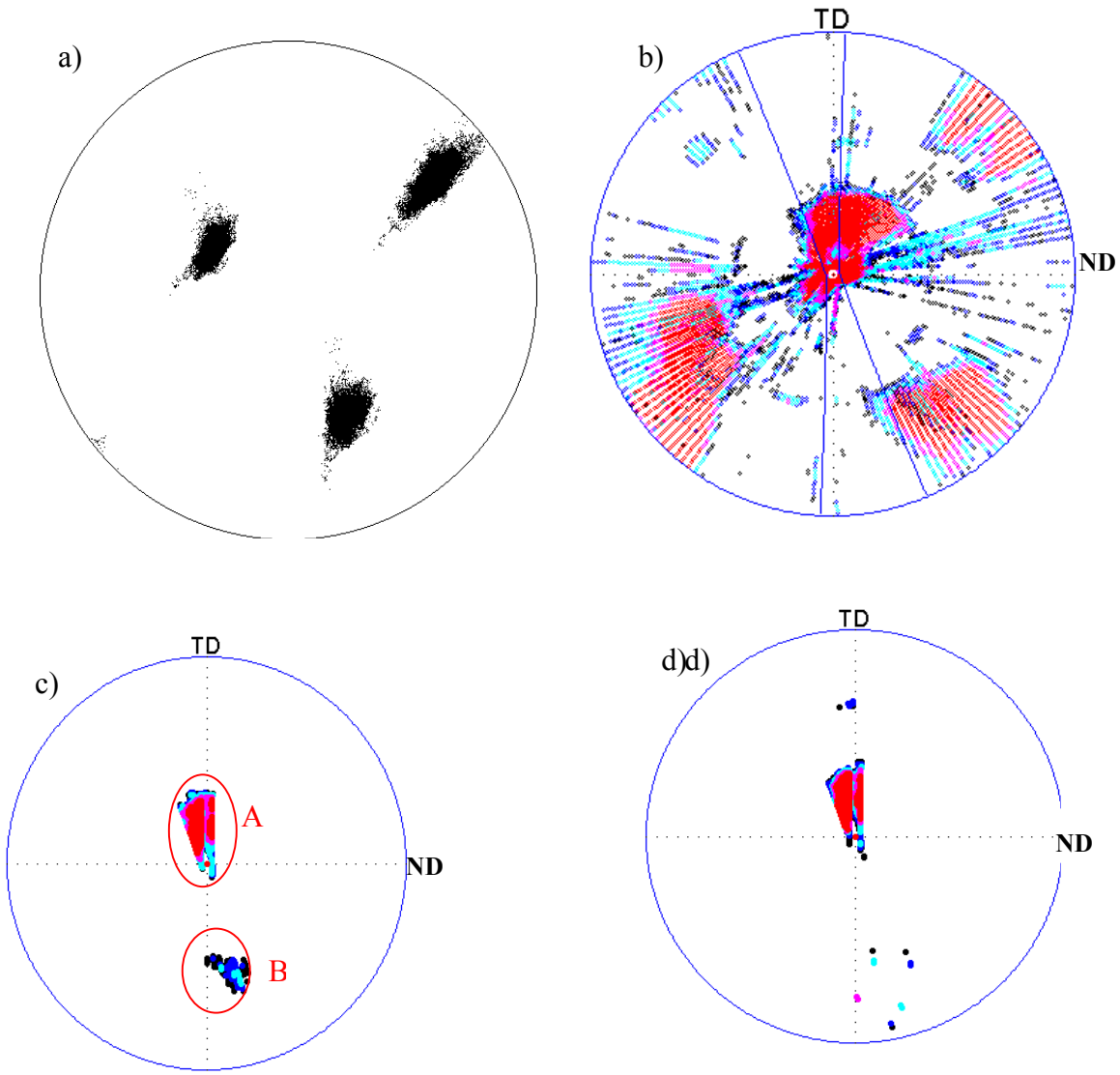

Figure 7.9.
{200} pole figures of the 2 mm thick deformed Al single crystal in the as-deformed state (a,b,c) and after 5 minutes of annealing (d). (a) is generated by EBSP based on 27,000 positions on the surface. The orientations found are marked as dots. (b,c,d) are generated by 3DXRD measurements on selected 240,000 μm^3 sub-volumes of the specimen. (b) is a full pole figure. To save time the characterisation was in general based on data acquisition within a limited ω-range of [0^o 20^o]. The corresponding part of the pole figure is indicated by two solid lines. (c,d) Partial pole figures for one and the same position within the (y,z)-grid. The orientation distribution for (c) is divided into 2 components: A, B, which are further discussed in the text. The colour code for (b,c,d) is: [black, blue, cyan, magenta, red] for [1, 2, 5, 20, 100], with 1 corresponding to the signal-to-noise ratio. From [A12].

These results are consistent with the observations of "new orientations" by other methods. It is the first time such observations have been based on non-destructive bulk measurements within a volume comparable to the recrystallised grain size. Furthermore the limiting numbers in terms of volume and volume fractions are very superior to those of previous studies.

In outlook, adding measurements at a third point in time, after repeated annealing, would be sufficient to determine which of the emerging recovered cells actually became nuclei (this would be evident from the intensity increase.)

7.3.3 Outlook

If possible, it would be of major interest to extend the scheme presented in section 7.3.1 to *in-situ* studies of the structural rearrangements taking place during deformation. However, for such studies the thin foil approach is inadequate, as thicker specimens are required to ensure a mode representative of bulk deformation. This implies that conical slits sampling a smaller gauge volume must be produced.

7.4 Peak shape analysis

From the early days of x-ray diffraction, it has been recognized that the so-called line profile of powder diffraction patterns – the 2θ variation of the intensity within a single Debye-Scherrer cone - carry information on the "size" and "strain" of the microstructural elements. Hence, considerable effort has been put into the establishment of methods for deriving these parameters from the diffraction patterns [144,145]. The main application has been the study of plastically deformed metals.

The most frequently used method, due to Warren and Averbach [146], is to decompose the line profiles into a set of Fourier coefficients. These are then interpreted in terms of an average size and strain, although it may not be clear what type of "domains" (dislocation cells, cell-blocks, sub-grains etc) these terms are referring to. As an alternative, the line profiles may be simulated based on a model of the microstructure. Matching the experimental and simulated profiles, parameters of choice can be optimised. Typically, such models are based on analytical expressions for the displacement field arising from specific lattice defects such as dislocation arrangements (*e.g.* [147-148]). The output may be for instance an estimate of the dislocation density.

Despite substantial refinement in the methodology [145] it may be argued that the impact of line profile analysis on materials science has been rather limited. In the author's opinion this is due to the indirect way conclusions are obtained. More specifically

1. The measured line profiles constitute an average over contributions from various types of microstructural elements and configurations, over the distributions of these as well as over possible macroscopic heterogeneities. In particular, the lattice strain is the combined response to inter-grain, intra-grain and macroscopic stresses. Furthermore, the line profiles are only partly specific to the crystallographic orientation, as they comprise contributions from a set of elements with parallel reflecting planes, but different orientations around the plane normal.

2. The information content in the one-dimensional profiles is rather limited. Hence, only a few parameters can be optimised reliably based on a set of such profiles. This again limits the complexity of the models used.

3. Due to the above effects, results generally rely on the validity of various simplifying assumptions. It may be difficult to prove or disprove these by independent means. Even the Warren-Averbach method, which seemingly is model independent, does make the critical assumption that the strain is uncorrelated and randomly distributed. This is typically not the case.

The 3DXRD methodology derived in chapter 3 has the potential to overcome a number of these shortcomings. More specifically, it is suggested to characterise the intensity distribution of individual diffraction spots with respect to the three angular variables ω, η and 2θ (or equivalent parameters such as reciprocal space units). This distribution is termed the peak shape. Furthermore to compare models of the microstructure with sets of such peak shapes, all originating from the same element. In principle such an approach can be applied to any type of microstructural elements, provided they are observable in the form of distinct diffraction spots. However, for simplicity, in the following the elements will be assumed to be grains.

In comparison to macroscopic line profile investigations, peak shape analysis has several advantages:

1. The measurements are specific to each grain. As such, the amount of averaging over various heterogeneities is substantially reduced. Furthermore, the importance of variations in size, stress conditions etc. can be judged by comparing results from different grains.
2. The full orientation of the grain is known.
3. Instead of measuring a few one-dimensional profiles, for each grain 10-100 3D distributions are available, one for each reflection characterised. Hence, the information content in the data is substantially enhanced. This should allow for more reliable fitting procedures to potentially more complex models, as well as for internal consistency checks, by comparing crystallographically equivalent entities.
4. An independent measurement of size can be obtained from the integrated intensity.

Formally, for each grain the set of 3D peak shapes may be interpreted in terms of a 9D projection within the 12D lattice space introduced in chapter 3. The spatial degrees of freedom have been integrated out by choice of detector resolution, while the strain and angular parts remain.

Two studies of the evolution of peak shapes with tensile deformation have been performed at APS, on Cu and Al. To minimise the instrumental contribution to broadening in the radial direction configuration C was used. At a distance of L = 2500 mm the minimum width of the peak is $\Delta 2\theta/2\theta = 10^{-4}$, while a shift in the CMS position of the peak – corresponding to a change in the elastic strain – can be determined with a precision of 10^{-5}. In this configuration, the active area of the detector covers only a small part of the full diffraction pattern, see Fig 3.2. Hence, to characterise the diffraction spots of interest, the specimen had to be rotated around at

least two rotation axes. In practice, the specimen was mounted in a small stress rig, which was fixed to a Eulerian Cradle.

In the peak shapes analysed so far, radial profiles made at different ω and η positions within the same diffraction spot were identical within experimental error. Hence, it appears that the 9D characterisation can be simplified to two independent measures for each grain, one describing the orientation spread, the other being a set of *radial peak profiles*, each of these integrated over the orientation spread.

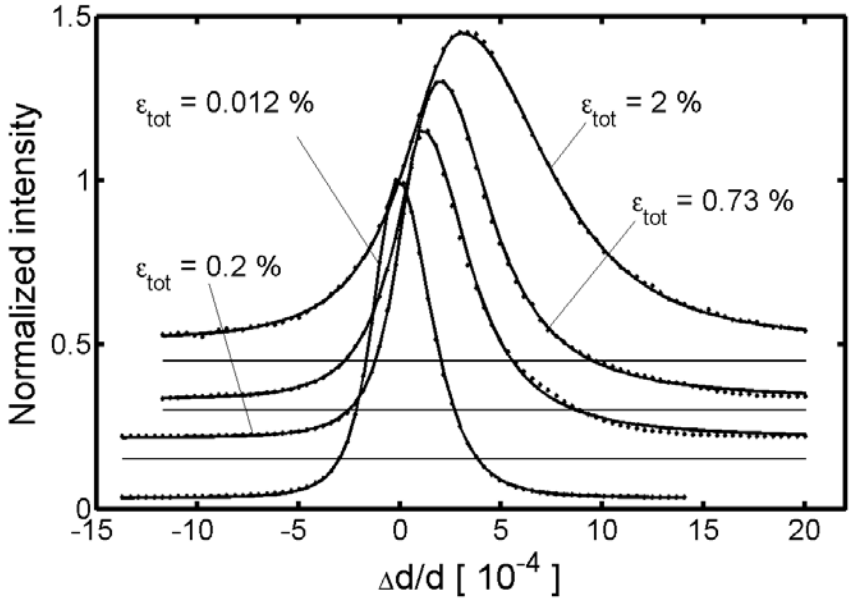

Figure 7.10
Radial peak profiles associated with an embedded grain in a pure Cu specimen. The evolution of a {440} diffraction spot is shown as a function of tensile strain. The profiles are scaled to equal peak values and vertically off-set for clarity, the loads are indicated. The elastic strain is visible as peak shifts. Also visible are the emerging peak broadening and asymmetry. The symbols are the experimental data points and the lines are fitted split Pearson VII profiles. From [A32].

In the study on pure Cu, the peak shapes of 20 {440} reflections – arising from different grains - were characterised [A32]. An example of the evolution of the radial peak profile for one of these diffraction spots is shown in Fig 7.10. In the experiment on commercial purity Al, by means of *GRAINDEX*, the evolution of the radial peak profiles from 19 reflections associated with the same grain was followed as a function of strain up to 4.5% elongation. Hence, at the time of writing, the feasibility of peak profile studies on the single grain level has been verified.

The main limitation of the above methodology is, once more, the issue of spot overlap. This restricts the technological applications substantially, as most components are strained to 30% or more. However, for some fundamental studies the small strain region is of interest, as this is where the initial formation of dislocation structures takes place. Moreover, by comparison to macroscopic line profiles, it should be possible to test some of the underlying assumptions in the field.

More generally, the integral method presented here may be seen as a route to "bridge the length scales" between the 3DXRD methods for studying plasticity on the grain

and sub-grain scale presented in section 7.1 and the 3DXRD methods for studying the dynamics of individual dislocation structures, presented in section 7.3. Combining the three types of characterisation on the same sample would provide a very comprehensive description of plastic deformation.

7.5 Phase transformations

An understanding of phase diagrams and phase transformation mechanisms is the starting point for much of materials science [149,150]. However, for reasons similar to those outlined for studies of deformation, recovery and recrystallization in metals, traditional experimental tools are often inadequate. In particular, the phase diagrams are often complex and the dynamics is characterised by a number of reactions taking place simultaneously within a heterogeneous structure and with substantial differences in the diffusion path lengths involved.

To a large extent, the 3DXRD methodology introduced in sections 7.1-7.3 can be transferred to studies of phase transformations. If the lattice parameters associated with the phases are known approximately *a priori*, applications like *GRAINDEX* can be run successively for each phase. Furthermore, as discussed in chapter 6 complementary dynamic and/or static studies using absorption contrast tomography may be relevant.

The main limitation for such studies is the grain size, which often will be smaller than the present spatial resolution of the 3DXRD microscope. However, as demonstrated in section 7.3 dynamic studies can be performed using ”orientation contrast”. This concept can be extended for multi-phase systems, as some frequently encountered transformation mechanisms imply a specific orientation relationship between a “grain” of the old phase and a “grain” of the new phase. In the simplest case one phase is replacing another within the contours of an existing grain boundary. In other cases such as peritectic overgrowth a new-phase grain is formed on top of an old-phase grain without necessarily consuming any of the old-phase grain. In any case, it is relevant to search the output from *GRAINDEX* for corresponding pairs of grains. If found, the time evolution of the diffraction spots originating from the two grains can be correlated. In this way information on the governing mechanisms can be obtained on a *local* scale, even though the grains may be too small for mapping.

The potential use of 3DXRD for phase transformation studies covers a wide range of topics, including diffusionless transformations, second phase precipitation, solidification and phase separation. Two examples of work are summarised in the following. In section 7.5.1, diffusion controlled solid-state transformations in steel are investigated. This work is a part of the external user program of the 3DXRD microscope, a collaboration with S.E. Offerman, J. Sietsma and co-workers at Delft University of Technology. In section 7.5.2 an applied study on phase transformations in ceramics is presented.

The two studies are first-of-kind, performed at a time when the full methodology presented in this thesis was not available. As such a substantial amount of additional information is expected, if the experiments were repeated, *e.g.* with an ω-range sufficiently broad that orientations of “old-phase” and “new-phase” grains could be

correlated. Nevertheless, both studies clearly demonstrate the shortcomings of present models.

7.5.1 Steel

Phase transformations in steel have been investigated more extensively than those in any other material, due to their intricate nature as well as their technological importance.

Carbon steels exists within three stable phases: austenite with an fcc structure, ferrite with a bcc structure and cementite (Fe_3C) with an orthorhombic structure. The transformation from the high-temperature austenite to the medium-temperature ferrite phase is accompanied by a carbon enrichment of the remaining austenite, as the solubility of C in ferrite is much lower than in austenite. At lower temperatures the remaining austenite decomposes into pearlite, a lamellar structure comprising ferrite and cementite. These structural changes are illustrated in the top part of Fig 7.11.

In [A13] the first 3DXRD results are reported for the annealing behaviour of a carbon steel. The experimental set-up was similar to the one used for the two recrystallization studies [A10, A11] with detector configuration B and an 80 keV 100 x 100 μm^2 beam. The carbon steel was annealed at 900 ^oC to produce mono-phase austenite and subsequently cooled to 600 ^oC over 1 hour. During this process the nucleation and growth of ferrite and pearlite grains was inferred from the evolution of distinct diffraction spots originating from the ferrite in either of the two phases.

The number of ferrite reflections observed are plotted as function of temperature in Fig 7.11 a). This curve is differentiated and the resulting nucleation rate is compared to the prediction from a classical nucleation model in Fig 7.11 b). This model was based on two assumptions: that the driving force for the nucleation - the decrease in Gibbs free energy – can be determined from thermodynamic reference data, and that the nucleus is shaped as a pillbox with coherent and semi-coherent interfaces [151].

From the figure it is apparent that the predicted and measured activation energies differ by more than two orders of magnitude. Two explanations are suggested for this disagreement:

- It is questionable whether thermodynamics, based on a continuum description, can be used to predict nucleation phenomena, when the number of atoms participating in the process may be as low as 100.
- The specific assumption on the shape of the grains and the energy of the interfaces may be wrong. Further theoretical work is required on the effect of alternative nucleation geometries.

Four types of growth behaviour were identified for the ~60 nuclei observed. Typical examples of growth curves are shown in Fig 7.12. The interpretation of these curves is as follows: in the most frequent type, (a), the ferrite grains grow in accordance with the parabolic growth model of Zener [152] until they impinge. These grains are not influenced by passing the transition temperature for pearlite formation at T_{pearl} = 685 ^oC. In contrast, for grains of type (b), pearlite colonies are nucleated at the boundary of the ferrite grain when passing T_{pearl}. The ferrite in these colonies has the same

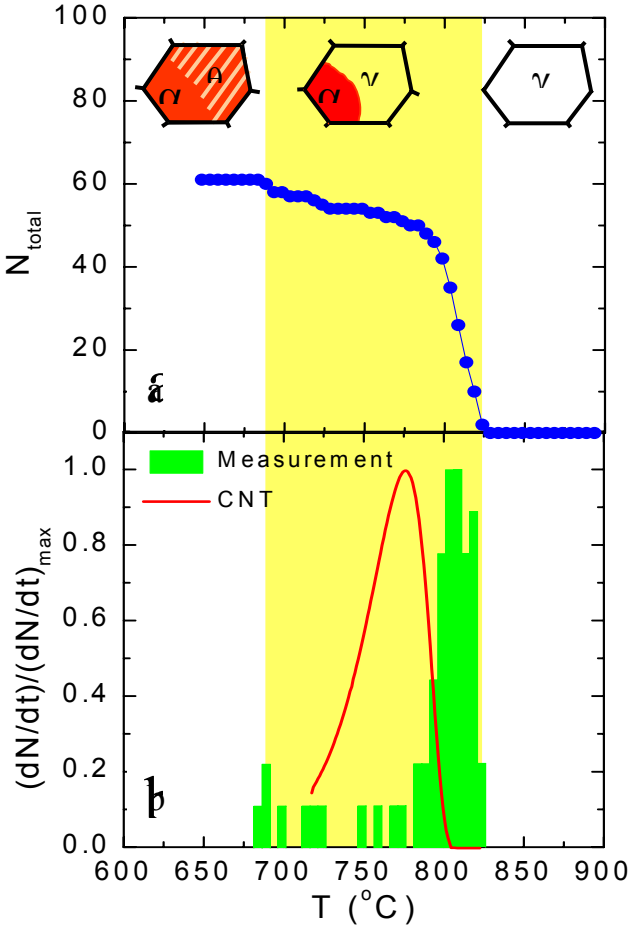

Figure 7.11.
Nucleation and growth of ferrite and pearlite grains during cooling of a C steel. Above the total number of ferrite diffraction spots observed is shown as a function of temperature (a). Below the normalised observed nucleation rate (bars) is compared to theoretical prediction (line) based on a classical model [151] (b). The different stages during the phase transformations in steel are schematically drawn at the top of the figure. The three phases are: austenite (γ), ferrite (α) and pearlite, a lamellar phase comprising ferrite and cementite (θ). From [A13].

orientation as the ferrite in the original ferrite grain. Hence, the steep increase in intensity of the diffraction spots at T_{pearl}. Noting that only 3 nuclei with new orientations were formed at or below T_{pearl} in Fig 7.11 it is concluded that this type of nucleation is the dominant mechanism for pearlite formation. For grains of type (c) the nucleation and growth of ferrite grains is retarded, due to a local enrichment in the C content in the austenite, caused by the growth of other ferrite nuclei in the neighbourhood. In the least frequent type of growth (d), the complex growth pattern is speculated to reflect the relaxation of boundaries between impinged ferrite grains.

In continuation of this study, the "growth curves" for the disappearing austenite grains have been analysed by Offerman [153]. The results corroborate the above interpretations.

In outlook, the relationship between the stability of an austenite grain and its orientation, size, average C content and stress condition can be studied. Similar to the

work on recrystallization reported in [A11], these parameters can be cross-correlated by means of statistical tests. However, as two additional parameters have been added (strain and stoichiometry) the number of grains needed for a full statistical analysis will be substantially larger. Initial 3DXRD work of the stability of austenite grains in TRIP steels has been performed by Kruijver and co-workers [A43].

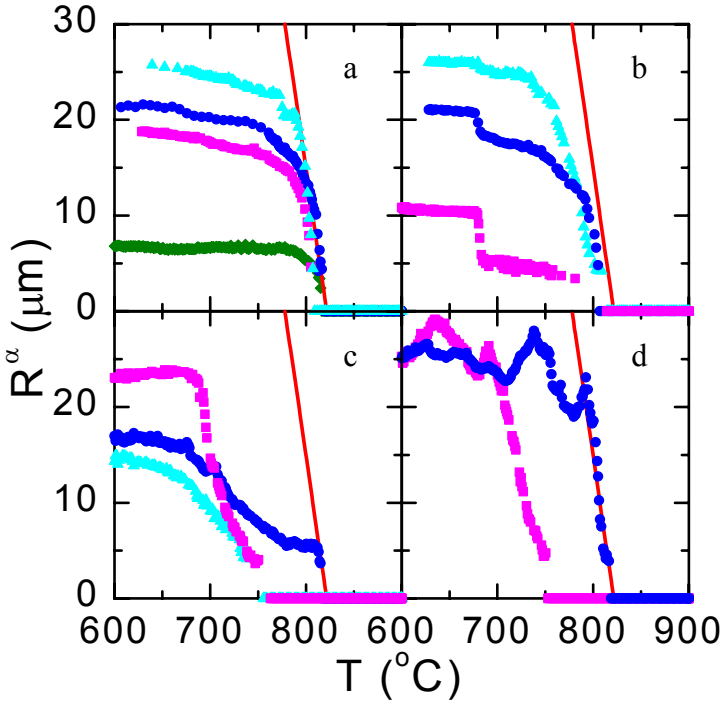

Figure 7.12
Examples of growth curves for individual ferrite grains during continuous cooling from 900 °C to 600 °C. Four types of behaviour are illustrated: a), b), c), and d), to be further discussed in the text. The lines are predictions based on the parabolic growth model of Zener. From [A13].

7.5.2 Optimisation of high T_c superconducting tapes

One of the most promising applications of the copper-oxide high T_c superconductors is as cables for resistance-free transport of electric power. Typically the design for such cables comprise a set of Ag-sheathed tapes with a core of high T_c material, all cooled with liquid N_2 in order to keep the device below the critical temperature for superconductivity. The tapes are produced by the so-called "powder-in-tube" technique [154,155] where a randomly oriented powder of $(Bi,Pb)_2Sr_2CaCu_2O_x$ (Bi-2212) and secondary phases are filled into a Ag tube. The tube is flattened by a series of drawing and rolling steps. The resulting tape is annealed around 830 °C to convert the powder into the relevant superconducting phase $(Bi,Pb)_2Sr_2Ca_2Cu_3O_x$ (Bi-2223). During the annealing the c-axis of the grains align to some extent with the tape normal.

It is crucial for the commercial use that the individual tape can carry as much superconducting current as possible. Otherwise, the component and cooling costs outweigh the gain from the lack of resistance. Hence, numerous laboratories have put a major effort into optimising the superconducting critical current density, J_c. Nevertheless the best values are still around 60-70 kA/cm^2. In comparison the best

values for the same material deposited as thin films exceed 1 MA/cm^2. Hence, it is evident that the transport potential of the tapes is far from being fully exploited. To increase J_c, the following issues need addressing:

- The c-axis of neighbouring Bi-2223 grains should be better aligned with respect to each other (implying a more pronounced macroscopic texture).
- The final tape should contain as pure and dense a Bi-2223 phase as possible.
- The interface between Bi-2223 grains should be free of secondary phase and the amount of micro-cracks should be negligible (to provide a path for the superconducting current).

Black-box approaches to optimisation along these lines have been slow. The reason is that the processes involved are very complex. The chemical phase space is large, and the relevant reactions take place within a narrow region in temperature and composition space. Furthermore, the Ag influences the processes substantially, chemically as well as by serving as a template for nucleation of Bi-2223. Hence, the material is inhomogeneous, and the reactions take place under far-from equilibrium conditions. As a result, reproducibility is a concern.

For these reasons, at Risø a major effort has been put into characterizing the structural details, in order to understand the microstructural dynamics [A28,A44-A49]. An extended summary of the results is given in [A14]. This work was performed as part of a general collaboration on tape optimisation with the manufacturer NST A/S, and the Technical University of Denmark. The resulting tapes were used for the first fully implemented high T_c power cable in the world, a 30 m long 3 kA demonstration cable, installed at a power utility in Copenhagen in 2001.

The structural studies reported in [A14] were made by a range of complementary methods. However, the main technique is the use of 100 keV x-rays for powder diffraction. The hard x-rays can penetrate the Ag, providing unique *in-situ* information on reactions, coarsening processes and texturing mechanisms. As an example of results, the concentration of the dominant crystalline phases is shown as a function of annealing time and temperature in Fig 7.13.

The article [A14] also contains the results of a feasibility study on the annealing of tapes using the 3DXRD microscope. The set-up was based on detector configuration B and an 80 keV 5x40 μm^2 beam. It is demonstrated that the individual Bi-2212 and Bi-2223 grains give rise to distinct diffraction spots. Growth curves were derived for 4 grains, as shown in Fig 7.14. It is illustrative to compare these curves to the macroscopic phase evolution, reproduced in Fig 7.13:

The average phase evolution suggests that the formation of Bi-2223 is due to a slow reaction, where the material is supplied by Bi-2212, $(Ca,Sr)_2CuO_3$ and a liquid phase. (The evidence for the role of the liquid is mainly from TEM studies [A14].) Implicit in this model is the assumption that all Bi-2212 grains are present from the beginning of the process; that is from the time t_0 of reaching the operation temperature. This assumption is contradicted by the 3 Bi-2212 grains in Fig 7.14, which nucleate 4-7 h after t_0. Similarly, the powder diffraction data would conventionally be interpreted such that the Bi-2223 grains, once formed would not disappear or shrink. This assumption is also contradicted by the growth curves of Fig 7.14.

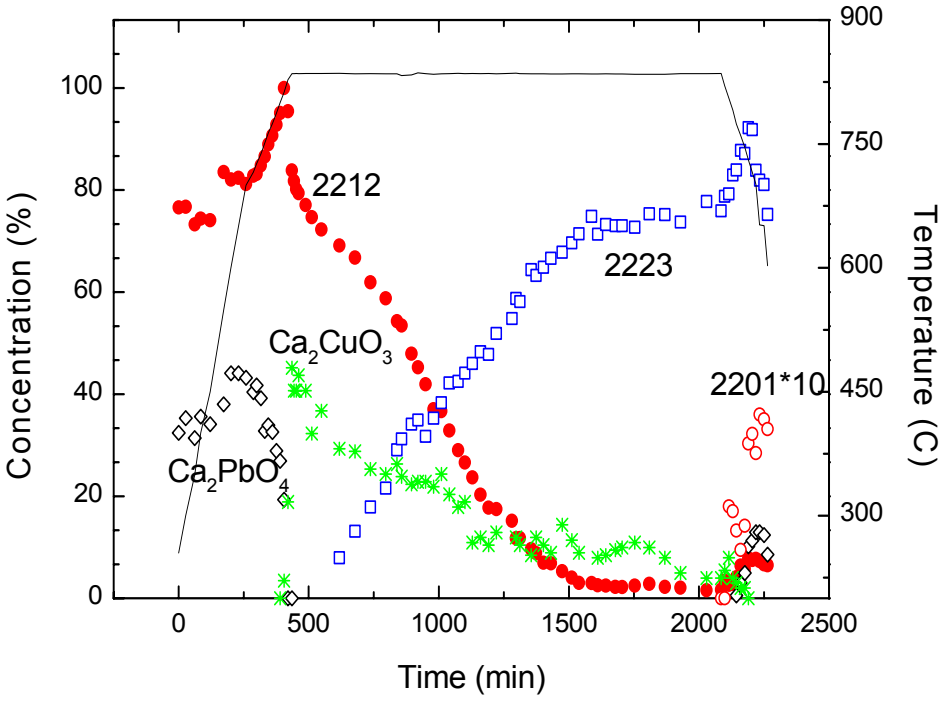

Figure 7.13
The relative concentration of the dominant crystalline phases during *in situ* annealing of a Ag clad Bi-2212 tape in air. The symbols refer to Bi-2212 (●), Bi-2223 (□), Bi-2201 (○), $(Ca,Sr)_2PbO_4$ (◊) and $(Ca,Sr)_2CuO_3$ (*). To ease visualization the Bi-2201 concentration is multiplied by 10. The line marks the temperature profile with reference to the temperature scale at the right hand of the figure. From [A14].

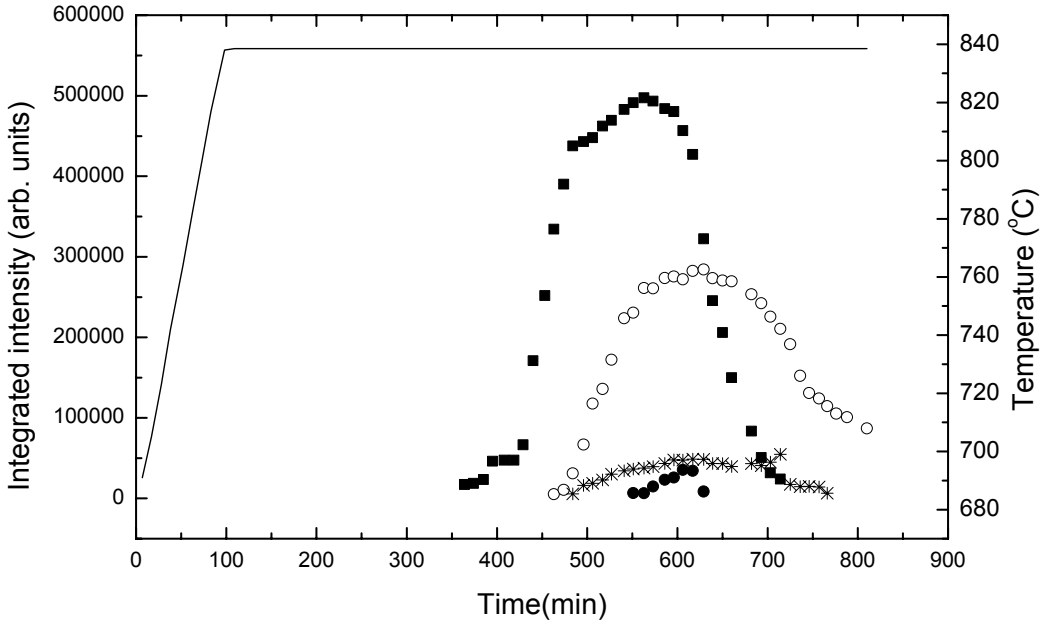

Figure 7.14
The 4 valid growth curves found during *in situ* annealing of a Ag clad Bi-2212 tape in air. Three of the curves relate to Bi-2212 grains (■, *, ●) and one to a Bi-2223 grain (o). The raw integrated intensity is shown as function of annealing time. The line marks the temperature profile with reference to the temperature scale at the right hand of the figure. From [A14].

The conditions in the two studies were similar. To reconcile the macroscopic and meso-scopic results, it is suggested that the microstructural evolution is dominated by the pronounced heterogeneity present in the material. Depending on local differences in the concentration and stoichiometry of phases present, the Bi-2212 to Bi-2223 reaction may run forwards or backwards, at times leading to dissolution of Bi-2223 grains and formation of new Bi-2212 grains. Only on average is the direction of the reaction deterministic. This difference in local behaviour may be important for the performance of the tapes, as the current path is disrupted by the remaining secondary phase particles.

It is noteworthy that many ceramics of current interest display phase diagrams of similar complexity. Hence, it is speculated that such heterogeneous reactions may appear quite frequently, accentuating the relevance of 3DXRD studies.

7.6 Grain size distributions

The grain size distribution is of fundamental importance for the properties of most polycrystals and powders. The standard method to obtain this distribution is by means of optical or electron microscopy; in the last case in particular by EBSP. The process of unfolding the 3D grain size distribution from two-dimensional data is a key problem in stereology [12]. As such it is well known to be non-trivial and associated with three major shortcomings. Firstly a critical assumption is needed on the shape of the grains. Typically these are all taken to be spheres, in which case the algorithms of Saltykov [156] or refinements thereof can be applied. In practice the shape varies substantially from grain to grain and this variation is often a function of size. Secondly, the unfolding is mathematically an ill-conditioned problem, implying that a small variation in the measured data can lead to a much larger error in the results. Hence, a large ensemble of grains is needed just to obtain reasonable counting statistics. And thirdly, the statistical approach only works if the sampling is uniform, isotropic and random. In order to provide such a sampling in general it is required to characterise a set of sections – a tedious task.

Obviously, these shortcomings can be overcome by provision of 3D data. In the past this has been attempted by means of microscopy in combination with serial sectioning. Gundersen has shown that data acquisitions from two parallel and adjacent sections in principle is sufficient – the so-called disector method [157]. However, independent of the number of sections, such methods are associated with their own problems. The requirement to co-planarity of the sections is a challenge to state-of-the-art sectioning equipment. Worse, typically a large number of sections are required in order to provide a sufficiently large ensemble of grains.

By contrast, 3DXRD is an ideal tool. True 3D volumes can be derived, by normalisation of the diffraction data from a reference (see section 3.3 and [A10]). Applying *GRAINDEX*, a box beam and detector configuration B, a large number of grains can be characterised in a relatively short time. Furthermore, the relative error on the determined size of a grain will tend to be small due to the fact that it is the grain volume that is observed. As an example, assume a grain volume is determined from 3DXRD with an accuracy of 20%. Then standard error propagation implies that the size is determined to 6%. In addition, it is of interest that the *GRAINDEX*-based

analysis provides a range of other information about the grains simultaneously, cf. chapter 3.

However, the main advantage of the 3DXRD method is likely to be the ability to measure the size distribution *in-situ.* This opens up for a broad range of coarsening studies, for instance in relation to abnormal grain growth in metals and sintering of powders.

By analogy to the presentation for recrystallization in section 7.2, such studies may be seen as "statistical studies". The complementary "first principles studies" of coarsening will require 3D mapping of the grain boundary network and determination of dihedral angles etc. The relevant methodology for the "first principles approach" was outlined in section 7.2.3, and a feasibility study on abnormal grain growth has been performed by Suter and co-workers [158]. However, for most powders, the current spatial resolution of the 3DXRD microscope prohibits a "first principles approach", emphasising the relevance of "statistical studies".

The main limitation of the suggested 3DXRD method for determining grain size distributions is the constraint on the size, currently ~200 nm. To get around this limitation combined analysis with EM or SANS may be of relevance.

In the following some methodological concerns are discussed.

7.6.1 Methodological concerns

To provide a statistically valid characterisation of the grain size distribution four issues need to be addressed:

- The *sampling of all grains once and only once*. This can be ensured by polycrystalline indexing. As discussed in chapter 3, a program like *GRAINDEX* will also serve as an efficient filter, dismissing peaks arising from stray reflections or from multiple scattering events.
- The *sampling of small grains.* Typical grain size distributions span at most 6 decades in volume. Using 14-18 bit detectors it is possible to cover this range with two exposures, one with and one without a suitable attenuator.
- The *sampling of sub-volumes*. To provide sufficient grain statistics as well as a sampling independent of local fluctuations it may be required to characterise a set of sub-volumes within a larger specimen. An efficient way to do this is by sampling in a 3-dimensional (ω,y,z)-grid, as discussed in section 3.5. The volumes of grains extending over two or more grid points are then found by adding the integrated intensities.
- *The boundary problem.* The grains at the surfaces of a polycrystal are normally cut, and as such not representative. Likewise, the external boundaries of the 3D (ω,y,z) grid introduced above may be internal to the specimen (*e.g.* in the case of the specimen being an extended plate). The grains at these internal boundaries will also be cut in terms of illumination by the beam. In the following two approaches are proposed for dealing with these grain at the external and internal boundaries. The first is a 3D guard-zone technique; the second is based on perturbation analysis.

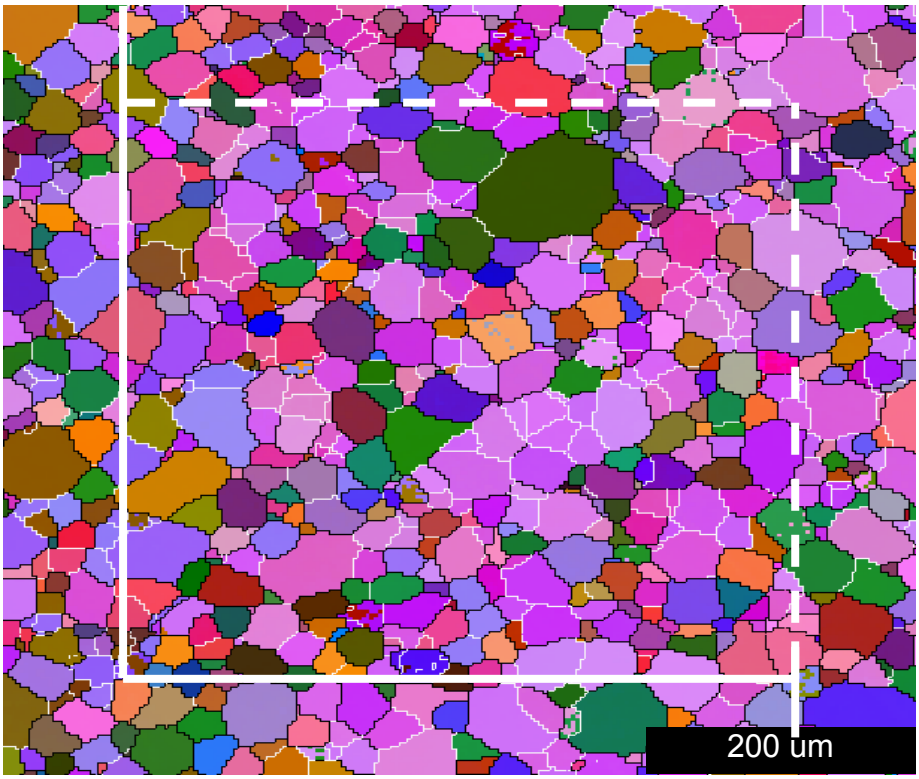

Figure 7.15
Illustration of the guard zone concept in 2D on an EM micrograph of a grain assemblage. The solid white line is the exclusion line. The box-shaped area within the solid and dashed white lines is defined as the internal area, while the remainder is known as the guard zone. All grains that are situated only in the internal area, are included in the statistical analysis, while those situated only in the guard zone are not. Grains situated at the boundary between the guard zone and the internal area are included if and only if they do not cross the exclusion line. The micrograph is from [159].

Treating boundary problems in 2D by introducing guard-zones is standard in stereology [12,157]. The essence of the method is illustrated in Fig 7.15. Grains that protrude from the inner part into the guard zone are included if and only if they do not cross the exclusion line.

A 3DXRD solution would be to acquire data in the (ω,y,z)-grid introduced above. The grid should be a real 3D grid implying that data is acquired around two ω settings 90^{o} apart. (To avoid cutting plate shaped specimens the two settings would be at angles of -45^{o} and 45^{o} to the plate normal.) Based on this grid a 3D "guard frame" and "exclusion planes" are drawn.

The 3D guard zone approach ensures a statistically-correct sampling. However, it is somewhat time-consuming. As a faster but less precise alternative a perturbation analysis may be applied. The underlying concept is first to accept the experimental size distribution. Then based on this distribution and an assumption of spherical grains to simulate the number of grains cut as function of size, and correct the experimental distribution accordingly. The accuracy will depend on the surface-to-volume ratio in the 3D grid.

For characterization of powders the last two of the four issues addressed above can be circumvented by deposition of the powder onto a microscope slide in a thin layer with an average thickness around 1 grain. In this case the issue of the external surfaces is irrelevant, as no grains have been cut, and with a thin specimen the beam size can be made much larger than the grain size, such that the number of grains cut by the internal surfaces is negligible. Likewise, the number of grains rotating out of the beam will be small.

7.7 Crystallography

Traditionally, x-ray crystallography is based on either powder diffraction data or single crystal studies. Both methods have their distinct advantages. Single crystal data are indispensable for structural refinement of large molecules, in particular proteins, and for high accuracy work such as the generation of charge density maps. Powder diffraction, on the other hand, is required for *in-situ* dynamic studies and for use whenever suitable single crystals are not available. This includes most applied studies.

The work presented in this thesis points to a third route, based on indexing of polycrystalline data. In the following a discussion is made of the potential use of the tools presented in chapter 3-4 more generally, including applications outside materials science. The focus is on two topics: structural solution and refinement in general, and the identification and characterisation of structural phases appearing in parts-per-million (ppm) concentrations.

7.7.1 Structure determination from polycrystalline data

Single crystal data are clearly preferable for structural solutions and refinement due to the better signal-to-noise ratio, the larger number of independent reflections and the provision of multiple symmetry-equivalent reflections. By contrast, the information content in a powder diffraction pattern is much reduced. Recently, significant progress in powder diffraction methodology has been reported [160-163]. Nevertheless, a structural solution is often impossible, in particular for structures with more than 20 atoms in the unit cell.

Hence, there are numerous cases where a structure determination today is impossible, due to the lack of suitable single crystals. These arise for instance in relation to studies in extreme environments, studies involving first-order transitions or cases where a suitable synthesis route has not been found. In addition, existing polycrystalline samples may be too precious or fragile to be fragmented into individual crystals.

As an alternative route to structural solutions and refinement, in [A15] it is suggested to characterise the individual grains within a polycrystal or a powder. A two-step analysis is applied: first diffraction spots are sorted with respect to the grain of origin by an indexing program such as *GRAINDEX*. Then any conventional single crystal refinement program is used for determining the crystal structure of the grains. Depending on whether the grains can be assumed to be crystallographically identical a set of refinements of the individual grains or an average refinement based on all the diffraction spots can be performed.

The feasibility of this scheme is demonstrated in [A15] by refining the grains within a sintered plate of a reference material, α-Al_2O_3. From 1500 grains in the gauge volume the 57 largest ones were selected. Refinements to individual grains as well as to the grain average are found to have a quality comparable to single crystal studies – and out perform powder diffraction data.

It appears that the *only* differences between the requirements for a single-crystal and a multi-crystal refinement are the issues of spot-overlap and secondary extinction. These issues have been dealt with previously, in sections 3.2 and 2.4, respectively.

For an implementation of the method it is likely that *GRAINDEX* needs to be substituted by a new multi-grain indexing and spot integration program. In *GRAINDEX*, the integration of a spot is performed by summing over the intensities within an area-of-interest in the image. In the new program this should be replaced by fitting to a 3D peak profile as is customary in crystallography. This would increase the accuracy. By applying the program iteratively overlapping spots could be refined. Such a program is presently being developed at ESRF [164].

The potential for application is wide-ranging. As examples:

- In the context of *biochemistry* it is remarkable that there is no direct limitation on the number of atoms in the unit cell in the multi-crystal refinement scheme. Hence, it appears that *GRAINDEX* might be applied to large molecules, where powder diffraction will fail. Furthermore, many grains from a single sample can be refined simultaneously, allowing complete and redundant data to be acquired with only a small sample rotation. This is of interest in connection with highly radiation-sensitive samples.
- In *high pressure* studies, whether related to geo-science or condensed matter physics, single crystal specimens will often undergo phase transformations which unavoidably turn them into polycrystals.
- In *materials science* phases are often non-stoichiometric. The characterisation of the stoichiometry for each grain may be based on the lattice parameters, as discussed in sections 3.3 and 7.5. However, in some cases the lattice parameter changes will be masked by strain or the relationship between lattice parameter and stoichiometry is unknown. In such cases it is relevant to perform full structural refinements.

7.7.2 Structural phases appearing in ppm concentrations

The identification and characterisation of structural phases appearing in minute volume fractions is of interest in many fields, *e.g.* materials science, forensic science, geosciences and environmental sciences. Trace analysis of the atomic elements can be performed by numerous methods, including mass spectrometry and x-ray fluorescence analysis. In favourable cases these can probe concentrations as small as 10^{-15}. However, such methods cannot reveal information on the structural phase involved. Furthermore, they are either destructive or only sensitive to surface regions.

Minority phases can be identified non-destructively by x-ray powder diffraction, down to concentrations of the order of 10^{-3}. The ultimate limit is the background arising from incoherent scattering within the specimen. Notably, increasing the size of

the illuminated volume doesn't alleviate the problem, as both the signal and the background are proportional to volume.

In comparison, use of 3DXRD is very advantageous, provided the grains of the minority phase are larger than the detection limit of currently ~ 200 nm. The distinct diffraction spots are much more visible than the powder diffraction rings. Substituting "novel phase" by "novel orientation", the case was outlined in section 7.3.2. Concentrations of the order of $10^{-6} – 10^{-5}$ can be found by a single ω scan. Moreover, by repeating this procedure at other sample positions, the required volume fraction is reduced proportionally. Hence, particles occurring in a concentration of 10^{-9} can be identified within some hours of beam time. For each of these, the analysis tools of chapter 3 can be applied, providing a complete structural description in terms of position, orientation, elastic strain, etc. Once positions are known detailed on-line investigations can be performed in the neighbourhood of the particle. Alternatively, the particles may be exposed to surface sensitive analysis tools by proper sectioning.

8. Outlook

So far the 3DXRD microscope has mainly been applied to fundamental studies in metallurgy. As demonstrated in sections 7.1-7.5 the method is sufficiently developed to answer a range of basic questions, which cannot be addressed directly in any other way. In passing, one may note that it is of interest to repeat the experiments already performed for other metals and alloys to study the influence of for example, the stacking fault energy of the material, the grain size, the presence of alloying elements or the annealing temperature.

Technically, the ultimate aim for this type of research is a complete *in-situ* characterization of the microstructural dynamics for a given specimen during a series of deformation and annealing steps. It is too early to conclude the feasibility of such studies. However, some major milestones can be identified: 6D reconstructions of deformed materials, and an improvement of the spatial resolution of both 2D detectors and conical slits.

The prospect of applying 3DXRD to other classes of hard materials such as ceramics, intermetallics and composites equals that for metals. Some examples were given in section 7.5. Two other areas, where experiments recently have been made are:

- *Domains:* Many classes of materials form domains, which have characteristic orientation relationships to each other. Important examples are the twins occurring in ferro-elastic and co-elastic crystals [165] and the domains in ferro- and piezo-electric materials [166]. Quite often the domains are sufficiently large that they can be detected by 3DXRD. Hence, it seems feasible to study the switching between individual domains within single crystals or polycrystals subject to an external mechanical or electric field. Orientation contrast suffices to index the diffraction spots and therefore to determine which domains belong to the same grain. For reasons similar to those related to polycrystalline deformation, such *bulk* studies of the microstructural dynamics would provide unique tests of the constitutive models for these materials.

- *Nano materials:* nano-scale structures of hard materials are of great interest for the development of materials with new or improved mechanical, electrical or magnetic properties. Characterizing these structures can be seen as the ultimate challenge to 3DXRD. First results for structures with a grain size of 200 nm were presented in section 7.3. Individual grains in the nano regime below 100 μm cannot as yet be detected. Nevertheless 3DXRD studies can be of interest, namely in connection with studies of the stability of such structures. It is not known how the increased interfacial area, which is a natural consequence of the structural refinement, affects the dynamics of thermally-activated processes. *In-situ* measurements of the coarsening kinetics during annealing would provide vital information in that respect.

More generally, it should be emphasized that the 3DXRD method applies universally to studies of polycrystals. As such applications may be foreseen within a variety of fields including geo-science, mineralogy, environmental science, crystallography and high pressure physics.

In the following, foreseeable hardware improvements are presented. Then, a discussion is given as to what extent the 3DXRD methodology can be transferred to use with laboratory x-ray, neutron and electron sources. Next, recent x-ray diffraction studies by other groups are summarized. These either aim at 3D structural characterization or the method used could be extended to such studies. They are based on scanning methods, using lower x-ray energies.

8.1 Hardware improvements

Flux:
The ultimate limiting factor for 3DXRD is the photon flux impinging on the relevant part of the specimen. This flux is determined by the properties of the synchrotron, the insertion devices used at the beamline and the focusing optics.

In the short term, beamline ID11 at ESRF will be equipped with a new insertion device, an in-vacuum undulator. That should increase the flux by a factor of 4. With respect to the focusing optics, the present detection limit of 200 nm was determined in section 7.3 from measurements performed with a 7x7 μm^2 beam. By use of the optimal setting of 2x5 μm^2 another factor of 4 is expected. Summing the two flux gains, characterization of 100 nm sized structures should be within reach with the 3DXRD microscope.

There are two ways to lower the detection limit even further. The first is to focus to a spot-size smaller than the 2x5 μm^2 presently obtainable. This will be feasible with a new generation of x-ray optics, or alternatively by reducing the distance from the focusing optics to the specimen. The second is to perform experiments at lower x-rays energies, at the expense of penetration power. Such studies cannot be performed with the current 3DXRD microscope, though.

In the long-term, several new synchrotron facilities will be built. The PETRA-II ring in Hamburg will be converted to a dedicated synchrotron source from 2007. Likewise, one or more energy-recovery-linacs are likely to be built within the next decade or two. These linacs will allow for a much better focusing of the beam.

Even more spectacular is the plan to construct an x-ray laser in Hamburg, the XFEL [167]. Once completed in 2012, this facility will provide completely unprecedented, in fact revolutionary, opportunities for structural studies. Instead of basing structural information on integrated intensities (diffraction), the microstructure can be reconstructed from observations of the phase shift of the x-rays. Hence, the XFEL will allow 3D structural studies to be performed with (near-) atomic resolution, at least for small specimens of a size of a few micrometres. Feasibility studies of this kind using 3rd generation synchrotrons – which are partially coherent - have been performed recently [168,169]. A discussion of reconstruction by means of phase methods is not within the scope of this thesis. However, it is noteworthy that the XFEL in addition to generating a laser pulse in the 10 keV range also will give rise to spontaneous emission in the hard x-ray region. This part of the spectrum may be used for 3DXRD experiments of the type outlined in this thesis, with an estimated gain in flux of 100 in the 50-100 keV range. Furthermore, the number of photons is estimated

to be appreciable up to 1 MeV, which would provide a penetration power of at least 5 mm in all materials [167].

Spatial resolution:
In chapter 4 the spatial resolution was shown to be limited by the width of the point-spread-function of the high-resolution 2D detector. The point-spread-function in turn is a function of the thickness of the fluorescence screen.

At the time of writing, the plan is to equip the 3DXRD microscope with a new 2D detector, based on the same optics principle but equipped with a thinner screen, an 800 nm thick Gd_2O_3:Eu single crystal. This detector is specified to have a spatial resolution (FWHM) of ~2 μm at 60 keV. At the same time, for the same thickness the efficiency of the fluorescing crystal should be 10 times higher than the one presently used.

However, it is unlikely that the present detector principle will be able to provide a resolution below 1 μm. Generally speaking, the intensity per pixel decreases in proportion to pixel area and in proportion to the thickness of the screen. Hence, a compromise between spatial resolution and time resolution is required.

There are two potential roads to obtain a sub-micrometre spatial resolution, the first being the development of new types of detectors and the second the use of scanning principles. The schemes based on scanning the sample with respect to the beam are inherently much slower than the "tomographic" procedures presented in chapter 3 and 4. This disqualifies them for general mapping purposes. However, they might have a potential as an add-on for optimal resolution, provided coarser maps are generated by other means.

To illustrate the use of a scanning principle, a schematic drawing of the so-called *focusing analyzer scheme* [A50] is reproduced in Fig 8.1. In this scheme, a focusing optical element such as a multi-layer (ML) is inserted in the beam path between the sample and the detector, and adjusted to a specific reflection. The sample is illuminated by a pencil beam. This scheme has the intriguing features that:

- the projection of the illuminated line through the specimen is magnified.
- the strain and spatial degrees of freedom are separated by construction.
- the distance from the sample to the ML can be 10-30 centimetres.

Hence, the scheme has the potential to increase the spatial resolution as well as to overcome two of the main limitations related to deformed specimens. Unfortunately, there are also severe disadvantages:

- the ML only probes the material at a given azimuthal setting. In order to sample orientation space, the specimen must therefore be scanned around at least one extra axis of rotation in addition to the scan around the ω axis. Hence, to probe a given part of the specimen fully a 4-dimensional scan is required.
- the ML characterizes only one family of reflections, say {311}. Realigning the ML for another family would be very time consuming.

The focusing analyser scheme was verified in a test experiment using available optics [A50]. The depth resolution inferred was 10 μm, limited by aberrations in the optics. This number can be improved substantially by the use of a dedicated ML design. However, substantial additional work would be required to turn the focusing analyser scheme into a tool for routine operation.

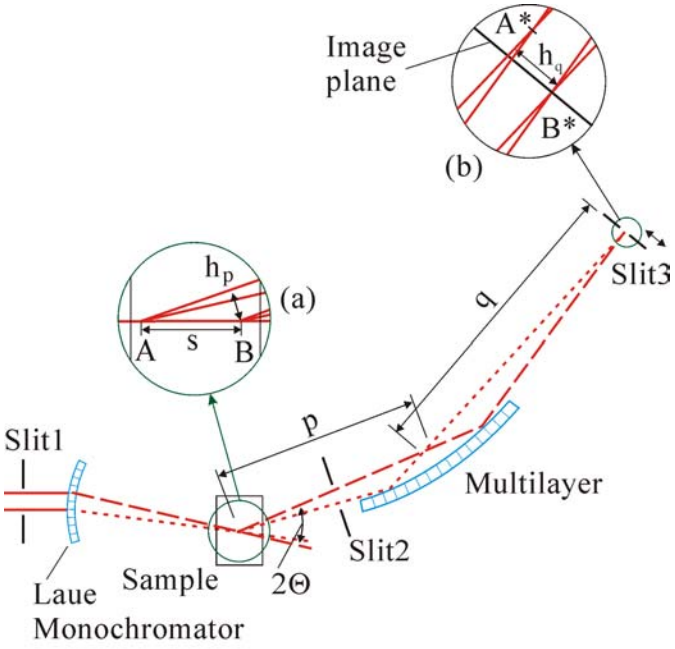

Figure 8.1
Sketch of the focusing analyser set-up when used in combination with a Laue crystal monochromator. X-rays are reflected by the Laue monochromator within a certain energy band. The path of the low/high energy part of this band is indicated by long/short dashed lines. The insets (a) and (b) clarify the focal properties in the object and image plane, respectively. The multilayer is adjusted such that B and B^* are in the focal points. The projection of the distance AB, h_p, is magnified in the image plane: $h_q = h_p*(q/p)$. From [A50].

Spot overlap:
Reducing the spot overlap seems only possible by further reducing the gauge volume. With the manufacturing technology presently used - wire electro-discharge machining – it is unlikely that conical slits can be produced with gaps smaller than 10 μm. Hence, further development of the lateral resolution will require the use of alternative technologies, *e.g.* lithography (LIGA) or the use of a Focused Ion Beam (FIB).

8.2 Applying 3DXRD methods to other sources

Most of the geometric principles outlined in chapters 3 and 4 are applicable to studies with a laboratory x-ray source. What is required is a W target for generation of hard x-rays, a rotation stage and a suitable 2D detector – all standard equipment. In addition focusing optics are generally needed, otherwise the flux becomes prohibitively low. Suitable focusing optics for hard x-rays are not readily available, but have to be developed according to specifications of the actual set-up. Furthermore, *GRAINDEX* and the *ART* reconstruction routines need minor modifications such as taking beam divergence into account.

The fraction of laboratory x-ray diffractometers equipped with a W source is small. Commonly, instruments are equipped with Cu, Mo or Ag targets, generating x-rays in the 8 - 22 keV range. In comparison to work with W targets, there is a substantial gain in both flux and scattering cross sections. Furthermore, focusing optics are available and the projection angle becomes less steep, see Fig 2.3. Disadvantages are the lack of penetration power and the prominence of extinction, cf. chapter 2. However, with respect to the 3DXRD technique the main disadvantage is the fact that the scattering angles are too large to enable the full diffraction pattern to be monitored by standard 2D detectors, which are flat.

In any case, in a laboratory-based set-up the flux is reduced by many orders of magnitude in comparison to the synchrotron, implying a degradation of the detection limit and the spatial resolution. For static studies, this can be partly compensated by very long exposure times. As pointed out by Hirsch and Kellar [16-18], in favourable cases structures with a size around 1 μm can be identified.

The prospect for use of 3DXRD algorithms with neutrons is similar. Existing neutron diffractometers qualify as the equivalent of the x-ray set-up with a box beam and detector configuration B. *GRAINDEX* and the associated algorithms can be directly applied, with the exception that the 2D detectors typically are curved and not flat. The clear disadvantage of neutron 3DXRD in comparison to synchrotron 3DXRD is the flux. The detection limit with current reactor sources is in the range 20-100 μm. On the other hand, the neutrons can in principle handle larger specimens, in particular for components comprising heavy elements. At the same time the aspect ratio of gauge volumes will be close to 1:1, as the scattering angles typically are close to 90 degrees.

A simple application of neutron 3DXRD could be for parametric studies. The suggestion is to assemble an artificial polycrystal from a set of single crystals corresponding to the different parameter settings. These can then be studied simultaneously, saving beam time. Likewise, it is often the case that crystals of optimal size cannot be synthesized for neutron diffraction studies. Using 3DXRD a set of identical crystals can be studied simultaneously, increasing the statistical accuracy.

Combining 3DXRD with EM is more troublesome, due to the limited penetration, the smaller Bragg angles and in particular the dynamical scattering effects. The most promising approach might be to implement *GRAINDEX* for use with Selected Area Diffraction (SAD) images of polycrystals. (Extinction is in this case less of a concern, as the indexing program in configuration B only relies on intensities in the sense that the diffraction spots must be visible.) This would require that the size-broadening from the thin foil is taken into account.

8.3 Other 3D resolved x-ray diffraction work

Independently of the work in this thesis, two other approaches for 3D diffraction studies have been developed. The first method is due to Ice, Larson and co-workers from Oak Ridge [3, 170-172]. Their method is an extension of the Laue method, well known from single crystal crystallography [31]. A polychromatic beam is used with an energy band sufficiently broad that all illuminated microstructural elements give

rise to diffraction simultaneously, without the need for a rotation in ω. A polycrystal indexing scheme for the Laue method was developed by Chung and Ice [173].

Three-dimensional information is obtained by triangulation, using an incoming beam focused to a sub-micrometre size. Between the specimen and a 2D detector a highly absorbing wire is positioned. For fixed sample position the wire is scanned transverse to the beam, and the absorption of the diffracted signal caused by the wire is monitored. By additional scanning of the specimen in y and z, complete information is obtained in 3D of the position, orientation and elastic strain of the microstructural elements. The method has been implemented at APS using energies around 20 keV.

Comparing the 3DXRD and the Laue methods with respect to their specifications at the time of writing, typically the penetration power of 3DXRD is several orders of magnitude larger, due to the difference in x-ray energy. Likewise, for the same set-up a Laue-based method always generates more diffraction spots than a (monochromatic) rotation-based method. Hence, the spot overlap issue is accentuated. On the other hand, the spatial resolution of the Oak Ridge method is superior, presently slightly better than 1 μm [3]. Furthermore, this method enables three-dimensional maps of the elastic strains.

However, the main conceptual difference between the methods is the distinction between a “tomographic approach” and a “scanning approach”. As argued at length in this thesis tomographic approaches are faster.

The second method is due to Wroblewski and co-workers from HASYLAB [4]. Using an 8 keV beam, their set-up comprises a 4-circle diffractometer and a micro-channel plate in front of a CCD. The micro-channel plate serves as a set of collimators, arranged in a 2D grid. The spatial resolution reported is 12 μm. This set-up provide a large degree of parallel data output, as all positions within one plane in the specimen can be characterised with respect to a fixed angle simultaneously. Hence, it can provide extended maps in the powder limit, *e.g.* the position of various fine-grained phases. The method could be extended to depth-resolved meso-scopic studies. However, for complete characterisation a 4D scan would be required.

9. Conclusions

A novel method, 3DXRD, is established for structural characterisation of polycrystals and powders. The method is based on the use of a monochromatic beam of high energy x-rays from a synchrotron source ($E \geq 50$ keV). It involves a "tomographic" approach to diffraction, enabled by the acquisition of data by a set of area detectors. Uniquely, the method provides a non-destructive and essentially complete 3D characterization of the individual microstructural elements (grains and sub-grains) within millimetre-to-centimetre sized specimens. Furthermore, the dynamics of the individual elements can be monitored during typical processes such as deformation or annealing. Hence, for the first time information on the interaction between elements can be obtained directly.

More specifically,

- A universal polycrystal-indexing program, *GRAINDEX*, has been developed. In favourable cases several thousand grains can be indexed simultaneously. Based on this program, the individual grains can be characterised with respect to their position, volume, average orientation and average elastic strain tensor. *GRAINDEX* supports all space-groups and applies to multi-phase as well as single-phase materials. In addition to studies of grains it is also used for studies of individual embedded dislocation structures, inclusions or domains. There are only two limitations: the structural elements must be larger than the detection limit, and the diffraction spots should not overlap. The latter limitation can to a certain extent be overcome by inserting a conical slit between the specimen and the 2D detector. *GRAINDEX* has been used extensively, for static as well as dynamic studies.

- A mathematical formalism for reconstructing the microstructure of a specimen from 3DXRD data has been established. It is based on generalisations to higher dimensional spaces of principles known from medical imaging. At the time of writing, the formalism has been used for generation of 3D grain maps for undeformed specimens. Following the completion of a general-purpose program the aim is to generate maps of the microstructure also for deformed specimens, and to enable structural characterisation in general for the case of overlapping diffraction spots. A conclusion on the latter prospect must await experimental tests.

- A suite of unique experimental tools has been developed for characterisation of plastic deformation. These tools complement each other with respect to length scale, information content and the degree of deformation accepted. The tools have been implemented to a varying degree, ranging from "routine operation" to "analysis of feasibility study in progress". Specifically, by 3DXRD the average plastic response of a given grain can be derived from measurements of the rotation of the grain, the evolution in the associated lattice strains or by comparing the grain morphology before and after deformation. The variation in response within a grain can be characterised in direct space by reconstruction of the local changes in orientation, and in an integral way by peak shape analysis. In addition the displacement gradient

tensor can be mapped directly by tracing the displacement of dispersed marker particles by absorption contrast tomography. In outlook, by combining the tools a very comprehensive description of plastic deformation is enabled. Hence, a direct determination of active slip systems should be possible.

- A dedicated instrument for 3DXRD studies, the 3DXRD microscope, has been established at ESRF. The spatial resolution is determined by the available detectors; at present it is 5 μm. The detection limit is much smaller: 200 nm, while the time resolution varies between 1 second and 1 hour, depending on application. Since the commissioning of the instrument at the end of 1999 a diverse user community has emerged, with experimentalists coming from more than 20 laboratories in Europe and the US.

- Selected fundamental issues in metallurgy have been pursued by 3DXRD. Annealing experiments, whether in connection with recrystallization or phase transformations, whether on Al, steel or ceramics, display large variations in the nucleation and growth behaviour of the grains, due to the influence of the local environment. The results demonstrate the gross simplification made by standard models such as JMAK, which assume all grains (of the same orientation) to exhibit the same dynamics. Studies of polycrystal deformation in Al demonstrate that the rotation paths for the individual grains exhibit a clear dependence on initial grain orientation, while the effect of grain-grain interaction is relatively small. The paths do not match predictions from standard models. A first study of the evolution of lattice strains indicates that the variation between a set of equivalent grains is substantially smaller than expected from FEM simulations. This is interpreted as an indication of the strain fields being screened by the emerging dislocation structures.

- The multi-grain approach to diffraction may be seen as a third route in crystallography, an alternative to powder diffraction and single crystal diffraction. In particular, a multi-grain refinement procedure has been demonstrated on a sintered plate of α-Al_2O_3, with results of a quality that equals those from single crystal studies. The procedure as such is independent of the size of the unit cell. Hence, it is expected that it will be of use within a broad range of fields, also outside of materials science, *e.g.* in the field of macromolecular chemistry.

Acknowledgments

Synchrotron instrumentation requires by nature a collaborative effort. Hence, the 3DXRD methodology has been developed by a team comprising Xiaowei Fu, Stephan Garbe, Carsten Gundlach, Axel Larsen, Erik Mejdal Lauridsen, Lawrence Margulies, Rene Martins, Søren Fæster Nielsen and Søren Schmidt. The implementation at ESRF was only possible thanks to the dedication and expertise by the in-house staff, in particular, Andy Goetz, Åke Kvick, and Gavin Vaughan from beamline ID11, Miguel Nicola from the metrology group, and Heinz Graafsma from the detector group.

The 3DXRD applications with relation to metallurgy have emerged from discussions within the Materials Science Department at Risø. As such, it is a pleasure to acknowledge the contributions from my colleagues: Jacob Bowen, Roger Doherty, Niels Hansen, Xiaoxu Huang, Oleg Mishin, Torben Leffers, Torben Lorentzen, Wolfgang Pantleon, John Wert, and Grethe Winther. Most importantly, I thank Dorte Juul Jensen for her continuous support and for a rewarding, friction-less and wide-ranging collaboration over the last 7 years.

The work on superconducting tapes was performed with colleagues Lotte G. Andersen, Niels Hessel Andersen, Thomas Frello, Jean-Claude Grivel, Bruno Kindl and Yi-Lin Liu at Risø. This and other work at the DORIS synchrotron has benefited strongly from the collaboration with the group of Jochen Schneider at HASYLAB, including Felix Beckmann, Jens Homeyer, Thomas Lippmann, Thomas Tschentscher and Martin von Zimmermann.

It is a pleasure to acknowledge a long-standing collaboration with Ulrich Lienert, who has been a driving force behind first the development of the x-ray optics, then the strain scanning principle for materials engineering and lately for establishment of the set-up at APS. The collaboration on shape analysis further involves John Almer, and Wolfgang Pantleon.

With the external use of the 3DXRD microscope, collaboration on a number of projects has naturally emerged. Among these are work on fatigue with Wolfgang Ludwig and Jean-Yves Buffiere from EMSA, Lyon, work on recovery with Julian Driver from Ecoles des Mines, St. Etienne, and work on martensitic phase transformations with Erik Offerman, Suzelotte Kruijver, Jilt Sietsma and coworkers from the University of Delft.

For the possibility to test various components at beamline ID15 at ESRF, I am indebted to Thomas Buslaps and Veijo Honkimäki. Furthermore, for discussions on image analysis, reconstruction and texture representations I acknowledge Robert M. Suter, Jan Teuber, Adam Morawiec, Gabor Herman and Sine Jensen. For very skilful help with experimental work in general I am grateful to Cliver Klitholm, Palle Nielsen, Helmer Nilsson, Preben Olesen and Ove Rasmussen.

Finally, I'm grateful to Roger Doherty, Dorte Juul Jensen and Brian Ralph for reading and discussing this manuscript.

References

Authors Publications

A1. H.F. Poulsen, S. Garbe, T. Lorentzen, D. Juul Jensen, F.W. Poulsen, N.H. Andersen, T. Frello, R. Feidenhans'l, and H. Graafsma (1997). *J. Synchrotron Rad*. **4,** 147-154.

A2. E.M. Lauridsen, S. Schmidt, R.M. Suter, and H.F. Poulsen (2001). *J. Appl. Cryst*. **34,** 744-750.

A3. H.F. Poulsen, S.F. Nielsen, E.M. Lauridsen, S. Schmidt, R.M. Suter, U. Lienert, L. Margulies, T. Lorentzen and D. Juul Jensen (2001). *J. Appl. Cryst*. **34,** 751-756.

A4. H.F. Poulsen and X. Fu (2003). *J. Appl. Cryst.*, **36**, 1062-1068.

A5. H.F. Poulsen and S. Schmidt (2003). *J. Appl. Cryst*. **36**, 319-325.

A6. H.F. Poulsen (2003). *Phil. Mag.* **83**, 2761-2778.

A7. S.F. Nielsen, H.F. Poulsen, F. Beckmann, C. Thorning, and J.A. Wert (2003). *Acta Mat*. **51**, 2407-2415.

A8. L. Margulies, G. Winther, and H. F. Poulsen (2001). *Science* **291**, 2392-2394.

A9. H.F. Poulsen, L. Margulies, S. Schmidt, and G. Winther (2003). *Acta Mat.* **51**, 3821-3830.

A10. E.M. Lauridsen, D. Juul Jensen, H. F. Poulsen, and U. Lienert (2000). *Scripta mater.* **43,** 561-566.

A11. E.M. Lauridsen, H.F. Poulsen, S.F. Nielsen and D. Juul Jensen (2003). *Acta Mat*. **51**, 4423-4435.

A12. H.F. Poulsen, E.M. Lauridsen, S. Schmidt, L. Margulies, and J.H. Driver (2003). *Acta Mat*., **51**, 2517-2529.

A13. S.E. Offerman, N.H. van Dijk, J. Sietsma, S. Grigull, E.M. Lauridsen, L. Margulies, H.F. Poulsen, M.T. Rekveldt, and S. van der Zwaag (2002). *Science* **298**, 1003-1005.

A14. L.G. Andersen and H.F. Poulsen (2001). In *Studies of high temperature superconductors*, *Ed: A. Narlikar* (Nova Science, New York), **36,** 29-87.

A15. S. Schmidt, H.F. Poulsen and G.B.M. Vaughan (2003). *J. Appl. Cryst*., **36**, 326-332.

A16. H.F. Poulsen and D. Juul Jensen (1995). *Proc. of 16th Risø Int. Symp. on Mat. Science, Risø 4-8 September 1995, Eds: N. Hansen et al.* (Risø Nat. Lab., Roskilde, Denmark), pp 503-508

A17. S. Garbe, H.F. Poulsen, and D. Juul Jensen (1996). *Proc. of ICOTOM-11, Xi'an, 16-20 Sep 1996, Eds: Z. Liang, L. Zuo, Y. Chu, International Academic Publishers, Beijing*, **1**, 100-105.

A18. T. Lorentzen, A.P. Clarke, H.F. Poulsen, S. Garbe and H. Graafsma (1997). *Composites A* **28,** 667-674.

A19. H.F. Poulsen, T. Lorentzen, R. Feidenhans'l, and Y.L. Liu (1997). *Metall. Mater. Trans. A* **28,** 237-243.

A20. U. Lienert, C. Schulze, V. Honkimäki, T. Tschentscher, S. Garbe, O. Hignette, A. Horsewell, M. Lingham, H.F. Poulsen, N.B. Thomsen, and E. Ziegler (1998). *J. Synchrotron Rad.* **5,** 226-231.

A21. S.F. Nielsen, A. Wolf, H.F. Poulsen, M. Ohler, U. Lienert, and R.A. Owen (2000). *J. Synchrotron Rad.*, **7**, 103-109.

A22. J.R. Schneider, R. Bouchard, T. Brückel, M. Lippert, H.-B. Neumann, H.F. Poulsen, U. Rütt, T. Schmidt and M. von Zimmermann (1994). *J. Phys. IV France* **4,** 415-421.
A23. R. Bouchard, D. Hupfeld, T. Lippmann, J. Neuefeind, H.-B. Neumann, H.F. Poulsen, U. Rütt, T. Schmidt, J.R. Schneider, J. Sussenbach, and M. von Zimmermann (1998). *J. Synchrotron Rad.* **5,** 90-101.
A24. H.F. Poulsen, J. Neuefeind, H.-B. Neumann, J.R. Schneider, and M.D. Zeidler (1995). *J. Non-Cryst. Solids* **188**, 63-74.
A25. P. Schleger, R. Hadfield, H. Casalta, N.H. Andersen, H.F. Poulsen, M. von Zimmermann, J.R. Schneider, R. Liang, P. Dosanjh, and W.N. Hardy (1995). *Phys. Rev. Lett.* **74**, 1446-1449.
A26. H.-B. Neumann, H.F. Poulsen, U. Rütt, J.R. Schneider, and M. von Zimmermann (1995). *Phase Transit*. **55**, 17-35.
A27. T. Lippmann, P. Blaha, N.H. Andersen, H.F. Poulsen, T. Wolf, J.R. Schneider and K.-H. Schwarz (2003). *Acta Cryst.* **A59**, 437-451.
A28. H.F. Poulsen, T. Frello, N.H. Andersen, M.D. Bentzon, and M. von Zimmermann (1998). *Physica C* **298,** 265-278.
A29. O.V. Mishin, E.M. Lauridsen, N.C. Krieger Lassen, G. Brückner, T. Tschentcher, B. Bay, D. Juul Jensen and H.F. Poulsen (2000). *J. Appl. Cryst.,* **3**, 364-371.
A30. U. Lienert, S. Grigull, Å. Kvick, R.V. Martins, and H.F. Poulsen (2001). *Proc. of ICRS-6 Oxford (UK), July 2000*, 1050-1057.
A31. L. Margulies, T. Lorentzen, H.F. Poulsen and T. Leffers (2002). *Acta Mat.* **50**, 1771-1779.
A32. U. Lienert, L. Margulies, S.F. Nielsen, S. Schmidt, T. Leffers, and H.F. Poulsen. Submitted.
A33. S. Kruijver, J. Sietsma, S.E. Offerman, N. van Dijk, L. Margulies, E.M. Lauridsen, S. Grigull, H.F. Poulsen, and S. van der Zwaag (2002). *Steel Res.* **73,** 236-241.
A34. D. Juul Jensen, Å. Kvick, E.M. Lauridsen, U. Lienert, L. Margulies, S.F. Nielsen and H.F. Poulsen (2001). *Proc. of 5. MRS Fall meeting, Boston, 29 Nov - 3 Dec 1999. Eds.: S.R. Stock et al. , Mat. Res. Soc. Symp. Proc.* **590,** 227-240.
A35. G. Winther, L. Margulies, H.F. Poulsen, S. Schmidt, A.W. Larsen, E.M. Lauridsen, S.F. Nielsen and A. Terry (2002). *Mat. Science Forum* **408-412**, 287-292.
A36. U. Lienert, R. Martins, S. Grigull, M. Pinkerton, H.F. Poulsen and Å. Kvick (2000). *Mat. Res. Soc. Symp. Proc.* **590**, 241-246.
A37. H.F. Poulsen, D. Juul Jensen, T. Tschentscher, L. Wcislak, E.M. Lauridsen, L. Margulies and S. Schmidt (2001). *Textures & Microstructures* **35**, 1, 39-54.
A38. X. Fu, H.F. Poulsen, S. Schmidt, S.F. Nielsen, E.M. Lauridsen, and D. Juul Jensen (2003). *Scr. Mater*. **49**, 1093-1096 .
A39. U. Lienert, H.F. Poulsen, and Å. Kvick (2001). *AIAA Journal*, **39**(5), 919-923.
A40. U. Lienert, S. Keitel, W. Caliebe, C. Schulze-Briese, and H.F. Poulsen (2001). *Nucl. Instr. Meth. Phys. Res.* A, **467-468**, 659-662.
A41. S.F. Nielsen, W. Ludwig, D. Bellet, E.M. Lauridsen, H.F. Poulsen, and D. Juul Jensen (2000). *Proc of the 21st Risø Int. Symp. on Mat. Science*, *Ed: N. Hansen et al*. (Risø Nat. Lab., Roskilde, Denmark:), pp 473-478.
A42. G. Winther, L. Margulies, S. Schmidt and H. F. Poulsen. Submitted.

A43. S.O. Kruijver, L. Zhao, J. Sietsma, E.M. Lauridsen, H.F. Poulsen, S.E. Offerman, N.H. van Dijk, L. Margulies, S. Grigull, and S. van der Zwaag (2003). *J. Phys. IV* **104**, 499-502.
A44. T. Frello, H.F. Poulsen, L.G. Andersen, N.H. Andersen, M.D. Bentzon and J. Schmidberger (1999). *Supercond. Sci Technol*. **12**, 293-300.
A45. H.F. Poulsen, L.G. Andersen, T. Frello, S. Pratontep, N.H. Andersen, S. Garbe, J. Madsen, A. Abrahamsen, M.D. Bentzon, and M. von Zimmerman (1999). *Physica C* **315**, 254-262.
A46. L.G. Andersen, H.F. Poulsen, T. Frello, N.H. Andersen, and M von Zimmermann (1999). *IEEE Trans. Appl. Supercond*. **9**, 2758-2761.
A47. L.G. Andersen, H.F. Poulsen, A.B. Abrahamsen, B.A. Jacobsen and T. Tschentscher (2002). *Supercond. Sci. Technol*. **15**, 190-201.
A48. H.F. Poulsen, N.H. Andersen, L.G. Andersen and U. Lienert (2002). *Physica C* **370**, 141-145.
A49. L.G. Andersen, S. Bals, G. van Tendeloo, H.F. Poulsen and Y.L. Liu (2001). *Physica C,* **353** , 251-257.
A50. U. Lienert, H.F. Poulsen, V. Honkimäki, C. Schulze, and O. Hignete (1999). *J. Synchrotron Rad*. **6**, 979-984.

Other publications

1. H.C. Sörby (1886). *J. Iron Steel Inst. (London)*, 140.
2. M. Knoll and E. Ruska (1932). *Z. Physik* **8**, 18.
3. B.C. Larson, W. Yang, G.E. Ice, J.D. Budai, and T.Z. Tischler (2002). *Nature* **415**, 887-890.
4. T. Wroblewski, O. Clauss, H.-A. Crostack, A. Ertel, F. Fandrich, Ch. Genzel, K. Hradil, W. Ternes, and E. Woldt (1999). *Nucl. Instr. Meth. A* **428,** 570-582.
5. D.B. Williams and C.B. Carter (1996). *Transmission Electron Microscopy* (Plenum Press, New York).
6. J.I. Goldstein, D.E. Newbury, P. Echlin, D.C. Joy, A.D. Romig, Jr., C.E. Lyman, C. Fiori, and E. Lifshin (1992). *Scanning Electron Microscopy and X-ray Analysis* (Plenum Press, New York).
7. M.N. Alam, M. Blackman and D.W. Pashley (1954)**.** *Proc. Royal Soc. A* **221**, 224-242.
8. J.A. Venables, C.J. Harland, and R. bin-Jaya (1981). *Development in Electron Microscopy and Analysis* (Academic Press, London).
9. D.J. Dingley (1984). *Scan. Electron Micr*. **11**, 569-575.
10. N.C.K. Lassen, D. Juul Jensen, and K. Conradsen (1992). *Scanning Microsc*. **6**, 115-121.
11. F.J. Humphreys and I. Brough (1999). *J. Microsc. V* **195,** 6-9.
12. J.C. Russ and R.T. Dehoff (1999). *Practical Stereology* (Plenum Press, New York).
13. M.V. Kral and G. Spanos (1999). *Acta Mat.* **47,** 711-724.
14. N. Hansen (1977). *Acta Metall*. **25**, 863.
15. A. Taylor (1961). *X-ray metallography* (John Wiley & Sons, New York).
16. P.B. Hirsch and J.N. Kellar (1958), *Acta Cryst*. **5**, 162-167.
17. P.B. Hirsch (1958), *Acta Cryst*. **5**, 168-171.
18. P.B. Hirsch (1958), *Acta Cryst.* **5**, 172.

19. G.E. Ice, J.S. Chung, J.Z. Tischler, A. Lunt, and L. Assoufid (2000). *Rev. Sc. Instr*. **71**, 2635-2639.
20. S. Tamura, K. Murai, N. Kamijo, K. Yoshida, H. Kihara, and Y. Suzuki (2000). *Vacuum* **59**, 553-558.
21. P.J. McMahon, A.G. Peele, D. Paterson, J.J.A. Lin, T.H.K. Irving, I. McNulty, and K.A. Nugent (2003). *Optics Com.* **217**, 53-58.
22. A. Snigirev, V. Kohn, I. Snigireva, and B. Lengeler (1996). *Nature* **384**, 49-51.
23. C.G. Schroer, J. Meyer, M. Kuhlmann, B. Benner, T.F. Gunzler, B. Lengeler, C. Rau, T. Weitkamp, A. Snigirev, and I. Snigireva (2002). *Appl. Phys. Lett*. **81**, 1527-1529.
24. F. Pfeiffer, C. David, M. Burghammer, C. Riekel, and T. Salditt (2002). *Science* **297**, 230-234.
25. H. Biermann, B.V. Grossmann, S. Mechsner, H. Mughrabi, T. Ungar, A. Snigirev, I. Snigireva, A. Suovorov, M. Kocsis, and C. Raven (1997). *Scripta Mat.* **37**, 1309-1314.
26. A. Guinier and G. Fournet (1955). *Small-angle scattering of x-rays* (J.Wiley Inc, New York).
27. A.C. Kak, and M. Slaney (1988). *Principles of Computerized Tomographic Imaging* (IEEE Press, New York).
28. G.T. Herman (1980). *Image Reconstructions from Projections. The Fundamentals of Compterized Tomography.* (Academic Press, New York).
29. F. Beckmann, U. Bonse, and T. Biermann (1999). *Proc. SPIE Conf. Vol 3772: Developments in X-ray Tomography II, Denver Colorado, July 1999*, pp 179-187.
30. J. Baruchel, P. Cloetens, J. Hartwig, W. Ludwig, L. Mancini, P. Pernot, and M. Schlenker (2000). *J. Synchrotron Rad*. **7**,196.
31. C. Giacovazzo, H.L. Monaco, D. Viterbo, F. Scordari, G. Gilli, G. Zanotti, and M. Catti. *IUCr Texts on Crystallography 2: Fundamentals of Crystallography* (Oxford University Press, Oxford).
32. J. Als-Nielsen and D. McMorow (1999). *Elements of X-ray Physics* (Wiley, New York).
33. J.R. Schneider, J.E. Jørgensen and G. Shirane (1986). *Phase Transitions* **8**, 17-34.
34. P. Bastie, F. Troussaut, M. Vallade, and C.M.E. Zeyen (1987). *J. Appl. Cryst*. **20**, 475-481.
35. A. Palmer and W. Jauch (1993). *Phys. Rev. B* **48**, 10304-10310.
36. J.B. Hastings, D.P. Siddons, J.R. Schneider, and L.E. Berman (1989). *Rev. Sci. Instrum*. **60**, 2398-2401.
37. A. Vigliante, M. von Zimmermann, J.R. Schneider, T. Frello, N.H. Andersen, J. Madsen, D.J. Buttrey, D. Gibbs, and J.M. Tranquada (1997). *Phys. Rev*. B **56** 8248-8251.
38. H.-B. Neumann, U. Rütt, R. Bouchard, and J.R. Schneider (1994). *J. Appl. Cryst*. **27**, 1030-1038.
39. M. Lippert, T. Brückel, T. Köhler, and J.R. Schneider (1994). *Europhys. Lett*. **27**, 537-541.
40. T. Lippmann and J.R. Schneider (2000). *J. Appl. Cryst.* **33**, 156-167.
41. K.D. Liss, A. Magerl, R. Hock, A. Remhof, and B. Waibel (1997). *Europhys. Lett*. **40,** 369-374.
42. C.A. Tulk, C.J. Benmore, J. Urquidid, D.D. Klug, J. Neuefeind, B. Tomberli and P. Egelstaff (2002). *Science* **297**, 1320-1323.

43. U. Rütt, M.A. Beno, J. Strempfer, G. Jennings, C. Kurtz, and P.A. Montano (2001). *Nucl. Instr. Meth. Phys. Res.* A **467-468**, 1026-1029.
44. H. Ohno, S. Kohara, N. Umesaki, and K. Suzuya (2001). *J. Non-cryst. Solids* **293**, 125-135.
45. V. Petkov, S.J.L. Billinge, S.D. Shastri, and B. Himmel (2001). *J. Non-cryst. Solids* **293,** 726-730.
46. A.R. Yavari, A. Le Moulec, A. Inoue, G.B.M. Vaughan, and Å. Kvick (2002). *Annales de Chimie-Science des Materiaux,* **27**, 107-112.
47. H. Reichert, O. Klein, H. Dosch, M. Denk, V. Honkimäki, T. Lippmann, and G**.** Reiter (2000). *Nature* **408**, 839-841.
48. H. Reichert, V.N. Bugaev, O. Shchyglo, A. Schops, Y. Sikula, and H. Dosch (2001). *Phys. Rev. Lett*. **87**, 236105.
49. M.J. Kramer, L. Margulies, A.I. Goldman, and P.L. Lee (2002) *J. Alloys Comp*. **338**, 235-241.
50. S. Giraud, J.P. Wignacourt, S. Swinnea, H. Steinfink, and R. Harlow (2000). *J. Sol. St. Chem.* **151**, 181-189.
51. L. Wcislak, H. Klein, H.J. Bunge, U. Garbe, T. Tschentscher, and J.R. Schneider (2002). *J. Appl. Cryst.* **35**, 82-95.
52. M.R. Daymond and P.J. Withers (1996). *Scripta Mat*. **10**, 1229-1234.
53. A.M. Korsunsky, K.E. Wells, and P.J. Withers (1998). *Scripta Mat*. **39**, 1705-1712.
54. A. Wanner and D.C. Dunand (2000). *Metall. Mater. Trans.* **31A**, 2949-2962.
55. A. Pyzalla (2000). *J. Nondestructive Eval*., **19,** 21-31.
56. A. Pyzalla, B. Reetz, J. Wegener, A. Jacques, O. Ferry, J.-P. Feiereisen, and T. Buslaps (2002). *Mat. Sc. Forum*, **404-407**, 535-540.
57. J.C. Hanan, G.A. Swift, E. Üstündag, I.J. Beyerlein, J.D. Almer, U. Lienert, and D.R. Haeffner (2002). *Metall. Mat. Trans.* **33A**, 3839-3845.
58. J. Almer, U. Lienert, R.L. Peng, C. Schlauer, and M. Oden (2003). *J. Appl. Phys.,* accepted.
59. R.V. Martins, U. Lienert, L. Margulies, and A. Pyzalla (2001), *Proc. of TMS Fall meeting 2001, Indianapolis, Session VI: Affordable Metal-Matrix Composites for High Performance Applications,* pp 285-295.
60. R.V. Martins, S. Grigull, U. Lienert, L. Margulies, and A. Pyzalla (2000). *Proc. ICRS-6, Oxford, United Kingdom*, **1**, 90-97.
61. U.F. Kocks, C.N. Tome, and H.R. Wenk (1998). *Texture and Anisotropy* (Cambridge University Press, Cambridge).
62. H.J. Bunge (1969). *Matematische Methoden der Texturanalyse* (Akademie Verlag, Belin).
63. F.C. Frank (1988). *Metall. Trans. A* **19**, 403.
64. L.D. Landau and E.M. Lifshitz (1959). *Course of theoretical physics, vol 7: Theory of elasticity* (Pergamon, Oxford).
65. A. Allen, M.T. Hutchings, and C.G. Windsor (1985). *Adv. Phys*. **34**, 445-473.
66. R.V. Martins, L. Margulies, S. Schmidt, H.F. Poulsen, and T. Leffers. *Mat Sci. Eng.*, in press.
67. N.R. Barton, D.E. Boyce, and P.R. Dawson (2002). *Textures and Microstructures*, **35,** 113-144.
68. H. Weiland, J.M. Fridy, and E. Llewellyn (2002). *Mat. Sc. Forum* **408-412**, 101-106.
69. R. V. Martins and V. Honkimäki (2003). *Textures Microstr* **35**, 145-152.

70. S.R. Deans (1983). *The Radon Transform and some of its applications* (Wiley, New York).
71. R. Gordon, R. Bender and G.T. Herman (1970). *J. Theor. Biol*. **29**, 471-481.
72. S. Helgason (1980). *The Radon Transform. Progress in Math., Vol. 5* (Birkhäuser, Boston).
73. A.M. Cormack (1981). *Proc. American Math. Soc*. **83**, 325-330.
74. G.T. Herman and A. Kuba, Eds (1998). *Discrete Tomography*. (Boston, Birkhäuser).
75. www.esrf.fr/UsersAndScience/Experiments/MaterialsScience/ID11/
76. www.risoe.dk/afm/synch/
77. C. Schulze, U. Lienert, M. Hanfland, M. Lorenzen and F. Zontone (1998). *J. Synchrotron Rad.* **5**, 77-81.
78. P. Kirkpatrick, A.V. Baez, and A. Newell (1948). *Phys. Rev.* **73**, 535-536.
79. P. Suortti and C. Schulze (1995). *J. Synchrotron Rad.* **2**, 6-12.
80. S.D. Shastri, K. Fezzaa, A. Mashayekhi, W.K.Lee, P.B. Fernandez, and P.L. Lee (2002). *J. Synchrotron Rad.* **9**, 317-322.
81 A. Koch, C. Raven, P. Spanne, and A. Snigirev (1998). *J. Opt. Soc. America A* **15**, 1940-1951.
82. J. P. Moy (1994). *Nucl. Instr. Meth. A*, **348**, 641-644.
83. M. Preuss, P.J. Withers, E. Maire, and J.Y. Buffiere (2002). *Acta Mat*. **50**, 3175-3190.
84. S.R. Stock (1999). *Int. Mater. Rev*. **44,** 141-164.
85. S.R. Stock, J. Barss, T. Dahl, A. Veis, and J.D. Almer (2002). *J. Struct. Bio*. **139**, 1-12.
86. P.J. Desre (1997). *Scripta Mat.* **37**, 875-881.
87. E. Rabkin (1998). *Scripta Mat.* **39**, 685-690.
88. W. Ludwig, J.-Y. Buffiere, S. Savelli, and P. Cloetens (2003). *Acta Mat*. **51**, 585-598.
89. M.F. Bartholomeusz and J.A. Wert (1994). *Mater Charact.* **33**, 337.
90. Y.L. Liu and G. Fischer (1997). *Scripta Mater*. **36**, 1187.
91. A. Tatschl and O. Kolednik (2003). *Mater. Sci. Eng. A,* **339**, 265-280.
92. J.A. Wert (2002). *Acta Mat.* **50,** 3125.
93. H. Mughrabi, Ed. (1993). *Materials Science and Technology, Vol 6: Plastic deformation and fracture of materials* (VCH, Weinheim).
94. G.I. Taylor (1937). *J. Inst. Met*. **62,** 307.
95. G. Sachs (1928). *Z. verein deut Ing.* **72**, 734.
96. E. Kröner (1961). *Acta Metall*. **9**,155.
97. J.W. Hutchinson (1970). *Proc. R. Soc. London* **A319**, 247.
98. D.P. Mika and P.R. Dawson (1998). *Mater. Sci. Eng.* **A257**, 62.
99. B. Bay, N. Hansen, D. Hughes and D. Kuhlmann-Wilsdorf (1992). *Acta metal mater*. **40**, 205-219.
100. N. Hansen and D. Juul Jensen (1999). *Phil. Tr. Royal Soc. London A*, **357**, 1447-1469.
101. N. Hansen (2001). *Metall. Mater. Trans A* **32**, 2917-2935.
102. Q. Liu and N. Hansen (1995). *Phys. Stat. Sol*. **149**, 187-199.
103. X. Huang and N. Hansen (1997). *Scr. Mater*. **37**, 1-7.
104. G. Winther (2003). *Acta Mat*. **51**, 417-429.
105. S.R. MacEwen, N. Christodoulou, C. Tome, J. Jackman, T.M. Holden, J. Faber, Jr., and R.L. Hitterman (1988). *Proc of ICOTOM-8, Santa Fe 1987, Eds: J.S. Kallend and G. Gottstein.* (The Metallurgical Soc., Warrendale) pp 825-836.

106. B. Clausen, T. Lorentzen, and T. Leffers (1998). *Acta Mat*. **46**, 3087-3098.
107. P.R. Dawson, D. Boyce, S. MacEwan, and R. Rogge (2000). *Metall. Mater. Trans.* **31A**, 1543.
108. P.R. Dawson, D. Boyce, S. MacEwan, and R. Rogge (2001). *Mater. Sci. Engng.* **A313**, 123.
109. P.R. Dawson. Private communication.
110. F.J. Humphreys and M. Hatherly (1995). *Recrystallization and related annealing phenomena* (Pergamon, Oxford).
111. P.A. Beck (1954). *Advances in Physics* **3**, 245.
112. A.N. Kolmogorov (1937). *Izv. Akad. Nauk. USSR-Ser. Matemat*. **1**, 355-359.
113. W.A. Johnson and R.F. Mehl. (1939). *Trans AIME* **135**, 416-458.
114. M. Avrami (1939). *J. Chem. Phys*. **7**, 1103-1109.
115. M. Avrami (1940). *J. Chem. Phys*. **8**, 212-224.
116. M. Avrami (1941). *J. Chem. Phys*. **9**, 177-184.
117. R.A. Vandermeer (1995). *Proc. 16th Risø Int. Symp. on Mat. Sc., Eds. N. Hansen et al.,* (Risø Nat. Lab., Roskilde, Denmark) pp 193-213.
118. K.W. Mahin, K. Hanson, and J.W. Morris (1980). *Acta metall*. **28**, 443-453.
119. D. Juul Jensen (1992). *Scripta metall. mater*. **27**, 1551-1556.
120. J.W. Cahn, and W.C. Hagel (1962). In *Decomposition of Auestenite by Diffusional Processes. Eds. V.F. Zackay, H.I. Aaronson* (Interscience), pp 131-196.
121. D. Juul Jensen (1992). *Scripta metall. mater*. **27**, 533-538.
122. H.W. Hesselbarth, L. Kaps and F. Haessner (1993). *Mat. Sci. Forum* **113-115**, 317-322.
123. F.J. Humphreys (1992). *Scripta metal. Mater*. 27, 1557-1562.
124. E.M. Lauridsen (2002). *Ph.D. Thesis. Report R-1266* (Risø Nat. Lab., Roskilde).
125. R.A. Vandermeer and D. Juul Jensen (1998). *Interface Science*, **6,** 95.
126. R.A. Vandermeer and D. Juul Jensen (2001). *Acta Mat.* **49,** 2083.
127. W.H. Press, S.A. Teukolsky, W.T. Vetterling, and B.P. Flannery (1992). *Numerical Recipes in C* (Cambridge University Press, Cambridge).
128. J. Savoie, H.L. Yiu, E.M. Lauridsen, L. Margulies, S.F. Nielsen, S. Schmidt, M. Ashton and R. Sebald (2002). *Mat. Science Forum* **408-412**, 833-838.
129. H.L. Yiu, J. Savoie, E.M. Lauridsen, A. Bosland, L. Margulies, S.F. Nielsen, S. Schmidt, and M. Zeng (2002). *Mat. Science Forum* **408-412**, 1501-1506.
130. S.F. Nielsen, S. Schmidt, E.M. Lauridsen, H. Yiu, J. Savoie, M. Zeng and D. Juul Jensen (2003). *Scripta Mat*. **48**, 513-518.
131. S. Schmidt. Private communication.
132. P.J. Hurley and F.J.Humphreys (2003). *Acta Mat.* **51**, 1087-1102.
133. A. Godfrey, D. Juul Jensen and N. Hansen (2001). *Acta Mat*. **49**, 2429-2440.
134. H. Hu (1962). *Trans. Metall. Soc. A.I.M.E.* **224**, 75.
135. P. Beck and P.R. Sperry (1950). *J. Appl. Phys.* **21**, 150-152.
136. I.L. Dillamore, P.L. Morris, C.J.E. Smith and W.B. Hutchinson (1972). *Proc. Royal Soc. London* **329A**, 405-420.
137. R.D. Doherty, I. Samajdar, C.T. Necker, H.E. Vatne and E. Nes (1995). *Proc. 16th Risø Int. Symp. Mat. Sc. Eds.: N.Hansen et al.* (Risø Nat. Lab., Roskilde, Denmark), pp 1-23.
138. S. Zaefferer, T. Baudin and R. Penelle (2001). *Acta Mat*. **49**, 1105-1122.
139. V.M. Segal (1995). *Mater. Sci. Eng*. A**197**, 157-164
140. J.R. Bowen, P.B. Prangnell, and F.J. Humphreys (2000). *Mat. Sci. Techn.,* 1246-1250.

141. S. Kikuchi, E. Kimura and M. Koiwa (1992). *J. Mat. Science*. **27**, 4927-4934.
142. D. Juul Jensen (1999). *Proc. 4th Int. Conf on Recrystallization and Related Phenomena. Eds T. Sakai and H.G. Suzuki*. (JIM) pp 3-14.
143. H. Paul, J. H. Driver, C. Maurice and Z. Jasienski (2002). *Acta Mat*. **50**, 4339-4355
144. M.A. Krivoglaz (1969). *Theory of x-ray and neutron scattering by real crystals* (Plenum, New York).
145. R.L. Snyder, J. Fiala, and H.J. Bunge (1999). *Defect and microstructure analysis by diffraction* (Oxford University Press, Oxford).
146. B.E. Warren and B.L Averbach (1950). *J. Appl. Phys*. **21**, 595.
147. H. Mughrabi, T. Ungar, W. Kienle, and M. Wilkens (1986). *Phil. Mag*. **53**, 793.
148. R.I. Barabash and P. Klimanek (1999). *J. Appl. Cryst*. **32,** 1050-1059.
149. J.W. Christian (1981). *The theory of transformations in metals and alloys* (Pergamon, Oxford).
150. R.W. Cahn and P. Haasen, E.J. Kramer, Eds (1991). *Materials Science and Technology. Vol 5: Phase transformation in materials.* (VCH, Weinheim).
151. W.F. Lange III, M. Enornoto, and H.I Aaronson (1988). *Metall. Trans.* **19A**, 427.
152. C. Zener (1949). *J. Appl. Phys*. **20**, 950.
153. S.E. Offerman, N.H. van Dijk, J. Sietsma, E.M. Lauridsen, L. Margulies, S. Grigull, H.F. Poulsen, and S. van der Zwaag (2004). Submitted.
154. K. Heine, J. Tenbrink, and M. Thoner (1989). *Appl. Phys. Lett*. **55**, 2441.
155. M.D. Bentzon, Z. Han, L.O. Andersen, J. Goul, P. Bodin and P. Vase (1997*). IEEE Trans. Appl. Supercond.* **7**, 1411.
156. S.A. Saltykov (1958). *Stereometric Metallography* (Metalurgizdat).
157. H.J.G. Gundersen, P. Bagger, T.F. Bendtsen, S.M. Evans, L. Korbo, N. Marcussen, A. Møller, K. Nielsen, J.R. Nyengaard, B. Pakkenberg, F.B. Sørensen, A. Vesterby, and M.J. West (1988). *Acta Path. Microbiol. Immuno. Scan.* **96**, 857-881.
158. R.M. Suter. Private communication.
159. A. Gholina, J.R. Bowen, J.S. Hayes, Z.C. Wang, F.J. Humphreys, and P.B. Prangnell (2000). *Proc 21st Risø Int. Symp. on Mat. Science, Eds: N. Hansen et al.* (Risø Nat. Lab., Roskilde, Denmark) pp 345-351.
160. L.B. McCusker, R.B. Von Dreele, D.E. Cox, D. Louër, and P. Scardi (1999). *J. Appl. Cryst.* **32,** 36-50.
161. K.D.M. Harris, M. Tremayre, and B.M. Kariuki (2001). *Angew. Chemie, Int. Ed*. **40,** 1626-1651.
162. R.A. Young, Ed. (1995) *The Rietveld Method* (Oxford University Press, Oxford).
163. W.I.F. David, K. Shankland, L.B. McCusker, and Ch. Baerlocher, Eds. (2002). *Structure Determination from Powder Diffraction Data* (Oxford University Press, Oxford).
164. G.B.M. Vaughan. Private communication.
165. E.K.H. Salje (1990). *Phase transitions in ferroelastic and co-elastic crystals* (Cambridge University Press, New York).
166. J.E. Huber, N.A. Fleck, C.M. Landis, and R.M. McMeeking (1999). *J. Mech. Phys. Sol*. **47**, 1663-1697.
167. The technical design report for the XFEL is available at www-hasylab.desy.de.
168. I.K. Robinson, I.A. Vartanyants, G.J. Williams, M.A. Pfeifer, and J.A. Pitney (2001). *Phys. Rev. Lett.* **87**, 195505.

169. J. Miao, T. Ohsuna, O. Terasaki, K.O. Hodgson, and M.A. O'Keefe (2002). *Phys. Rev. Lett*. **88**, 88303.
170. G.E. Ice and B.C. Larson (2000). *Adv. Eng. Mat*. **2**, 643-646.
171. R. Barabash, G.E. Ice, B.C. Larson, G.M. Phar, K.S. Chung, and W. Yang (2001). *Appl. Phys. Lett.* **79**, 749-751.
172. R.I. Barabash, G.E. Ice, B.C. Larson, and W.G. Yang (2002). *Rev. Sci. Instr*. **73**, 1652-1654.
173. J.-S. Chung and G.E. Ice (1999). *J. Appl. Phys*. **86,** 5249-5255.

Dansk Resume (Summary in Danish)

Denne afhandling præsenterer en ny metode, 3DXRD, til strukturelle undersøgelser af polykrystaller og pulvre. Metoden er baseret på brugen af en monokromatisk Røntgenstråle med høj energi ($E \geq 50$ keV), genereret af en synkrotron kilde. En "tomografisk" tilgang til diffraktion er udviklet, muliggjort af brugen af et sæt af areal detektorer. Metoden muliggør som den eneste en ikke-destruktiv 3D karakterisering af de enkelte elementer i mikrostrukturen (korn og under-korn) indeni prøver med en størrelse på mm til cm. Videre kan dynamikken af de enkelte elementer følges under typiske processer såsom deformation og varmebehandling. Hermed bliver det for første gang muligt af foretage direkte observationer af vekselvirkningen mellem elementer.

Afhandlingen omhandler for det første det teknikske grundlag for metoden: de geometriske principper og deres implementering. For det andet præsenteres en række anvendelser indenfor materialeforskning, hvor metoden allerede har bidraget væsentligt videnskabeligt. Arbejdet er rapporteret dels i selve afhandlingen, dels i 15 udvalgte publikationer (A1-A15) som er medtaget i appendix.

De primære resultater, der er opnået, er følgende:

- Der er etableret et universelt program til indicering af polykrystaller: *GRAINDEX*. I gunstige tilfælde kan flere tusinde korn indiceres samtidigt. Baseret på dette program, kan de enkelte korn karakteriseres med hensyn til deres position, volumen, gennemsnitlige orientering og den elastiske tøjnings-tensor midlet over kornet. *GRAINDEX* understøtter alle krystallografiske rum grupper og kan anvendes til såvel en-fase som fler-fase systemer. Udover studier af korn kan programmet også anvendes til studier af individuelle indlejrede dislokations strukturer, inklusioner eller domæner. Der er kun to begrænsninger: de strukturelle elementer skal være større end detektions-grænsen og diffraktions pletterne må ikke overlappe hinanden. Den sidste begrænsning kan i et vist omfang omgås ved indsættelse af en kegleformet slit imellem prøven og detektoren. *GRAINDEX* har fundet bred anvendelse til såvel statiske som dynamiske studier.

- Der er etableret en matematisk formalisme for rekonstruktion af mikrostrukturen af en prøve ud fra 3DXRD data. Formalismen er baseret på en generalisering af principper kendt fra medicinsk billedbehandling til højere dimensionale rum. I skrivende stund er formalismen blevet anvendt til 3D kortlægninger af kornstrukturer for ikke-deformerede prøver. Et generelt program er ved at blive færdiggjort. Med dette er det formålet at generere kort over mikrostrukturen også for deformerede prøver, herunder at muliggøre en strukturel karakterisering i tilfælde af overlappende pletter.

- Der er udviklet en serie af unikke eksperimentelle værktøjer til karakterisering af plastisk deformation. Disse værktøjer komplementerer hinanden med hensyn til længdeskala, informations indhold og graden af deformation, som de kan håndtere. Den gennemsnitlige plastiske respons af et givet korn kan således bestemmes udfra 3DXRD målinger af enten kornets rotation,

ændringerne i dets gittertøjning eller ved at sammenligne morfologien af kornet før og efter deformationen. Variationerne i respons indeni kornet kan karakteriseres rumligt ved rekonstruktion af de lokale orienteringsændringer, og integralt via en analyse af formen af diffraktions pletterne. Videre kan forskydnings-gradient tensoren kortlægges direkte ved at følge forskydningen af indlejrede markør partikler med absorptions kontrast tomografi. Ved at kombinere alle disse værktøjer, muliggøres en meget omfattende beskrivelse af plastisk deformation. Således skulle det være muligt at bestemme de aktive slip systemer direkte.

- Der er etableret et dedikeret instrument for 3DXRD studier på ESRF: 3DXRD mikroskopet. Den rumlige opløsning er bestemt af de forhåndenværende detektorer, og er i øjeblikket 5 μm. Detektions-grænsen er betydeligt lavere: 200 nm, mens den tidslige opløsning varierer mellem 1 sekund og 1 time, afhængig af anvendelsen. Siden ibrugtagningen sidst i 1999, har instrumentet fundet bred anvendelse med deltagelse af eksperimentalister fra mere end 20 laboratorier i Europa og USA.

- 3DXRD er blevet anvendt til fundamentale undersøgelser af udvalgte problemstillinger indenfor metallurgi. Studier af nukleering og vækst under varmebehandlinger har vist at der er store variationer mellem opførslen af de enkelte korn. Dette resultat er uafhængigt af hvorvidt der var tale om studier af rekrystallisation, recovery eller fase overgange og uafhængigt af hvorvidt der måltes på Al, stål eller keramer. Disse resultater demonstrerer den grove simplificering som standard modeller såsom JMAK anvender, idet de antager at alle korn (af en bestemt orientering) opfører sig ens. Studier af polykrystal deformation i Al har demonstreret at rotationen af de enkelte korn udviser en klar afhængighed af deres oprindelige orientering, mens effekten af vekselvirkningen mellem korn er relativt lille. De målte rotationer modsvares ikke af forudsigelser fra standard modeller. Et første studie af udviklingen i gitter tøjning som funktion af træk indikerer at variationen mellem et sæt af ækvivalente korn er betydelig mindre end forventet fra FEM simuleringer. Dette ses som en indikation af at tøjningerne bliver afskærmet af de generede dislokations strukturer.

- 3DXRD kan ses som en tredje vej i krystallografi, et alternativ til pulver diffraktion og målinger på enkrystaller. Specielt er en multi-korn raffinerings metode blevet demonstreret på et α-Al_2O_3 emne, med resultater af en kvalitet der modsvarer enkrystal-studier. Metoden er uafhængig af størrelsen af enheds-cellen. Den forventes derfor at kunne finde bred anvendelse, også udenfor materialeforskning, f.eks. indenfor makro-molekylær kemi.

List of abbreviations

3DXRD:	Three-dimensional x-ray diffraction
ART:	Algebraic Reconstruction Technique
bcc:	body-centered cubic
CCD:	Charge-coupled-device
CMS:	Center of mass
CT:	Computerized tomography
EBSP:	Electron back-scatter pattern
ECAE:	Equi-channel angular extrusion
EM:	Electron microscopy
FBP:	Filtered back-projection
fcc:	Face-centered cubic
FEM:	Finite element modelling
FIB:	Focused Ion Beam
FWHM:	Full-width-at-half-maximum
JMAK:	The Johnson-Mehl-Avrami-Kolmogorov model
ML:	Multi-layer
ODF:	Orientation distribution function
PET:	Positron emission tomography
SAD:	Selected Area Diffraction
SANS:	Small angle neutron scattering
SEM:	Scanning electron microscope
TEM:	Transmission electron microscope

APPENDIX

A1. H.F. Poulsen, S. Garbe, T. Lorentzen, D. Juul Jensen, F.W. Poulsen, N.H. Andersen, T. Frello, R. Feidenhans'l, and H. Graafsma (1997). *J. Synchrotron Rad*. **4,** 147-154.

A2. E.M. Lauridsen, S. Schmidt, R.M. Suter, and H.F. Poulsen (2001). *J. Appl. Cryst*. **34,** 744-750.

A3. H.F. Poulsen, S.F. Nielsen, E.M. Lauridsen, S. Schmidt, R.M. Suter, U. Lienert, L. Margulies, T. Lorentzen and D. Juul Jensen (2001). *J. Appl. Cryst*. **34,** 751-756.

A4. H.F. Poulsen and X. Fu (2003). *J. Appl. Cryst.*, **36**, 1062-1068.

A5. H.F. Poulsen and S. Schmidt (2003). *J. Appl. Cryst*. **36**, 319-325.

A6. H.F. Poulsen (2003). *Phil. Mag.* **83**, 2761-2778.

A7. S.F. Nielsen, H.F. Poulsen, F. Beckmann, C. Thorning, and J.A. Wert (2003). *Acta Mat*. **51**, 2407-2415.

A8. L. Margulies, G. Winther, and H. F. Poulsen (2001). *Science* **291**, 2392-2394.

A9. H.F. Poulsen, L. Margulies, S. Schmidt, and G. Winther (2003). *Acta Mat.* **51**, 3821-3830.

A10. E.M. Lauridsen, D. Juul Jensen, H. F. Poulsen, and U. Lienert (2000). *Scripta mater* **43,** 561-566.

A11. E.M. Lauridsen, H.F. Poulsen, S.F. Nielsen and D. Juul Jensen (2003). *Acta Mat*. **51**, 4423-4435.

A12. H.F. Poulsen, E.M. Lauridsen, S. Schmidt, L. Margulies, and J.H. Driver (2003). *Acta Mat*., **51**, 2517-2529.

A13. S.E. Offerman, N.H. van Dijk, J. Sietsma, S. Grigull, E.M. Lauridsen, L. Margulies, H.F. Poulsen, M.T. Rekveldt, and S. van der Zwaag (2002). *Science* **298**, 1003-1005.

A14. L.G. Andersen and H.F. Poulsen (2001). In *Studies of high temperature superconductors*, *Ed: A. Narlikar* (Nova Science Pubs, New York), **36,** 29-87.

A15. S. Schmidt, H.F. Poulsen and G.B.M. Vaughan (2003). *J. Appl. Cryst*., **36**, 326-332.

A1

J. Synchrotron Rad. (1997). **4**, 147–154

Applications of High-Energy Synchrotron Radiation for Structural Studies of Polycrystalline Materials

H. F. Poulsen,[a] S. Garbe,[a] T. Lorentzen,[a] D. Juul Jensen,[a] F. W. Poulsen,[a] N. H. Andersen,[b] T. Frello,[b] R. Feidenhans'l[b] and H. Graafsma[c]

[a]Materials Department, Risø National Laboratory, DK-4000 Roskilde, Denmark, [b]Department of Solid State Physics, Risø National Laboratory, DK-4000 Roskilde, Denmark, and [c]European Synchrotron Radiation Facility, BP 220, F-38043 Grenoble, France. E-mail: henning.friis.poulsen@risoe.dk

(*Received 24 September 1996; accepted 31 January 1997*)

The large penetration power of high-energy X-rays (>60 keV) raises interesting prospects for new types of structural characterizations of polycrystalline materials. It becomes possible in a non-destructive manner to perform local studies, within the *bulk* of the material, of the fundamental materials physics properties: grain orientations, strain, dislocation densities *etc.* In favourable cases these properties may be mapped in three dimensions with a spatial resolution that matches the dimensions of the individual grains. Imbedded volumes and interfaces become accessible. Moreover, the high energies allow better *in-situ* studies of samples in complicated environments (industrial process optimization). General techniques for research in this energy range have been developed using broad-band angle-dispersive methods, on-line two-dimensional detectors and conical slits. Characterizations have been made at the level of the individual grains and grain boundaries as well as on ensembles of grains. The spatial resolution is presently of the order of 10–100 μm. Four examples of applications are presented along with an outlook.

Keywords: high-energy synchrotron radiation; texture; residual stress; Bi-2223; solid-oxide fuel-cell concept (SOFC); industrial process optimization.

1. Introduction

Dedicated beamlines for high-energy X-ray diffraction (>60 keV) have recently become available at several synchrotrons. Their use for research on single crystals and amorphous materials is now established (*cf.* Schneider *et al.*, 1994). In this report we focus on their applicability for studies of polycrystalline materials such as metals, alloys and ceramics.

High-energy X-rays are associated with a large penetration power, which makes it possible to investigate millimetre- to centimetre-sized samples. This is crucial, as polycrystalline research is often concerned with structural materials, where processing or application in general put restrictions on the sample dimensions. At the same time there may be unwanted surface effects, *e.g.* strain relaxation, corrosion, friction or atypical grain growth. The optimum X-ray energy, which is mostly a trade-off between penetration depth and photon flux, is for many applications with materials of medium atomic number, including steel, nickel, copper and various ceramics, in the range 60–100 keV.

With state-of-the-art insertion devices, such as small-gap undulators at the APS (Shastri, Dejus, Haeffner & Lang, 1995), the available flux at 100 keV may be as high as 2×10^{13} photons s^{-1} (0.1% bandwidth)$^{-1}$ through a 5 × 2 mm pinhole at 30 m distance. The unique combination of flux and penetration power raises prospects for performing local studies in the bulk of materials. This is obviously interesting for applications with imbedded volumes or interfaces, *e.g.* thick multilayers. Perhaps more importantly, the minimal gauge volume may in favourable cases be comparable with or smaller than the grain size. For the first time, it therefore becomes possible to measure non-destructively the fundamental microstructural parameters related to the individual grains: crystallographic orientation, strain, size, dislocation density, as well as the topology of the grain boundaries. Predictions of the macroscopic properties of the materials, such as texture, flow stress, fatigue strength, corrosion resistance, magnetization and superconducting critical current, depend heavily on these parameters. It therefore seems likely that being able to map the microstructure in three dimensions will significantly enhance our capability of predicting the macroscopic properties.

Another important aspect of the large penetration power is the improved option for performing *in-situ* studies of samples in complicated environments. This is especially of interest for applied work (industrial process optimization). Finally, for some applications, including dislocation density measurements, it may also be of importance that the primary extinction vanishes, implying that kinematical models can be used.

The other main difference between diffraction at high energies and at conventional energies (5–20 keV) is the smaller Bragg angles. These imply that the Q-space resolution becomes worse. However, a poor resolution can often be tolerated as most samples of interest consist of (a small number of) well known phases with small unit cells. Actually, from a practical point of view, it may be more important that the smaller Bragg angles make it easier to use a two-dimensional detector, as the whole diffraction pattern can be acquired on a flat device such as an image plate or a CCD camera. The small Bragg angles also imply that the local gauge volumes tend to have a long dimension along the beam direction. In some situations this problem can be overcome by scanning the sample in the direction of the beam and defining the grain boundary as positioned at the intensity half point.

2. Experimental technique

The work presented here was performed almost exclusively on beamlines BW5 at HASYLAB and ID11 at ESRF, and with X-ray energies between 80 and 100 keV. In this section we will use the experimental configuration for determination of local texture/grain orientations, shown in Fig. 1, as an example of technique.

Texture determinations do not put high demands on angular resolution, 1–3° is normally sufficient. The energy bandpass can therefore be as broad as 1%, with the limit actually being set by geometrical demands related to how the local volume is defined (*cf.* below). So far, broad-band focusing optics have not been implemented at high-energy beamlines. At present, the experiments are therefore performed with an unfocused beam and with mosaic monochromator and analyzer crystals. Initially, we have mostly used $SrTiO_3$ crystals. However, experience has shown that this material has drawbacks in terms of homogeneity as well as radiation damage. A better choice might be Si-$TaSi_2$ (Neumann, Schneider, Süssenbach, Stock & Rek, 1996), Cu or plastically deformed Ge.

Experiments at high energies tend to be intensity limited. Full use should therefore be made of two-dimensional detectors. Image plates and CCD cameras, coupled either to an image intensifier or to a phosphor by tapered fibre optics, can all be manufactured to have a reasonable efficiency up to 100 keV. However, stability concerns rule out the use of image intensifiers. The spatial resolution (FWHM) of commercially available devices is in all cases 100 μm or worse. We have used a modified XIOS-II camera from Photonics Science – a 12-bit tapered fibre-optics CCD with an area of 77 × 83 mm^2.

The poor spatial resolution of the available detectors rules out tomographic techniques, where the origin of the diffracted signal is inferred from the detector itself. Instead, the gauge volume must be defined by a cross-beam technique, where both the incoming and the outgoing beam are defined by mechanical devices (slits). For the local texture/grain orientation experiments we have used a combination of a square pinhole on the entry side and a conical slit on the exit side, *cf.* Fig. 1 (Garbe, Thomson, Graafsma, Poulsen & Juul Jensen, 1996). The conical slit is a 5 mm-thick Ta plate with two 20 μm-thick conical openings corresponding to the ⟨311⟩ and ⟨200⟩ reflections of an f.c.c. system. In addition to those shown in Fig. 1, several other slits were introduced to serve as guard slits.

The Q-space resolution of a high-energy X-ray triple-axis diffractometer has been described in detail by Rütt, Neumann, Poulsen & Schneider (1995). With perfect monochromator and analyzer crystals the longitudinal resolution, $\Delta Q_{\|}$, in a dispersive set-up is simply proportional to $1/\lambda$:

$$\Delta Q_{\|} = (4\pi/\lambda)\Delta_{\mathrm{div}}|1 - (d_{M/A}/d_s)|. \qquad (1)$$

Here, Δ_{div} is the divergence of the beam hitting the monochromator, d_s is the d spacing of the sample and

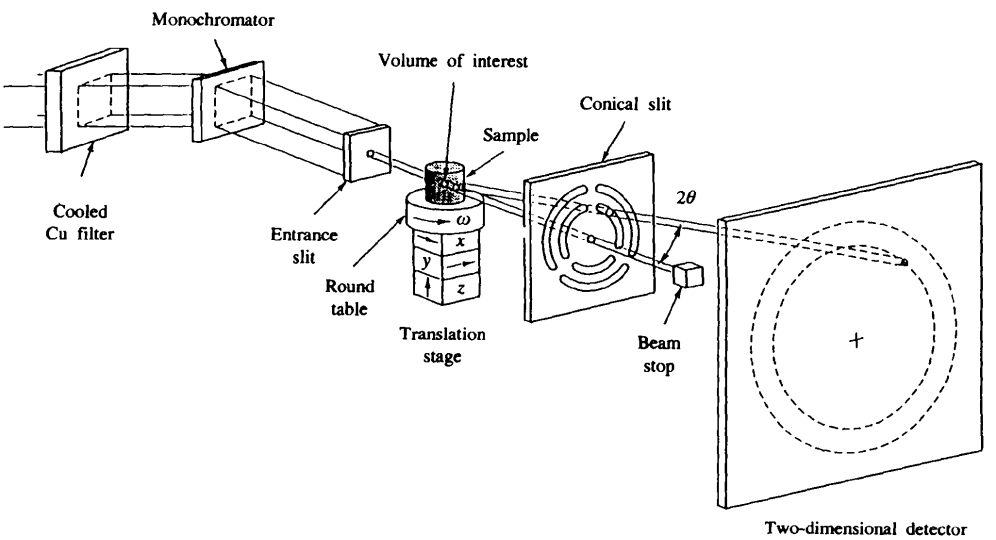

Figure 1
Experimental set-up for local texture/local grain orientation measurements. Transmission geometry is used throughout.

$d_{M/A}$ is the common d spacing of the monochromator and analyzer. For the case of imperfect crystals, a d_s-independent term has to be added to (1). In both cases it follows that $\Delta Q_{\parallel}$ may be improved by insertion of slits in the primary beam. The in-plane transverse resolution is for most applications, *e.g.* strain and texture determinations, much better than needed, *i.e.* of the order of minutes of arc. It may therefore be advantageous to vibrate the sample in ω during measurements. Turning next to a two-axis set-up, the direct-space contribution to the 2θ resolution tends to dominate. For fixed gauge volume and fixed sample-to-detector distance, this implies that the 2θ resolution deteriorates linearly with $1/\lambda$. The dimensions of the experimental hutches are therefore a major concern.

The obtainable spatial resolution depends drastically on Z (atomic number), sample thickness, degree of deformation and grain size.

The analysis of the two-dimensional images is simplified in the cases where the scattering from the local volume can be approximated as powder or single-grain diffraction. For the 'grey area' between these extremes, which cannot be neglected here, the available software is limited.

A texture/powder integration program, *CONE*, has been developed at Risø (Jensen, Schou, Carstensen, Poulsen & Garbe, 1996). This program deals with a set of complications that arise for the present applications. Firstly, the signal-to-noise ratio is often poor due to the simultaneous demands for fast and local measurements, and the use of complicated sample environments. The background subtraction therefore has to be based on an analysis of the local variations within the image. Secondly, it is non-trivial to parameterize the traces of the cones in the image as partial data sets are often recorded. Centre positions may therefore be unknown. Images also deviate from the ideal circular shape due to misalignments *etc.* Combined with the fact that the texture components are often rather sharp, this makes it necessary to employ image-processing methods to find the parameters of the traces. In the present case they are found by a combination of a circular Hough transform and non-linear least-squares fitting.

3. Residual strain in metal-matrix composites

The incorporation of stiff inclusions in a ductile metal is known to strengthen the metal and to improve creep properties and wear resistance. The exact strengthening mechanism in the resulting metal-matrix composite and, in particular, the influence of the mismatch in elastic/plastic behaviour of the two components, is a central issue in materials research. Experimentally, neutron diffraction has been used to determine the volume average deformations of the two constituents, while electron microscopy has given qualitative information on a local scale (results are severely influenced by the sectioning).

We have used high-energy X-rays to determine the three-dimensional strain fields around single inclusions in two model systems. Conventional 2θ scans were performed with a scintillation counter as detector. Various strain components were successfully measured with a precision of $\Delta\varepsilon = 1 \times 10^{-4}$. The results have added new elements to our understanding of these systems. Similar types of experiment may, in the future, be used for direct tests of some of the fundamental assumptions in present-day models (*e.g.* the underlying continuum mechanics formalism).

In the first experiment (Lorentzen, Clarke, Poulsen, Garbe & Graafsma, 1997), composite cylindrical samples were produced by casting copper around a long single-fibre inclusion of tungsten. Samples were subsequently wire drawn to reduce the grain size sufficiently that measurements were essentially 'powder-like'. Eight of these samples, with varying thermal history, were characterized within 48 h of beamtime at ESRF. The gauge volume was $20 \times 100 \times 270\,\mu m^3$. Most notable among the results, all samples showed evidence of large gradients in the axial strain between the sample surface and the fibre/matrix interface. These strain variations were independent of axial position even when measurements were made far from the end of the fibres. On the other hand, the radial lattice strain varied only weakly (of the order of $\pm 3 \times 10^{-4}$). As an example, the axial strain results for one of the samples are shown in Fig. 2.

Such observations are not consistent with the residual strain variations being due to thermal expansion, or plastic/elastic mismatch between the W fibre and Cu matrix. Instead we attribute them to deformations of the Cu matrix by the W fibre as the fibre slips relative to the matrix during wire drawing. This results in a uniaxial compressive stress in the core of the Cu matrix balanced by tensile stresses towards the sample surface similar to the process of inducing biaxial stresses by grinding or shot-peening.

In the second experiment (Poulsen, Lorentzen, Feidenhans'l & Liu, 1997) we investigated an analogous

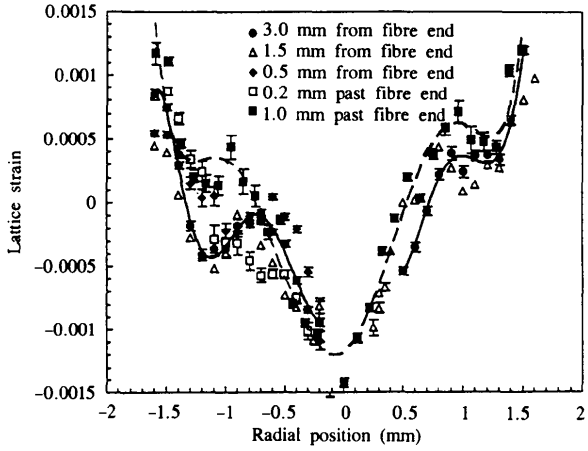

Figure 2
Cu (111) axial lattice strain as a function of radial position at several axis positions in a 3.2 mm-diameter cylindrical Cu sample with an imbedded 4.5 mm-long, 0.5 mm-diameter W fibre along the axis. The solid line is a polynomial fit to the closed circles and the dashed line is a fit to the closed squares. They are included as guides to the eye.

metal-matrix composite model system with aluminium replacing copper as the matrix material. Aluminium being lower in Z, the experiment was performed at BW2, HASYLAB, with 26 keV radiation. The gauge volume was $10 \times 10 \times 170\,\mu m^3$. Two specimens were investigated with typical Al grain sizes of 1 and 30 μm, respectively. In the former the intra-granular strains were mapped, *cf.* Figs. 3 and 4. In the latter the strains for individual grains with a given distance to the fibre were sampled and averaged. For both specimens we found no variation of the radial and transverse strain components with distance to the fibre, indicating either a complete debonding of the system or interface deterioration.

The use of two-dimensional detectors and conical slits would speed up this type of experiment, partly because 2θ scanning becomes superfluous and partly because it becomes easier to find and align the individual grains in single-grain-type experiments. However, in order to cover the full Debye–Scherrer circle with sufficient accuracy, pixel arrays of $10^4 \times 10^4$ would be needed. Also, the necessary software has, to our knowledge, not been developed.

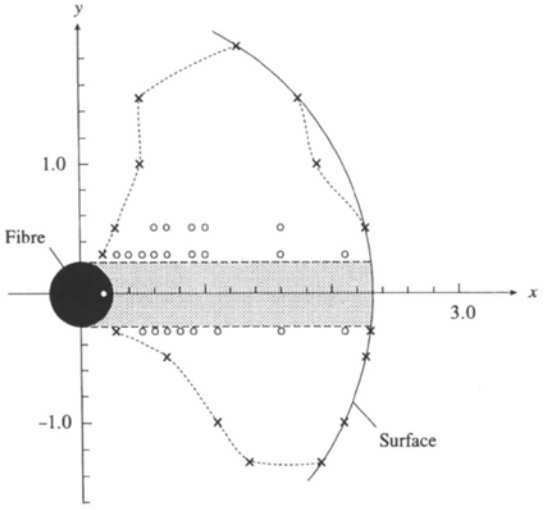

Figure 3
A sectional view through an Al/W composite with large Al grains. The crosses and dashed line mark the circumference of the grain of interest as determined by the experiment. Local strain measurements were performed at the positions marked with circles. The scattering vector was kept fixed, corresponding to the incident beam at all times being directed along the positive x axis. The shaded part of the grain was inaccessible for strain measurements with this particular scattering vector, due to absorption in the fibre.

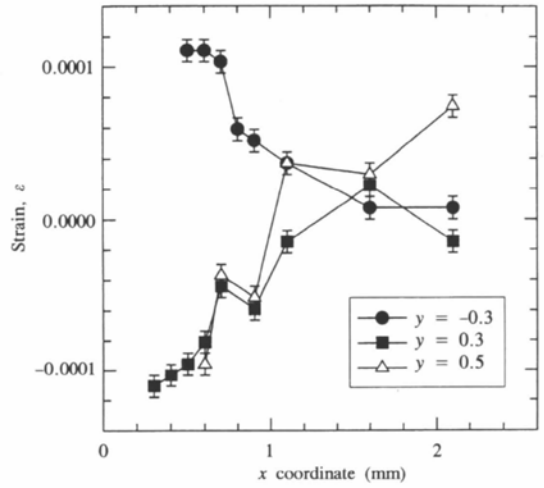

Figure 4
Strain profiles within the plane shown in Fig. 3. Error bars mark the reproducibility of the data. The intra-granular strain is seen to build up close to the grain boundary.

4. Growth studies of single grains during recrystallization

The set-up shown in Fig. 1 is well suited for local texture studies. A large aluminium sample has been used as a test case (Garbe, Poulsen & Juul Jensen, 1996). The deformed

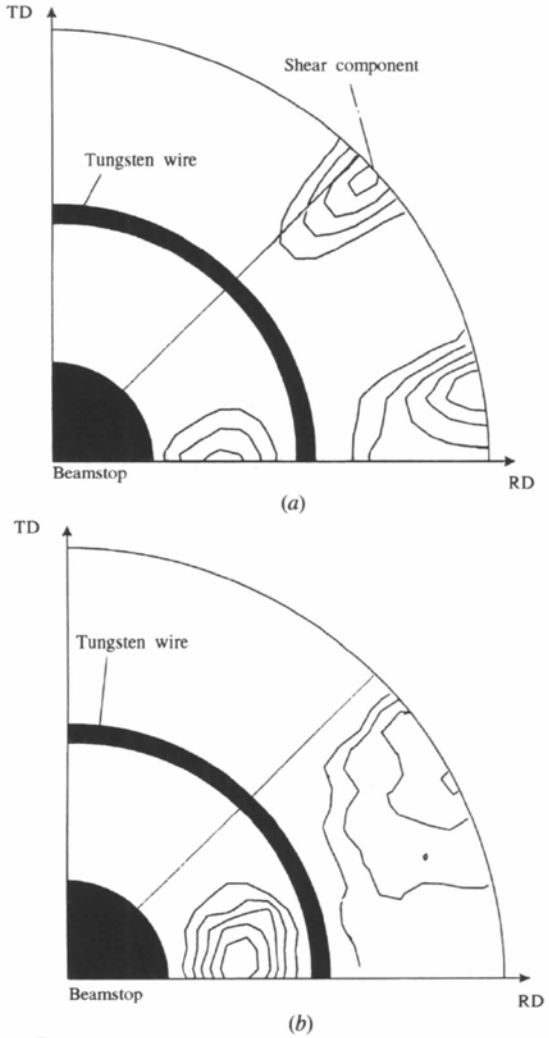

Figure 5
(200) Pole figures for two selected volumes at different depths from the surface in a deformed Al sample: (*a*) $d = 50\,\mu m$ and (*b*) $d = 850\,\mu m$. No information about the shaded parts was obtained due to the beam stop and W wires, used to keep the conical slit together, *cf.* Fig. 1. RD and TD denote rolling and transverse directions, respectively.

sample was annealed *in-situ* in order to follow the spatial as well as temporal evolution of the local texture. Texture components were found to change progressively with the distance to the surface of the sample. An example of resulting pole figures for the as-deformed sample is given in Fig. 5.

Our prime motivation for this type of work is to study the kinetics of recrystallization on a more local scale. The prospect of the technique is to perform *in-situ* measurements of the growth of individual grains and to correlate this growth to the texture of the surrounding deformed material. The establishment of growth laws in turn is a key ingredient for predictions of the final texture. This kind of local information cannot be achieved by other means as surface methods such as electron backscattering patterns do not give representative results. An account of a first experiment of this kind is given by Poulsen & Juul Jensen (1995).

It is also relevant to focus on the 'late-stage' regime, after complete recrystallization, where the grains start to coarsen and a characteristic topology of grain boundaries arises. To characterize a specific boundary in this network fully it is necessary to determine the crystallographic orientation of the two adjacent grains as well as the three-dimensional position of the interface. Obtaining such information, which is relevant for grain-boundary engineering purposes (Aust, 1994), is troublesome with sectioning techniques. In a feasibility study at ESRF we have partially characterized the (static) grain-boundary topology in a $4 \times 5 \times 1.4\,mm^3$ Ni sample (Garbe, Thomson *et al.*, 1996). The intensities of the reflections were mapped in two dimensions within five sheets in the sample and with a step size of 50 μm. An example of the results is given in Fig. 6. An advantage of the technique is that the accuracy of the crystallographic orientation determination can be made sufficiently small that misorientations between intra-grain cell structures can be studied.

5. *In-situ* studies of superconducting tapes

Some of the most promising applications of the high-T_c superconductors are related to the use of wires and tapes of the $(Bi,Pb)_2Sr_2Ca_2Cu_3O_y$ material (abbreviated as the 2223 phase). Risø is involved in manufacturing such tapes in collaboration with other Danish institutes and the industrial partner NKT Research Centre. Precursor powder, consisting mainly of the 2212 phase $[(Bi,Pb)_2Sr_2Ca_1Cu_2O_y]$, is filled into Ag tubes, which are subsequently rolled and annealed at temperatures between 1073 and 1123 K several times. During this treatment, oxygen diffuses through the Ag sheet, the 2212 phase is transformed into 2223, the superconducting grains grow and they develop a strong *c*-axis alignment. The final tapes have cross sections of approximately 3 mm × 200 μm.

The critical current density J_c at 77 K is the crucial parameter to optimize. There seems to be ample room for substantial improvements from the state-of-the-art J_c = 20–40 kA cm^{-2}, but in order to do so it may be necessary to determine exactly what happens during the thermomechanical processing, especially during the first annealing. This is complicated by the fact that conventional diffraction tools, including neutron diffraction, cannot penetrate the silver

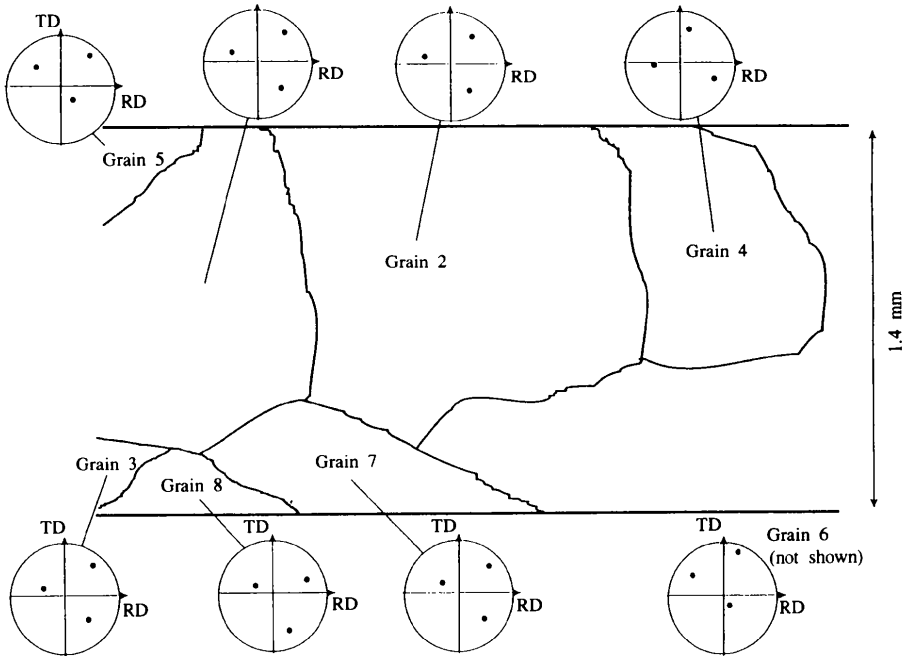

Figure 6
Slide section of eight grains in an imbedded plane in a 1.4 mm-thick Ni sample. Also shown are the determined ⟨200⟩ pole figures for the individual grains.

while on the other hand removal of the Ag sheet is known to change the results drastically.

Using 100 keV photons at HASYLAB, we have recently performed what to our knowledge are the first *in-situ* studies of the annealing process (Frello *et al.*, 1996; Poulsen, Frello *et al.*, 1996). The texture development and kinetics of the 2212 and 2223 phases, as well as some secondary phases, can clearly be followed. An example of the raw data for a multifilament tape is given in Fig. 7. The annealing process is rather slow (~2 d), while exposure times are ~1 min. The furnace was therefore designed in such a way that many tapes could be mounted in parallel and measured sequentially. This also made it possible to perform some process optimization of temperatures, oxygen partial pressures, cooling rates *etc.*

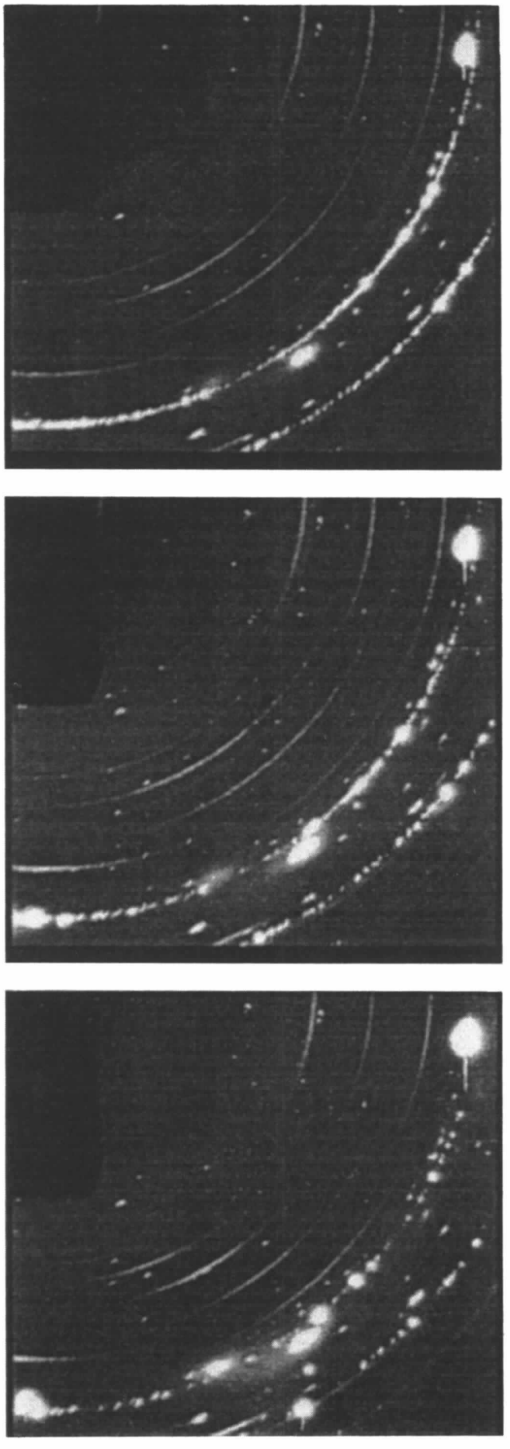

Figure 7
Exposures of a monofilament Ag/$(Bi,Pb)_2Sr_2Ca_2Cu_3O_y$ superconducting tape after 0 (top), 6 (middle) and 26 h (bottom) of annealing at 1108 K. The set-up shown in Fig. 1 was used except for the conical slit (bulk data). The superconducting grains are small and give rise to smooth segments while the silver is recrystallized and gives rise to 'dotted' segments.

6. *In-situ* studies of fuel-cell electrodes

The solid-oxide fuel-cell concept (SOFC) is being studied intensively as a means of a more efficient and cleaner electricity-generation method, compared with conventional steam and gas-turbine technology. Cells typically consist of five layers of current collectors, electrodes and a solid-state electrolyte. They are operated at temperatures between 1050 and 1300 K. Risø National Laboratory is leading a Danish SOFC programme and an EU programme with international and local partners.

High-energy X-rays offer unique possibilities for *in-situ* characterization of fuel cells, and batteries in general, under operating conditions. In an initial study (Sörby, Poulsen, Poulsen & Garbe, 1996) we have focused on the effect of temperature and current on the structure of the 'air electrode', a 5–50 μm-thick imbedded layer of $(La,Sr)MnO_{3\pm\delta}$. Under current production we find that

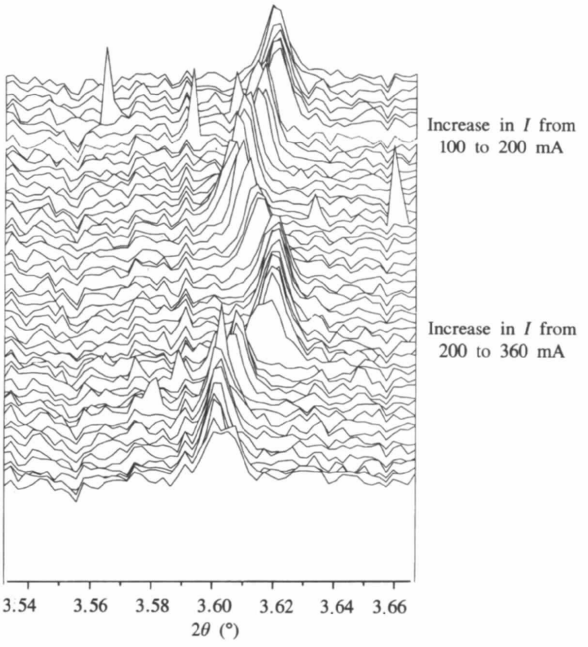

Figure 8
A close-up on the (2,0,4) $(La,Sr)MnO_{3\pm\delta}$ (LSM) peak in a time-resolved set of diffractograms from polarizing an Ag/$(Y,Zr)O_2$/LSM fuel cell at 1113 K. The data were reduced to the format shown here from exposures made by a CCD camera.

the air electrode adjusts to steep gradients in oxygen potential by changing the oxygen stoichiometry (δ) leading to large reversible structural changes, *cf.* Fig. 8. This type of composition-driven structural adjustment of fuel-cell electrodes has not been reported before.

7. Outlook

From the polycrystalline research point of view the high-energy X-rays fill a gap in (spatial resolution, penetration power) space between SEM and neutron diffraction. Improving the spatial resolution is therefore a main concern. It is equally important to find better ways of measuring many local volumes in parallel, as applications tend to require the coverage of many samples as well as many local positions within each sample. We will here discuss various angle-dispersive solutions to these problems. White-beam solutions have been ruled out due to lack of suitable detectors.

The requirements to Q-space resolution are as mentioned relatively relaxed for many applications, including local strain and texture determinations as well as, in some cases, local structure identification. Broad-band focusing is therefore an option. Optic devices such as multilayers (Høghøj, 1994), Fresnel zone plates (Snigirev, 1995) and bent crystals (Suortti, Lienert & Schulze, 1994) have all been shown to give reasonable reflectivities at energies up to 100 keV. However, these devices have not yet been implemented at high energies. As a first attempt to find the optimal solution, we plan to test a combination of a bent Laue/Bragg monochromator in the horizontal and a bent multilayer in the vertical direction at ESRF. We estimate this combination will increase the flux by a factor of 50 with respect to the set-up with mosaic crystals. In the long term, a considerable flux increase may be expected from new sources, such as PETRA, the 12 GeV storage ring at Hamburg, and new insertion devices, such as small-gap undulators.

Little was done to minimize the background in the experiments presented here. Most noteworthy, a nosepiece that connects the two-dimensional detector directly to the defining slit system should be constructed. This should reduce the background significantly. From the combined effect of improvements in optics and background suppression we estimate that gauge volumes of the order of $5 \times 5 \times 50\,\mu m^3$ should be within reach (best-case scenario).

With decreasing gauge volume, the machining of mechanical devices such as slits becomes a problem. Plans are to make the next generation of conical slits with the LIGA lithography technique (Bacher, Menz, Mohr, Müller & Schomburg, 1994). This also has the advantage that five or more 'rings' can be placed in one slit, allowing a full texture determination to be measured without any sample rotations. The LIGA technology can also be envisaged to have other interesting applications, such as two-dimensional Soller collimators.

Ideally, the spatial information should be extracted from the detector itself (tomography). In order to have a reasonable spatial resolution it will be necessary to incorporate high-Z material in the detector such that the photoelectric effect dominates over scattering and the diameter of the 'Compton cloud' becomes as small as possible. It is conceivable that such detectors can be manufactured in the long term. Provided a suitable detector is available, the origin of a specific signal can be traced by translating the detector forwards and backwards in the direction of the beam. The 'track' of the ray will then be estimated in much the same way as is done in high-energy physics using three-dimensional detectors. Small translation scans of the detector may also serve as a general way of improving the accuracy by which the centre of a given signal can be determined. This 'trick' may actually be sufficient to circumvent some of the previously mentioned problems of using two-dimensional detectors for strain measurements.

The ultimate microfocus set-up would be a close analogue to the SEM. Hence, it would be natural to combine microdiffraction with high-resolution high-energy imaging, an interesting undeveloped field in itself (the direct equivalent to industrial radiography).

Turning next to other applications of high-energy X-rays for materials research, we note that the local volumes are already sufficiently small that thick multilayers may be characterized by entering the beam from the side of the multilayer. A pilot experiment at BW5, HASYLAB, has shown that the intensity is sufficient for determining the strain profile in a Cu/Ni multilayer with a layer thickness of 10 μm. High-energy X-rays may also be of interest for determining dislocation densities and in general for studies of peak profiles. Individual bulk grains can be studied, which clearly helps when performing diffuse studies. As mentioned, it may also be significant that the kinematic approximation will nearly always be valid. In this case, of course, broad-band focusing is not an option.

Finally, time-resolved studies are an interesting alternative. Millisecond sampling of bulk data is likely to be of importance *e.g.* for studies of stress relaxation after thermal shocks.

The authors would like to thank J. R. Schneider and the staff at beamline BW5, HASYLAB, for continuous help and encouragement. We are grateful to U. Lienert, P. Klimanek and A. Horsewell for fruitful discussions related to optics, dislocation densities and strain measurements on multilayers, respectively. Moreover, we are much indebted to A. Abrahamsen, Y. L. Liu, A. P. Clarke, P. Olesen, C. Klitholm, M. D. Bentzon, L. Sörby, C. Thomson, J. Süssenbach, D. Novikov and M. von Zimmermann for help with sample preparation and synchrotron experiments. Support for this work was provided by the Danish Research Councils through the Engineering Science Centre at Risø and through DanSync, by the Danish Energy Agency and by the companies NKT Research Centre, ELSAM and ELKRAFT.

References

Aust, K. T. (1994). *Can. Metall. Q.* **33**(4), 265–274.

Bacher, W., Menz, W., Mohr, J., Müller, C. & Schomburg, W. K. (1994). *Naturwissenschaften*, **81**(12), 536–545.

Frello, T., Poulsen, H. F., Bentzon, M. D., Garbe, S., von Zimmermann, M., Abrahamsen, A. & Andersen, N. H. (1996). Unpublished.

Garbe, S., Poulsen, H. F. & Juul Jensen, D. (1996). *Proc. ICOTOM 11; 11th Int. Conf. Text. Mater.* Xian, China.

Garbe, S., Thomson, C., Graafsma, H., Poulsen, H. F. & Juul Jensen, D. (1996). Preprint available.

Høghøj, P. (1994). PhD thesis, Niels Bohr Institute, University of Copenhagen, Denmark. ISSN 0906-0286-1994-03.

Jensen, R. F., Schou, J., Carstensen, M., Poulsen, H. F. & Garbe, S. (1996). Preprint available.

Lorentzen, T., Clarke, A. P., Poulsen, H. F., Garbe, S. & Graafsma, H. (1997). *Composites A*. In the press.

Neumann, H.-B., Schneider, J. R., Süssenbach, J., Stock, S. R. & Rek, Z. U. (1996). *Nucl. Instrum. Methods*, A**372**(3), 551–555.

Poulsen, H. F., Frello, T., Bentzon, M. D., Garbe, S., Novikov, D. & Andersen, N. H. (1996). Preprint available.

Poulsen, H. F. & Juul Jensen, D. (1995). *Proc. 16th Risø Int. Symp. Mater. Sci.*, edited by N. Hansen, D. Juul Jensen, Y. L. Liu & B. Ralph. Risø National Laboratory, Roskilde, Denmark.

Poulsen, H. F., Lorentzen, T., Feidenhans'l, R. & Liu, Y. L. (1997). *Metall. Mater. Trans. A*. In the press.

Rütt, U., Neumann, H.-B., Poulsen, H. F. & Schneider, J. R. (1995). *J. Appl. Cryst.* **28**, 729–737.

Schneider, J. R., Bouchard, R., Brückel, T., Lippert, M., Neumann, H.-B., Poulsen, H. F., Schmidt, T. & von Zimmermann, M. (1994). *Proc. Eur. Symp. Front. Sci. Technol. Synchrotron Rad.* Aix-en-Provence.

Shastri, S. D., Dejus, R. J., Haeffner, D. R. & Lang, J. C. (1995). *Rev. Sci. Instrum.* **66**(9), 1–3.

Snigirev, A. (1995). *Rev. Sci. Instrum.* **66**, 2053–2058.

Sörby, L., Poulsen, F. W., Poulsen, H. F. & Garbe, S. (1996). Unpublished.

Suortti, P., Lienert, U. & Schulze, C. (1994). *Nucl. Instrum. Methods*, A**338**, 27–32.

A2

Journal of
Applied Crystallography
ISSN 0021-8898

Received 28 March 2001
Accepted 29 August 2001

Tracking: a method for structural characterization of grains in powders or polycrystals

E. M. Lauridsen,[a] S. Schmidt,[a] R. M. Suter[b] and H. F. Poulsen[a]*

[a]Materials Research Department, Risø National Laboratory, DK-4000 Roskilde, Denmark, and [b]Department of Physics, Carnegie Mellon University, Pittsburgh, PA 15213, USA. Correspondence e-mail: henning.friis.poulsen@risoe.dk

A method is presented for fast and non-destructive characterization of the individual grains inside bulk materials (powders or polycrystals). The positions, volumes and orientations of hundreds of grains are determined simultaneously. An extension of the rotation method is employed: a monochromatic beam of high-energy X-rays, focused in one dimension, impinges on the sample and the directions of the diffracted beams are traced by translation of two-dimensional detectors. Algorithms suitable for on-line analysis are described, including a novel indexing approach, where the crystal symmetry is used directly by scanning in Euler space. The method is verified with a simulation of 100 grains.

1. Introduction

Many of the properties of metals and ceramics are determined by the structure and interactions of individual grains. Both in powders and polycrystalline materials, the agglomerate is often highly heterogeneous with grains varying in size, shape, crystallographic orientation and stress state, as well as in their relationships to neighbouring grains. As such, it is remarkable that state-of-the-art models in general only deal with average properties. A major cause for this situation is the almost exclusive use of surface probes (electron microscopy and standard laboratory X-ray diffraction) for structural characterization. Due to surface effects such as strain relaxation, pinning and atypical diffusion, samples must be treated and then sectioned before investigation to obtain results representative of bulk behaviour. This destructive procedure prohibits studies of the dynamics of individual grains. Hence, only static and statistical information is obtained.

A need is therefore identified for a non-destructive technique that provides three-dimensional mappings of the pertinent grain characteristics. The technique must enable analysis over an ensemble of 10–1000 grains for significant conclusions to be drawn. Likewise, the data acquisition speed must be sufficient to perform *in situ* processing studies.

We present here an X-ray diffraction technique that fulfils the above requirements. By coupling the monochromatic 'rotation method' with ray tracing, the positions, volumes and orientations of hundreds of grains are determined simultaneously. The technique is limited to undeformed or weakly deformed samples with grains exhibiting a mosaic spread of less than a few degrees. Kinematical diffraction is assumed. The technique applies to all X-ray energies, but emphasis is on the use of high energies, $E > 40$ KeV. These provide the necessary penetration power for three-dimensional mapping of bulk hard condensed matter (Bouchard *et al.*, 1998; Poulsen *et al.*, 1997), and extinction is in general negligible. The technique is named 'tracking' by analogy to reconstruction procedures in particle physics.

First results based on parts of this methodology and a few grains have been presented elsewhere (Lauridsen *et al.*, 2000; Juul Jensen *et al.*, 2000; Juul Jensen & Poulsen 2000; Nielsen, Ludwig *et al.*, 2000; Margulies, Winther *et al.*, 2001; Margulies, Lorentzen *et al.*, 2001). This article gives a comprehensive view of the tracking technique, emphasizing the situation with many grains. As the main topic, an algorithm is developed for sorting and analyzing the vast quantity of data produced. The outcome is a program called *GRAINDEX*, which has been implemented at the three-dimensional X-ray diffraction (3DXRD) microscope at beamline ID11, European Synchrotron Radiation Facility (ESRF) (Lienert *et al.*, 1999). The algorithm is outlined in Fig. 1. Initially, all grains are associated with the same *a priori* known space group and lattice parameters, representing, for example, a stoichiometric and strain-free reference material. The ray tracing provides a list of reflections characterized by their centre-of-mass origin and integrated intensity. The reflections are sorted with respect to their grain of origin by the central indexing algorithm. Next, the positions, volumes and crystallographic orientations of the grains can be fitted.

Once the grains are indexed, single-crystal refinements may be applied. Alternatively, the relevant part of the data may be reinvestigated for a stress analysis. Depending on grain size, it may also be possible to produce a three-dimensional map of grain boundaries. These topics will be treated in a following publication. First examples of grain-boundary mapping and strain data have been reported by Nielsen, Ludwig *et al.* (2000) and Margulies, Lorentzen *et al.* (2001), respectively.

The article will follow the flow of the data analysis. Having established the geometry, we present details of the tasks identified in Fig. 1. Emphasis is on a fast indexing routine,

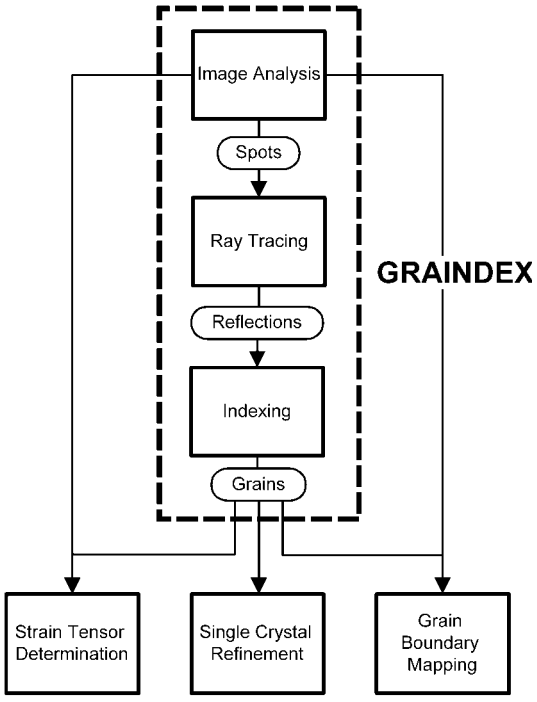

Figure 1
A flow chart for the tracking method using the *GRAINDEX* algorithm. *GRAINDEX* generates a list of grains with associated positions and orientations as well as sets of indexed reflections with associated integrated intensities. The output may be used for crystallographic refinements of the grains or, with a reanalysis of the raw data, for determining the average strain tensors. Furthermore, for coarse-grained materials the grain boundaries can be mapped in three dimensions.

enabling on-line data analysis. Finally, limitations are discussed based on results of a computer simulation.

2. Tracking principle

The experimental geometry is sketched in Fig. 2. The sample is mounted on an ω rotation stage. A beam of monochromatic high-energy X-rays is focused in one direction in order to define a layer in the sample, which is perpendicular to the ω rotation axis. Some of the grains intersected by this layer will give rise to diffracted beams, which are transmitted through the sample to be observed as spots by a flat two-dimensional detector. The detector is aligned perpendicular to the incident beam. In addition, an optional slit is placed before the sample.

The tracking algorithm works as follows. Images are acquired at a number of rotation-axis-to-detector distances, L_1 to L_N (typically $N = 3$). Equivalent spots, generated by the same reflection, are identified and a best fit is determined to a line through the centre-of-mass (CM) positions of these spots. This determines the scattered wavevector, which we specify in terms of the scattering angle, 2θ, and the azimuthal angle, η. Extrapolating the fitted line to its intersection with the incident beam determines the CM position of the illuminated section of the grain of origin, specified by (x_l, y_l). For definitions of zero points and positive directions, see Fig. 2.

To obtain information from all grains in one layer, the X-ray tracing is repeated at a number of ω settings in steps of $\Delta\omega$. During each exposure, the sample is oscillated by $\pm\Delta\omega/2$. Typically, an ω range of 25–40° provides a sufficient number of Bragg peaks from each grain. If the ω range is expanded to 180°, all reflections are illuminated with the exception of those lying in two small 'blind' spots on the unit sphere (centred on the ω axis) with a total spherical area of $4\pi[1 - \cos(\theta)]$, where θ is the Bragg angle. For high-energy X-rays with wavelength, λ, much less than the lattice constant, this area is negligible for low-order reflections. This observation justifies the use of a sample stage with only one rotation.

Finally, for a complete mapping, the procedure is repeated for a set of layers by translating the sample in z. In this way a six-dimensional space, consisting of the $(x, y, z, \omega, 2\theta, \eta)$ coordinates for the various reflections, is probed with essentially a two-dimensional scan over ω and z.

As a variation of the tracking method, we consider the monochromatic beam being restricted in two directions, either by focusing or by slits. This is an option if the overlap between spots arising from the grains in the full layer is too severe. For each ω setting, the beam then defines a stripe through the sample. Upon rotation, only grains close to the rotation axis will remain fully illuminated. The majority of the spots therefore need to be discarded from the analysis, and a full mapping requires additional scanning with translations x and y on top of the rotation table.

In the following, as default we will assume that the beam defines an ideal horizontal plane. Furthermore, we assume that the energy bandwidth and divergence of the beam are negligible. (As an example, the numbers for the 3DXRD instrument are at most 0.1% and 0.5 mrad, which leads to negligible contributions to the uncertainty in Euler angle determination.)

3. Coordinate transformations

The algebra for associating scattering observations with reciprocal space is well described for single crystals (Busing & Levy, 1967). The polycrystal case differs by the need for one extra coordinate system since the sample and grains are different objects. For reference purposes we present the equations, following the single-crystal formalism of Busing & Levy (1967) as close as possible (our sign convention for ω, however, is opposite to theirs). Four Cartesian coordinate systems are introduced: the laboratory system, the ω-axis system, the sample system and the Cartesian grain system.

We describe the coordinate transformations for an arbitrary scattering vector, $\mathbf{G}$. The laboratory system $(\mathbf{x}_l, \mathbf{y}_l, \mathbf{z}_l)$ is defined in Fig. 2. It has $\mathbf{x}_l$ pointing along the incoming beam, $\mathbf{y}_l$ transverse to it in the horizontal plane and $\mathbf{z}_l$ positive upwards, parallel to the ω rotation axis. In this system, vectors are given the subscript l: $\mathbf{G}_l$. The ω system $(\mathbf{x}_\omega, \mathbf{y}_\omega, \mathbf{z}_\omega)$ is rigidly attached to the ω turntable. For $\omega = 0$, the ω and laboratory systems are the same. Hence, the scattering vector transforms as $\mathbf{G}_l = \mathbf{\Omega}\mathbf{G}_\omega$ with

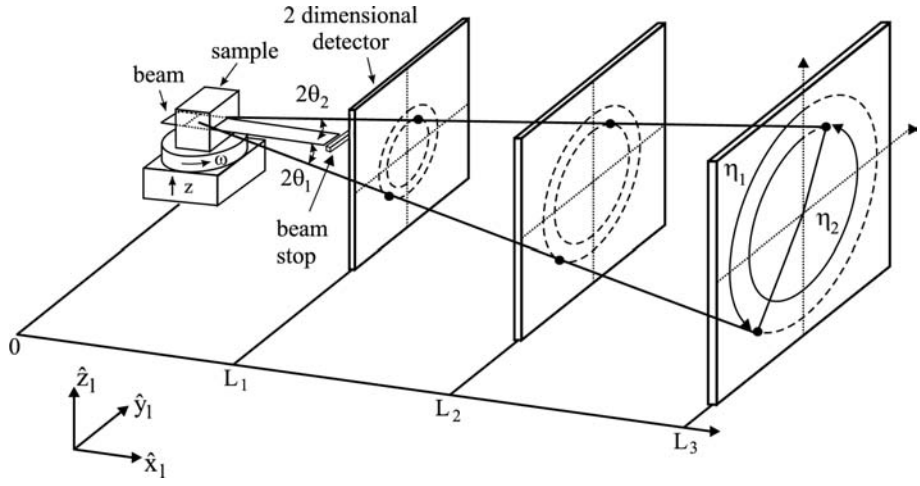

Figure 2
Illustration of the tracking principle. Spots arising from the same reflection at different sample–detector distances are identified. Linear fits through these are extrapolated to give the position of the grain within the illuminated layer in the sample. The angles $(2\theta, \eta, \omega)$ are defined, as well as the laboratory coordinate system $(\mathbf{x}_l, \mathbf{y}_l, \mathbf{z}_l)$.

$$\mathbf{\Omega} = \begin{bmatrix} \cos(\omega) & -\sin(\omega) & 0 \\ \sin(\omega) & \cos(\omega) & 0 \\ 0 & 0 & 1 \end{bmatrix}. \quad (1)$$

The sample system $(\mathbf{x}_s, \mathbf{y}_s, \mathbf{z}_s)$ is fixed with respect to the sample, *e.g.* defined by deformation axes (RD, TD, ND). The orientation of the sample on the ω turntable is given by the **S** matrix: $\mathbf{G}_\omega = \mathbf{S}\mathbf{G}_s$. **S** must be provided by the user and is typically used to swap axes, in order to simplify the data analysis.

The crystallographic orientation of a grain with respect to the sample is given by the **U** matrix: $\mathbf{G}_s = \mathbf{U}\mathbf{G}_c$, where index c refers to the Cartesian grain system $(\mathbf{x}_c, \mathbf{y}_c, \mathbf{z}_c)$. This is fixed with respect to the reciprocal lattice $(\mathbf{a}^*, \mathbf{b}^*, \mathbf{c}^*)$ in the grain. We use the convention that $\mathbf{x}_c$ is parallel to $\mathbf{a}^*$, $\mathbf{y}_c$ is in the plane of $\mathbf{a}^*$ and $\mathbf{b}^*$, and $\mathbf{z}_c$ is perpendicular to that plane. Let **G** be represented in the reciprocal-lattice system by the Miller indices $\mathbf{G}_{hkl} = (h, k, l)$. The correspondence between the Cartesian grain system and reciprocal space is then given by the **B** matrix: $\mathbf{G}_c = \mathbf{B}\mathbf{G}_{hkl}$, with

$$\mathbf{B} = \begin{bmatrix} a^* & b^*\cos(\gamma^*) & c^*\cos(\beta^*) \\ 0 & b^*\sin(\gamma^*) & -c^*\sin(\beta^*)\cos(\alpha) \\ 0 & 0 & c^*\sin(\beta^*)\sin(\alpha) \end{bmatrix} \quad (2)$$

and

$$\cos(\alpha) = \frac{\cos(\beta^*)\cos(\gamma^*) - \cos(\alpha^*)}{\sin(\alpha^*)\sin(\beta^*)}. \quad (3)$$

Here $(a, b, c, \alpha, \beta, \gamma)$ and $(a^*, b^*, c^*, \alpha^*, \beta^*, \gamma^*)$ symbolize the lattice parameters in direct and reciprocal space, respectively.

The orientation matrix **U** can be parameterized in numerous ways (well known from texture analysis). As default, we use the $(\phi, \varphi_1, \varphi_2)$ Euler angle notation (Bunge, 1982):

$$\begin{pmatrix} \mathbf{U}_{11} & \mathbf{U}_{12} & \mathbf{U}_{13} \\ \mathbf{U}_{21} & \mathbf{U}_{22} & \mathbf{U}_{23} \\ \mathbf{U}_{31} & \mathbf{U}_{32} & \mathbf{U}_{33} \end{pmatrix} = \begin{bmatrix} \cos(\varphi_1)\cos(\varphi_2) - \sin(\varphi_1)\sin(\varphi_2)\cos(\phi) & -\cos(\varphi_1)\sin(\varphi_2) - \sin(\varphi_1)\cos(\varphi_2)\cos(\phi) & \sin(\varphi_1)\sin(\phi) \\ \sin(\varphi_1)\cos(\varphi_2) + \cos(\varphi_1)\sin(\varphi_2)\cos(\phi) & -\sin(\varphi_1)\sin(\varphi_2) + \cos(\varphi_1)\cos(\varphi_2)\cos(\phi) & -\cos(\varphi_1)\sin(\phi) \\ \sin(\varphi_2)\sin(\phi) & \cos(\varphi_2)\sin(\phi) & \cos(\phi) \end{bmatrix} \quad (4)$$

Equations and diagrams with reference to pole figures and the high-energy X-ray setup can be found in work by Mishin *et al.* (2000).

Next, we deduce the basic diffractometer equations. In order for a given scattering vector **G** to give rise to a diffraction spot it must fulfil Bragg's law:

$$|\mathbf{G}| = 4\pi\sin(\theta)/\lambda. \quad (5)$$

From the geometry in Fig. 2 we have

$$\mathbf{G}_l = \frac{2\pi}{\lambda}\begin{bmatrix} \cos(2\theta) - 1 \\ -\sin(2\theta)\sin(\eta) \\ \sin(2\theta)\cos(\eta) \end{bmatrix}. \quad (6)$$

The coordinate transforms introduced above lead to

$$\mathbf{G}_l = \mathbf{\Omega}\mathbf{S}\mathbf{U}\mathbf{B}\mathbf{G}_{hkl}. \quad (7)$$

4. Image analysis and X-ray tracing

Initially all images are scanned for bright objects that satisfy certain criteria on area, connectivity and maximum intensity. These criteria depend on the experimental conditions and generally have to be found by trial-and-error. Additional criteria may apply, such as the location of an object in the image. Objects meeting the criteria are defined as spots. Spots

are associated with a CM pixel position, an ω position (the middle of the $\Delta\omega$ interval) and an integrated intensity.

Depending on mosaic spread, the same reflections may give rise to spots appearing at several consecutive ω settings. *GRAINDEX* identifies such groups as single spots, adds integrated intensities and assigns pixel positions and ω positions based on weighted averages.

Next, valid spots in images acquired at different detector distances are grouped into a reflection and the linear fitting (orthogonal regression) is performed. Three criteria are applied to discriminate against erroneous groupings, typically caused by spot overlap. First, tolerances are set on the χ^2 of the fit and the variation in integrated intensity within corresponding spots. Second, the fitted 2θ value is compared with calculated ones. If the observed value matches, within a tolerance, one of the calculated values, the reflection is put in a list with others of that $\{hkl\}$ family; otherwise it is disregarded. If the observed 2θ could be associated with more than one $\{hkl\}$, list entries corresponding to each $\{hkl\}$ family are created. The erroneous reflections are sorted out later. Third, the fitted CM origin obtained by extrapolation of the fitted line to the incident beam plane should be positioned within the illuminated region of the sample.

The integrated intensity of the reflection is taken to be that of the outermost L setting. For comparison between reflections it is multiplied by polarization Debye–Waller and Lorentz factors. With our conventions the Lorentz factor is

$$\mathrm{Lor}(2\theta, \eta) = 1/[\sin(2\theta)|\sin(\eta)|]. \tag{8}$$

Note that spots appearing near $\eta = 0$ and $\eta = 180^\circ$ have to be discarded as the Lorentz factor is diverging at this point and parts of the mosaic spread may be situated in the inaccessible areas on the unit sphere near the rotation axis. Also such spots will tend to appear at several consecutive ω settings, adding to noise in the summed intensity. In practice, this restriction is handled by defining certain η ranges to be void.

5. Indexing

Indexing is not straightforward, partly because of the overlap of spots, and partly because of their magnitudes. Three criteria may be applied to sort reflections according to grain: the position (x_ω, y_ω), the crystallography, and the integral intensities (area of grain section). Among these, the latter is considered the least robust. One reason is the issue of the 'grains at the boundary'. In many cases, samples will have a plate- or rod-like geometry with dimensions that are too large for the entire section to be illuminated by the incident beam. Hence, there will be a number of grains which will be partly illuminated and which will tend to rotate in and out of the illuminated area. The spots arising from these pieces of grains will still be assigned correct orientations and X-ray tracing will place the CM of the pieces within the area of the full grains. In contrast, the intensities will be reduced. In the limit of the grain dimensions being much larger than the accuracy with which the X-ray tracing defines the CM positions, it is possible to rely primarily on the position criterion.

In the limit of the grains being much smaller than the error on the CM position, indexing must rely on the crystallographic criteria. Let us therefore consider the case of equal-sized grains, all placed at the origin. At first, it seems relevant to compute the angles between all pairs of observed reflections and compare these to a list of allowed angles, dictated by the space-group symmetry. Grains are then defined by groups of reflections, where all pairs mutually fulfil the angle criterion. However, as n reflections give rise to 2^n possible groups, the speed of analysis becomes prohibitive for large n. Instead, space-group symmetry can be probed directly, leading to an algorithm for which the speed is almost independent of n. By rearranging (7) as

$$\mathbf{G}_s = \mathbf{UBG}_{hkl}, \tag{9}$$

the measurements of $\mathbf{G}_s$ and crystallographic properties ($\mathbf{B}$, $\mathbf{G}_{hkl}$) are separated. Note that the number, n, of measured reflections $(\mathbf{G}_s)_i$ increases with the number of grains, whereas the number M_0 of theoretical reflections $(\mathbf{BG}_{hkl})_j$ is constant.

The underlying principle of the algorithm is to scan through all orientations and for each orientation $\mathbf{U}$ count the number, $M_{\rm exp}$, of (hkl)'s for which there is at least one observation $\mathbf{G}_s$ that matches $\mathbf{UBG}_{hkl}$. Grains are defined by completeness and uniqueness criteria. The former requires $M_{\rm exp} \geq (1 - \alpha)M_0$, where the tolerance α is rather small. The latter requires that the set of matching (hkl)'s is not a sub-set of the set of matching (hkl)'s for another $\mathbf{U}$ setting. Naturally, scanning through all orientations in a strict mathematical sense is not possible. However, by incrementing the three Euler angles defining $\mathbf{U}$ by finite steps *and* allowing a corresponding mismatch between the left- and right-hand sides of (9), the number of orientations to test becomes finite.

To sample Euler space homogeneously, we use the metric (Hansen *et al.*, 1978)

$$\mathrm{d}\mathbf{U}(\phi, \varphi_1, \varphi_2) = (1/8\pi^2)\sin(\phi)\,\mathrm{d}\phi\,\mathrm{d}\varphi_1\,\mathrm{d}\varphi_2. \tag{10}$$

Furthermore, the crystal symmetry of each grain implies that only a subset of the full $[0, \pi] \times [0, 2\pi] \times [0, 2\pi]$ Euler space needs to be sampled. As an example, 1/24 of the volume is sufficient for cubic symmetry and this yields a corresponding increase in speed of the algorithm. For a discussion of the symmetries in Euler space, see work by *e.g.* Randle & Engler (2000).

To allow an effective search for the $(\mathbf{G}_s)_i$'s, initially these are placed in look-up tables, one for each $\{hkl\}$ family. In these, the unit vectors $\mathbf{G}_s/|\mathbf{G}_s|$ are represented by spherical coordinates (ψ_1, ψ_2). For a given $\mathbf{UBG}_{hkl}$, an area around the theoretical $(\psi_1, \psi_2)^0$ is searched and the matching observations found (if any). The size of the search area reflects the measuring errors and the step size in the scan over Euler space.

For a given step in Euler space, the calculated $\mathbf{G}_{hkl}$'s are grouped as follows.

Group A: reflections that have no matching observations.

Group B: reflections that have one matching observation.

Group C: reflections that have two or more matching observations.

Provided that the number of A-type reflections is small enough to fulfil the completeness criteria, a linear least-squares fit is made to the orientation of the grain based on the $\mathbf{G}_s$ vectors associated with group B. To linearize equation (9) in ϕ, φ_1 and φ_2, we expand to first order around the nominal step position in Euler space. Hence, for a given step $(\phi^0, \varphi_1^0, \varphi_2^0)$ and corresponding $\mathbf{U}^0 = \mathbf{U}(\phi^0, \varphi_1^0, \varphi_2^0)$ we have

$$\mathbf{U}_{mn} = \mathbf{U}^0_{mn} + \frac{\delta \mathbf{U}}{\delta \phi}(\mathbf{U}^0)_{mn}\Delta\phi + \frac{\delta \mathbf{U}}{\delta \varphi_1}(\mathbf{U}^0)_{mn}\Delta\varphi_1 + \frac{\delta \mathbf{U}}{\delta \varphi_2}(\mathbf{U}^0)_{mn}\Delta\varphi_2. \quad (11)$$

For step sizes of a few degrees in ϕ, φ_1 and φ_2, this is an excellent approximation. The fit is weighted with respect to the estimated experimental errors in ω and η:

$$\chi^2 = \sum_{i,j} \frac{\{(\mathbf{G}_s)_j - [\mathbf{U}(\Delta\phi, \Delta\varphi_1, \Delta\varphi_2)\mathbf{B}(\mathbf{G}_{hkl})]_j\}^2_i}{\sigma^2_{ij}(\Delta\omega, \Delta\eta)}. \quad (12)$$

Here index i runs over the spatial coordinates, $i = 1, 2, 3$, while j enumerates the members of group B. σ^2_{ij} is the error on $\mathbf{G}_s$ vector number j in the point $\mathbf{U}^0$, calculated by error propagation using equations (1) and (6).

This approach, trusting the group B reflections, has one pitfall. Assume a reflection from the grain to be found is lacking, *e.g.* because of overlap, but one stray reflection is positioned within the same search area in (ψ_1, ψ_2). Then the stray reflection will be assigned as a group B reflection. This reflection is likely to move the least-squares fit minimum substantially as it contributes with a large weight. To discard such 'outliers', the fit is performed in iterative steps using a reweighting scheme. Alternative methods for producing a more robust fit with less or no weight on outliers can be found in the book by Press *et al.* (1992).

The final result of the fit to the group B reflections is used to choose among observations in group C. For a given (hkl), the $\mathbf{G}_s$ observation that is closest and within $\Delta\omega$ and $n\Delta\eta$ of the expected position is chosen (if any).

Returning to the general case of grains of various sizes, which on average are comparable with the error in the CM positions, *GRAINDEX* uses a modification of the Euler scan procedure just outlined. Once an orientation is found fulfilling the completeness criterion, the associated B- and C-type reflections are sorted by CM position and/or integrated intensity.

6. Grain position, volume and orientation

Having indexed the grains, optimized positions and volumes can be found from the set of associated reflections. *GRAINDEX* determines the position as a weighted average of the (x_ω, y_ω) coordinates. The volume is defined by conventional single-crystal refinement. The necessary intensity normalization can be obtained *e.g.* by summing all the reflections from all the grains in the layer of interest, *i.e.* by acquiring data through a complete ω sweep from -90 to 90°.

The precise determination of the orientation matrix is complicated by the large relative uncertainties on ω. In fact, by simply associating a reflection with the middle position in the $\Delta\omega$ interval, the assumption of Gaussian distributed data underlying least-squares routines fails. Hence, maximum-likelihood methods may be relevant. In practice, *GRAINDEX* does use the least-squares formalism of equation (12), associating errors of $\Delta\omega$ with the ω observations.

7. Simulations

To verify the indexing procedure we have performed Monte Carlo simulations. The grains were assumed to have random orientations and to appear as ideal intensity spikes in the images. Furthermore, they were assumed to be of the same size and to be positioned on top of each other, such that the indexing relied on the crystallographic criteria only. An example of the results is shown in Fig. 3 for 100 grains of f.c.c. symmetry. The simulated data covered an ω range from -45 to 45° in steps of 1° and included only the four $\{hkl\}$ families with highest d spacings. In total, 2498 reflections were generated. *GRAINDEX* was operated with a 1° step in the Euler angles and estimated errors of $\Delta\omega = 0.5^\circ$ and $\Delta\eta = 0.3^\circ$. The completeness and uniqueness criteria were 0.9 and 0.2, respectively. Computing time was 1 min.

Exactly 100 grains were identified and indexed by *GRAINDEX*. Histograms are shown in Fig. 3. These provide statistics over the grain distributions of the completeness factor (the number of reflections found by *GRAINDEX*, correct or not, divided by the number of reflections generated) and purity factor (the number of correct reflections divided by the number of reflections found). The average values for the two distributions are 99.4 and 99.8%, respectively. The result is found to be robust with respect to changes in the *GRAINDEX* parameters.

8. Discussion

The method outlined is implemented at the 3DXRD microscope at beamline ID11, ESRF. This instrument operates in the 50–100 keV range with broadband optics (Lienert *et al.*, 1999). Typically, the line focus is produced with a bent Laue monochromator. With a focal distance of 2 m and a divergence of <0.5 mrad, the spot size is presently 1–2 μm. The flux is sufficient to observe grains of size 0.3 μm (Jensen & Poulsen, 2000). The spatial resolution is mainly limited by the two-dimensional detectors available, which at present have point-spread functions of 20 μm. With typical exposures times of 1 s, one plane in the sample is characterized within a few minutes.

The program *GRAINDEX* runs on a Windows platform. It utilizes the commercial software *Image Pro Plus* for visualization and some of the image analysis tasks. It supports all space groups. Running on a 1.4 GHz Pentium, one layer is indexed within approximately 1 min. Hence, the speed is sufficient for on-line analysis of the positions, volumes and orientations.

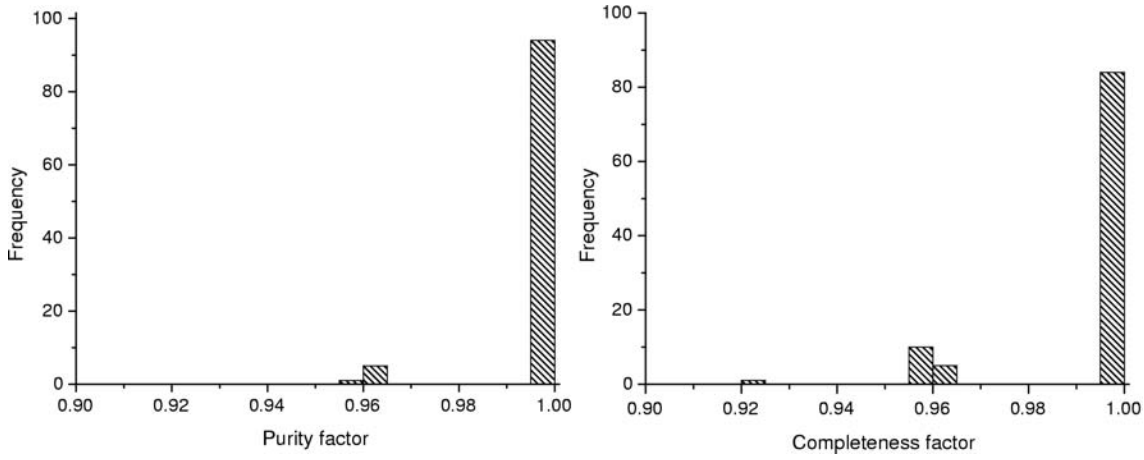

Figure 3
Histograms of the outcome of *GRAINDEX* when provided with input from a simulation of 100 randomly oriented grains (2498 diffraction spots). *GRAINDEX* identified all 100 grains. For each grain, the completeness factor is defined as the number of reflections found (correct or not) divided by the number of reflections generated. Likewise, the purity factor is defined as the number of correct reflections divided by the number of reflections found.

There are three main limitations of the tracking technique. Firstly, deformation will lead to broadening of spots and eventually to spot overlap. The image analysis part then breaks down. So far grains have been partially indexed up to 11% deformation (Margulies *et al.*, 2001). Secondly, even for non-deformed grains there is a limit to the number of spots that can be indexed. In the case of small grains with random orientations in a crystal with cubic symmetry, we estimate that this limit is around 1000. Thirdly, the grains at the boundary of the illuminated volume will give rise to a background of spots, which do not fulfil the completeness criteria. To include these, a more extensive analysis is needed.

One remedy to some of these problems could be to combine tracking with the use of a conical slit (Nielsen, Wolf *et al.*, 2000). The conical slit then defines an interior gauge volume, centred at the ω rotation axis. Only spots arising from this 'area of interest' will reach the detector. Another is to install a slit in front of the sample and monitor the intensity of all the spots as a function of the width of the beam (Lauridsen *et al.*, 2000). Spots arising from grains fully illuminated by the beam are easily identified in this way.

In parallel with the efforts presented here, Ice and co-workers from Oak Ridge National Laboratory have developed a white-beam technique (Chung & Ice, 1999) for studying local texture and strain. Their technique has the intriguing aspect that sample rotation is not needed. However, the number of spots per image increases substantially, leading to a reduced upper limit on the number of grains in the gauge volume. With their point-focus beam, the sample has to be mapped by scanning in both y and z at the expense of speed. With respect to the actual implementation, another major difference is that the Oak Ridge instrument operates with $\sim$20 keV X-rays and shorter focal lengths, enabling better spatial resolution at the expense of a substantially lower penetration power (*e.g.* for Fe the penetration depth is 50 μm and 2100 μm for 20 and 80 keV, respectively) and less space for sample surroundings.

We thank P. Kirkegård, B. S. Johansen, D. Hennessy and C. Xiao for discussions, S. F. Nielsen for manual tests of some of the algorithms, Å. Kvick and G. Vaughan at ESRF for general support, as well as our colleagues U. Lienert, L. Margulies, T. Lorentzen and D. Juul Jensen who took part in experiments. This work was supported by the Danish Natural Science Research Council *via* Dansync. RMS also received support from the MRSEC program of the US National Science Foundation under Award DMR-0079996.

References

Bouchard, R., Hupfeld, D., Lippmann, T., Neuefeind, J., Neumann, H.-B., Poulsen, H. F., Rütt, U., Schmidt, T., Schneider, J. R., Sussenbach, J. & von Zimmermann, M. (1998). *J. Synchrotron Rad.* **5**, 90–101.
Bunge, H. J. (1982). *Texture Analysis in Materials Science.* London: Butterworths.
Busing, W. R. & Levy, H. A. (1967). *Acta Cryst.* **22**, 457–464.
Chung, J.-S. & Ice, G. E. (1999). *J. Appl. Phys.* **86**, 5249–5255.
Hansen, L., Pospiech, J. & Lücke, K. (1978). *Tables of Texture Analysis of Cubic Crystals.* Berlin: Springer-Verlag.
Juul Jensen, D., Kvick, Å., Lauridsen, E. M., Lienert, U., Margulies, L., Nielsen, S. F. & Poulsen, H. F. (2000). *Mater. Res. Soc. Symp. Proc.* **590**, 227–240.
Juul Jensen, D. & Poulsen, H. F. (2000). *Proceedings of the 21st Risø International Symposium on Materials Science*, Roskilde, Denmark, pp. 103–124.
Lauridsen, E. M., Juul Jensen, D., Poulsen, H. F. & Lienert U. (2000). *Scr. Mater.* **43**, 561–566.
Lienert, U., Poulsen, H. F. & Kvick, Å. (1999). *Proceedings of the 40th Conference of AIAA on Structures, Structural Dynamics and Materials*, St Louis, USA, pp. 2067–2075.
Margulies, L., Lorentzen, T., Poulsen, H. F. & Leffers, T. (2001). *Acta Mater.* Submitted.
Margulies, L., Winther, G. & Poulsen, H. F. (2001). *Science*, **291**, 2392–2394.

Mishin, O. V., Lauridsen, E. M., Krieger Lassen, N. C., Brückner, G., Tschentscher, T., Bay, B., Juul Jensen, D. & Poulsen, H. F. (2000). *J. Appl. Cryst.* **33**, 364–371.

Nielsen, S. F., Ludwig, W., Bellet, D., Lauridsen, E. M., Poulsen, H. F. & Juul Jensen, D. (2000). *Proceedings of the 21st Risø International Symposium on Materials Science*, Roskilde, Denmark, pp. 473–478.

Nielsen, S. F., Wolf, A., Poulsen, H. F., Ohler, M., Lienert, U. & Owen, R. A. (2000). *J. Synchrotron Rad.* **7**, 103–109.

Poulsen, H. F., Garbe, S., Lorentzen, T., Juul Jensen, D., Poulsen, F. W., Andersen, N. H., Frello, T., Feidenhans'l, R. & Graafsma, H. (1997). *J. Synchrotron Rad.* **4**, 147–154.

Press, W. H., Teukolsky, S. A., Vetterling, W. T. & Flannery, B. P. (1992). *Numerical Recipes in FORTRAN*, pp. 694–700. Cambridge University Press.

Randle, V. & Engler, O. (2000). *Introduction to Texture Analysis, Macrotexture, Microtexture and Orientation Mapping.* London: Gordon and Breach.

A3

Journal of
Applied Crystallography
ISSN 0021-8898

Received 2 May 2001
Accepted 30 August 2001

Three-dimensional maps of grain boundaries and the stress state of individual grains in polycrystals and powders

H. F. Poulsen,[a]* S. F. Nielsen,[a] E. M. Lauridsen,[a] S. Schmidt,[a] R. M. Suter,[b] U. Lienert,[c] L. Margulies,[a,c] T. Lorentzen[a] and D. Juul Jensen[a]

[a]Materials Research Department, Risø National Laboratory, DK-4000 Roskilde, Denmark, [b]Department of Physics, Carnegie Mellon University, Pittsburgh, PA 15213, USA, and [c]European Synchrotron Radiation Facility, BP 220, F-38043 Grenoble CEDEX, France. Correspondence e-mail: henning.friis.poulsen@risoe.dk

A fast and non-destructive method for generating three-dimensional maps of the grain boundaries in undeformed polycrystals is presented. The method relies on tracking of micro-focused high-energy X-rays. It is verified by comparing an electron microscopy map of the orientations on the 2.5 × 2.5 mm surface of an aluminium polycrystal with tracking data produced at the 3DXRD microscope at the European Synchrotron Radiation Facility. The average difference in grain boundary position between the two techniques is 26 μm, comparable with the spatial resolution of the 3DXRD microscope. As another extension of the tracking concept, algorithms for determining the stress state of the individual grains are derived. As a case study, 3DXRD results are presented for the tensile deformation of a copper specimen. The strain tensor for one embedded grain is determined as a function of load. The accuracy on the strain is $\Delta\varepsilon \simeq 10^{-4}$.

1. Introduction

At Risø we have recently developed several methods for non-destructive characterization of the individual grains inside bulk materials (Poulsen *et al.*, 1997; Lienert, Poulsen, Honkimäki *et al.*, 1999; Nielsen, Wolf *et al.*, 2000; Juul Jensen, Kvick *et al.*, 2000). The methods are based on diffraction of high-energy X-rays ($E \geq 50$ keV), enabling three-dimensional studies within specimens of millimetre-to-centimetre thickness. In collaboration with the European Synchrotron Radiation Facility (ESRF), the methods have been implemented at the three-dimensional X-ray diffraction (3DXRD) microscope, a dedicated instrument situated at the ID-11 Materials Science Beamline (Lienert *et al.*, 1999). The instrument operates with monochromatic micro-focused beams in the 50–100 keV range. The focal spot sizes are 1 μm × 1 mm and 5 × 5 μm for beams focused in one and two dimensions, respectively.

For undeformed or weakly deformed polycrystals or powders, tracking is the method of choice. Tracking combines the conventional 'rotation method' with ray tracing of the diffracted beams. A program, *GRAINDEX*, has been established that can index the reflections from several hundred grains simultaneously and derive the positions, volumes and orientations of the grains. The data acquisition procedures and software algorithms are both fast, typically requiring of the order a few minutes. Hence, studies of grain dynamics under realistic processing conditions are possible. As such, the first applications of the tracking method relates to *in situ* studies of recrystallization (Lauridsen *et al.*, 2000; Juul Jensen & Poulsen, 2000) and deformation (Margulies *et al.*, 2001) of metals. The details of the tracking principle and the *GRAINDEX* algorithm are presented by Lauridsen *et al.* (2001).

In this article, we extend the tracking concept in two ways. First we establish the geometry and algorithms for a fast and conceptually simple method of mapping the grain boundaries in three dimensions. A combined 3DXRD and electron microscopy study verifies the method, which works for undeformed and coarse-grained specimens. Next, we discuss two approaches to determine the elastic strain tensors of the grains. One of these is verified by an *in situ* deformation study of a copper polycrystal.

2. Review of the tracking principle

The tracking procedure combines the monochromatic 'rotation method' with X-ray tracing. The principle is sketched in Fig. 1. The incoming beam is focused in one dimension to illuminate a layer in the sample. The divergence of this beam is assumed to be negligible. The sample is mounted on an ω rotation table, with the rotation axis perpendicular to the illuminated plane. For a given ω setting, some of the grains intersected by the layer will give rise to diffracted beams, which are transmitted through the sample to be observed as spots by a flat two-dimensional detector. The detector is aligned perpendicular to the monochromatic beam. In addition, an optional slit can be placed before the sample.

The tracking algorithm works as follows. Images are acquired at a number of rotation-axis-to-detector distances, L_1

to L_N. Equivalent spots, relating to the same reflection, are identified and a best fit to a line through the centre-of-mass (CM) positions of these spots is determined. Extrapolating the line to its intersection with the layer defined by the monochromatic beam, the CM position of the section of the grain, (x_l, y_l), is found, as well as the Bragg angle 2θ and the azimuthal angle η. For definitions of zero points and positive directions of these angles see Fig. 1.

To obtain information from all the grains in one layer, the X-ray tracing is repeated at a number of ω settings in steps of $\Delta\omega$. During each exposure, the sample is oscillated by $\pm\Delta\omega/2$. For high-energy X-rays, an ω range of 180° assures that virtually all reflections can be included in the analysis; this justifies the use of a sample stage with only one rotation. However, typically an ω range of 25–40° is sufficient. Finally, for a complete three-dimensional mapping, the procedure is repeated for a set of layers by translating the sample in z.

For each layer, the program *GRAINDEX* sorts the reflections and identifies grains, complete with an orientation matrix **U** and a list of indexed reflections. For the details of the data analysis, see the paper by Lauridsen *et al.* (2001); however, for reference purposes we present the basic equation

$$\mathbf{G}_l = \mathbf{\Omega S U B G}_{hkl}. \tag{1}$$

Here $\mathbf{G}_l$ is the scattering vector as determined in the laboratory system defined in Fig. 1. $\mathbf{\Omega}$, **S** and **U** are rotation matrices between the laboratory system (index l), a system rigidly attached to the ω turntable (index ω), a sample system (index s) and a Cartesian coordinate system for a specific grain (index c): $\mathbf{G}_l = \mathbf{\Omega G}_\omega$, $\mathbf{G}_\omega = \mathbf{S G}_s$, $\mathbf{G}_s = \mathbf{U G}_c$. $\mathbf{G}_{hkl}$ is a vector comprising the Miller indices, $\mathbf{G}_{hkl} = (h, k, l)$. The reciprocal-lattice parameters are contained in the **B** matrix

$$\mathbf{B} = \begin{bmatrix} a^* & b^*\cos(\gamma^*) & c^*\cos(\beta^*) \\ 0 & b^*\sin(\gamma^*) & -c^*\sin(\beta^*)\cos(\alpha) \\ 0 & 0 & c^*\sin(\beta^*)\sin(\alpha) \end{bmatrix} \tag{2}$$

with

$$\cos(\alpha) = \frac{\cos(\beta^*)\cos(\gamma^*) - \cos(\alpha^*)}{\sin(\alpha^*)\sin(\beta^*)}. \tag{3}$$

Here $(a, b, c, \alpha, \beta, \gamma)$ and $(a^*, b^*, c^*, \alpha^*, \beta^*, \gamma^*)$ symbolize the lattice parameters in direct and reciprocal space, respectively.

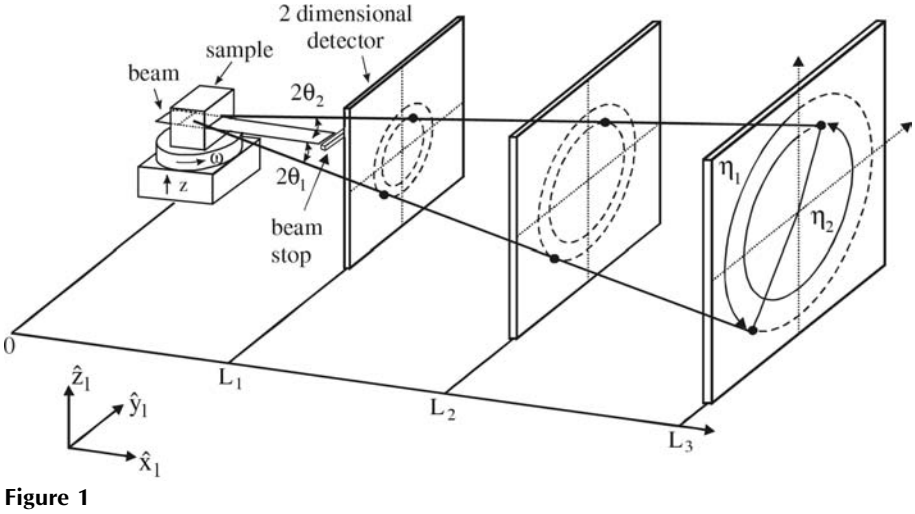

Figure 1
Sketch of the tracking principle. The diffraction spots appearing in exposures of the area detector at different sample–detector distances are projected back to the illuminated plane in the sample. The angles $(2\theta, \eta, \omega)$ are defined as well as the laboratory coordinate system.

3. Mapping of the grain-boundary topology

For a 'perfect' grain with no orientation spread and an ideal instrument there will be a one-to-one correspondence between the shape of the illuminated cross section of a grain and the shape cross section of any associated diffraction spot. Hence, the position of the grain boundary can be determined by back-projecting the periphery of the diffraction spot along the line established by the X-ray tracing. Introducing a local coordinate system $(y_{\rm det}, z_{\rm det})$ around the CM of the spot and analogously a system $(\Delta x, \Delta y)$ around the CM of the grain section, the projection becomes

$$y_{\rm det} = \Delta y, \quad z_{\rm det} = \Delta x \tan(2\theta)\cos(\eta). \tag{4}$$

For high-energy X-rays with small Bragg angles, the projection is seen to be very anisotropic. Typically, a square grain section is projected into a rectangular diffraction spot with an aspect ratio of 10:1. Furthermore, for η = 90° and η = 270°, the projection collapses into a line. Hence, diffraction spots appearing within a certain η range around these limits cannot be part of the analysis.

In metallurgy and ceramics research, the grains are seldom truly perfect. Moreover, the instrumental resolution is an issue. Hence, the intensity distribution of a spot on the detector, $I_{\rm det}(y_{\rm det}, z_{\rm det})$, can be seen as the idealized response of a 'perfect' grain, I_0, convoluted with the instrumental resolution function, Res, and the orientation spread of the reflection, Q. Res can be determined with a high degree of accuracy; its main components are the detector response function and the smearing caused by the oscillation in ω during acquisition. In contrast, Q varies from reflection to reflection and is *a priori* unknown. (However, provided that the detector is sufficiently close to the sample, there is no noticeable spread in 2θ.)

The existence of an orientation spread within each grain also implies that some of the reflections will be associated with several diffraction spots appearing in images acquired at neighbouring ω settings. As the ω axis is a fixed point for the rotation, this effect is pronounced for reflections appearing near the axis, *i.e.* for spots with $\eta \simeq 0$ and $\eta \simeq 180°$.

To handle these complications, it seems relevant to use space-filling algorithms based on either intensity conservation constraints or fits to the local orientation function (Monte Carlo simulations). The establishment

of such algorithms is outside the scope of this article. Instead, we pursue the simple approach of determining the outlines of the diffraction spots and we back-project the outlines into the sample plane. This approach can be seen as a fast procedure for obtaining a coarse map, to be refined later in the analysis by more advanced algorithms.

We have tested two approaches. In the first, the outline of a given spot was determined by an intensity threshold, fixed at a certain percentage of the maximum pixel intensity within the spot. In the second, the outline was defined by the points of steepest descent. The image-processing program *Image Pro* used by *GRAINDEX* provides routines to find the outline of any object by either method. It is found that the steepest-descent method is more robust. Consequently, this has been used for the data presented here. The problem of a reflection breaking up into several spots is solved by merging the back-projected outlines of the individual parts.

For a given reflection, the back-projected outline can be associated with two types of error. The first is related to the uncertainty in the CM projection. The second reflects the anisotropy in the projection; *cf.* equation (4). Based on these errors, the resulting grain boundary can be determined from a fit to the back-projected outlines of all the reflections associated with the grain. Alternatively, the grain boundary is determined as the back-projected outline of the reflection which has superior projection properties. That is, the one associated with a minimum orientation spread and with the most favourable angular setting, *i.e.* the largest projection factor $\tan(2\theta)\cos(\eta)$ [*cf.* equation (4)].

4. Verification and discussion of the grain mapping principle

To verify the principle, a combined synchrotron and electron microscopy study was performed on a coarse-grained 99.996%-pure aluminium polycrystal. Initially the grains at one surface of the sample were mapped by the electron back-scattered pattern (EBSP) method. In this way, the local orientations on the surface were sampled in a 20×20 μm grid. Some 50 grains were identified.

Next, the sample was aligned with the same surface parallel to the beam at the 3DXRD microscope. The tracking was performed with a line-focused beam of dimensions 800×5 μm. The beam was parallel to the surface and incident at a layer 10 μm below it. The X-ray energy was $E = 50$ keV and the bandwidth was $\Delta E/E = 0.5\%$. The two-dimensional detector is equipped with a powder scintillator screen, which is coupled by focusing optics (lenses) to a charge-coupled device (CCD). The resulting pixel size is 4.3 μm, but the point-spread function is substantially larger, with a full width at half-maximum (FWHM) of 16 μm.

The range of orientation variations within the grains was found on average to be of the order of 1°. The surface dimensions of the sample were 2.5×2.5 mm, making it necessary to acquire information from three strips across the sample. For each strip, the tracking procedure was performed with 22 equidistant ω settings with $\Delta\omega = 2°$ and with detector distances $L_1 = 7.6$, $L_2 = 10.3$ and $L_3 = 12.9$ mm. With a 1 s exposure time, the total data acquisition time was less than 4 min.

An example of a set of images acquired at L_1, L_2 and L_3 is given in Fig. 2. The diffraction spots are seen to move outwards from the centre of the images when the detector is translated away from the sample. The error on the linear fit to the CM of such corresponding spots does on average correspond to an uncertainty of ±17 μm along the beam direction in the sample plane.

Fig. 3 is an example of a reflection, where the diffracted intensity is divided into four spots. This kind of break-up into a few large flakes is found to be typical of the specimen. The tracking algorithm associated the four diffraction spots with directions that differed by less than 2°. Hence, the corresponding four outlines were merged into one, defined as the circumference of the total area enclosed by any of the four outlines. Analogously, diffraction spots associated with the same reflection but appearing in different strips were identified by their common direction, and the outlines once again were merged by superposition.

The outlines of three reflections associated with the same grain are compared in Fig. 4. The direction of the incident beam is in all cases within a few degrees parallel to the vertical direction in the images. The corresponding larger uncertainty on the outlines in this direction is evident. Furthermore, we observe that the reflection with the most favourable angular settings (largest 2θ and η furthest away from the equatorial plane) gives rise to the best correspondence with the EBSP

Figure 2
Diffraction patterns from the aluminium polycrystal at sample–detector distances of 7.6 mm (left), 10.3 mm (middle) and 12.9 mm (right). The rectangular spots near the centre of the images are artefacts caused by the tails of the incident beam. The horizontal length of the rectangular spots is 0.8 mm.

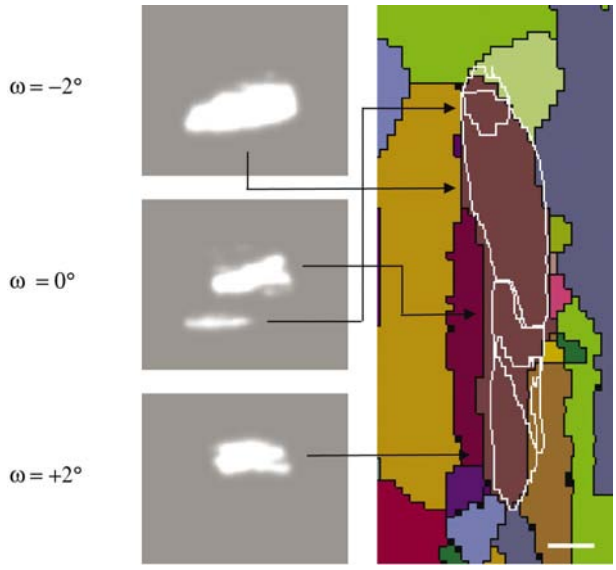

Figure 3
Example of the effect of grain break-up. For this particular reflection, the diffracted intensity is distributed over three images, acquired at $\omega = -2$, 0 and 2°. Left: identical sections of the images acquired at the three ω settings. Right: the back-projection of the outlines of the four spots into the sample plane (white lines). These are superimposed on an EBSP image of the same section of the sample surface (colours and black lines). The white scale bar at the bottom is 100 μm.

data. Also shown in Fig. 4 is the weighted average of the three outlines. For reasons of robustness and simplicity, we choose to consider only the best reflection in the following.

The grain orientations determined by the tracking routine and by EBSP agreed within 1°. For comparison, the tracking procedure produced grain orientations with an accuracy of better than ±0.1°, as determined by the scatter between reflections from the same grain. The difference between the techniques is therefore thought mainly to arise from EBSP and alignment errors.

In Fig. 5, the resulting EBSP and 3DXRD grain boundaries are superposed. As mentioned, the 3DXRD boundaries are based on data with no interpolation or averaging between reflections from the same or neighbouring grains. The misfit between the tracking and the EBSP boundaries was found by linear intercept to be 26 μm on average with a maximum of 40 μm. These data should be compared with the 16 μm point-spread function of the detector, the 20 μm step size in the EBSP data, and also the 10 μm difference in z.

The degree of correspondence obtained with the crude outline algorithm illustrates the potential of mapping grains in three dimensions. In fact, the quality of the map is sufficient for many basic studies. A first application of such a mapping, namely a study of the wetting of aluminium grain boundaries by liquid gallium, has been published elsewhere (Nielsen, Ludwig *et al.*, 2000). The use of difference maps should also enable grain-boundary mobility studies. More generally, simplified descriptions of the grain morphology in terms of centroids (centre-of-mass position, volume and aspect ratio) can be very useful, especially for classifying grains. Furthermore, it should be recalled that many annealed polycrystals exhibit orientation spreads substantially smaller than 1°.

Ultimately, for near-perfect grains the limit on the mapping accuracy is governed by the width of the focal line, the detector resolution and the accuracy of the sample movements. With present technology these factors can all be reduced to 1 μm. Indeed, for synchrotron-based X-ray tomography, which is also based on a projection of high-energy X-rays on two-dimensional detectors, a spatial accuracy below 1 μm has been reached (Baruchel *et al.*, 2000).

For grains with an orientation spread above 1°, the outline formalism breaks down. Two routes can then be followed. The first is to restrict the incoming beam in both directions, such that only a line through the specimen is illuminated. In this

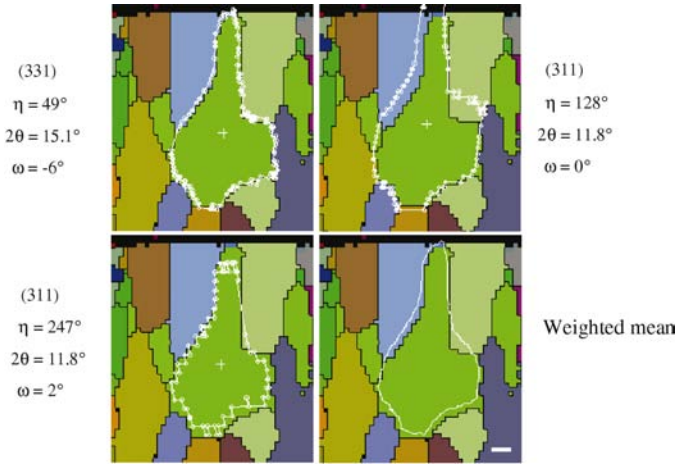

Figure 4
The outline of one grain as determined from three different reflections (white lines). These are superimposed on an EBSP image of the same section of the sample surface (colours and black lines). The image in the lower right corner is a weighted fit to the grain boundary based on the three outlines and estimates of their errors. The white scale bar in the right corner is 100 μm.

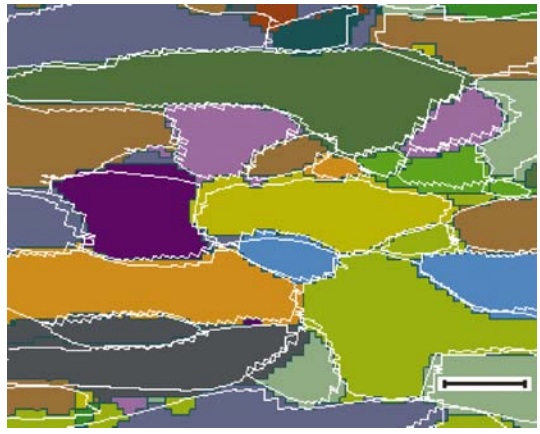

Figure 5
Validation of the X-ray tracing algorithm. Colours and black outlines mark the grains and grain boundaries on the surface of the aluminium polycrystal as determined by electron microscopy (EBSP). Superposed as white lines are the grain boundaries resulting from the synchrotron experiment. The scale bar at the bottom is 400 μm.

case, the fact that the orientation spread does not have a radial (2θ) component implies that the one-to-one correspondence can be regained. However, the mapping becomes much slower, as the sample needs to be scanned in both y and z. As an alternative, a conical slit can be inserted between the sample and the detector for a full three-dimensional definition of the gauge volume, at the cost of further reduced data acquisition speed. First mappings with the conical slit were presented by Poulsen *et al.* (1997) and Nielsen, Wolf *et al.* (2000). The second route is to ray-trace the individual parts of the diffraction spot by means of Monte Carlo simulations. Work along both routes as well as work on space-filling routines in general is in progress.

5. Strain formalism

For strain analysis, it is suggested to extend the tracking algorithm by including data at a large sample–detector distance, L_N. The larger distance facilitates a superior 2θ resolution. In practice, two detectors may be used: a moveable and semitransparent one with a small pixel size at short sample–detector distances, and a fixed detector with a larger field of view placed at a large distance.

The elastic strain is a property of the unit cell in each grain. Hence, for each grain we define a Cartesian system with axes ($\mathbf{x}_d$, $\mathbf{y}_d$, $\mathbf{z}_d$) and with $\mathbf{x}_d$ parallel to $\mathbf{a}$, $\mathbf{y}_d$ in the plane of $\mathbf{a}$ and $\mathbf{b}$, and $\mathbf{z}_d$ perpendicular to that plane. In analogy with equation (2), the transformation between the two systems is given by the matrix

$$\mathbf{A} = \begin{bmatrix} a & b\cos(\gamma) & c\cos(\beta) \\ 0 & b\sin(\gamma) & -c\sin(\beta)\cos(\alpha^*) \\ 0 & 0 & c\sin(\beta)\sin(\alpha^*) \end{bmatrix}. \quad (5)$$

Let $\mathbf{A}_0$ refer to the lattice of a reference grain, typically representing an unstrained situation. Let $\mathbf{A}$ refer to the lattice of the same grain in a strained situation. We then define the matrix $\mathbf{T}$ by

$$\mathbf{T} = \mathbf{A}\mathbf{A}_0^{-1}. \quad (6)$$

By definition, the strain tensor is

$$\varepsilon_{ij} = \tfrac{1}{2}(\mathbf{T}_{ij} + \mathbf{T}_{ji}) - \mathbf{I}_{ij}, \quad (7)$$

where $\mathbf{I}$ is the identity matrix.

We identify two approaches to the strain analysis. In the first, the tensor elements are derived from a linear fit to the 2θ shifts. In the second, a full refinement of the unit-cell parameters is performed, based on the combined shift in ω, η and 2θ. We outline a formalism for both methods.

The analysis of the 2θ shift of the reflections is similar to the one used for macroscopic stress and strain determination with neutron diffraction (Allen *et al.*, 1985), with the exception that the sample reference system is replaced by the grain system. For each reflection i, we determine the components (l, m, n) of the unit vector $\mathbf{G}_c/|\mathbf{G}_c|$. For hard X-rays, with small Bragg angles, to a very good approximation there is a linear relation between the shift in 2θ and the strain ε_i:

$$\begin{aligned} \varepsilon_i &= (d_i - d_0)/d_0 \\ &= [\sin(\theta_i) - \sin(\theta_0)]/\sin(\theta_0) \\ &= \begin{pmatrix} l_i & m_i & n_i \end{pmatrix} \begin{pmatrix} \varepsilon_{11} & \varepsilon_{12} & \varepsilon_{13} \\ \varepsilon_{12} & \varepsilon_{22} & \varepsilon_{23} \\ \varepsilon_{13} & \varepsilon_{23} & \varepsilon_{33} \end{pmatrix} \begin{pmatrix} l_i \\ m_i \\ n_i \end{pmatrix}. \end{aligned} \quad (8)$$

This equation can be solved by the singular-value decomposition procedure for over-determined linear systems. In addition to being simple, this approach is robust towards the grain rotations associated with plastic deformation. The only error sources are therefore the experimental accuracy in 2θ and the provision of a strain-free reference material.

The experimental setup may be simplified by using only one detector and one detector setting L_N. This requires that the grain positions are found in another way, *e.g.* by placing a slit in the incoming beam and monitoring the intensity of reflections while translating the sample with respect to the slit. Small deviations from the assumed position with respect to the rotation axis may also be included as fit parameters. As an example, consider an *in situ* deformation experiment. Assume that the reference values $(2\theta)_0$ for a given grain are defined by the CM of the diffraction spots for the non-deformed sample, determined with the grain centred exactly on the rotation axis. Assume further that in the deformed state, the same grain is offset by $(\Delta x, \Delta y)$ with respect to the axis in the ω system, with Δx and Δy parallel to $\mathbf{x}_\omega$ and $\mathbf{y}_\omega$, respectively. Then

$$\begin{aligned} \varepsilon_i = &\begin{pmatrix} l_i & m_i & n_i \end{pmatrix} \begin{pmatrix} \varepsilon_{11} & \varepsilon_{12} & \varepsilon_{13} \\ \varepsilon_{12} & \varepsilon_{22} & \varepsilon_{23} \\ \varepsilon_{13} & \varepsilon_{23} & \varepsilon_{33} \end{pmatrix} \begin{pmatrix} l_i \\ m_i \\ n_i \end{pmatrix} \\ &- [\cos(\omega_i) + \sin(\omega_i)\sin(\eta_i)/\tan(\theta_i)](\Delta x/L_N) \\ &- [\sin(\omega_i) + \cos(\omega_i)\sin(\eta_i)/\tan(\theta_i)](\Delta y/L_N). \end{aligned} \quad (9)$$

The ω range covered should be large. Otherwise, only a subset of the elements in the strain tensor will be determined by equation (8) and the triangulation in equation (9) will be associated with a large uncertainty in one of the two positional parameters.

The second approach, using the full angular information, is potentially more powerful, but also more complex. We will only sketch a solution, with some similarities to the algorithm suggested by Chung & Ice (1999) for white-beam characterization. First we note that the plastic deformation of a grain will be accompanied by a rotation. The suggestion is therefore to fit the matrices $\mathbf{U}$ and $\mathbf{B}$ simultaneously, using equation (1). These can be parameterized by the three Euler angles and the reciprocal-lattice parameters, respectively. Next, the direct lattice constants are derived from the reciprocal ones and inserted into $\mathbf{A}$. From equations (6) and (7), this leads to the strain tensor.

The nine-parameter fit is bound to be non-trivial. In particular, the observations are asymmetric with large errors on ω. Likewise, during deformation, the diffraction spots will spread out substantially along η, making the CM derivation prone to error. Furthermore, the spatial distortions in the detector may render the derivation of an absolute metric impossible. Hence,

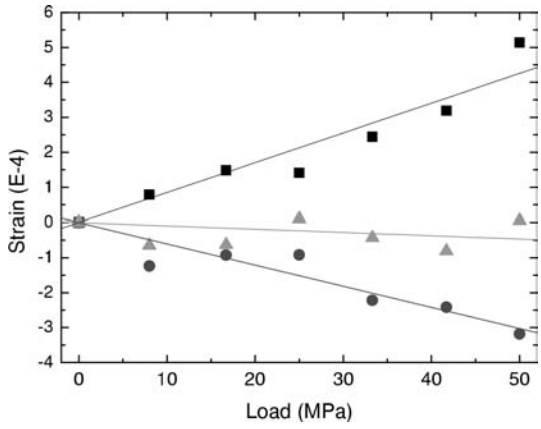

Figure 6
Evolution of selected strain components for an embedded copper grain during tensile deformation. ε_{22} (squares) and ε_{33} (circles) represent directions along the tensile axis and transverse to it, respectively. ε_{23} (triangles) is the associated shear component. Lines represent linear fits to the data.

to facilitate difference measurements, $\mathbf{A}_0$ should be a measured quantity. The advantage of this approach is the complementarity of the 2θ and η variations.

In both cases, the stress tensor σ_{ij} can be derived from the strain tensor by Hooke's law:

$$\sigma_{ij} = \sum_{kl} \mathbf{C}_{ijkl}\varepsilon_{kl}, \tag{10}$$

where $\mathbf{C}_{ijkl}$ is the compliance tensor, containing the elastic constants.

6. Example of strain-tensor characterization

We report on the first experiment involving strain characterization of single grains as a function of tensile deformation. The experiment was performed at the 3DXRD microscope using an 80 keV X-ray beam focused to a line of 5 μm height. One fixed two-dimensional detector (a Frelon CCD coupled to an image intensifier) was placed 520 mm behind the sample. An undeformed copper specimen with dimensions $3 \times 8 \times 50$ mm was mounted in a 25 kN stress rig. The average grain size was 200 μm. One grain in the middle of the sample was singled out. After each loading step, this grain was centred over the rotation axis and the tracking algorithm performed for an ω range of -30 to 30° and $\Delta\omega = 2^\circ$. The exposure time was 1 s. *GRAINDEX* indexed 21 reflections for this grain, of which four were associated with background problems. Using equation (8), the strain determination was based on the remaining 17 reflections. The result is shown in Fig. 6. Generally, the accuracy $\Delta\varepsilon$ on the strain measurements is given by the stability of the setup. For the present setup, $\Delta\varepsilon \simeq 10^{-4}$, consistent with the scatter in Fig. 6.

7. Conclusions

We have derived and verified unique methods for mapping the grain boundaries in a polycrystal as well as studying the evolution in the elastic strain in the embedded grains. With the added possibility of grain orientation mapping, the tracking concept is seen to provide a complete structural description on the grain level. The algorithms presented are universal and sufficiently fast (in terms of both hardware and software) that on-line analysis during many types of *in situ* processing studies is feasible.

We thank B. S. Johansen for programming, N. C. Krieger Lassen for providing the EBSP map, T. Leffers, D. Hennessy and C. Xiao for discussions, and Å. Kvick, A. Goetz and G. Vaughan for general support. This work was supported by the Danish Research Councils SNF *via* Dansync and STVF *via* the Engineering Science Centre at Risø. RMS also received support from the MRSEC program of the National Science Foundation under Award DMR-0079996.

References

Allen, A., Hutchings, M. T. & Windsor, C. G. (1985). *Adv. Phys.* **34**, 445–473.
Baruchel, J., Cloetens, P., Härtwig, J., Ludwig, W., Mancini, L., Pernot, P. & Schlenker, M. (2000). *J. Synchrotron Rad.* **7**, 196–201.
Chung, J.-S. & Ice, G. E. (1999). *J. Appl. Phys.* **86**, 5249–5255.
Juul Jensen, D., Kvick, Å., Lauridsen, E. M., Lienert, U., Margulies, L., Nielsen, S. F. & Poulsen, H. F. (2000). *Mater. Res. Soc. Symp. Proc.* **590**, 227–240.
Juul Jensen, D. & Poulsen, H. F. (2000). *Proceedings of the 21st Risø International Symposium on Materials Science*, Roskilde, Denmark, pp. 103–124.
Lauridsen, E. M., Juul Jensen, D., Poulsen, H. F. & Lienert U. (2000). *Scr. Mater.* **43**, 561–566.
Lauridsen, E. M., Schmidt, S., Suter, R. M. & Poulsen, H. F. (2001). *J. Appl. Cryst.* **34**, 744–750.
Lienert, U., Poulsen, H. F., Honkimäki, V., Schulze, C. & Hignete, O. (1999). *J. Synchrotron Rad.* **6**, 979–984.
Lienert, U., Poulsen, H. F. & Kvick, Å. (1999). *Proceedings of the 40th Conference of AIAA on Structures, Structural Dynamics and Materials*, St Louis, USA, pp. 2067–2075.
Margulies, L., Winther, G. & Poulsen, H. F. (2001). *Science*, **291**, 2392–2394.
Nielsen, S. F., Ludwig, W., Bellet, D., Lauridsen, E. M., Poulsen, H. F. & Juul Jensen, D. (2000). *Proceedings of the 21st Risø International Symposium on Materials Science*, Roskilde, Denmark, pp. 473–478.
Nielsen, S. F., Wolf, A., Poulsen, H. F., Ohler, M., Lienert, U. & Owen, R. A. (2000). *J. Synchrotron Rad.* **7**, 103–109.
Poulsen, H. F., Garbe, S., Lorentzen, T., Juul Jensen, D., Poulsen, F. W., Andersen, N. H., Frello, T., Feidenhans'l, R. & Graafsma, H. (1997). *J. Synchrotron Rad.* **4**, 147–154.

A4

Journal of
Applied Crystallography
ISSN 0021-8898

Received 5 February 2003
Accepted 19 May 2003

Generation of grain maps by an algebraic reconstruction technique

H. F. Poulsen* and Xiaowei Fu

Centre for Fundamental Research: 'Metal Structures in Four Dimensions', Risø National Laboratory, DK-4000 Roskilde, Denmark. Correspondence e-mail: henning.friis.poulsen@risoe.dk

A reconstruction method is presented for the generation of three-dimensional maps of the grain boundaries within powders or polycrystals. The grains are assumed to have a mosaic spread below 1°. They are mapped layer by layer in a non-destructive way by diffraction with hard X-rays. First the diffraction spots are sorted with respect to grain of origin by the indexing program *GRAINDEX*. Next for each grain the reconstruction is performed by *ART* – an iterative algebraic algorithm. The method is optimized by simulations. It is verified by a 50 keV study on one embedded layer in an aluminium specimen. The layer comprises ∼50 grain sections of an average size of 100 μm. Based on the use of five reflections per grain, a resolution of ∼5 μm is inferred.

1. Introduction

Mapping the grain structure is a vital part of most materials studies of polycrystals or powders. Until recently, for monophase materials maps could only be provided by optical or electron microscopy on surfaces. The generation of three-dimensional maps required serial sectioning. Sectioning is a tedious procedure, which furthermore, and very importantly, is incompatible with dynamic studies.

To enable dynamic studies of individual embedded grains, diffraction with high-energy ($E \geq 50$ keV) X-rays from synchrotrons has been introduced (Poulsen *et al.*, 1997; Lauridsen *et al.*, 2000; Margulies *et al.*, 2001; Offermann *et al.*, 2002; Poulsen & Juul Jensen, 2002). The hard X-rays have a penetration power in the millimetre-to-centimetre range. A method known as three-dimensional X-ray diffraction (3DXRD) has been established at the ID11 beamline of the European Synchrotron Radiation Facility, ESRF. In short, the X-ray beam defines a two-dimensional plane, namely a 'layer-of-interest', in the sample. Diffraction spots are acquired with a virtual three-dimensional detector, while rotating the sample around one axis. The spots are sorted with respect to the grain of origin by an indexing algorithm, *GRAINDEX* (Lauridsen *et al.*, 2001). Simultaneously, the position, volume, elastic strain tensor and crystallographic orientation of each grain are found (Poulsen *et al.*, 2001).

For coarse-grained well annealed specimens, 3DXRD can also provide grain maps. This was demonstrated by Poulsen *et al.* (2001) and applied to a study of grain-boundary wetting by Nielsen *et al.* (2000). The approach is simple: for each grain the contour of one of the diffraction spots is projected back into the layer of interest. Three-dimensional maps are generated by stacking layers. With the available detector, a spatial resolution of 25 μm was obtained. To improve this number, a better map-generation algorithm is required. In particular, the back-projection method cannot deconvolute the point spread function of the detector, it only uses a fraction of the information available and it is difficult to extend it to interpolate between reflections.

In this article we demonstrate that the 3DXRD mapping problem as stated above is similar to reconstruction tasks in other fields, such as X-ray tomography (CT), electron microscopy and positron emission tomography (PET). In all cases, the acquired data are approximately one-dimensional projections of the three-dimensional density distributions in real space. Such problems are typically solved either by Fourier filtering or by algebraic methods (see *e.g.* Kak & Slaney, 1988; Herman, 2002). These methods do not suffer from the limitations mentioned.

Next we generate 3DXRD maps by superposing partial reconstructions comprising sets of neighbouring grains. For each set the problem is formulated in terms of a set of linear equations. This is solved iteratively by a variant of the algebraic reconstruction technique (ART), as devised by Gordon *et al.* (1970). Simulations are used to optimize the algorithm and to estimate the spatial resolution in the absence of instrumental noise.

The proposed method is validated by experimental 3DXRD data for a few neighbouring grains in a single layer of an aluminium polycrystal. In the discussion, a number of differences between ART for 3DXRD and 'classical' ART for CT or PET are outlined. Furthermore, the main limitations with the present setup and software are identified.

2. Algebraic formulation

The geometry underlying the 3DXRD method is described in detail by Lauridsen *et al.* (2001) and Poulsen *et al.* (2001). A sketch is provided in Fig. 1. In summary, a beam of monochromatic hard X-rays is focused in one direction to illuminate a layer in the sample. The sample is mounted on an ω rotation

stage, with the rotation axis perpendicular to the beam. Some of the grains will give rise to diffracted beams, which are transmitted through the sample to be observed as spots by a flat two-dimensional detector. The detector exhibits a high spatial resolution and is positioned at a small sample–detector distance L_1. It is aligned perpendicular to the monochromatic beam. Acquisitions are made at a set of equiangular ω settings in steps of $\Delta\omega$. During each exposure, the sample is oscillated by $\pm\Delta\omega/2$, in order to sample the diffracted intensity uniformly. As an option the whole procedure may be repeated one or more times at larger sample–detector distances, $L_2, \ldots, L_N$. The data obtained at the larger distances are used only for *GRAINDEX*, not for the reconstruction part.

Assume a ray is diffracted from position (x, y) in the sample system, with $(x, y) = (0, 0)$ along the ω rotation axis. The direction of the diffracted beam is given by the Bragg angle 2θ and the azimuthal angle η, both defined in the Fig. 1. Then the associated spot on the detector is centred at $(L_1, y_{\rm det}, z_{\rm det})$:

$$\begin{aligned} x_l &= x\cos(\omega) - y\sin(\omega),\\ y_l &= x\sin(\omega) + y\cos(\omega),\\ y_{\rm det} &= -(L_1 - x_1)\tan(2\theta)\sin(\eta) + y_1 - y_{\rm det}(0),\\ z_{\rm det} &= (L_1 - x_l)\tan(2\theta)\cos(\eta) - z_{\rm det}(0). \end{aligned} \tag{1}$$

Here $[y_{\rm det}(0), z_{\rm det}(0)]$ denotes the intersection of the detector plane with the incoming (non-diffracted) ray.

We proceed to derive an algebraic approach to the reconstruction of the in-plane shape of a single grain.

Let $\rho(x, y)$ be the density of the intersection between the grain and the illuminated layer. This distribution is approximated by pixelated values, ρ_{ij}. For all pixels except those at the boundary, we expect either $\rho_{ij} = \rho_0$ or $\rho_{ij} = 0$ (ρ_0 is a constant to be determined from the experimental data). The pixelated values are listed in the one-dimensional array x.

The indexing program *GRAINDEX* provides the orientation of the grain and an associated list of diffraction spots. Following that, for each of the associated diffraction spots we identify an area-of-interest (AOI) on the detector. The AOI is centred on the projected centre-of-mass (CMS) of the grain. The background-corrected pixel intensities within the AOI are normalized to the structure factor and the Lorenz factor for the reflection. For each reflection, r, the normalized intensities are saved in an array b^r. It is essential that the complete integrated intensity of each diffraction spot is included in the analysis. Any overlapping spots or diffraction spots that are split over several ω settings (due to a minor mosaic spread) therefore have to be excluded from the analysis.

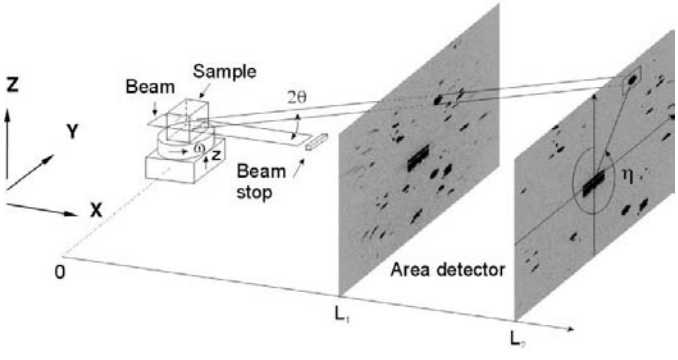

Figure 1
Sketch of the experimental geometry. Spots arising from the same reflection at different sample–detector distances are identified. The angles $(2\theta, \eta, \omega)$ are defined.

Central to the method is the assumption of kinematical scattering, *i.e.* a linear relationship between density and integrated intensity. Then for each reflection, r, we may write

$$A^r x = b^r, \tag{2}$$

where A^r comprises the information on geometry, *cf.* equation (1).

Next we pile the A^r values for the reflections into a block matrix A and define the compound array b:

$$A = \begin{pmatrix} A^1 \\ A^2 \\ \vdots \end{pmatrix}; \qquad b = \begin{pmatrix} b^1 \\ b^2 \\ \vdots \end{pmatrix}. \tag{3}$$

With these definitions the basic equation for the reconstruction of the shape of the grain is

$$\sum_{j=1}^{N} A_{ij}x_j = b_i; \qquad i = 1, , M \tag{4}$$

with the constraint

$$0 \le x_i \le \rho_0; \qquad \forall i. \tag{5}$$

A full grain map may be obtained by superposing the solutions (the shapes) of the individual grains. However, such a map will not be space filling as boundaries from neighbouring grains may overlap or leave 'voids' in the map. To avoid this we extend the method to simultaneous reconstruction of two neighbouring grains, symbolized by 1 and 2. Let $A_1x_1 = b_1$ and $A_2x_2 = b_2$ be the one-grain equations as defined above, with x_1 and x_2 referring to the same pixels. Then we define the compound system

$$A = \begin{pmatrix} A_1 & 0 \\ 0 & A_2 \end{pmatrix}; \qquad b = \begin{pmatrix} b_1 \\ b_2 \end{pmatrix}; \qquad x = \begin{pmatrix} x_1 \\ x_2 \end{pmatrix}. \tag{6}$$

With these definitions equation (4) applies again. In the vicinity of the boundary between the two grains, the constraint of equation (5) becomes

$$0 \le x_{1i} \le \rho_0; \quad 0 \le x_{2i} \le \rho_0; \quad x_{1i} + x_{2i} = \rho_0; \quad \forall i. \tag{7}$$

Generalization to three or more neighbours is straightforward. Three is sufficient as a maximum of three grains will be adjacent to one another in one layer.

3. The ART routine

In general M and N will be large, the rank of A *a priori* unknown and the set of equations may be underdetermined as well as overdetermined. For such situations iterative solutions are attractive. In this article we attempt to solve equation (4) by the ART algorithm (Gordon *et al.*, 1970), a variant of Kaczmarz's classical iterative method. Solutions x^{k+1} are

found by progressively projecting the previous solutions x^k on hyperplanes represented by the kth equation:

$$x^{k+1} = x^k + \lambda \left[\left(b_{i(k)} - \sum_{j=1}^{N} A_{i(k)j} x_j^k \right) \Big/ \sum_{j=1}^{N} A_{i(k)j}^2 \right] a_{i(k)} \qquad (8)$$

with $a_{i(k)} = [A_{i(k)1}, \ldots, A_{i(k)N}]$. The term within brackets is a scalar, representing a normalized difference between the measured intensity in the pixel with index $i(k)$, b_i, and the simulated intensity in that pixel given the solution x^k. Following the proofs by Kaczmarz (1937) and Tanabe (1971) this algorithm is known to converge to the minimum-norm solution for $M < N$. For overdetermined systems the 'solution' will oscillate in the neighbourhood of the intersection of the hyperplanes.

To improve the rate of convergence, the order of the rows are permuted $i = i(k)$ such that consecutive hyperplanes are more orthogonal to each other. Furthermore, a so-called relaxation parameter, $0 < \lambda < 1$, is introduced, which empirically has been shown to improve convergence. For details on optimization of these parameters, see Herman & Meyer (1993).

For the single grain reconstruction [equations (4) and (5)] we apply two restrictions after each step.

(i) Fully constrained:

$$x^k = \min[\rho_0, \max(0, x^k)]. \qquad (9a)$$

(ii) Compact support:

$$x_j^k = 0, \qquad (9b)$$

if the projection of pixel j is outside any of the AOIs.

The ART algorithm is repeated until convergence is obtained. Once a solution is found this is 'binarized' by setting a threshold: pixel j is defined as belonging to the grain if and only if $x_j > \rho_0/2$.

For the simultaneous reconstruction of neighbouring grains, the constraint in equation (7) is implemented in a similar way. Once a solution is found, it is binarized by associating pixel j with grain 1 if and only if $x_{1j} > x_{2j}$.

Note that the restrictions in equations (9*a*) and (9*b*) are projections onto convex sets, in the sense that if x_1 and x_2 are solutions fulfilling the restrictions, then so are $\alpha x_1 + (1 - \alpha)x_2$ with $0 \leq \alpha \leq 1$. For some inverse problems it has proven to be critical to include such projections in order to reach a solution (Press *et al.*, 1992). Specifically, if the set of equations (8) is consistent, convergence is assured when applying these restrictions.

4. Implementation and optimization

For numerical and instrumental reasons the algorithm needs modification. Firstly, it is well known that saving and extracting the full matrix A is problematic when A is large. Secondly, the layer of interest as defined by the incoming beam will have a finite thickness. Thirdly, detectors of the type used in the experiment (see below) are associated with a point spread function with rather long tails. To accommodate these issues we apply the concept of a footprint, as described *e.g.* by Matej & Lewitt (1996).

For a given reflection we first replace the pixels by voxels, which are square in the (x, y) directions, and with a shape in the z direction that mimics that of the beam profile. We calculate the projection of this object on the detector. The result is a function $h(\mathrm{d}y - \mathrm{d}y0, \mathrm{d}z - \mathrm{d}z0)$, centred around $(\mathrm{d}y0, \mathrm{d}z0)$, the projection of the centre of the voxel. The footprint g is then given by the convolution of h with the isotropic detector point spread function psf

$$g(\mathrm{d}y, \mathrm{d}z) = \mathrm{psf}(\mathrm{d}y^2 + \mathrm{d}z^2)^{1/2} \otimes h(\mathrm{d}y, \mathrm{d}z). \qquad (10)$$

The footprint can be tabulated, eliminating the need for storage of the full matrix A.

Another experimental concern is the assumed proportionality between scattering volume and integrated intensity. This is only approximate owing to absorption, inhomogeneities in the beam profile and spatial fluctuations in detector response. Hence, there will be a scatter between the normalized integrated intensities from the various reflections of the same grain. This in turn implies that the apparent ρ_0 vary between reflections. To handle this issue, the integrated intensity over each of the AOIs is normalized to 1. What remains is to fit a global ρ_0, the procedure for which is presented below.

With respect to the ART algorithm itself, for simplicity the rows were permuted randomly [more elaborate schemes are presented by Herman & Meyer (1993)]. The initial guess x^0 was set to an array of zeros. This eliminates the possibility of being misguided by 'ghosts' left over from the initial guess.

To characterize the convergence the 1-norm was used as a figure-of-merit function, FOM1:

$$\mathrm{FOM1} = ||Ax - b||_1 / ||b||_1. \qquad (11)$$

Evidently, FOM1 = 1 for x^0 and FOM1 $\rightarrow$ 0 for ideal solutions.

The algorithm as described was implemented in *MATLAB* (http://www.mathworks.com).

Simulations were performed to optimize the convergence parameters and to estimate the spatial accuracy of the method in the absence of experimental errors. The geometry was kept fixed, using parameters of relevance for the 3DXRD microscope.

The simulated two-dimensional object was generated by hand. It comprised 15 grains of random orientations. The object had the shape of a square with 100 $\times$ 100 pixels, each 1.15 $\times$ 1.15 µm in size. It was assumed to be fully illuminated. Detector images were simulated for kinematical scattering of grains with no mosaic spread or strain. The detector was assumed to be homogeneous, without any point spread function and with a pixel size of 2.3 $\times$ 2.3 µm. The field-of-view was as described in §5. It was placed in a distance of 4.2 mm from the ω rotation axis. Images were generated for ω settings from -45 to 45° in steps of $\Delta\omega = 1°$. Reflections from the eight $\{hkl\}$ families with the largest d spacings were included. Among these, most reflections did not give rise to diffraction spots owing to the geometry of the detector. As a result, for each grain ~23 useful spots were detected.

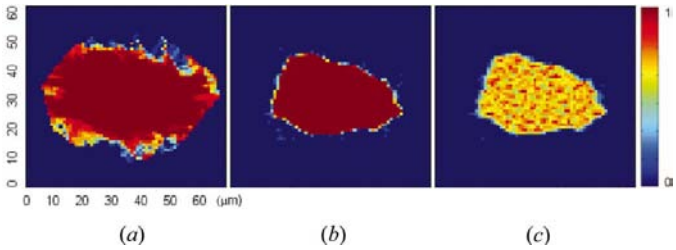

Figure 2
Reconstructed density maps for simulated data representing one grain. The upper limit on density ρ_0 is varied: (*a*) $\rho_0 = 0.25\rho_{\rm theory}$; (*b*) $\rho_0 = \rho_{\rm theory}$, (*c*) $\rho_0 = 5\rho_{\rm theory}$, where $\rho_{\rm theory}$ is the theoretical density. The (*x*, *y*) coordinate system is shown in units of μm. The colour code is shown to the right with red representing the maximum density in the map (ρ_0). The colour code is linear.

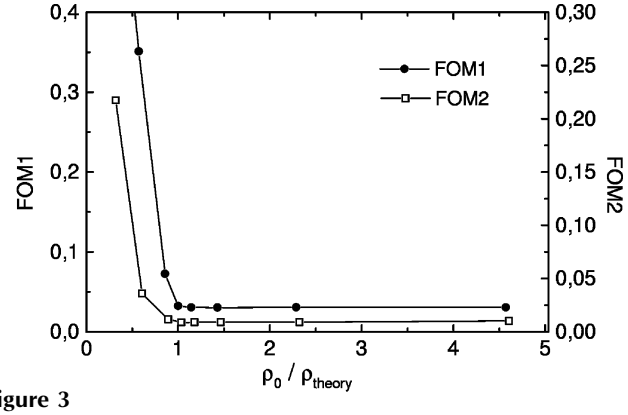

Figure 3
The variation of FOM1 (circles) and FOM2 (squares) with the upper limit on density ρ_0. The figure-of-merit functions are defined in the text [equations (11) and (12)]. The density is normalized to the theoretically correct density, $\rho_{\rm theory}$.

Results are reported for one internal grain with a size of 872 pixels. The grid size of the reconstructed maps was identical to the original: 1.15 × 1.15 μm . To measure the deviation between the original $x^{\rm orig}$ and the reconstructed $x^{\rm sol}$ the relative number of incorrectly assigned pixels was used:

$$\mathrm{FOM2} = ||x^{\rm orig} - x^{\rm sol}||_1 / ||x^{\rm orig}||_1. \qquad (12)$$

Evidently, FOM2 = 1 for x^0 and FOM2 → 0 for ideal solutions.

First λ was optimized using the theoretical value of ρ_0 ($\rho_0 = \rho_{\rm theory}$) and all 23 reflections. A broad minimum was found in both FOM1 and FOM2, centred around λ = 0.1. With this optimized setting, the density variable ρ_0 was varied. Three representative maps for $\rho_0 < \rho_{\rm theory}$, $\rho_0 = \rho_{\rm theory}$ and $\rho_0 > \rho_{\rm theory}$ are shown in Fig. 2. Furthermore, the variation of FOM1 and FOM2 with ρ_0 is shown in Fig. 3. The interpretation is straightforward: for $\rho_0 > \rho_{\rm theory}$, pixelation errors lead to pronounced 'salt and pepper' noise. Lowering ρ_0, a uniform density distribution is enforced in the grain interior and as a result FOM2 shows a minimum at $\rho_0 = \rho_{\rm theory}$. Lowering ρ_0 further, the missing density in the grain interior is added to the grain boundary areas, implying a larger apparent grain size. As a result both figures of merit rapidly increase.

Next for optimized λ and ρ_0, the number of reflections Nr was varied. Maps for 1, 4 and 23 reflections are shown in Fig. 4. The two former maps are based on reflections with $|\eta| < 45°$ only. [Note that the information content in the diffraction spots approximately scales with $|\tan(2\theta)\cos(\eta)|$ due to the projection, *cf.* equation (1).] Furthermore, the variation of FOM2 as function of number of reflections is shown in Fig. 5. Our interpretation is as follows: for Nr = 1, the system is strongly underdetermined with a large null space. Picking a solution in this null space is not likely to give a good result. With increasing Nr the solution is forced closer to the ideal one. As a result, FOM2 decreases and eventually saturates.

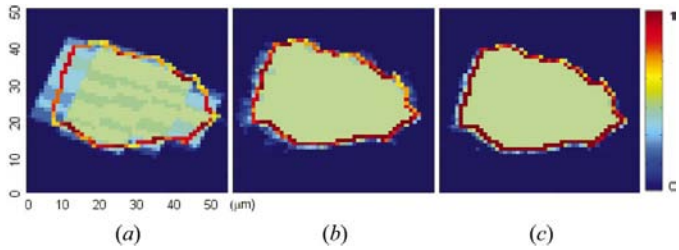

Figure 4
Reconstructed density maps for simulated data representing one grain. The number of diffraction spots used for the analysis is varied: (*a*) one spot, (*b*) four spots and (*c*) all 23 spots. The colour code is shown to the right. Superposed on each image is the outline of the original grain. The (*x*, *y*) coordinate system is shown in units of μm.

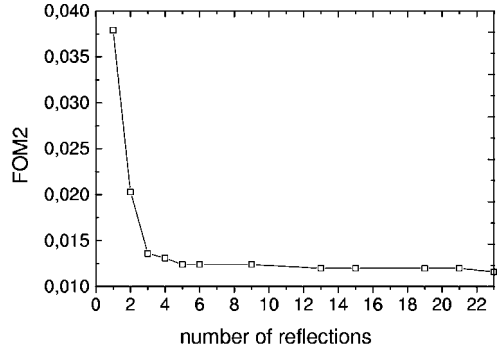

Figure 5
The variation of the figure-of-merit function FOM2 (squares) with the number of reflections used for the reconstruction. FOM2 is defined in equation (12).

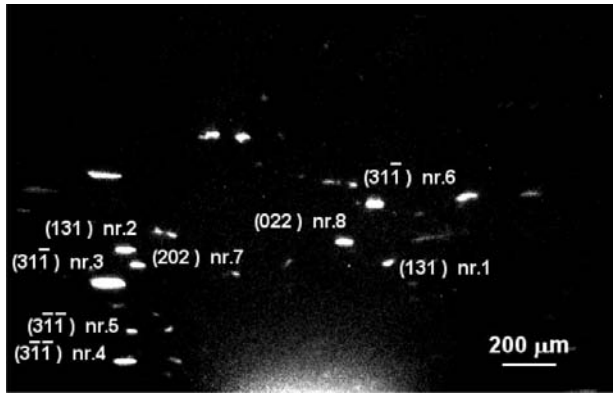

Figure 6
Background-subtracted raw image obtained at a sample–detector distance of 4.2 mm. White corresponds to 50 counts pixel^{-1}. The monochromatic beam passes the detector just below the bottom part of the image. The result of the indexing procedure is shown for a few selected spots as combinations of (*hkl*) indices and grain numbers.

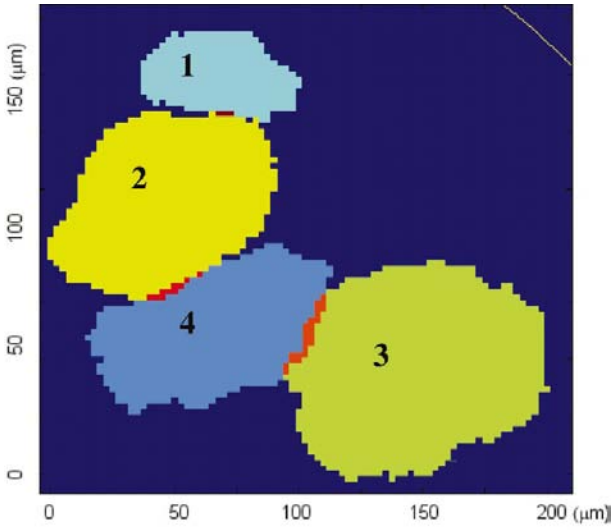

Figure 7
Independent reconstruction of four neighbouring grains. These are marked by number, for comparison with Fig. 6, as well as by different colours. Regions of overlap between the grains are marked by red. The surface of the polycrystal is indicated by a solid yellow curve.

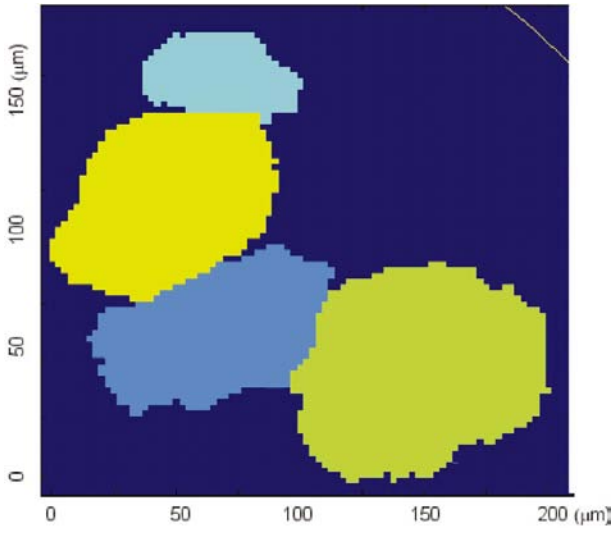

Figure 8
Combined reconstruction of the same data set as used in Fig. 7.

For optimized ART parameters: FOM2 = 0.012. That corresponds to an average uncertainty of ∼0.2 pixel units on the position of the grain boundary. With the detector pixel size being twice that of the pixel size in the reconstructed map, this clearly demonstrates that super-resolution is obtainable, even with only five reflections.

5. Experimental verification

The experimental verification was performed on a well annealed aluminium polycrystal with an average three-dimensional grain size of 150 μm (as deduced from optical microscopy). It exhibited a weak texture. A cylindrical specimen was used with a height of 3 mm and a radius of 0.4 mm. The experiment was performed at the 3DXRD microscope at ESRF. A monochromatic beam of 50 keV was focused to an elongated spot of 2 × 1000 μm. This spot illuminated a layer near the centre of the specimen, which was mounted with the cylindrical axis parallel to the ω axis. Images were acquired over an ω range of 90°, in steps of $\Delta\omega = 1°$. The exposure time was 5 s. Three centre-of-rotation to detector distances were used: 4.2, 5.7 and 7.2 mm, respectively.

The two-dimensional detector comprises a 1536 x 1024 pixel CCD camera coupled to a 14 μm thick LAG:Tb fluorescence screen by microscope optics. The effective pixel size is 2.3 × 2.3 μm. Empirically, the detector point spread function is found to be reasonably described by a Lorentzian to the power $n = 1.45$ and a width of $\sigma = 4.6$ μm:

$$\mathrm{psf}(r) = [1 + (r/\sigma)^2]^n. \quad (13)$$

To avoid excessive scattering from the non-diffracted monochromatic beam, the detector is designed such that this beam passes just below the detector screen. Hence only diffraction spots on one hemisphere can be detected.

Images are corrected for spatial distortion by the program *FIT2D* (Hammersley *et al.*, 1996). A background is subtracted, determined for each pixel as the median over the full ω range. An example of a corrected image is shown in Fig. 6. Diffraction spots are clearly visible, with maximum pixel intensities of 900 counts for {111} reflections. On the other hand, reflections with a smaller d spacing than {222} are very faint and deemed useless for further analysis.

For each grain, initially we eliminate the invalid overlapping or incomplete spots. This is done by performing a non-linear least-squares fit to the centre-of-mass positions of the spots on the detector and removing the outliers. The fitting parameters are the average grain orientation and the centre of mass of the intersection of the grain with the beam. Typically 30% of the reflections were found to be invalid.

In the following we focus on four neighbouring grains of medium size. For each of these the five valid spots with spot positions closest to the fitted values were chosen. The resulting standard deviation between simulated and observed spot positions varied between 0.9 and 2.4 μm for these grains. With a reconstructed pixel size of 2.3 μm, the matrix A was typically nearly square with a size around 2500 × 2500. The relaxation parameter λ was set to 0.1. The variation in FOM1 with ρ_0 was plotted analogously to Fig. 3. The two graphs exhibit very similar properties. By scaling to the known ρ_{theory} from the simulations, the optimal ρ_0 was found.

The results for the independent reconstruction of the four grains based on five reflections each are shown in Fig. 7. The FOM1 values were in the range 0.15–0.24, with the scatter mainly reflecting the size of the AOI used. From the overlap and voids in the three boundary regions in Fig. 7 we may derive a crude estimate of the spatial resolution. The result is ∼5 μm, less than the width of the point spread function.

The corresponding results for the simultaneous refinement of the same four grains is shown in Fig. 8. The FOM1s were in this case in the range 0.20–0.30.

More grains were analysed with similar results. Pending the establishment of fully automated software, a complete map will be presented elsewhere.

6. Discussion

First we outline three inherent differences between the well established tasks of density reconstruction for CT or PET, and the generation of grain maps by 3DXRD.

(i) In CT or PET, the projection angles can be chosen almost at will. With single-grain diffraction, the angles are pre-defined to a set defined by the orientation of the grain. In addition, only the reflections with the largest d spacings can be included in the analysis, as the integrated intensities decrease rapidly with Bragg angle. Furthermore, some reflections must be discarded due to overlap. As a result the number of valid projections will be an order of magnitude smaller than the 360–720 conventionally used in tomography. In the present experiment, in addition 85% of the reflections were inaccessible due to detector geometry and the 90° ω range, leading to on average only five useful reflections.

(ii) Strictly speaking, the 3DXRD geometry does not conform to the 'parallel-beam X-ray transform' (Natterer, 1986) underlying most reconstruction problems. That would imply that the diffraction spots were one-dimensional projections of the two-dimensional sample plane (in the absence of a point spread function: lines on the detector). Instead, additional information is available. Hence, the number of projections can be reduced.

(iii) With CT or PET the whole specimen needs to be reconstructed simultaneously. In contrast, the 3DXRD algorithm presented here divides the task into a set of minor reconstructions, namely those for individual grains (or clusters of neighbouring grains). This, in combination with the smaller number of projections, reduce the size of A very significantly.

In view of these differences it is relevant to discuss alternative approaches to solving equation (4). The reconstruction literature is abundant with various solutions, including maximum-entropy and expectation-maximization methods (for a recent overview see Herman, 2002). Specific to the 3DXRD case, the reduced size of A implies that direct matrix-inversion methods might be relevant (Conn *et al.*, 1992). Likewise, the discrete nature of grain mapping suggests binary approaches such as Monte Carlo simulations. However, a comparative study of various algebraic reconstruction schemes is beyond the scope of this article. Our aim has been to demonstrate that the reconstruction of 3DXRD maps is feasible using an established algorithm, which suitably optimized has proven to be 'second to none' in several fields (*e.g.* Herman & Meyer, 1993).

Further refinement of the implementation of the ART routine for 3DXRD is foreseeable. In particular, it has been repeatedly demonstrated that reconstruction in terms of square pixels (in three-dimensions: cube shaped voxels) is inferior to the use of overlapping volume elements which gradually decay to zero with increasing distance from their centres. The solutions have substantially less 'salt and pepper' noise. In particular, the generalized Kaiser–Bessel window functions have been shown to have attractive properties (Lewitt, 1990; Matej & Lewitt, 1996).

Comparing simulations and experimental data, it is clear that the spatial resolution with the present setup is limited by the setup itself, not the ART routine. Likewise, the small deviation between observed and predicted CMS positions of the spots implies that the main error is not related to instrumental alignment. Instead we consider the main error sources to be as follows.

(i) Detector characteristics and calibration. In particular the tails of the point spread function need to be known with high precision.

(ii) Mosaic spread of the grains. With the present pixel size and sample–detector distance, the angular spread of each grain needs to be less than $\sim$0.5°.

For completeness we mention two other general limitations. The first is the kinematical scattering 'ansatz'. Typically, extinction effects are negligible for metallic or ceramic polycrystals examined with hard X-rays. The absorption may be negligible as well; otherwise it can easily be incorporated in the program. The second is the number of illuminated grains. *GRAINDEX* requires that most of the diffraction spots are not overlapping in order to work. As calculated by Schmidt *et al.* (2003), the maximum number of grains allowed in the illuminated part of the layer depends critically on the mosaic spread. For a spread of 0.1°, the number of grains allowed is in the range of 5000, while for a spread of 1° it is 100, numbers that in most cases not are prohibitive.

7. Conclusion

The task of 3DXRD mapping of near-perfect grains has been formulated in terms of a set of linear equations. Depending on grain size, the number of valid reflections and the spatial resolution required, this may be solved in many ways, including Monte Carlo and maximum-entropy approaches and even direct matrix inversion. The algebra is easily extended, *e.g.* to true three-dimensional reconstructions, to materials with several phases and to include absorption.

A fully constrained ART algorithm has been implemented to solve the set of linear equations.

In comparison with standard ART applications (CT, PET) the size of the matrix is much reduced, due to the division in sub-reconstructions. The total number of projections (for 3DXRD the number of grains times the number of valid reflections per grain) is similar.

Simulations showed that super-resolution is possible even with only five reflections. This was confirmed by the experiment. The resulting resolution of $\sim$5 μm is comparable to the best results obtained with X-ray tomography in the hard X-ray range (3 μm as reported by Lame *et al.*, 2003).

The main limitations of the method are the restriction to grains with vanishing mosaicity (in practice <1° total width), the spot overlap issue and the detector characteristics.

S. F. Nielsen, E. M. Lauridsen, L. Margulies, S. Schmidt and A. Terry are acknowledged for participating in the synchro-

tron experiment, P. B. Olesen for sample preparation and S. Schmidt, P. Kirkegård and G. T. Herman for discussions on algebra and reconstruction. The ESRF is acknowledged for provision of beam time. This work was supported by the Danish National Research Foundation through the 'Centre for Fundamental Research: Metal Structures in Four Dimensions', and by the Danish Natural Science Research Council *via* Dansync.

References

Conn, A. R., Gould, N. I. M. & Toint, P. L. (1992). *Lancelot: a Fortran Package for Large-Scale Non-Linear Optimization. Springer Series in Computational Mathematics*, Vol. 17. Berlin: Springer Verlag.

Gordon, R., Bender, R. & Herman, G. T. (1970). *J. Theor. Biol.* **29**, 471–481.

Hammersley, A. P., Svensson, S. O., Hanfland, M., Fitch, A. N. & Häusermann, D. (1996). *High Pressure Res.* **14**, 235–248.

Herman, G. T. (2002). *Encyclopedia of Imaging Science and Technology*, Vol. 2, edited by J. P. Hornak, pp. 1404–1411. New York: John Wiley.

Herman, G. T. & Meyer, L. B. (1993). *IEEE Trans Med Imag.* **12**, 600–609.

Kaczmarz, S. (1937). *Bull. Int. Acad. Pol. Sci. Lett. A*, **35**, 355–357.

Kak, A. C. & Slaney, M. (1988). *Principles of Computerized Tomographic Imaging*. New York: IEEE Press.

Lame, O., Bellet, D., Di Michiel, M. & Bouvard, D. (2003). Unpublished.

Lauridsen, E. M., Juul Jensen, D., Poulsen, H. F. & Lienert, U. (2000). *Scr. Mater.* **43**, 561–566.

Lauridsen, E. M., Schmidt, S., Poulsen, H. F. & Suter, R. M. (2001). *J. Appl. Cryst.* **34**, 744–750.

Lewitt, R. M. (1990). *J. Opt. Soc. Am. A*, **7**, 1834–1846.

Margulies, L., Winther, G. & Poulsen, H. F. (2001). *Science*, **291**, 2392–2394.

Matej, S. & Lewitt, R. M. (1996). *IEEE Trans. Med. Imag.* **15**, 68–77.

Natterer, F. (1986).*The Mathematics of Computerized Tomography*. Chichester: Wiley.

Nielsen, S. F., Ludwig, W., Bellet, D., Lauridsen, E. M., Poulsen, H. F. & Juul Jensen, D. (2000). *Proceedings of the 21st Risø International Symposium on Materials Science*, edited by N. Hansen, X. Huang, D. Juul Jensen, E. M. Lauridsen, T. Leffers, W. Pantleon, T. J. Sabin & J. A. Wert, pp. 473–478. Risø National Laboratory, Roskilde, Denmark.

Offermann, S. E., van Dijk, N. H., Sietsma, J., Grigull, S., Lauridsen, E. M., Margulies, L., Poulsen, H. F., Rekveldt, M. Th. & van der Zwaag, S. (2002). *Science*, **298**, 1003–1005.

Poulsen, H. F., Garbe, S., Lorentzen, T., Juul Jensen, D., Poulsen, F. W., Andersen, N. H., Frello, T., Feidenhans'l, R. & Graafsma, H. (1997). *J. Synchrotron Rad.* **4**, 147–154.

Poulsen, H. F. & Juul Jensen, D. (2002). *Mater. Sci. Forum*, **408–412**, 49–66.

Poulsen, H. F., Nielsen, S. F., Lauridsen, E. M., Schmidt, S., Suter, R. M., Lienert, U., Margulies, L., Lorentzen, T. & Juul Jensen, D. (2001). *J. Appl. Cryst.* **34**, 751–756.

Press, W. H., Teukolsky, S. A., Vetterling, W. T. & Flannery, B. P. (1992). *Numerical Recipes in C*. Cambridge University Press.

Schmidt, S., Poulsen, H. F. & Vaughan, G. B. M. (2003). *J. Appl. Cryst.* **36**, 326–332.

Tanabe, K. (1971). *Numer Math.* **17**, 203–214.

A5

electronic reprint

Journal of
Applied Crystallography
ISSN 0021-8898

Reconstruction of grain boundaries in polycrystals by filtered back-projection of diffraction spots

Henning Friis Poulsen and Soeren Schmidt

Journal of
Applied Crystallography
ISSN 0021-8898

Received 7 February 2002
Accepted 27 January 2003

Reconstruction of grain boundaries in polycrystals by filtered back-projection of diffraction spots

Henning Friis Poulsen* and Soeren Schmidt

Center for Fundamental Research: 'Metal Structures in Four Dimensions', Risø National Laboratory, DK-4000 Roskilde, Denmark. Correspondence e-mail: henning.friis.poulsen@risoe.dk

A reconstruction method is presented for the generation of three-dimensional maps of the grain boundaries within powders or polycrystals. The grains are assumed to have a mosaic spread below 1°. They are mapped non-destructively by diffraction with hard X-rays, using a uniform mm^2-sized beam. First the diffraction spots are sorted with respect to grain of origin by the indexing program *GRAINDEX*. Next, for each grain the reconstruction is performed by a variant of the filtered back-projection algorithm. The reconstruction method is verified by a simulation over ten grains. Using 64 reflections for each grain, sub-pixel accuracy is obtained. The potential of the method is outlined.

1. Introduction

The physical, chemical and mechanical properties of polycrystals and powders tend to be strongly influenced by the structure of the grain agglomerate. The agglomerate is often highly heterogeneous with properties depending on the size, shape and crystallographic orientation of the grains, as well as the topology of the grain boundaries and the misorientations across these. Mapping a representative part of the grain structure is therefore an integral part of many materials studies. Until recently, for mono-phase materials, maps could only be provided by optical or electron microscopy on surfaces. Three-dimensional maps are then produced by serial sectioning. The precision of such maps is given by the accuracy of the sectioning, which at best is 1–5 μm (Krac & Spanos, 1999).

Sectioning is incompatible with dynamic studies. To enable such studies, we have recently introduced the idea of using diffraction with focused high-energetic ($E \geq 50$ keV) X-rays from synchrotrons. The hard X-rays have the necessary penetration power for three-dimensional mappings of hard condensed matter (Bouchard *et al.*, 1998; Poulsen *et al.*, 1997). A dedicated instrument, the three-dimensional X-ray diffraction (3DXRD) microscope, has been built at the Materials Science beamline of the European Synchrotron Radiation Facility, ESRF (Lienert *et al.*, 1999; Juul Jensen & Poulsen 2000). Using this a number of results have emerged for the dynamics of individual grains during deformation (Margulies *et al.*, 2001), recrystallization (Lauridsen *et al.*, 2000) and phase transformations (Poulsen *et al.*, 2002).

Central to the 3DXRD studies have been the development of a mapping strategy, known as tracking, and a corresponding program, *GRAINDEX*. The details of these have been described by Lauridsen *et al.* (2001) and Poulsen *et al.* (2001). In short, a monochromatic beam is focused in one dimension. This impinges on the sample and defines a layer-of-interest within it. Diffraction spots are acquired with a virtual three-dimensional detector, while rotating the sample around one axis. By means of ray tracing a list of reflections is provided, characterized by their direction and integrated intensity. The reflections are sorted by the *GRAINDEX* indexing algorithm with respect to the grain of origin. Next, for each grain, the contour of one of the diffraction spots is projected back into the layer of interest. Finally, three-dimensional mapping is provided by mapping layers sequentially.

In this article, we present an alternative reconstruction method. We still rely on *GRAINDEX* to sort the diffraction spots and we perform the mapping of each grain separately. However, the grains are now fully illuminated by a uniform beam and the reconstruction of each grain is performed by a variant of the Fourier technique known as filtered back-projection (Bracewell & Riddle, 1967). The latter is used extensively in a number of fields, including absorption contrast tomography, where it has been shown to reconstruct density distributions with remarkable accuracy (see *e.g.* Kak & Slaney, 1988).

In comparison with the original tracking concept the present algorithm has a number of advantages.

(i) Experimentally, mapping the whole grain in three dimensions at once instead of stabling layers is obviously faster. The method is also more robust with respect to beam fluctuations.

(ii) The original tracking geometry essentially requires the use of a third-generation synchrotron, as this is the only source capable of focusing a hard X-ray beam to a micrometre-sized line in an effective way. In contrast, the wide-beam geometry used in the new method is also suited for work on second-generation synchrotrons, and in addition, for coarse-grained samples, it is suitable for work with laboratory X-ray sources.

(iii) The fact that the geometry and parts of the analysis are similar to those used in tomography should ease combined diffraction and absorption contrast studies.

(iv) It is not straightforward to interpolate between the back-projected contours of diffraction spots arising from the same grain. In contrast, the Fourier method is an ideal interpolation tool.

The main disadvantage is the loss of information. The original tracking is built on a one-to-one mapping of a grain segment onto the detector, while the new concept implies that the intensity in one pixel of the detector is the sum over contributions from diffraction taking place along a line in the grain. Hence, it is not clear *a priori* that an adequate number of independent measurements (reflections) is available. In addition, we emphasize that both methods require a complete separation between the diffraction spots used. In the case of moderately to heavily deformed grains, *GRAINDEX* does not work.

In this article, we establish the algorithm and present the necessary modifications of the standard filtered back-projection method. Next, simulations are performed to verify the methodology. Simultaneously, we address the questions of accuracy and numbers of reflections needed. Finally, we discuss the intrinsic limitations of the method. First applications will be published elsewhere.

2. Geometry

The experimental geometry is similar to that used for parallel-beam tomography. It is sketched in Fig. 1. A uniform and parallel beam of monochromatic hard X-rays of wavelength λ illuminates the sample. The sample is mounted on an ω rotation stage, with the rotation axis perpendicular to the beam. Some of the grains, namely those fulfilling the Bragg condition, will give rise to diffracted beams, which are transmitted through the sample to be observed as spots by a flat two-dimensional detector. This detector has a high spatial resolution and is positioned at a small sample–detector distance L_1. The directions of the reflections are given by their Bragg angles 2θ and azimuthal angles η, both defined in Fig. 1. The detector is aligned perpendicular to the incident beam.

Acquisitions are made at a set of equiangular ω settings. With a step size of $\Delta\omega$, the full range required by the reconstruction algorithm is 180°. During each exposure the sample is oscillated by $\pm\Delta\omega/2$, in order to sample the diffracted intensity uniformly. The whole procedure is then repeated at least once and possibly more times at larger sample–detector distances, $L_2, \ldots, L_N$. The data obtained at larger distances are used only for *GRAINDEX*, not for the reconstruction part.

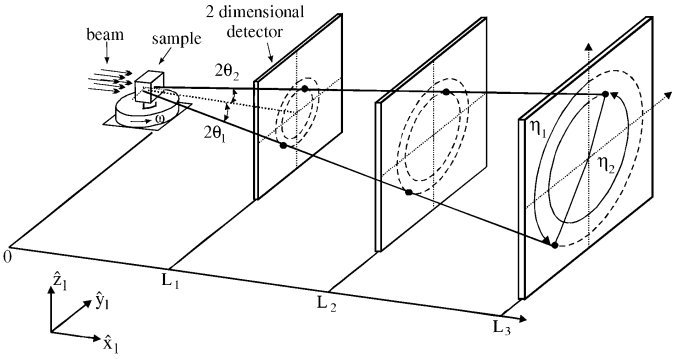

Figure 1
Sketch of the experimental geometry. Spots arising from the same reflection at different sample–detector distances are identified. The angles $(2\theta, \eta, \omega)$ are defined, as well as the laboratory coordinate system $(\hat{x}_l, \hat{y}_l, \hat{z}_l)$. L_i is the distance between the centre of rotation of the ω table and the detector in position i.

We introduce two coordinate systems: the laboratory coordinate system, $\mathbf{R}_l = (x_l, y_l, z_l)$, and a system fixed to the sample, $\mathbf{R}_\omega = (x_\omega, y_\omega, z_\omega)$, called the ω system. We define $(x_l, y_l) = (x_\omega, y_\omega) = (0, 0)$ along the ω rotation axis. With the chosen positive direction of ω (see Fig. 1) we have $\mathbf{R}_l = \mathbf{\Omega R}_\omega$, with

$$\mathbf{\Omega} = \begin{bmatrix} \cos(\omega) & -\sin(\omega) & 0 \\ \sin(\omega) & \cos(\omega) & 0 \\ 0 & 0 & 1 \end{bmatrix}. \qquad (1)$$

In the following we describe the geometry for one grain in the rotated system. For grains with no strain and a mosaic spread smaller than the divergence given by one detector pixel, the diffracted beam from a particular reflection consists of parallel rays. Further assuming kinematical scattering, the intensity distribution on the detector is a projection of the grain along a straight line. The direction of the line is $\mathbf{V}_\omega$

$$\mathbf{V}_\omega = \mathbf{\Omega}^{-1} \begin{bmatrix} \cos(2\theta) \\ -\sin(2\theta)\sin(\eta) \\ \sin(2\theta)\cos(\eta) \end{bmatrix}. \qquad (2)$$

The relationship between a ray diffracted from position $\mathbf{R}_l = \mathbf{\Omega R}_\omega$ in the sample and the associated diffraction point on the detector $(L_1, y_{\rm det}, z_{\rm det})$ is

$$\begin{aligned} y_{\rm det} &= -(L_1 - x_1)\tan(2\theta)\sin(\eta) + y_1 - y_{\rm det}(0) \\ z_{\rm det} &= (L_1 - x_1)\tan(2\theta)\cos(\eta) + z_1 - z_{\rm det}(0). \end{aligned} \qquad (3)$$

Here $[y_{\rm det}(0), z_{\rm det}(0)]$ denotes the intersection of the detector plane with the incoming (non-diffracted) ray passing through $\mathbf{R}_\omega = (0, 0, 0)$.

It appears that for each $z_{\rm det}$, the acquired intensity distribution $P(y_{\rm det})$ is proportional to a projection of the density in a two-dimensional layer of the grain. These layers in the grain are all tilted by the same angle of $\sin(\alpha) = \sin(2\theta)\cos(\eta)$ with respect to the x–y plane. Noting that the Bragg angle 2θ is small for hard X-rays and that most diffracted spots will have η values around $\pi/2$ and $-\pi/2$, we will make the approximation of neglecting this out-of-the-layer angle α. This approximation implies that the various z layers in the grain can be reconstructed independently.

The projection geometry of one such z layer is shown in Fig. 2. The geometry is seen to be equivalent to that for parallel-beam tomography, with the exception of the angle ω being substituted by the angle γ between $\mathbf{V}_\omega$ and the x_ω axis. We define γ to be positive for increasing ω:

$$\tan(\gamma - \omega) = \tan(2\theta)\sin(\eta). \qquad (4)$$

The density of the layer is given by

$$\rho(x_\omega, y_\omega) = 1, \quad (x_\omega, y_\omega) \text{ inside the grain,}$$
$$\rho(x_\omega, y_\omega) = 0, \quad (x_\omega, y_\omega) \text{ outside the grain.} \tag{5}$$

Let t be the minimal distance between the diffracted beam of interest and the centre of rotation (*cf.* Fig. 2). The intensity distribution P_γ is

$$P_\gamma(t) = \iint \rho(x, y)\, \delta[t = x\sin(\gamma) + y\cos(\gamma)]\, \mathrm{d}x\, \mathrm{d}y. \tag{6}$$

The intensity distribution on the detector is then

$$P_\gamma(y_{\rm det}) = P_\gamma\left[t = \frac{y_{\rm det} - y_{\rm det}(0)}{\cos(\gamma - \omega)}\right]\cos(\gamma - \omega). \tag{7}$$

The term $\cos(\gamma - \omega)$ reflects the fact that the detector is not perpendicular to the diffracted beams. For hard X-rays, this term will often be negligible, owing to the small Bragg angles [see equation (4)].

The data analysis consists of three separate parts. First the diffraction spots must be sorted with respect to which grain they come from. Furthermore, for each reflection we need to know the directional vector $\mathbf{V}_\omega$ with an accuracy matching the divergence given by one detector pixel. For this task we rely on *GRAINDEX*. Initially the program uses ray-tracing principles to group diffraction spots at different sample–detector distances into reflections. Simultaneously, the directions and the integrated intensities of the reflections are found. Next, the reflections are grouped into a set of grain orientations by scanning over Euler space. The result is a list of associated reflections and diffraction spots for each illuminated grain. For details the reader is referred to Lauridsen *et al.* (2001).

To enable a comparison between various diffraction spots, the background-corrected intensities must be normalized to the beam current, the structure factors and the Lorentz factors. For the present geometry, the Lorentz factor is

$$\mathrm{Lor}(2\theta, \eta) = 1/[\sin(2\theta)|\sin(\eta)|]. \tag{8}$$

It is essential that the complete integrated intensity of each diffraction spot is included in the analysis. Any diffraction spot that is split over several ω settings (due to a minor mosaic spread) therefore has to be combined into one spot or excluded from further analysis.

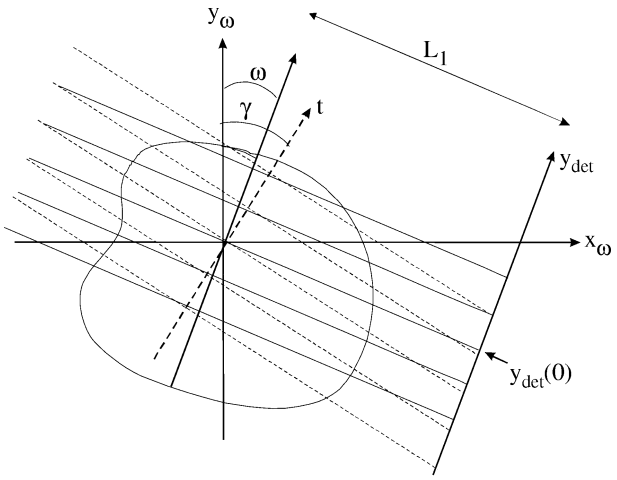

Figure 2
The projection geometry for one z layer in one grain and one reflection. The parallel set of incoming rays (full lines) and the projection of the diffracted rays on the x–y plane (hatched lines) are offset by an angle of $\gamma - \omega$. The projection radius t and the detector coordinate $y_{\rm det}$ are defined.

The second part of the analysis is the reconstruction. Here we consider only the data from the detector setting which is closest to the sample. With the approximation introduced, the reconstruction can be performed separately for each grain, and within one grain separately for each z layer. Simultaneously with the shape of the grain, we also determine its position within the sample. In order to apply a Fourier method we first interpolate the projected intensities P_γ on an equiangular γ' grid spanning a range of π.

The filtered back-projection procedure as such is standard (see *e.g.* Kak & Slaney, 1988). It involves first a Fourier transform of the projections

$$S_{\gamma'}(w) = \int_{-\infty}^{\infty} P_{\gamma'}(t)\exp(-i2\pi wt)\, \mathrm{d}t. \tag{9}$$

Then the multiplication by a filter $|w|H(w)$ and a reverse transform

$$Q_{\gamma'}(t) = \int_{-\infty}^{\infty} S_{\gamma'}(w)|w|H(w)\exp(i2\pi wt)\, \mathrm{d}w. \tag{10}$$

Finally, the filtered projections $Q_{\gamma'}$ are back-projected to produce the reconstructed density distribution $f(x_\omega, y_\omega)$ of the grain:

$$f(x_\omega, y_\omega) = \int_0^{\pi} Q_{\gamma'}[x_\omega\sin(\gamma') + y_\omega\cos(\gamma')]\, \mathrm{d}\gamma'. \tag{11}$$

These equations can be handled fast and precisely by means of Fast Fourier Transform (FFT) algorithms. To speed up the algorithm and avoid 'dishing' of images, the length of the projections $P_\gamma(t)$ is increased by adding zeros until the number of digits is a power of 2. The filter H is an optional smoothing algorithm, which serves as an apodization function. In this article we will use the Hamming filter

$$H(w) = \{\tfrac{1}{2}[1 + \cos(\pi w/w_c)]\}^n. \tag{12}$$

Here w_c is the Nyquist frequency and n is an exponent, to be fitted for best results.

The third part of the analysis is the derivation of a grain boundary. Here we can either derive the boundaries for each grain individually or interpolate between them to obtain a 1:1 map. In the first case, we define a threshold at a fraction of the average intensity in the interior of the grains of the reconstructed density distribution. In the second case, each voxel is associated with the grain which has the highest reconstructed density at that position.

3. Simulations

Simulations were performed to verify the equations and estimate the spatial accuracy of the method in the absence of experimental errors. The geometry was kept fixed, using parameters of relevance for the 3DXRD microscope. Instead, the parameters of the reconstruction were varied, in particular the number of reflections.

The simulated object, namely an aluminium polycrystal, was generated by hand. It comprised ten grains of random orientations. For simplicity, the grains were columnar, that is the object exhibited a translational symmetry along the z axis. The object had the shape of a cube with 100 × 100 × 100 voxels, each 2.5 × 2.5 × 2.5 μm in size. It was assumed to be fully illuminated.

Detector images were simulated for kinematical scattering of grains with no mosaic spread or strain. The wavelength was 0.248 Å (50 keV). The detector was assumed to be homogeneous, distortion free and with 5 × 5 μm square pixels. It was placed at a distance of 3.75 mm from the ω rotation axis. Images were generated for ω settings from 0 to 180° in steps of $\Delta\omega = 1°$. Reflections from the six $\{hkl\}$ families with the largest d-spacings were included, resulting in a total of ∼64 simulated diffraction spots per grain. The average and maximum α values were 4.9 and 13.4°, respectively. These numbers represent typical experimental conditions.

As expected, *GRAINDEX* retrieved all the grains with the correct orientation. The filtered back-projection algorithm was implemented in *MATLAB*. The interpolation in γ was handled simply by using the closest projection. Reconstructions were performed with a voxel size of 2.5 × 2.5 × 2.5 μm, and the Hamming filter with exponent $n = 1$. The threshold for definition of the boundary was set at 50% of the average density in the interior of the reconstructed objects.

In the following, focus is placed on the results for one layer in one randomly chosen grain. The reflections were rather uniformly distributed in γ, with a maximum separation of 7°. In Fig. 3(*a*) we have stacked the original 64 projections below each other in order of increasing ω. From this, five projections with overlapping spots are easily identified. These were excluded. The remaining were interpolated to give an equiangular set of projections. The corresponding stacked projections, a figure known as a sinogram, is shown as function of γ in Fig. 3(*b*).

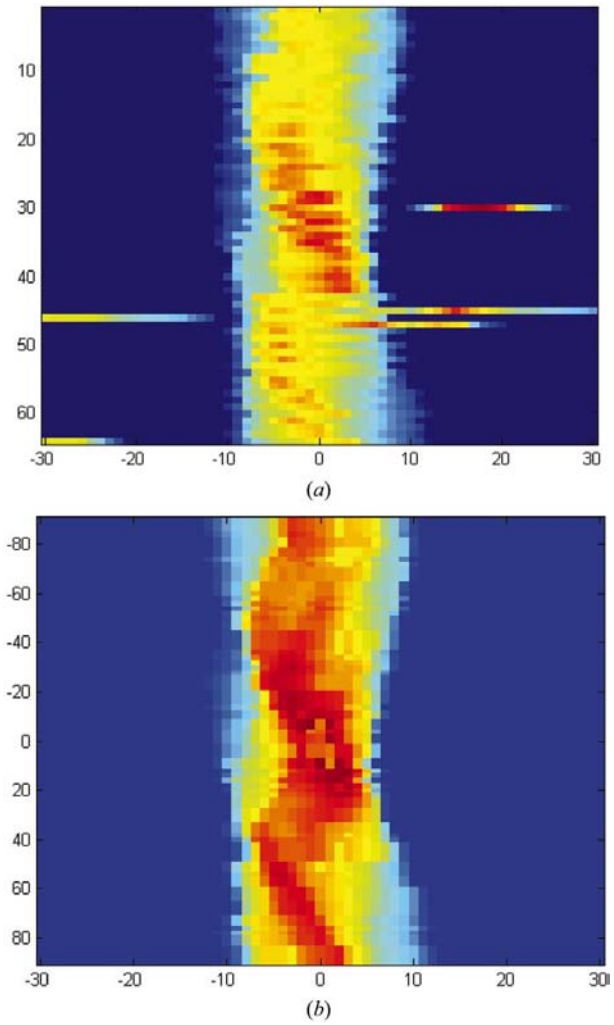

Figure 3
Sinograms for the reconstruction of one z layer in one grain. In (*a*) the original projections are stabled below each other in order of increasing ω. In (*b*) the interpolated projections are shown as a function of γ.

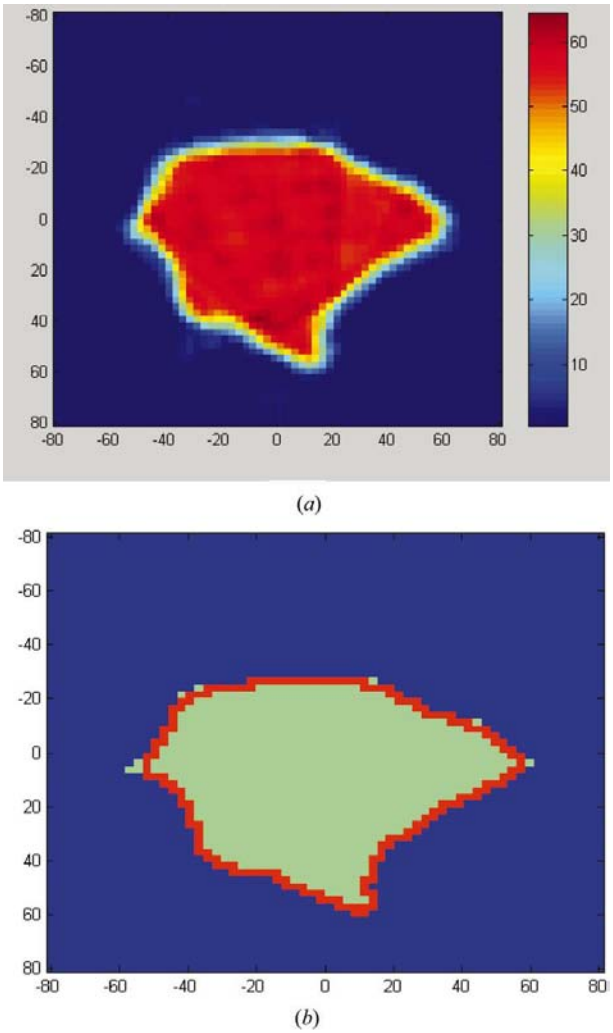

Figure 4
(*a*) The reconstructed density profile of the grain from Fig. 3 using the 59 non-overlapping reflections. (*b*) The corresponding outline defined at the 50% level (red) is compared with the original of the simulations (green). The outline is defined to be the set of pixels which have intensity above the threshold and which have at least one neighbour with an intensity below the threshold. The (x_ω, y_ω) coordinate system shown is shifted such that the origin is near the grain centre; the units are μm.

The resulting reconstruction for the grain is shown in Fig. 4(*a*). The density fluctuations in the interior of the grain are of the order of 5%. The corresponding outline is shown in Fig. 4(*b*) together with the original. The average deviation between the two is below 2.5 µm, to be compared with the detector pixel size of 5 µm. (A similar reconstruction including also the overlapping projections gave almost identical results.)

The reconstruction for the full sample layer is compared with the original in Figs. 5(*a*) and 5(*b*). In Fig. 5(*a*) the individual boundaries are shown, as found by setting a threshold of 0.5. The outlines are defined as the set of pixels which have an intensity above the threshold and which have at least one neighbour with an intensity below it. This implies that in the ideal case the red grain boundaries should be two pixels wide. The quality of the map is generally good. In Fig. 5(*b*) interpolation is performed. The correspondence is now excellent, with on average a sub-voxel accuracy. In comparison, the pixel size of the detector is twice that of the grid used for reconstruction.

To estimate the effect of symmetry, the grain in the upper-right corner was associated with a specific orientation, namely the so-called cube orientation with (100), (010) and (001) aligned with x, y and z, respectively, for $\omega = 0$. In this highly symmetric case, the number of independent projections decreases substantially. Nevertheless, the correspondence is still good.

To investigate further the influence of the number of reflections, we introduce a cut-off on the maximum deviation of a reflection from the x–y plane, $\alpha_{\rm cut}$. Results for $\alpha_{\rm cut} = 5^\circ$ and 2.5° are shown in Figs. 6(*a*) and 6(*b*), respectively. The associated number of valid non-overlapping projections are 30 and 13. Evidently, 30 reflections are sufficient for the reconstruction, while the resolution has deteriorated in Fig. 6(*b*).

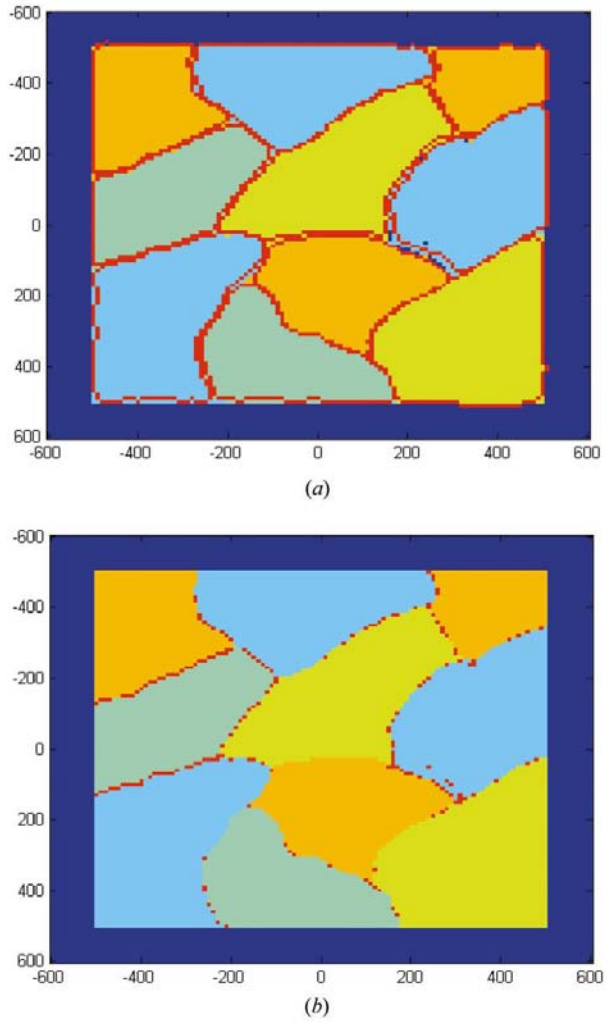

Figure 5
The result of the reconstruction for one layer in the material as compared with the original of the simulations. The grain segments of the latter are shown in arbitrary colours. In (*a*) the individual outlines of the reconstructed grains are shown as red lines. In (*b*) interpolation is performed: each pixel is associated with the grain exhibiting the highest reconstructed density at that position. Shown are only the points (red) where there is a difference between the original and the interpolated map. The units of the (x_ω, y_ω) coordinate system are µm.

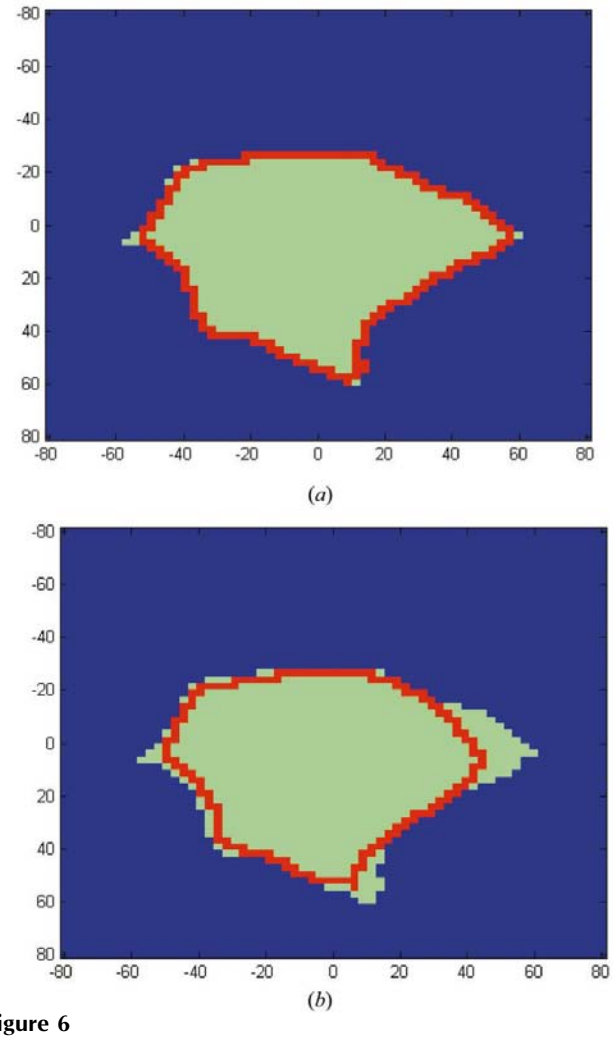

Figure 6
Effect of rejecting projections where the reflection has an angle α with the x–y plane above a threshold. The outlines (red) are compared with the original of the simulations (green) as in Fig. 4. Shown are the results of a cut of $|\alpha| < 5^\circ$ (*a*) and $|\alpha| < 2.5^\circ$ (*b*).

To estimate the influence of extinction, simulations were made in which each projection was multiplied by a random fraction, $p + (1 - p)r$, where p is fixed and $0 < r < 1$ is a random number specific to each reflection. Results for $p = 0.7$ and 0.1 are shown in Figs. 7(*a*) and 7(*b*), respectively. Evidently, the reconstruction is robust towards a moderate amount of extinction.

4. Discussion

A final assessment of the method cannot be made until it has been used on a set of materials science problems. This is outside the scope of this article. Instead we discuss a number of intrinsic limitations.

(*a*) In order for *GRAINDEX* to work, the amount of overlap of diffraction spots has to be small. This limits the number of simultaneously illuminated grains and the degree of texture in the sample. The limit can be shifted at the expense of time resolution by the use of a smaller $\Delta\omega$.

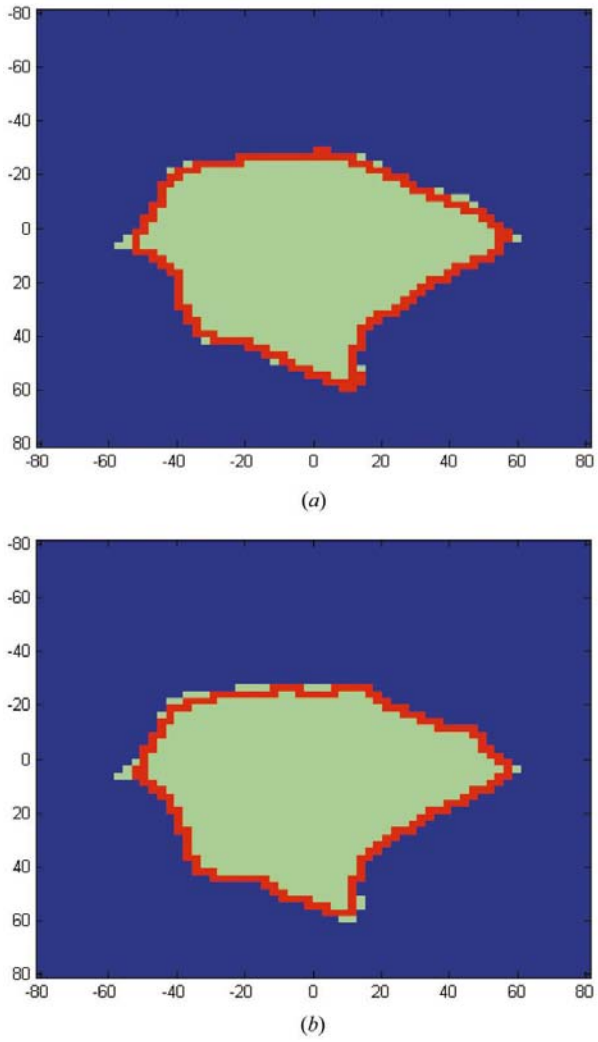

Figure 7
Effect of extinction. The outlines (red) are compared with the original of the simulations (green) as in Fig. 4. The extinction is simulated by weakening the intensities in the projection profiles by a random factor, specific to each reflection. Shown are results for a maximum of (*a*) 30% extinction and of (*b*) 90% extinction.

(*b*) Kinematical scattering. Both absorption and extinction effects diminish strongly with increasing X-ray energy. Moreover, the absorption can be calculated with high precision from the diffraction map (or from a tomogram of the whole sample). With respect to extinction, the simulations have shown that the method is relatively robust.

(*c*) Mosaic spread. There is a limit to how close the detector can be to the centre of rotation. This limit might be set by sample dimensions or the requirement to be able to separate the diffraction spots from the transmitted part of the incoming beam. With state-of-the-art specifications as used in the simulations, it appears that the mosaic spread of each reflection should be below 1°.

(iv) The approximation of $\alpha = 0$ evidently leads to a smearing of the resulting three-dimensional map in the z direction. A possible remedy is to repeat the data acquisition procedure for a number of small tilts of the sample. Combining data from different tilts, all reflections can be measured with an arbitrarily small α angle.

An additional constraint should be considered: the method as outlined above requires the diffraction geometry to be known with a high precision, *e.g.* for the setup of the simulations L_1 should be known within ± 20 µm and the spatial distortion in the detector should be calibrated to better than ± 2 µm. In that context two facts are helpful. Firstly, it is well known from tomography that alignment errors on *e.g.* $y_{\rm det}(0)$ can be estimated and corrected by inspection of the sinograms. Secondly, we may reformulate the reconstruction part of the algorithm such that a global coordinate system is not needed. This can be done by determining the projections relative to the centre of mass of each diffraction spot, as these are bound to have the same origin in the grain.

Alternative methods for solving the reconstruction problem exist (Davies, 1983). In particular, iterative reconstruction methods, also known as algebraic methods, where the voxels are treated as unknowns to be solved by a set of linear equations given by the projections. (For tomography-related work, see *e.g.* Gordon *et al.*, 1970; Andersen & Kak, 1984; Kak & Slaney, 1988). Closely related are maximum entropy methods (Minerbo, 1979; Steenstrup, 1990). Both types of method are known to be substantially more demanding in terms of computing time than the filtered back-projection approach. However, they do not require the set of projections to be uniformly distributed within a given plane. Hence, if applied to the present problem, the approximation of $\alpha = 0$ would not needed. Likewise, it would not be necessary to interpolate in γ. Furthermore, the algebraic methods may be of interest when the number of non-overlapping reflections becomes very small.

5. Conclusion

We have established a three-dimensional mapping scheme for polycrystals based on two independent parts: indexing of the reflections and reconstruction of each grain. For an f.c.c. structure we find from simulations that of the order of 30 reflections are sufficient to use the filtered back-projection

method. The method is relatively robust towards extinction and exhibits sub-pixel accuracy. It is fast and therefore relevant for studies of grain dynamics. In addition, it seems well suited for simultaneous characterization with absorption contrast tomography.

We thank D. Juul Jensen for discussions. This work was supported by the Danish Natural Research Foundation through the 'Center for Fundamental Research: Metal Structures in Four Dimensions', and by the Danish Natural Science Research Council *via* Dansync.

References

Andersen, A. H. & Kak, A. C. (1984). *Ultrason. Imag.* **6**, 81–94.
Bouchard, R., Hupfeld, D., Lippmann, T., Neuefeind, J., Neumann, H.-B., Poulsen, H. F., Rütt, U., Schmidt, T., Schneider, J. R., Sussenbach, J. & von Zimmermann, M. (1998). *J. Synchrotron Rad.* **5**, 90–101.
Bracewell, R. N. & Riddle, A. C. (1967). *Astrophys. J.* **150**, 427–434.
Davies, S. R. (1983). *The Radon Transform and some of its Applications*. New York: John Wiley.
Gordon, R., Bender, R. & Herman, G. T. (1970). *J. Theor. Biol.* **29**, 471–481.
Juul Jensen, D. & Poulsen, H. F. (2000). *Proceedings of the 21st Risø International Symposium on Materials Science*, Risø National Laboratory, Roskilde, Denmark, pp. 103–124.
Kak, A. C. & Slaney, M. (1988). *Principles of Computerized Tomographic Imaging*. New York: IEEE Press.
Krac, M. V. & Spanos, G. (1999). *Acta Mater.* **47**, 711–724.
Lauridsen, E. M., Juul Jensen, D., Poulsen, H. F. & Lienert, U. (2000). *Scr. Mater.* **43**, 561–566.
Lauridsen, E. M., Schmidt, S., Poulsen, H. F. & Suter, R. M. (2001). *J. Appl. Cryst.* **34**, 744–750.
Lienert, U., Poulsen, H. F. & Kvick, Å. (1999). *Proceedings of the 40th Conference of AIAA on Structures, Structural Dynamics and Materials*, St. Louis (USA), pp. 2067–2075. American Institute of Aeronautics and Astronautics.
Margulies, L., Winther, G. & Poulsen, H. F. (2001). *Science*, **291**, 2392–2394.
Minerbo, G. (1979). *Comput. Graph. Image Process.* **10**, 48–68.
Poulsen, H. F., Andersen, N. H., Gottschalck Andersen, L. & Lienert, U. (2002). *Physica C*, **370**, 141–145.
Poulsen, H. F., Garbe, S., Lorentzen, T., Juul Jensen, D., Poulsen, F. W., Andersen, N. H., Frello, T., Feidenhans'l, R. & Graafsma, H. (1997). *J. Synchrotron Rad.* **4**, 147–154.
Poulsen, H. F., Nielsen, S. F., Lauridsen, E. M., Schmidt, S., Suter, R. M., Lienert, U., Margulies, L., Lorentzen, T. & Juul Jensen, D. (2001). *J. Appl. Cryst.* **34**, 751–756.
Steenstrup, S. (1990). *Phys. Med. VI*, **3–4**, 273–276.

A6

PHILOSOPHICAL MAGAZINE, 21 August 2003
VOL. 83, NO. 24, 2761–2778

Taylor & Francis
Taylor & Francis Group

A six-dimensional approach to microtexture analysis

H. F. POULSEN†

Centre for Fundamental Research: Metal Structures in Four Dimensions,
Materials Research Department, Risø National Laboratory,
DK-4000 Roskilde, Denmark

[*Received 6 January 2003 and accepted in revised form 12 May 2003*]

ABSTRACT

A mathematical framework is presented for microtexture derivation and analysis. A six-dimensional space is introduced, defined as the product of direct space (x, y, z) and orientation space, parametrized by the Rodrigues vector (r_1, r_2, r_3). The framework is adapted to diffraction experiments, where orientation information from many grains or deformation microstructures is recorded in parallel, with the prime aim of allowing fast measurements and thus the ability to study microstructure dynamics. Assuming the use of a monochromatic beam the geometry of the projection surfaces is deduced. The derivation of the microtexture is formulated as an inverse problem similar to reconstruction problems in absorption or emission tomography. The applicability of the two major types of reconstruction algorithm, namely transform methods and algebraic methods, is discussed. An explicit solution in terms of the iterative algebraic reconstruction technique algorithm is given. The choice of basis function is discussed. Furthermore, the framework is applied to a number of important simplifying cases. These include grain-by-grain reconstruction, classical pole figure inversion and the generation of three-dimensional maps of non-deformed grains.

§1. INTRODUCTION

During the last 10–15 years, experimental studies, which combine the characterization of the local structure and the local crystallographic orientation, have become immensely popular (for example Lee (2002)). The major parts of these studies have been performed by techniques such as electron backscatter pattern (EBSP) and Kikuchi line analysis, where the position and shape of the orientational elements of the microstructure (the grains, subgrains, cells, etc.) are mapped and each local volume is associated with one and only one orientation. Alternatively, methods such as selected-area diffraction are applied where the size of the gauge volume is larger than the dimension of the typical microstructural element. The resulting local orientation distributions are generally referred to as microtextures. Characteristic for both approaches is that the material is probed subvolume by subvolume by scanning either the microfocused beam or the sample. Furthermore, as most of these techniques are based on probes with limited penetration, such as electrons or visual light, bulk properties cannot be characterized non-destructively.

† E-mail: henning.friis.poulsen@risoe.dk.

Philosophical Magazine ISSN 1478–6435 print/ISSN 1478–6443 online
http://www.tandf.co.uk/journals
DOI: 10.1080/1478643031000147308

The object of this work is to provide the mathematical framework for an alternative approach, where the microstructure within an extended three-dimensional (3D) volume, consisting of many elements, is characterized simultaneously. Experimentally this is achieved by the use of a penetrating monochromatic beam, which is much wider than the size of the average element. Diffraction patterns are acquired with a high-resolution two-dimensional (2D) detector, while rotating the sample around one or more axes. In addition the detector may be positioned at several distances to the sample. The microtexture is then derived ('reconstructed') from the intensity distribution in these images. Similar approaches have been used with great success in fields such as absorption contrast tomography and positron emission tomography (for example Deans (1983), Kak and Slaney (1988) and Herman (2002)). The relevance for microtexture characterization is above all an increase in speed of data acquisition. Compared with scanning, the tomographic approach can be several orders of magnitude faster.

While the framework to be presented is applicable to electron diffraction, neutron diffraction or X-ray diffraction (XRD), the main motivation comes from the emergence of the 3DXRD method. This is based on the use of high-energy ($E \geqslant 50$ keV) X-rays from a synchrotron source. The hard X-rays have a penetration power in the millimetre to centimetre range and are associated with relatively small Bragg angles, which makes it possible to measure the complete diffraction pattern with charge-coupled device-based detectors (Poulsen *et al.* 1997). A dedicated instrument, the 3DXRD microscope, has been established at the European Synchrotron Radiation Facility. With this, the position, volume, elastic strain tensor and crystallographic orientation of 100–1000 embedded grains can be determined simultaneously (Lauridsen *et al.* 2001, Poulsen *et al.* 2001, Poulsen and Juul Jensen 2002). The accuracy is of the order of 1 μm for positions, 10^{-4} for strain and 0.2° for orientations. Furthermore, 3D grain-boundary maps can be generated (Nielsen *et al.* 2000a). However, the algorithms applied cannot handle overlap between diffraction spots arising from different grains. So far this has limited the use of the method to plastic strains below 20%. For grain-mapping purposes, the restriction is more severe; only undeformed grains can be handled. Hence, to make 3DXRD a more universal tool for studies of the dynamics of the microstructural elements, more powerful reconstruction methods are required.

A distinction can be made between a reconstruction where each sample position is associated with one orientation and one where each position is associated with an orientation distribution. Focus will here be on the second type, for a number of reasons. Firstly, this is the more general case. Secondly, the spatial resolution of the 3DXRD microscope is 5 μm at present (Poulsen and Fu 2002). This value should be contrasted with typical cell dimensions in deformed metals of 100 nm–1 μm, and the even smaller dimensions involved in characterization of nanomaterials. Thirdly, an experimental compromise between resolution, inspection volume and data acquisition speed is generally needed. Hence, even if the microscope can be operated with a spatial resolution better than the size of the typical element, such a setting may not be relevant.

The task is therefore to reconstruct the density of a six-dimensional (6D) space, one composed of the product of direct space and orientation space. Introducing such a high-dimensional space makes discretization an issue. To represent, say, orientation elements of a size of $(0.5^\circ)^3$ over $100 \times 100 \times 10$ positions in the sample, a set of approximately 10^{11} '6D voxels' is required. Fortunately, the vast majority

of this space will in most cases be empty, a fact which can, and should, be used in the analysis.

From a mathematical point of view the task is an 'inverse problem'. Driven by applications in numerous fields, such problems have been investigated in great detail. The resulting reconstruction principles can broadly be categorized as belonging to one of two categories: transform methods and algebraic methods (Herman 2002). In the transform methods the projection is treated as an operator: a generalized Radon transform. Solutions are typically based on theorems that couple Radon transforms and Fourier transforms (FTs). The algebraic methods are similar to the so-called 'direct methods' in texture analysis (Matthies 1979) in the sense that the geometry is formulated as a constrained set of linear equations. With both types of method, routinely the density in a grid with 10^9–10^{10} volume elements is reconstructed with accuracy in the 1% range.

In this paper, microtexture reconstruction is discussed in terms of transform methods and algebraic approaches, specifically as follows.

(i) The 6D reconstruction space H is represented as the product of direct space and Rodrigues space. The geometric properties of this space are derived.
(ii) The relative merits of transform methods versus algebraic methods are discussed.
(iii) A solution in terms of an implementation of the iterative algebraic reconstruction technique (ART) routine (Gordon *et al.* 1970) is presented.
(iv) A number of simplifying conditions are investigated, one being element-by-element reconstruction of the microstructure elements and others being reconstruction in lower-dimensional spaces such as generation of grain maps of non-deformed grains and pole figure inversion for classical texture analysis.
(v) The choice of basis function is discussed. Functions with superior properties to 6D voxels are suggested.

The methodology is derived for the geometry of the 3DXRD microscope, but the equations are valid for any set-up based on diffraction with a monochromatic beam and assuming kinematic scattering. A first application of the ART reconstruction method was recently presented for the case of mapping non-deformed grains (Poulsen and Fu 2002). That article also gives a discussion of implementation and an experimental verification. Similarly, a simulation demonstrating the use of transform methods for mapping of non-deformed grains was reported by Poulsen and Schmidt (2002). The formalisms developed in these two articles constitute subsets of the full methodology presented here.

§ 2. Diffraction geometry

The geometry underlying the 3DXRD method has been described in detail by Lauridsen *et al.* (2001). In this section the relevant equations are partly summarized and partly cast in a new form, more suitable for establishing a reconstruction formalism.

A sketch of the set-up is provided in figure 1. The sample is illuminated by a parallel monochromatic beam. It is mounted on an ω rotation stage, with the axis perpendicular to the beam. Diffraction spots are acquired on a 2D detector while the sample is scanned in equiangular steps of $\Delta\omega$. During each acquisition the sample is oscillated by $\pm\Delta\omega/2$ to provide an intensity-conserving sampling.

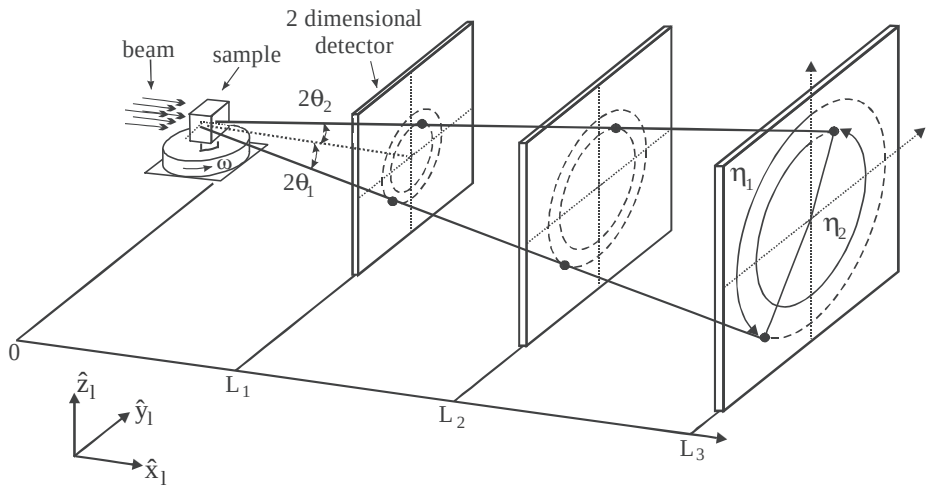

Figure 1. Sketch of the assumed experimental geometry. The angles 2θ, η and ω are marked for two diffraction events at three sample-detector distances L_1 to L_3. The laboratory coordinate system (x_l, y_l, z_l) is defined.

The detector is aligned perpendicular to the (non-diffracted) incident beam. It exhibits a high spatial resolution and is positioned at a small sample–detector distance L_1. As an option the whole procedure is repeated one or more times at larger sample–detector distances $L_2, \ldots, L_N$.

Initially we assume the relevant part of the sample to be fully illuminated at all ω settings by a homogenous beam. For a given position, a given ω setting and a given sample–detector distance L, we describe the geometry of one ray.

Assume that the ray is diffracted from position (x, y, z) in the sample system, with $(x, y) = (0, 0)$ along the ω rotation axis. The direction of the ray is determined by the Bragg angle 2θ and the azimuthal angle η, both defined in figure 1. The intersection between the ray and the detector plane is $(L, y_{\mathrm{det}}, z_{\mathrm{det}})$:

$$\begin{aligned} y_{\mathrm{det}} &= -(L - x_l)\,\tan(2\theta)\,\sin(\eta) + y_l, \\ z_{\mathrm{det}} &= (L - x_l)\,\tan(2\theta)\cos(\eta) + z. \end{aligned} \tag{1}$$

with

$$\begin{pmatrix} x_l \\ y_l \\ z \end{pmatrix} = \Omega \begin{pmatrix} x \\ y \\ z \end{pmatrix} = \begin{pmatrix} \cos(\omega) & -\sin(\omega) & 0 \\ \sin(\omega) & \cos(\omega) & 0 \\ 0 & 0 & 1 \end{pmatrix} \begin{pmatrix} x \\ y \\ z \end{pmatrix}. \tag{2}$$

Here we have defined $(y_{\mathrm{det}}, z_{\mathrm{det}}) = (0, 0)$ for the intersection of the detector plane with the incident ray passing through $(x, y, z) = (0, 0, 0)$. In equations (1) and (2), and throughout this paper, the subscript l refers to the laboratory system.

The normalized diffracting vector in the laboratory system $\mathbf{G}_l/\|\mathbf{G}_l\|$ can be expressed as

$$\frac{\mathbf{G}_l}{\|\mathbf{G}_l\|} = \Omega \mathrm{S}\mathbf{y} = \Omega \mathrm{S}\mathrm{g}^{-1}\mathbf{h} = \cos(\theta) \begin{pmatrix} -\tan(\theta) \\ -\sin(\eta) \\ \cos(\eta) \end{pmatrix}. \tag{3}$$

Here S defines the orientation of the sample on the ω turntable. By default $S = I$, but at times it is convenient to choose the axes of the sample system at will. **y** is the normalized diffraction vector in the sample system. The matrix g refers to the crystallographic orientation of the material at the point of origin of the ray. (This definition of g is standard in texture literature. g is the inverse of the matrix U, as used by Lauridsen *et al.* (2001).) The unit vector **h** is defined by

$$\begin{pmatrix} h_1 \\ h_2 \\ h_3 \end{pmatrix} = \frac{\lambda}{4\pi \sin(\theta)} \mathrm{B} \begin{pmatrix} h \\ k \\ l \end{pmatrix}, \tag{4}$$

where λ is the wavelength, (h, k, l) are the Miller indices and B is the metric

$$\mathrm{B} = \begin{pmatrix} a^* & b^* \cos(\gamma^*) & c^* \cos(\beta^*) \\ 0 & b^* \sin(\gamma^*) & -c^* \sin(\beta^*) \cos(\alpha) \\ 0 & 0 & c^* \sin(\beta^*) \sin(\alpha) \end{pmatrix}, \tag{5}$$

with $(a, b, c, \alpha, \beta, \gamma)$ and $(a^*, b^*, c^*, \alpha^*, \beta^*, \gamma^*)$ symbolizing the lattice parameters in the direct and reciprocal spaces respectively.

Inserting in equation (1) we obtain

$$\begin{pmatrix} cL \\ y_{\mathrm{det}} \\ z_{\mathrm{det}} \end{pmatrix} = \begin{pmatrix} cx_l \\ y_l \\ z \end{pmatrix} + \frac{(L - x_l)\tan(2\theta)}{\cos(\theta)} \Omega \mathrm{S} \mathrm{g}^{-1} \begin{pmatrix} h_1 \\ h_2 \\ h_3 \end{pmatrix}. \tag{6}$$

The constant $c = 1 - 1/\cos(2\theta)$ is immaterial. The first equation is better expressed by the first index in a vector

$$\sin(\theta) = -\left[\Omega \mathrm{S} \mathrm{g}^{-1} \mathbf{h}\right]_1. \tag{7}$$

It constitutes a quadratic equation for determination of ω, given g and **h**.

For experimental set-ups with a different choice of rotation axes, that is a three- or six-circle diffractometer, the equations above are still valid provided that Ω is replaced with the appropriate rotation matrix.

In the following we shall perform a number of estimates of the validity of simplifying assumptions on geometry. For this we define a *standard* 3DXRD setting, defined by $L = 4\,\mathrm{mm}$, $2\theta = 10^\circ$ and a detector pixel size of $2.5\,\mu\mathrm{m}$. The assumptions will be said to fail when the deviation introduced by the simplification corresponds to a distance of 1.0 pixel or more on the detector.

§ 3. Reconstruction formalism

3.1. *Rodrigues space*

As pointed out by Frank 1988, Rodrigues space is a natural choice for representation of orientation space. For use in the rest of the article, certain key features are reviewed (Morawiec and Pospiech 1989, Neumann 1991, Morawiec and Field 1996, Kumar and Dawson 2000).

Any rotation operator g can be represented in a unique way by a rotation axis **n** and a rotation angle ϕ, defined on $[0\ \pi]$. In the Rodrigues parametrization these are coupled in the definition of the Rodrigues vector **r**:

$$\mathbf{r} = \tan\left(\frac{\phi}{2}\right)\mathbf{n}. \tag{8}$$

The vector $\mathbf{r}$ can be treated as a vector in $\mathbf{R}^3$, with exception of points with a rotation angle of π, which are represented by two opposite points in infinity. The axes of this space are collinear with those of the sample system in the sense that a vector $\mathbf{r} = (r_1, 0, 0)$ describes a rotation around the sample x axis.

The relationship to g is given by

$$g_{ij} = \frac{1}{r^2}\left[\left(1 - r^2\right)\delta_{ij} + 2r_i r_j - 2\varepsilon_{ijk} r_k\right], \tag{9}$$

where $r^2 := r_k\, r_k$, and ε_{ijk} is the permutation tensor. The metric d_{ij} and the volume element $\mathrm{d}V$ are

$$d_{ij} = \frac{1}{\left(1 + r^2\right)^2}\left[\left(1 + r^2\right)\delta_{ij} - 2r_i r_j\right], \tag{10}$$

$$\mathrm{d}V = \left[\det(d_{ij})\right]^{1/2} = \frac{\mathrm{d}r_1\, \mathrm{d}r_2\, \mathrm{d}r_3}{1 + r^2}. \tag{11}$$

A key fact is that rotations with a fixed axis and varying rotation angle (geodesics in $SO(3)$) are straight lines in Rodrigues space. From this follows first of all that the fundamental region Ω_{fr} is a polyhedron with the faces aligned with the symmetry axes. As an example, for cubic crystal symmetry the fundamental zone is a truncated cube. For a detailed calculation of the shape of the fundamental zone and the boundary conditions for various crystal symmetries, see Morawiec and Field (1996).

Another consequence of the theorem on geodesics is that the projection lines (integration paths) for pole figure generation are straight lines. Specifically, for a given set of vectors $\mathbf{h}$ and $\mathbf{y}$, the projection line is given by

$$\mathbf{r} = \mathbf{r}^0 + t\frac{\mathbf{h} + \mathbf{y}}{1 + \mathbf{h} \cdot \mathbf{y}}, \quad -\infty < t < \infty, \tag{12}$$

$$\mathbf{r}^0 = \frac{\mathbf{h} \times \mathbf{y}}{1 + \mathbf{h} \cdot \mathbf{y}} = \tan\left(\frac{\phi_0}{2}\right)\mathbf{n}, \tag{13}$$

where $\mathbf{r}^0$ is the rotation from $\mathbf{h}$ into $\mathbf{y}$ with the minimum rotation angle ϕ_0. The second term in equation (12) corresponds to an arbitrary rotation around the symmetric position $\mathbf{h} + \mathbf{y}$.

Confining the solution to Ω_{fr} the projection line extending through the full Rodrigues space is transformed into a set of projection lines, as defined by the various symmetry operations including the inversion in origin.

Of particular interest are the properties of Rodrigues space close to the origin. For $\phi \to 0$, rotations become commutative. This is reflected in the fact that the metric (equation (10)) becomes linear. As an example, for orientation distributions characterized by $\phi < 10^\circ$, the space is Euclidean within an accuracy of better than 1%. Furthermore for $\phi \to 0$ the expression for the projection line simplifies to

$$\mathbf{r} = \frac{1}{2}(\mathbf{h} \times \mathbf{y}) + \frac{t}{2}(\mathbf{h} + \mathbf{y}). \tag{14}$$

3.2. *The six-dimensional reconstruction space*

Based on the properties of Rodrigues space it is natural to define the 6D reconstruction space H as the outer product between direct space $\mathbf{x} = (x, y, z)$ and Rodrigues space $\mathbf{r} = (r_1, r_2, r_3)$: $H = \mathbf{x} \otimes \mathbf{r}$. Again the axes r_i correspond to rotations

around x, y and z for $i = 1$, 2 and 3 respectively. H is bounded in $\mathbf{x}$ by the dimension of the sample and confined in $\mathbf{r}$ to Ω_{fr}. The metric is the product: $\det(H) = \det(I \otimes d) = \det(d)$.

The parametrization of the space will be in terms of a base consisting of functions that individually span a small part of H (sometimes called local interpolants). In the simplest case, H is tessellated into '6D voxels', each in the shape of a 6D cube. For illustration, we shall refer to such 6D voxels below; other choices of base functions are discussed in § 7.

In the following the projection surface in H is derived. By definition, the integrated intensity in a given pixel $(y_{\mathrm{det}}, z_{\mathrm{det}})$ at a given ω setting and a given distance L is proportional to a weighted sum of the density along this surface. As we shall see later, the geometry of the projection surface is important for deciding which reconstruction method to choose.

The projection surface is 3D. The spatial part can be derived from equation (1):

$$(y_{\mathrm{det}} - y_{\mathrm{l}})^2 + (z_{\mathrm{det}} - z)^2 - (L - x_{\mathrm{l}})^2 \tan^2(2\theta) = 0, \quad x_{\mathrm{l}} < L. \tag{15}$$

Evidently, the surface is a set of cones, defined by Bragg's law. There is one cone for each distinct scattering angle 2θ, which can be observed experimentally. The cones all have their top at $\Omega^{-1}(L, y_{\mathrm{det}}, z_{\mathrm{det}})$ and their rotation axis in the (x, y) plane at an angle of $-\omega$ from the x axis. When mirrored in the detector plane they form the familiar set of Debye–Scherrer cones for a hypothetical powder placed at $\Omega^{-1}(L, y_{\mathrm{det}}, z_{\mathrm{det}})$. A schematic drawing of the spatial part of the projection surface as seen from the laboratory system is given in figure 2 (*a*).

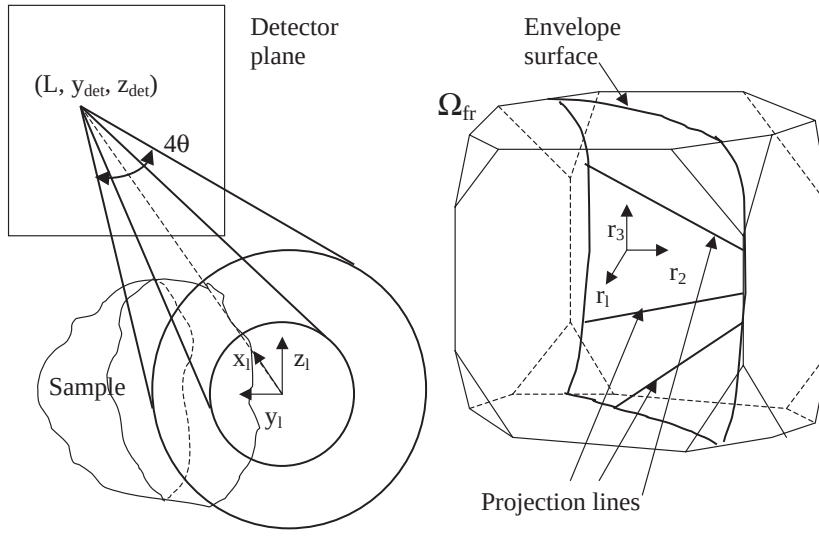

Figure 2. (*a*) The geometry of the projection surface in the 6D reconstruction space. For a given acquisition and detector position $(y_{\mathrm{det}}, z_{\mathrm{det}})$ the spatial part of the surface is a set of cones with opening angles of 4θ. In the laboratory system the cones are aligned with the x_{l} axis. The surface is restricted by the extension of the sample. (*b*) The angular part of the projection surface is a set of straight projection lines in the Rodrigues space. These are embedded within a curved envelope surface. Confining the geometry to the fundamental zone Ω_{fr}, the embedded surface is transformed into a set of surfaces, as defined by the relevant symmetry operations (not shown).

For a fixed (x_l, y_l, z) point on one of the projection cones the corresponding projection surface in Rodrigues space is a set of straight lines (cf. § 3.1). Let us consider one of these (in the following called the Rodrigues projection line). From equation (3), the Rodrigues projection line is seen to be fixed for constant η, corresponding to traversing the projection cone along a straight line passing through the top point. When traversing the cone along the circle at any fixed x_l, the Rodrigues projection lines precess. All the projection lines for a given cone are embedded in a curved 2D plane defined by equation (7), the envelope surface. A schematic drawing of the angular part of the projection surface is given in figure 2.

The shape and position of the projection cone and the Rodrigues projection line are functions of the parameters y_{det}, z_{det}, L and ω. Varying the three former parameters correspond to simultaneous translations of all the projection cones. For a given 2θ and η the Rodrigues projection line is fixed. Changing ω, on the other hand, implies a simultaneous rotation of the projection cones in the (x, y) plane and a rotation of the envelope surface.

The projections through a given 6D voxel are determined by crystallography. For an ω range of 180° the number of projections is equal to the number of L settings multiplied by the number of observable reflections including multiplicity. It is noticeable that this is independent of the detector resolution and $\Delta\omega$. This property makes reconstruction of diffraction data distinctly different from reconstruction of absorption and emission tomography data, where the direction and number of projections can be determined at will by configuration of the experimental set-up.

3.2.1. *Element-by-element reconstruction*

A powerful simplification arises if the density distribution in H can be divided into disjunct sets, which form diffraction patterns that are separated on the detector. Most notably, experiments may be designed such that the majority of the diffraction spots, arising from the individual microstructural elements within the gauge volume, are not overlapping with each other. In such cases it is possible to sort the diffraction spots with respect to element of origin by the indexing program, GRAINDEX (Lauridsen *et al.* 2001). The data analysis can then be performed sequentially on each set of diffraction spots, and the elements therefore be reconstructed individually. (The probability of spot overlap has been calculated by Schmidt *et al.* (2002) as a function of texture, number of elements and the orientation spread within each element. For non-deformed specimens it is demonstrated that 3000 elements can be identified simultaneously.)

Most of the 3DXRD results mentioned in the introduction have been generated using GRAINDEX as a stand-alone program. Then the algorithm provides the centre-of-mass position, the volume and the average orientation of each element. The issue here is for each element to use the output of the indexing program to identify the relevant part of the diffraction pattern on which to base the reconstruction.

To derive the projection surface for one microstructural element, it is convenient to set S equal to the average orientation of the element. Then the relevant part of orientation space becomes a small subset of Ω_{fr}, centred on the origin. In this case, there is only one cone (we know which reflection a given diffraction spot is associated with) and only one Rodrigues projection line, expressed by equation (14). Moreover, for small orientation spreads the envelope surface becomes straight.

Furthermore for small element sizes we can perturb equation (15) around the grain centre. In this way, the projection cone is approximated by the tangential

plane. With this approximation the geometry is completely linearized. H is a Euclidian space and the 3D projection surface has zero curvature.

For the *standard* 3DXRD setting we find that element dimensions must be smaller than 100 μm for the tangential approximation to be valid.

3.3. *Reconstruction space in lower dimensions*

In the following we adopt the general formalism to some simplifying cases, where the dimension of reconstruction space is reduced.

3.3.1. *Layer-by-layer reconstruction*

In this case the incoming beam is defined (by focusing and/or the use of slits) in z such that the cross-section is an infinitesimally thin line parallel to y_l. This beam defines a layer in the sample, and the reconstruction is confined to this layer. 3D information is obtained by repeating the procedure while scanning the sample in z and, in the end, stacking the reconstructed layers.

The projection surface is now 2D. Inserting $z = 0$, equation (15) reduces to

$$(y_{\mathrm{det}} - y_l)^2 - (L - x_l)^2 \tan^2(2\theta) = -z_{\mathrm{det}}^2, \quad x_l < L. \tag{16}$$

For $z_{\mathrm{det}} \neq 0$, this equation defines one branch of a hyperbola, centred at $\Omega^{-1}(L, y_{\mathrm{det}}, 0)$. For $z_{\mathrm{det}} = 0$ the solution is two straight lines, corresponding to $\eta = 90^\circ$ and $\eta = 270^\circ$. The angular part of the projection surface remains as before.

In comparison with the method discussed in § 3.2, the data acquisition rate for layer-by-layer reconstruction is inherently slower. On the other hand, the reduced dimensionality will in general lead to a superior resolution, and in some cases it may be the only choice as either the information content provided by full illumination data or the associated computational effort does not allow a reconstruction at all. Furthermore, for small 2θ values the tangential approximation is better to the hyperbola than to the cone.

3.3.2. *Texture characterization*

If the detector resolution is larger than the dimensions of the illuminated sample volume, the set-up reduces to that of a classical texture experiment. This is typically accommodated using an area detector with a large pixel size placed at a fixed distance far from the sample. One sample–detector distance is sufficient.

Obviously, in this case, H is identical with Rodrigues space, with projection geometry as described in § 3.1. The methodology is similar to that developed by Barton *et al.* (2002) and by Weiland *et al.* (2002), with the exception of a different choice of interpolation functions (cf. § 7).

3.3.3. *Mapping large non-deformed grains by full illumination*

Let a grain be fully illuminated by a uniform beam, and assume that the associated diffraction spots are non-overlapping with any other diffraction spots. If the mosaic spread of the grain is negligible, reconstruction space is identical with direct space. From equation (1) it follows that the reconstruction surface is a straight line defined by

$$-(y_{\mathrm{det}} - y_l)\sin(\eta) + (z_{\mathrm{det}} - z)\cos(\eta) - (L - x_l)\tan(2\theta) = 0. \tag{17}$$

For the *standard* 3DXRD setting the mosaic spread must be less than 0.4° (full width) to be negligible. A large group of polycrystals fulfil this criterion.

3.3.4. *Mapping large non-deformed grains in a layer-by-layer reconstruction*

Finally for layer-by-layer reconstruction of a grain with a negligible mosaic spread, reconstruction space is the 2D (x, y) plane. Apart from the singularities at $\eta = -90^\circ$ and $\eta = 90^\circ$ there is no projection surface, but a one-to-one relationship between the grain section and the diffraction spot. Hence, it appears that a map of the layer in the grain can be produced by back projecting the density profile of the diffraction spot. Indeed this simple approach was the basis for the first grain maps, as reported by Nielsen *et al.* (2000a) and Poulsen *et al.* (2001).

However, the projection is not area conserving, as seen from equation (1). Hence, the spatial resolution in the resulting grain map varies with choice of reflection and direction in the (x, y) plane. Reconstruction schemes are therefore superior to the back-projection method, as they make use of all available information and enable interpolation between diffraction spots at different ω settings. This was the topic of the previous publication on reconstruction by ART (Poulsen and Fu 2002).

A summary of the geometry for the various cases is given in table 1.

§ 4. Transform methods

Most reconstructions in other areas are based on the so-called transform methods (for example Deans (1983), Natterer (1986) and Kak and Slaney (1988)). We briefly introduce the basic concepts by summarizing the simplest case of reconstructing a 2D Euclidean space (x, y) from all the linear projections through that space.

Let f be a function defined on $\mathbf{R}^2$. The Radon transform $\mathfrak{R}f$ is then a function defined on the set of hyperplanes (straight lines) in $\mathbf{R}^2$. For a given line ξ it is the projection of f along that line:

$$\mathfrak{R}f\,(\xi) = \int_{\xi} f\,(x, y)\,\mathrm{d}s. \tag{18}$$

Direct inversion formulae exist if f is continuous and has compact support, that is zero outside a finite region. However, in applications these are seldom used as they involve differentiation. The broad applicability arises from the relationship between Radon transforms and Fourier transforms. The Fourier-slice theorem states that

$$f = \mathfrak{F}_2^{-1}(\mathfrak{F}_1 \mathfrak{R}f\,). \tag{19}$$

Table 1. Summary of the geometric properties for the various reconstruction cases, as defined in the text. H symbolizes the reconstruction space and PS the projection surface. The dimension of the beam is the dimension of its cross-section. 'Element by element' refers to small elements.

	Dimension			Topology	
	Beam	H	PS	H	PS
General case	2	6	3	Elliptic	Cone × line
	1	5	2	Elliptic	Hyperbola × line
Element by element	2	6	3	Euclidean	Plane
	1	5	2	Euclidean	Plane
Large non-deformed grains	2	3	1	Euclidean	Line
	1	2	0	—	—
Classical texture	—	3	1	Elliptic	Line

Here $\mathfrak{F}_1$ is the one-dimensional Fourier Transform along the radial direction and $\mathfrak{F}_2$ is the conventional 2D Fourier Transform. This solution has the drawback that an interpolation is required between polar and Cartesian coordinates in Fourier space. Instead the following relation to the dual transform $\mathfrak{B}$ is used ($|k|$ is the radius in Fourier space)

$$f = \mathfrak{B}\mathfrak{F}_1^{-1}(|k|\mathfrak{F}_1\mathfrak{R}f). \tag{20}$$

This solution is known as the filtered back-projection algorithm. Using the fast Fourier transform algorithm for the two Fourier transforms involved the resulting reconstruction is fast, essentially assumption free and robust to noise.

In the following we investigate the feasibility of generalizing the transform method to the task of microtexture reconstruction. This task differs from that summarized above in four ways.

(i) The reconstruction space H is n dimensional and the projection surface is k dimensional, with $k \neq n-1$.
(ii) H is a curved space.
(iii) The projection surfaces are conical sections and not zero-curvature planes.
(iv) A complete sampling of all k-dimensional surfaces is not possible, as the set of projections going through a given Rodrigues vector $\mathbf{r}$ is defined by the set of experimentally observable (h, k, l) values.

The relevant generalization is the k-plane Radon transform. Let $f = f(x)$ be a function defined on $\mathbf{R}^n$. The k-plane Radon transform $\mathfrak{R}^k f$ is then a function defined on the set of k-dimensional planes in $\mathbf{R}^n$. For a given plane ξ it is the projection of f along that plane:

$$\mathfrak{R}^k f(\xi) = \int_\xi f(x)\,\mathrm{d}m(x), \tag{21}$$

where $\mathrm{d}m$ is the induced metric. Inversion formulae have been given for both Euclidean and elliptic spaces by Helgason (1980) (see also Jensen (2002)). The Fourier-slice theorem (equation (19)) can be generalized (S. R. Jensen, 2003, private communication), but an equivalent to the filtered back-projection algorithm (equation (20)) is not known to the present author.

With respect to issue (iii), Cormack (1981) reported inversion formulae for the Radon transform on a family of curves in the plane including the hyperbola. However, the simple relationship between Radon and Fourier transforms is lost. Likewise, the restricted sampling (issue (iv)) complicates the use of Fourier transforms.

Hence, it appears that the task of 6D microtexture reconstruction cannot be handled by state-of-the art transform methods. However, the concept can be applied to some of the lower-dimensional cases. As an example the task described in § 3.3.3 defined above was solved by means of an implementation of the filtered back-projection algorithm by Poulsen and Schmidt (2002). The Radon transform has also been discussed in connection with pole figure inversion by Savyolova (1994) with an approach based on ultrahyperbolic differential equations.

§ 5. Algebraic formulation

We proceed to derive an algebraic approach to the reconstruction for the general 6D case.

Let the densities in the 6D voxels, that is the unknowns, be listed in the vector $\mathbf{x}$. Correspondingly, let $\mathbf{b}$ list the background subtracted and flux normalized intensities of the individual pixels in the acquired images. Furthermore, let $\mathbf{b}^r$ symbolize the fraction of that intensity arising from reflection number r. Then, kinematic scattering implies a linear relationship between $\mathbf{x}$ and $\mathbf{b}^r$:

$$\mathrm{A}^r\mathbf{x} = \mathbf{b}^r. \tag{22}$$

Each element A^r_{ij} is a product of three known terms. The first is the fraction of the diffracted beam from voxel number i in H space that is absorbed in pixel number j, assuming all parts within voxel i to diffract with equal intensities. The second is the product of the three crystallographic normalization factors: the Lorentz, polarization and structure factors. The third is the volume element, as given by equation (11).

Next we sum the A^r and $\mathbf{b}^r$ values for the various reflections to produce A and $\mathbf{b}$. Hence, $\mathrm{A}\mathbf{x} = \mathbf{b}$. In practice, a tensor notation is useful. Let $\mathbf{x}$ be described by x_{jklmnp} with the first three and the last three indices referring to the spatial and angular degrees of freedom respectively. With these definitions the basic equation for the reconstruction is

$$A_{ijklmnp}x_{jklmnp} = b_i, \quad i = 1, \ldots, M, \tag{23}$$

with the following constraints (A) and (B).

(A) $0 \leqslant x_j \leqslant \rho_0, \ \forall j.$ (24)

(B) For positions not at the surface of the sample (for multiphase materials, not at an interface),

$$\sum_{mnp} x_{jklmnp} = \rho_0, \quad \forall jkl. \tag{25}$$

Here ρ_0 is the density of the material.

It is crucial to reduce the size of the system as much as possible. In particular, 6D voxels that point to pixels on the detector with a vanishing intensity should be discarded from further analysis. One way to do that is to scan through $\mathbf{b}$ and for each zero-value index to remove both the index from $\mathbf{b}$ and all the associated 6D voxels on the projection surface from $\mathbf{x}$. Another way is to scan through reconstruction space and for each voxel test whether any of the forward projections points to pixels with a vanishing intensity.

The formalism for the simplifying cases of §§ 3.2.1 and 3.3 follows immediately from the general case above.

§ 6. The algebraic reconstruction technique routine

Solving the constrained set of linear equations (23)–(25) can be achieved in numerous ways (Kak and Slaney 1988, Herman 2002). For smaller systems, singular-value decomposition, linear programming or maximum-entropy methods (for example Minerbo (1979)) are relevant. In this article we focus on the general case, where the size of A can be enormous, up to $10^8 \times 10^{11}$. Here it is impossible to store A in the memory, and an iterative solution with in-line evaluation of the matrix elements is the method of choice.

The ART algorithm (Gordon *et al.* 1970) is a variant of Kaczmarz' classical iterative method. Suitably optimized it has proven second to none in several cases

(Herman and Meyer 1993). Solutions $\mathbf{x}^{k+1}$ are found by progressively projecting the previous solutions $\mathbf{x}^k$ on hyperplanes represented by the kth equation:

$$\mathbf{x}^{k+1} = \mathbf{x}^k + \lambda \frac{b_{i(k)} - \sum_{j=1}^{N} A_{i(k)j} x_j^k}{\sum_{j=1}^{N} A_{i(k)j}^2} \mathbf{a}_{i(k)}, \tag{26}$$

with $\mathbf{a}_{i(k)} = (A_{i(k)1}, \ldots, A_{i(k)N})$. Following the proofs by Kaczmarz (1937) and Tanabe (1971) this algorithm is known to converge to the minimum-norm solution if the set of equations is consistent.

To improve the rate of convergence, the order of the rows are permuted $i = i(k)$ such that consecutive hyperplanes are more orthogonal to each other. Furthermore, a so-called relaxation parameter $0 < \lambda < 1$ is introduced, which empirically has been shown to improve convergence. For details on the optimization of these parameters see Herman (1993). If some observations are believed to be more accurate than others, λ can also be made dependent on the index in $\mathbf{b}$.

The constraints given by equations (24) and (25) may be applied after each step. A further useful constraint is that of compact support. Mathematically, these restrictions are all projections on to convex sets, in the sense that, if $\mathbf{x}_1$ and $\mathbf{x}_2$ are solutions fulfilling the constraints, then so are $\alpha\mathbf{x}_1 + (1-\alpha)\mathbf{x}_2$. Provided that the set of equations is consistent, convergence is assured when using such restrictions.

To accommodate the in-line evaluation of elements A_{ij} we apply the concept of a footprint (Matej and Lewitt 1996). For a given 6D voxel, a given reflection and fixed ω and L, we calculate the projection of this object on the detector. The result (the footprint) is a function centred on the projection of the centre of the voxel. Provided that the footprint has the same shape for a large set of 6D voxels, it can be tabulated. The use of look-up tables is well known to provide efficient programming. We shall return to this subject in § 7.

The ART routine can be generalized to a group-iterative version with identical convergence properties and a potential for much faster solutions (Eggermont *et al.* 1981). For this to be relevant the matrix A should be subdivided into groups of rows where the equations within each group are approximately disjoint. This is the case if the 6D projection surfaces do not overlap. An example of such a division is to group detector positions within one image with a constant z_{det}.

§ 7. Choice of basis functions

The issue of which basis functions to choose has been discussed in depth in the literature on inverse problems. Lewitt (1990) lists the following set of requirements, with specific address to reconstruction from line integral data.

(i) The basis functions are localized in space.
(ii) The Fourier transforms of the basis functions are effectively band limited.
(iii) The basis functions (and their Fourier transforms) have rotational symmetry in n dimensions.
(iv) Convenient formulae exist for calculation in n dimensions of the Fourier transform, the k-plane Radon transform and the gradient of the basis function.
(v) The basis functions can be constructed to have any finite number of derivatives.

The full argumentation behind this set is beyond the scope of this article. However, two points should be emphasized. Firstly, the rotational symmetry is important because it makes the projection on to the detector (for fixed 2θ and η) independent of ω, thereby facilitating the use of a look-up table. Secondly, the fact that the basis functions are band limited removes the 'salt-and-pepper' noise, which otherwise typically is removed in an *ad hoc* manner by smoothing, with a loss of resolution as result.

It is clear that the conventional cube-shaped voxels (in this case 6D cubes) essentially do not fulfil any of the requirements listed except the first. As an alternative, in connection with pole figure inversion, it has been suggested that a finite-element representation is used (Barton *et al.* 2002). Those fare better but fail, for example, on the rotational symmetry.

Addressing the list of requirements, Lewitt suggests the use of generalized (or modified) Kaiser–Bessel window functions. These are known in the literature as 'blobs'. They have the form

$$b_m(r) = \begin{cases} \dfrac{\left[1-(r/a)^2\right]^{m/2} I_m\left\{\alpha\left[1-(r/a)^2\right]^{1/2}\right\}}{I_m(\alpha)}, & 0 < r < a, \\ 0, & r > a. \end{cases} \tag{27}$$

Here r is the distance to the blob's centre, I_m denotes the modified Bessel function of order m and a is the radial dimension of the blob. The parameter m controls the continuity conditions at the blob boundary. For $m=0$ the blob is not continuous at the radius a. For $m > 0$ the blob is a continuous function with $m-1$ derivatives. The parameter α controls the blob's shape. The blobs fulfil all requirements.

The superiority of reconstructions based on blobs instead of voxels has been demonstrated in a number of cases (Matej *et al.* 1994). Hence, it is suggested that the 6D versions of blobs are used as the basis functions for the algebraic methods discussed in §§ 5 and 6. For explicit formulae for the Radon transform of the blobs, etc., see Lewitt (1990).

§ 8. Discussion

It is conventional in materials science to describe the microstructure in terms of a hierarchical set of elements (e.g. for a deformed metal, grains, subgrains, cell blocks and cells). Moreover, typically the smallest element can be associated with a negligible internal orientation spread. With this contribution it is argued that nevertheless it is often relevant to use a 6D description of the microstructure. The reason is the difficulty of 'bridging the length scales'. In other words, if one wishes to study a volume sufficiently large to be statistically representative of bulk behaviour, then one cannot at the same time characterize the material at the level of the smallest elements. Most notably, this schism between representability and spatial resolution is characteristic of experiments and simulations alike. Hence, the establishment of a mathematical framework for 6D microtexture analysis is believed also to be of relevance for modelling.

Focusing on experimental characterization of the microtexture, direct extensions of classical texture methods are found to be less relevant. The use of spherical harmonics (Roe 1965, Bunge 1969) is ruled out by truncation problems. A high angular resolution is needed, partly because the microtexture tends to consist of elements (grains, cell blocks or cells) with a small or vanishing mosaic spread, and

partly because spatial resolution and angular resolution are inherently linked. The 'direct methods' (Matthies 1979) are similar to those called algebraic here in the sense that a solution is sought in terms of a constrained set of linear equations. However, existing programs are confined to 3D systems with direct matrix inversion, and in most cases the use of voxels and a representation in terms of Eulerian angles.

Instead microtexture characterization is presented as an example of the more general class of 'inverse problems'. This has two potential benefits. Firstly, a large set of tools is available from the literature. Secondly, it simplifies the combination of microtexture characterization with mapping of other types of structural information. Specifically, the potential for combining XRD and X-ray absorption contrast tomography data is emphasized. Noticeably, both the hardware set-up and the reconstruction algorithms presented here are similar to those used in tomography. Hence, simultaneous or even combined reconstructions can be envisaged. This is of vital interest for many materials science studies involving multiphase materials or materials with voids and cracks (for a first study see Nielsen *et al.* (2000a)). Furthermore, based on tomography and suspended marker particles a universal method for characterizing the plastic strain in three dimensions has been demonstrated recently (Nielsen *et al.* 2002). Hence, by combining diffraction and absorption contrast the microstructure can be characterized in terms of both microtexture and plastic strain. A combined analysis could also provide a powerful additional constraint on microtexture data for multiphase materials in terms of the shape of the individual constituents.

A conclusion about which reconstruction method is better cannot be made without comparison of experimental data. Furthermore, the answer is likely to be different for the different cases lined up in § 3, owing to the large variation in geometry, size of reconstructed volume and sampling conditions. However, for a universal solution, the curved projection surfaces and the size of the problem point to an iterative algebraic solution, such as the ART algorithm with blobs as basis functions.

Algebraic methods have the additional advantage that they easily adapt to additional experimental constraints. As examples, the ART algorithm may be used to handle absorption and the introduction of a conical slit, see below. Likewise, the effect of a detector point-spread function was included in the previous work (Poulsen and Fu 2002).

The ultimate limit for reconstruction is the relation between the information content in H and in the experimental data. Here one may distinguish between two situations.

(i) The reconstruction is in principle possible but the number of projections provided is insufficient. In that connection it is worth mentioning that the number of projections can be increased by introducing rotations of the sample around additional axes and/or by varying the X-ray energy. (An additional contrast can be obtained by acquiring data for a set of sample temperatures. Assuming the microstructure to be frozen over the temperature range applied, the number of projections remain constant but the ratios between integrated intensities of various reflections are altered, owing to the change in Debye–Waller factors.)

(ii) Independent of the number of projections the complexity of H is too large to allow a reconstruction. In this case the only remedy is to decrease the size of

the illuminated volume. For thick specimens, typically the best way to do this is to define an intrinsic 'volume of interest' by inserting a conical slit between the sample and the detector (Nielsen *et al.* 2000b).

Two further limitations of the methodology are worth mentioning. The first arises in connection with deformed samples, where the sample–detector distance must be rather small to avoid broadening due to strain. As an example, the *standard* 3DXRD set-up, as defined in § 2, is able to accommodate a broadening of up to $\Delta d/d = 7 \times 10^{-3}$.

The second limitation relates to the central assumption on kinematic scattering, as expressed in the linear relationships (21) and (23). For neutrons and hard X-rays alike, extinction in polycrystalline specimens is generally negligible and effects due to absorption can be calculated to a high degree of accuracy and corrected for within the ART methodology. For electrons and X-rays of lower energy this is not the case. Possible extensions of the 6D formalism to include dynamic scattering or secondary extinction effects are outside the scope of this presentation.

§ 9. Conclusions

A universal 6D framework has been presented for microtexture analysis. It is of relevance for both experimental characterization and modelling, whenever the spatial resolution is not sufficient to characterize the smallest individual elements in the microstructure. This is often the case when studies are required to be statistically representative of bulk behaviour.

The focus in this presentation has been on reconstructions from tomographic type measurements. From a geometric analysis the following conclusions emerge.

(1) The representation of the crystallographic orientation by Rodrigues parameters is essential, as the straight projection lines and the lack of a singularity at the origin vastly simplifies the analysis. For a number of cases the reconstruction space even become Euclidean.
(2) The projection surface can be described by a combination of conical sections.
(3) The facts that the reconstruction space in the general case is curved and the sampling not on a regular grid imply that transform methods are less suited to reconstruction.
(4) The iterative ART algorithm is ideal. Full use is made of simplifications in geometry or additional constraints. The algorithm can be scaled up and it easily adapts to additional experimental constraints. Furthermore it can be extended to handle combined diffraction and absorption contrast tomography data.
(5) A number of concepts well known to the tomography community with benefit can be introduced in the context of microtexture. These include blobs, footprints, group-iterative solutions and the k-plane Radon transform.

Specifically, for 3DXRD the suggested reconstruction algorithms overcome the limitation given by spot overlap. Hence, the mathematical framework is provided for 3DXRD to become a universal method for characterizing the dynamics of the microstructural elements within a macroscopic volume.

Acknowledgements

I thank S.R. Jensen, A. Morawiec and G.T. Herman as well as my colleagues at Risø, W. Pantleon, S. Schmidt, X. Fu and D. Juul Jensen, for scientific discussions. This work was supported by the Danish National Research Foundation through the Center for Fundamental Research: Metal Structures in Four Dimensions.

References

Barton, N. R., Boyce, D. E., and Dawson, P. R., 2002, *Textures Microstruct*., **35**, 113.

Bunge, H. J., 1969, *Matematische Methoden der Texturanalyse* (Berlin: Akademie).

Cormack, A. M., 1981, *Proc. Am. Math. Soc*., **83**, 325.

Deans, S. R., 1983, *The Radon Transform and Some of its Applications* (New York: Wiley).

Eggermont, P. P. B., Herman, G. T., and Lent, A., 1981, *Linear Algebra Applic*., **40**, 37.

Frank, F. C., 1988, *Metall. Trans*. A, **19**, 403.

Gordon, R., Bender, R., and Herman, G. T., 1970, *J. theor. Biol*., **29**, 471.

Helgason, S., 1980, *The Radon Transform. Progress in Mathematics*, Vol. 5 (Boston: Birkhauser).

Herman, G. T., 2002, *Encyclopedia of Imaging Science and Technology*, Vol. 2, edited by J. P. Hornak (New York: Wiley), pp. 1404–1411, and references therein.

Herman, G. T., and Meyer, L. B., 1993, *IEEE Trans. Med. Imaging*, **12**, 606.

Jensen, S. R., 2003, Preprint.

Kaczmarz, S., 1937, *Bull. Inst. Acad. Pol. Sci. Lett*. A, **35**, 355.

Kak, A. C., and Slaney, M., 1988, *Principles of Computerized Tomographic Imaging* (New York: IEEE).

Kumar, A., and Dawson, P. R., 2000, *Acta mater*., **48**, 2719.

Lauridsen, E. M., Juul Jensen, D., Poulsen, H. F., and Lienert, U., 2000, *Scripta mater*., **43**, 561.

Lauridsen, E. M., Schmidt, S., Poulsen, H. F., and Suter, R. M., 2001, *J. appl. Crystallogr*., **34**, 744.

Lee, D. N. (editor), 2002, *Proceedings of the 13th International Conference on the Texture of Materials*, Seoul, South Korea, 26–30 August 2002.

Lewitt, R. M., 1990, *J. opt. Soc. Am*. A, **7**, 1834.

Matej, S., Herman, G. T., Narayan, T. K., Furuie, S. S., Lewitt, R. M., and Kinahan, P. E., 1994, *Phys. Med. Biol*., **39**, 355.

Matej, S., and Lewitt, R. M., 1996, *IEEE Trans. Med. Imaging*, **15**, 68.

Matthies, S., 1979, *Phys. Stat. sol*. (b), **92**, K135.

Minerbo, G., 1979, *Comput. Graph Image Processing*, **10**, 48.

Morawiec, A., and Field, D. P., 1996, *Phil. Mag*. A, **73**, 1113.

Morawiec, A., and Pospiech, J., 1989, *Textures Microstruct*., **10**, 243.

Natterer, F., 1986, *The Mathematics of Computerised Tomography* (Chichester, West Sussex: Wiley).

Neumann, P., 1991, *Textures Microstruct*., **14–18**, 53.

Nielsen, S. F., Ludwig, W., Bellet, D., Lauridsen, E. M., Poulsen, H. F., and Juul Jensen, D., 2000a, *Proceedings of the 21st Risø International Symposium on Materials Science*, edited by N. Hansen, X. Huang, D. Juul Jensen, E. M. Lauridsen, T. Leffers, W. Pantleon, T. J. Sabin and J. A. Wert (Risø, Roskilde: Risø National Laboratory), pp. 473–478.

Nielsen, S. F., Poulsen, H. F., Beckmann, F., Thorning, C., and Wert, J. A., 2002, *Acta mater*., **51**, 2407.

Nielsen, S. F., Wolf, A., Poulsen, H. F., Ohler, M., Lienert, U., and Owen, R. A., 2000b, *J. Synchrotron Radiat*., **7**, 103.

Poulsen, H. F., and Fu., X., 2003, *J. appl. Crystallogr*., in press.

Poulsen, H. F., Garbe, S., Lorentzen, T., Juul Jensen, D., Poulsen, F. W., Andersen, N. H., Frello, T., Feidenhans'l, R., and Graafsma, H., 1997, *J. Synchrotron Radiat*. **4**, 147.

Poulsen, H. F., and Juul Jensen, D., 2002, *Mater. Sci. Forum*, **408–412**, 49.

Poulsen, H. F., Nielsen, S. F., Lauridsen, E. M., Schmidt, S., Suter, R. M., Lienert, U., Margulies, L., Lorentzen, T., and Juul Jensen, D., 2001, *J. appl. Crystallogr.*, **34**, 751.

Poulsen, H. F., and Schmidt, S., 2002, *J. appl. Crystallogr.*, **36**, 319.

Roe, R. J., 1965, *J. appl. Phys.*, **36**, 2024.

Savyolova, T. I., 1994, *Mater. Sci. Forum*, **157–162**, 419.

Schmidt, S., Poulsen, H. F., and Vaughan, G. B. M., 2002, *J. appl. Crystallogr.*, **36**, 326.

Tanabe, K., 1971, *Numer. Math.*, **17**, 203.

Weiland, H., Fridy, J. M., and Llewellyn, E., 2002, *Mater. Sci. Forum*, **408–412**, 101.

A7

Available online at www.sciencedirect.com
SCIENCE DIRECT®
Pergamon
Acta Materialia 51 (2003) 2407–2415
Acta MATERIALIA
www.actamat-journals.com

Measurements of plastic displacement gradient components in three dimensions using marker particles and synchrotron X-ray absorption microtomography

S.F. Nielsen [a,*], H.F. Poulsen [a], F. Beckmann [b], C. Thorning [a], J.A. Wert [a]

[a] *Center for Fundamental Research: Metal Structures in Four Dimensions, Risø National Laboratory, 4000 Roskilde, Denmark*
[b] *Hamburger Synchrotronstrahlungslabor HASYLAB at Deutsches Elektronen-Synchrotron DESY, Notkestrasse 85, 22607 Hamburg, Germany*

Received 6 September 2002; received in revised form 22 January 2003; accepted 23 January 2003

Abstract

A universal method is presented for characterising the three-dimensional (3D) plastic displacement gradient field in bulk materials that contain particles or voids observable by X-ray tomography. Millimetre sized samples are investigated by absorption contrast microtomography using high intensity X-rays from a synchrotron source. The positions of dispersed marker particles are determined as a function of imposed strain. The particle diameter can be in the micrometre range, and the volume fraction can be less than 1%. The method is demonstrated by evaluation of compression deformation of a cylindrical Al specimen containing W marker particles. By interpolating the displacement gradient components determined at each particle on a $30 \times 30 \times 30$ μm^3 grid, 3D maps of the displacement gradient components are obtained with a resolution of 10^{-2} in each component. Limitations of the method are discussed, and the potential for application in materials science is outlined.

Keywords: Synchrotron radiation; Plastic deformation; X-ray tomography; Image analysis; Aluminium

1. Introduction

The local plastic strain is likely to deviate from the imposed (macroscopic) plastic strain in materials that contain voids or cracks, in materials such as composites that contain second phases with elastic or plastic properties unlike those of the matrix, and in graded materials with gradients of elastic or plastic properties. Even in single phase polycrystalline metal aggregates the elastic and plastic properties of the individual grains depend on crystal orientation, with the result that the plastic strain state within a grain deviates from the externally imposed strain state. At external plastic strains larger than 10 or 20%, the original grains subdivide into smaller crystal orientation domains, a process that reflects the variation of plastic strain within an original grain.

Methods to assess local plastic strains primarily

* Corresponding author. Tel.: + 454677-5762; fax: + 454677-5758.
E-mail address: soeren.faester.nielsen@risoe.dk (S.F. Nielsen).

1359-6454/03/$30.00 © 2003 Published by Elsevier Science Ltd on behalf of Acta Materialia Inc.
doi:10.1016/S1359-6454(03)00053-3

focus on surface characterisation. Scratches, etched patterns or grids deposited on the surface of samples have been used to measure grain boundary shear and to measure the relative creep rates of the deforming phases in multiphase materials [1,2]. A recent version of such techniques is the grid distortion technique described by Fisher et al. involving deposition of a regular array of marker particles on a surface and measurement by optical diffraction [3–6]. In addition, irregularly distributed etch pits have been used to assess plastic strain distributions within grains on the surface of polycrystalline samples [7]. The spatial resolution of these methods depends on the marker grid scale, it is on the micrometre scale when photolithography methods are used for grid deposition. Photogrammetric methods can be adapted to the problem of assessing surface topology [8,9].

Laser speckle pattern techniques have been developed for the measurement of local elastic and plastic strains [10]. Although the strain resolution is excellent, the spatial resolution of current laser speckle techniques is of the order of 0.1 mm [11]. These techniques have been applied to strain mapping during the deformation of polycrystalline metals and ceramics as well as biological materials.

Unfortunately, the extension of surface strain mapping methods to strain fields in three dimensions has been limited. Wire or grid markers have been used for studies of deformation processes but the scale of the internal grids is usually coarser than 0.1 mm, insufficient to detect localised phenomena [12,13]. In addition, sample preparation usually involves welding or brazing, which can alter the properties of the material in the vicinity of the markers. The perturbing influences of the sample preparation method and the lack of spatial resolution limit the applicability of such three-dimensional (3D) strain mapping methods.

Recently, high energy synchrotron X-ray diffraction has been introduced as a probe for examining the local crystal orientation of individual grains embedded in a polycrystal [14]. The hard X-rays can penetrate millimetres to centimetres of material. Under favourable conditions a simultaneous description can be given of the position, volume, crystal orientation and elastic strain of up to several hundred grains [15–18]. Furthermore, for coarse-grained materials, the topology of the grain boundaries can be mapped [18]. This diffraction method, known as 3DXRD, can also be used to probe crystal rotation in individual grains during straining [14]. However, crystal rotation is not a direct manifestation of plastic strain; it is a manifestation of the coupling between microscopic shear deformation mechanisms and constraints imposed either on the sample or on an individual grain by its neighbours. Furthermore, the 3DXRD method is inherently limited to crystalline materials and, at present, is limited to modest deformations, up to about 20%.

The objective of this article is to present a universal method for mapping the plastic displacement gradient tensor in bulk materials that contain particles or voids observable by X-ray tomography, with a spatial resolution in the micrometre range. X-rays from a synchrotron source are used as a probe and imaging is performed by means of X-ray absorption contrast microtomography. To enable the microtomographic measurements, marker particles with strong absorption contrast are added to the matrix prior to deformation. The particle trajectories are identified as functions of imposed strain and the local plastic deformation gradient tensor is revealed by subsequent analyses. The method is verified by a study of a compacted Al powder specimen in which W particles have been added as markers.

2. Sample preparation and deformation conditions

The sample was prepared using Al powder with a mean particle diameter of 6.5 μm. The marker particles were W powder of an initially coarser size, sieved so that the largest remaining particles were about 10 μm diameter. The Al and W powders were blended such that the volume fraction of W was about 1%. The powder blend was cold compacted at 30 MPa pressure in a cylindrical double acting die with a diameter of 24 mm and was subsequently hot compressed at 60 MPa pressure in a blind die at 825 K for 5 min. Prior experiments demonstrated that these processing conditions produce compacted aluminium cylinders with a den-

sity equal to the accepted value for aluminium. Thus, the initial sample is assumed to be free of voids, within the accuracy of the density measurements. This resulted in a powder compact with a relatively uniform dispersion of W particles and virtually no voids, as confirmed by optical metallography and electron backscatter imaging. The grain size of the Al remains at about 10 μm during processing, as a consequence of the Al_2O_3 films originally present on the powder particle surfaces and incorporated into the compacted alloy. The small size of the oxide particles and the slight difference in attenuation between Al_2O_3 and Al make the oxide invisible to the present microtomographic method. The dispersion of W particles in the consolidated alloy was evaluated using SEM backscatter imaging; a representative image is shown in Fig. 1. The W particles are revealed as bright areas and the dark Al_2O_3 particle films outline the original Al powder particles. An image analysis confirmed that the average size of the W particles is about 10 μm and that they are equally distributed in the observed section.

A small cylinder with dimensions 1 mm diameter and 2 mm height was machined from the compacted billet. Projected absorption images of this sample were obtained in the unstrained condition and after uniaxial compression of 2.7%, 6.2% and 9.5% (engineering strain). The compression faces were not lubricated.

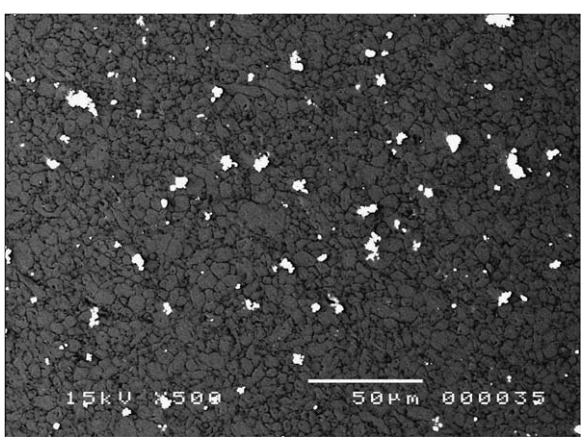

Fig. 1. SEM backscatter image showing W particles in the Al matrix after hot compression. The W particles are white and the Al particles are grey.

3. Measurement technique

The principles of X-ray tomography were developed in the late 1970s [19,20]. The method is based on measuring a set of radiograms while rotating the sample around an axis perpendicular to the beam direction. The tomographic reconstruction yields a 3D representation of the linear attenuation coefficient μ for every volume element inside the sample. The high intensity of synchrotron X-ray radiation together with very low beam divergence facilitates microtomographic imaging since reconstruction artefacts are reduced substantially compared to tomography based on conventional laboratory X-ray sources. Another main advantage is the availability of monochromatic radiation, since tomography with a polychromatic beam leads to artefacts in the reconstructed volumes. As a result, synchrotron-radiation-based microtomography routinely generates maps with a spatial resolution of 1–2 μm [21,22].

The present experiment was performed at the dedicated microtomography instrument at beamline BW2 at HASYLAB [21]. The energy provided by a double-bounce monochromator was 24 keV with an energy bandwidth of 10^{-3}. Images were collected at 0.25° intervals over a total rotation range of 180°; an image with the sample moved out of the beam was acquired after each degree of rotation to correct for spatial intensity fluctuations during the tomography run. Typical exposure times for the CCD camera were 10 s. The effective pixel sizes in the reconstructed images and field of view were 1.5 μm and 1.5×1.5 mm^2, respectively. The achieved spatial resolution in the reconstructed volumes was 2.8 μm in all three dimensions.

4. Results

Reconstruction was performed slice by slice using the standard Fourier back-projection algorithm [19]. The slices were then merged to produce a map of the total $1 \times 1 \times 1.5$ mm^3 volume. Typical results are shown in Figs. 2 and 3, which reveal that the W particles are approximately uniformly distributed apart from a small region near the outer surface of the cylinder at the bottom of both figures

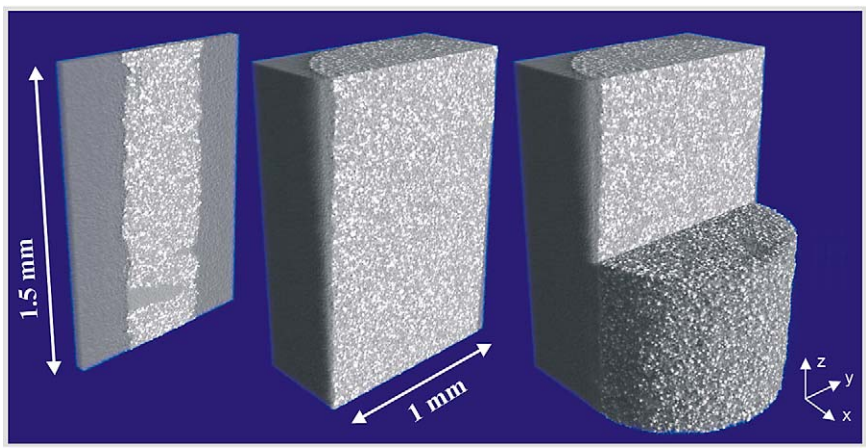

Fig. 2. Visualisation of the AlW sample after about 10% compression. Vertical slices and 3D representation of the data set are shown. The W particles are white, the cylindrical Al sample is light grey, the reconstructed air around the sample is dark grey and the background is black.

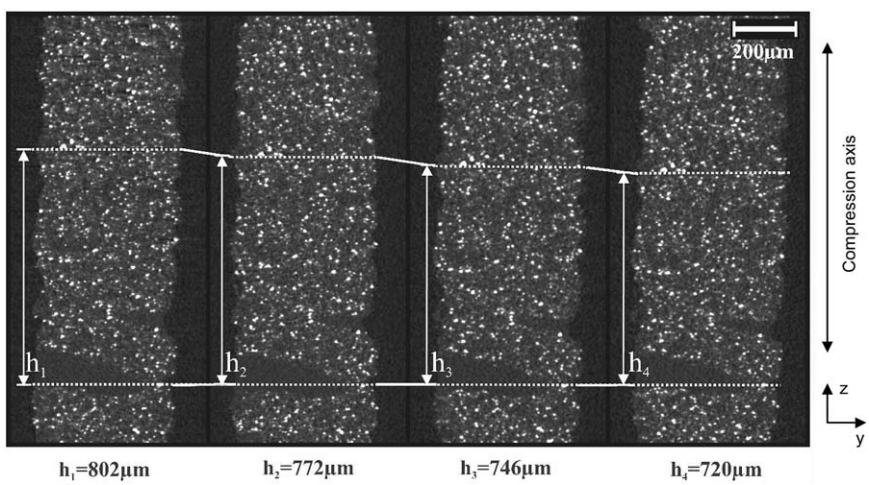

Fig. 3. Vertical slices through the 3D-reconstruction volumes of four tomographical scans of the Al–W sample at 0%, 2.7%, 6.2% and 9.5% deformation, respectively. Corresponding heights in the different slices indicate the compression of the sample.

where no W particles were blended into the original powder billet.

Equivalent cross-sections through the tomographic reconstruction for different imposed strain levels are illustrated in Fig. 3. The lines drawn on each image are based on the position of specific particles. The difference in spacing of the lines reveals compression strains of 3.2, 6.9 and 10.2% for this interval of the gauge length, close to the macroscopic compression strain increments imposed on the cylindrical sample. Detailed inspection of Fig. 3 reveals that particles change diameter or disappear from the section, as a function of strain, indicating that particles move in and out of the selected plane during the course of deformation.

Since the present experiment tracks particle displacement as a function of imposed strain, the local displacement gradient tensor $\boldsymbol{e}$ can be determined from the results. If desired, the displacement gradient tensor can be separated into local strain $\boldsymbol{\varepsilon}$ and rigid body rotation tensors $\boldsymbol{\omega}$ in the standard way.

Although the sample as a whole does not experience rigid body rotation during plastic deformation, local rigid body rotations may develop as a consequence of the inhomogeneity of plastic deformation. If the results are presented as local plastic strain components, the portion of inhomogeneous deformation reflected as local rigid body rotation is lost. Thus, in the remainder of the present article, all results are expressed as displacement gradient tensor components. To extract 3D maps of the displacement gradient tensor from the tomographic images, an analysis procedure has been implemented, as follows.

- Particles were identified in each 3D tomogram as isosurfaces, using a fixed intensity threshold.
- The intensity weighted centre of mass and the volume of each particle were determined. Since the centre of mass is determined from the tomograms by an averaging process over all the pixels in the vicinity of the particle location, this allows the intensity weighted centre of mass to be identified with a resolution of order 0.3 μm.
- An initial set of a few *matching particles* (minimum three) was identified manually in the particle fields at successive imposed strain levels by comparing the intensity weighted centre of mass and the volume of prominent particles.
- Due to the ex situ deformation, matching particles in different data sets were used to align the data sets with respect to each other. The alignment includes a rotation and a translation of the particle fields. The alignment was optimised by minimising the sum of the distances between matching particles.
- The full set of matching particles was identified automatically by selecting those particles that had moved less than the average distance between neighbouring particles during one imposed strain increment.

Alignment of the data sets for different imposed strain levels and the identification of matching particles between different tomograms were conducted as iterative processes. A volume of 450 × 450 × 450 μm^3 containing ~5000 particles was analysed, and a total of 2544 matching particles were identified and used in the alignment process. The trajectories of matching particles constitute joined vector segments of particle displacement. Some errors happened in the identification of particles. This was observed in a few cases where a smooth trajectory changed direction sharply in one imposed strain interval. The shape of these particles was inspected to determine whether this was due to truly discontinuous displacements or errors in the particle identification. In case of the latter, the particle was rejected from further evaluation. The displacement field of the remaining particles between the initial and the final imposed strain levels is plotted in Fig. 4.

The components of the displacement gradient tensor are defined as

$$e_{ij} = \left(\frac{\partial u_i}{\partial x_j}\right) \quad \forall\, i,j, \tag{1}$$

where u_i are displacement components and x_j are position components. The tensor $\boldsymbol{e}$ is not the strain tensor, since displacements may reflect rigid body rotation, which affects the derivatives in Eq. (1).

The displacement gradient tensor for each particle was obtained by a least square fit to the relative displacements of the eight nearest particles. In this way, a local displacement gradient tensor is identified at each particle location. The local $\boldsymbol{e}$ components can be represented as distributions;

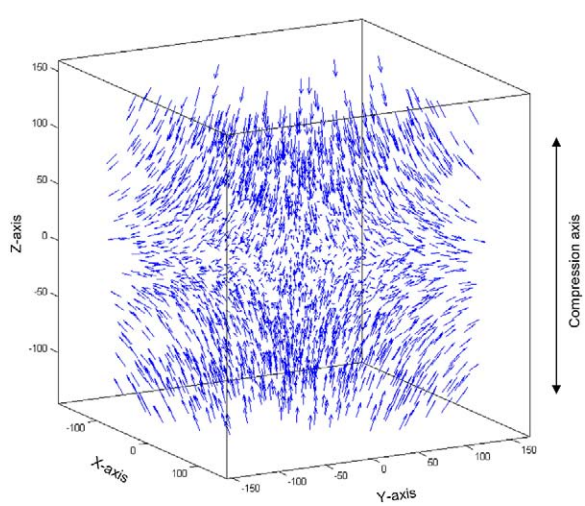

Fig. 4. 3D map of the particle displacement field for deformation of 0–9.5%. The numbers on the axes are in units of pixels of 1.5 μm.

the e_{11} and e_{12} components for all matching particles in the initial and final data sets are plotted as histograms in Fig. 5.

The trace of the displacement gradient tensor should be zero for all the particles as a result of volume conservation during the plastic deformation. The distribution of the calculated quantity $(e_{11} + e_{22} + e_{33})/3$ has an FWHM of 0.020 (see Fig. 5). This constitutes an upper limit on the instrumental resolution and implies that the technique is capable of determining shifts in the particle positions of $\pm$ 0.3 μm over a distance of 30 μm. The distributions of each of the displacement gradient components are broader than 0.020, and their widths can therefore be seen as a convolution of an instrumental effect and a "real" fluctuation. This indicates real plastic displacement gradient fluctuations of the order of 0.01–0.02 for the present experimental conditions. To our knowledge, this is the first time such numbers have been measured.

To visualise the displacement gradient tensor in three dimensions, each ***e***-component was interpolated on a regular (x, y, z) grid with an internode distance of 30 μm and plotted layer by layer (see Figs. 6 and 7). The interpolation was done simply by averaging over all markers within a radius of 15 μm. The interpolated intensity in each node is symbolised by a greyscale. The greyscale ramps from -0.15 (white) to $+0.15$ (black) around the average value of the component. At some locations there are no marker particles within 15 μm from the grid point, and in these cases, the voxel is associated with a white dot on a black background.

The displacement gradient component maps in Figs. 6 and 7 reveal quite homogeneous deformation of the analysed volume. This is as expected for a powder metallurgical sample with aluminium grains of approximately the same dimension as the marker particles. No dependence of the local crystallographic orientation can be expected when the aluminium grains do not contain internal marker particles as in the present case. Nevertheless, some heterogeneities in the straining are observed. There do exist clusters of voxels that strain differently than the rest (e.g. see the bottom three images in Fig. 6 near $x = 150$ and $z = 90$).

5. Discussion

Prior attempts to characterise the particle distribution in 2024 aluminium using tomography have been reported by Quan et al. [23]. In addition, the effect of strain on the void formation process in Al/TiN metal matrix composite samples has been assessed by Crostack et al. [24] using X-ray microtomography. In their study, the appearance of voids in the vicinity of particles as a function of strain was evaluated, but a quantitative analysis of the observations has not been reported. In contrast to both studies, in the present case particle motion as a function of imposed strain has been measured using X-ray microtomography, and an analysis system for tracking the motion of individual particles and transforming that information into local deformation gradient maps has been developed.

We identify the following limitations of the method:

1. The marker size is limited by the tomographic method, mainly by the effective pixel size of

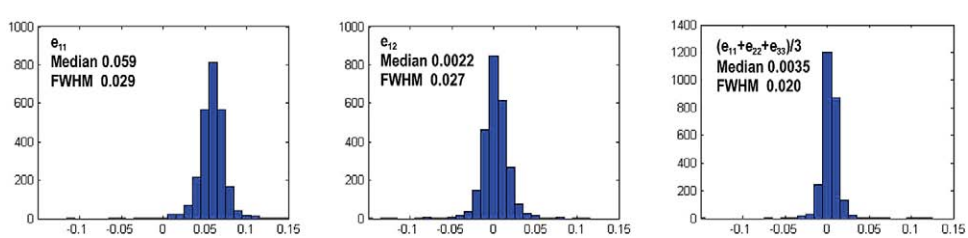

Fig. 5. The displacement gradient component e_{11} and e_{12} for all the matching particles. The FWHM of the quantity $(e_{11} + e_{22} + e_{33})/3$ constitutes an upper limit on the instrumental resolution, as the trace of the displacement gradient tensor should be zero due to volume conservation during deformation.

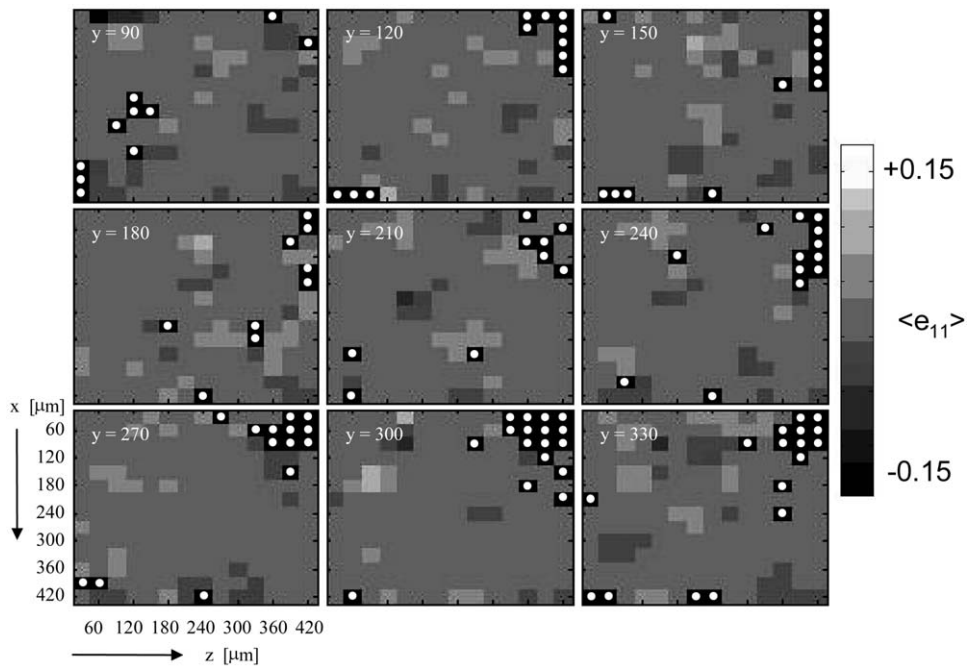

Fig. 6. Intensity maps representing the 3D displacement gradient component e_{11}. The black voxels with the white dots indicate that no particles are present within a radius of 15 μm from the grid node, and no value is therefore assigned to the voxel during the interpolation on a regular grid.

present-day detectors. At best, marker particles of diameter down to 1 μm can be detected.

2. For a given average marker particle size, the volume fraction of the markers and their average spacing are inversely related. Hence, a compromise is required between enhancing the spatial resolution of the displacement gradient component maps and the perturbing effect of the marker particles on the plastic deformation processes.
3. The tomographic method can, as a rule of thumb, provide a 1:1000 ratio between spatial resolution and specimen size. For large marker particles, the limiting specimen dimension is determined by penetration of the X-rays, which is a strong function of the X-ray energy. The ultimate limit for X-rays in the range of 100 keV is of order 40 mm for Al and 4 mm for Fe.
4. To be able to identify the same marker particle at each imposed strain level, the imposed strain increment cannot be arbitrarily large. However, it can be substantially larger than the increment used here, provided that the process of matching particles in different tomograms is based on both particle position and particle size. Particle morphology may also contribute to the identification process in the case of nonequiaxed particles.

The technique described in this article uses marker particles to detect material flow. In this context, it is necessary to consider whether the particles perturb the plastic flow process. In the Al–W alloy used to demonstrate the technique, the W particles are harder than the Al matrix. When a metallic alloy containing nondeforming particles is plastically strained, strain incompatibility generates high local stresses that induce plastic strain gradients in the matrix near each particle [25]. At low macroscopic strain such plastic relaxation leads to the formation of dislocation loops in the vicinity of each particle, the geometry of which depends on the particle diameter and macroscopic strain. At higher strains, the supplementary dislo-

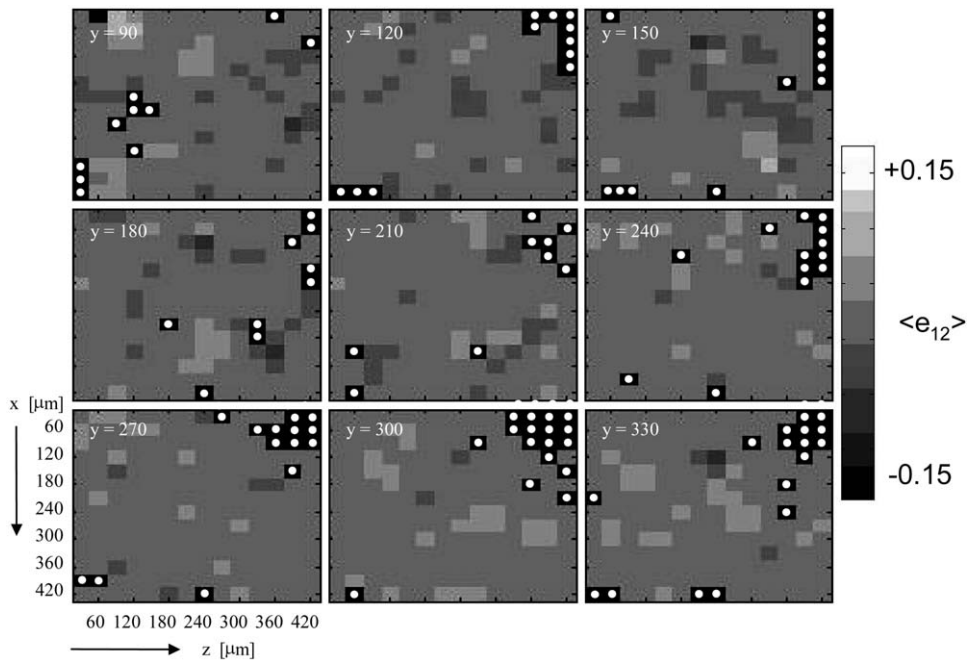

Fig. 7. Intensity maps representing the 3D displacement gradient component e_{12}. The black voxels with the white dots indicate that no particles are present within a radius of 15 μm from the grid node, and no value is therefore assigned to the voxel during the interpolation on a regular grid.

cations resulting from plastic relaxation evolve into a local dislocation cell structure containing lattice orientations distinct from those present in the matrix texture. This local deformation zone extends into the surrounding matrix about one particle diameter from the particle surface. However, since the present technique uses particle motion to detect displacement gradients on the scale of particle spacing, it is insensitive to the formation of strain gradients local to individual W marker particles.

A second consideration involves the possibility that the marker particles experience displacements different from those in the Al matrix. Plastic flow constitutes a nonuniform displacement field of zero divergence experienced by a material body. Since no additional fields act differently on the particles and the nearby matrix, the W particle motion is expected to faithfully represent the displacements that occur as the material body is deformed. Future work will describe measurements of the effect of particle volume fraction on the measured displacement gradients as a way to experimentally evaluate possible effects of particles on the displacement field. In addition, we note that while the Al–W system was selected to demonstrate the potential of the technique, future studies will examine additional alloy systems as well as variations of grain size and other matrix characteristics.

Apart from these restrictions, the method seems applicable to a broad range of materials science problems. Hence, most conventional deformation processing and sample straining methods (rolling, extrusion, drawing, tension, torsion, etc.) can be studied, with the deformation tool placed either on or near the synchrotron X-ray source. The method is compatible with high levels of deformation as long as a suitable number of intermediate strain increments are used and the marker particles do not fragment. Furthermore, it is foreseeable that this method can be used for studies of deformation of multiphase materials, amorphous metals, and phase transformations involving localised shear.

6. Conclusions

A universal method has been formulated for characterising the 3D plastic displacement gradient component field in bulk materials that contain particles or voids observable by X-ray tomography. The method is based on X-ray absorption microtomography as a means of identifying marker particle position at successive imposed strain levels. The method has been demonstrated using an Al alloy containing W particles. The displacement gradient component resolution is 10^{-2} while the spatial resolution depends on particle spacing, in the present case 30 μm.

Acknowledgements

We thank P.B. Olesen and P. Nielsen for technical support and J. Homeyer, W. Drube and H. Schulte-Schrepping for help with the tomographic experiment. We acknowledge the Danish National Research Foundation for supporting the Center for Fundamental Research: Metal Structures in Four Dimensions. Additional support was provided by the Danish Natural Science Research Council (via Dansync).

References

[1] Bartholomeusz MF, Wert JA. Mater Charact 1994;33:377.
[2] Thorsen PA, Bilde-Sørensen JB. Deposition of material at grain boundaries in tension interpreted in terms of diffusional creep. Mater Sci Eng A 1999;265:140–5.
[3] Liu YL, Fischer G. Scr Mater 1997;36:1187.
[4] Berka L, Sova M, Fischer G. Exp Tech 1998;22:22.
[5] Soppa E, Schmauder S, Fischer G, Thesing J, Ritter R. Comput Mater Sci 1999;16:323.
[6] Crostack HA, Fischer G, Soppa E, Schmauder S, Liu YL. J Microsc Oxford 2001;201:171.
[7] Tatschl A, Kolednik O. Mater Sci. Eng. A 2003;339:265.
[8] Wert JA, Roberson WM. Metallography 1982;15:367.
[9] Marschall HU, Danzer R, Pippan R. J Am Ceram Soc 2000;83:223.
[10] Yamaguchi I. J Phys E Sci Instrum 1981;14:1270.
[11] Sjodahl M. Electronic speckle photography: increased accuracy by nonintegral pixel shifting. Appl Opt OT 1994;33:6667.
[12] Tarnovskii IYa, Pozdeyev AA, Lyashkov VB. Deformation of metals during rolling. Oxford: Pergamon Press, 1965.
[13] Wert JA. Acta Mater 2002;50:3125.
[14] Margulies L, Winther G, Poulsen HF. Science 2001;291:2392.
[15] Poulsen HF, Garbe S, Lorentzen T, Juul Jensen D, Poulsen FW, Andersen NH, Frello T, Feidenhans'l R, Graafsma H. J Synchrotron Rad 1997;4:147.
[16] Juul Jensen D, Kvick Å, Lauridsen EM, Lienert U, Margulies L, Nielsen SF, Poulsen HF. Mater Res Soc Symp Proc 2000;590:227.
[17] Lauridsen EM, Schmidt S, Suter RM, Poulsen HF. J Appl Crystallogr 2001;34:744.
[18] Poulsen HF, Nielsen SF, Lauridsen EM, Schmidt S, Suter RM, Lienert U, Margulies L, Lorentzen T, Juul Jensen D. J Appl Crystallogr 2001;34:751.
[19] Kak AC, Slaney M. Principles of computerized tomographic imaging. New York: IEEE Press, 1988.
[20] Hounsfield Gen. Computed medical imaging. Nobel lecture, Dec. 8, 1979. J Comput Assist Tomogr 1979;4(5):665–74.
[21] Beckmann F, Bonse U, Biermann T. In: Developments in X-ray Tomography II, Denver, CO, 1999 July. Proceedings of the SPIE Conference, vol. 3772. p. 179–87.
[22] Baruchel J, Cloetens P, Hartwig J, Ludwig W, Mancini L, Pernot P, Schlenker MJ. Synchrotron Rad 2000;7:196.
[23] Quan G, Beckmann F, Lippmann T, Heerens J, Brocks W. In: HASYLAB Annual Report; 2001.
[24] Crostack H-A, Nellesen J, Beckmann F, Fischer G, Czayka W. In: HASYLAB Annual Report; 2001.
[25] Humphreys FJ. In: Loretto MH, editor. Dislocations and properties of real materials. London: Institute of Metals, 1985. p. 175–204.

A8

reference potential as well as slight decomposition (as indicated by a small amount of black precipitate collecting on the electrodes after several hours). The ~2-min rise and decay times of the IR absorption are due to cell geometry and the slow mobility of the nanocrystals. Larger nanocrystals exhibit slower time constants.

Applying a potential to a solution of CdSe nanocrystals also induces quenching of the band-edge photoluminescence. Whether delocalized in a quantum-confined state or localized in a surface state, charges can cause marked quenching of the photoluminescence in semiconductor nanocrystals (*16*). The same effect is observed in the electrochemical electron injection. The "on/off" behavior of the photoluminescence properties of CdSe/ZnS core/shell nanocrystals is seen (Fig. 4A) as the electrochemical potential is varied (set at either 0 or −1.5 V). The photoluminescence spectra of CdSe/ZnS (Fig. 4B) correspond to points (i), (ii), and (iii) in Fig. 4A. The photographs of the sample under UV illumination (Fig. 4C) show that photoluminescence quenching is readily observed by eye and occurs mostly near the working-electrode disk. The spatial selectivity of photoluminescence quenching may be desirable in display applications.

At −1.5 V, the photoluminescence quenches to ~40% of the initial value in 1 min and recovers completely in ~60 min after the potential is reset to 0 V. The slower photoluminescence recovery rate with respect to the IR absorption decay may be attributed to the effects of surface charges; that is, the IR absorption depends only on the electrons in the 1S state, whereas the photoluminescence can be strongly quenched by charges in the surface band-gap states. For the photoluminescence to recover to its maximum, electrons in both the 1S state and surface states need to be removed. Improvements in surface passivation, experimenting with different electrolytes and different materials, and investigating thin solid-film electrodes are likely to lead to technologically practical and efficient electrochemical switching of the optical properties of colloidal nanocrystal quantum dots.

References and Notes

1. M. Nirmal, L. E. Brus, *Acc. Chem. Res.* **32**, 407 (1999).
2. A. P. Alivisatos, *Science* **271**, 933 (1996).
3. C. B. Murray, C. R. Kagan, M. G. Bawendi, *Science* **270**, 1335 (1995).
4. M. A. Kastner, *Phys. Today*, 24 (1993).
5. R. C. Ashoori, *Nature* **379**, 413 (1996).
6. V. Colvin, M. Schlamp, A. P. Alivisatos, *Nature* **370**, 354 (1994).
7. B. O. Dabbousi, M. G. Bawendi, O. Onitsuka, M. F. Rubner, *Appl. Phys. Lett.* **66**, 1316 (1995).
8. B. O'Regan, M. Grätzel, *Nature* **353**, 737 (1991).
9. T. Yamase, *Chem. Rev.* **98**, 307 (1998).
10. C. G. Granqvist, *Sol. Energ. Mat. Sol. Cells* **60**, 201 (2000).
11. U. zum Felde, M. Haase, H. Weller, *J. Phys. Chem. B* **104**, 9388 (2000).
12. C. B. Murray, D. J. Norris, M. G. Bawendi, *J. Am. Chem. Soc.* **115**, 8706 (1993).
13. M. A. Hines, P. Guyot-Sionnest, *J. Phys. Chem. B* **102**, 3655 (1998).
14. O. I. Micic *et al.*, *J. Phys. Chem.* **98**, 4966 (1994).
15. M. Shim, P. Guyot-Sionnest, *Nature* **407**, 981 (2000).
16. M. Shim, C. Wang, P. Guyot-Sionnest, *J. Phys. Chem. B*, in press.
17. P. Hoyer, H. Weller, *Chem. Phys. Lett.* **221**, 379 (1994).
18. M. A. Hines, P. Guyot-Sionnest, *J. Phys. Chem.* **100**, 468 (1996).
19. R. E. Wittrig, C. P. Kubiak, *J. Electroanal. Chem.* **393**, 75 (1995).
20. We have not yet observed hole injection most likely because of other oxidative processes that prevent it. Applying a positive potential (0 to +3 V) to the samples did not cause changes in the visible absorption or photoluminescence properties of the nanocrystals. Successful hole injection will require an optimization of solvent and electrolyte combination as well as nanocrystals that are stable after oxidation.
21. N. M. Dimitrijevic, D. Savic, O. I. Micic, A. J. Nozik, *J. Chem. Phys.* **88**, 4278 (1984).
22. B. Enright, G. Redmond, D. Fitzmaurice, *J. Phys. Chem.* **98**, 6195 (1994).
23. The confinement energy, $E_x - E_g$, can be approximated as $\hbar^2/2m^*R^2$ and the charging energy, E_c, as $e^2/2\varepsilon R$. E_x is the first exciton transition energy, E_g is the bulk band gap, R is the radius of the nanocrystals, m^* is the effective mass of the electron, and ε is the dielectric constant of the solvent. With the bulk reduction potential, V_0, the reduction potential, V_R, of nanocrystals can be expressed as $[(E_x - E_g) + E_c]/e + V_0$.
24. R. Memming, *Top. Curr. Chem.* **169**, 105 (1994).
25. R. J. D. Miller, G. L. McLendon, A. J. Nozik, W. Schmickler, F. Willig, *Surface Electron Transfer Processes* (VCH, New York, 1995), p. 44.

26. Funded by a grant from the National Science Foundation (DMR-9731642). Experiments made use of the Materials Research Science and Engineering Centers Shared Facilities supported by a grant from the National Science Foundation (DMR-9400379).

28 November 2000; accepted 1 February 2001

In Situ Measurement of Grain Rotation During Deformation of Polycrystals

L. Margulies,[1,2] G. Winther,[1] H. F. Poulsen[1]*

Texture evolution governs many of the physical, chemical, and mechanical properties of polycrystalline materials, but texture models have only been tested on the macroscopic level, which makes it hard to distinguish between approaches that are conceptually very different. Here, we present a universal method for providing data on the underlying structural dynamics at the grain and subgrain level. The method is based on diffraction with focused hard x-rays. First results relate to the tensile deformation of pure aluminum. Experimental grain rotations are inconsistent with the classical Taylor and Sachs models.

Most metals and ceramics are aggregates of crystalline grains. The crystalline lattice of each grain has a characteristic orientation, and a polycrystal is thus characterized by a distribution of orientations—its texture. The texture plays a role in virtually every modern industry, determining phenomena as disperse as the weight of beer cans and the prospect of high-temperature superconducting cables. The orientation difference between neighboring grains is the focus of an emerging technology termed "grain boundary engineering." At the same time, textures in minerals and rocks are vital sources revealing information about geological processes.

Textures evolve during plastic deformation, where a polycrystal changes its shape. At the grain level, each grain changes its shape and its crystallographic lattice rotates. The external force produces line defects (dislocations) in the lattice. The dislocations move in certain directions (slip directions) within certain planes (slip planes), causing the two sides of the plane to slide with respect to each other. The change in grain shape is the result of millions of such operations. The dynamics of the grains are coupled, because the two sides of any grain boundary at all times must adjoin and be in stress equilibrium. To facilitate this process, the grains have to change shapes in different ways, and their crystallographic orientations must rotate with respect to each other.

Various texture models have been presented in the literature for more than 50 years. They predict which possible slip systems (combinations of slip plane and slip direction) are operational and calculate the resulting texture and other macroscopic properties,

[1]Materials Research Department, Risø National Laboratory, 4000 Roskilde, Denmark. [2]European Synchrotron Radiation Facility, BP 220, 38043 Grenoble, France.

*To whom correspondence should be addressed. E-mail: henning.friis.poulsen@risoe.dk

such as the yield stress. However, many central issues remain unsolved, because the grain dynamics have not been observed directly. In particular, conventional techniques, such as optical and electron microscopy as well as laboratory-based x-ray diffraction, probe the near surface. The free surface leads to stress relaxation, which makes dynamic studies using these techniques irrelevant. Hence, experimental verification is only possible by averaging over grains, typically by a statistical analysis.

Because of the lack of local-scale experimental input, models are based on global assumptions without taking the different surroundings of individual grains into account. These assumptions deal with the ambiguity in choosing between a number of possible operational slip systems, which have nearly the same energy, and the issue of which strain and stress conditions to impose on the grain boundaries. The classical models are the Taylor model (*1*), which assumes that all of the grains are subject to the same strain, and the Sachs model (*2*), which assumes only the most stressed slip system to be operational. Self-consistent models that consider the interaction between a grain and a surrounding matrix representing the average bulk behavior are also used (*3*). In general, these models and refinements thereof (*4*) exhibit mathematical singularities and differ substantially. For example, the predicted number of operational slip systems varies between 1 and 8.

Despite the huge modeling effort, present models cannot account for texture evolution; most noteworthy is the general overestimation of the rate of texture development (*4*). Another feature not grasped by any of the models is that, during deformation, grains break up on a micrometer scale into fairly regular deformation structures with different crystallographic orientations (*5*). To facilitate the establishment of models taking such features into account, one needs local-scale dynamic data.

Here, we present results on the rotation and subdivision of bulk grains during deformation. Such studies have been attempted twice before with split samples (*6, 7*). In both cases, the internal surfaces of split samples were investigated, then fitted together. After deformation, the samples were disassembled and the internal surfaces were reinvestigated. The results are questionable, because the effect of the interface is unknown and the experiment only allows two-dimensional characterization of the grain surroundings. In contrast, our method of choice investigates a grain while it is deeply embedded in a polycrystal. Furthermore, the method can be extended to provide a characterization in three dimensions.

The method is three-dimensional (3D) x-ray diffraction microscopy, recently developed and put into use at the European Synchrotron Radiation Facility (*8–11*). The experimental setup is shown in Fig. 1. The tensile specimen is high-purity aluminum (99.996%) with a thickness of t = 3 mm and an average grain size of 300 μm. It is mounted in a stress rig, which is fixed to a sample stage, that allows x, y, and z translations as well as a rotation of magnitude ω about the z axis. A hard x-ray beam with an energy of 50 keV (and a penetration power of centimeters) is focused on the specimen and illuminates a volume of 5 μm by 300 μm by t. Some of the grains within this volume will give rise to diffracted beams (reflections) that are transmitted through the sample to appear as spots on a charge-coupled device camera. At each strain, 25 images were recorded while stepping from –12° to 12° in ω, around the position ω = 0°, where the tensile axis is perpendicular to the beam. All of the images were acquired in 1 s while oscillating the sample by 1° in ω around its nominal value to ensure full integration of the intensity for grains with some intragranular orientation spread. In this way, each grain gives rise to a minimum of six recorded reflections. Measurements were made for strains of 0, 2, 4, 5, 7, 9, and 11%.

Four grains positioned near the center of the specimen were identified by x-ray tracing (*9, 10*). At each strain level, these grains were centered in the y and z directions by examining the integrated intensity of a reflection during translation of the sample. As sketched in the enlarged part of Fig. 1, the illuminated volume contains many grains. An automatic indexing program was used to sort out the reflections from the four grains of interest from a background arising from all other grains and to calculate the orientations of the four grains (*10*).

Examples of raw data are shown in Fig. 2. Initially, any reflection appears as a spike in one image that corresponds to one specific ω setting. With increasing strain, the reflection moves on the unit sphere, so that the spot appears at a different ω setting and moves along the azimuthal direction η (see Fig. 1 for definition of η). The spots also broaden in the two directions, which eventually leads to an overlapping of spots. With the present setting, a sufficient number of non-overlapping reflections were available at all strain levels.

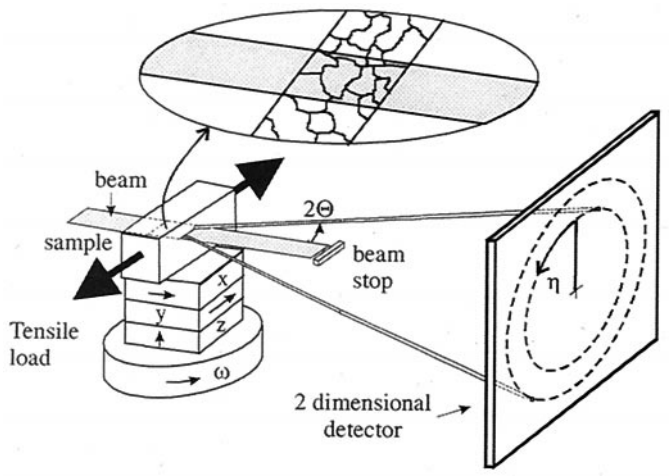

Fig. 1. Sketch of experimental setup. Coordinate system (x, y, z) and angles (ω, 2Θ, η) are defined. All of the grains within the stripe illuminated by the beam will give rise to diffracted spots during the scanning of ω. Spots are further characterized by their Bragg angle 2Θ and their position on the Debye-Scherrer ring given by η.

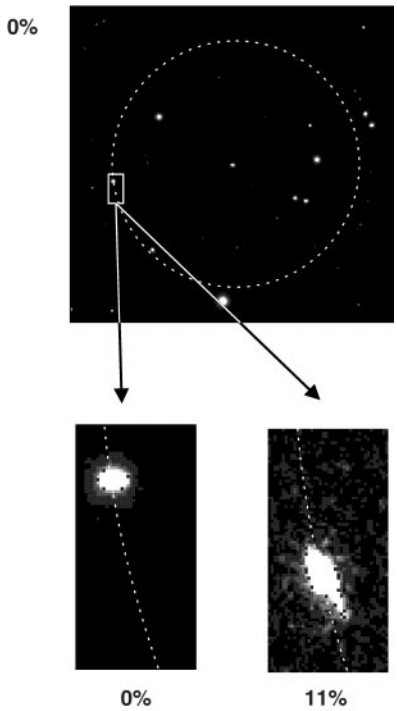

Fig. 2. Example of raw data for ω = 1° and 0% strain (top). The circle marks the (220) Debye-Scherrer ring, and the box identifies a spot related to grain 1. The enlarged areas (bottom) show the movement of this spot on the ring, by comparison with a corresponding image at ω = –5° and 11% strain.

The average rotation and the spread of orientations developed during deformation are illustrated in Fig. 3 for the same reflection as depicted in Fig. 2. The average rotation velocity is 5.5° per 11% deformation. The spread at a strain of 11% is ~2°, which is consistent with transmission electron microscopy measurements of typical misorientation angles across deformation-induced dislocation boundaries in the same material (*12*). The increase in spread is one-fourth the rotation rate. Here, a ratio of, say, 1:1 would imply a direct rejection of all present models, whereas a ratio of 1:20 or more would indicate that grain breakup can be neglected.

The rotations of the tensile axis for the four grains are presented in Fig. 4. The results are compared with predictions of the classical Taylor and Sachs models by using the antisymmetric part of the strain tensor to calculate the crystallographic grain rotations. These models are usually regarded as upper and lower bound models with respect to the applied work. (Corresponding results for the rotation of the sample normal perpendicular to the tensile axis are consistent with the conclusions below.)

For the Taylor model, all of the solutions to the ambiguity problem with the same five slip systems (or as similar as possible in the case of rotation to orientations where new slip systems are activated) are shown in Fig. 4A; that is, the model predicts any linear combination of the solutions shown. For grain 1, the model has substantial ambiguity, and thus rotation in any direction except toward the ⟨110⟩ corner is predicted. The experimental data fall within this large span of directions. For grain 3, the Taylor model is also associated with a large ambiguity, but the experimentally observed rotation toward the ⟨111⟩ corner is totally unpredicted. For grains 2 and 4, the experimental rotations clearly lie to the left of the narrow span of predicted rotation directions.

The Sachs model has no ambiguity (Fig. 4B). Here, model predictions of the direction agree well with the experimental data for grain 4 but lie to the left of the experimental data for the other three grains. The correct prediction of the final orientation of grain 2 appears to be accidental because the model clearly fails in predicting the path to this orientation. We conclude that neither model works, but for three out of the four grains, the experimental rotation of the tensile axis lies between the predictions of the Taylor and Sachs models; that is, the grains move toward the predicted dominant stable orientation in the ⟨111⟩ corner.

The experimental rotation rates follow the Taylor model well and are lower than the predictions from the Sachs model. The reason for the difference between models is that the Taylor model operates with more slip systems (five to eight active systems) than does the Sachs model (one system) and that coactive slip systems tend to counterbalance each other. Hence, the results indicate that the grains deform by multislip.

A ratio of grain size versus specimen size of 1:15 has been shown to eliminate surface effects on the mechanical properties of the whole specimen (*13*). It is therefore concluded that the four grains analyzed, which were situated in the center of the specimen with a 1:10 ratio, must represent the bulk. In general, limitations of specimen thickness are set by the penetration power of the hard x-rays (penetration of several millimeters is universally available and can be as much as 5 cm for aluminum). Limitations on the grain size are set by the breakup, which smears out the peaks. For the strain levels used here, a grain size of 10 μm is realistic.

The technique presented above allows simultaneous measurements on a number of grains and enables statistical analysis for ensembles of grains. Moreover, by scanning the detector parallel to the incoming beam, a 3D grain map can be extracted (*10*). Hence, information on neighboring relations is available. Simultaneously, by generating 3D maps of grain boundaries before and after the deformation, the shape changes of the grains can be produced. All of the necessary information for the establishment and tests of local models, such as finite-element algorithms, is then provided. Simultaneously, the described technique bridges the grain and subgrain length scales (compare with Fig. 3). Definite answers to the question of texture evolution seem therefore finally at hand.

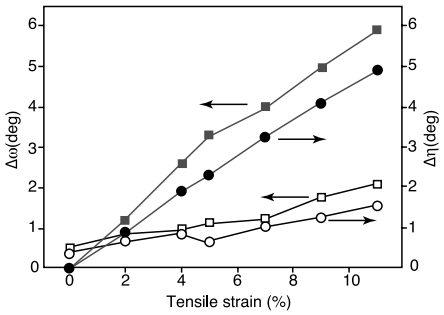

Fig. 3. Experimental data for the average rotation (solid symbols) of the reflection singled out in Fig. 2, compared with the spread in orientation (full width at half maximum) of the same reflection (open symbols). Shown are the components along the change in two experimental angles, Δω and Δη, defined in Fig. 1.

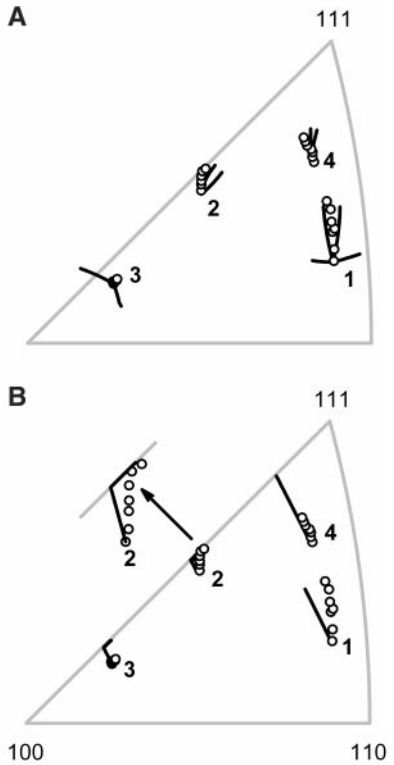

Fig. 4. The dynamics of four embedded aluminum grains during tensile deformation. Experimental data (open circles) are shown as inverse pole figures, which represent the position of the tensile axis in the reciprocal space of the grains. Strain levels were 0, 2, 4, 5, 7, 9, and 11%. The instrumental errors are substantially smaller than the symbol size. A comparison is performed with the evolution path from 0 to 11% (solid line) as predicted by (**A**) a full-constraints Taylor model and (**B**) a Sachs model. Several lines associated with the same grain represent degenerate solutions. To show the comparison, we enlarged the data set for grain 2.

References and Notes

1. G. I. Taylor, *J. Inst. Met.* **62**, 307 (1938).
2. G. Sachs, *Z. Ver. Dtsch. Ing.* **72-22**, 734 (1928).
3. E. Kröner, *Acta Metall.* **9**, 155 (1961); J. W. Hutchinson, *Proc. R. Soc. London Ser. A* **319**, 247 (1970).
4. U. F. Kocks, C. N. Tomé, H.-R. Wenk, *Texture and Anisotropy: Preferred Orientations in Polycrystals and Their Effect on Materials Properties* (Cambridge Univ. Press, New York, 1998).
5. B. Bay, N. Hansen, D. A. Hughes, D. Kuhlmann-Wilsdorf, *Acta Metall. Mater.* **40**, 205 (1992).
6. C. S. Barrett, L. H. Levenson, *TMS-AIME* **137**, 112 (1940).
7. S. Panchanadeeswaran, R. Becker, R. D. Doherty, K. Kunze, *Mat. Sci. Forum* **157-162**, 1277 (1994).
8. H. F. Poulsen *et al.*, *J. Synchrotron Radiat.* **4**, 147 (1997).
9. D. Juul Jensen *et al.*, *Mater. Res. Soc. Symp. Proc.* **590**, 227 (2000).
10. D. Juul Jensen, H. F. Poulsen, in *Proceedings of the 21st Risø International Symposium on Materials Science, Risø 4–8 September 2000*, N. Hansen *et al.*, Eds. (Risø National Laboratory, Roskilde, Denmark, 2000), p. 103; S. F. Nielsen *et al.*, in *Proceedings of the 21st Risø International Symposium on Materials Science, Risø 4–8 September 2000*, N. Hansen *et al.*, Eds. (Risø National Laboratory, Roskilde, Denmark, 2000), p. 473.
11. S. F. Nielsen *et al.*, *J. Synchrotron Radiat.* **7**, 103 (2000).
12. X. Huang, personal communication.
13. N. Hansen, *Acta Metall.* **25**, 863 (1977).
14. This work was supported by the Danish Natural Science Research Council through Dansync. We thank N. Hansen, T. Lorentzen, R. M. Suter, U. Lienert, D. Juul Jensen, and T. Leffers for advice and help with experimental work.

1 December 2000; accepted 13 February 2001

A9

Available online at www.sciencedirect.com
SCIENCE DIRECT®
Pergamon
Acta Materialia 51 (2003) 3821–3830
Acta MATERIALIA
www.actamat-journals.com

Lattice rotations of individual bulk grains Part I: 3D X-ray characterization

H.F. Poulsen [a,*], L. Margulies [a,b], S. Schmidt [a], G. Winther [a]

[a] *Center for Fundamental Research: Metal Structures in Four Dimensions, Risø National Lab., DK-4000, Roskilde, Denmark*
[b] *European Synchrotron Radiation Facility, BP 220, F-38043 Grenoble Cedex, France*

Received 19 February 2003; received in revised form 6 April 2003; accepted 8 April 2003

Abstract

Three-dimensional X-ray diffraction has been applied to characterise the plastic deformation of individual grains deeply embedded in a 99.6% pure aluminium specimen. The specimen is 4 mm thick with an average grain size of 75 μm. The average lattice rotation for each grain as well as the degree of internal orientation spread within the grain is measured in-situ during 6% elongation. The rotation paths for 95 grains with nearly random initial orientations are reported. The quality of this data set is sufficient to make distinctions between plasticity models. The rotation paths exhibit a clear dependence on the initial orientation, while the influence of grain interaction is relatively small. All grains deform plastically. Averaged over grains and reflections the rotation of the tensile axis and the FWHM of the internal spread is 2.0 and 0.8°, respectively, at 6% strain.

Keywords: Plastic deformation; X-ray diffraction; Aluminium; Texture; Synchrotron radiation

1. Introduction

Polycrystal plasticity models describing texture evolution are based on the prediction of active slip systems in individual grains and calculation of the resulting lattice orientation [1–6]. The field has been impeded by lack of suitable experimental data on the dynamics of individual grains. Studies of lattice rotations within surface or near-surface grains do exist (e.g. [7]), but the dynamics of such may not be representative of bulk behaviour.

In order to mimic bulk conditions a set of experiments were performed by Barrett and Levenson [8] and later by Panchanadeeswaran, Doherty and co-workers [9–11]. In these studies, two metal surfaces were pressed tightly together during deformation and characterisation was performed by surface probes on these two "interior" surfaces before and after deformation. While demonstrating that individual grains do not behave as average grains, it is unclear to what extent the interface influenced the results.

Recently, we have demonstrated the feasibility of monitoring the lattice rotation of deeply embed-

* Corresponding author. Tel.: +45 4677 5739; fax: +45 4677 5758.
E-mail address: henning.friis.poulsen@risoe.dk (H.F. Poulsen).

1359-6454/03/$30.00
doi:10.1016/S1359-6454(03)00206-4

ded grains in-situ during deformation [12,13]. This was accomplished by means of diffraction with high energy (50–100 keV) X-rays. The hard X-rays provide a penetration power of up to 4 cm in light materials such as aluminium [14]. Furthermore when generated by synchrotrons such X-rays can be focused to provide a very intense beam of micron dimensions. These properties have been exploited in the so-called 3-dimensional X-ray diffraction (3DXRD) microscope, situated at beamline ID11 at the European Synchrotron Radiation Facility (ESRF) [15–17].

The two previous articles introduced the 3DXRD technique as applied to Al [12] and Cu [13] deformed in tension. In these preliminary studies information was extracted only on a few grains. In the present article we report on further developments of the method. As a result we present data for the tensile deformation of ~100 grains embedded within a commercial purity aluminium polycrystal. Information is extracted both on the average rotation of each grain and on the emerging orientation spread within the grains. The quality of the data and the grain statistics are discussed and argued to be sufficient to make clear distinctions between plasticity models.

A detailed analysis of the rotation data in terms of the dependence on initial orientation and a comparison with classical texture models is provided in a subsequent article [18].

2. Experimental

The sample material was 99.6% pure Al AA1050. This had been cold rolled to 60% reduction and annealed at 400 °C for 2 hs. From EBSP characterisation the material was found to be nearly equi-axed with an average grain size of ~75 μm. Based on EBSP as well as X-ray diffraction data, the texture is found to be rather weak with a predominant cube component [19]. A tensile specimen was prepared with a cross section of 4 × 8 mm^2 and with the tensile direction parallel to the original rolling direction.

The experiment was performed at the 3DXRD microscope at ESRF. The set-up is sketched in Fig. 1. The X-rays from the synchrotron are focused by a combination of a bent Laue crystal and a bent and graded multilayer [20]. The resulting 55.0 keV monochromatic beam had a negligible divergence of ~0.2 mrad. At the focal point the beam dimensions were 5 × 5 μm^2. At this point the beam impinged on the specimen, which was placed in a 25 kN stress-rig equipped with an extensometer. The stress-rig was mounted on top of an (x,y,z)-translation stage and a horizontal (ω) rotation stage. The tensile axis was horizontal and transverse to the beam for $\omega = 0$. Between the focusing optics and the specimen an adjustable entry slit was mounted in order to reduce the background. Diffraction spots were recorded on a two-dimensional detector, a FRELON CCD coupled to an Image Intensifier. This detector has an approximate resolution of 225 μm and an effective area of 230 × 230 mm^2.

A conical slit was placed between the sample and the detector [21]. The conical slit contains 6 conical shaped openings, placed in accordance with the {111}, {200}, {220}, {222}, {331} and {422} powder rings of Al. The gap of each opening is 20 μm. The conical slit was aligned such that its focal point coincided with the ω rotation-axis. In this way the conical slit ensures that only diffraction spots arising from a small intrinsic gauge volume are seen by the detector. The dimension of the gauge volume is in the present case 5 μm × 5 μm × d, where the depth resolution d varies between 250 and 350 μm, depending on 2θ.

Prior to actual measurements a reference grain was aligned such that the beam illuminated the center of it and simultaneously the center of the grain is positioned on top of the ω rotation axis. For the actual data taking, images were acquired while stepping in ω with equi-angular steps of $\Delta\omega = 0.25°$. During each acquisition the sample was oscillated by $\pm\Delta\omega/2$ in order to perform a space-filling and intensity-conserving sampling. The ω-range was from −11 to 11°. This procedure was repeated for a total of 24 reference grains, separated from each other in the y-direction by 100 μm or more. All reference grains were placed within 100 μm from the center line of the specimen.

Next the sample was elongated to a strain of 6% in steps of 2%. At each strain level reference grains were re-aligned with respect to the beam and the

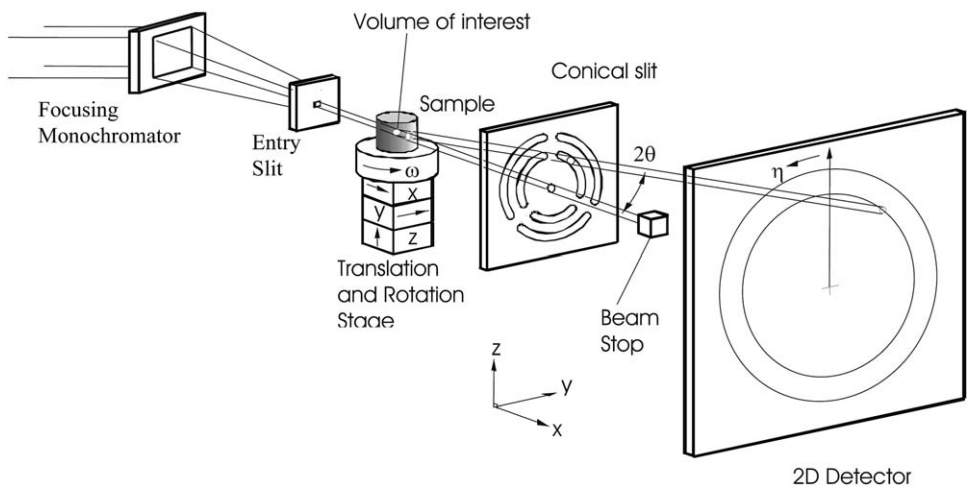

Fig. 1. Sketch of the experimental set-up. The co-ordinate system (x,y,z) and angles 2θ (Bragg angle) ω (sample rotation) and η (azimuthal angle) are defined. The axis of the mounted tensile rig (not shown) is parallel to y for $\omega = 0$.

rotation axis. Then the measuring sequence was repeated. The ramping between strain levels was performed without overshoot and with a strain rate of 1.6 10^{-4} sec^{-1}.

3. Data analysis

An example of the evolution of a typical diffraction spot is given in Fig. 2. For the un-deformed sample the reflection appears as a nearly point-like feature in a given exposure. With increasing strain the reflection moves on the unit sphere, so that the spot appears at a different ω-setting and moves in the azimuthal direction η (see Fig. 1 for a definition of η). The spot also broadens in the two directions, reflecting the development of a certain orientation spread within the grain.

For each y-position and strain-level the diffraction spots observed arise partly from the reference grain, partly from neighbouring grains within the gauge volume. Some of the neighbouring grains gave rise to only a few stray reflections as they "rotate out" of the gauge volume during the ω rotation. Others—closer to the centre of rotation—were illuminated at all ω settings. The indexing program GRAINDEX [15] identifies all the spots and determines the center-of-mass (CMS) of their (ω,η) distributions. Next it sorts the spots with respect to grain of origin. For grains with a near complete set of reflections GRAINDEX derives their average orientation by a least-square fit to the calculated CMS positions of the spots. Hence, for each y-position and each strain level information is obtained not only for the reference grain but also for a small set of neighbouring grains. For the further analysis and the results it makes no difference whether a grain is a reference grain or not.

With increasing load the probability of diffraction spots overlapping each other becomes larger. GRAINDEX cannot handle such cases. Hence, reflections corresponding to overlapping spots were discarded. For each grain, to ensure a uniform sampling a fixed set of non-overlapping reflections was used at all strain levels. Setting the lower limit on the number of such fixed reflections at 5, the rotation paths of 95 grains were determined. From the geometry of section 2 it follows that all of these were positioned within 250 μm from the center line.

4. Results

4.1. Grain rotations

The rotation paths of the tensile axis for each of the 95 grains are shown in the standard stereo-

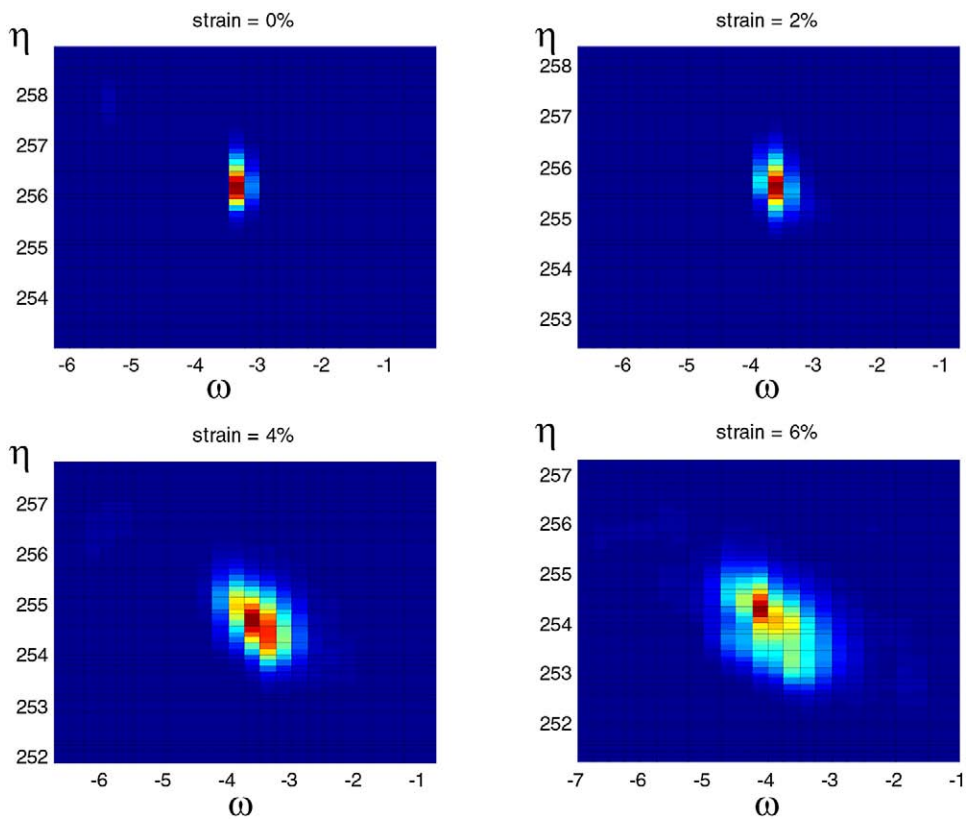

Fig. 2. Example of evolution of a diffraction spot with load. The intensity distributions are plotted with respect to the ω and η axes, see Fig. 1. The colour code is linear with red representing the maximum intensity and blue the background.

graphic triangle in Fig. 3. A corresponding plot of the frequency of the rotation angle is provided in Fig. 4 for the 6% strain level. Similarly, the degree of rotation around the tensile axis is shown in Fig. 5. (The sign is selected such that positive angles correspond to rotations clockwise around the tensile axis when looking in the direction of the axis.) The corresponding plot of the frequency of this angle is provided in Fig. 6 for the 6% strain level.

From Fig. 3 the grains are seen to have nearly random initial orientations. Furthermore, with possible exception of the <111> corner, the grain statistics are sufficient to derive conclusions on the dependency of the initial orientation.

Some statements can be derived immediately from Figs. 3–6

- From Fig. 3 it is evident that there are strong correlations between the initial orientation and the rotation behaviour of the tensile axis.
- In the right hand part of the triangle, grains with almost identical initial orientation display in most cases nearly parallel rotation paths. As the grains in such a set will have different neighbour configurations, this indicates that the effect of grain interaction is relatively small. However, there are also examples of grains with similar initial orientation exhibiting distinctly different rotation paths. Two examples are encircled and marked as A in Fig. 7. Hence, the rotation of an individual grain is not uniquely determined by its initial orientation.
- In the left part of Fig. 3 the rotations are more stochastic in nature.
- The rotation paths are in general approximately straight.

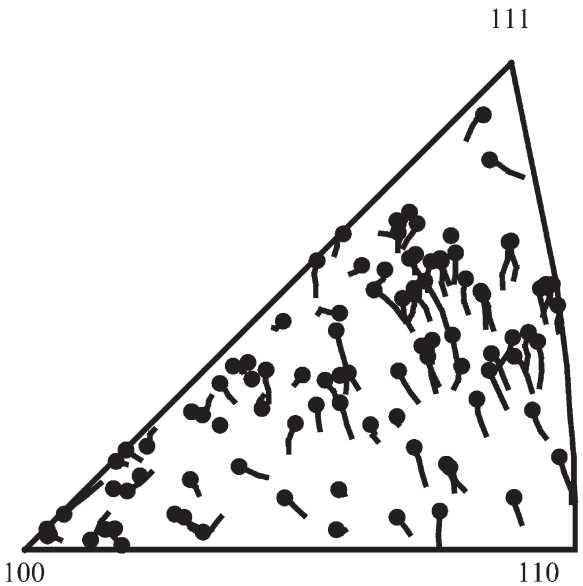

Fig. 3. The rotation of the tensile axis of each of the 95 embedded grains expressed in the stereographic triangle. The curves are the observed paths for the average orientation of each grain during tensile deformation from 0 to 6%. The final orientation of the axis is marked with a filled circle.

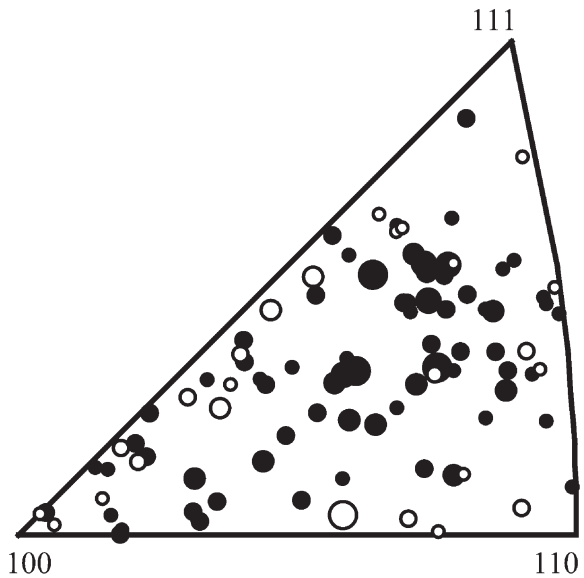

Fig. 5. The rotation around the tensile axis of each of the 95 embedded grains. The symbols are placed in the stereographic triangle according to the initial position of the tensile axis, for direct comparison with Fig. 3. Filled and open circles represent negative and positive rotations, respectively. The size of symbols is proportional to the rotation angle, with the largest symbols representing a rotation of 2.5°.

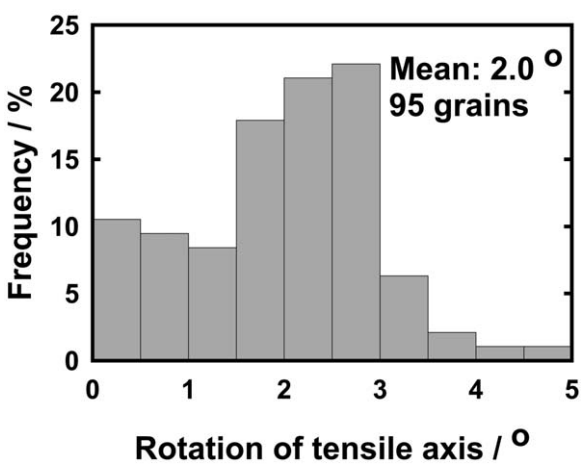

Fig. 4. Frequency of the rotation angle of the tensile axis at 6% elongation.

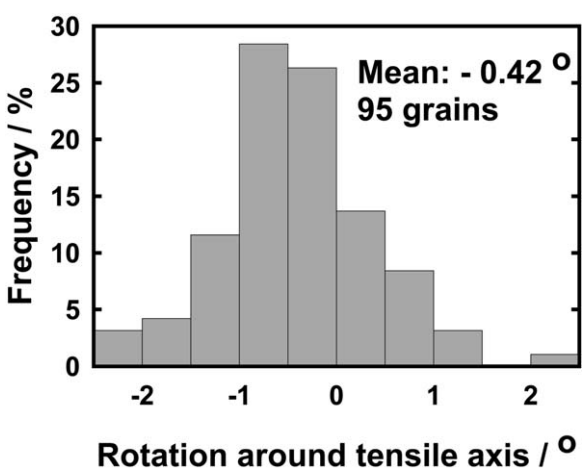

Fig. 6. Frequency of the rotation angle around the tensile axis at 6% elongation.

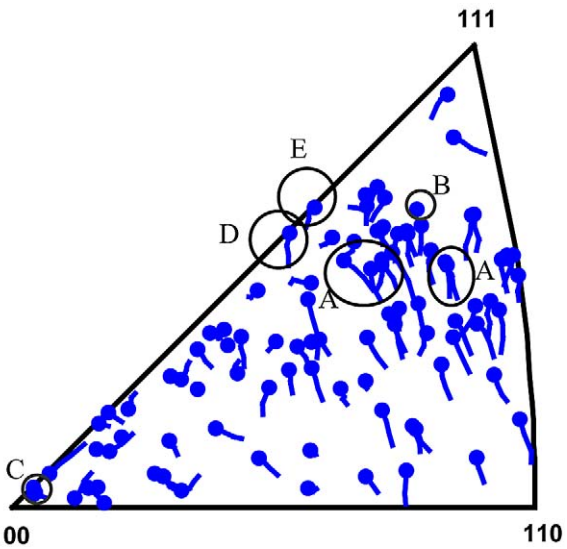

Fig. 7. Copy of data presented in Fig. 3 with specific grains pinpointed. Regions marked A are examples of set of grains with initially close orientations which rotate in very different directions. Grains marked B and C are the grains that exhibits the minimum total rotation (0.2°). Grains D and E are examples of grains that rotate out of triangle if no symmetry operations are applied. Grain D is analysed further in Fig. 8.

- The rotation around the tensile axis is on average smaller and slightly more random in nature than the rotation of the tensile axis itself. 3/4 of grains rotate in the negative direction. Those performing a positive rotation around the tensile axis are with two exceptions all placed near the borders of the standard triangle.
- For a few grains the tensile axis stays approximately fixed during the deformation (most notably the ones marked B and C in Fig. 7). At 6% elongation the minimum total rotation for any grain is 0.2°. The maximum total rotation of any grain is 5.5°.

It should be added that a few grains, including those marked D and E in Fig. 7, actually rotates out of the standard triangle if no symmetry operations is applied.

4.2. Orientation spread within grains

The analysis of the emergence of an orientation spread within the grains was based on (ω,η)-plots of the type shown in Fig. 2.

The diffraction spots analysed exhibited a range of behaviour. Some diffraction spots essentially just broadened, cf. Fig. 2. Others divided into a small set of sub-peaks—typically 2–4—which split progressively with increasing load. An example with 2 peaks is shown in Fig. 8. In this case a similar split was observed for 3 of the 5 valid reflections associated with this grain—the remaining 2 did not split. As a result for the highest load GRAINDEX identified two components of the grain and indexed both of them. As shown in Fig. 8(b), this particular split appeared when the rotation path of the grain on average met the <100>–<111> line. Other grains split at positions within the triangle.

Due to the complexity of the splitting behaviour and the small amount of fixed reflections for each grain it is questionable whether the data can be used to quantify the orientation spread for specific grains. However, we can apply a statistical analysis to determine a distribution of spreads of the individual diffraction spots as averaged over grains. To do so 88 randomly chosen reflections were analysed. For each of these the FWHM of the intensity distribution in the ω-direction was determined from the associated (ω,η)-plots. To obtain numbers representing distances on the unit sphere the results were multiplied by the Lorentz-factor $|\sin(\eta)|$ [15]. Fig. 9 shows the spread defined in this way as a histogram for 6% load. The average spread is 0.9° with a standard deviation of 0.4°. A minor instrumental broadening from the ω-binning ($\Delta\omega$ = 0.25°) has not been subtracted from these data, so the actual orientation spreads are ~0.1° smaller.

From Fig. 9 it is seen that all reflections have broadened significantly. A similar analysis for the reflections associated with the grains with a small total rotation revealed that these do all spread. Hence, it is clear that all grains deform plastically at 6%. (This result is also true for 4% strain).

5. Discussion

To the authors' knowledge, the data set presented above is the first true, statistically sound, measurement of the full rotation of bulk grains during deformation.

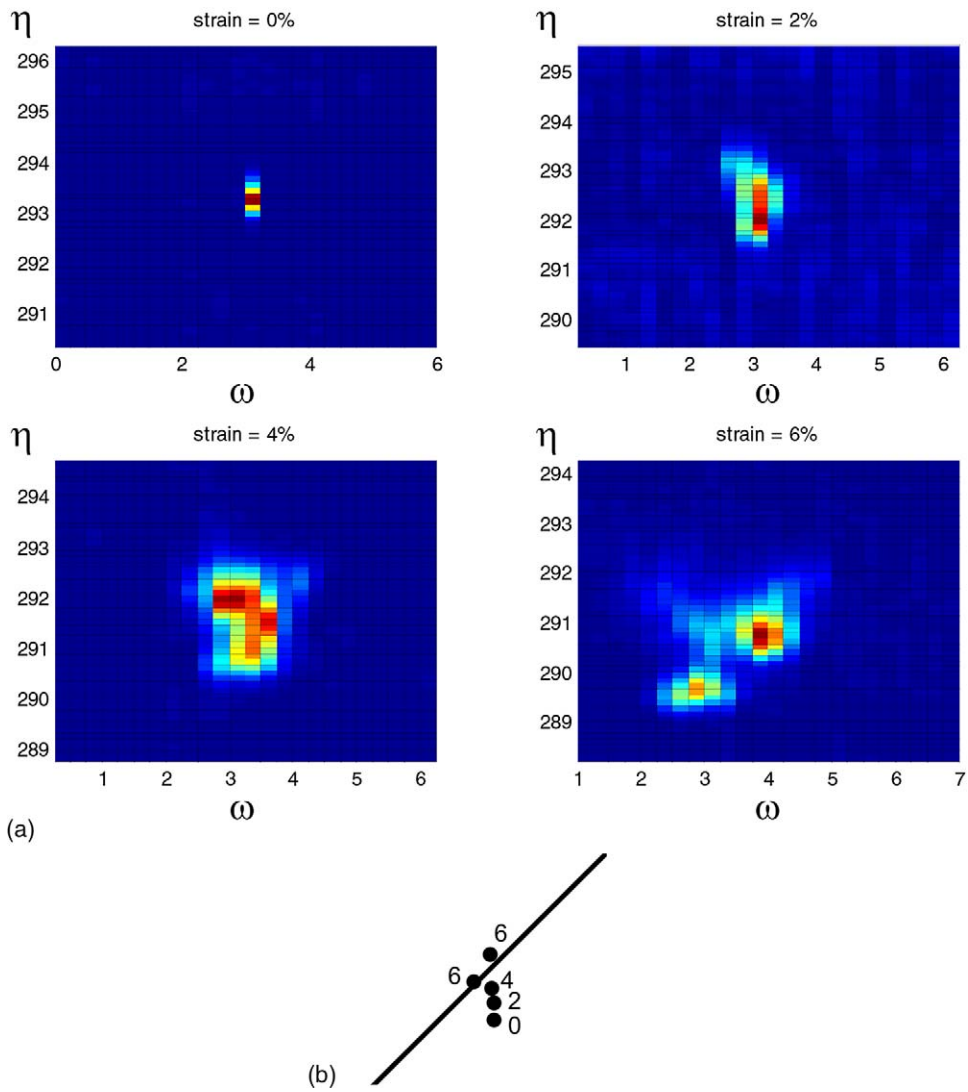

Fig. 8. Example of evolution of a diffraction spot with strain for the case of a grain breaking up into two components. In part a) (ω,η)-plots are shown with symbols and colour code as for Fig. 2. In part b) the average rotation of the corresponding grain is shown as function of strain. (The grain is marked in Fig. 7 as D.) When approaching the <100>–<111> line two distinct orientations are found by the indexing software.

5.1. Grain rotations

A potential problem should be addressed. The issue is that the grains are not fully illuminated. Hence, strictly speaking the orientation of a given grain as determined by GRAINDEX is based on diffraction arising from a sub-volume of the grain, not the full grain. However, the sub-volume actually probed for each of the 95 grains remains approximately throughout the experiment due to the re-alignment of reference grains preceding each strain increment. Furthermore there are several indications that the difference between the rotation of the whole grain and rotation of the sub-volume is negligible:

- The movement of the CMS of the diffraction

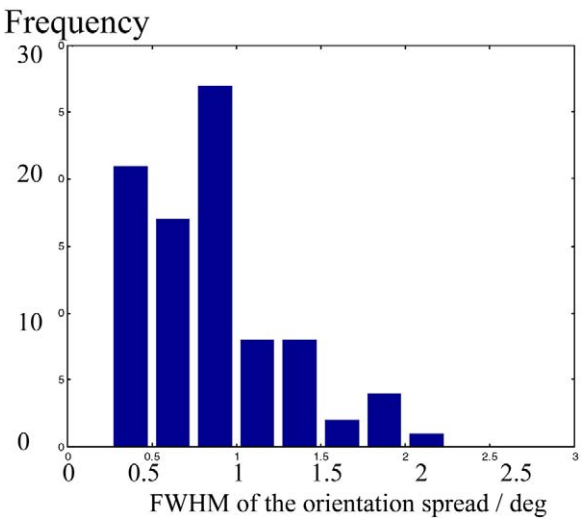

Fig. 9. The FWHM of the intensity distribution for 88 randomly chosen reflections. For each of these (ω-η)-plots were made. Plotted are the projected widths along the ω direction, normalised by the appropriate geometric factor |sin(η)|.

spots (average rotation) is typically larger than the width of the spots.

- The fact that the rotation paths in Fig. 3 in some regions, e.g. close to <221>, are straight and nearly parallel with respect to the paths of grains of approximately the same initial orientation.
- In the previous study on Cu this question was addressed by observing the apparent average rotation of 3 different parts of a large grain. The differences were close to the noise [13].

To estimate the uncertainty on the orientations we use the average spherical angle between the observed scattering vectors and the calculated ones based on the result of GRAINDEX. For most grains the uncertainty is found to be nearly constant as function of load—of order 0.3°, reflecting the step size in ω. In addition there may be a global error arising from misalignments of the instrument. This is estimated to be less than 1°. Notably, to correct for this error the orientation of all grains at all loads should be rotated by the same amount, so relative to each other the rotation paths are not affected by the error.

To shed some light on whether the results are universal, we compare them with those obtained in the two feasibility studies [12–13]. The parameters of the three studies are summarised in Table 1. By inspection of figures the results for the three studies can be seen as reflecting the same rotation field. Hence, within the limitations of the grain statistics, there is no evidence for a dramatic effect of changing the average grain size by a factor of 4 or of replacing Al by Cu. However, to settle these issues, more data is required for other materials.

5.2. Orientation spread within grains

It is well known from electron microscopy that grains "break up" during deformation. In other words that a distinct orientation sub-structure is generated on a rather coarse scale. This phenomenon is reflected here in a pronounced tendency for the intensity distribution in the (ω,η)-plots to be concentrated in a few spikes, cf. Fig. 8. The number derived for the average orientation spread can be compared to values from the literature on the average misorientation angle across dislocation boundaries as determined by TEM [22]. At 6% tensile deformation the two numbers are 0.8 and ~1°, respectively.

It is of interest to estimate the importance of the effect of grain brake-up. To do so we suggest for each grain to use as a parameter the ratio between the width of the emerging orientation spread and the rotation of the grain on average. In the previous study on aluminium [12] a ratio of 1:4 was reported for this parameter. However, that result was based on analysis of a single reflection from a single grain.

The present data set provides a statistically sound estimate of the ratio when averaged over all grains. Assuming an isotropic spread, by compar-

Table 1
Comparison of parameters for the three 3DXRD experiments performed so far with relation to grain rotation

Material	Sample thickness	Grain size	No. grains studied
99.996% pure Al [12]	3 mm	300 μm	4
99 % pure Cu [13]	2 mm	35 μm	7
99.6% pure Al (this work)	4 mm	75 μm	95

ing Figs. 4 and 9 we find the ratio to be 2:5. By inspection of the (ω-η)-plots we find that there often are tails spreading considerably further, up to the same magnitude as the grain rotation. However, the fraction of volume associated with these tails is rather small.

Implicit in the derivation of the ratio, is the approximation that the width of the orientation spread within each illuminated volume (a rod through a grain) is identical to the width associated with the full grain. We argue, that this is a reasonable approximation, as the GRAINDEX estimates for the CMS positions for diffraction spots in general fall within 0.3° of the observed positions.

5.3. Outlook

The method presented is applicable to a broad range of polycrystalline materials. The hard x-rays can penetrate 1 mm of material independent of composition and the flux is sufficient to observe (un-deformed) grains with an initial size as small as 300 nm [17]. The main restriction is the GRAINDEX requirement that diffraction spots do not overlap. As the probability of spot overlap is a steep function of the width of the intrinsic orientation spread, this restriction imposes a limitation on the amount of deformation applied. However, a recent feasibility test has demonstrated that the method with a few modest modifications can be applied up to 20% tensile deformation.

The method can be supplemented by other 3DXRD methods, currently under development. Importantly, for coarse-grained samples the grain boundary topology can be mapped in 3D in the undeformed state [16,17]. Very recently, a reconstruction formalism has also been developed with the aim of mapping deformed specimens [23]. The spatial resolution at the instrument at ESRF is at present ~5 μm.

Likewise, for small strains, rotation data may be supplemented by gathering of information on the average lattice strain within each grain. By indexing of reflections, the evolution of the elastic strain tensor can be followed grain-by-grain [16]. A first application of this method to tensile deformation of Cu to 2% elongation has recently been performed by Lienert and co-workers at the APS synchrotron [24]. They report on the lattice strain of 20 grains lying in the <110> corner of the triangle (rotation data were not acquired). The standard deviation of the scattering of the strains is found to be only 10% of the yield strain, indicating again a small effect from grain interactions.

With such combinations of 3DXRD tools it is clear that the requirements for full and direct comparison with plasticity models such as FEM simulations can be met.

6. Conclusion

A unique data set is provided for evaluation of models for polycrystal deformation. Results are produced on both the grain and sub-grain scale. The method can be applied to polycrystals in general, with the main limitation being the degree of deformation obtainable.

95 grains with nearly random initial orientations are characterised. It is found that

- all grains undergo plastic deformation as evidenced by spot broadening
- the total rotations at 6% elongation vary between 0.2 and 5.5°.
- the rotation paths are approximately straight.
- the rotation of the tensile axis exhibit a clear dependence on initial grain orientation. This is to a lesser extent also true of the rotation around the tensile axis.
- the effect of grain interaction on the average rotation path of a grain is relatively small.

Acknowledgements

We thank N. Hansen, R.D. Doherty and D. Juul Jensen for scientific discussions, A.W. Larsen and A. Terry for help with the synchrotron experiment, A. Goetz, P.B. Olesen, and P. Nielsen for technical support. ESRF is acknowledged for provision of beamtime. This work was supported by the Danish National Research Foundation through the “Center for Fundamental Research: Metal Structures in Four Dimensions” and by the Danish Natural Science Research Council via Dansync.

References

[1] Taylor GI. J Inst Met 1938;62:307.
[2] Sachs G. Z verein deut Ing 1928;72:734.
[3] Kröner E. Acta Metall 1961;9:155.
[4] Hutchinson JW. Proc R Soc London 1970;A319:247.
[5] Mika DP, Dawson PR. Mater Sci Eng 1998;A257:62.
[6] Kocks UF, Tome CN, Wenk H-R. Texture and anisotropy. New York: Cambridge University Press, 1998.
[7] Bunge HJ, Fuchs R. Phys Stat Sol 1969:32:169.
[8] Barrett CS, Levenson LH. TMS-AIME 1950;137:112.
[9] Panchanadeeswaran S, Doherty RD. Scripta Metall Mater 1993;28:23.
[10] Panchanadeeswaran S, Doherty RD, Becker R. Acta Metall Mat 1996;44:1233.
[11] Bhattacharyva A, El-Danaf E, Kalindindi SR, Doherty RD. International J of Plasticity 2001;17:861.
[12] Margulies L, Winther, G, Poulsen HF. Science 2001;291:2392.
[13] Winther G, Margulies L, Poulsen HF, Schmidt S, Larsen AW, Lauridsen EM, Nielsen SF, Terry A. Mat Science Forum 2002;408–412:287.
[14] Bouchard R, Hupfeld D, Lippmann T, Neuefeind J, Neumann HB, Poulsen HF et al. J Synchrotron Rad 1998;5:90.
[15] Lauridsen EM, Schmidt S, Poulsen HF, Suter RM. J Appl Crystallogr 2001;34(6):744.
[16] Poulsen HF, Nielsen SF, Lauridsen EM, Schmidt S, Suter RM, Lienert U et al. J Appl Crystallogr 2001;34(6):751.
[17] Poulsen, HF, Juul Jensen D. Mat Science Forum 2002;408–412:49.
[18] Winther G, Margulies L, Schmidt S, Poulsen HF. Preprint.
[19] Mishin OV, Bay B, Juul Jensen D. Met Mater Trans 2000;31A:1653.
[20] Lienert U, Schulze C, Honkimäki V, Tschentscher T, Garbe S, Hignette O et al. J Synchrotron Rad 1998;5:226.
[21] Nielsen SF, Wolf A, Poulsen HF, Ohler M, Lienert U, Owen RA. J Synchrotron Rad 2000;7:103.
[22] Hansen N, Huang X, Hughes DA. Mat Sci Eng 2001;A317:3.
[23] Poulsen, HF. Phil Mag, in print.
[24] Lienert U, Margulies L, Nielsen SF, Schmidt S, Leffers T, Poulsen HF. Acta Met (submitted for publication).

A10

PERGAMON

Scripta mater. 43 (2000) 561–566

Scripta MATERIALIA

www.elsevier.com/locate/scriptamat

KINETICS OF INDIVIDUAL GRAINS DURING RECRYSTALLIZATION

E.M. Lauridsen, D. Juul Jensen and H.F. Poulsen
Materials Research Department, Risø National Laboratory, DK-4000 Roskilde Denmark

U. Lienert
ESRF, BP 220, F-38043 Grenoble Cedex, France

(Received January 26, 2000)
(Accepted in revised form April 11, 2000)

Keywords: Recrystallisation; Nucleation; Growth; X-ray diffraction; Synchrotron radiation

Introduction

The nucleation and growth process occurring during recrystallization have been extensively studied both experimentally and theoretically [e.g. 1–3] A plethora of models exist to simulate the recrystallization, ranging from purely geometrical numerical models to fundamental analytical models. A common characteristic of the models is that focus is on the *average* behaviour of the nuclei. The main reason therefore is the lack of experimental data for the behaviour of the individual nuclei.

Many experimental techniques commonly available can be used for static characterisation of recrystallization. Typically a series of samples are annealed for various times at a given temperature to achieve various volume fraction of recrystallized material (V_v) within the samples. By quantitative characterisation, statistically significant data is then collected for each sample. These data may be used either to give a static description of the individual samples or merged to give an *average* kinetic description of the nucleation and growth processes occurring during the recrystallization.

Several experimental techniques may also be used for *in-situ* characterisation during annealing, for example by electron microscopy and neutron diffraction. Clearly the microscope techniques only reveal the recrystallization kinetics in the sample surface which may not be representative of the bulk kinetics and because of the limited spatial resolution the neutron diffraction techniques can typically not resolve individual nuclei.

The aim of the present paper is to introduce hard x-rays (above 50 keV) from a synchrotron source as a tool to provide *in-situ* bulk information of the behaviour of the individual nuclei. With the recently commissioned 3 Dimensional X-Ray Diffraction microscope [4,5] at beamline ID11 at the ESRF synchrotron we have succeeded in focusing such a beam to a micron-size spot. In this way a unique combination of high penetration power (millimetres to centimetres) and high intensity is obtained as well as a spatial resolution comparable to the size of the nuclei. The technique has been used for *in-situ* measurements of the growth of individual nuclei in the bulk of an aluminium sample (AA 1050) cold rolled to 90% reduction in thickness. The main reason for choosing this material is that it has already been characterised in detail by microscopy and neutron diffraction [6] and a model has been developed to simulate the recrystallization [7,8].

PII: S1359-6462(00)00430-9

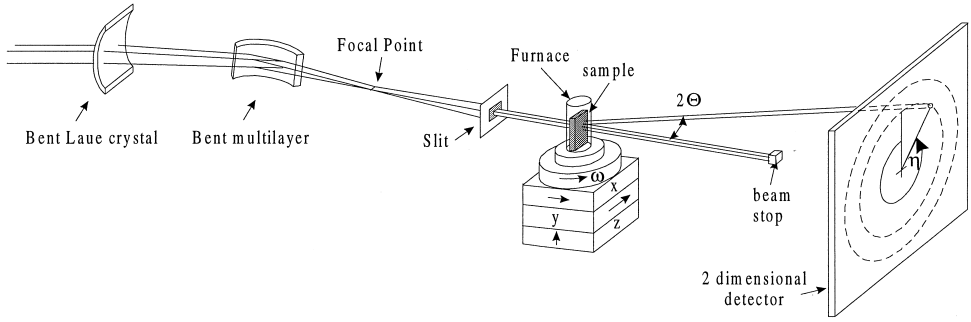

Figure 1. Sketch of the experimental set-up, including definition of angles 2θ (Bragg angle), ω (sample rotation) and η (azimuthal angle around Debye-Scherrer cones).

Experimental

The experiment was performed at the 3DXRD microscope using the set-up sketched in Fig 1. A focused monochromatic x-ray beam with an energy of 50 keV was obtained by combining a bent Laue crystal for vertical focusing with a bent and laterally graded multilayer for horizontal focusing [9]. The resulting focal spot size was 5×10 μm^2 with a divergence and bandwidth of the incoming beam of 0.5 mrad and 0.6%, respectively. The flux was $1.3\ 10^{11}$ cps. The sample was placed off-focus (Fig 1). In this way, by means of a slit, the illuminated area on the sample could be varied continuously with fixed optics up to 100×100 μm^2. The slit also served to remove the tails of the beam. The resulting beam profile was characterised and found to be homogeneous within 15%. Images of the diffracted beams were acquired in transmission geometry by a CCD.

The specimen was 1 mm thick and mounted with (TD) along the beam (ND) upwards in a small furnace. Operated in vacuum, the annealing involved an initial ramping of the temperature from RT within 2 minutes, after which the temperature was kept constant at 270 ± 0.5 °C for 162 minutes. At this point the recrystallisation is 96% complete [8].

The measuring procedure aimed at determining the volume of the grains giving rise to the diffraction spots by measuring the integrated intensity of spots. To do so the slit gaps were set to 70 μm, thereby defining a gauge volume of $V_{gauge} = 70 \times 70 \times 1000$ μm^3, and the sample was oscillated by $\Delta\omega =$ 0.2 deg during exposures. With these settings subsequent exposures were recorded during the entire annealing with a time resolution of 50 seconds. In order to observe diffraction spots of various strengths two exposure times were used: 0.5 and 10 seconds. After 60 minutes these values were changed to 0.1 and 0.5 seconds, to avoid saturation of the detector. During the measurements the sample was kept fixed. This means that only nuclei within the selected gauge volume are recorded and among these only the ones fulfilling the Bragg condition is detected.

Measuring Procedure and Data Analysis

For illustration, raw images acquired at the beginning and end of the thermal treatment are shown in Figure 2. The diffraction pattern for the as-deformed specimen displays the characteristic segmented Debye-Scherrer rings associated with a rolling texture. The diffraction pattern for the annealed specimen comprises $\approx$ 200 sharp diffraction spots, with an average mosaicity less than the instrumental resolution of 0.05°. Virtually no intensity is left in the powder rings, indicating that the recrystallisation is almost complete. (A few spurious powder segments from a slit blade can easily be discarded, due to

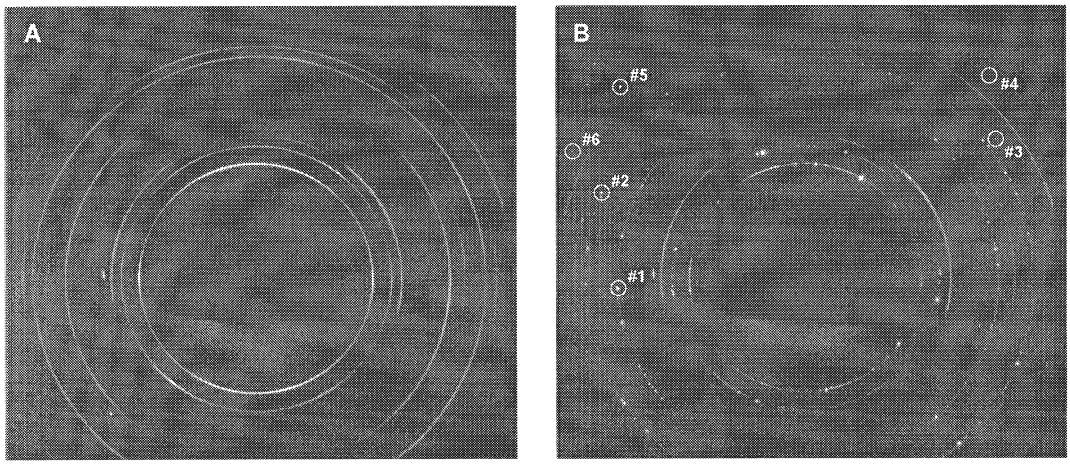

Figure 2. Diffraction patterns measured by the position sensitive detector during annealing at 270°C. Left: At t = 0 min (start of annealing). Right: At t = 162 min, where the recrystallisation is 96% completed. The 6 grains analysed are marked by circles.

their distinct Bragg angles.) The integrated intensities of the diffraction spots were found by summing the pixel intensities and subtracting the background from the deformed material (the powder segments). To convert the integrated intensities of the spots to grain volumes the summed intensity of the 111 ring, I^p_{111}, of the as-deformed sample was used as an internal calibration. The following relationship then exists between the grain volume V_{grain} and the integrated intensity of a specific (h,k,l) reflection, I^g_{hkl}:

$$\mathrm{V}_{\text{grain}} = \frac{\Delta t_p}{\Delta t_g} \frac{m_{111}|F_{111}|^2}{|F_{hkl}|^2} \frac{\Delta\omega|\sin\eta|\sin 2\theta_{hkl}}{4\sin\theta_{111}} \frac{I^g_{hkl}}{I^p_{111}} V_{gauge} \qquad (1)$$

Here F, m, θ and Δt symbolise structure factor, multiplicity, Bragg angle and the acquisition times, respectively. The $\sin(\eta)$ term relates to the fact that the scattering vector does not necessarily lie in the plane of oscillation. To enable comparison with EBSP data the resulting grain volumes are converted into equivalent sphere radia $\mathrm{R} = \sqrt[3]{3V/(4\pi)}$. (It is realised that normalisation using I^p_{111} (Eq. 1) is not fully correct due to the fact that the material has a non-random texture, however, based on a neutron diffraction texture determination, it is found that at maximum $\mathrm{V}_{\text{grain}}$ (Eq. 1) is underestimated by a factor of 0.8 and that the error in the grain radius, taking the cube root, thus is negligible).

Before adding the kinetics of a diffraction spot to the statistics of grains it is necessary to perform two tests. Firstly, the integration over the reflection must be complete (*i.e.* the grain must be situated fully within the gauge volume and the mosaic spread of the reflection must be contained by the oscillation range). To test this, images were acquired at regular intervals with two so-called validation settings: $\mathrm{V}_{\text{gauge}} = 100 \times 100 \times 1000\ \mu\mathrm{m}^3$ combined with $\Delta\omega = 0.2$ deg and $\mathrm{V}_{\text{gauge}} = 70 \times 70 \times 1000\ \mu\mathrm{m}^3$ combined with $\Delta\omega = 0.4$ deg. If the integrated intensity obtained by any of the validation settings were $\geq 5\%$ higher than the results for the normal setting, the grain was considered not valid. Secondly, grains situated within 100 μm of the free surfaces (4 times the average recrystallised grain size) have to be excluded. This information is obtained by comparing the center-of-mass position of a given spot on the detector with the envelope of the positions of a large number of spots of roughly the same orientation.

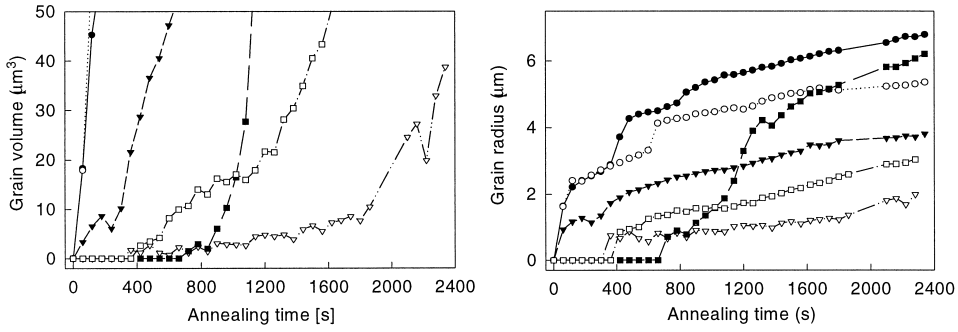

Figure 3. The initial evolution of the 6 grains marked in Fig 2: grain #1 (●), #2 (○), #3 (▼), #4 (▽), #5 (■), and #6 (□). Left is shown the grain volume and right the equivalent sphere radius.

Results and Discussion

In total ≈50 valid grains were found by the procedure outlined above. However as the full data analysis is done manually and thus is very time consuming, only 6 grain picked at random have been analysed so-far. The results of these are presented in the following. Focusing first on the nucleation part, the kinetics during the initial 2400 seconds is shown in Fig 3. The noise limit for observing the nuclei is seen to be R ≈ 1 μm, comparable to the nuclei size found by microscopy techniques [10]. Defining the nucleation time t_{nucl} by $R(t_{nucl}) = 1.3$ μm, (slightly above our detection limit) immediate nucleation is seen to take place for grain # 1, 2, while the others are retarded by t_{nucl} = 300, 1860, 900 and 600 seconds for grains 3, 4, 5 and 6, respectively. The observation of such an incubation periode t_{nucl} of up to more than 15% of the total recrystallization time is a new finding. As the material is only 99.5% pure aluminium and contains large $FeAl_3$ particles which stimulates nucleation [1], instantaneous nucleation without incubation is generally assumed in models. Within the limits of the technique, the nuclei are found to be perfect crystals with no mosaicity from the beginning, that is with no spread along η.

Turning next to the actual growth of the nuclei, the kinetics for the whole process is plotted as R(t) and as the growth velocity G = dR/dt in Fig. 4. Also included in Fig. 4 is a curve of the overall average growth rate determined based on EBSP data. Linear intercept grain size values determined by EBSP in a series of partly recrystallised samples are converted to equivalent circle diameter values and dR/dt is calculated. As can be seen in Fig. 4 the synchrotron results and the EBSP results are of the same order

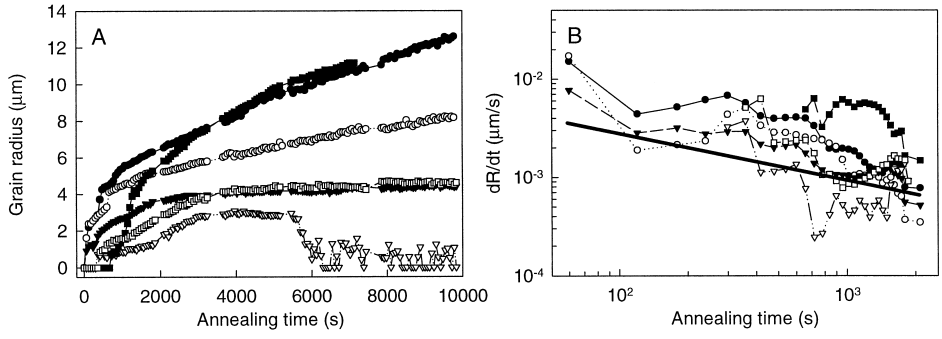

Figure 4. The full evolution of the 6 grains marked in Fig 2: grain #1 (●), #2 (○), #3 (▼), #4 (▽), #5 (■), and #6 (□). Left is shown the equivalent sphere radius R_{grain} and right – for the first 2400 seconds - $G_{grain} = dR_{grain}/dt$. The data were smoothed before differentiation. Also shown are EBSP results (straight line) for the average growth velocity for all grains [10].

of magnitude. That the two sets of results do not agree perfectly may be ascribed to variations in growth rate from nucleus to nucleus, which relate both to the orientation of the nucleus and to the local surroundings which change in space as well as in time as the nucleus grow. Previous EBSP results have shown that nuclei of cube orientation on average grow approximately 1.5 times faster than other nuclei in the present material [6]. Furthermore, from the figure it is clear that there are large fluctuation in growth rates both within and between the 6 different synchrotron curves. Notice in particular the growth velocity of nucleus #5, which at its maximum is 0.0061 μm/second, 1 order of magnitude above the average. In interpreting the curves in Fig. 4, it is essential to remember that the synchrotron data represent the movement of the total (free plus impinged) surface area. This is in particular important at longer annealing times where the impingement between nuclei is significant. Fig. 4 show that even, for $t<2000$ seconds – where $V_v = 0.15$ [8], there are large fluctuations from nucleus to neuclus and as a function of time. It is believed the fluctuations not only reflect different impingement conditions for the different nuclei but also is a consequence of the specific deformed matrix surrounding the individual nuclei. At 90% reduction in thickness, the deformed matrix is heavily subdivided into small μm-sized volume elements of different crystallographic orientations [11]. As both the driving force for recrystallization and the mobility of the recrystallization front may depend on these crystallographic orientations, it seems not surprising that large fluctation in growth rate are observed both as a function of annealing time and between the individual nuclei.

Another interesting feature is the abrupt disappearance of nucleus # 4 around $t = 6000$ when it has reached a size of $R \simeq 2.5$ μm. (The scatter in the data for $t > 6000$ reflects the background noise for the short acquisition time – by direct inspection of the images no trace of the grain is found.) Optical microscopy revealed that annealing of a sample at 270°C for a very extended period of time ($t > 120$h) does not lead to significant grain growth. The disappearance of nucleus #4 is therefore believed to be a local discrete grain growth phenomenon and not a consequence of standard "macroscopic" grain growth.

Future Developments

In the present work focus has been on determination of nucleation and growth rates of individual nuclei in the bulk. In the near future analysis of the data and more diffraction spots and the crystallographic orientations of the nuclei will be determined. These orientations can be calculated directly knowing the η angle (see Figs. 1 and 2) of the diffraction spot of the nucleus and the sample alignment relative to the X-ray beams. Other parameters important for the nucleation growth may be studied after future developments of the technique. For the nucleation part, the sample can be positioned closer to the focus, lowering the detection limit on nuclei (R) significantly, at the expense of grain statistics. For the growth part the use of several consecutive ω-settings during the same run will improve the grain statistics at expense of time resolution. A conical slit with openings along the relevant Debye-Scherrer cones [12] might also be inserted between the sample and the detector. It would lead to the definition of a truly three-dimensional intrinsic gauge volume and thus enable analysis of local surrounding of a nucleus. Finally, the x-ray tracing procedure used for rejecting surface-near grains can be extended to encompass a determination of the centre-of-mass, orientation and aspect ratios of all grains in the gauge volume, using the recently developed tracking algorithm [13]. Such information would indicate on a local scale when the nuclei impinge as well as clarify whether clustering of the nuclei takes place. Moreover $V_v(t)$ and the nuclei density could be determined in this way.

Conclusion

A new equipment—the so called 3D x-ray microscope—has been used for *in-situ* investigation of nucleation and growth of individual nuclei during recrystallization of a 90% cold rolled aluminium sample. Six nuclei have been analysed. It was found that:

- The nucleation differ from nucleus to nucleus. Two of the nuclei form instantaneously upon annealing whereas the remaining 4 have a distinct incubation period before the onset of growth.
- The growth rates of the 6 nuclei vary significantly. The variations exceed one order of magnitude. Also the growth rate of the single nuclei vary significantly in time – for example a nucleus is observed first to grow fast then slower and then faster again. These variations in time and the variations between the individual nuclei match well with the subdivided nature of the deformed matrix.
- The experimental set-up used here applies to not only to aluminium but to all metals and alloys as the penetration depth of 1mm is universally obtainable with hard x-rays.

Acknowledgments

Support for this work was provided by the Danish research councils SNF (via Dansync) and STVF. We thank P.B. Olesen and F. Lemming for technical assistance and R.A. Vandermeer and L. Margulies for fruitful discussions.

References

1. F. J. Humphreys and M. Hatherley, Recrystallization and Related Annealing Phenomena, Pergamon Press, New York (1995).
2. N. Hansen, et al., ed. Proceedings of the 16th Risø International Symposium on Materials Science “Microstructural and Crystallographic Aspects of Recrystallization,” Risø (1995).
3. T. Sakai and H. G. Suzuki, ed., Proceedings of ReX’99: The Fourth International Conference on Recrystallization and Related Phenomena (1999).
4. H. F. Poulsen, S. Garbe, T. Lorentzen, D. Juul Jensen, F. W. Poulsen, N. H. Andersen, T. Frello, R. Feidenhans’l, and H. Graafsma, J. Synchrotron Rad. 4, 147 (1997).
5. U. Lienert, H. F. Poulsen, and Å. Kvick, Proceedings of the 40th Conference of the AIAA on Structures, Structural Dynamics and Materials, St. Louis, MO, April 1999.
6. D. Juul Jensen, Acta Metall. Mater. 43, 4117 (1995).
7. R. A. Vandermeer and D. Juul Jensen, Acta Metall. Mater. 42, 2427 (1994).
8. R. A. Vandermeer, private communication.
9. U. Lienert, C. Schulze, V. Honkimäki, T. Tschentscher, S. Garbe, O. Hignette, A. Horsewell, M. Lingham, H. F. Poulsen, N. B. Thomsen, and E. Ziegler, J. Synchrotron Rad. 5, 226 (1998).
10. B. Bay and N. Hansen, Metall. Trans. A. 10A, 279 (1972).
11. N. Hansen and D. Juul Jensen, Phil. Trans. R. Soc. Lond. 357, 1447 (1999).
12. S. F. Nielsen, A. Wolf, H. F. Poulsen, M. Ohler, U. Lienert, and R. A. Owen. J. Synchrontron Rad. in press.
13. H. F. Poulsen, S. F. Nielsen, E. M. Lauridsen, U. Lienert, R. M. Suter, and D. Juul Jensen, submitted.

A11

Available online at www.sciencedirect.com
SCIENCE DIRECT®
Pergamon
Acta Materialia 51 (2003) 4423–4435
Acta MATERIALIA
www.actamat-journals.com

Recrystallization kinetics of individual bulk grains in 90% cold-rolled aluminium

E.M. Lauridsen *, H.F. Poulsen, S.F. Nielsen, D. Juul Jensen

Centre for Fundamental Research: Metal Structures in Four Dimensions, Materials Research Department, Risø National Laboratory, Frederiksborgvej 399, DK-4000, Roskilde, Denmark

Received 27 January 2003; received in revised form 7 May 2003; accepted 14 May 2003

Abstract

The recrystallization kinetics of a 90% cold-rolled commercial aluminium alloy AA1050 annealed at 270 °C has been investigated by use of 3-dimensional X-ray diffraction (3DXRD) microscopy. For the first time growth curves of a large number of individual bulk grains have been measured in situ during recrystallization providing unique information on the nucleation and growth behaviour of the individual grains. From observations of 244 individual growth curves, it is found that each grain has its own growth kinetics. The orientation dependencies of the recrystallization kinetics are investigated by grouping the measured growth curves into *cube*, *rolling* and *other* orientation classes. Based on analysis of the growth curves, distributions of nucleation time, grain size and growth rate has been derived, and are used for a discussion of the recrystallization kinetics of aluminium AA1050.

Keywords: Recrystallization; Synchrotronradiation; X-ray diffraction; Nucleation; Aluminium

1. Introduction

During recrystallization new strain free grains nucleate and grow in a deformed matrix. One of the fundamental questions is how the *individual* grains grow in the deformed microstructure and in spite of great effort this question is still not solved [1]. A main reason for this is experimental limitations given by the available characterization techniques. The experimental studies of the recrystallization process have been typically based on microscopy techniques such as optical microscopy or electron microscopy. Common for the microscopy techniques is that they provide high spatial resolution but only of the surface of the samples. As such they are ideal for static characterization at discrete processing intervals, but not for in situ characterization of the dynamics of structural development in the bulk.

By optical microscopy, the classic Beck experiment [2] has revealed that all grains may not grow with the same rate and the crystallographic orientation of a grain may be an important parameter affecting the growth rate (e.g. [3]). However, sample purity and annealing temperature may also be of importance [4,5]. In heavily deformed polycrys-

* Tel.: +45-4677-5760; fax: +45-4677-5758.
E-mail address: erik.mejdal@risoe.dk (E.M. Lauridsen).

1359-6454/03/$30.00
doi:10.1016/S1359-6454(03)00278-7

tals, the extended Cahn-Hagel method [6] has revealed that sometimes growth rates vary with orientation [7], whereas for other sample material or processing conditions it does not [8,9]. However these types of measurements only give information on the *average* growth rate of grains within given orientation classes, and not on the growth of individual grains. It is therefore not known how large the variations, if any, are between grains in general or between grains within one orientation class.

Detailed characterization of the deformation microstructure in typical metals and alloys deformed to medium to high strain have shown that the original grains are heavily subdivided by deformation induced dislocation boundaries and that there are significant local variations (for an overview see e.g. [10]). Given that the growth rate of a given grain during recrystallization depends on the local deformed microstructure surrounding the grain, which defines both the driving force and the mobility (misorientation), it is likely that there will also be significant variation in the growth rates of different grains.

It is now possible to non-destructively measure the growth kinetics of individual bulk grains in situ by 3-dimensional X-ray diffraction (3DXRD) microscopy. A preliminary study using 3DXRD focusing on six grains in the bulk of an aluminium sample showed that these six grains all grew with different rates [11].

The aim of the present work is to use 3DXRD for an analysis of the nucleation and growth of a statistically significant number of grains. The sample material chosen for this investigation is the same as used in the preliminary study [11] as well as in a detailed study using the extended Cahn-Hagel method to determine the average growth rate [12,13]. This choice ensures validation of the new type 3DXRD data against results obtained by a well-established method.

In this paper, the nucleation and growth of 244 individual grains are followed in situ. Distributions of nucleation times, of the evolution in grain size as well as of growth rates are determined. Also the effect of crystallographic orientation is investigated. The results are compared to the previous results obtained by the electron back-scattering diffraction (EBSD) technique [12,13]; reasons for the observed variation are discussed as are the implications on orientation dependencies.

2. Experimental

2.1. Material

The AA1050 aluminium alloy used in the current study was continuously cast, annealed at 600 °C followed by slow cooling and hot rolling at 400 °C to 75% reduction. Finally the material was recrystallized at 450 °C for 1 h (for further details see [12]). The treatment resulted in a material with a weak initial texture and a uniform distribution of second phase particles with an average diameter of 1.7 μm. The average recrystallized grain size was 100 μm [12].

For the present investigation, this starting material was cold-rolled to a thickness reduction of 90%. Samples were cut from the centre of the cold-rolled sheet having dimensions of 8 mm along the rolling direction (RD), 1 mm along the transverse direction (TD), and 3 mm along the normal direction (ND). A series of partly recrystallized samples were characterized using EBSD [14] in a JEOL 840 scanning electron microscope prior to the synchrotron experiment. The volume fractions recrystallized vs. annealing time were estimated according to the procedure devised by Krieger Lassen and Juul Jensen based on the measured orientation imaging maps (OIMs) [15]. A total of four samples were investigated during the synchrotron experiments.

2.2. 3DXRD measurements

The experiments were performed using the 3DXRD microscope situated at the Materials Science beam line at the European Synchrotron Radiation Facility (ESRF) in Grenoble, France [16,17]. The basic idea behind the experiment was to measure the diffracted intensity of a number of individual reflections during annealing. A complete measure of the recrystallization kinetics of the individual nuclei from the moment they nucleate until they reach their final recrystallized grain size is obtained exploiting the fact that the diffracted

intensity is proportional to the volume of the associated nucleus/grain.

The experimental set-up is shown in Fig. 1. True bulk characterization was ensured by use of high-energy X-rays ($E = 50$ keV), which provides a penetration depth of more than 1 cm in aluminium. A wide beam with a homogeneous profile illuminated the sample. A set of slits in front of the sample was used to define a 100 μm × 100 μm × 1000 μm illuminated channel through the sample, where the last dimension is given by the thickness of the sample. The sample was mounted in an X-ray transparent furnace. The furnace is operated in an inert gas atmosphere and has a heating rate of approximately 150 °C/min. It is capable of keeping the temperature constant within ±0.5 °C. The furnace was mounted on top of a sample stage with motorised (x,y,z)-translations and an ω-rotation (see Fig. 1 for definitions). The diffracted signal was recorded by a 14-bit fast readout Frelon CCD coupled to an image intensifier.

During the experiment, the sample was annealed in situ at 270 °C while diffraction images were acquired repeatedly cycling through a number of consecutive ω-positions. The integrated intensity was obtained by oscillating the sample by $\Delta\omega$ at each ω-position, where $\Delta\omega$ is the angular distance between two consecutive ω-positions.

Only grains fulfilling the Bragg condition will give rise to diffraction for a given ω-position. The experiment was restricted to a narrow ω-range around $\omega = 0$ to increase the time resolution. Hence, only a fraction of the grains inside the illuminated channel were detected.

An example of the acquired images is shown in the right part of Fig. 1. Each of the rings corresponds to a family of reflections, i.e. {1 1 1}, {2 0 0}. The image shown was acquired when the sample was partly recrystallized. Hence, the diffracted signal consists both of continuous broad arc-segments originating from the deformed matrix and sharp spots originating from the emerging new grains [18].

In addition to the kinetics reflected by the intensity changes of the diffraction spots, information on the orientation of the diffracting grain was obtained from the position of the diffraction spot. A one-to-one correlation between the detector-coordinates of a diffraction spot and the coordinates in the corresponding pole figure is obtained by a stereographic projection of the scattering vector onto the (RD,TD)-plane of the sample [19–21]. In the present study, the samples were mounted with the TD-direction along the x-axis (parallel to the X-ray beam), the ND-direction along the y-axis and the RD-direction along the z-axis. This corresponds to measurements along two slightly curved lines aligned with the RD-axis in the pole figures for $\omega = 0$ [20].

It must be verified that the grain is fully contained within the illuminated channel and that the intrinsic orientation spread is fully covered by the angular oscillation range to ensure that the integrated intensity of a given diffraction spot is pro-

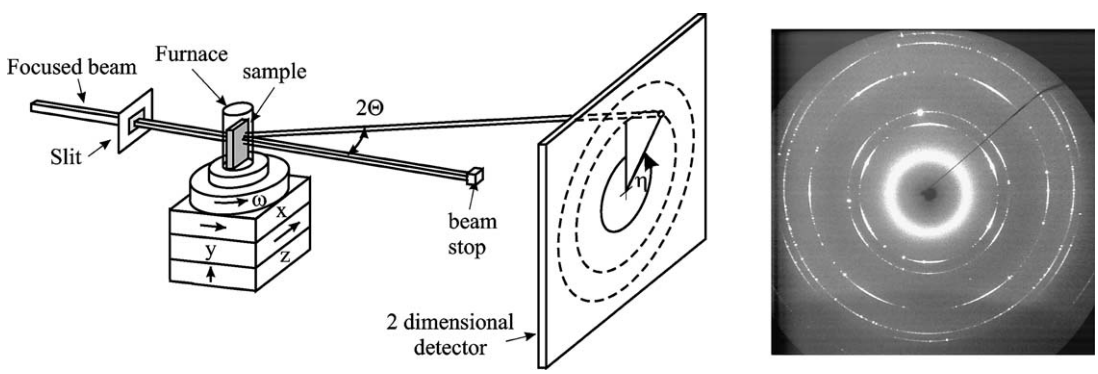

Fig. 1. Left: Experimental set-up at the 3DXRD microscope for measuring growth curves. Right: An example of the raw data from a partly recrystallized sample.

portional to grain volume. The first criterion was validated by regularly opening up the slits in both directions, and hence illuminating a wider channel through the sample. If opening up the slits resulted in an increase in the integrated intensity, the grain was not fully imbedded in the gauge volume and was therefore rejected. An example of a grain dissatisfying this criterion is shown in Fig. 2. This procedure also prevents grains growing into the illuminated channel from neighbouring volumes to be incorrectly treated at new nucleation events. The second criterion was validated by the use of consecutive ω-settings and by requiring that no tails from a diffraction spot was present in the images taken at neighbouring ω-settings. Hence, the first and last ω-settings were used only for validation purposes.

Finally, the measurement of bulk behaviour was ensured by the fact that the thickness of the sample was much larger than the grain size, and thereby the fraction of surface grains was negligible compared to the fraction of bulk grains. An alternative way of avoiding contributions from surface grains is by use of a conical slit [22], this will, however, increase the complexity of the experimental set-up and was not used in the current experiment.

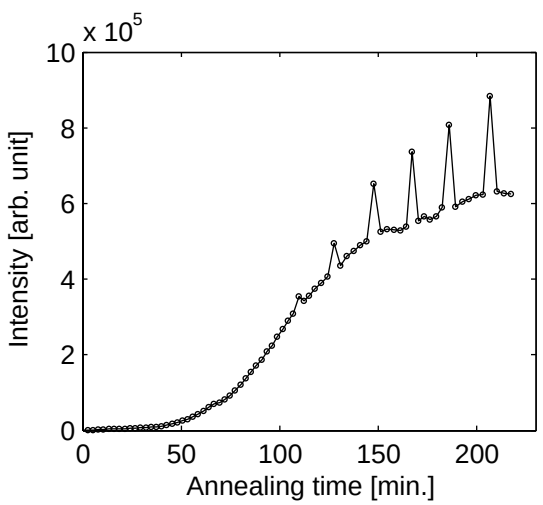

Fig. 2. Example of a grain not satisfying the position validation criteria. In the beginning of the annealing the grain lies entirely inside the illuminated channel but after approximately 100 min annealing the grain starts to grow outside the channel apparent by the increase in intensity at the validation points.

2.3. Data analysis

The analysis of the integrated intensities of the diffraction spots originating from the recrystallizing grains requires that they can be separated from the diffraction signal of the deformed matrix. This was done utilizing the fact that the texture of the deformed matrix is a slowly varying function compared to the sharp Bragg peaks from the recrystallizing grains. Growth curves of the individual grains were obtained by integrating the background corrected intensities of the corresponding diffraction spots as a function of annealing time and converting them into grain volumes. To simplify the data analysis, only diffraction spots that were well separated from neighbouring ones were included. See [19] for detailed information.

3. Results

3.1. Overall recrystallization kinetics

A total of 244 valid individual growth curves were extracted using the procedure outlined above. A random subset of the measured growth curves is shown in Fig. 3. Inspection of the growth curves clearly reveals that every grain has its own kinetics; no two growth curves are alike. Some grains start to grow immediately after the onset of

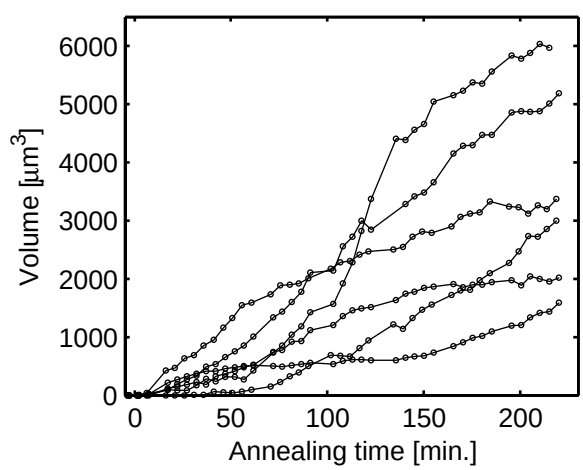

Fig. 3. A selection of the measured growth curves showing large variations in the growth kinetics of the individual grains.

annealing, whereas others have significant incubation periods before nucleation. Another interesting feature is that the growth varies substantially as a function of annealing time for some grains. As an example, some grains exhibit a fast initial growth, followed by a period with almost a stagnation of growth, after which the grains resume growth.

Apart from the direct information on the variety of growth behaviours accessible from the individual growth curves, they also form the foundation for a statistical analysis of some of the fundamental parameters describing the recrystallization process.

3.1.1. Nucleation times

By inspection of the measured growth curves, the detection limit is found to be at an equivalent sphere radius, R, of approximately 1 μm, which is comparable to or slightly smaller than the nuclei size found by TEM in similar materials [23]. Hence, by defining the nucleation time t_{nuc} as the time where the radius of the grains has just exceeded the detection limit (here $R(t_{nuc}) = 1.3$ μm) the nucleation times were determined for all 244 analysed grains. The result is shown in Fig. 4. From the distribution of nucleation times, it is clear that the majority of the nuclei nucleate within the very early stage of the recrystallization (about 80% nucleate within the first 10 min corresponding to a volume fraction recrystallized, $V_V < 0.10$). There are, however, a number of nuclei with nucleation times up to 75 min, corresponding to $V_V \approx 0.35$.

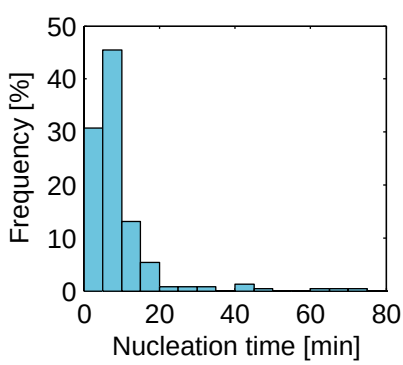

Fig. 4. Distribution of nucleation times determined from 244 individual growth curves.

3.1.2. Growth rates

The growth kinetics of the individual grains can be quantified by means of a derived "growth rate". The growth rate of a grain after a given time, t, of growth is determined by first transforming the grain volume into an equivalent grain radius, R. The growth rate is then given by the tangent ($\mathrm{d}R/\mathrm{d}t$) of the radius curve vs. time. Fig. 5 shows the obtained growth rates at $t = 10$ min ($V_V = 0.10$). It is seen that the spread in growth behaviour observed for the few selected grains in Fig. 3 is a real feature of the recrystallization kinetics. The mean and maximum growth rate of the distribution is found to be 2.5×10^{-3} and $7.3 \times 10\mathrm{m}^{-3}$ μm/s, respectively. It has to be noted that impingement between neighbouring grains cannot be detected with the present set-up. Therefore, the growth rate is determined at an early stage of the recrystallization process where impingement is assumed negligible.

3.2. Orientation dependence

Based on the pole figure coordinates (α, β) associated with each growth curve, the measured growth curves were examined for orientation dependencies of the recrystallization process. To classify the grains, the following three orientation classes were used: *cube* {1 0 0}<0 0 1>, *rolling* (consisting of Br {1 1 0}<1 1 2>, S {1 2 3}<6 3 4> and Cu {1 1 2}<1 1 1>), and

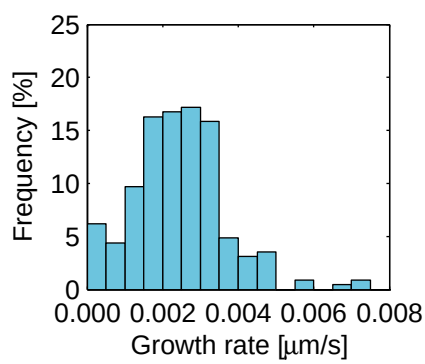

Fig. 5. Distribution of growth rates after 10 min of annealing corresponding to a volume fraction recrystallized of 0.10. Due to the limited degree of impingement at this early stage of the recrystallization process, the distribution may be taken as the real "free to grow" growth rate distribution.

Table 1
Result of the orientation analysis of the 244 grains based on their pole figure projection

Orientation class	Number of grains
Cube orientation	14
Rolling orientations (Br, S, and Cu)	124
Other orientations	106
Total	244

other, sometimes referred to as *random*, which consists of everything not belonging to the *cube* or *rolling* orientations. An angular deviation of 10° from the ideal texture components was allowed and in cases when the pole figure projection lies within 10° of several standard texture components the closest projection was chosen. The result of the grouping is summarized in Table 1. The distribution of grains between the three orientation classes does not necessarily reflect the macroscopic texture of the sample, but is given by the part of orientation space investigated (cf. Section 2.2).

3.2.1. Individual growth curves

The measured growth curves of the 14 *cube* grains are shown in Fig. 6. As in the case of the randomly selected grains shown in Fig. 3, the *cube* grains also shows a large variation in growth behaviour.

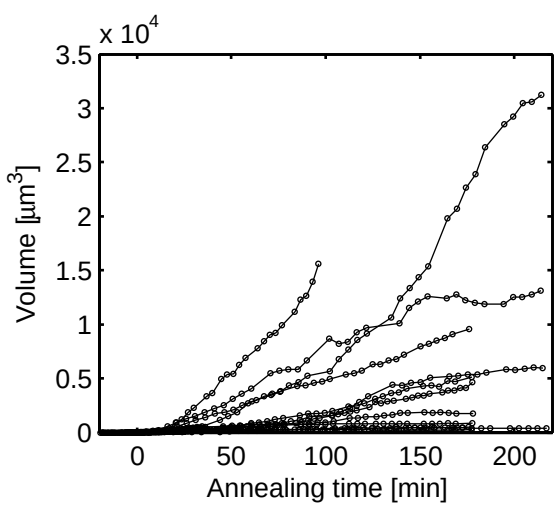

Fig. 6. Growth curves for the 14 grains observed with *cube* orientation. The different durations of the growth curves is caused by different annealing times of the four samples, or due to the fact that a grain no longer satisfy the validation criteria (see Fig. 2).

3.2.2. Nucleation times

The distribution of nucleation times shown in Fig. 4 was examined with regard to the three orientation classes. As seen in Fig. 7 the time dependence of the nucleation behaviour for the three orientation classes appear similar. The obtained mean values for the distributions are 7 min for the *cube* grains and 9 min for the *rolling* and *other* grains. A noticeable difference is that none of the grains having significant retarded nucleation was found among the *cube* grains. This can, however, simply be related to the poor statistics of the *cube* grains. The fact that the time dependence of the nucleation behaviour is fairly similar for the three orientation classes is supported by the results of a Kolmogorov–Smirnov (K–S) test, which is a statistical test used to see if two distributions are consistent [24]. The results of the pair wise K–S test of the three distributions in Fig. 7 are shown in Fig. 8. For the K–S test of *cube* vs. *rolling* (Fig. 8a) and *cube* vs. *other* (Fig. 8b) it is found that the probabilities of the two distributions being identical given the limited counting statistics are 53% and 94%, respectively. For the K–S test of *rolling* vs. *other* (Fig. 8c), the corresponding probability is 19% indicating that the two distributions may not be strictly identical. However, it is seen that both distributions have similar shape and mean value from inspections of the corresponding cumulative distribution functions (Fig. 8c).

3.2.3. Grain sizes

The final recrystallization texture of the AA1050 alloy is dominated by a *cube* texture and a retained *rolling* texture [7]. The late stages of the growth curves were examined with respect to the different orientation classes to check whether this finding is related to an orientation dependence of the final recrystallized grain sizes. The result of the investigation is shown in Fig. 9. There is a significant spread in the grain sizes *within* each orientation class reflecting the observed variety in growth behaviour. The average grain sizes for the *cube*, *rolling* and *other* orientations at this late stage of

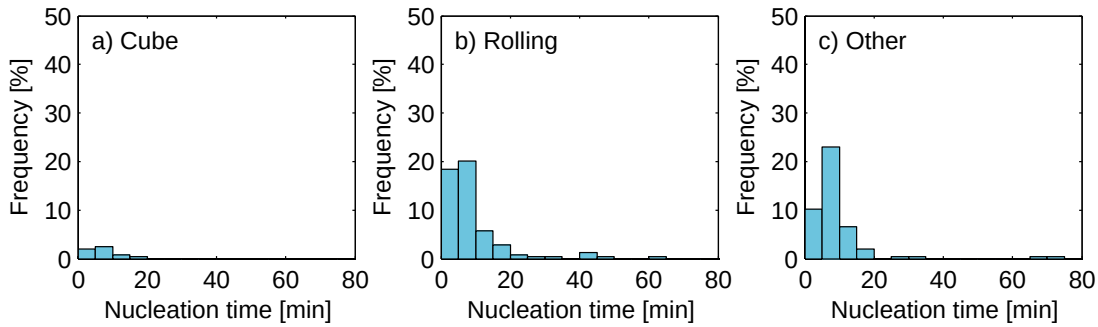

Fig. 7. Orientation dependence of the nucleation times. The data has been grouped into (a) *cube* grains, (b) *rolling* grains, and (c) *other* grains. The frequency shown on the *y*-axis is referring to the total number of grains, i.e. 244, hence the sum of the three distributions gives the distribution shown in Fig. 4.

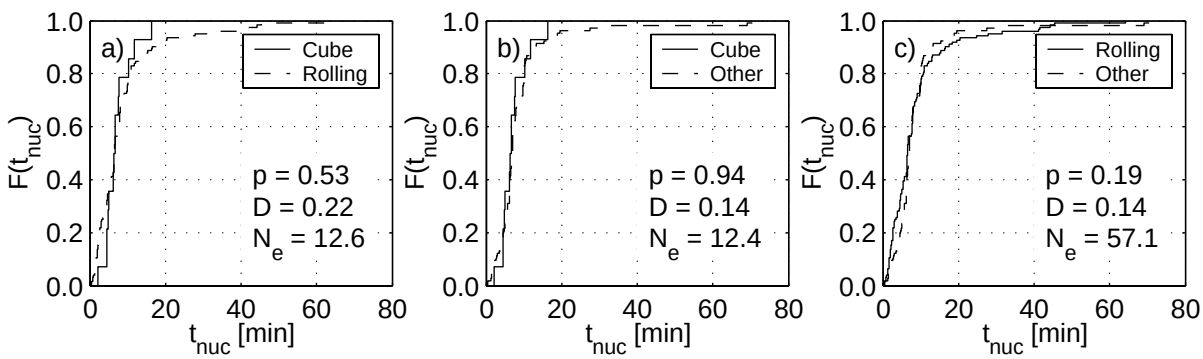

Fig. 8. Plots of the pair wise comparison of the cumulative distribution functions for the distributions shown in Fig. 7. These are used in the Kolmogorov–Smirnov tests for (a) *cube* vs. *rolling*, (b) *cube* vs. *other* and (c) *rolling* vs. *other*. Also shown is the probability, *p*, that the two data sets are drawn from the same distribution, the maximum distance between the cumulative distribution functions, *D*, and the effective number of data points, N_e [25].

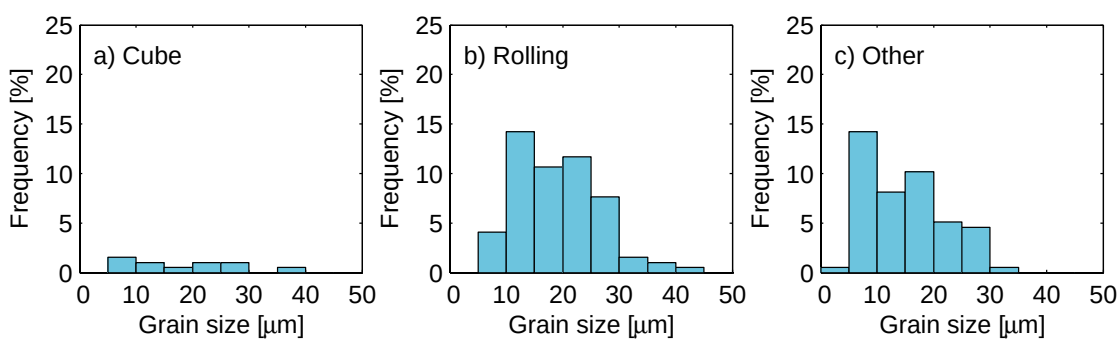

Fig. 9. Orientation dependence of the grain size after 175 min of annealing for (a) *cube* grains, (b) *rolling* grains, and (c) *other* grains. The frequency shown on the *y*-axis is referring to the total number of grains.

the recrystallization process ($t = 175$ min) are 18.7, 19.2 and 15.0 μm, respectively.

Information concerning the orientation dependence of the grain size evolution can be obtained by analysing the grain size distribution of the individual orientation classes as function of annealing time. This is illustrated in Fig. 10 where the average equivalent grain diameter for the different orientation classes are shown as a function of annealing time. As seen in this figure, the measured average grain sizes of grains having *cube* or *rolling* orientation end up being approximately 1.3 times larger than that for grains having *other* orientations.

3.2.4. Growth rates

The growth rate distribution after 10 min of annealing shown in Fig. 5 was examined with respect to orientation dependence. The result of the analysis is shown in Fig. 11. As with the grain size distributions shown in the previous section these results also show a significant spread within the individual orientation classes. The average growth rates are 2.9×10^{-3} μm/s for *cube* grains, 2.6×10^{-3} μm/s for *rolling* grains and 2.3×10^{-3} μm/s for *other* grains.

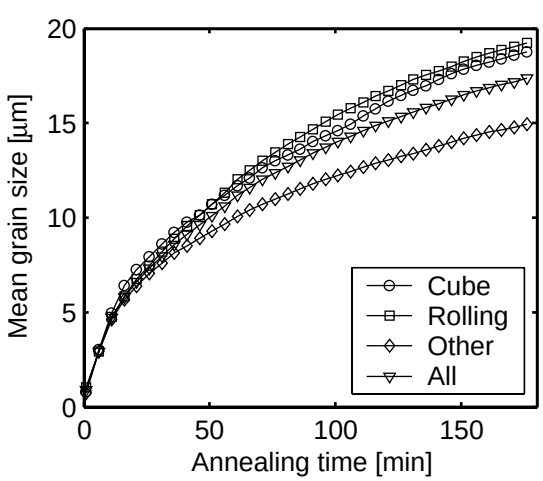

Fig. 10. Evolution of the mean grain size (equivalent sphere diameter) for grains of different orientations during recrystallization. The *cube* and *rolling* grains are found to become significantly larger than grains having *other* orientations.

3.2.5. Impingement

As mentioned in Section 3.1.2, the present technique does not allow for the impingement between grains to be measured directly. Some information on the impingement behaviour can, however, be obtained indirectly by looking at the evolution of the growth rate distribution. Given that the time dependence of the nucleation behaviour is similar for all orientation classes (cf. Section 3.2.2), and assuming that any concurrent recovery taking place during the annealing will happen uniformly throughout the sample, any observed differences in the decrease of the average growth rate of the different orientation classes may be ascribed to differences in the impingement conditions, hence to differences in the spatial distribution of the nuclei. The evolution of the average (impingement influenced) growth rate is plotted in Fig. 12 as a function of annealing time for the three different orientation classes. Apart from the absolute values of the growth rates, the average growth rates of the different texture components seem to decrease in a similar manner.

4. Discussion

4.1. The 3DXRD technique

On one hand, electron microscopy provides detailed static characterization of the microstructure on a plane of polish, and on the other hand neutron diffraction provides in situ characterization of the evolution of the overall bulk texture. Both techniques provide important information on the recrystallization process, but a need exists for in situ characterization of the growth of individual bulk grains.

The results presented above show that the 3DXRD microscope is capable of providing such information. Using this technique, it is possible to measure in situ the growth of a large number of individual bulk grains. Based on investigations of the measured growth curves, information regarding the growth kinetics can be obtained, including important parameters such as time of nucleation, growth rate and grain size of individual grains in the bulk. In addition, the technique provides infor-

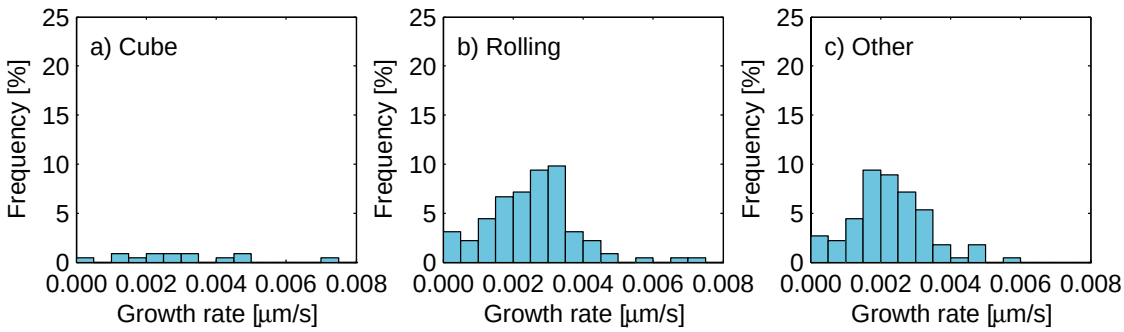

Fig. 11. Orientation dependence of the growth rate after 10 min of annealing for (a) *cube* grains, (b) *rolling* grains, and (c) *other* grains. The frequency shown on the *y*-axis is referring to the total number of grains, hence the sum of the three distributions gives the distribution shown in Fig. 5.

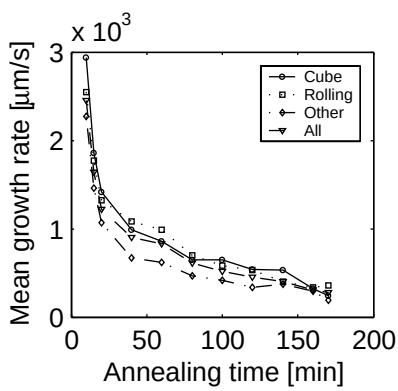

Fig. 12. Evolution of the growth rate during recrystallization. The growth rate values plotted are affected by impingement and no impingement corrections are applied.

mation on the orientation of the grains allowing investigations of orientation dependence on the growth kinetics.

The limitations of the technique, in its present state, include the need for compromises between the part of orientation space that is probed and the time resolution achieved. This means that not all grains, but only a certain subset, have been monitored in the present investigation. Ongoing development of the 3DXRD microscope, however, has resulted in a significant increase in the acquisition speed thereby allowing for a larger part of orientation space to be covered without decreasing the time resolution. Another limitation is that the partial information on grain orientation that can be derived from a single Bragg reflection may not be sufficient for some purposes. Algorithms have however been developed which allow the full orientation of the grains to be determined [25]. Together, these improvements will enable a complete classification with regard to the orientations present in the sample. Furthermore, it is believed that these improvements will enable the monitoring of all grains within the given gauge volume, and not only a certain subset as in the current study, thereby allowing the nucleation rates to be determined. This will also allow for an investigation of the number frequency of nuclei belonging to the different orientation classes to see if there are any preferred orientations [26]. Finally, the fact that the presented technique does not provide spatial information on the location of the nuclei/grains makes the interpretation of the measured growth curves somewhat more difficult. This is believed to be overcome in future experiments by combining the described technique for measuring grain kinetics with other techniques developed for the 3DXRD microscope which provide *non-destructive* spatial information on the individual grains [27,28].

4.2. Kinetics of individual grains

The present study reveals that none of the 244 measured growth curves is identical. In other words, each recrystallizing grain has its own nucleation and growth characteristics. The same conclusion was reached in the preliminary work using the same technique and material but monitor-

ing only six individual grains [11]. It is thus now considered proven that this conclusion was real and not an artefact caused by the limited number of observations.

The present result for the 244 grains shows that most of the nuclei (about 80%) form early in the recrystallization process at annealing times less than 10 min, i.e. at V_v values below 0.1. To a first approximation, site saturation is thus a reasonable assumption for the observed nucleation. This is encouraging as most recrystallization modelling is applying this assumption [29,30]. In particular, it verifies the previous microstructural path modelling result of the present sample material [31], which showed that a good match between stereologically determined microstructural parameters could be obtained assuming site saturation [12]. The present AA1050 material contains approximately 0.5 vol% second phase particles with an average size of 1.7 μm [7]. These second phase particles are large enough to act as preferential nucleation sites and particle stimulated nucleation (PSN) [32] is therefore assumed to be the dominating nucleation mechanism in the material [12]. As PSN is generally considered to lead to rapid nucleation [32], the present direct observation of site saturation is in good agreement with this assumption.

Remaining are, however, about 20% of the nuclei which are observed to form later in the recrystallization process; some form as late as 75 min after the annealing has started when the material is approximately 35% recrystallized. The nucleation sites of these late nuclei are not known and the spatial resolution of the 3DXRD microscope achieved so far does not allow an experimental investigation of this.

It is however clear that the distribution of nucleation times is a fairly continuous function of time (see Fig. 4) and the nucleation is likely to occur in sequential order: the first nucleus at the best site which could be the largest particle, a group of particles or a particle situated near another preferential nucleation site, e.g. a grain boundary [33], the second nucleus at the next best site etc. So the smaller particles or less good nucleation sites in the deformed matrix may be activated later in the recrystallization process.

The measured kinetic curves show very large variations in growth rates: every grain grows with a rate different to that of the others and the growth rate for a given grain varies with time having a periodicity not matching other grains.

That the growth rates vary with time for the individual grains is not too surprising considering the heavy subdivision of the deformation microstructure after 90% rolling reduction [34]. Earlier observations have shown that after such strain, the deformation microstructure is subdivided by deformation induced dislocation boundaries with very large misorientations across the boundaries. In the present material, it is observed that the distance between high angle boundaries on average is 2.3 μm along the normal direction and 4.4 μm along the rolling direction [35]. A nucleus will thus be surrounded by matrix material with different orientations at different parts of its periphery and the surroundings will constantly change during its growth. As these deformation surroundings may affect the local stored energy and thus the driving force for recrystallization, as well as the misorientation across segments of the nucleus boundary and thus the mobility, the boundary velocity will also be affected. Such an effect of the local variations in deformation microstructure on the overall increase in volume of a given recrystallizing grain, will be most dominating for small grain sizes, where the size of the recrystallizing grain is comparable to the scale of the subdivision of the deformation microstructure.

The measured kinetics curves not only show variations with time for the individual grains but also large variations between the grains: not any two grains of the 244 studied have the same curve. It is clear that some of this variance relate to the actual orientation of the grain. It is for example shown that on average the *cube* oriented grains grow faster and become larger than the *other* grains (see Fig. 10). There are also very large variations even within just one orientation category (see Fig. 6) and therefore effects of the surrounding deformation microstructure have to be considered. The small-scale effects of this have already been discussed, but also on a larger scale, e.g. on the scale of the original grain size, it will contribute to the individual nature of the growth of the grains. From

single crystal work, it is known that different crystallographic orientations may lead to different dislocation boundary morphologies with different stored energy [36,37]. For example, it is generally found that the stored energy in crystals with *brass* orientation is lower than for *S* orientations. Also in polycrystals such variations are seen and it has been shown that even after large strain deformation ($\varepsilon > 2$), the deformation microstructure "remembers" the original grain structure in the sense that the elements (e.g. cell blocks) of the microstructure are not randomly mixed but relate to the original grain orientation [38,39]. It is therefore to be expected that a grain of a given orientation nucleated for example in an original *brass* grain will grow differently from a similar one nucleated in an original grain of another orientation. Here also the actual misorientation between the recrystallizing grain and the surrounding deformation matrix would play a role. If misorientations favourable for growth form, fast growth is expected whereas if a lower angle boundary is surrounding the recrystallizing grain partly or fully, orientation pinning [7,40] occurs and therefore slower growth may be observed.

It is still an open question if growth variations as observed in this investigation are a general phenomenon or not. However, if they are, this can have significant consequences for modelling recrystallization. In a recent microstructural path modelling investigation, it has been shown that a distribution of growth rates may lead to deviations from the usual kinetics curves for example leading to transients in the overall kinetics [41].

4.3. Comparison with EBSD results

The choice of the AA1050 alloy was primarily motivated by the fact that the exact same material has been thoroughly characterized by Juul Jensen and Vandermeer using both neutron diffraction and linear intercept measurements with the EBSD technique [42]. They found that annealing at 280 °C leads to a change in the volume fraction of *cube* grains from virtually zero in the as-deformed sample to approximately 10% in the fully recrystallized sample [7]. This has been correlated to an average growth advantage of grains belonging to the *cube* texture component as compared to grains of *other* orientation [42]. A later study by the same authors, on the same alloy but using lower annealing temperatures (245–265 °C), however, did not reveal any growth advantages for the *cube* grains. Why this discrepancy between high and low annealing temperatures is observed is still not well understood.

In the following a comparison of the results of the current study and those of the investigations of Vandermeer and Juul Jensen [12,13] will be made. In the current study, the average growth rate at $V_v \approx 0.10$ is 2.5×10^{-3} μm/s with an annealing temperature, *T*, of 270°C. This value falls nicely between the corresponding values of the Cahn-Hagel growth rates obtained for $T = 265$ and $T = 280$ °C by Vandermeer and Juul Jensen [12]. Also the observation that the average growth rate for *cube* grains is 1.3 times the average growth rate of *other* grains, is consistent with the observation by Vandermeer and Juul Jensen. They find an average growth advantage of *cube* grains of 1.5 at $T = 280$ °C [13]. With respect to grain sizes, the obtained ratio of 1.3 between the average recrystallized grain size ($V_v \approx 0.90$) of the *cube* grains and *other* grains in the current study is in nice agreement with the value of 1.4 at $T = 280$ °C found by Juul Jensen [7].

The observed growth and size advantage for the *rolling* grains is however a new finding, and is in disagreement with the observations of Vandermeer and Juul Jensen [7,13].

One possible explanation of this discrepancy could be related to the fact that the set-up used in the present investigation only probes a small part of orientation space (cf. Sections 2.2 and 4.1). As a result, there is a larger probability of measuring *copper* and *brass* grains than measuring grains having *S*-orientation. Hence, the range of measured *rolling* orientations of our paper differs from the work by Juul Jensen and Vandermeer using EBSD [7]. A related concern is the ambiguity in classifying reflections on Debye-Scherrer rings with high multiplicity (e.g. {3 1 1} reflections). To test the significance of this ambiguity the data analysis were repeated excluding all {3 1 1} reflections. However, similar conclusions regarding the orientation dependence of the recrystallization kinetics

were reached irrespective of the {3 1 1} reflections being included in the data analysis or not. It should be noted that both issues are likely to be avoided in future experiments due to the recent improvements of the 3DXRD technique as described in Section 4.1. Finally, since only diffraction spots well separated from neighbouring spots in orientation space were included in the analysis (cf. Section 2.3) biasing of the sampling of grains belonging to the relatively strong retained *rolling* texture was inevitable. Further development of the analysis routines is currently taking place to remove such biasing in future experiments.

4.4. Why larger cube grains?

Investigation of orientation distribution functions (ODFs) measured with EBSD showed that the volume fraction of the *cube* orientation changed from virtually nothing to approximately 5% after annealing at 270 °C. Investigation of the measured growth curves of the individual grains showed that the strengthening of the *cube* texture found in the ODF might be related to the observed larger mean *cube* grain size. A larger mean grain size can be obtained by one of the following three mechanisms or a combination of these; (1) early nucleation, (2) higher growth rate, or (3) less impingement.

From an analysis of the data depicted in Fig. 7, it was found that the time dependence of the nucleation behaviour for the three orientation classes were similar. Hence, mechanism 1 is not likely to explain the observed size advantage of the *cube* grains. The investigation of the initial growth rate (believed to be the "true" growth rate) revealed that *cube* grains on average have a higher growth rate than *other* grains (cf. Fig. 11). Hence, mechanism 2 might explain the observed size advantage. Finally, investigations of the evolution of the average growth rates as a function of time indicate that the impingement conditions are the same for the three investigated orientation classes (cf. Fig. 12), and as such mechanism 3 does not seem to contribute to the observed size advantage of the *cube* grains. Hence, preferential growth is found to be the main mechanism responsible for the observation of an average size advantage of the *cube* grains in 90% cold-rolled AA1050 commercial purity aluminium when annealed at 270 °C.

5. Summary and conclusions

The nucleation and growth of individual bulk grains in 90% cold rolled aluminium have been followed in situ during recrystallization at 270 °C by 3DXRD microscopy.

It was found that

- 3DXRD is a powerful tool for investigations of recrystallization kinetics. It enables, for the first time, in situ measurements of nucleation times and real 3D sizes for a large number of individual bulk grains during recrystallization. From these data (impingement influenced) growth rates for the individual grains can be derived and the evolution of the grain size distribution monitored. Furthermore, information on the crystallographic orientation is obtained and can be used for investigations of orientation effects.
- Each grain is characterized by its own nucleation and growth kinetics. The growth rate not only varies between grains, but also in time. These variations are related to the fine and medium scale heterogeneities of the deformed microstructure. Such observations are in clear contradiction to the classical models of recrystallization kinetics, which assume identical growth behaviour for all grains.
- To a first approximation, site saturation is a reasonable assumption for the nucleation rate in the present material as 78% of the nuclei form within the first 10 min of annealing ($V_v < 0.1$). A remarkable observation is, however, that the remaining 22% form over a significant time interval, which may be related to less potential nucleation sites.
- The crystallographic orientation is observed to affect the growth rate of grains, although even within a single orientation class, there are significant variations in nucleation and growth of the individual grains.
- On *average* the *cube* grains grow to become larger than grains of *other* orientations. By analysing the individual kinetics curves, it is concluded that a growth advantage of the cube grains is at least part of the explanation.

Acknowledgements

The authors gratefully acknowledge the Danish National Research Foundation for supporting the Centre for Fundamental Research: Metal Structures in Four Dimensions, where this work was performed. Additional support for this work was provided by the Danish research council SNF (via Dansync). The authors thank S. Schmidt and L. Margulies for help with the synchrotron experiment and R.D. Doherty, W. Pantleon and R.A. Vandermeer for valuable discussions.

References

[1] Doherty RD, Hughes DA, Humphreys FJ, Jonas JJ, Juul Jensen D, Kassner ME et al. Mat. Sci. Eng. 1997;A238:219.
[2] Beck PA. Adv. Phys. 1954;3:245.
[3] Ibe G, Lücke K. Arch. Eisenhüttenwesen 1968;39:693.
[4] Aust KT, Rutter JW. Trans AIME 1959;215:119.
[5] Aust KT, Rutter JW. Trans AIME 1960;218:50.
[6] Juul Jensen D. Scr. Metall. Mater. 1992;27:533.
[7] Juul Jensen D. Acta Metall. Mater. 1995;43:4117.
[8] Magnusson H, Juul Jensen D, Hutchinson B. Scr. Mater. 2001;44:435.
[9] Vandermeer RA, Juul Jensen D. Acta Mater 2003;51(10):3005–18.
[10] Hansen N. Metall. Mater. Trans. 2001;A32:2917.
[11] Lauridsen EM, Juul Jensen D, Poulsen HF, Lienert U. Scr. Mater. 2000;43:561.
[12] Vandermeer RA, Juul Jensen D. Acta Mater. 2001;49:2083.
[13] Vandermeer RA, Juul Jensen D. Interface Sci. 1998;6:95.
[14] Krieger Lassen NC, Juul Jensen D, Conradsen K. Scan. Microsc. 1992;6:115.
[15] Krieger Lassen NC, Juul Jensen D. In: Szpunar JA, editor. Proceedings of the 12th international conference on textures of materials. 1999. p. 854–9.
[16] Poulsen HF, Garbe S, Lorentzen T, Juul Jensen D, Poulsen FW, Andersen NH et al. J. Synch. Rad. 1997;4:147.
[17] Juul Jensen D, Kvick Å, Lauridsen EM, Lienert U, Margulies L, Nielsen SF, et al. Mat Res Soc Symp Proc 2000;227–40.
[18] Poulsen HF, Juul Jensen D. In: Hansen N, Huang X, Juul Jensen D, Liu YL, Ralph B, editors. Microstructural and crystallographic aspects of recrystallization. Roskilde, Denmark: Risø National Laboratory; 1995. p. 503–8.
[19] Lauridsen EM. Thesis: The 3D X-ray diffraction microscope and its application to the study of recrystallization kinetics. Risø-R-1266(EN): Risø National Laboratory; 2001.
[20] Lauridsen EM, Schmidt S, Margulies L, Poulsen HF, Juul Jensen D. In: Gottstein G, Molodov DA, editors. Recrystallization and grain growth. Berlin: Springer-Verlag; 2001. p. 589–94.
[21] Mishin OV, Lauridsen EM, Lassen NCK, Bruckner G, Tschentscher T, Bay B et al. J. Appl. Cryst. 2000;33:364.
[22] Nielsen SF, Wolf A, Poulsen HF, Ohler M, Lienert U, Owen RA. J. Synch. Rad. 2000;7:103.
[23] Bay B, Hansen N. Metall. Trans. 1979;10A:279.
[24] Press WH, Teukolsky SA, Vetterling WT, Flannery BPN. Numerical recipes in FORTRAN. Cambridge: Cambridge University Press, 1992 p. 694.
[25] Lauridsen EM, Schmidt S, Suter RM, Poulsen HF. J. Appl. Cryst. 2001;34:744.
[26] Doherty RD. Scr. Metall. 1985;19:927.
[27] Poulsen HF, Nielsen SF, Lauridsen EM, Schmidt S, Suter RM, Lienert U et al. J. Appl. Cryst. 2001;34:751.
[28] Poulsen HF, Schmidt S. J. Appl. Cryst. 2003;36:319–25.
[29] Vatne HE, Furu T, Nes E. In: McNelley TR, editor. Proc ReX'96, The Third International Conference on Recrystallization and Related Phenomena. Monterey, USA: MIAS; 1996. p. 95–108.
[30] Weiland H. In: Hansen N, Huang X, Juul Jensen D, Liu YL, Ralph B, editors. Microstructural and crystallographic aspects of recrystallization. Roskilde, Denmark: Risø National Laboratory; 1995. p. 215–28.
[31] Vandermeer RA. In: Hansen N, Huang X, Juul Jensen D, Lauridsen EM, Leffers T, Pantleon W, editors. Recrystallization—fundamental aspects and relations to deformation microstructure. Roskilde, Denmark: Risø National Laboratory; 2000. p. 179–200.
[32] Humphreys FJ, Hatherly M. Recrystallization and related annealing phenomena. Oxford: Pergamon Press, 1995.
[33] Bay B, Hansen N. Metall. Trans. 1984;15A:287.
[34] Hansen N, Juul Jensen D. Phil. Trans. Roy. Soc. London 1999;A357:1447.
[35] Juul Jensen D. In: Hansen N, Huang X, Juul Jensen D, Liu YL, Ralph B, editors. Microstructural and crystallographic aspects of recrystallization. Roskilde, Denmark: Risø National Laboratory; 1995. p. 119–37.
[36] Bardal A, Lindseth I, Vatne HE, Nes E. In: Hansen N, Huang X, Juul Jensen D, Liu YL, Ralph B, editors. Microstructural and crystallographic aspects of recrystallization. Roskilde, Denmark: Risø National Laboratory; 1995. p. 261–6.
[37] Godfrey A, Juul Jensen D, Hansen N. Acta Mater. 2001;49:2429.
[38] Juul Jensen D. Mat. Sci. Eng. 1997;A234:762.
[39] Bowen JR, Mishin OV, Prangnell PB, Juul Jensen D. Scr. Mater. 2002;47:289.
[40] Doherty RD. Prog. Mat. Sci. 1997;42:39.
[41] Juul Jensen D, Lauridsen EM, Vandermeer RA. In: Ankem S, Pande CS, Ovid'ko I, Ranganathan S, editors. Science & technology of interfaces. Warrendale: TMS; 2002. p. 361–74.
[42] Vandermeer RA, Juul Jensen D. Textures Microstruct. 1996;26-27:263.

A12

Available online at www.sciencedirect.com
SCIENCE DIRECT®
Pergamon
Acta Materialia 51 (2003) 2517–2529
Acta MATERIALIA
www.actamat-journals.com

3D-characterisation of microstructure evolution during annealing of a deformed aluminum single crystal

H.F. Poulsen [a,*], E.M. Lauridsen [a], S. Schmidt [a], L. Margulies [a,b], J.H. Driver [c]

[a] *Center for Fundamental Research: Metal Structures in Four Dimensions, Risø National Lab., DK-4000, Roskilde, Denmark*
[b] *European Synchrotron Radiation Facility, BP 220, F-38043 Grenoble Cedex, France*
[c] *Ecole des Mines, St. Etienne, France*

Received 8 October 2002; accepted 10 January 2003

Abstract

The microstructure within a 3D volume of a deformed Al single crystal is studied by a novel diffraction method before and after annealing for 5 min at 300 °C. The 99.996% pure single crystal of the S-orientation was channel die deformed to a strain of ϵ=1.5, producing a cell-block structure with distances of about 1 μm between dislocation boundaries. By means of micro-focused hard X-rays from a synchrotron the orientations within a volume of $0.2 \times 0.2 \times 2$ mm^3 were mapped non-destructively. Cells or cell-blocks with orientations far from those of the principal poles can be identified individually with a resolving limit of 0.6 μm. The diffraction pattern related to these parts of the orientation distribution show little correlation between the as-deformed and annealed states. They indicate the emergence of recovered cells and/or nuclei with orientations not present in the deformed state.

Keywords: Recovery; Recrystallisation; X-ray diffraction; Aluminium; Texture

1. Introduction

When annealing deformed metals or alloys, the structural changes taking place during the early phases—recovery and nucleation—play an important role in determining the final properties. Traditionally these phenomena have been examined by either bulk probes, such as calorimetry, resistivity or hardness measurements, or by electron microscopy. Such studies have provided much important information, for instance on the processes involved in recovery and the correlation of nucleation sites with the deformed microstructure (for a review see e.g. Ref. [1]).

Nevertheless, it should be realised that both types of techniques have their limitations. Use of the bulk probes implies averaging over all the processes and over the heterogeneity of the sample. The electron microscope can only probe relatively small areas in typical heterogeneous samples, and only on sectioned surfaces. Furthermore, it is difficult to obtain realistic *in situ* information on structure evolution during annealing. In particular,

* Correspondence author. Tel.: +1-45-4677-5739; fax: +1-45-4677-5758.
E-mail address: henning.friis.poulsen@risoe.dk (H.F. Poulsen).

1359-6454/03/$30.00
doi:10.1016/S1359-6454(03)00048-X

it can be argued that the free surface will influence growth rates and that results therefore may not be representative of bulk dynamics. Moreover, dislocations will tend to migrate to the surface and the wedge-shaped specimen geometry typical of TEM samples leads to an additional driving force.

It is evident that data on the microstructure evolution within the *bulk* of the material would be a major step forward. Providing such data requires a probe that is both penetrating and able to span a large range in length scale. Note in particular that the deformed structure is characteristically subdivided on a *sub-micron scale* into what we shall call structural units (cells, cell blocks and subgrains). The annealed state is characterised by nucleation, which is a rare event. Depending on nucleation frequencies, volumes as large as 1 mm^3 need to be characterised. Hence, the probe should be able to detect volume fractions of the order of 10^{-9}.

Over the last 5 years, methods have emerged for non-destructive characterisation of well-annealed polycrystals by means of diffraction with high energy (50–100 keV) X-rays [2–7]. When generated by synchrotrons such hard X-rays exhibit a unique combination of a large penetration power—1 mm universally and up to 4 cm in light materials, such as aluminium—and high flux [2]. By focusing, three-dimensional information is provided on the length-scale of the individual grains. In connection with novel reconstruction software the position, volume, orientation and elastic strain can be determined in hundreds of grains simultaneously [3,4]. Likewise, for coarse-grained materials a three-dimensional map of the grain boundaries can be generated [4,5]. With the dedicated 3-dimensional X-ray diffraction (3DXRD) microscope at the ESRF synchrotron, these methods have been employed to *in situ* studies of the grain dynamics during recrystallisation [6,7]. The spatial resolution is a function of the available hardware, and is presently of order 5 μm [5].

This resolution is insufficient to map deformation microstructures. However the flux of a focused synchrotron X-ray beam is such that crystalline structures with a submicron size will give rise to diffraction spots. Hence, provided the orientation of a given dislocation cell or subgrain is sufficiently unique that the associated diffraction spots do not overlap with those of other units, such units are observable. This was verified recently in a feasibility experiment [8], which also demonstrated that the volume and volume fractions probed by 3DXRD match the above requirements.

In this article, we report on a first application of 3DXRD for studies of deformation microstructures. The issue of choice is an outstanding problem in recovery/recrystallisation studies: do new orientations emerge or do all the recovered cells and nuclei develop by growth of specific cells already present in the microstructure [9–13]? For this study we have chosen a cold-deformed Al single crystal of the S-orientation, a system where previous TEM investigations already had indicated that new orientations may arise during heat treatment following channel die deformation [14]. The same volume is investigated in the as-deformed state and after 5 min annealing at 300 °C. After this treatment the recrystallised volume fraction is zero within the detection limit of optical and electron microscopy. With 3DXRD the orientation distribution away from the poles is characterised. Local pole figures for these parts of orientation space change character completely.

The structure of the article is as follows. Initially, a description of the methodology is provided, including a number of details not dealt with in Ref [8]. With this background the 3DXRD results are presented. Following a discussion of instrumental limitations, an interpretation of the annealing phenomena is given based on results from both 3DXRD and electron and optical microscopy.

2. Sample

The specimens used were prepared from a single crystal of 99.996% pure aluminium of the S-orientation {123}<634>. The crystal was channel die deformed to a strain of $\epsilon = 1.5$ at room temperature using a Teflon film lubricant [15]. The crystal was cut into four pieces with a slow speed saw, and the two middle sections used for synchrotron and electron microscopy work, respectively. Both specimens had dimensions of $11 \times 7 \times 2$ mm^3 along RD, TD and ND, respectively. To avoid any poten-

tial recovery at room temperature all specimens were kept in a deep freeze before and between investigations.

The as-deformed and the annealed state were characterised by EBSP [16]. The resulting {200} pole figures are shown in Fig. 1. (Small rotations have been applied to both pole-figures to compensate for specimen misalignments.) The orientation distributions are seen to be similar, both representative of a spread S-texture. The main difference is that the spread of the annealed specimen (b) is significantly smaller than that of the as-deformed one (a). Based on the EBSP data and optical microscopy no recrystallisation has taken place after 5 min.

Additional characterisation was performed on longitudinal sections by TEM. Typical micrographs are shown in Fig. 2. The as-deformed specimen exhibits a deformation microstructure composed of two sets of extended dislocation boundaries. It appears homogeneous on a 100 μm scale. In general the microstructure is elongated along the band directions. Histograms of cell dimensions as they appear on the micrographs (linear intercept) are shown in Figs 3a and b, for the short and long direction, respectively. The average of the distributions are 0.9 and 1.5 μm, respectively. Dislocations are seen in most cells at this strain level.

The annealed specimen exhibited two types of regions. One was similar to that for the deformed specimen. The other was typical of a recovered specimen, with more equi-axed dislocation-free cells and dihedral angles around 120°. For these regions, the average linear intercept length is 1.3 μm. The largest cells seen in the micrographs had dimensions of ~ 5 μm.

3. Experimental

The 3DXRD microscope installed at the ESRF synchrotron was used. A bent Laue monochromator was used to focus the beam vertically to a spot with a width of order 15 μm. By means of a slit, placed just in front of the sample, a uniform 11 × 11 μm^2 spot was produced. The energy was 50.0 keV, corresponding to a wavelength of 0.249 Å. The divergence of the beam and the energy bandwidth were 0.2 mrad and 0.5%, respectively.

The sample was mounted in a small furnace, enabling *in situ* annealing in an inert atmosphere. The temperature was calibrated to within 5°. The furnace was fixed on a sample tower comprising

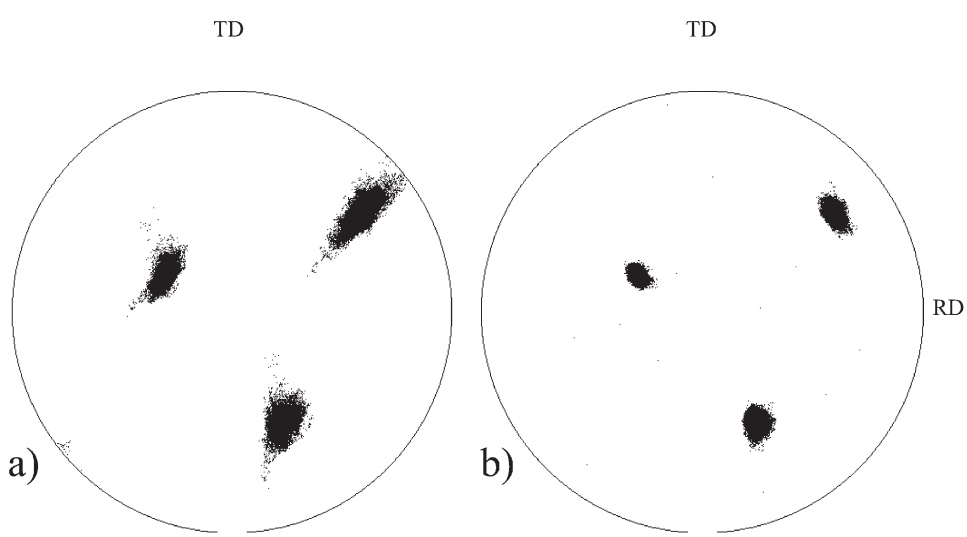

Fig. 1. {200} pole figure generated by EBSP of the $\epsilon = 1.5$ deformed Al single crystal in the as-deformed (a) and annealed state (b). With a grid size of 1 × 1 μm^2 27 000 and 66 000 orientations were measured respectively. Only data with five out of eight lines correctly indexed are included in the figure.

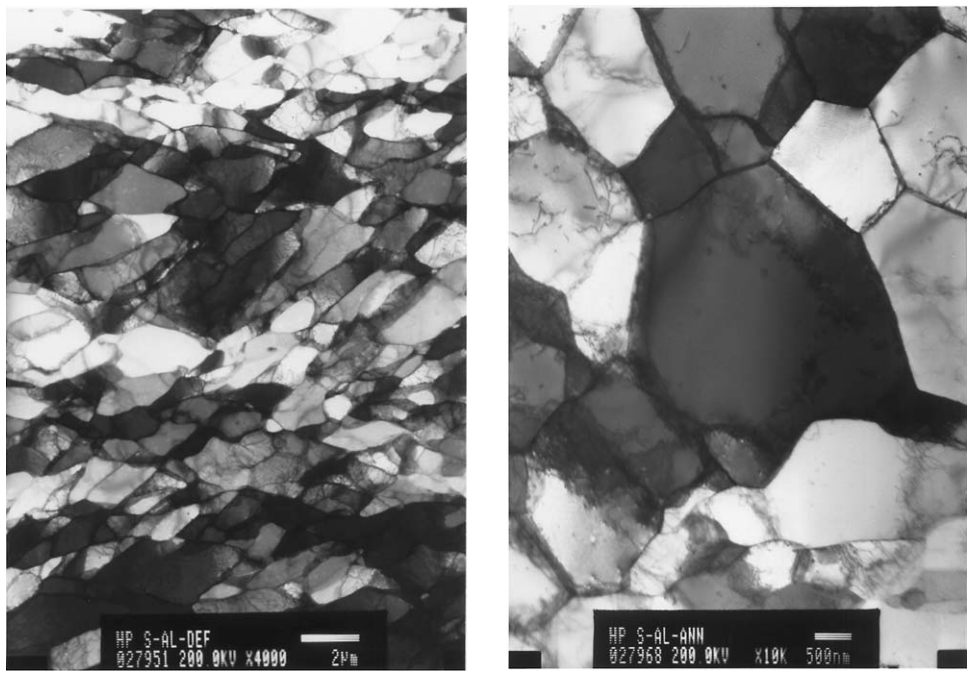

Fig. 2. TEM micrographs of as-deformed (left) and annealed state (right). The micrograph to the right includes one of the largest structural features found. The scale bars are 2 μm and 500 nm, respectively.

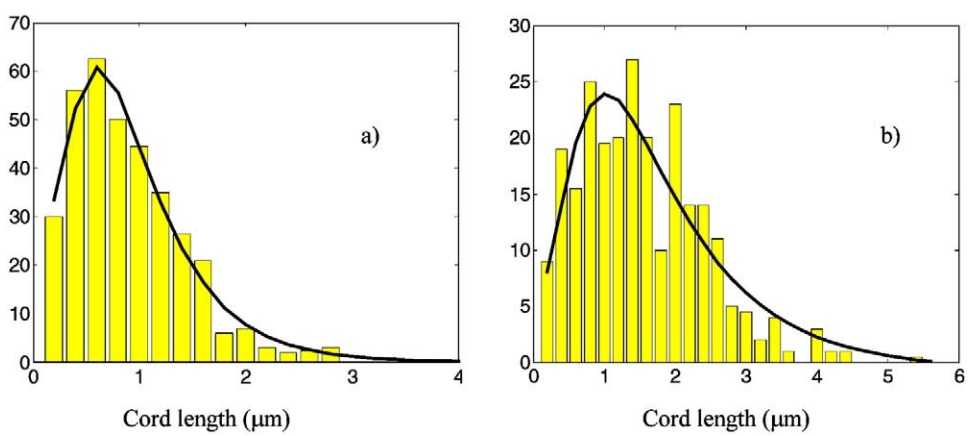

Fig. 3. Histograms of chord-length distributions from TEM studies of the as-deformed specimen (bars). Lines are drawn along directions TD and RD in (a) and (b), respectively. Also shown are best fits to a microstructure model based on a log-normal cell size distribution (lines).

an (x,y,z) translation unit and an ω-rotation stage. The vertical rotation-axis (along z) was coincident with RD, and ND was parallel to the monochromatic beam (along x) for $\omega = 0$. Hence, for a given ω-setting, the beam illuminates a channel through the sample with a volume of $V_0 = 11 \times 11 \times 2000/\cos(\omega)$ μm^3. The diffracted beam from structural units within this gauge volume which fulfil the Bragg condition produce spots on an area detector (transmission geometry). The detector was

an image intensifier coupled to a FRELON type CCD with an effective pixel size of 175 μm and an active area of 185 × 185 mm^2. The detector is 16 bits and exhibits anti-blooming. It was placed at a fixed distance from the sample, such that all spots arising from {111}, {200} and {220} reflections were acquired.

Measurements were performed by the 'rotation-method', which is ideally suited for orientation measurements with hard X-rays [3,17]. That is by acquiring images while stepping in ω with equidistant steps of $\Delta\omega$. During each acquisition the sample is oscillated by $\pm\Delta\omega/2$ in order to perform a space-filling and intensity-conserving sampling. By choosing an ω-range of 180° complete pole figures are obtained. However, as discussed in Ref [8] the gauge volume is not fixed during such a rotation.

The first aim of the experiment was to produce a space-filling grid of local orientation maps for the as-deformed state within a fixed volume of 2000 × 190 μm × 210 μm, along x, y and z, respectively. This was done by acquiring data at each point in a three-dimensional regular (y, z, ω) grid—a method introduced in Ref [8]. The grid comprised an outer loop of 19 points in z, in steps of 10 μm, 21 points in y, in steps of 10 μm, and an inner loop of 10 points in ω, in steps of $\Delta\omega$ = 2°. The ω-range was [0°, 20°]. The exposure time was 15 s per image.

In addition a two-dimensional (z,ω) grid was applied to the same total volume. In this case the incoming beam was defined to an 11 × 200 μm^2 spot. Each z-layer was then characterised by the same ω-scan, that was applied to each (y,z) position in the first grid. Hence, the speed of data acquisition was 21 times faster at the expense of resolving power.

Furthermore a full pole figure was generated at the centre position of the grids, with an illuminated area of 11 × 11 μm^2. This was done twice in order to enhance the effective dynamic range of the detector. The first setting was identical to the one for the fine grid. The second differed by an added beam attenuator and a shorter exposure time. The two data sets were combined to provide valid data on both the high and low intensity parts on the pole figure.

The total time spent on these maps was 34 h. At regular intervals during this time, reproducibility tests were performed. This, in connection with a comparison of the coarse and fine grid, enables us to state that the stability within 1 h was of the order of 1 μm while the long-term positional drifts were at most 5 μm.

Next, the sample was heated to 300 °C within 4 min with no overshoot. After 5 min at the operation temperature, it was cooled first within 10 min to 80 °C and then within another 10 min to room temperature. After a careful test of shift of position, the acquisition of the two grids with partial pole figures was repeated. However, to minimise beam-time the fine grid was performed for the two top-most layers only. The stability matched that of the grids for the as-deformed specimen.

4. Data analysis

The analysis of the synchrotron data followed the steps outlined in Ref [8]. Results were derived for the {200} data set, associated with the lower multiplicity and therefore less overlap of diffraction spots.

An example of raw data is shown in Fig. 4a. The poles appear as dominant ring segments, broadened radially due to saturation of the detector. In addition, far from the principal 'S' poles, minor spikes are clearly visible. The first step in the data analysis is to make a polar transformation of the data and plot the background and Lorentz factor corrected intensities as a function of the azimuthal angle, η(defined in Fig. 4a). A typical η-plot is shown in Fig. 4b. From such plots it was evident that a noise threshold of five counts can be defined. Spikes with a maximum intensity above the threshold are identified as arising from structural units in the microstructure. Arguments to the point that these spikes are not caused by instrumental artefacts such as higher harmonics and background were given in Ref [8], and apply here as well. (The issue of Renninger peaks will be dealt with in the discussion.) In addition we note that the width of the spikes in the η-direction for the as-deformed specimen is typically a few degrees. That is substantially broader than the angular resolution of the

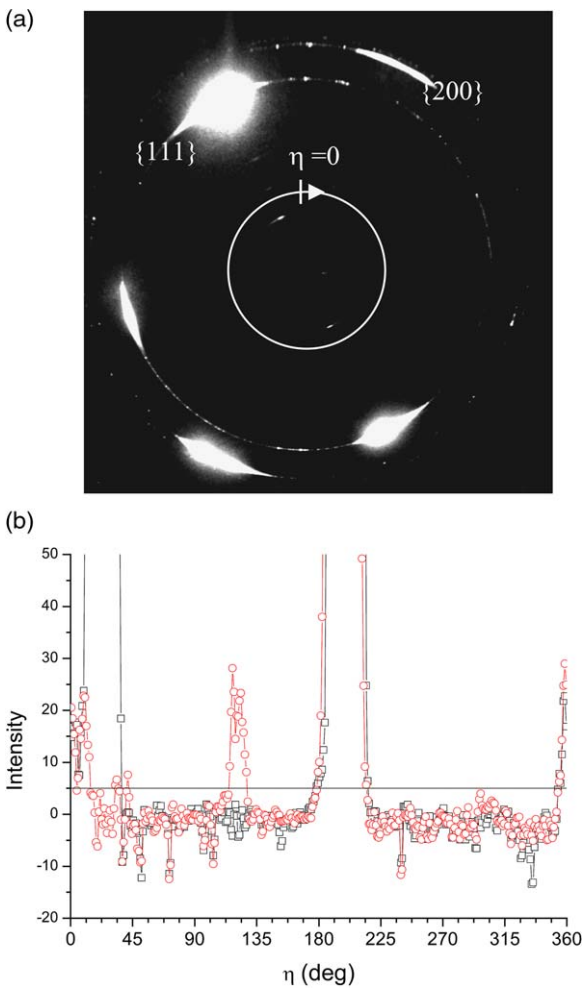

Fig. 4. Example of an exposure (a). A grey scale is used with white indicating the more intense regions. The textured Debye-Scherrer rings of the {111} and {200} reflections are seen. In addition the azimuthal angle η is defined. The corresponding background corrected intensity of the {200} ring is shown as function of η for two ω-settings (b). The straight solid line indicates the defined noise threshold of five counts.

instrument, and fits reasonably with the expected orientation variation within individual cell-blocks, as determined by TEM on a similar sample [14].

For completeness we mention that 6 small negative spikes are also present in Fig. 4b. These are found in all exposures and relate to detector black spots and to η-regions where tails of the {111} distribution radially extends into regions used for estimating the background for the {200} data. These small negative spikes are of no relevance to the further data analysis.

The full pole figure generated for the as-deformed specimen at the centre of the grid is shown as a contour plot in Fig. 5a. Let the summed intensity over this pole figure be I_{tot} and V_0 be the illuminated volume for a single exposure. Then, for a given area in the pole-figure (associated e.g. with a pole or a spike) with a summed intensity of I, we can derive the volume fraction V/V_0 of the corresponding texture component by scaling:

$$\frac{V}{V_0} = m\frac{I}{I_{tot}}. \quad (1)$$

Here m is the multiplicity of the {200} reflection.

The contour-plot presentation used in Fig. 5a necessarily involves smoothing of the data. An alternative pole figure with intensities plotted directly as a colour map is provided in Fig. 5b. Several additional faint texture components are now visible. Evidently, the contour-plot algorithm tends to 'wash out' isolated spikes, and the second representation is the one that will be used in the following. (A tendency towards radial streaks is evident in Fig. 5b. This is explained by the fact that each ω-setting probes two radial lines in the pole figure [17], and that different ω-settings probe different gauge volumes. Hence, a structural unit giving rise to a diffraction spot which should extend over several ω-settings may show up in only one of them, as the unit has rotated out of the active gauge volume.)

As previously mentioned, for the actual grid only partial pole figures were measured. The part characterised is marked in Fig. 5b by solid lines.

5. Results

Initially we present the result from the (y,z) grid made for the as-deformed specimen. The partial pole figures for the four corners of the grid are shown in Fig. 6. By inspection of these and the rest of the set of 19∗21 pole figures[1] we make the following observations:

[1] Access to the full set of pole figures for the specimen in the as-deformed and annealed states can be provided by the corresponding author.

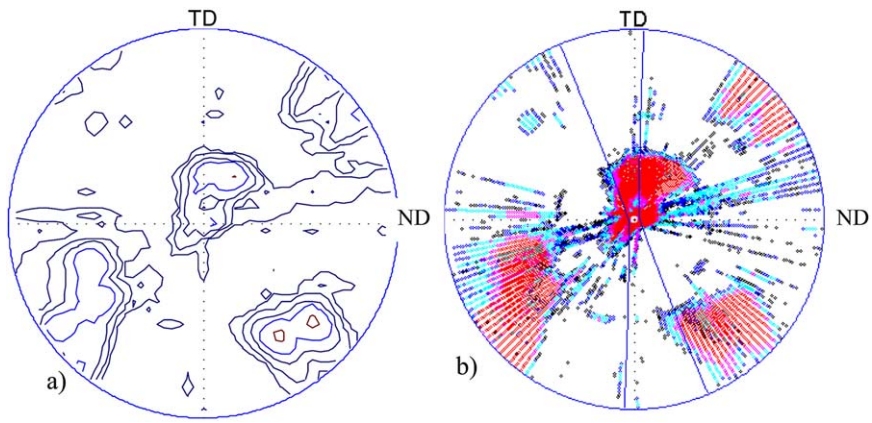

Fig. 5. {200} pole figures of one $11 \times 11 \times 2000$ μm^3 subvolume of the as-deformed specimen. (a) As contour-lines [1, 10, 100, 1000, 10000] with 1 being the noise-limit. These data are smoothed by a Watson distribution with a FWHM of 2°. The maximum intensity is 14 500. (b) The low intensity part of the same data plotted as a colour-map without any smoothing. The colour code is: [black, blue, cyan, magenta, red] for [1, 2, 5, 20, 100]. The part of the pole figure covered by the chosen [0° 20°] ω-interval is indicated by two solid lines. There is a 'black spot' in the centre of both pole figures with a radius of 4°.

1. At all grid positions there is a saturated, near-S principal pole above the centre and the tail of another pole below it. These are marked as A and B in Fig. 6b. The A and B pole distributions are approximately homogeneous within the grid. By scaling (Eq. 1), the volume-fraction of material associated with B is found to be of order 6×10^{-5}.
2. Through all the z-layers there is a gradient in the y-direction with the pole figures at one end—to the right in Fig. 6—containing only the A and B distributions, while those in the other end—to the left—in addition contain a broad and weak distribution identified as C. Th volume fraction of this part is at most 2.4×10^{-4}. In addition, the tail of the central pole, A, becomes broader in the left part.
3. In three non-connected parts of the grid there is also a component in the upper left part, D. These parts all extend over 30–50 μm in both directions. The D component is confined within a narrow angular range of less than 5°, see Fig. 6a. The volume fraction as shown is 3×10^{-6}.
4. When overlaying all the partial pole figures it becomes evident that there are still large areas in the {200} pole figures without any spikes.

As mentioned, measurements for the annealed state were made for the same grid-points but only for the first two z-layers. Two examples of the resulting partial pole figures are shown in Fig. 7. They refer to the two extreme y positions within layer 1, such that direct comparisons can be made with Figs 6a and b. By inspection of these and the rest of the set of 2∗21 pole figures we make the following observations:

1. The orientation distribution for the specimen in the annealed state comprises the poles and a set of distinct spikes. The minor components B, C and D have disappeared. The saturated pole area A remains.
2. The spikes outside the pole area are fewer than for the as-deformed sample and they are more isolated in orientation space. They tend to be very sharp with a mosaic spread given by the instrumental resolution. Outside the principal 'S' poles there is virtually *no correlation* between the orientation distributions before and after. This is also true if one compares to neighbouring grid points (assuming some positional shifts to have occurred).
3. The spikes are distributed rather uniformly across the grid, with a tendency toward more spikes in the left part. The volume fractions of spikes outside the poles are 1.5×10^{-4} and 5×10^{-4} for Figs 7a and b, respectively.
4. If one interprets the individual spikes as arising

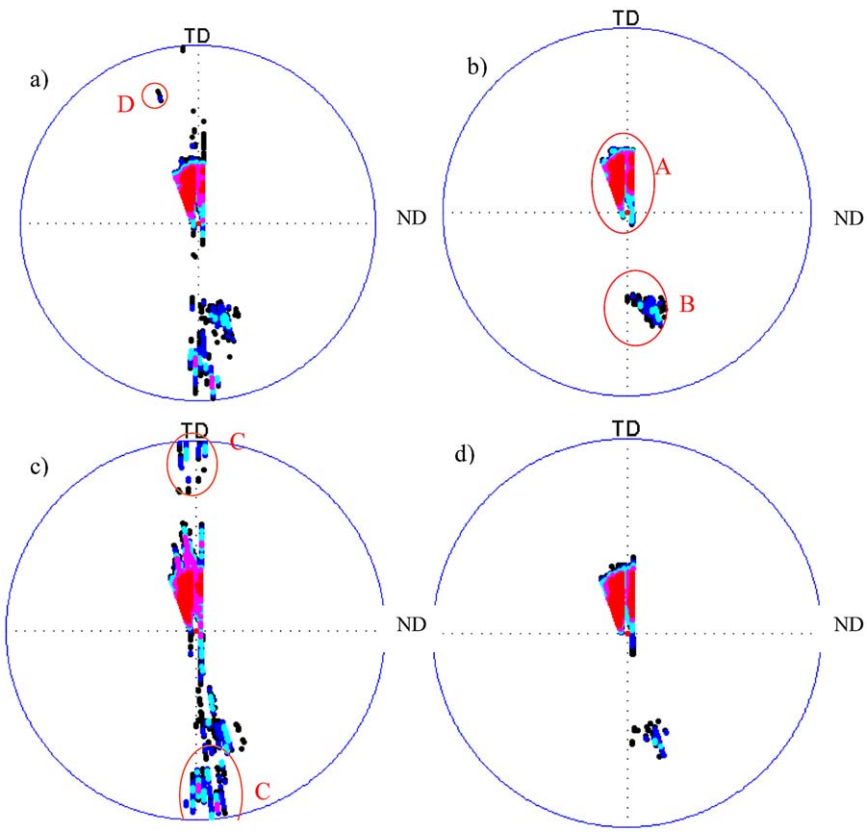

Fig. 6. Partial {200} pole figures for the as-deformed state. The four extreme positions of the (y,z)-grid are shown: (a) z-layer 1, y-position 1, (b) z-layer 1, y-position 21, (c) z-layer 19, y-position 1, (d) z-layer 19, y-position 21. The orientation distribution is divided into four components: A, B, C and D, as discussed in the text. The data representation and colour code are the same as for Fig. 5b.

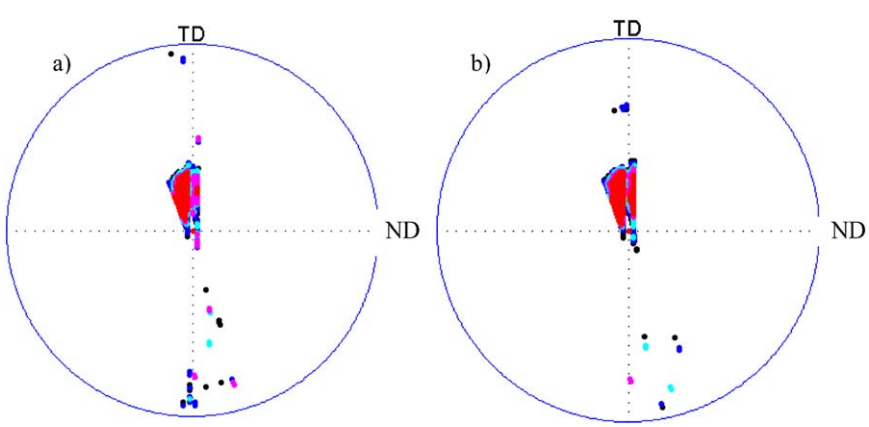

Fig. 7. Partial {200} pole figures for the annealed state. The two extreme positions of the (y,z)-grid are shown: (a) z-layer 1, y-position 1, and (b) z-layer 1, y-position 21. The data representation and colour code are the same as for Fig. 5b.

from single structural units, the larger ones have a volume of up to (2.5 μm^3).

To enable a comparison between the as-deformed and annealed states over the full mm^3-sized volume, we focus on layers instead of grid points. For all layers of the specimen in the as-deformed state and for the two first layers in the annealed state we may overlay the spikes of the 21 individual pole figures. Fig. 8 shows the resulting 'summed pole figures' for layer 1 before and after annealing. Evidently the observations made from inspection of individual grid points remain valid.

To perform the analysis for the remaining z-layers, we introduce three pole figures per layer. Two of them are generated based on the data produced before and after annealing with the 11 × 200 μm^2 beam. These are directly comparable. The third is the summed pole figure for the as-deformed state, as introduced above. Two examples of such a set of three pole figures are given in Fig. 9—for layers 7 and 13, respectively. As expected, the two representations of the as-deformed state are identical, except for the higher sensitivity of the 'summed pole figures' towards weak spikes. Comparing the as-deformed and annealed state, it is seen that the observations made above once more remain valid. In particular the lack of correlation between the distributions before and after is striking.

We further note that some of the emerging spikes have orientations that are not represented in any of the 19∗21 pole figures of the as-deformed state. One example is marked as E in Fig. 9. Likewise the spike marked F in Fig. 9 is not represented in the corresponding z-layer of the as-deformed specimen, nor in the adjacent layers. The integrated intensities of the E and F structures correspond to volumes of (2.3 μm^3) and (9.4 μm^3), respectively. The spike marked F also appears in the two neighbouring layers of the annealed state, although with reduced intensities.

6. Discussion

6.1. Instrumental limitations

The main limitation of the 3DXRD method is the problem of spot-overlap, which in the present case prohibits gathering information on the dynamics of microstructure evolution associated with orientations near the average (i.e. the vast majority). The information obtained here therefore relates to off-average orientations. In the following we discuss two other possible shortcomings.

6.1.1. Multiple scattering

It is well known from work on near-perfect single crystals that spurious peaks—the so-called Renninger peaks—can arise from the beam being diffracted twice on two different reflections [18].

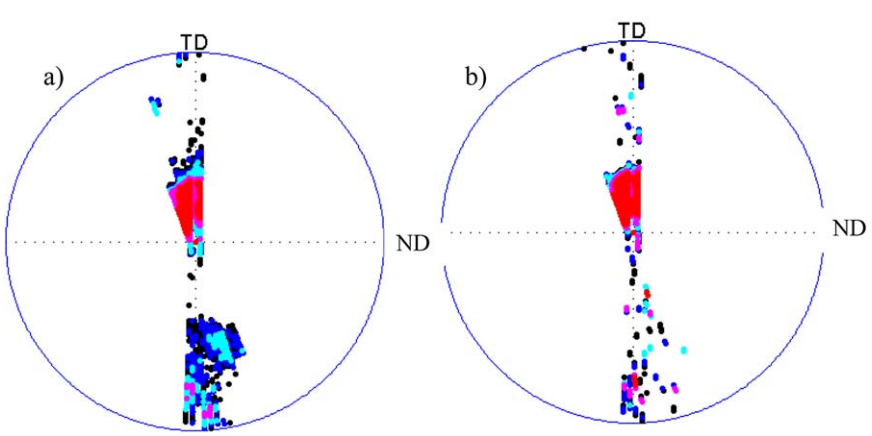

Fig. 8. Partial {200} pole figures for layer 1 in the as-deformed (a) and annealed state (b). The figures are made by overlaying the individual 21 pole figures associated with that layer in the grid. The data representation and colour code are the same as for Fig. 5b.

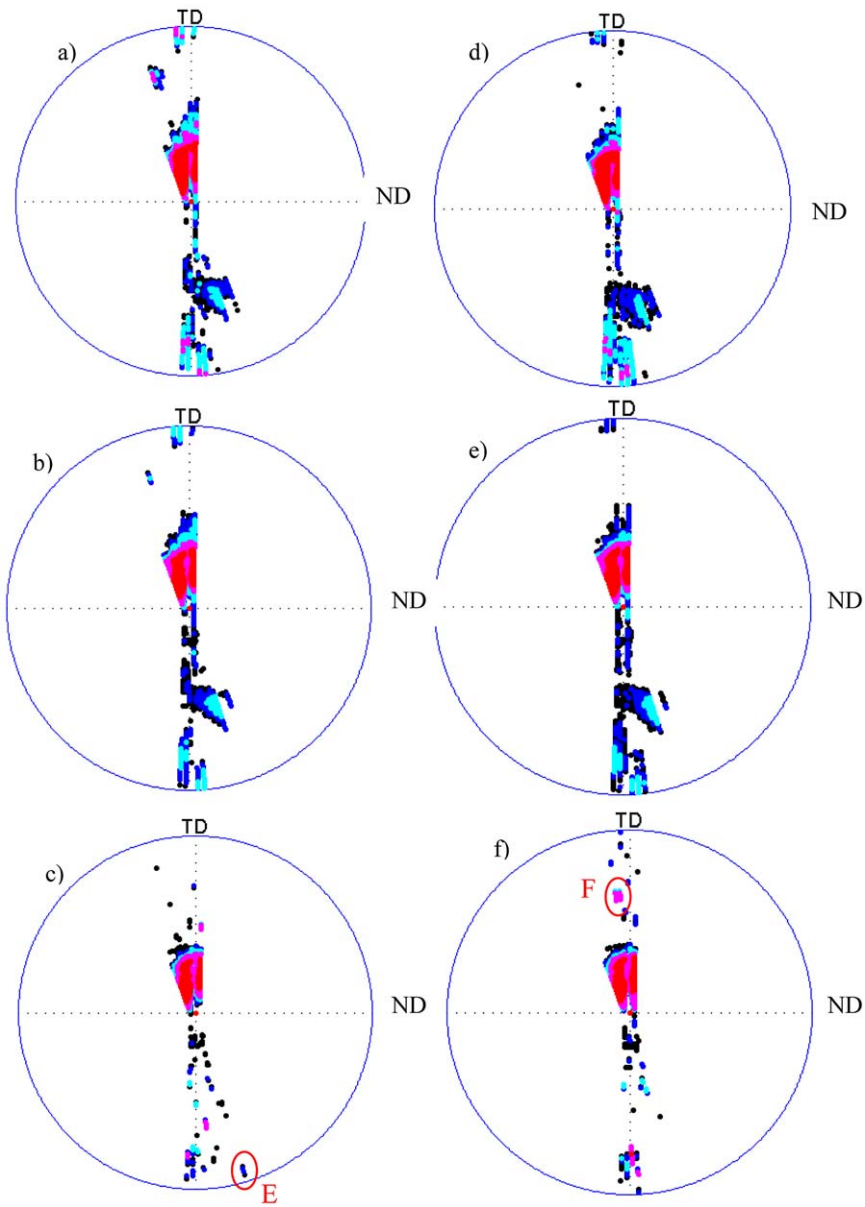

Fig. 9. Partial {200} pole figures for layers 7 (right) and 13 (left). Panels (a) and (d) represent an overlay of the results for the grid-points within the layer in the as-deformed state. The data representation and colour code are the same as for Fig. 5b. Panels (b) and (e) represent the results of measuring the full layer at once in the as-deformed state. Panels (c) and (f) represent the results of measuring the full layer at once in the annealed state. The colour code for (b), (c), (e) and (f) is [black, blue, cyan, magenta, red] for [10, 20, 50, 200, 1000]. Features E and F are marked for further discussion in the text.

This effect falls off dramatically with an increasing mosaic spread of the single crystal—in our case with the deformation—and with increasing X-ray energy. We have performed an analytical estimate for the most favourable geometry, multiple scattering on {111}/{111}. The resulting doubly diffracted beam is found to be at most a factor of 2 above the noise threshold of five counts. For most settings the intensity is clearly below the threshold. Likewise, the character of the diffuse scattering reported here is incompatible with what one would expect if the spikes were in fact Renninger peaks. In particular, the position of the peaks is not correlated with 'favourable settings'. Likewise, the observed y- and z-dependency cannot readily be explained on this basis.

6.1.2. Surface effects

For each exposure we probe the structure through the thickness of the specimen. Noting the small volume fractions involved, it appears that in principle the diffuse features could all arise from near-surface regions. There are ways to gather information on the depth of origin for each spike, namely by inserting a knife-edge [19] or a conical slit [20] between the sample and the detector, or by using the X-ray tracing concept developed for grain mapping [3,4]. For time reasons, these were not applied. Instead we have analysed a few spikes manually, looking for cases where we could identify more than one reflection as belonging to the same structural unit. This involved using the Friedel pair, that is (h,k,l) and ($\bar{h}$,$\bar{k}$,$\bar{l}$). By triangulation the approximate position within the sample was then derived. Most of the spikes, including features E and F in Fig. 9, are found to be positioned in the bulk of the material.

Having listed these shortcomings, it should be emphasised that the present data clearly allow both qualitative and quantitive statements on the microstructural dynamics. The emerging features, such as the lack of correlation between the orientation of the spikes before and after the first 5 min of annealing, cannot be explained solely in terms of background or surface effects.

6.2. Comparison of 3DXRD and TEM size distributions

The 3DXRD method probe volumes while size distributions in TEM only can be quantified via measurements of linear intercept or section area. To compare the results in principle a full stereological analysis is required. This is prohibited by the limited statistics provided by TEM. However, for the arguments of relevance here estimates of sufficient quality can be made from a microstructural model.

To interpret the TEM data we assume a system of box-shaped cells with a constant ratio a/c = b/c between the long axis c and the two shorter axes a and b. The size-distribution is log-normal. Shown in Fig. 3 is the best fit of the linear intercept data to such a model. The optimised parameters for the Gaussian are midpoint values of 1.27 μm (along c) and 0.77 μm (along a). The widths are σ_c = 0.55 μm and σ_a = 0.48 μm, respectively.

With respect to 3DXRD, the volume fraction of material giving rise to diffraction within one bin (of 2 × 2°) of the pole figure is provided in a model-independent way by Eq. (1). In this way the noise threshold of five counts is found to correspond to a limiting volume fraction of 9×10^{-7}. Furthermore, we may assume the structural units of relevance to have an internal orientation spread of less than 2°. Then we can derive a detection limit on the volume of such structures: V_{limit} = 0.6^3 μm^3. This limit is estimated to be associated with an error of less than 50%, implying an error of less than $\sqrt[3]{1.5}-1 = 14\%$ on the size.

With these assumptions we can derive the fraction of cells in the as-deformed state that has a size below the noise threshold. The number is 8%. This result is reasonable robust towards change in models. More importantly is the fact that adjacent cells with a mis-orientation angle of less than 2° are counted as separate units by TEM, but not by 3DXRD. Hence, the fraction of non-detectable cells is likely to be significantly smaller then the 8%.

6.3. Annealing behaviour

We proceed with an interpretation of the data based on both the electron microscopy and

synchrotron results. Simultaneously we compare with the results reported by Godfrey, Juul Jensen and Hansen [14]—hereafter referred to as GJH. Using a nearly identical single crystal with the same orientation, they performed extensive EBSP and TEM analysis on specimens as-deformed and quenched after annealing for 5, 30 and 60 min at 300 °C.

In the as-deformed state, the orientations of the different parts of the microstructure sum up to produce broad poles. The FWHM of these distributions as determined by EBSP and 3DXRD are similar. The tails of the 3DXRD data extend further than those generated by EBSP, as a direct consequence of the higher sensitivity towards small volume fractions by 3DXRD.

The diffuse features marked C and D in Fig. 6 are too weak to be detected by EBSP. The fact that they exhibit a clear variation with y position—that is approximately along TD—in the (y,z) grid despite the fact that the illuminated volume is much longer in the x-direction—along ND—indicates that these structures are likely to be clustered within a fraction of the illuminated volume. Hence, while the existence of localised extreme orientations as such may be representative of the sample, we cannot conclude that these orientations are generic.

The electron microscopy work presented here and in GJH both indicate that a major part of the structure has recovered after 5 min of annealing. This conclusion is based on the disappearance of most dislocations within cells, as well as the observed morphology changes: change of aspect ratio and dihedral angles. The recovery is found in GJH to be associated with a marked decrease in the number of high angle misorientations as determined by EBSP. This is consistent with the markedly sharper poles (compare Fig. 1a and b) and the disappearance of the tail component B in the 3DXRD data. To summarise, these observations are consistent with subgrain growth by migration of low angle boundaries.

Uniquely, the 3DXRD results reveal the existence of minority orientation components, clearly not encompassed by the tails of the poles. The total volume fraction of these is of the order of 2×10^{-4}. Based on the homogeneity and the fact that some spikes were traced to the bulk of the material, these orientation components are believed to be generic and representative of bulk behaviour.

We interpret the new orientation components as arising from isolated recovered cells and/or from nuclei. In favour of the former interpretation is the fact that the optical microscopy work here and in GJH both indicates that the recrystallisation process has not started after 5 minutes and that the maximum cell size is around 5 μm. Furthermore GJH reports that the recrystallised volume fraction after 30 min is less than 1%. However, the statistics of such observations is not sufficient to rule out nucleation completely. In favour of the second interpretation is the fact that at least one of the spikes presented in Fig. 9—the one marked F—resembles a grain in terms of an apparent size of 10 μm. However, GJF report on a recovered cell size in the non-recrystallised parts of up to 10 μm after 60 min of annealing. Noting the stochastic nature of the processes at play it is reasonable that at least one large cell is produced after 5 min within the 10^5 larger volume probed by 3DXRD. Alternatively the spike may be seen as superposed of a number of cells with near identical orientations.

Generally we may state that all parts of the deformed microstructure with orientations away from the poles are highly mobile, as there is no correlation between the pole figures for the as-deformed and the annealed state. This should be compared with the fact that TEM work in the present case indicates that part of the majority component microstructure resembles that of the deformed specimen, and that the sub-grain dynamics in those parts therefore presumably is slow or absent.

7. Conclusions

The 3DXRD technique has been modified to enable in situ studies of microstructural dynamics during the early stages of annealing of deformed metals. The method is applied to annealing of a cold deformed Al single crystal of the S orientation. Changes in individual structural units with orientations far from the poles are monitored within a 0.08 mm^3 volume and with a detection

limit of 0.6 μm. There is virtually no correlation between the orientation distributions before and after 5 minutes of annealing.

There are two ways the new minority orientation components can be generated:

1. They emerge by rotation from the vast majority of the deformed structure, associated with the poles.
2. They emerge (with or without orientation conservation) from very rare parts of the deformed structure, associated with a volume fraction of less than 9×10^{-7}. In addition, if these parts have an intrinsic orientation spread of less than 2° (as one would normally assume for deformation induced dislocation cells), they *all* have an unusual small size of less than 0.6 μm. This corresponds to the 8% fractile of the overall cell size distribution. However, as they are likely to be associated with a size distribution, their size is seen to be at the very tail of the distribution, as well as substantially below the classical nucleation threshold. Furthermore such hypothetical parts of the deformed specimen must be surrounded by high angle boundaries.

These results are consistent with recent observations of 'new orientations' by other methods—see e.g. Refs. [21,22]. It is the first time such observations have been based on non-destructive bulk measurements within a volume comparable to the recrystallised grain size. Furthermore the limiting numbers in terms of volume and volume fractions are superior to those of previous studies.

The results suggest the new orientations to arise during recovery as opposed to nucleation. However, the use of only two time steps prohibits a final conclusion on this matter.

Acknowledgements

We thank A. Godfrey, D. Juul Jensen, N. Hansen and G. Winther for scientific discussions, A.W. Larsen for help with data analysis, X. Huang for performing the TEM investigation, A. Goetz, P.B. Olesen, H. Nilsson, and G. Christiansen for technical support and the staff at ID11, ESRF for general support. This work was supported by the Danish National Research Foundation through the 'Center for Fundamental Research: Metal Structures in Four Dimensions' and by the Danish Natural Science Research Council via Dansync.

References

[1] Humphreys FJ, Hatherly M. Recrystallization and related annealing phenomena. Oxford: Pergamon Press, 1995.
[2] Poulsen HF, Garbe S, Lorentzen T, Juul Jensen D, Poulsen FW, Andersen NH, Frello T, Feidenhans'l R, Graafsma H. J Synchrotron Rad 1997;4:147–54.
[3] Lauridsen EM, Schmidt S, Poulsen HF, Suter RM. J Appl Cryst 2001;34(6):744–50.
[4] Poulsen HF, Nielsen SF, Lauridsen EM, Schmidt S, Suter RM, Lienert U, Margulies L, Lorentzen T, Juul Jensen D. J Appl Cryst 2001;34(6):751–6.
[5] Poulsen HF, Fu X. J Appl Cryst, in print.
[6] Lauridsen EM, Juul Jensen D, Poulsen HF, Lienert U. Scripta Mater 2000;43:561–6.
[7] Poulsen HF, Juul Jensen D. Proc ICOTOM-13, Seoul 2002;:49–67.
[8] Poulsen HF, Juul Jensen D, Tschentscher T, Wcislak L, Lauridsen EM, Margulies L, Schmidt S. Textures and Microstructures 2001;35(1):39–54.
[9] Hu H. Trans Metall Soc AIME 1962;224:75.
[10] Chan HM, Humphreys FJ. Acta Metall 1984;32:235.
[11] Kikuchi S, Kimura E, Koiwa M, Materials J. Science 1992;27:4927–34.
[12] Kamijo T, Katao S, Inagaki H. Acta Metal Mater 1993;41:1713–20.
[13] Kashiara K, Tagami M, Inoko F. Materials Transactions JIM 1996;37:572–8.
[14] Godfrey A, Juul Jensen D, Hansen N. Acta Mater 2001;49:2429–40.
[15] Orlans-Joliet B, Driver JH, Montheillet F. Acta Metall Mater 1990;38(4):581–94.
[16] Krieger Lassen NC, Juul Jensen D, Conradsen K. Scanning Microsc 1992;6:115–21.
[17] Mishin OV, Lauridsen EM, Krieger Lassen NC, Brückner G, Tschentscher T, Bay B, Juul Jensen D, Poulsen HF. J Appl Cryst 2000;33:364–71.
[18] Giacovazzo C, Monaco HL, Viterbo D, Scordari F, Gilli G, Zanotti G, Catti M. IUCr Texts on Crystallography 2: Fundamentals of Crystallography. Oxford University Press, 1992 p 191.
[19] Larsen BC, Yang W, Ice GE, Budal JD, Tischler JZ. Nature 2002;45:887–90.
[20] Nielsen SF, Wolf A, Poulsen HF, Ohler M, Lienert U, Owen RA. J Synchrotron Rad 2000;7:103–9.
[21] Juul Jensen D. In: Sakai T, Suzuki HG, editors. Proc 4th Int. Conf on Recrystallization and Related Phenomena, JIM 3-14. 1999.
[22] Paul H, Driver JH, Maurice C, Jasienski Z. Acta Mater 2002;50:4339.

A13

Grain Nucleation and Growth During Phase Transformations

S. E. Offerman,[1,2]* N. H. van Dijk,[1] J. Sietsma,[2] S. Grigull,[3] E. M. Lauridsen,[4] L. Margulies,[3,4] H. F. Poulsen,[4] M. Th. Rekveldt,[1] S. van der Zwaag[2]

The mechanical properties of polycrystalline materials are largely determined by the kinetics of the phase transformations during the production process. Progress in x-ray diffraction instrumentation at synchrotron sources has created an opportunity to study the transformation kinetics at the level of individual grains. Our measurements show that the activation energy for grain nucleation is at least two orders of magnitude smaller than that predicted by thermodynamic models. The observed growth curves of the newly formed grains confirm the parabolic growth model but also show three fundamentally different types of growth. Insight into the grain nucleation and growth mechanisms during phase transformations contributes to the development of materials with optimal mechanical properties.

Grain nucleation and growth are important phenomena in polycrystalline materials such as metals and most ceramics. They govern the kinetics of many phase transformations and recrystallization processes that take place during processing. The final average grain size after the transformation is directly related to the strength of the material. In general, a smaller average grain size results in a stronger material. Despite the various transformation models that have been proposed in the past 60 years, the kinetics of these phase transformations is still poorly understood. Most of these models are based on the classical nucleation theory (CNT) (*1*) and the law of parabolic grain growth as derived by Zener (*2*), which describe the behavior of individual grains in the bulk of the material.

The experimental techniques that have been available to verify these nucleation and growth models are limited to either observations at the surface or the determination of the average grain growth behavior in the bulk (*3*). The development of x-ray microscopes at synchrotron sources with focused high-energy x-rays has created the opportunity to study individual grains in the bulk of a material (*4*–*7*). In addition, these measurements give unique information about the grain nucleation during the phase transformation. Because of a combination of fundamental scientific interest and technological importance, the phase transformations in steel have been investigated more extensively than those in any other material, and steel is the material studied here.

Carbon steel consists of iron and carbon [up to 2 weight % (wt %)], with small quantities of alloying elements, and exists in three stable crystalline phases: austenite with a face-centered cubic structure, ferrite with a body-centered cubic structure, and cementite (Fe_3C) with an orthorhombic structure. The principal transformation reaction in steel, which is a typical diffusion-controlled solid-state transformation, is from the high-temperature austenite phase to the low-temperature ferrite phase. Because the solubility of carbon in ferrite is much lower than in austenite, the transformation is accompanied by a carbon enrichment of the austenite. At lower temperatures, the carbon-rich austenite decomposes into pearlite, which consists of a lamellar structure of two interpenetrating single crystals of ferrite and cementite (Fig. 1).

In order to study the time evolution of individual grains during the phase transformations, a relatively small volume of steel was illuminated with a monochromatic beam of hard x-rays from a synchrotron source. Through a slight rotation of the sample around an axis perpendicular to the beam, a number of grains gave rise to diffraction spots on a two-dimensional detector. Figure 2 shows a diffraction pattern halfway through the austenite-to-ferrite transformation. From the standard diffraction theory it can be shown that the intensity of each spot is proportional to the volume of the grain it originates from. The intensity of the spot is normalized with respect to the total intensity of the diffraction ring at the end of the transformation (*4*), by assuming that the equilibrium ferrite fraction is then reached. By repeated acquisition of images, the nucleation and growth of the individual grains were studied, with a typical time resolution of 10 s.

The steel was annealed at 900°C for 10 min in order to form the austenite phase and was subsequently continuously cooled to 600°C in 1 hour. By counting the number of valid diffraction spots, the number of ferrite grains (with a grain radius above the detection limit of about 2 μm) was obtained as a function of temperature (Fig. 3A). The number of ferrite nuclei increased most rapidly just below the austenite/ferrite transition temperature of 822°C for this steel, but new ferrite nuclei were continuously formed over a large temperature range until the austenite/pearlite transformation started at 685°C. Only a very small number of new pearlitic ferrite nuclei were formed in the pearlite transition temperature range. Figure 3B shows the normalized experimental nucleation rate, which is compared to the CNT (*1*). The shape of the theoretical curve is in qualitative agreement with the measurements. The most striking

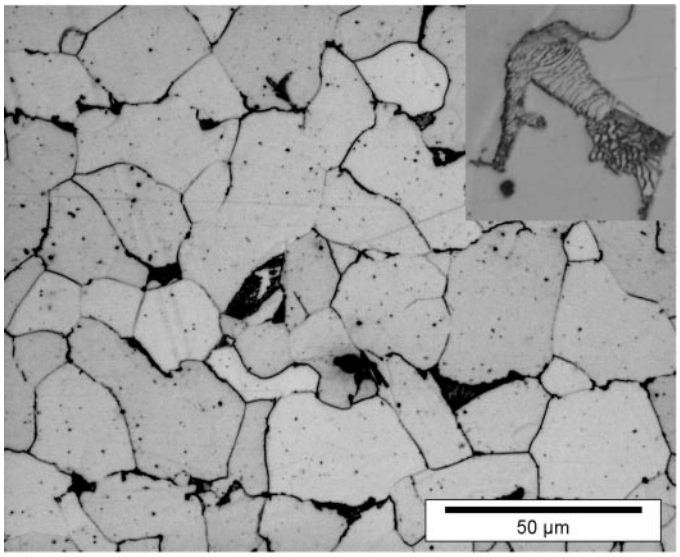

Fig. 1. Optical microscopy images of the construction steel (0.21 wt % C, 0.51 wt % Mn, and 0.20 wt % Si) at room temperature. The light regions correspond to ferrite and the dark regions to pearlite. The insert in the top right corner shows the lamellar structure of pearlite (magnification is three times that of the main image).

[1]Interfaculty Reactor Institute, Delft University of Technology, Mekelweg 15, 2629 JB Delft, Netherlands. [2]Department of Materials Science, Delft University of Technology, Rotterdamseweg 137, 2628 AL Delft, Netherlands. [3]European Synchrotron Radiation Facility, BP 220, 38043 Grenoble Cedex, France. [4]Center for Fundamental Research: Metal Structures in 4D, Materials Research Department, Risø National Laboratory, 4000 Roskilde, Denmark.

*To whom correspondence should be addressed. E-mail: Offerman@IRI.TUDelft.nl

difference is that the maximum nucleation rate occurred at a higher temperature than predicted by the CNT.

According to the CNT, the driving force for nucleation is the decrease in Gibbs free energy per unit of volume of the system during the phase transformation Δg_V, which depends on the chemical composition and temperature. However, the creation of a new nucleus also requires energy because of the formation of an interface between the nucleus and the original phase. According to the CNT, the nucleation rate can be expressed as

$$\frac{dN}{dt} \propto (1-f)\,\frac{kT}{h}\exp\left[-\frac{\Delta G^* + Q_D}{kT}\right] \quad (1)$$

where the factor $(1-f)$ takes into account the decrease in the number of potential nucleation sites with increasing fraction f (in this case, the ferrite fraction f^α), k is the Boltzmann constant, h is the Planck constant, and T is the temperature. The mobility of the (iron) atoms in the original (austenite) phase is taken into account by the activation energy for diffusion Q_D. The energy that is necessary to form a critical nucleus is referred to as the activation energy for nucleation ΔG^*, which can in general be written as $\Delta G^* = \Psi/\Delta g_V^2$. The factor Ψ accounts for the energy of the interface (boundary) between the nucleus and the original phase and the geometry of the nucleus.

It is the uncertainty in Ψ that makes predictions of the nucleation rate very difficult, so models have been developed in order to estimate Ψ (*8*, *9*). These models have in common that a certain shape is assumed for the nucleus, which is then applied to all the nuclei in the system. One of the early models by Clemm and Fisher (*8*) predicts $\Psi_{CF} = 3.3 \times 10^{-3}$ J^3/m^6 for grain corner nucleation of nuclei with incoherent grain boundaries. A more recent model by Lange *et al.* (*9*) gives $\Psi_{LEA} = 2.1 \times 10^{-6}$ J^3/m^6 for a pillbox shape of the nucleus with coherent and semicoherent interfaces. A best fit of our experimental data to Eq. 1 gives $\Psi_{exp} = 5 \times 10^{-8}$ J^3/m^6, when $Q_D = 4.72 \times 10^{-19}$ J (*10*). This means that the activation energy for nucleation as determined in this experiment is at least two orders of magnitude smaller than the models predict.

The difference between experiment and theory cannot solely be explained by varying Δg_V and/or Q_D within a realistic range. The low experimental value for the activation energy for nucleation indicates a close balance between the energy that is released by the removal of incoherent austenite/austenite grain boundaries and the energy that is required for the formation of coherent and incoherent austenite/ferrite grain boundaries. This could be related to recent computer simulations of nucleation in a system of colloidal particles. These calculations indicate that it is possible that the initial nucleus has a metastable crystallographic structure, which transforms in a stable structure upon growth (*11*). Moreover, it may be questioned whether conventional continuum thermodynamics accurately predicts the driving force Δg_V, because the critical nucleus only consists of 10 to 100 atoms.

We determined the growth behavior of individual ferrite grains and pearlite colonies by continuously monitoring the intensity of the diffraction spots (Fig. 4). The ferrite grain volume V^α that was derived from the measured intensity is transformed into a grain radius R^α by assuming that the grain shape is spherical. Four types of ferrite growth could be distinguished, as shown in the four panels of Fig. 4. In each panel, the experimental growth curves are compared with the theoretical prediction of the classical Zener model (*2*), which predicts a parabolic growth for a spherical grain when the growth rate is limited by diffusion. This theory is commonly used to describe the growth of ferrite grains in construction steels during the transformation from austenite. Because the solubility of carbon in ferrite is two orders of magnitude lower than in austenite, the carbon

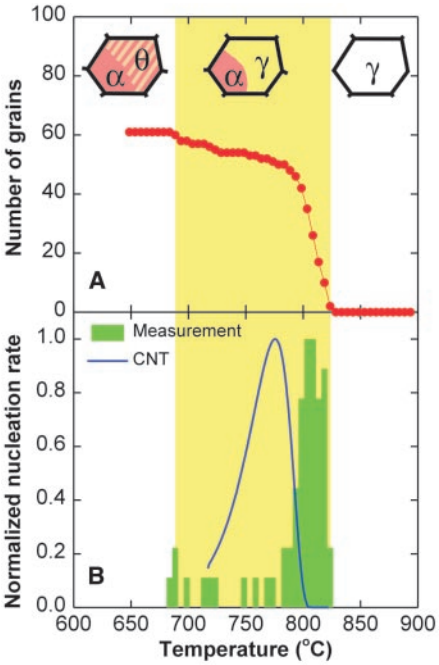

Fig. 3. Nucleation as a function of temperature during continuous cooling of the steel from 900° to 600°C in 1 hour. (**A**) The total number of valid ferrite reflections. (**B**) The normalized experimental nucleation rate (green bars) compared to the CNT (line) as given by Eq. 1. The ferrite fraction f^α was assumed to develop according to thermodynamic equilibrium and was calculated from the thermodynamic database MTDATA. The driving force for nucleation Δg_v was determined through the parallel-tangent construction with the standardized data from the Scientific Group Thermodata Europe (SGTE) under the assumption that the alloying elements were homogeneously distributed. For Ψ, the value determined by Lange *et al*. (*9*) was used: $\Psi_{LEA} = 2.1 \times 10^{-6}$ J^3/m^6. The nucleation rate was normalized to the maximum nucleation rate. The first ferrite reflections were observed at a temperature of 822°C and the pearlite started to form at 685°C. The different stages during the phase transformations in steel are schematically drawn at the top of the figure, which shows the three phases: austenite (γ), ferrite (α), and cementite (θ).

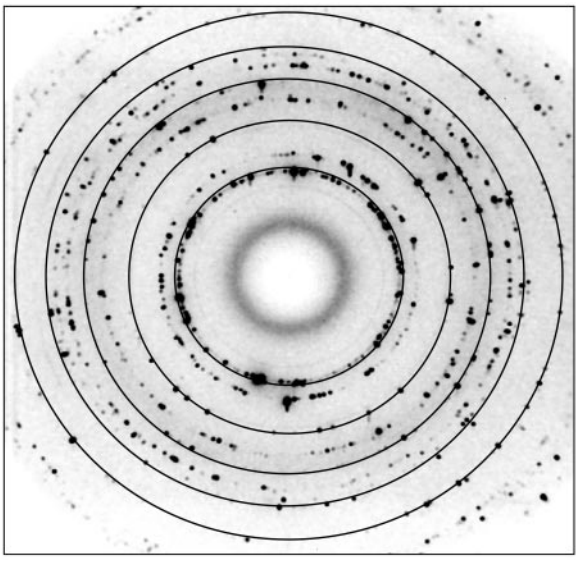

Fig. 2. X-ray diffraction pattern of the steel showing the austenite and ferrite reflections at 763°C. The solid rings indicate the expected scattering angles from the ferrite grains illuminated by the x-ray beam. The energy of the monochromatic x-rays corresponded to 80 keV (with a wavelength of 1.55×10^{-2} nm), the beam size to 94×97 μm^2, and the thickness of the sample to 400 μm. During the exposure, the sample was continuously rotated around the vertical axis over an angle from –0.8° to 0.8°. In order to determine whether a diffraction spot was valid, we took additional exposures for rotation angles from –2.4° to –0.8° and 0.8° to 2.4°, which told us whether the complete integrated intensity was observed in the central exposure. Once every six exposures, the beam size was expanded to 139×139 μm^2 in order to check whether the total volume of the grain was illuminated by the small central beam. For the experiment, we used the three-dimensional x-ray diffraction microscope (3DXRD) at beam line ID11 of the European Synchrotron Radiation Facility in transmission geometry.

piles up at the moving interface and diffuses into the bulk of the austenite phase. This forms the rate-limiting process for the ferrite grain growth during the phase transformation. According to the Zener model, R^{α} as a function of time t is given by

$$R^{\alpha}(t) = \chi \sqrt{D_C^{\gamma}(t - t_s)} \qquad (2)$$

where, in the case of the austenite/ferrite transformation, χ is a parameter that is determined by the carbon solubilities in ferrite and austenite; D_C^{γ} is the carbon diffusion coefficient in the bulk of the austenite, which depends on temperature and carbon concentration (*12*); and t_s is the moment of nucleation of the grain. Equation 2 only applies to the initial stages of the transformation, during which the growth of the individual grain is not limited by interactions with neighboring grains because of overlapping diffusion fields (soft impingement) or existing grain boundaries (hard impingement).

The first and most frequently observed type of ferrite grain growth is initially in agreement with the theory (Fig. 4A). This means that the grains initially do not interact with growing neighboring grains. For each of the grains, the growth curves start to deviate from the Zener theory at different levels, depending on the local impingement conditions. Figure 4B shows the second type of growth, in which some ferrite grains continue to grow with the same crystallographic orientation during the pearlite formation as part of a pearlite colony. This remarkable behavior has so far only been observed by Thompson and Howell (*13*), who performed transmission electron microscopy measurements at the interface between ferrite and pearlite. This mechanism of continued growth of preexisting ferrite appears to be the dominant mechanism for pearlite formation. This is evidenced by the fact that very few new pearlite nuclei were found in the pearlite transformation temperature range (Fig. 3A). These growth curves also show that the pearlite colony reaches a larger final size when the initially formed ferrite grain is smaller. Another difference between the austenite/ferrite and austenite/pearlite transformation is that at the low imposed cooling rate, all the pearlite colonies start to grow at a well-defined temperature of 685°C for this steel. Once pearlite formation is initiated, the intercalated cementite takes up all the carbon, which increases the growth rate.

The final two types of grain growth have not been observed or postulated before. Figure 4C shows the third type of ferrite growth, in which ferrite nucleation and growth are retarded. An enrichment of carbon in the austenite causes a local decrease in transition temperature, which leads to retarded nucleation. The retarded growth is caused by indirect interaction with growing neighboring grains. The neighboring grains do not directly touch each other but interfere via surrounding diffusion and stress fields (*14*). The last class of ferrite grain growth is characterized by complex growth behavior (Fig. 4D). In this least frequently observed growth mode, ferrite grains not only grow but also temporarily shrink upon continued transformation. This behavior is due to a complex grain-boundary migration caused by direct interaction with neighboring grains. The neighboring grains directly touch, but their grain boundaries are not yet in their equilibrium position. It is known that some grain boundaries are more stable than others, depending on the curvature (*15*). Because the growth is a dynamic process, the forces on the grain boundaries may change irregularly, resulting in the growth behavior shown in Fig. 4D. Thus, on the level of individual grains we can distinguish four types of grain growth: There are grains that do not interact with neighboring grains, grains that continue to grow with the same crystallographic orientation into another phase, grains that indirectly interact, and grains that directly interact with neighboring grains.

Our measurements show that the activation energy for grain nucleation is at least two orders of magnitude smaller than that predicted by thermodynamic models. The observed growth curves of the newly formed grains confirm the parabolic growth model but also show three fundamentally different types of growth. We conclude that the current models do not accurately predict the phase transformation kinetics in polycrystalline materials. Future nucleation models should give a better prediction of the optimum size and shape of the critical nucleus, which initially may have a metastable crystallographic structure, with respect to the energy of the interfaces. Future growth models should incorporate the interactions between growing neighboring grains. From a technological perspective, these new insights are of importance to the modern materials production process, which relies heavily on grain nucleation and growth models to produce tailor-made materials.

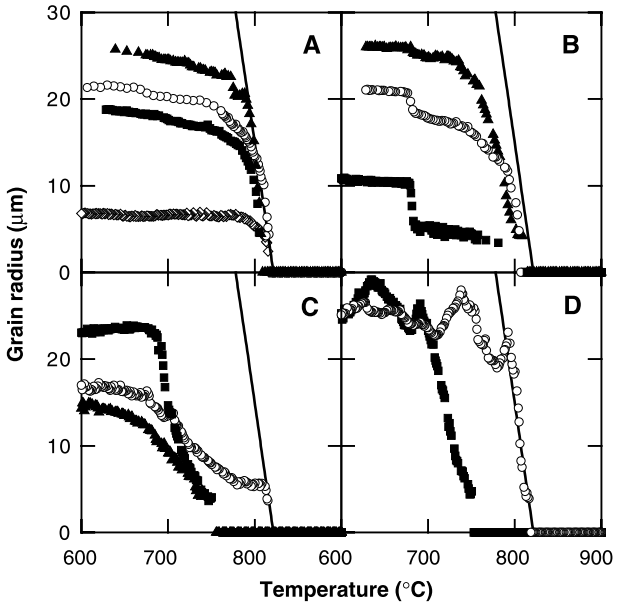

Fig. 4. Particle radius of individual ferrite grains as a function of temperature during continuous cooling of the steel from 900° to 600°C in 1 hour. Symbols indicate the growth curves of individual grains, and the solid line indicates the Zener theory. (**A**) Ferrite grains that started to grow according to the classical Zener theory (line). (**B**) Ferrite grains that continued to grow with the same crystallographic orientation during the pearlite formation as part of a pearlite colony. (**C**) Retarded ferrite growth. (**D**) Complex ferrite growth.

References and Notes

1. J. W. Christian, *The Theory of Transformations in Metals and Alloys* (Pergamon, Oxford, 1981).
2. C. Zener, *J. Appl. Phys.* **20**, 950 (1949).
3. C. E. Krill III *et al.*, *Phys. Rev. Lett.* **86**, 842 (2001).
4. E. M. Lauridsen, D. J. Jensen, H. F. Poulsen, U. Lienert, *Scripta Mater.* **43**, 561 (2000).
5. L. Margulies, G. Winther, H. F. Poulsen, *Science* **292**, 2392 (2001).
6. H. F. Poulsen *et al.*, *J. Appl. Crystallogr.* **34**, 751 (2001).
7. B. C. Larson, W. Yang, G. E. Ice, J. D. Budal, J. Z. Tischler, *Nature* **415**, 887 (2002).
8. P. C. Clemm, J. C. Fisher, *Acta Metall.* **3**, 70 (1955).
9. W. F. Lange III, M. Enomoto, H. I. Aaronson, *Metall. Trans. A* **19A**, 427 (1988).
10. J. Kučera, K. Stránský, *Mater. Sci. Eng.* **52**, 1 (1982).
11. S. Auer, D. Frenkel, *Nature* **409**, 1020 (2001).
12. J. Ågren, *Scripta Metall.* **20**, 1507 (1986).
13. S. W. Thompson, P. R. Howell, *Scripta Metall.* **22**, 1775 (1988).
14. M. Onink, F. D. Tichelaar, C. M. Brakman, E. J. Mittemeijer, S. van der Zwaag, *J. Mater. Sci.* **30**, 6223 (1995).
15. D. A. Porter, K. E. Easterling, *Phase Transformations in Metals and Alloys* (Chapman and Hall, London, 1981).

16. We thank S. O. Kruijver and L. Zhao for assistance during the synchrotron measurements, S. Schmidt for the use of his software, and E. R. Peekstok for the optical microscope images. Financially supported in part by the Foundation for Technical Sciences (STW) of the Netherlands Organisation for Scientific Research (NWO), the Danish National Research Foundation, and the Danish Research Council SNF (via Dansync).

29 July 2002; accepted 20 September 2002

A14

MICROSTRUCTURAL DYNAMICS IN Bi-2223/AG TAPES

Lotte Gottschalck Andersen and Henning Friis Poulsen

Materials Research Department, Risø National Laboratory, P.O. Box 49, DK-4000 Roskilde, Denmark.

1 INTRODUCTION

A large number of laboratories are presently involved in the research and development of high temperature superconducting (HTSC) tapes in kilometer length. While coated conductors may be the technology of the future, commercial products have so far only been obtained by producing polycrystalline Bi-2223 tapes by the so-called powder-in-tube (PIT) technique [1, 2]. Here a randomly oriented powder of $(Bi,Pb)_2Sr_2CaCu_2O_x$ (Bi-2212) and secondary phases are filled into a silver tube. The tube is flattened by a series of drawing and/or rolling steps, and the resulting tapes are stacked and put into another tube, which, in turn, is deformed once more. Finally, and most importantly, the powder is converted into $(Bi,Pb)_2Sr_2Ca_2Cu_3O_x$ (Bi-2223) by a series of annealing steps with intermediate deformations. During the annealing the c-axis of the Bi-2223 grains aligns to some extent to the tape normal. As a result, textured multi-filamentary tapes are produced with typical cross-sections of 3 mm $\times$ 0.2 mm.

The focus of the field is the optimization of the superconducting critical current density J_c, where values for tapes still are below 100 kA/cm^2, while thin films has been reported to have J_c's of order 1600 kA/cm^2. The limits for the critical current density

are ultimately defined by the flux pinning properties of Bi-2223, but as of today it is generally recognized that an optimization of the structural properties of the ceramic core is crucial.

The relevant structural features, in turn, relate to length-scales ranging from the macroscopic to the atomic level. In particular, emphasis is on controlling the phase purity of the core, its density and the dimensions of the filaments (macroscopic), the *c*-axis alignment of the Bi-2223 grains (mesoscopic), the structure of the interfaces between the grains (atomic) and the amount of cracks (all scales). At the same time the chemical phase space is very large, and the reactions are complex due to effects such as the use of non-stoichiometric and inhomogeneous powders, a small operation window in temperature, and an interaction with the Ag tube. Due to this complexity empirical 'black-box' approaches to optimization have been slow. As an alternative several groups have put a major effort into characterizing the structural details.

At the Materials Research Department at Risø structural characterizations of tapes have been going on for almost a decade – always in collaboration with the tape manufacturer Nordic Superconductor Technologies A/S (NST). We have focused on understanding the *dynamics* of the microstructure, which in turn has lead us to develop several new instrumental techniques. In particular, we note two short-comings of the 'conventional' diffraction tools: electron microscopy and Cu K_α X-rays. Firstly, they cannot penetrate the silver. Hence, investigations have to be performed on quenched and sectioned samples, which always rise the question of representability, in particular the formation of phases during quenching. (The reactions in pellets is clearly different from those in tapes, due to the influence of the Ag sheeting on the phase diagrams [3, 4, 5].) Secondly, the kinetics cannot be followed directly on the relevant length scales. Neutron diffraction is associated with some of the same problems. Again the absorption by the silver is a problem, and the time- and spatial resolution is not optimal [6].

The instrumental developments relate to the use of *hard X-rays* for diffraction studies. While conventional X-ray powder diffraction (with say 8 keV Cu K_α sources) only probes a few microns into the specimen, the penetration power can be increased dramatically by increasing the energy of the X-rays, as shown in Fig. 1. The necessary energy depends on the question at hand. If there is no need for separating diffraction peaks arising from Bi-2212 and Bi-2223 the tapes may be investigated with the incoming beam perpendicular to the normal direction of the tape for a minimum X-ray path length within the tape. In that case 24 keV is sufficient, as shown in the figure and demonstrated by the tape studies performed by Thurston *et al.* [7, 8]. However, for a complete diffraction analysis including a separation of peaks and a full texture analysis the tape needs to be investigated with ND positioned at an angle to the beam. As discussed later an angle of 75° is ideal. As illustrated by Fig. 1 energies of order 100 keV is then required.

With this motivation, in 1995–1996 we established a dedicated set-up for tape studies at the HASYLAB synchrotron in Hamburg, Germany [9]. Operating at 100 keV, the instrument is an all-round powder diffraction instrument, providing information on the phase concentrations, the texture, the strain and the stoichiometry of the phases within the ceramic core. As such the technique provides bulk data, averaging over

1–2 mm^2. The equipment has been used for a number of *in situ* studies, representative of typical annealing procedures. In addition, it has served as a tool for optimization and screening of many hundred tapes at room temperature.

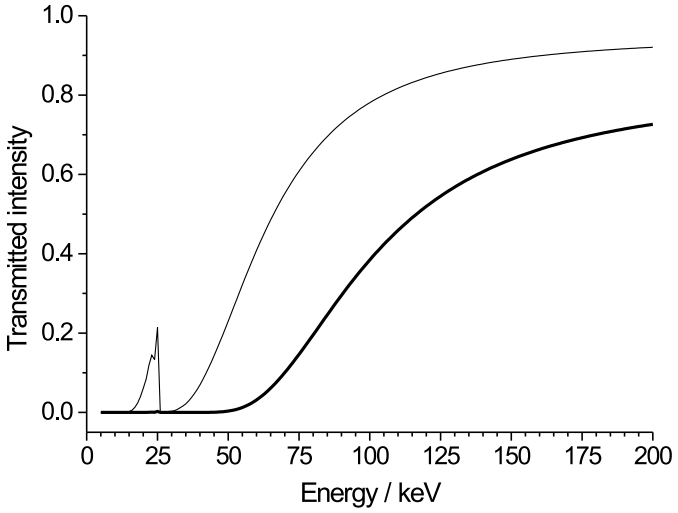

Figure 1: The transmitted fraction of X-rays penetrating a 200 μm thick Bi-2223/Ag tape as function of X-ray energy. A filling factor of HTSC:Ag = 1:3 is assumed. Simulated results are shown for the tape normal (ND) positioned parallel to the beam (thin line) and with ND at angle of 75° to the beam (thick line). The peak at 24 keV is related to an X-ray absorption edge of silver.

The second instrumental development involved pushing the hard X-ray concept one step further – namely by focusing the X-ray beam. Three-dimensional mappings of the local structure can then be realized. This idea has lead to the establishment of a so-called 3-Dimensional X-Ray Diffraction (3DXRD) microscope at the European Synchrotron Radiation Facility (ESRF) in Grenoble, France [10, 11]. Developed by Risø in collaboration with ESRF, the microscope was put in operation at the end of 1999. In favorable cases, it enables a complete non-destructive structural characterization at the grain level of a powder or polycrystal. For each grain the position, volume, crystallographic orientation, elastic strain and stoichiometry can be determined. In addition, for coarse-grained materials the topology of the grain boundaries can be mapped. So far the method has mainly been used in connection with studies of grain kinetics during processing of metals [12]. The main limitation is the spatial resolution, which at present is of order 20 μm. However, grains as small as 0.3 μm can be resolved with the microscope provided they have a unique orientation.

For Bi-2223 studies, the technique seems to be relevant for powder studies in general, e.g. the phase transformation can be studied as function of size, stoichiometry and alignment of the Bi-2212 grains. Furthermore, as hard X-rays are used, the kinetics of the individual ceramic grains within the tape can be followed. This statement has been verified by a feasibility study. Further advancement along this route is depending

on the development of software, which is able to index grains in colonies. Such work is in progress.

In this chapter we summarize our work on tapes with hard X-rays. In addition, we report on transmission electron microscopy (TEM) studies performed in collaboration with the group of van Tendeloo at EMAT in Antwerp, Belgium. TEM gives the opportunity to gain insight into the current path (sub-micron scale) including the grain thickness, colony thickness and the grain boundary angles [13, 14, 15]. Furthermore, by high-resolution TEM (HRTEM) one can investigate the grain boundaries on an atomic scale and detect the possible presence of non-superconducting phases. Also the intergrowth of Bi-22$(n-1)n$ phases with $n \neq 3$ can be studied. Using the same tapes for both hard X-ray diffraction and TEM studies, relevant complementary information is obtained.

The chapter is based partly on previously published results [16, 17, 18, 19]. In addition, we have included new material relating to the first use of the 3DXRD technique and *in situ* annealing in 8% O_2. In continuation of the work presented here numerous optimization studies have been performed. Some of these have been published elsewhere [20, 21].

The outline is as follows: in section 2 we give details of the experimental set-up in HASYLAB and the associated data analysis. Next, in section 3 we present *in situ* hard X-ray diffraction data for tapes subject to 'standard' annealing schemes with constant operating temperatures both in technical air and in an atmosphere of 8% O_2. The results for texture and phase evolution are compared to various models of the microstructural evolution. In section 4 we present the outcome of another hard X-ray experiment on tapes, describing the reversibility of the phase reactions and the role of the liquid. Section 5 comprises the results of a feasibility experiment with the 3DXRD technique. Section 6 contains our TEM results, again related to tapes that have been subject to 'standard' annealing conditions. These are compared with the synchrotron data. Finally, a summary of our results for the microstructural evolution in Bi-2223/Ag tapes is given in section 7.

2 HARD X-RAY DIFFRACTION SET-UP

In this section the hard X-ray powder diffraction set-up at the HASYLAB synchrotron is presented along with the corresponding data analysis. We illustrate the quality of the data and the analysis procedure by some of our first results for a mono-filamentary tape annealed in air [16]. The data were obtained at room temperature for the green tape (as-rolled) and for the tape in the fully processed state (after 2nd annealing).

2.1 Experimental set-up

The set-up for *in situ* studies of tapes is established at the BW5 beamline at HASYLAB [9, 10, 16, 22]. This beamline was built as the first dedicated source for experiments with energies above 60 keV [23]. As discussed in section 1, the energy is typically chosen to be 100 keV, corresponding to penetration depths of $\mu = 650$ μm and $\mu = 600$ μm in

Ag and fully dense, pure Bi-2223, respectively. A photo of the set-up is given in Fig. 2.

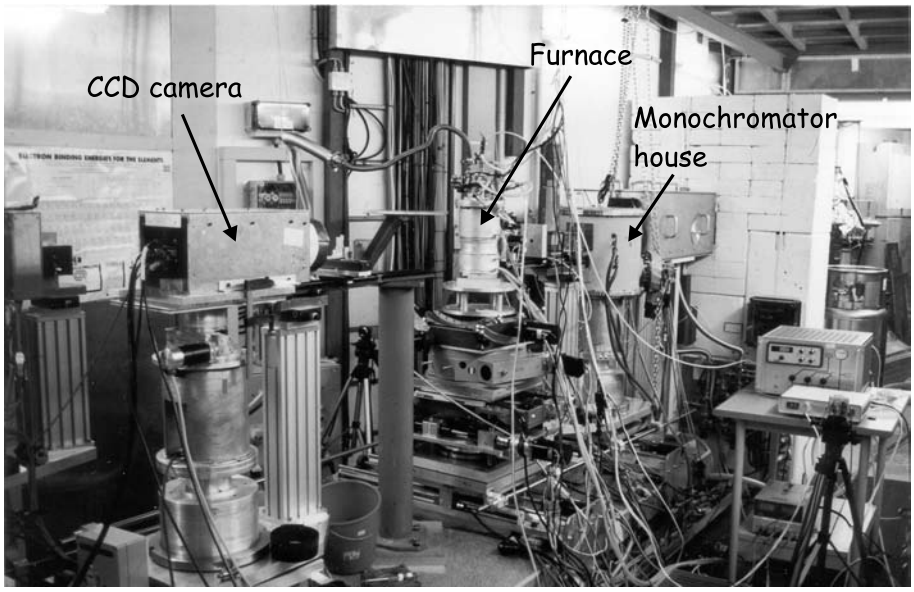

Figure 2: The experimental hutch at the BW5 beamline at HASYLAB with the setup used for *in situ* annealing experiments.

The underlying geometry of the set-up is illustrated in Fig. 3. The un-focused beam is monochromatized by a broad band monochromator in order to maximize the number of photons impinging on the sample. For our first experiments – annealing in air – we chose an imperfect $SrTiO_3$ crystal with a mosaic spread of FWHM = 40", using the (200) reflection in Laue geometry. For the later studies in 8% O_2 this was replaced by a Si/Ge (111) gradient crystal [24]. A slit is used to define the size of the incoming beam. The gaps are typically set at 1 mm horizontally and 1 mm vertically. With this setting, the incoming flux on the sample is measured to be of order 10^{11} photons/s. Powder patterns are recorded on-line using either a CCD camera or an image plate. The CCD camera is a 12 bit tapered camera with an effective area of 77×83 mm^2. It is typically operated in a 600×650 pixel mode, having a read-out time of $\sim$1 s. The Image-Plate system is an on-line MAR345 system. In this case, the recorded image contains more pixels, typically 1800×1800 pixels. Unfortunately, the read-out time is also much longer – of order 2 min. Results presented in this section will all refer to the use of the $SrTiO_3$ monochromator and the CCD camera.

A laboratory coordinate system (x, y, z) is defined with the beam along the y-axis and perpendicular to the plane of the detector, cf. Fig. 3. The z-axis is parallel to the vertical axis. The azimuthal angle around the Debye-Scherrer cones is called η. Tapes are mounted on a horizontal ω table with the rolling direction (RD) vertically and the normal direction (ND) parallel to the beam for $\omega = 0$.

In general, the CCD camera is mounted at a distance from the sample where slightly more than one quadrant of the relevant diffraction pattern is retained. The approximate resolution is then: $\Delta 2\theta = 0.02°$, $\Delta\eta = 1.2°$ and $\Delta\omega = 0.02°$. Numbers for the image plate are similar.

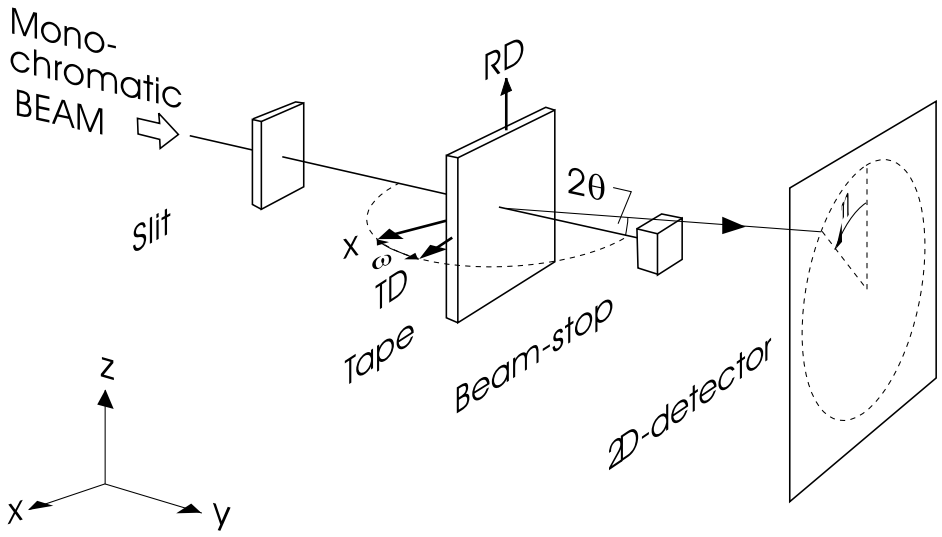

Figure 3: Schematic of the experimental set-up at beamline BW5, HASYLAB. The definitions of a laboratory coordinate system (x, y, z) and angles 2θ, η, ω are illustrated. RD and TD denotes the rolling and transverse directions of the tape, respectively.

2.2 Choice of diffraction geometry

In general, for a textured material a complete diffraction analysis requires the acquisition of images for a series of equidistant ω settings spanning the range from $-90°$ to $90°$. For specimens with broad textures, such as tapes, the step size should be of order $5°$. From such data the texture of the various phases can be determined in the form of pole figures. At the same time, for each phase the integrated intensities can be derived, leading to concentration determinations. The necessary coordinate transforms as well as an introduction to the use of the hard X-ray set-up for texture studies in general is provided in Ref. [22].

A simple way of visualizing textures is by means of pole figures. A pole figure is a stereographic projection. As an example the construction of a pole pole figure for a cubic single crystal is illustrated in Fig. 4.

To illustrate the pole figure construction for tapes, let us consider a selected powder ring on the detector for a given ω setting. The trace of such a ring transforms into two closely lying curves in the corresponding pole figure (one for each hemisphere). Tracks for selected ω values in the TD-RD plane are shown in Fig. 5.

Pole figures of tapes have been generated on several occasions, see e.g. Ref. [26]. Within experimental uncertainty (10%) the data all indicate that the Bi-2212 and Bi-2223 textures are fiber-symmetric with $(00l)$ aligned along ND. This is in accordance with a series of works performed by other groups [6, 27, 28, 29]. As discussed in more detail below, this implies that it is sufficient to acquire data for one well considered ω setting.

With respect to Fig. 5 and the Bi-2212 and Bi-2223 phases, a $(00l)$ reflection will appear as a peak at the center (ND). The (200)/(020) reflection will appear as a ring following the periphery, while the general (hkl) reflections will appear as rings at various distances from the center. The radial widths of any of these peaks/rings are indicative

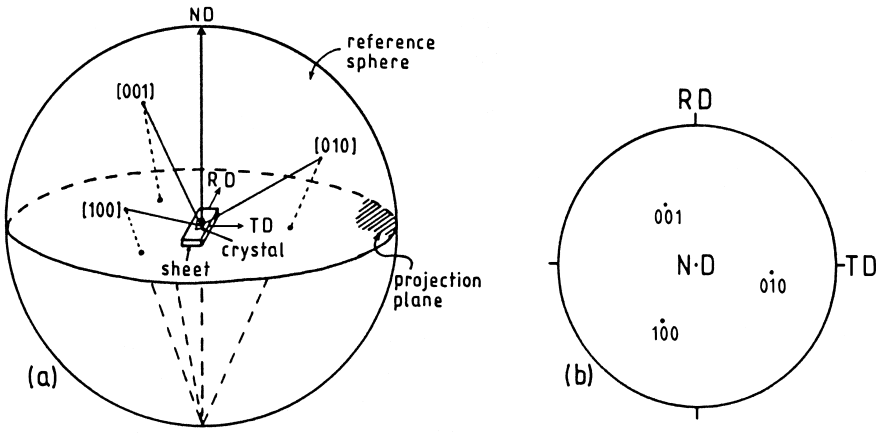

Figure 4: (a) An illustration of construction of a pole figure (b) The corresponding pole figure [25].

of the degree of c-axis alignment of the grains.

At a first glance $\omega = 90°$ seems ideal, as the trace of experimental data cuts through ND, cf. Fig. 5. However, absorption prohibits quantitative investigations with $|\omega| \geqslant 80°$. Instead $\omega = 75°$ is chosen, as the cut with the intense (115) and (117) rings will be nearly perpendicular. Furthermore, the tail of the distribution of the $(00l)$ peak is still available for analysis.

2.3 Data analysis

The data analysis is done primarily by means of the software package FIT2D [30]. Initially, images are normalized to primary intensity and exposure times. Next, the center of the diffraction patterns are found and the traces of the Debye-Scherrer cones in the images are parameterized. The radial off-set between the estimated traces and the texture segments in the exposures is found to be less than 1 pixel.

The further data analysis is based on various one dimensional projections of the images. Three projections are used: 2θ projections, line profiles and texture profiles. 2θ projections contain the radial intensity variation within the image, averaged for each 2θ value over the available η range. They are used for indexing and estimates of phase concentrations, 2θ widths and 2θ positions (d-spacings). Line profiles contain the intensity variation along a radial line in the image at a given azimuthal angle η. Intensities are averaged over 10 pixels in the direction perpendicular to the radial line. Hence, the data set are equivalent to conventional powder diffractograms obtained by a single detector with an aperture 1 pixel wide and 10 pixels high in front of the detector. Line profiles are used in certain cases for estimates of the 2θ widths of individual reflections. Finally, the texture profiles contain the intensity variations with η for fixed 2θ of the powder diffraction segments. For each η position in the texture profile the scattered intensity in the image is integrated radially within the 2θ range of the reflection. A linear background subtraction is employed.

With respect to the texture analysis, for a fiber symmetry the interesting distribu-

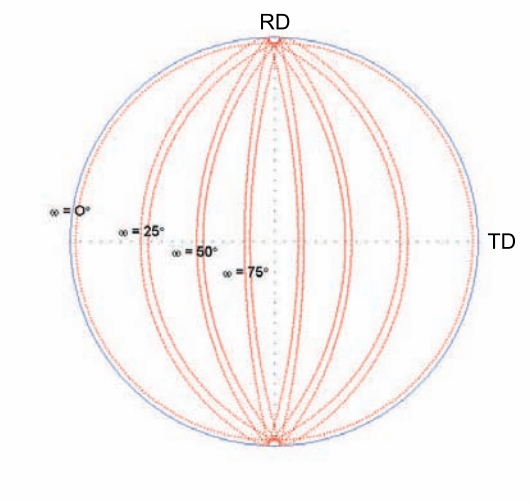

Figure 5: Construction of the pole figure: For each ω setting the data in a given Debye-Scherrer ring ($0° < \eta < 360°$) probes the pole figure along two narrow lying curves. Only the tracks of $\omega = 0°$, $25°$, $50°$ and $75°$ are shown.

tion is $P(\alpha)$, the probability of finding the scattering vector of interest with a spherical distance of α to ND. We will symbolize the width (FWHM) of this profile by $\Delta\alpha$. The transformation between η and α is derived in Ref. [16]. It is

$$\cos(\alpha) = |\cos(\theta)\sin(\eta)\sin(\omega) + \sin(\theta)\cos(\omega)|. \tag{1}$$

When the texture is distinct, the $P(\alpha)$ distributions for different reflections belonging to the same phase will to a good approximation have the same peak shape, and therefore also nearly identical $\Delta\alpha$'s.

Within the fiber symmetric approximation, the concentration, c, of the various phases may be found according to

$$c \propto \frac{\sin(\theta)}{\lambda^3 N_0^2 j_{hkl}|F_{hkl}|^2} \frac{1}{VA(\omega,\eta,\theta)} \int I_{norm}(\alpha)d\alpha \tag{2}$$

where $|F_{hkl}|^2$ is the structure factor including the atomic form factor, j_{hkl} the multiplicity, N_0 the number of units cells per unit volume, V the volume of the HTSC core illuminated by the beam, $A(\omega,\eta,\theta)$ the absorption coefficient, and $\int I_{norm}(\alpha)d\alpha$ the integrated intensity over the α-distribution (normalized to incoming photon count). However, structure factors are not known for several of the phases of relevance here, either because literature data are scarce (Bi-2223) or because the stoichiometry of the compounds vary, e.g. $(Ca,Sr)_2PbO_4$. We will therefore to some extent rely on scaling of $\frac{1}{VA}\int I_{norm}(\alpha)d\alpha$ to known abundances in the tapes before or after annealing. The exact procedure will be outlined in section 3.

For calculations of the absorption coefficient, A, we note that the penetration depths of Ag and HTSC are nearly the same at 100 keV. We therefore approximate the tape geometry by a single slab of thickness t, inclined at an angle $90 - \omega$ to the incoming

beam. Due to the small Bragg angles and the rather narrow texture profiles we may further to a good approximation set 2θ to 0. This leads to the following simple equation

$$A(\omega) = \exp\left(-\frac{t}{\mu\cos(\omega)}\right). \tag{3}$$

For the standard data analysis based on the HTSC (115) reflections at $\omega = 75°$ the absolute errors introduced by using Eq. (3) are of the order a few percent. Moreover, when comparing identical reflections of the Bi-2223, Bi-2212 and Bi-2201 ($Bi_2Sr_2CuO_x$) phases, the relative error will be much smaller. In general, we have therefore neglected absorption in our texture analysis, while Eq. (3) has been used to normalize integrated intensities when comparing measurements made at different ω's or on different samples.

We have not attempted to perform full structural refinements of the unit-cell parameters, e.g. Rietveld refinements. Instead, we present results for the evolution of the integrated intensities of selected reflections. By comparison with the corresponding line-shifts, we elucidate whether the intensity variations are due to changes in concentration or stoichiometry.

2.4 Example of room temperature data

The two specimens considered here as examples were cut from the same mono-filamentary tape, which had a nominal powder composition of $Bi_{1.84}Pb_{0.34}Sr_{1.91}Ca_{2.03}Cu_{3.2}O_{10+x}$. One specimen was investigated as a green tape (as-rolled) while the other was given a full heat treatment, using the standard employed at that time. The green tape had an average thickness of 260 μm and a width of 2.3 mm, while the fully processed tape was 190 μm thick. Synchrotron measurements were done at room temperature on both specimens [16], that is with the tapes mounted outside the furnace. Exposures were acquired for a series of ω values.

The raw exposures for the two specimens at $\omega = 75°$ are shown in Fig. 6 and Fig. 7. Exposure times were 30 s, and the resulting intensities in the main HTSC reflection are of order 3300 counts/pixel and 700 counts/pixel for the green tape and the fully processed tape, respectively. At 2θ angles below 2.0° the background is dominated by stray scattering from the hutch varying between 60 and 150 counts/pixel. At higher angles the combined diffuse and Compton scattering from the sample becomes dominant. For the HTSC reflections of main interest here, the two contributions are nearly of the same size.

The corresponding 2θ projections are shown for chosen ω settings in Fig. 8 and Fig. 9 for the green and fully processed tape, respectively. The indexing procedure involved the structural phases Ag, Bi-2201, Bi-2212, Bi-2223, and $(Ca,Sr)_2PbO_4$. In addition, a line at $d = 2.18$ Å is present in all data sets. Contributions from higher harmonics ($\lambda/2$, etc.) are only found for the strongest Ag lines – and easily separated. It should be noted, that the information content in the raw images is significantly higher than in the projections. Hence, inspection of the exposure shown in Fig. 7 showed small dots with d-spacings corresponding to the CuO (002)/(111) line, indicating the presence of relatively large and/or perfect CuO particles.

The results of the texture analysis for the Bi-2223 phase in the fully processed tape

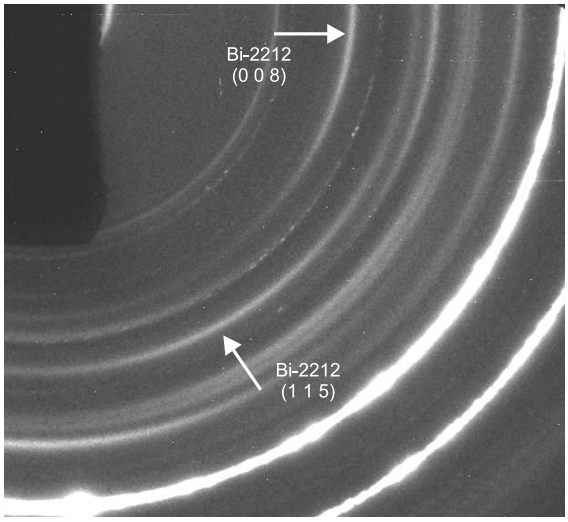

Figure 6: Room temperature exposure of the green tape at $\omega = 75°$. The image is dominated by the strong lines from the Ag sheet and the Bi-2212 reflections. To protect the detector a large beamstop was used, evident as a dark region in the upper left corner.

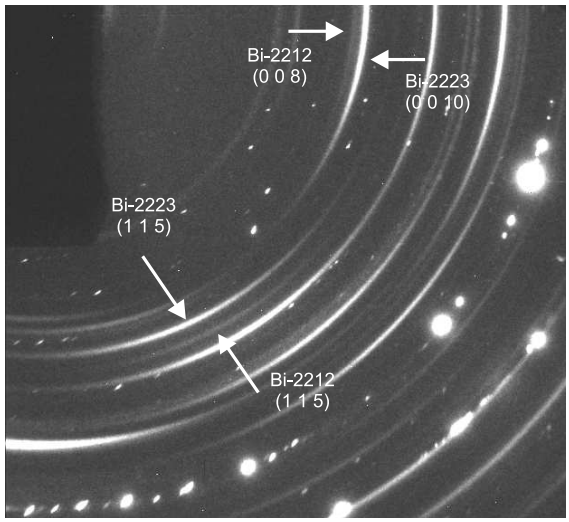

Figure 7: Room temperature exposure of the fully processed tape at $\omega = 75°$. The image is dominated by the strong lines from the Bi-2223 reflections. In comparison to Fig. 6 the Silver is seen to have recrystallized to form Bragg peaks in stead of powder rings.

are summarized in Fig. 10. The texture profile of the dominant (200) reflection at $\omega = 0°$ is shown as an insert. Evidently the deviation from a uniform profile is of order 5%, comparable to the degree of fluctuations within the sample. The profile of the chosen (115) standard reflection at $\omega = 75°$ is shown in the main of the figure – as function of α, cf. Eq. (1). Also shown is the result of fits to Gaussian, Lorentzian and Lorentzian squared functions. Clearly the Lorentzian squared – with a width (FWHM) of $\Delta\alpha = 21.9° \pm 0.2°$ – represents the data best. Similar results were obtained for other non-overlapping reflections: (117), (200), (0010), and (0012), with an average width of $\Delta\alpha = 21.4° \pm 1.0°$. Analysis of data obtained at other ω settings complied with these findings, and provided further validation of the assumption of a fiber-symmetric Bi-2223 texture.

The results of an analogue data treatment of the Bi-2212 phase in the green tape are shown in Fig. 11. Again the deviations from a uniform profile is small at $\omega = 0°$. At $\omega = 75°$ the (115) reflection is to a minor degree overlapping with (0010) due to a large 2θ spread, cf. below. After a suitable correction for this effect, the texture data are well described by a Lorentzian square function with best fit for $\Delta\alpha = 59.0° \pm 0.5°$. The corrected data set and the fit are compared in the main of Fig. 11.

The analysis of the $(Ca,Sr)_2PbO_4$ phase is based on the closely lying (110) and (020) reflections. In case of the green tape, the (110) is found to be aligned along ND in an approximate fiber symmetry. The width of the distribution is $\Delta\alpha = 160° \pm 30°$. The data for the fully processed tape are consistent with a similar type of distribution with $\Delta\alpha = 130° \pm 40°$. The texture of the Bi-2201 phase, on the other hand, is found

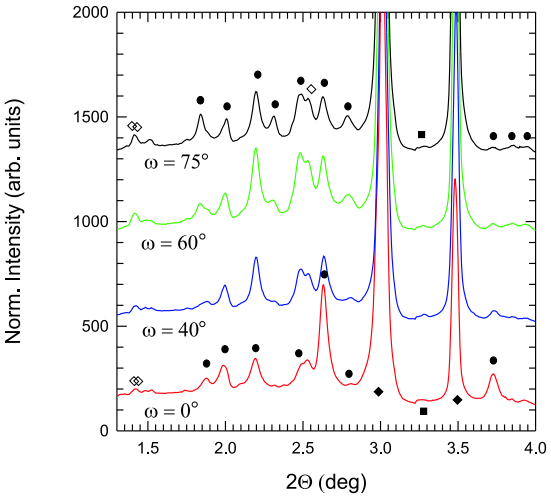

Figure 8: 2θ projections at various ω settings for the green tape. The $\omega = 75°$ data are based on an analysis of the image shown in Fig. 6. Intensities are normalized to acquisition time and primary intensity. The 2θ axis is normalized to a literature value for the Ag (111) line. Symbols refer to: (●) Bi-2212, (⧫) Ag, and (◇) $(Ca,Sr)_2PbO_4$. A non-identified phase with $d = 2.18$ Å is marked by ■.

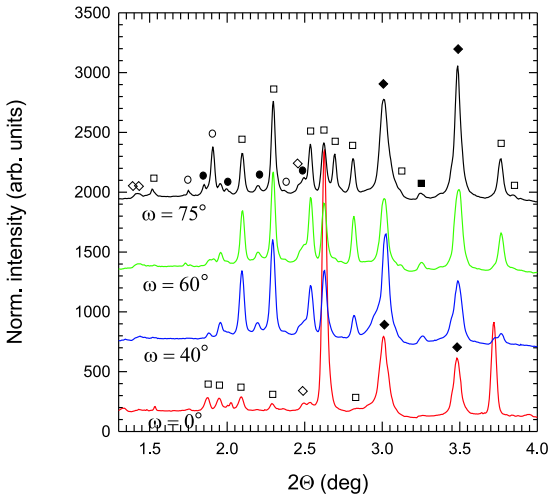

Figure 9: 2θ projections at various ω settings for the fully processed tape. The $\omega = 75°$ data are based on an analysis of the image shown in Fig. 7. Intensities are normalized to acquisition time and primary intensity. The 2θ axis is normalized to the Ag (111) line. Symbols refer to: (□) Bi-2223, (●) Bi-2212, (○) Bi-2201, (⧫) Ag, and (◇)$(Ca,Sr)_2PbO_4$. A non-identified phase with $d = 2.18$ Å is marked by ■.

to be similar to the ones for Bi-2212 and Bi-2223. In this case, the data analysis is based mainly on the (115) reflection.

For the line profile analysis we start by discussing data related to a set-up with a long sample to CCD distance (300 cm). Line profiles through selected reflections for the two tapes are shown in Fig. 12. The data sets are extracted from projections at $\eta = 90°$ through images made at $\omega = 75°$ – the same settings as those for the images displayed in Fig. 6 and Fig. 7. Both line profiles – as well as the others associated with the reflections of the two phases – are well approximated by Lorentzian peak shapes. The instrumental resolution on the other hand – as estimated from exposures of a pure Bi-2223 powder – is more Gaussian like. The full width at half maximum, $\Delta 2\theta$, for the as rolled tape is much broader than the width for the fully processed tape, indicating a larger particle size in the fully processed tape or relaxation of stresses as a result of the annealing. However, the 2θ variation of $\Delta 2\theta$ of the non-overlapping line profiles for the $(00l)$ reflections – shown in Fig. 13 – gives evidence that the broadening in both cases are caused predominantly by intergranular stresses with little contribution from particle size effects. This complies well with scanning electron microscopy investigations, which gave estimates of 1 μm for the as-rolled grain sizes. From linear fits through the points in Fig. 13, strains of $\varepsilon = -\Delta d/d = 1.7 \times 10^{-2}$ and $\varepsilon = 4 \times 10^{-3}$ is found for the $(00l)$

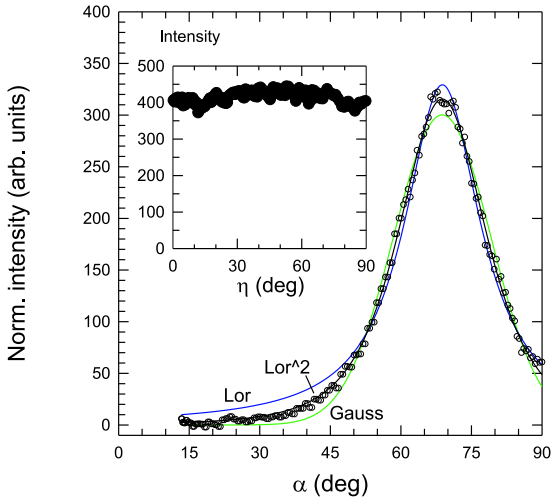

Figure 10: Texture analysis of the fully processed tape. The main part of the figure relates to a Bi-2223 (115) texture profile at $\omega = 75°$. The normalized data (○) are shown as function of α, along with best fits (——) to Gaussian, Lorentzian, and Lorentzian squared functions. The $\omega = 0°$ texture profile of the Bi-2223 (200) reflection is shown in the insert.

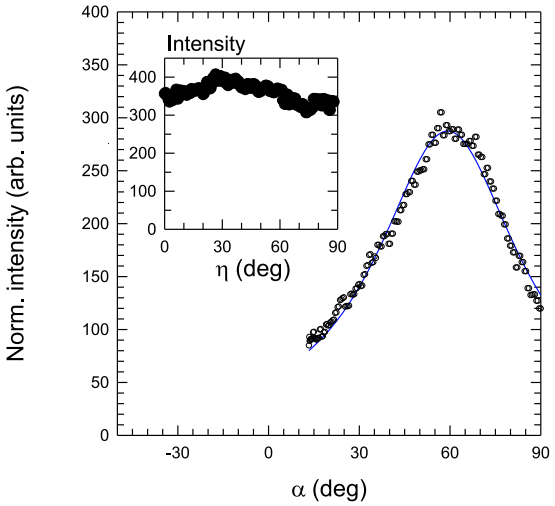

Figure 11: Texture analysis of the green tape. The main part of the figure relates to a Bi-2212 (115) profile at $\omega = 75°$. The normalized data (○) are shown as function of α, along with a best fit (——) to a Lorentzian squared function. The $\omega = 0°$ texture profile of the Bi-2212 (200) reflection is shown in the insert.

reflection along the ND direction for the green and fully processed tape, respectively.

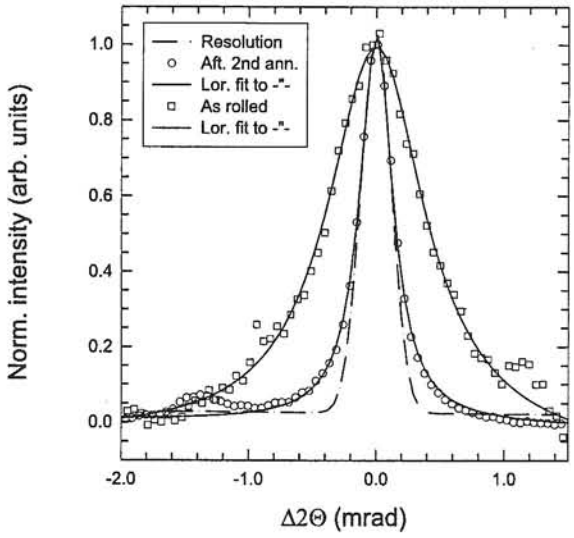

Figure 12: Peak profiles for the Bi-2212 (0010) reflection of the green tape (as-rolled) and the Bi-2223 (0014) reflection of the fully processed tape (after 2nd annealing). The setting is $\omega = 75°$ and $\eta = 90°$, corresponding to horizontal profiles through the upper rim of the images shown in Fig. 6 and Fig. 7. For sake of clarity of presentation, the data are normalized to a common maximum of 1. Best fits to Lorentzian peakshapes are shown, with resulting widths (FWHM) of $\Delta 2\theta = 0.93$ mrad and 0.31 mrad, respectively. The resolution function at the d-spacing of the Bi-2223 reflection is indicated as a dashed line.

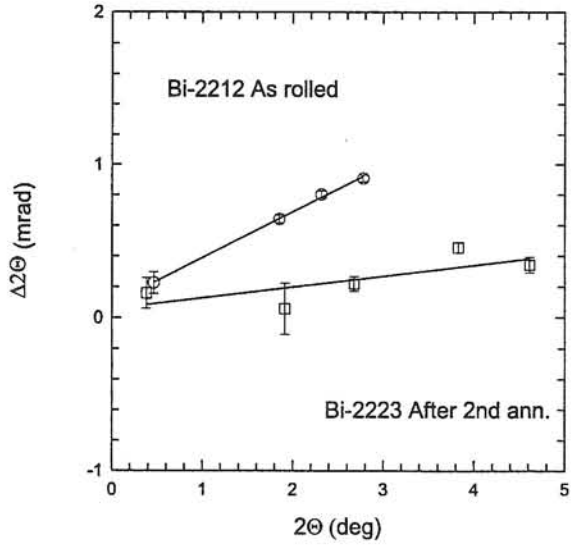

Figure 13: The full width at half maximum of various $(00l)$ peak profiles as function of 2θ for the standard setting of $\omega = 75°$ and $\eta = 90°$, cf. Fig. 12. Data points are the results of Lorentzian fits throughout. The instrumental broadening has been subtracted. Best linear fits to the points are indicated (——).

Line profile analysis for the standard set-up with the smaller sample to detector distance has been performed in a similar way. Results were similar but more uncertain due to the poorer resolution.

2.5 *In situ* studies

For *in situ* work tapes were mounted in parallel in a modified version of the neutron diffraction furnace presented in Ref. [31]. In addition to the main Kanthal heating element of the furnace, the inset comprise two small differential heaters positioned at different heights. Each of the heaters is associated with a tape holder, holding up to 8 tapes, with positions shifted horizontally. Hence, by translating the furnace in x and z up to 16 tapes can be studied during the same annealing. This feature has proven to be useful for optimization studies. Two chromel/alumel type thermocouples encapsulated in inconel were used. The operating temperatures were proven to be stable within $\pm$ 1 °C.

The background is dominated by scattering in the furnace, as both the diffracted and the incoming beam has to penetrate 1 mm Al, two 100-μm Ag heat shields and the 2.1 mm thick wall of a quartz tube.

The design of the sample holder required the specimens to be 2 cm long. Hence, specimens were cut in that length with scissors without attempting to seal the ends. We annealed several of such specimens and monitored the structure (phase composition and texture) as function of the distance to the ends. A clear degradation was found within the outermost 2 mm, while no effects could be observed further than 3 mm from the end. In comparison the *in situ* measurements always took place in the central part of the specimens.

For high quality tapes the structural fluctuations along the tape were found to be small. A texture variation, $\Delta(\Delta\alpha)$, of only 0.2° was measured in a long length tape at three places over ∼10 cm [26]. Nevertheless, to ensure that data are truly comparable, the furnace was translated up and down during heating and cooling such that the same volume within the tapes was illuminated by the beam at all times.

3 *IN SITU* HARD X-RAY DIFFRACTION STUDIES OF STANDARD HEAT TREATMENTS

In section 2 a detailed account of the experimental hard X-ray diffraction set-up and the procedures developed for the data analysis are found. Here we present the results from three *in situ* experiments: (1) a standard heat treatment of a green tape in an atmosphere of technical air [17], (2) a standard heat treatment of a green tape in 8% O_2 [26], and (3) the final annealing of a tape in 8% O_2 [26]. By standard conditions we imply a relatively slow ramp-up followed by annealing at a fixed operation temperature, T_{MAX}. T_{MAX} was chosen to be close to the middle of the temperature window, where Bi-2212 transforms to Bi-2223. Experimentally, we find the middle of this window to be the temperature where the kinetics is fastest. For each experiment the data is first presented, then followed by an interpretation and a discussion with respect to models

of the microstructure dynamics. A discussion of our results for the cooling part is outside the scope of this chapter – instead we refer to Ref. [32].

The results relate to mono-filamentary tapes: Similar studies on multi-filamentary tapes gave analogue results, however with substantially better alignment of the HTSC phases and a faster kinetics. The signal-to-noise ratio is somewhat worse in the multi-filamentary case due to the lower HTSC:Ag ratio.

3.1 1st annealing in air

The tape was produced from a powder with a nominal composition of $Bi_{1.84}Pb_{0.34}Sr_{1.91}$-$Ca_{2.03}Cu_{3.2}O_{10+x}$. The tape was first drawn then rolled to a final thickness of 238 μm for the green tape.

The *in situ* synchrotron annealing experiments took place in an environment of technical air, with an operating temperature of $T_{max} = 835$ °C. The temperature profile is shown in Fig. 14. The heating ramp was 100 °C/h up to 700 °C, then 50 °C/h. The cooling rate was 50 °C/h.

3.1.1 Results

The concentration of the dominant phases: Bi-2212, Bi-2223, Bi-2201 and $(Ca,Sr)_2PbO_4$ are shown as function of annealing time in Fig. 14. The concentrations C_{2212} and C_{2223} were determined by the constraints

$$\begin{aligned} C_{2212} &= 1 \qquad \text{when reaching } T_{max}, \\ C_{2212} &+ C_{2223} = 1 \qquad \text{at } T = 730\ ^\circ\text{C during cooling.} \end{aligned} \tag{4}$$

Results for secondary phases are based on scaling to the Bi-2212 phase by means of Eq. (2). The major features of Fig. 14 are the disappearance of the $(Ca,Sr)_2PbO_4$ reflections at 820 ±5 °C, the slow conversion of 97% of the Bi-2212 phase to (mainly) Bi-2223 within 19 h after the annealing temperature of 835 °C has been reached, and the appearance of secondary phases during cooling. It should be noted that crystalline Bi-2201 phase appears only during cooling.

In addition, a peak appears just before T_{MAX} is reached with a d-spacing of 2.50 Å. We identify this as the (011) peak of the $(Ca,Sr)_2CuO_3$ phase, with a being the longest axis of the orthorhombic unit cell. From results on other tapes the (200) and (301) reflections of this phase have been indexed as well (see also section 4). The relative concentration of $(Ca,Sr)_2CuO_3$ is determined by scaling the integrated intensity of the (011) reflection with respect to the integrated intensity of the Bi-2212 (115) reflection according to structure factors derived from Ref. [33, 34] for Bi-2212 and $(Ca,Sr)_2CuO_3$, respectively. In the raw two-dimensional images the diffraction pattern of $(Ca,Sr)_2CuO_3$ appears as a circle segment, not as dots, indicating a large number of rather small grains. The change in the $(Ca,Sr)_2CuO_3$ concentration with time is included in Fig. 14. Evidently the phase appears above 810 °C, peaks exactly when the operation temperature is reached, and then slowly decays at a rate which is very similar to the Bi-2212 to Bi-2223 conversion rate.

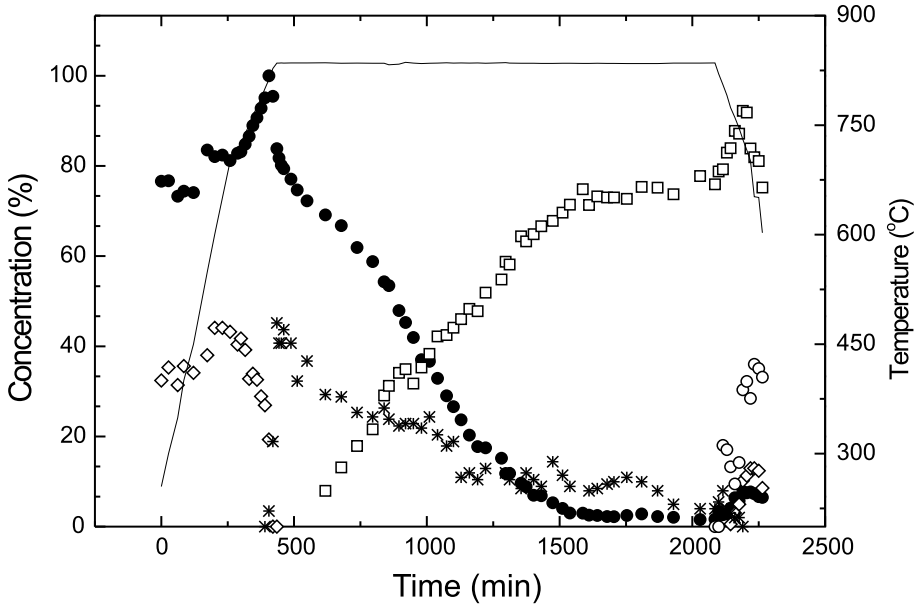

Figure 14: Integrated intensities of selected reflections during *in situ* annealing in air. The symbols refer to the (115) reflections of Bi-2212 (•), Bi-2223 (□) and Bi-2201 (○) as well as (110) for $(Ca,Sr)_2PbO_4$ (◇) and (011) for $(Ca,Sr)_2CuO_3$ (∗). The intensities are scaled to provide information on the relative concentrations, see the text. To ease visualization the Bi-2201 concentration is multiplied by 10. The line marks the temperature profile with reference to the temperature scale at the right hand of the figure.

The evolution of the average mis-alignment angle $\Delta\alpha$ of the two major superconducting phases is shown in Fig. 15. A major part of the texture development is seen to take place during the heating – before the Bi-2212 to Bi-2223 phase conversion. We also observe that the $\Delta\alpha$ widths of the two main phases are identical within experimental uncertainty within the second half of the time evolution. Note that for t $>$ 1500 min the uncertainty in the determination of the Bi-2212 texture is rather large due to the reduction of the scattered intensity. The final width of the Bi-2223 distribution is $\Delta\alpha = 23^\circ \pm 1^\circ$.

The evolution of the 2θ line-widths of the Bi-2212 (115) and Bi-2223 (115) peaks are shown in Fig. 16. While the Bi-2212 peak remains dominated by the instrumental resolution once the operating temperature has been reached, there is a distinct broadening of the Bi-2223 peaks. Initially, these are well described by Gaussians, as expected if finite-size effects cause the broadening, and at later stages they approach a Lorentzian squared lineshape. By a simple analysis of the 2θ variation of $\Delta(2\theta)$ we find that the broadening is dominated by finite-size effects, and that the thickness of Bi-2223 along the c-axis approaches 600 Å asymptotically.

In Fig. 17 the Bragg angle for the midpoint of the Bi-2212 (115) reflection is shown as function of annealing time. Substantial shifts are observed throughout the annealing. In order to understand this behavior the shifts during heating of three Bi-2212 peaks as well as one Ag peak are plotted as function of temperature in Fig. 18. From the

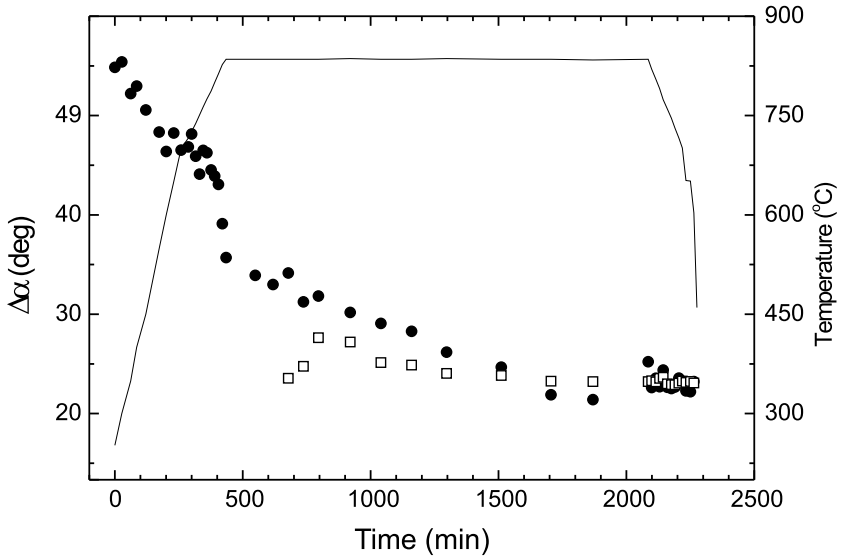

Figure 15: Texture evolution. The full-width-at-half-maximum – $\Delta\alpha$ – of the texture profiles of the Bi-2212 (•) and Bi-2223 (□) phases are shown. The analysis is based on the (115) reflections. The line marks the temperature profile with reference to the temperature scale at the right hand of the figure.

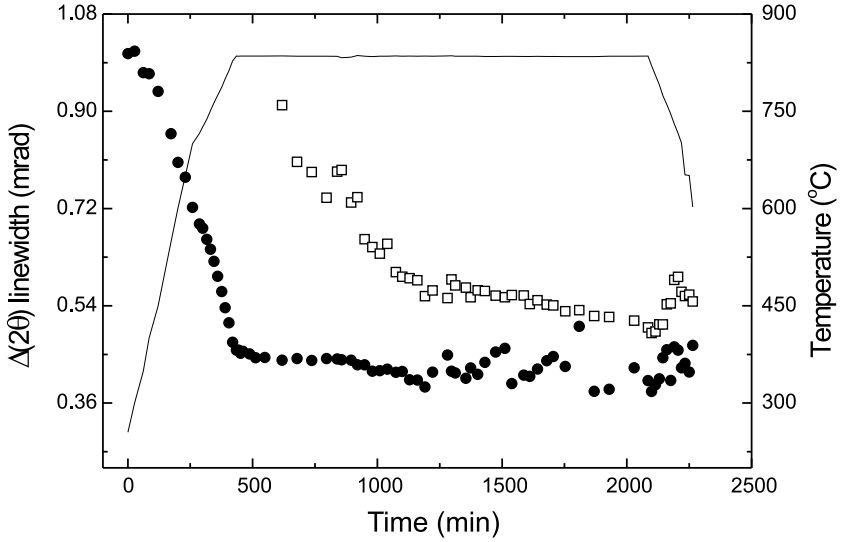

Figure 16: Evolution of the X-ray line-widths. The 2θ full-width-at-half-maximum of the (115) reflections of Bi-2212 (•) and Bi-2223 (□) are shown. The data points are not corrected for an instrumental broadening of estimated width 0.35 mrad. The erratic behavior of the Bi-2212 data between 1200 and 2000 min is an artifact of the fitting caused by the low concentration of this phase in this region.

figure, clearly for all four reflections the lattice expansion is nearly constant between 400 °C – where the silver softens – and 750 °C. From fits within this temperature range we find linear thermal expansion coefficients of $\alpha = 16 \times 10^{-6}$ K^{-1}, 19×10^{-6} K^{-1}, 22×10^{-6} K^{-1} and 26×10^{-6} K^{-1} for Bi-2212 (200), Bi-2212 (115), Bi-2212 (0010)

and Ag (111), respectively. With these coefficients at hand we may extrapolate the expected thermal expansion of the lattice for the rest of the annealing. The resulting model values for 2θ are shown as lines in Fig. 17 and Fig. 18.

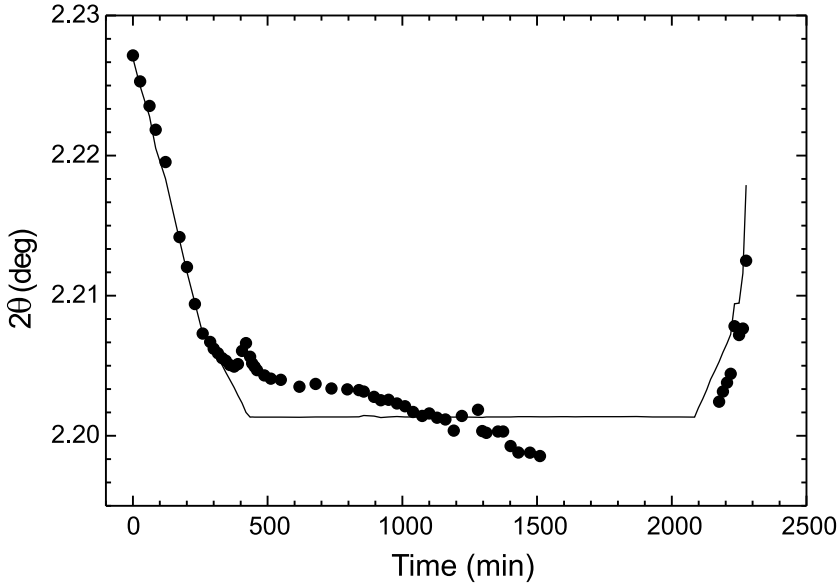

Figure 17: The lattice expansion of the (115) reflection of Bi-2212 during *in situ* annealing (•). Data points are left out when fitting becomes unreliable, due to vanishing intensities. A theoretical curve based on a shift caused only by thermal expansion is shown as a line.

With respect to the model calculation the lattice is seen from Fig. 18 to contract in all crystal directions by up to $\Delta d/d_0 = 0.0022$ at 825 °C. There are two possible causes of this: stress and change in stoichiometry. The latter is the dominant effect for two reasons. Firstly, the Ag expansion is approximately linear in temperature up to the operation temperature, cf. Fig. 18. Secondly, the integrated intensity of the Bi-2212 (115) increases between 700 °C and 815 °C where the relative contraction also takes place. Moreover, the integrated intensities of other Bi-2212 peaks do not all exhibit the same behavior – e.g. the (113) intensity is to a good approximation constant in the same temperature range. Hence, the Bi-2212 composition and thereby the scattering structure factors seem to change.

3.1.2 Structural evolution during ramp-up

In the following we interpret the data for the initial 500 min of the annealing. First, we note that the texture and strain curves are very similar up to 700 °C, with approximately constant values in the ranges 0–400 °C and 550–700 °C. We attribute the changes to grain growth of Bi-2212. Minor jumps appear at around 450 °C. These are attributed to softening of the Bi-2212 material.

The various results for the last part of the heating ramp and the first 30 min at 835 °C is summarized in Fig. 19. The curves are normalized as described in the caption in order to facilitate the comparison of phase and texture evolution. For quantitative

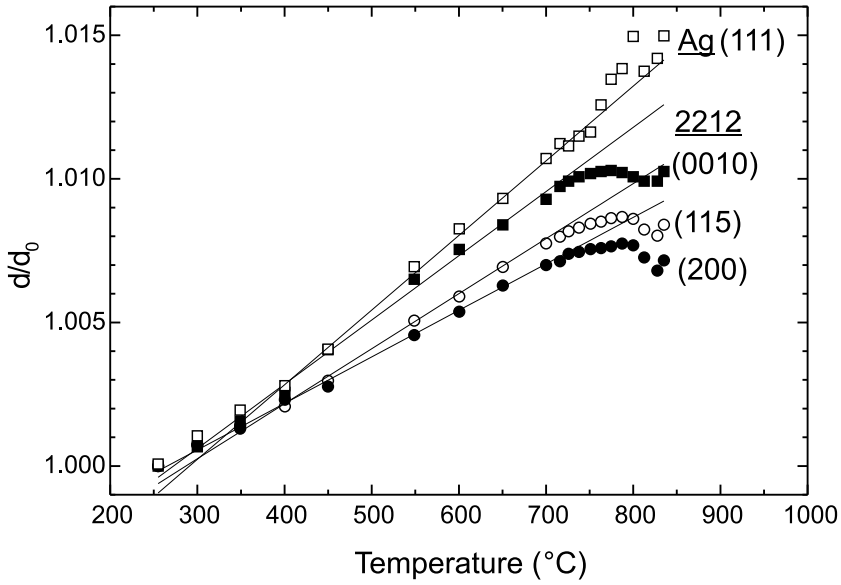

Figure 18: The lattice expansion of Bi-2212 and Ag during heating, where d_0 is the lattice spacing at 250 °C. Shown are data points for the Bi-2212 (200), (115) and (0010) peaks as well as for Ag (111). Linear fits are made to these curves within the temperature range of 400 °C to 700 °C. These fits – extrapolated to the full temperature range – are marked by straight lines.

information we refer to Fig. 14 and Fig. 15. The increase in the integrated intensity of the Bi-2212 (115) peak, which we have argued is due to a structure factor change, is seen to follow closely the decrease in $(Ca,Sr)_2PbO_4$ content. The texture evolution also mimics the $(Ca,Sr)_2PbO_4$ concentration curve, but possibly with a time delay of some 15 min. (Note that the texture development is much slower after reaching the operation temperature, cf. Fig. 15.) Finally, the strain release – not shown in Fig. 19 – follows the texture evolution closely.

These results are consistent with a model where Bi-2212 and $(Ca,Sr)_2PbO_4$ reacts to form Pb and/or Ca enriched Bi-2212 (and possibly a liquid, cf. section 4). The large temperature span over which $(Ca,Sr)_2PbO_4$ dissociates may either be related to slow kinetics or to a temperature dependent solubility limit of Pb in Bi-2212. The Pb and/or Ca incorporation takes place by a mechanism that involves a major growth of the Bi-2212 grains, explaining the strain release and the texture changes.

Several groups have reported on an incorporation of Pb and possibly Ca into the Bi-2212 lattice during the last part of the heating [35, 36]. The lattice contraction as function of increasing Pb content in $Bi_{2-z}Pb_zSr_2CaCu_2O_{8+d}$ was studied by Jeremie *et al.* [37]. Based on their work, if the lineshifts are caused solely by Pb incorporation, we estimate the change in Pb content to be approximately $\Delta z = 0.2$. Grader *et al.* [38] showed that $Bi_2Sr_{3-x}Ca_xCu_2O_{8+d}$ is associated with a monotonic variation of the room temperature lattice parameter in the $0.8 < x < 2.2$ range, increasing towards the Sr-rich composition. If the lineshifts we observe are caused solely by Ca incorporation, the numbers in that article point to an increase in the Ca content by $\Delta x = 0.6$.

Finally, we note the 20% dip in Bi-2212 integrated intensity above 812 °C, which

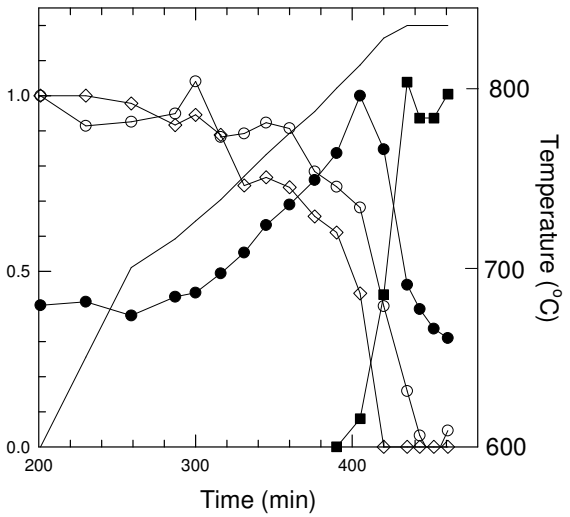

Figure 19: Qualitative summary of structural variations during the heating part above 600 °C and the first 30 min at the operating temperature. The line without dots marks the temperature profile with reference to the temperature scale at the right hand of the figure. The other curves are scaled and shifted to ease a comparison. The $(Ca,Sr)_2PbO_4$ (◇) and $(Ca,Sr)_2CuO_3$ (■) concentrations are normalized to 1 at 600 °C and 835 °C, respectively. The measured Bi-2212 (115) intensity (●) is normalized to 1 at the maximum, 812 °C, and – to ease the visualization – to 0.4 at 600 °C, cf. Fig. 14. Finally, the average mis-alignment ($\Delta\alpha$) of the Bi-2212 (115) reflection (○) is normalized to 1 and 0 at the temperatures of 600 °C and 835 °C, respectively.

appears simultaneously with the formation of $(Ca,Sr)_2CuO_3$, cf. Fig. 14 and Fig. 19. We interpret this as a partial dissociation of Bi-2212 into a liquid and $(Ca,Sr)_2CuO_3$.

3.1.3 Bi-2212 to Bi-2223 phase transformation

Next, we discuss the Bi-2212 to Bi-2223 transformation. To describe the reaction Kanai *et al.* [39] and later Matsubara *et al.* [40] have suggested to use the Johnson-Mehl-Avrami equation, as reported in the work of Hulbert [41]:

$$C(t) = 1 - \exp[-(Kt)^m] \qquad K = A\exp(-E/RT) \tag{5}$$

where C is the volume fraction transformed into the new phase, K is the rate constant, m the reaction order, E the activation energy, R the gas constant and T the temperature in Kelvin. The value of m gives information on what conversion mechanisms are involved during the phase transformation, provided that the phase conversion proceeds by nucleation and growth models [41].

Using the Bi-2223 concentrations displayed in Fig. 14 as measures of the fractional conversion rate, and setting $t = 0$ at the time the operating temperature is reached, the Johnson-Mehl-Avrami plot is shown in Fig. 20. A rather good linear fit gives $m = 1.43$ and $m\ln(K) = -9.81$. To test for systematic errors we may assume that the 'final' plateau reached after 1600 min in Fig. 14 actually corresponds to 100%

conversion. This gives rise to a slightly worse fit with $m = 1.78$. The good Avrami fit supports the assumption that the reaction mechanism involved in the Bi-2212 to Bi-2223 transformation does not change during the process before the saturation at the very end.

An analogue analysis is performed using $1-C(2212)$ as measure of the concentration rate, where $C(2212)$ is the Bi-2212 concentration. The results is shown in Fig. 21. A nice fit is obtained to the latter 2/3 of the data points, with resulting fit values of $m = 1.69$ and $m \ln(K) = -10.68$. The deviation in the first part could be due to the change in stoichiometry by incorporation of Pb/Ca as mentioned earlier.

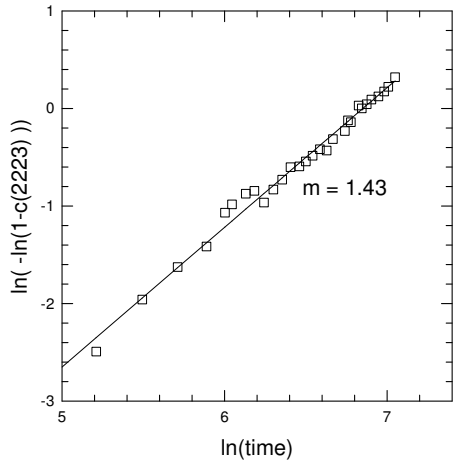

Figure 20: A Johnson-Mehl-Avrami type plot for the time variation of the Bi-2223 concentration (□). The data points are identical to those shown in Fig. 14. The line is the result of a linear fit to the data set. The fitted slope is $m = 1.43$.

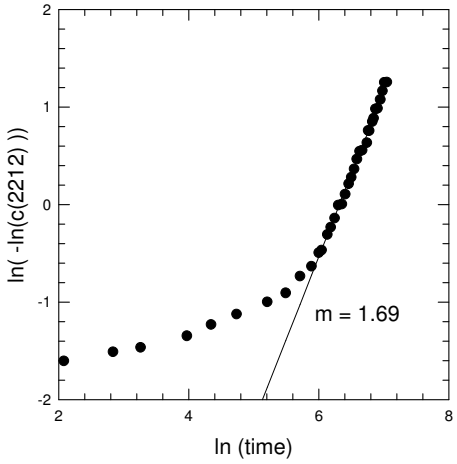

Figure 21: A Johnson-Mehl-Avrami plot for $1 - C(2212)$, where $C(2212)$ is the Bi-2212 concentration (•). The data points are identical to those shown in Fig. 14. The line is the result of a linear fit to the data set truncated by the first 10 points. The fitted slope is $m = 1.69$.

A key point in the Avrami analysis is that the exponent m in equation (5) depends critically on the growth dimension of the transformation, the nucleation rate (constant, zero, decreasing) and on whether the growth is phase-boundary controlled or diffusion controlled. It may be doubted whether such a type of analysis actually is meaningful for inhomogeneous powders such as the Bi-2223/Ag tapes. However, assuming it to be valid, the present result of $1 < m < 2$ is consistent with a transformation which is a diffusion controlled 2 or 3 dimensional process with decreasing nucleation rate.

The actual Bi-2212 to Bi-2223 reaction route cannot be deduced from the present work, as one or more phases – such as the liquid one – have disappeared in the background. Still, some important overall features can be extracted. The results in Fig. 14 points to a reaction between Bi-2212, $(Ca,Sr)_2CuO_3$ (and possibly a liquid) to form Bi-2223. And the line shift in between $t = 500$ min and $t = 1500$ min suggests that the average Pb and/or Ca content in the remaining Bi-2212 steadily decreases during the transformation, even to a value below the extrapolation from 700 °C. There are two

possible routes for the decreasing Pb/Ca content: new Bi-2212 grains with low Pb/Ca content nucleate throughout the transformation process, or the Pb/Ca rich Bi-2212 grains transform faster giving an average decrease of Pb/Ca-enriched Bi-2212. From our data alone we cannot exclude any of the two transformation mechanisms, but we can test which of the two routes is the most likely by the following analysis: We have taken the Bi-2212 (115) peak when it is largest just before the annealing temperature is reached. The peak of course consists of the scattered radiation from all the Bi-2212 grains present in the illuminated volume of the tape, both the Pb/Ca-poor and the Pb/Ca-rich grains. If the concentration of the Pb/Ca-poor grains was growing, the peak at later times would be growing at the side corresponding to a lower d-spacing (higher 2θ value). The opposite would be the case if the concentration of Pb/Ca-rich grains was increasing. By overlaying the Bi-2212 (115) peaks at different times during the transformation we observe that the progressively smaller peaks at later times are all encompassed by the envelope of the first and largest peak. Hence, no Bi-2212 grain growth is needed to explain the shift in Fig. 17.

The Bi-2212 to Bi-2223 transformation mechanism has been debated at length in the literature. We will refrain from a comprehensive review, and in stead quote the main arguments by summarizing a few of the articles devoted to this subject [42, 43, 44, 45, 46, 47, 48, 49].

A nucleation and growth model by means of a liquid droplet mechanism has been suggested by many authors. In general, the reports are based on SEM/EDS and TEM studies on quenched pellets, often with small amounts of Ag added to the powder in order to simulate the proximity of the Ag-sheet in the tapes. Some of the most compelling evidence is reported by Morgan *et al.* [43]. They observed small amount of liquid drop relics connected to the Bi-2223 platelets. The (Bi,Pb) concentration of the drops is higher than for Bi-2223, typically with a Bi:Pb ratio close to 1:1. From inspection of the micrographs the drops seem to migrate, depositing Bi-2223 phase in the form of ledges (steps) on top of existing platelets – these being Bi-2212 or Bi-2223 phase material. The intercalation mechanism on the other hand has been favored by – in particular – the group at Brookhaven [42, 44, 45]. Performing TEM investigations on quenched tapes they frequently observed intergrowth of Bi-2212 and Bi-2223 (mono) layers. At times, the layers were sufficiently ordered to form a new phase 4:4:3:5, with a unit cell defined by the stacking of half a Bi-2212 and half a Bi-2223 unit-cell along the c-axis [42]. The authors argue that such structures are formed without breaking the Bi-O bonds by intercalation of Ca-Cu-O Bi-layers into Bi-2212 and that the 4435 phase should be considered an 'intermediate phase' during the conversion process. It is proposed that diffusion takes place through displacements of edge dislocations at the growth front [44]. Such dislocations are indeed observed but only in a limited number, leading to the suggestion that the intercalation process – once nucleated at a particular site in a particular grain – is very rapid [45].

Finally, early on a disproportionation mechanism was suggested [46, 47], whereby the Bi-2212 phase is converted into Bi-2223 and Bi-2201 by the reaction $2Bi_2Sr_2CaCu_2O_x \rightarrow Bi_2Sr_2Ca_2Cu_3O_{x'} + Bi_2Sr_2CuO_{x''}$.

An argument against the intercalation as the only mechanism at play is that grain growth is generally observed during the transformation period by all groups. This

however does not exclude that some intercalation takes place. To shed more light on the transformation mechanism, Grivel *et al.* performed an extensive set of experiments [48, 49]. The main contribution comes from an ingenious use of SEM equipment, where pressed pellets repeatedly are investigated by SEM (and X-ray diffraction), inserted directly into a preheated furnace, annealed at the operation temperature for some time and quenched to room temperature, then re-investigated by SEM, etc. They clearly demonstrate that the morphological changes of the individual grains can be followed in the micro-graphs in this way [48]. As a result, a progressive rounding of edges, reduction and subsequent disappearance of the Bi-2212 grains are seen. Concurrently, new lamellar Bi-2223 grains appear and grow. The group has also performed statistics by means of TEM on tapes quenched after different sintering times [49]. For each tape the Bi-2212/Bi-2223 stacking was characterized in a number of grains. In contrast to the work at Brookhaven, only pure Bi-2212 grains or Bi-2223 grains with less than 30% Bi-2212 layers are present. This contradicts intercalation, unless the transformation within each grain takes place within a few minutes or less.

The present work adds to the knowledge we have of the transformation mechanism in several ways. Firstly, the simple Bi-2223 + Bi-2201 disproportionation mechanism clearly cannot be valid in this case, as no solid state Bi-2201 is observed at high temperatures. Secondly, the Bi-2223 texture development follows the Bi-2212 one closely. This feature is an obvious consequence of the intercalation model, while the simplest way to reconcile it with a nucleation and growth scheme is to assume that the Bi-2223 grains nucleate on the existing Bi-2212 platelets. Thirdly, the Bi-2212 line shifts indicate a change in the average stoichiometry during the transformation period.

The observation that the Bi-2212 linewidth is constant throughout the transformation at 835 °C (see Fig. 16) implies that the conversion to Bi-2223 only involves a limited strain and finite-size broadening of the Bi-2212 peaks. This narrows down the possible routes of the transformation process. We first consider the low or absent strain: During an intercalation process one would expect a considerable strain to be present along the *c*-axis as the intercalating CuO_2 layers propagate into the Bi-2212 crystal structure. Since any strain present is below our detection limit, this can only be reconciled with the intercalation model if there is a limited number of growth fronts at all times during the transformation. Fig. 22 shows schematically what possible situations we have: If many grains transform at the same time, the number of growth fronts must be small (Fig. 22(a)) while on the other hand if there is a large number of growth fronts, only a few grains at a time are transforming (Fig. 22(b)). The processes in Fig. 22(a) and Fig. 22(b) are both 2D-type intercalation in the *ab*-plane followed by a 1D growth along the *c*-axis. Turning to the lack of finite-size broadening, this tells us that there is a rather long-range order of the Bi-2212 crystalline phase within the single grains. This is hard to reconcile with the situation depicted in Fig. 22(a) with many grains transforming at the same time, as this should give a reduction of the phase-coherent distance leading to finite-size broadening of the peaks. And since we do not observe any broadening towards the end of the annealing this implies that only a few grains at the same time are close to full transformation, so on average no broadening is detected. A growth as depicted in Fig. 22(c) where the growing layers are stacked on top of each other, would give less loss of phase-coherence. But this

would be a purely 1-dimensional growth of the grains, and while the m value in the Johnson-Mehl-Avrami-fits is consistent with a 2D or 3D growth model ($1 < m < 2$) it barely fits with a 1D diffusion limited growth model ($0.5 < m < 1.5$). Thus, the intercalation can be reconciled with experimental data only if few grains transform at a time, and if the transformation of a grain is very fast. This is in accordance with the TEM studies of Grivel *et al.* as mentioned above [49].

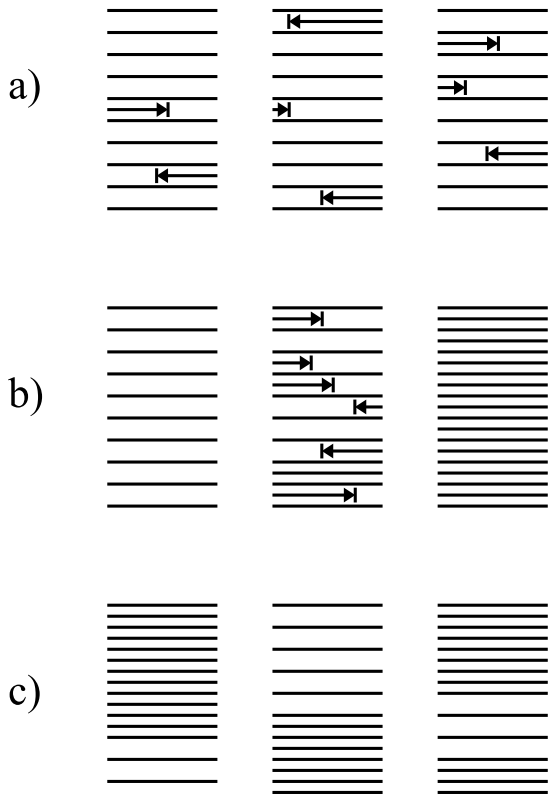

Figure 22: Different growth mechanisms of the intercalation model as discussed in the text. Distant lines represent the Bi-2212 phase, narrow lines represent the Bi-2223 phase, arrows indicate new growth fronts. (a) Few growth fronts in many grains. (b) Many growth fronts in few grains. (c) Stacking of growing layers.

A transformation model focusing on growth along the c-axis direction is most likely not very realistic, as the plate-like morphology of the Bi-2212/Bi-2223 grains reflects a much faster growth rate in the ab-plane than along the c-axis. A transformation model consistent with the experimental observations is a process where Bi-2212 grains are melting and transforming into the Bi-2223 phase by a nucleation and growth mechanism inside the plate-like cavities of the molten Bi-2212 grains. With the growth being predominantly along the ab-plane the Bi-2223 grains will have essentially the same morphology as the Bi-2212 grains. In order to make such a model consistent with the constant resolution limited Bi-2212 linewidth one must again require that the melting of the Bi-2212 grains occurs very fast and only for a few grains at a given time. There is however nothing in the experimental observations that contradict a slow growth of the Bi-2223 phase.

3.1.4 Texture development

The overall conclusion emerging from the results in Fig. 14, Fig. 15 and Fig. 16 is that the texturing mainly is caused by a substantial Bi-2212 grain growth. (In contrast, the intermediate pressing between annealings is found by hard X-ray diffraction [16] to increase $\Delta\alpha$.) Moreover, the final Bi-2223 and Bi-2212 alignment are identical, either because the Bi-2223 phase inherits the alignment (the Bi-2212 grain serves as templates during transformation) or due to the fact that the geometry for the two phases is the same (same aspect ratio of grains and same filamentary thickness).

One extra bit of information can be retrieved. The initial and final values for $\Delta\alpha$ of Bi-2223 are seen to be identical, while the intermediate values are higher. Similar results were demonstrated in a later *in situ* neutron diffraction study on a multi-filamentary tape in 8% O_2 by Fahr *et al.* [50]. To explain this phenomenon the authors investigated quenched tapes by SEM/EDS analysis. They found that initially the Bi-2223 grains appear only near the silver interface, where they form colonies of well aligned grains. During further annealing grains in the interior of the filament appears – these are associated with an inferior degree of alignment [50]. Since multi-filamentary tapes have a higher amount of silver interfaces this effect is more pronounced in the multi-filamentary tapes used by Fahr.

The fact that the initial growth of Bi-2223 takes place near the silver interface is likely to due to the fact that the presence of silver lowers the melting temperatures and thereby increases the amount of liquid, which also is important for the texturing [3, 5]. As such the results are in agreement with the previous work by Yi *et al.* [51], who also have found that the Bi-2223 phase always forms first (at lower temperatures) near the silver interface and that the Bi-2223 colonies align to the interface. In 1991 Yamada *et al.* [52] have also observed the improved texturing near the interface.

3.2 1st annealing in 8% O_2

For the experiment in 8% O_2 a 200 μm thick green tape was used with a nominal powder composition of $Bi_{1.8}Pb_{0.33}Sr_{1.87}Ca_2Cu_3O_x$. The temperature profile is shown in Fig. 23. The specimen was kept at the operation temperature of $T_{MAX} = 829.5$ °C for ∼11.5 h. The heating and cooling ramp rates were 100 °C/h.

The data was analyzed as explained in section 2.3 with one exception. The (00l) reflections were used for analysis of the phase development of Bi-2223 instead of the (115) reflection, as the latter was inaccessible due to the use of an Al_2O_3 tube in the furnace (a substitute for the quartz tube).

3.2.1 Results

The identified phases are Bi-2212, Bi-2223, Bi-2201, $(Ca,Sr)_2PbO_4$ and $(Ca,Sr)_2CuO_3$ (identified by one reflection at $d \approx 6.2$ Å). In Fig. 23 the kinetics of these phases is shown. During ramp up, at temperatures below ∼500 °C a constant amount of Bi-2212 and the secondary phases $(Ca,Sr)_2PbO_4$ and $(Ca,Sr)_2CuO_3$ is present in the tape. When the temperature reaches 790 °C the $(Ca,Sr)_2PbO_4$ phase decomposes quickly and disappears at 829 °C. The Bi-2212 content decreases just after the annealing temper-

ature is reached while the Bi-2223 phase appears and increases during the annealing. The Bi-2223 content saturates after 10 h annealing of a level of 93%. During cooling at 729 °C the $(Ca,Sr)_2PbO_4$ phase appears again and is present down to ∼500 °C, where the measurement was stopped. The Bi-2201 phase appears during cooling at the temperature of 740 °C and remains there until the measurement is stopped.

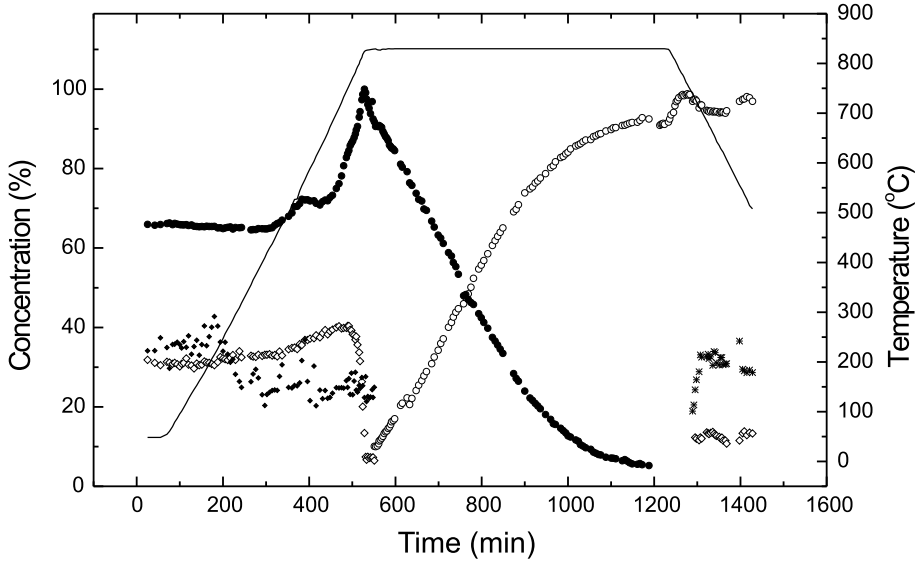

Figure 23: Integrated intensities of selected reflections during annealing in 8% O_2. The symbols refer to: (•) Bi-2212 (008), (○) Bi-2223 (0010), (∗) Bi-2201 (006), (◇) $(Ca,Sr)_2PbO_4$ (020), (⧫) $(Ca,Sr)_2CuO_3$ (200) and (—) Bi-2212 + Bi-2223. The intensities are scaled to provide information on the relative concentrations. However, Bi-2201 and $(Ca,Sr)_2CuO_3$ are in arbitrary units. The thick solid line marks the temperature profile with reference to the temperature scale at the right-hand side.

In Fig. 24 the evolution of the average mis-alignment angle $\Delta\alpha$ of the c-axis for Bi-2212 and Bi-2223 is shown. The texture evolution is seen to take place primarily during the initial stage of the first heat treatment before the conversion into Bi-2223. At the end of the heat treatment the $\Delta\alpha$ widths of the two phases become identical and level off to a value of $\Delta\alpha = 26° \pm 1°$. The Bi-2223 texture follows that of Bi-2212 most of the time, but is possibly associated with an initial knee of the same type as found for the case of annealing in air.

The evolution of the full width half maximum (FWHM) of a Bi-2212 and a Bi-2223 diffraction peak in the 2θ projection is presented in Fig. 25. The Bi-2212 linewidth decreases during heating and then levels off after the annealing temperature is reached (the subsequent increase of the Bi-2212 linewidth is caused by a fitting error). The linewidth of Bi-2223 decreases quickly in the beginning and levels off afterwards to a value higher than that for Bi-2212. No strain vs. crystal size analysis was performed in this case.

Fig. 26 shows the 2θ position of the midpoint of the Bi-2212 (008) and the Bi-2223 (0010) reflections during the annealing. The changes in 2θ due to the thermal lattice expansion/contraction are drawn as a line. At 700 °C the Bi-2212 2θ midpoint

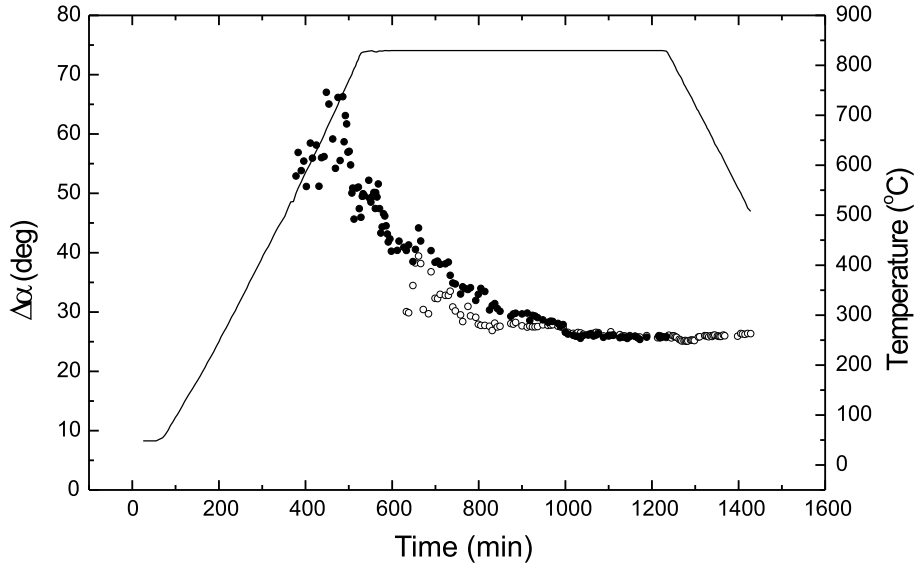

Figure 24: Texture evolution during the '1st annealing in 8% O_2'. The FWHM of the texture profiles ($\Delta\alpha$) of the Bi-2212 (115) (•) and the Bi-2223 (117)(∘). The line marks the temperature profile with reference to the temperature scale at the right-hand side.

begins to deviate from the theoretical curve. We note that the integrated intensity for the Bi-2212 peak increases steeply within the temperature range of 670 °C and 825 °C (Fig. 23) where this contraction takes place. The lattice spacing variation of the Bi-2223 reflection on the other hand is determined solely by the thermal expansion.

3.2.2 Comparison with study in air

By comparing the plots of relative concentration vs. annealing time of the annealings in 8% O_2 and air[1] (Fig. 23 and Fig. 14), we observe that the phases are the same and that the development of these has nearly identical trends. The conversion in 8% O_2 is however more than twice as fast as in air. In the same way, the texture developments obtained from annealing in air (Fig. 15) and in 8% O_2 (Fig. 24) are quite similar, with the same factor of 2 in difference between the rates. Moreover, the evolution in the data for linewidth and midpoint are very similar.

There are some differences though. Firstly, there is the dynamics of the $(Ca,Sr)_2CuO_3$ (2:1) phase. For the tape used in the annealing in 8% O_2 this phase is present from the beginning – this is not the case for the green tape annealed in air. More importantly, in air 2:1 appears when the Bi-2212 concentration starts to decrease and it decreases successively with a rate similar to Bi-2212. In 8% O_2 we do not observe the 2:1 phase at all at high temperatures.

Another difference is that for annealing in air the Bi-2212 lattice expands (the 2θ midpoint decreases) during the conversion into Bi-2223 (Fig. 17), indicating that the remaining Bi-2212 grains contain less and less Pb. In contrast to this the annealing in

[1]Note that the nominal powder composition of the tapes used in these two experiments are not identical.

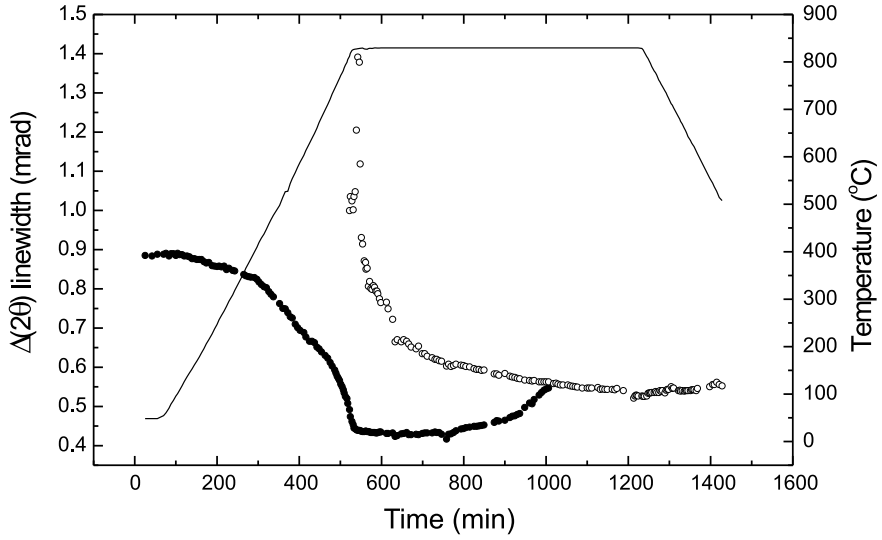

Figure 25: The evolution of the linewidth (2θ FWHM). The symbols refer to: (•) Bi-2212 (008) and (○) Bi-2223 (0010). Data points from Bi-2212 are removed after 1000 min because of an unreliable fitting due to vanishing intensities. The solid line marks the temperature profile with reference to the temperature scale at the right-hand side.

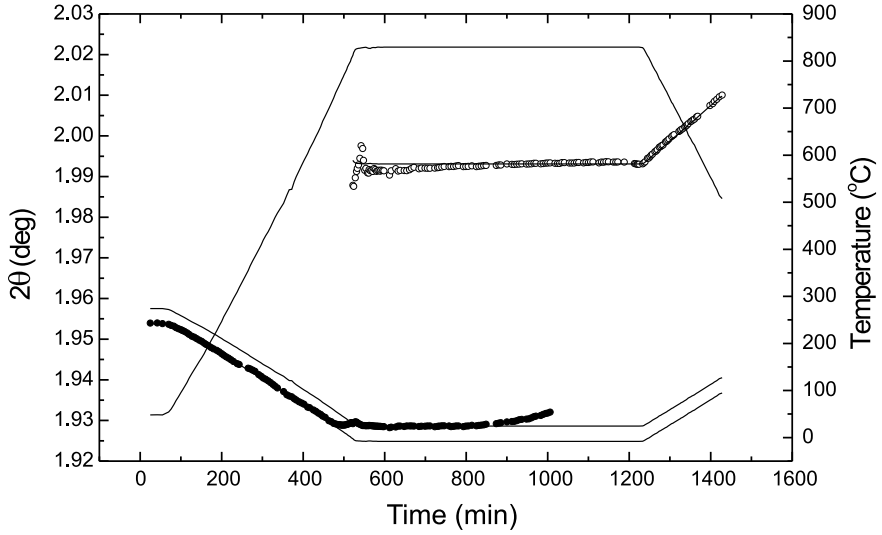

Figure 26: The position of the Bi-2212 (008) (•) and the Bi-2223 (0010)(○) peak mid-point in the 2θ projection as function of the annealing time. The lines are the theoretical lattice expansion curves under the assumption that the changes in the 2θ position only are related to thermal expansion/contraction. The linear thermal expansion coefficient is $\alpha = 19{\times}10^{-6}$ K^{-1} and $\alpha = 26{\times}10^{-6}$ K^{-1} for Bi-2212 and Bi-2223, respectively. Data points from Bi-2212 are removed after 1000 min because of an unreliable fitting due to vanishing intensities. A line is also marking the temperature profile with reference to the temperature scale at the right-hand side.

8% O_2 indicates no further stoichiometry changes after the incorporation of Pb.

Finally, by analyzing the steep increase of the Bi-2212 concentration during heating we observe an increase of ∼30% and ∼20% in the case of annealing in 8% O_2 (Fig. 23) and in air (Fig. 14), respectively. This is consistent with the fact that a lower oxygen partial pressure results in a higher Pb solubility of Bi-2212 [53].

3.2.3 Structural evolution during ramp-up

Our interpretation is that the role of the 2:1 phase in the high temperature kinetics is taken over by another alkaline-earth cuprate, the so-called 14:24 phase, with approximate stoichiometry $(Ca,Sr)_{14}Cu_{24}O_x$. This phase has proven very difficult to observe with the hard X-ray set-up, due to overlap of peaks. The reaction then becomes Bi-2212 → liquid + $(Ca,Sr)_{14}Cu_{24}O_x$.

This 'interpretation' is based on the outcome of a supplementary investigation of the phase evolution by Cu K_α XRD. As reported in Liu *et al.* [21, 54] multi-filamentary tapes were annealed at T_{MAX} = 830 °C in 8% O_2 for a variable amount of time – between 0 and 52 h – and then quenched in air. The XRD revealed that the 14:24 content peaks after 1 hour at T_{MAX}. Subsequently it decays at a rate similar to the Bi-2212 decay. In addition, CuO was found to appear after ∼10 h of annealing and Bi-2201 after 5 h. The latter phase, however, is known to arise from the cooling. Furthermore, small amounts of 2:1 was detected at all times with a maximum after 10 h, and no correlation with the Bi-2212 decay.

Fahr *et al.* [50] have by *in situ* neutron diffraction studied the phase development of a multi-filamentary tape during the first annealing for 25 h in a reduced oxygen atmosphere. The Bi-2223 phase, Ca_2PbO_4 and 14:24 are shown from the annealing temperature at 825 °C is reached [50]. The amount of 14:24 increases until 2.5 h annealing time and then decreases. The Ca_2PbO_4 phase disappears after ∼8 h annealing time. In our study this phase disappears before reaching T_{MAX}. This difference can be explained by the fact that the precursor powder used by Fahr *et al.* [50] contains more Pb (Pb = 0.4) than our powder (Pb = 0.33). In addition, the reaction rate of the study in Ref. [50] is slower, most probably due to the lower annealing temperature.

The reduction of the integrated intensity of the Bi-2212 peak at 825 °C, 23 min before the Bi-2223 phase appear, is interpreted as a partial dissolution of Bi-2212 into a liquid plus 14:24. This is confirmed by the fact that the background level, which is proportional to the amount of liquid, cf. section 4, begins to increase at this annealing time. This is also consistent with the neutron diffraction study by Giannini *et al.* [55] showing a decrease in the total crystalline matter at this stage.

3.2.4 Bi-2212 to Bi-2223 phase transformation

Johnson-Mehl-Avrami plots for Bi-2223 and Bi-2212 are shown in Fig. 27 and Fig. 28, respectively. They were generated in the same way as described for the analysis of the phase transformation in air. The resulting m values are again found to be in the range $1 < m < 2$. The arguments and conclusions for annealing in air can therefore be repeated with the appropriate substitution of the 1:2 phase by 14:24.

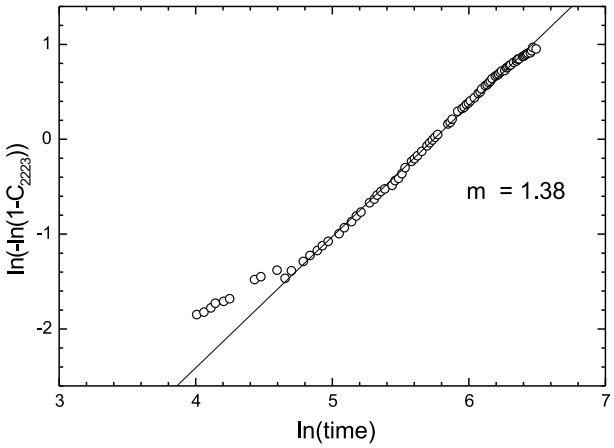

Figure 27: A Johnson-Mehl-Avrami plot (○) using the Bi-2223 concentrations displayed in Fig. 23 as the fractional conversion C, where $C(t) = 1 - \exp(-(Kt)^m)$ and K is the rate constant. The plot is constructed by setting t = 0 at 528 min, where the Bi-2212 concentration is 100% and the annealing temperature is reached (cf. Fig. 23). The line is a linear fit to the data set truncated by the first 9 points. The fitted slope is $m = 1.38$ and $m \ln K = -7.94$.

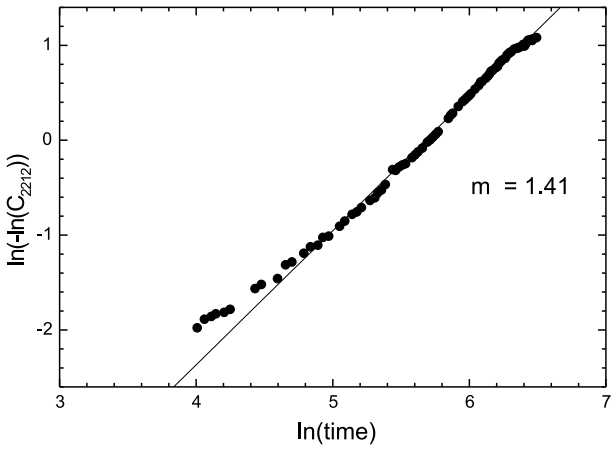

Figure 28: A Johnson-Mehl-Avrami plot for $1 - C_{2212}$, where C_{2212} is the Bi-2212 concentration (•). The line is a linear fit to the data set truncated by the first 8 points. The fitted slope is $m = 1.41$ and $m \ln K = -8.02$.

3.3 Last annealing in 8% O_2

To complement the study in 8% O_2 reported above, another piece of the same tape was fully processed in 8% O_2 with exception of the last annealing. This annealing was performed on-line using, once again, 8% O_2 and an operation temperature of 829.5 °C. Unfortunately, the furnace crashed after 480 min at T_{MAX}, such that the annealing period became truncated. The resulting temperature profile is shown in Fig. 29.

In the diffraction patterns we observed only reflections from $(Ca,Sr)_2PbO_4$ and Bi-2223. The background in the vicinity of the major $(Ca,Sr)_2PbO_4$ reflection prohibited a fit to the concentration of this phase. However, we can state that the phase is

present from the beginning at the experiment until 825 °C, based on inspection of the raw images. The (115) reflection was selected for analysis of the Bi-2223 phase development. The variation in concentration (in arbitrary units) is shown in Fig. 29. Within the uncertainty it is constant.

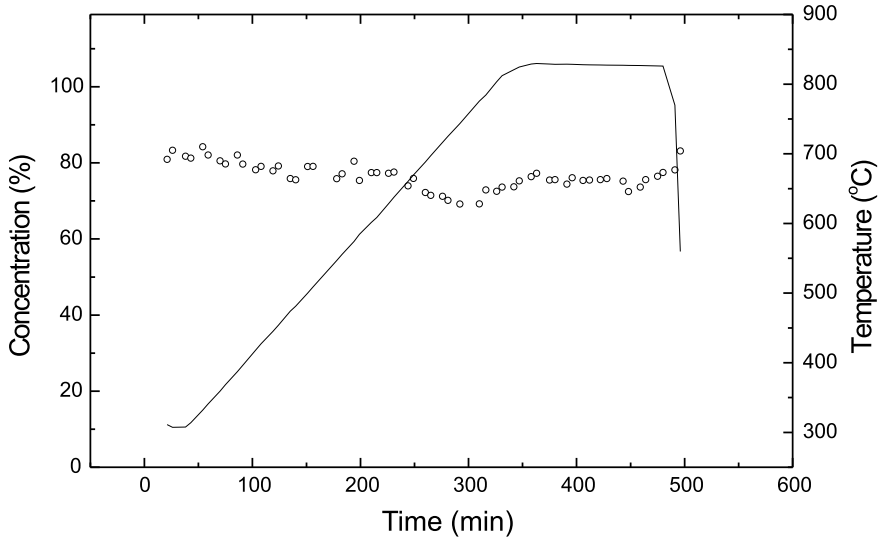

Figure 29: Concentration (in arbitrary units) of the Bi-2223 phase (○) during last annealing in 8% O_2. An injection of the synchrotron took place around 300 min. The solid line marks the temperature profile with reference to the temperature scale at the right-hand side.

The texture development as function of the annealing time is shown in Fig. 30. The average grain mis-alignment is constant within the uncertainty. However, the final $\Delta\alpha$ width is found to be $24^\circ \pm 1^\circ$, which by comparison is seen to be $\sim 2^\circ$ lower than after the 1st annealing in 8% O_2.

The evolution in the linewidth of Bi-2223 (115) reflection and the corresponding peak shifts are shown in Fig. 31 and Fig. 32, respectively. There is a trend in the linewidth data for a smaller width with time, indicative of grain growth, but it is barely outside the instrumental error. The evolution of the 2θ midpoint follows closely the thermal expansion curve (Fig. 32).

The interpretation of these results is straightforward. The volume percentage of material, where the phase composition favors reactions, is much smaller for the last annealing than for the first. The average kinetics rate is therefore much slower. Hence, within the time frame of the experiment no macroscopic dynamics can be observed.

The straight lines in the figures may also be seen as validations of the synchrotron technique.

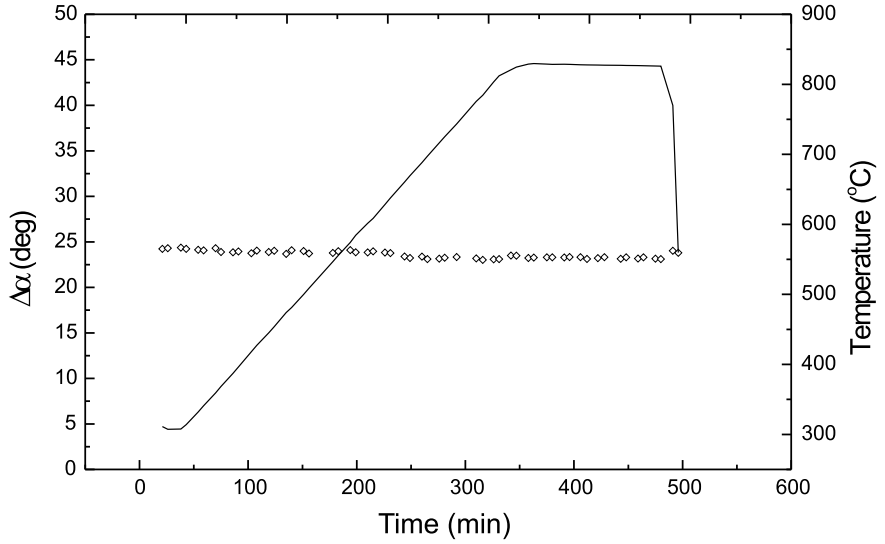

Figure 30: Texture evolution during the 'last annealing in 8% O_2'. The FWHM of the texture profile ($\Delta\alpha$) of the Bi-2223 (117)(∘). The line marks the temperature profile with reference to the temperature scale at the right-hand side.

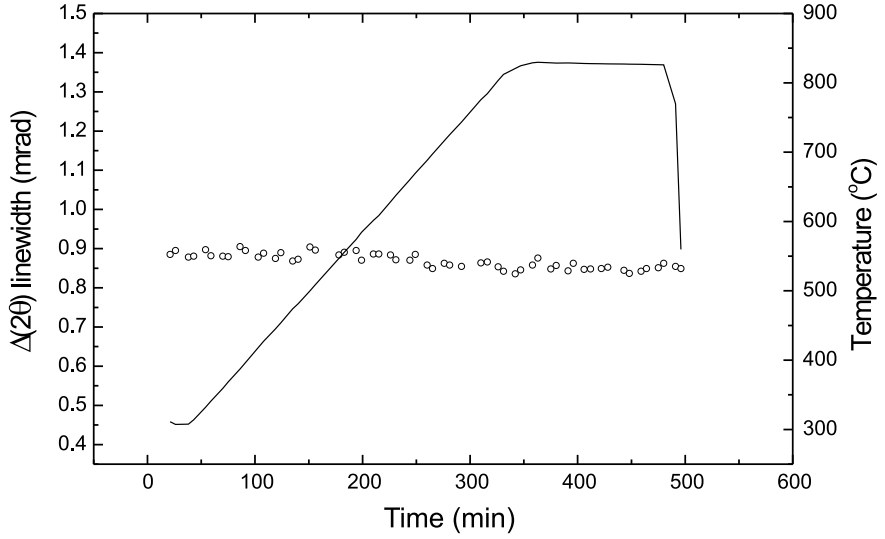

Figure 31: The evolution of the linewidth (2θ FWHM) of Bi-2223 (115)(∘). The solid line marks the temperature profile with reference to the temperature scale at the right-hand side.

4 A HARD X-RAY DIFFRACTION STUDY OF EQUILIBRIUM PHENOMENA AND REVERSIBILITY

As a complementary study [18] to the standard heat treatments presented in section 3 we present the results of a very slow initial ramp rate, followed by two temperature cycles between 845 °C and 860 °C. The temperature is changed in steps in order to learn about the kinetics. The cycles serve to investigate to what extent reactions are

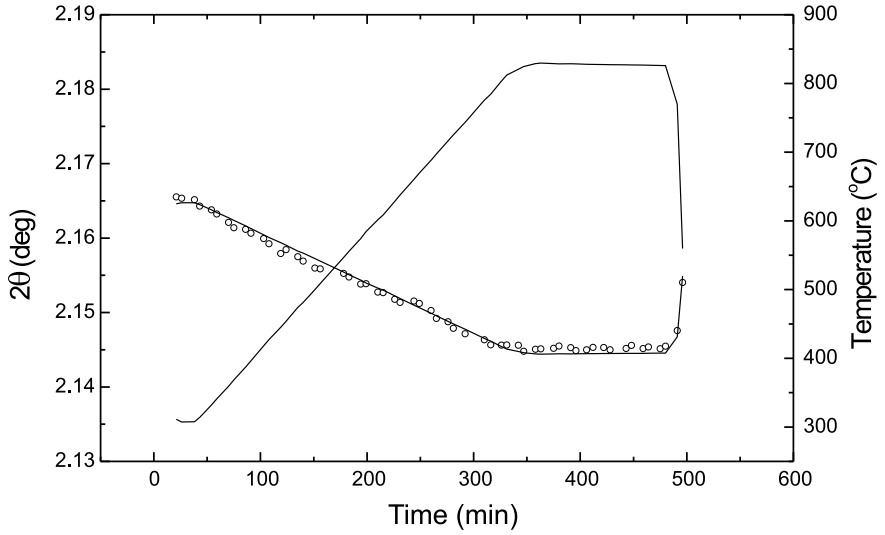

Figure 32: The position of the Bi-2223 (115) peak midpoint (○) in the 2θ projection as function of the annealing time. The line is the theoretical lattice expansion curve under the assumption that the changes in the 2θ position only are related to thermal expansion/contraction. The linear thermal expansion coefficient is $\alpha = 18{\times}10^{-6}$ K^{-1}. A line is also marking the temperature profile with reference to the temperature scale at the right-hand side.

reversible and to gain information on possible eutectic/peritectic parts of the phase diagram. In addition, we have succeeded in measuring the diffracted signal from the liquid phase during the annealing. This allows a more direct correlation between the liquid and the various crystalline phases than what may be obtained from quenched samples. The heat treatment is performed in an atmosphere of technical air.

We split the run into three temperature intervals: below 820 °C, between 820 °C and 840 °C and at 845 °C and above. The results for each interval are presented separately along with an interpretation and some comparison to other work, including the $T_{MAX} = 835$ °C work outlined in section 3.1. A discussion of the cooling part can be found in Ref. [32].

4.1 Experimental

The mono-filamentary tape used in the experiment had a nominal powder composition of $Bi_{1.8}Pb_{0.33}Sr_{1.87}Ca_{2.00}Cu_{3.00}O_{10+x}$. The green tape was rolled to a final thickness of 200 μm. The temperature profile is presented graphically jointly with the data in Figs. 36–38. The temperature T is initially ramped up by 2.8 °C/min to 620 °C, then by 1.6 °C/min to 765 °C. Next, T is increased in steps of initially approximately 10 °C, then 5 °C up to the maximum temperature of 860 °C. The temperature profile is then inverted while T is stepped down to 845 °C. Next, the temperature is increased directly from 845 °C to 860 °C, left there for 10 min, and then 'quenched' to 845 °C. This implies that we can learn about reversibility by comparing results for the three periods where the tape is at 845 °C – indicated in Fig. 37 – and about kinetics from

the 860 °C 'spike' in the temperature profile. Then, to observe solidification of possible liquid phases, T is decreased to 820 °C, and left there for 20 min. Finally, the furnace is cooled to 660 °C, left there for 20 min, and afterwards cooled to room temperature. All temperature changes above 765 °C as well as the final 'quench' to 660 °C took place within 1 min, and once set at a specific value, T was stable within 0.5°. Data acquisition took place every 1–5 min throughout the entire process.

Raw data – in the form of 2θ projections – are shown in Fig. 33 and Fig. 34 for the lowest and highest temperatures. The dominant peaks can be related to the Ag, $(Ca,Sr)_2PbO_4$, Bi-2212 and Bi-2223 phases. Also, the Bi-2201 phase appears during cooling. In addition, several minority phases are present, some of which have not been identified.

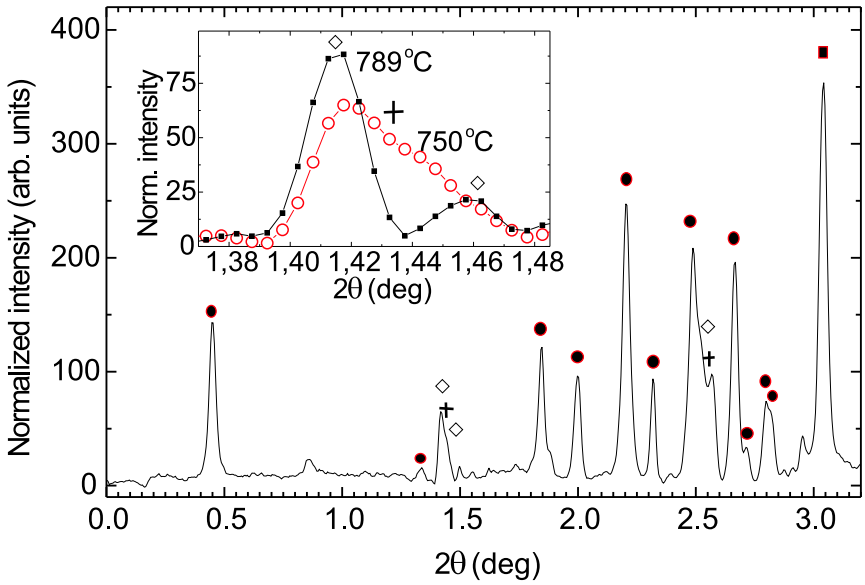

Figure 33: 2θ projection obtained at a temperature of 750 °C after 248 min of annealing. Symbols mark the identified peaks of the Bi-2212 (•), $(Ca,Sr)_2PbO_4$ (◇), 3221 (+) and Ag (■) phases. In the insert a comparison between 2θ projections at 750 °C and 789 °C is made, zooming in on the overlapping $(Ca,Sr)_2PbO_4$ and 3221 peaks around $2\theta = 1.43°$.

In Fig. 33 – at 750 °C – two peaks at $2\theta = 1.44°$ and $2\theta = 2.52°$ are associated with the so-called 3221 phase. This identification is based on the work of Grivel *et al.* [56, 57]. The stoichiometry of this phase is known to be very variable. The peak at 1.437° is situated between two $(Ca,Sr)_2PbO_4$ peaks – cf. the insert in Fig. 33 – so estimates of the integrated intensity are based on simultaneous fitting to three peaks. With no knowledge of structure factors we have refrained from making estimates of the phase concentration. In the raw two-dimensional images 3221 appears as continuous powder circles (or circle segments), indicating rather small grains. Additional peaks in the 2θ projections may tentatively be identified as reflections of CuO and of the 14:24 phase.

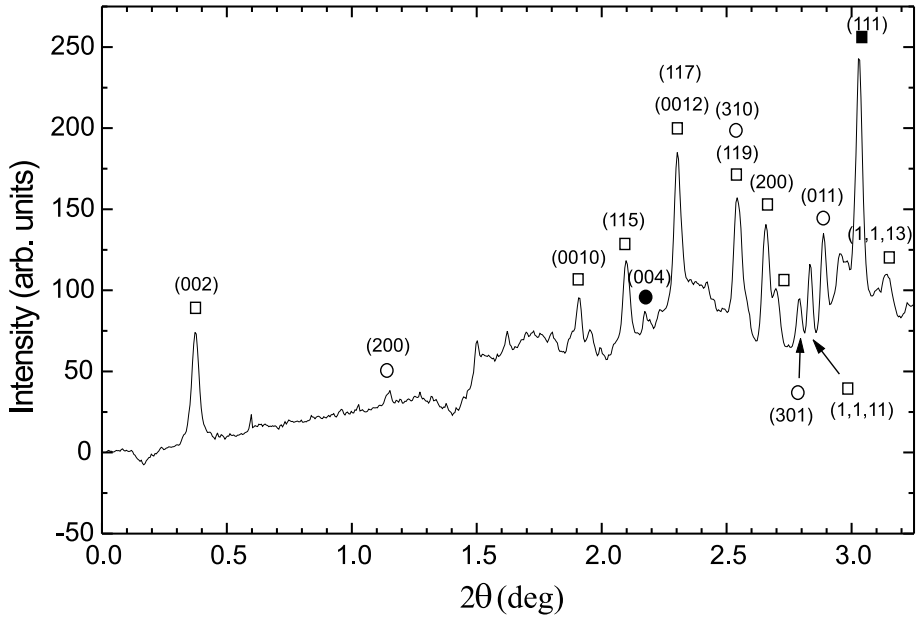

Figure 34: 2θ projection obtained at a temperature of 860 °C after 2440 min of annealing. Symbols mark the identified peaks for the Bi-2223 (□), Ag (■), and $(Ca,Sr)_2CuO_3$ (○) phases. The peak marked (•) may be the (004) reflection of the 14:24 phase. At this temperature there is almost no trace of the Bi-2212 phase.

At 860 °C we find peaks corresponding to the $(Ca,Sr)_2CuO_3$ (200), (310), (301) and (011) reflections, cf. Fig. 34. The relative concentration of $(Ca,Sr)_2CuO_3$ is determined by scaling the integrated intensity of the (011) reflection by a factor 4.5 with respect to the integrated intensity of the Bi-2212 (115) reflection (according to structure factors derived from Ref. [33, 34] for $(Ca,Sr)_2CuO_3$ and Bi-2212, respectively). In the raw two-dimensional images $(Ca,Sr)_2CuO_3$ appears as dots along the Debye-Scherrer circle, indicating rather large grains. The phase is weakly textured.

In Fig. 35, we compare the 2θ projections at 750 °C and 860 °C. Clearly, from the figure, at the higher temperature there is a substantial increase in the background in the 2θ range above 1.5°. We interpret this as the scattering from a partial liquid phase. As a measurement of the 'concentration' of this liquid phase, we use the background level at $2\theta = 2.15°$ – after subtraction of the 750 °C value. The scaling factor was arbitrarily set such that the total concentration of the liquid, Bi-2212 and Bi-2223 phases are 90% at 860 °C. As a test, an analogue data analysis of the background level was performed at $2\theta = 2.40°$ – with similar results.

4.2 Results

In Fig. 36, we compare the time variation of the Bi-2212, Bi-2223, 3221, $(Ca,Sr)_2PbO_4$ and liquid concentrations. A close-up of these curves for the last third of the annealing run is given in Fig. 37, which also comprises a comparison between the $(Ca,Sr)_2CuO_3$ and liquid concentrations. The 2θ midpoints for selected Bi-2212, Bi-2223, $(Ca,Sr)_2PbO_4$ and $(Ca,Sr)_2CuO_3$ peaks are shown as function of elapsed time in Fig. 38. For com-

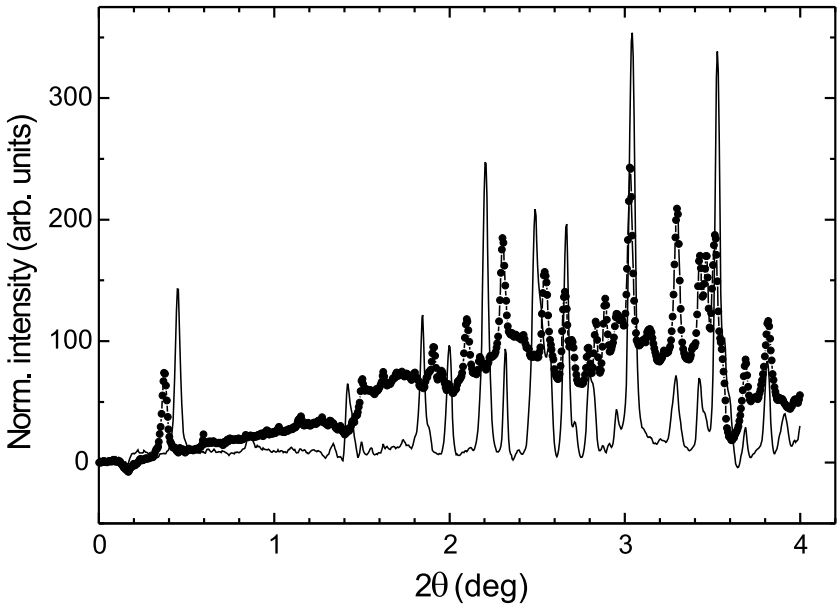

Figure 35: 2θ projections obtained during high temperature cycling. A comparison between data taken during heating at T = 750 °C (solid line) and at T = 860 °C (•). The corresponding elapsed annealing times are t = 248, and 2440 min, respectively. The increase of diffuse scattering in the interval above 1.5° is interpreted in terms of scattering from a liquid phase.

parison, the expected variation in the Bi-2212 curve as result of thermal expansion is also shown. (The high temperature expansion coefficient for Ag (111) was found in section 3 to be 26×10^{-6} K^{-1}.) The evolution of the 2θ widths of selected Bi-2212, Bi-2223 and $(Ca,Sr)_2PbO_4$ peaks are shown in Fig. 39. Data points are left out in these figures, when the fitting procedure becomes unreliable, due to minute or overlapping peaks.

As mentioned in the introduction, the time-evolution of these structural data may conveniently be separated into 3 parts: 3221 dissolution and strain relaxation ($t < 1550$ min, $T \leq 817$ °C), grain growth and transformation (1550 min $< t <$ 2220 min, 822 °C $\leq T \leq$ 839 °C), and high temperature cycling (2220 min $< t <$ 2610 min, $T \geq 845$ °C), where t is the annealing time. We will interpret the structural behavior of the time periods successively.

3221 dissolution and strain relaxation ($T \leq 817\,°C$)

Below 735 °C only two images were acquired, due to constraints on experimental procedure. However, the available results in Fig. 36 reveal a major crystallization process taking place in this temperature range, where e.g. the Bi-2212 peak intensities more than double while an amorphous/nano-crystalline background decreases. Above 735 °C the content of long-range ordered Bi-2212 continues to rise significantly. From Fig. 36 we furthermore observe that the 3221 phase dissolves, with the intensity totally vanished at 789 °C. It is likely that slower ramping would imply a completion of the dissolution at even lower temperatures. Similar behavior with Bi-2212 crystallization and

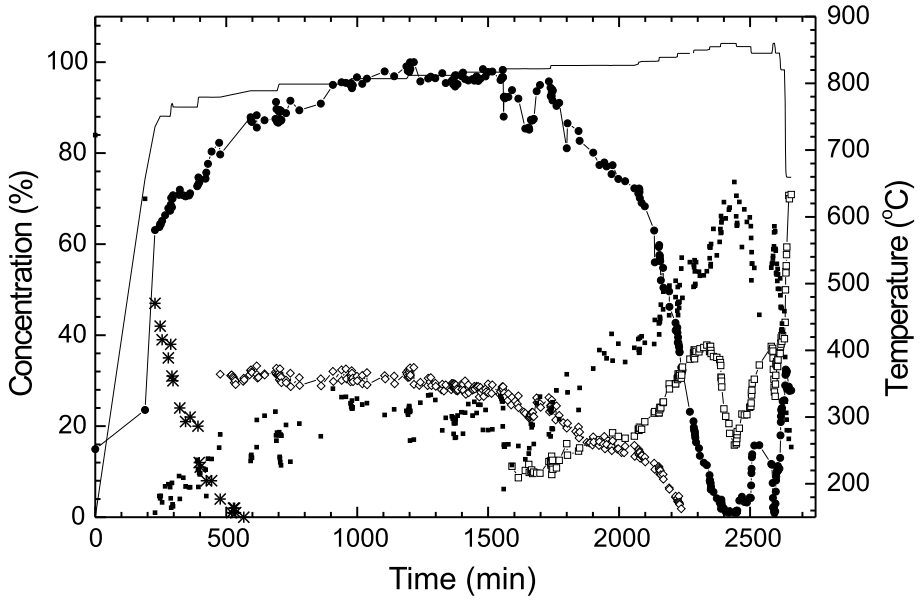

Figure 36: Integrated intensities of the Bi-2212 (115) (•), Bi-2223 (115) (□) and $(Ca,Sr)_2PbO_4$ (110) (◇) reflections during *in situ* annealing in air. These intensities are scaled to provide information on the relative concentrations. In addition, points proportional to the amount of 3221 and liquid are marked by (∗) and (■), respectively. The line marks the temperature profile with reference to the temperature scale at the right hand of the figure.

3221 appearing in an intermediate temperature range has been reported by Grivel *et al.* [56]. From Fig. 36 the amorphous/liquid background level is also seen to rise, while 3221 intensities decrease, and to stay constant once 3221 has disappeared.

In Fig. 38, the Bi-2212 (115) Bragg peak is seen to move to slightly larger Bragg angles at higher temperatures, in contrast with expectations based on thermal expansion. A more detailed analysis – shown in Fig. 40 – reveals that the *a*- and *c*-axes of Bi-2212 contract relatively by $\Delta d/d = 2 \times 10^{-4}$ and $\Delta d/d = 10 \times 10^{-4}$ between 765 °C and 820 °C, respectively. As discussed in section 3.1, the lattice contractions can be attributed to Ca and/or Pb incorporation in the Bi-2212 lattice. (Again we can rule out strain, as the midpoint of the Ag peak follows the thermal expansion line closely, cf. Fig. 38). The contraction for the (115) peak is almost identical for the 50 °C/h heating rate, reported in section 3.1, and for the present case. The Ca and/or Pb incorporation therefore seems to be an equilibrium feature.

The peak widths of the Bi-2212 (002) and (115) peaks are seen in Fig. 39 to decrease asymptotically with constant widths being obtained at 817 °C. An analysis of the 2θ variation in peak-width of additional reflections leads to the conclusion that this effect mainly reflects a decrease in the residual stress of the Bi-2212 grains. In addition, some grain growth takes place.

Grain growth and transformation ($822\,^\circ C \leq T \leq 839\,^\circ C$)

Upon reaching 822 °C, the $(Ca,Sr)_2PbO_4$ concentration starts to decrease significantly,

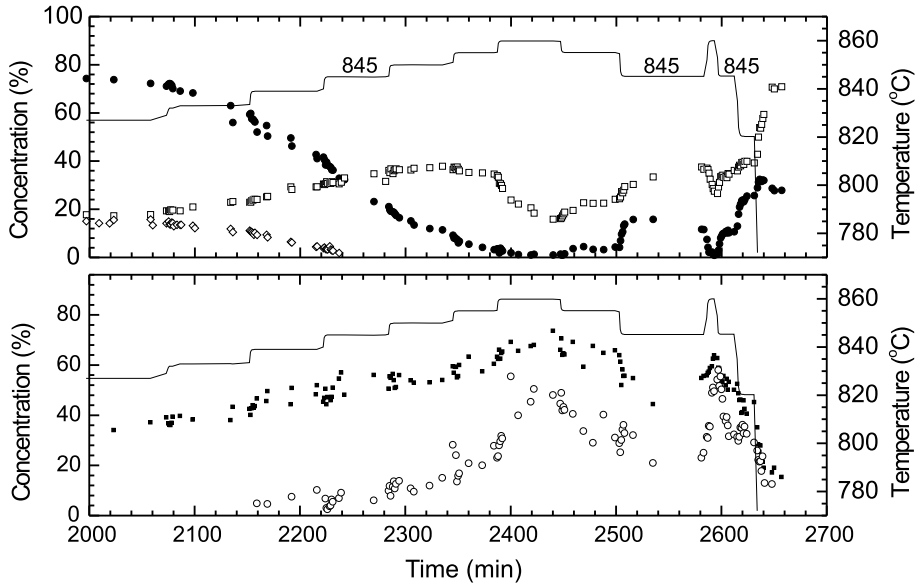

Figure 37: Close-up on the last third of the annealing. Shown above are the relative concentrations of Bi-2212 (•), Bi-2223 (□) and $(Ca,Sr)_2PbO_4$ (◇) (cf. Fig. 36). Shown below are the relative concentrations of $(Ca,Sr)_2CuO_3$ (○) and a liquid (■). The lines mark the temperature profile with reference to the temperature scale at the right hand of the figures. Comparisons between results for the 845 °C intervals – marked on the temperature profile above – are used to discuss how reversible reactions are.

cf. Fig. 36. The phase disappears 11 h later upon stepping from 839 °C to 845 °C. The $(Ca,Sr)_2PbO_4$ conversion is therefore 2 orders of magnitude slower than in the case of a standard heat treatment, cf. section 3, while the temperature range is approximately the same. Also, the $(Ca,Sr)_2PbO_4$ concentration is seen from Fig. 36 to approach a constant level during the extended time spent at 827 °C. Hence, it seems that the extended temperature interval is not caused by slow kinetics, but is an intrinsic property of the $(Ca,Sr)_2PbO_4$ dissolution.

From Fig. 38 the Bi-2212 *d*-spacing is seen to continue to contract, indicating more Ca and/or Pb incorporation. On the other hand, the width of the Bi-2212 reflections is constant, cf. Fig. 39. Hence, the Ca/Pb incorporation seems to be a bulk property effecting the majority of the Bi-2212 grains. Moreover, from Fig. 36 the liquid concentration is seen to grow in approximate proportion to the amount of $(Ca,Sr)_2PbO_4$ decomposed.

These properties are similar to the results for the standard heat treatment, cf. section 3, and may be explained in terms of a reaction between Bi-2212 and $(Ca,Sr)_2PbO_4$ producing Ca/Pb rich Bi-2212 and liquid. The Ca/Pb incorporation takes place by means of Bi-2212 grain growth. The Ca/Pb solubility limit of Bi-2212 varies with temperature. After each temperature increase, the $(Ca,Sr)_2PbO_4$ will therefore approach a constant value, with the dissolution process being halted by Ca/Pb saturation in the Bi-2212 grains.

The Bi-2223 reflections appear above the noise-level in Fig. 36 at T = 822 °C, that is shortly after the on-set of the $(Ca,Sr)_2PbO_4$ dissolution. This result should be

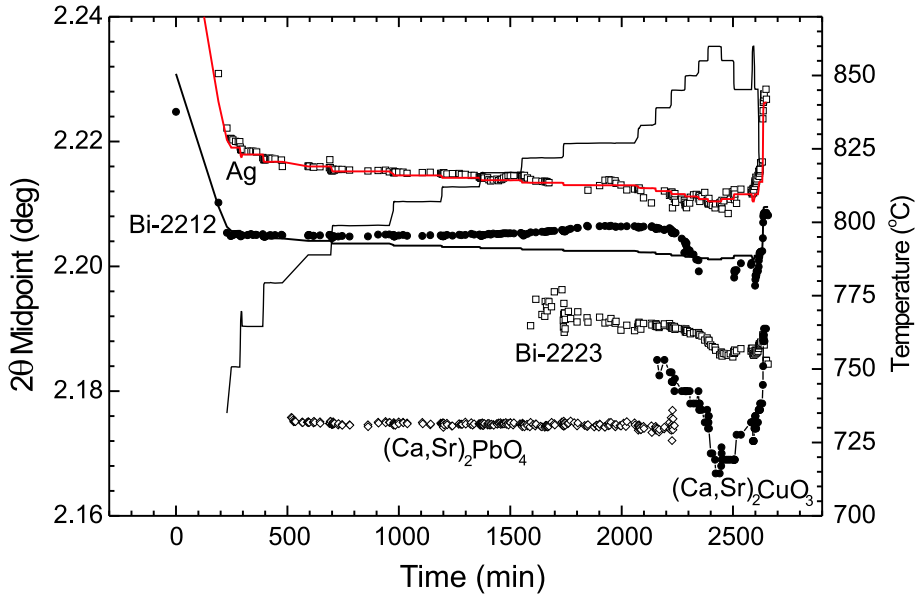

Figure 38: The midpoint of various peaks in the 2θ projections as function of annealing time. The following reflections are used: Ag (111), Bi-2212 (115), Bi-2223 (115), $(Ca,Sr)_2PbO_4$ (110) and $(Ca,Sr)_2CuO_3$ (011). To fit the five graphs into the same figure, constant off-sets of $-0.82°$, $0.088°$, $0.75°$ and $-0.72°$ have been added to the Bragg angle for the Ag, Bi-2223, $(Ca,Sr)_2PbO_4$ and $(Ca,Sr)_2CuO_3$ peaks, respectively. Shown as a solid line is the expected temperature variation for Ag – extrapolated from 799 °C using a thermal expansion coefficient of $\alpha = 26 \times 10^{-6}$ K^{-1}. In similar way the expected temperature variation for the Bi-2212 extrapolated from 760 °C is marked (with $\alpha = 19 \times 10^{-6}$ K^{-1}). Finally, for ease of interpretation, there is line marking the temperature profile with reference to the temperature scale at the right hand of the figure.

compared with the standard heat treatment, where the $(Ca,Sr)_2PbO_4$ dissolution was completed before any Bi-2223 peaks appeared. We assume the difference is a simple consequence of the very different ramp rates used in the two experiments. We also note that the Bi-2223 concentration jumps upward at every temperature step up to 839 °C.

High Temperature cycling ($T \geq 845$ °C)

The main result is the existence of fast nearly reversible changes, involving the Bi-2212, Bi-2223, $(Ca,Sr)_2CuO_3$ and liquid phases at temperatures above 833 °C, as evidenced by Fig. 37. The liquid concentration increases monotonically with temperature, but is the same within experimental error at the three 845 °C plateaus – as are the Bi-2223 concentrations. From the behavior introduced by the 860 °C temperature 'spike' near the end of the run – cf. Fig. 41 – the time constant is seen to be of the order of 10 min. $(Ca,Sr)_2CuO_3$ appears upon stepping from 833 °C to 839 °C. Again, the concentration increases monotonically with temperature. However, the reaction is less reversible in this case, with $(Ca,Sr)_2CuO_3$ concentrations of 14%, 36%, and 49% at the end of each of the three 845 °C plateaus. Also, the $(Ca,Sr)_2CuO_3$ formation and decomposition

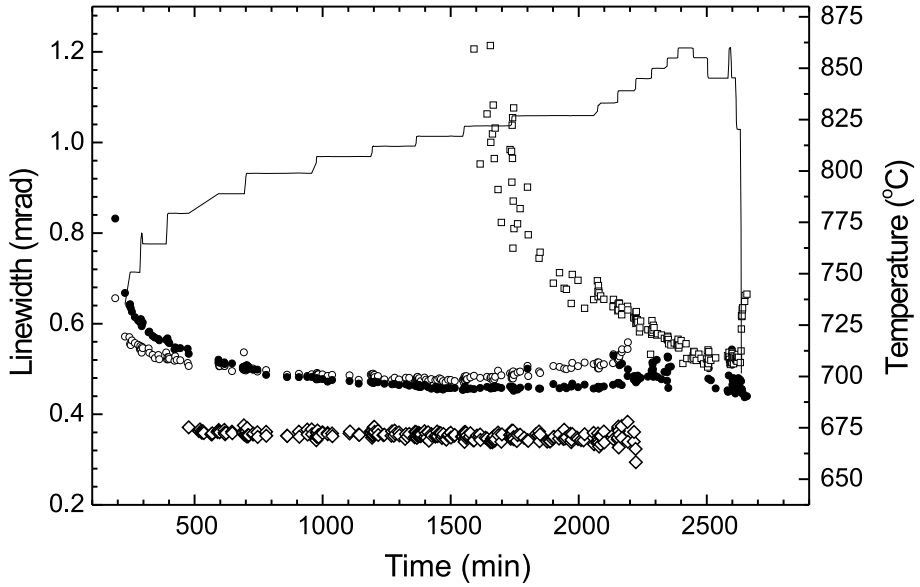

Figure 39: The full width at half maximum of various peaks in the 2θ projections as function of annealing time. Symbols refer to: (●) and (○) the (115) and (002) reflections of Bi-2212, (□) the (115) reflection of Bi-2223, and (◇) the (110) reflection of $(Ca,Sr)_2PbO_4$. The data points are not corrected for the instrumental broadening. The line marks the temperature profile with reference to the temperature scale at the right hand of the figure.

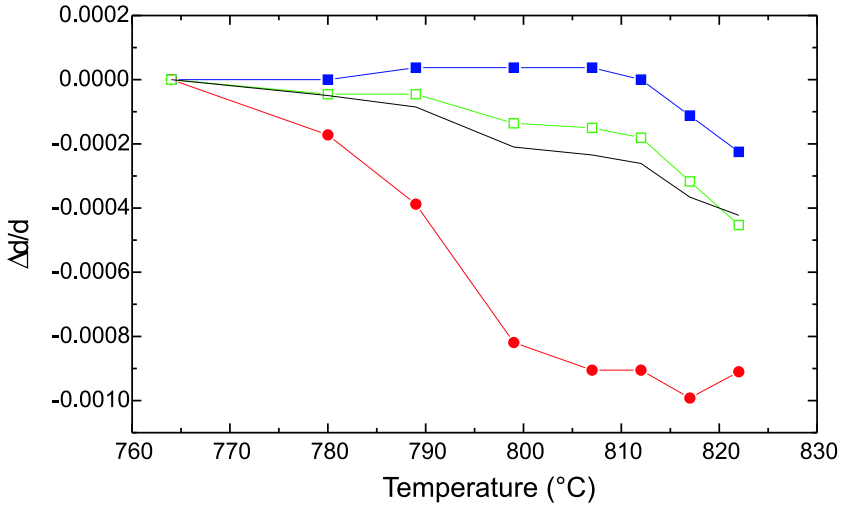

Figure 40: Contraction of the Bi-2212 *a*- and *c*-axes during the initial slow heating. Shown is the relative change in the *d*-spacing of the (020) (■) and (0010) (●) reflections with respect to values at 764 °C. To test data quality the relative change in *d*-spacing for (115) was calculated from these values (——) and compared with measured values (□).

kinetics are slower, cf. Fig. 41. This is likely to be related to the fact that the grains are much larger than those of the other phases (and appear as dots in the 2D images).

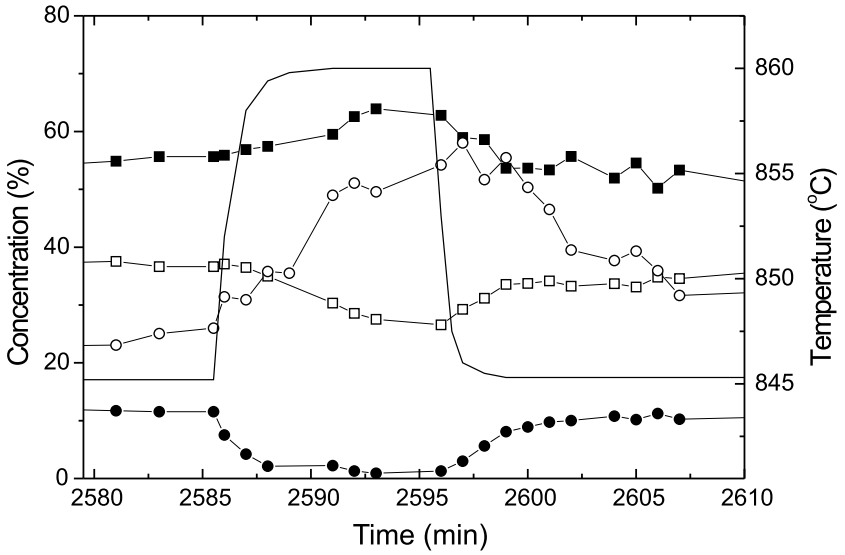

Figure 41: Results of the second high temperature cycle. The relative concentrations of Bi-2212 (•), Bi-2223 (□), $(Ca,Sr)_2CuO_3$ (○) and the liquid (■) are shown as a function of time. Data points are identical to the ones presented in Fig. 36 and Fig. 37. The line without dots marks the temperature profile with reference to the temperature scale at the right hand of the figure.

The behavior of Bi-2212 and Bi-2223 is governed by two things, which can be inferred from Fig. 37. Firstly, the liquid concentration always increases (decreases) when the sum of Bi-2212 and Bi-2223 concentrations decreases (increases). Secondly, for the duration of any of the temperature plateau the *available* Bi-2212 is always partly transformed to Bi-2223 (i.e., the ratio $c_{2223}/(c_{2212}+c_{2223})$ increases for constant T). In addition, the Bi-2212 phase is seen to decrease monotonically with T, while the Bi-2223 phase first decreases at 855 °C. Time constants – relating to the equilibrium with the melt – are of the order of 10 min for both phases, cf. Fig. 41.

Above 839 °C the Bi-2212 (115) lattice parameter expands drastically, cf. Fig. 38. As the midpoints of the Ag and Bi-2223 reflections behave in quite a different manner, we assume that the major cause of the line-shift is a change in stoichiometry. The variations take place within a few minutes. The final midpoint for the 3 plateaus at 845 °C is $2\theta = 2.2050°$, 2.2004° and 2.2008°, respectively. The latter two are seen from Fig. 38 to correspond to the expected values on the basis of thermal expansion only. On cooling to 820 °C in the end this correspondence continues to exist. Hence, it seems the Ca/Pb incorporation into Bi-2212 obtained during initial heating is lost during the first high temperature cycle. Next, we observe from Fig. 39, that the total change in Bragg angle for Bi-2212 (115) between 839 °C and 850 °C is less than 0.3 times the (almost constant) Bi-2212 line-width. Such a behavior is consistent with the Bi-2212 grains progressively melting from the Ca/Pb rich end of the (Bi,Pb) spectra.

The Bi-2223 lattice parameter exhibits a slow expansion below 850 °C, consistent with the thermal expansion. Above 850 °C the behavior is similar to that for Bi-2223, but less pronounced. Finally, the $Ca_{2-x}Sr_xCuO_3$ midpoint is seen to vary substantially

during the cycles. We tentatively attribute this to changes in the Ca/Sr ratio. Using room temperature d-spacings of Sr_2CuO_3 and Ca_2CuO_3 from the JCPDS database, and assuming identical thermal expansion coefficients for the two materials, the stoichiometry parameter x is estimated to be approximately 0 at 845 °C and 0.15 larger at 860 °C. The changes are not fully reversible, which again may be related to the sluggish kinetics associated with the $(Ca,Sr)_2CuO_3$ phase.

We interpret these results in terms of two types of reactions, a fast one that governs the equilibria between Bi-2212, Bi-2223 and the liquid, and a slow one, which governs the Bi-2212 to Bi-2223 conversion. Below 850 °C the Bi-2223 phase does not, to a first approximation, react with the melt. Bi-2212, on the other hand, is in equilibrium with the melt and (above 833 °C) $(Ca,Sr)_2CuO_3$ and possibly other phases as well. The rather large $(Ca,Sr)_2CuO_3$ concentration implies that the melt is more Bi-rich than Bi-2223, in accordance with electron microscopy results from the literature [43]. The Bi-2212 stoichiometry is shifted to the Ca/Pb deprived side at higher T – cf. Fig. 38 – which is likely to imply that the melt becomes Pb-rich in addition. At constant T, we found in section 3 that the Bi-2212 to Bi-2223 transformation implies the decomposition of $(Ca,Sr)_2CuO_3$. However, the temperature profile used here does not allow an observation of a decreasing $(Ca,Sr)_2CuO_3$ content at each plateau as the plateaus are too short. Above 845 °C, Bi-2223 is also in an equilibrium with the liquid and $(Ca,Sr)_2CuO_3$ (and possibly other phases).

In Fig. 39, the (002) and (115) lines of Bi-2212 are seen to broaden during heating. On 'quenching' back to 845 °C, the width immediately returns to the level of the instrumental resolution. The broadening during heating may either be a finite-size effect, or reflect that the variation in (Bi,Pb) stoichiometry of Bi-2212 becomes larger. The fact that the (002) peak starts to broaden before (115) favors the finite-size effect. Assuming this to be the case we compare the (115) widths at 845 °C before and after the first cycle. The width is significantly larger on heating. With approximately the same concentration of Bi-2212 on heating and cooling – cf. Fig. 37 – we argue that the Bi-2212 grains must on average be bigger during cooling. This points to a limited amount of Bi-2212 nucleation centers during cooling. That result, in turn, is consistent with precipitation mainly taking place by layer-on-layer growth on the surviving Bi-2212 grains, and the stoichiometry of the precipitated Bi-2212 reflecting the equilibrium, explaining the reversible behavior in Fig. 38.

The Bi-2223 line-width is less effected by the high temperature cycling – as was the line shift. From Fig. 39, the (115) line width is seen to decrease monotonically towards an asymptotic value of 0.52 mrad. A similar behavior was reported in section 3, and attributed to the finite thickness of the Bi-2223 grains in the direction of the c-axis.

These results are consistent with the Bi-2223 grain growth being mainly governed by the Bi-2212 to Bi-2223 transformation mechanism (and results therefore similar to those was reported in section 3). However, the results in Fig. 38 hints that at temperatures high enough that Bi-2223 and the liquid reacts, the associated melting/precipitation behavior exhibits the same features as the ones related to the Bi-2212/liquid equilibrium.

5 3DXRD FEASIBILITY STUDY

The hard X-ray setup at HASYLAB enables studies of the *average* properties of the Bi-2212 and Bi-2223 grains. As discussed in previous sections, with such data one cannot *directly* test models of the texture and transformation mechanisms, due to the fact that transformation rates etc. vary with grain size, grain stoichiometry and grain orientation. With the 3DXRD microscope [10, 11, 12, 58] we aim at overcoming this problem by following the kinetics of the individual embedded grains inside the Ag during annealing.

The 3DXRD microscope was put to use at the European Synchrotron Radiation Facility (ESRF) in 1999. It is dedicated toward 3D mappings of powders and polycrystals. The general aim is firstly to provide mappings of grain characteristics: size, shape, crystallographic orientation, stress-state and stoichiometry as well as neighboring relationships, and secondly to provide the dynamics over an ensemble of grains during processing. Methods have been established that provides such maps [11] and grain dynamics [12] in coarse-grained metals.

A preliminary annealing experiment with Bi-2223 tapes have been performed. The set-up was similar to the HASYLAB setup – see Fig. 3 – with the exception that the beam is focused vertically by a bent Laue crystal to form a 5 μm horizontal line. Horizontally, the 80 keV beam was limited by a slit to 40 μm. Hence, the gauge volume was much smaller than at HASYLAB. This implies that when the grains are sufficiently large the associated diffraction spots will no longer overlap to form a continuous ring (powder diffraction ring) but in stead appear as distinct spots on the detector. By oscillating in ω while exposing the integrated intensity of these spots can be deduced. As the grain volumes are directly proportional to the integrated intensity of the associated spots, the grain growth can be deduced in this way. At the same time the orientation of the grain is reflected in the position of the spots on the detector.

A mono-filamentary green tape was studied – of the same type as used in section 3.2. The tape was mounted in the standard way, shown in Fig. 3, in the same furnace as used in the studies at HASYLAB. The tape was annealed in air by initially ramping up from room temperature with a rate of 100 °C/h, followed by 12 h of operation at 838.5 °C. During this period exposures were made continuously by a CCD camera while oscillating the tape by 0.5° around $\omega = 75°$. The exposure time was 5 min.

At the beginning of the annealing the diffraction pattern consisted of segmented Debye-Scherrer powder rings. At 825 °C the diffraction spots from grains appeared. For the remaining period typically 60 diffraction spots were clearly visible on the CCD, cf. Fig. 42.

During the process so-called validation tests were made after every second exposure by either doubling the oscillation range or by opening the slit. By comparing the integrated intensities for the three settings (normal, larger oscillation range, larger gauge volume) we inferred whether the full grain was illuminated and whether the oscillation range was appropriate. In this way we ensured that the integration over intensity was complete and thereby that the deduced grain volume were valid. Unfortunately, it turned out that the majority of the grains 'rotated out' of the oscillation range during

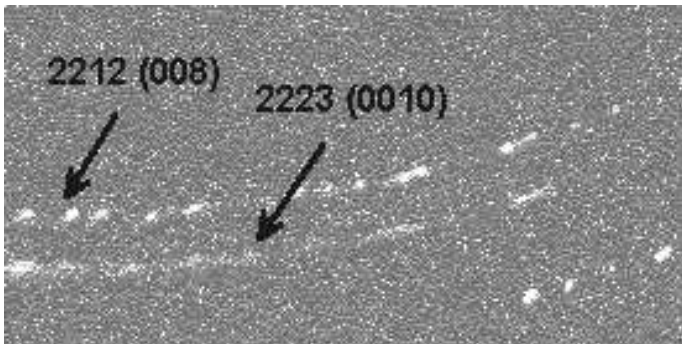

Figure 42: Detail of raw image acquired after 11.5 h of annealing at 838.5 °C in air. Dots appearing on the (008) and (0 0 10) Debye-Scherrer rings associated with the Bi-2212 and Bi-2223 phases, reflect the transformation from Bi-2212 to Bi-2223. The x and y axes of the figure are swapped in comparison to Fig. 6 and Fig. 7.

the period in question, most likely because the amount of liquid was sufficient to make the network of grains float to some extent. In total only 4 grains were found to valid during the entire period of their existence.

In Fig. 43 the evolution of the intensity of the four diffraction spots are shown. One of them is from a Bi-2223 grain (○) and the others are from Bi-2212. The integrated intensity, which is proportional to the grain volume, does in all cases increase to a maximum where after they decrease and finally disappear. The appearance of new Bi-2212 grains after ∼4–7 h annealing time indicates a dynamic behavior, where the individual grains crystallize again and transform at different times.

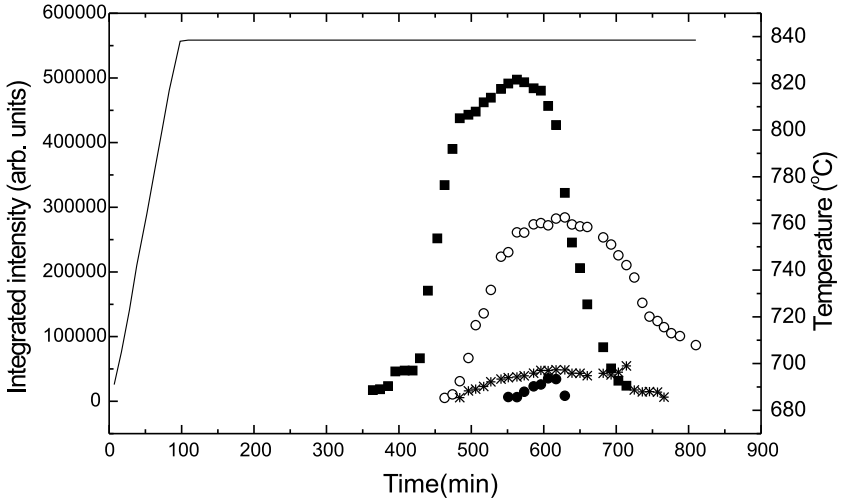

Figure 43: Relative integrated intensities of four diffraction spots originating from different grains during annealing in air. The symbols refer to: (•) Bi-2212 (117), (■) Bi-2212 (117), (○) Bi-2223 (119) and (∗) Bi-2212 (020). The solid line marks the temperature profile with reference to the temperature scale at the right-hand side.

While the results obtained from this feasibility study may seem somewhat meager, the potential should be underlined. In particular we note that

- The beam can be focused in both directions in stead of only one, leading to much shorter exposure times, and thereby the option of measuring at a number of consecutive ω positions. In this way the 'grain rotation problem' can be solved.
- Following the present measurements an indexing program GRAINDEX have been established [58]. This sorts the diffraction spots with respect to grain of origin. In this way the crystallographic orientation of the individual grains can be derived. Furthermore, by single crystal refinements to each grain we may deduce their stoichiometry.
- Essential information on transformation mechanism ('intercalation' vs. 'growth on top' vs. 'random nucleation') should be available in a rather direct way. Due to identical a/b-axes the transformation of Bi-2212 into Bi-2223 will give rise to spots appearing with identical azimuthal angle in the images, if and only if the grain orientation is conserved. Unfortunately, the number of valid grains in the present study was not sufficient.
- Likewise, we can infer whether Bi-2212 grains with a large Pb content transforms earlier than Bi-2212 grains with a small Pb content simply by making statistics over when the grains disappear as function of 2θ angle (radial distance from the center in the image). However, once more the number of valid grains in the present study was not sufficient.

One final complication still exist: the Bi-2212 and Bi-2223 grains typically form colonies, cf. section 6.2. The grains within the colony should have common $(00l)$ spots, but give rise to a set of spots for other reflections. Once the software is able to handle this complication it is clear that the kinetics really can be determined as function of the stoichiometry, orientation and grain size by the 3DXRD microscope.

6 TRANSMISSION ELECTRON MICROSCOPY INVESTIGATIONS

In this section TEM results [19] are presented with the aim of investigating the influence of the annealing time and the intermediate deformation process (pressing). A separation of the effect of the two processes was carried out by choosing three tapes for examination: a fully processed tape (1), a tape annealed once for less than 50 h (2) and a tape annealed once for 200 h (3). By comparing TEM results from tape 1 and 2 we infer the effect of annealing together with the intermediate pressing. Similarly, a comparison of tape 2 and 3 provides information on the effect of annealing time only.

The three 37-filamentary tapes were also examined by means of the hard X-ray set-up at HASYLAB. Within the limitations of that method they are all fully converted (no discernible Bi-2212 signal left).

6.1 Experimental

The three 37-filamentary tapes were annealed at the same temperature (830 °C) and in an atmosphere of 8% O_2. The samples are identified in Table 1. Also listed are the critical currents I_c, obtained by averaging results for three tapes, measured at 77 K in self-field. From each tape both a longitudinal and a transversal cross-section TEM sample were prepared by stacking two pieces of tape (cut at a length of 3 mm) together. This stack was sandwiched between two pieces of glass before it was mechanically polished to a thickness of ∼20 μm and glued on a copper grid. Finally the sample was thinned by ion-milling. The TEM studies were performed at the center for Electron Microscopy for Materials Science (EMAT) at University of Antwerp (RUCA). For grain morphology and grain boundary angle investigations a Philips CM20 (200 kV) was used. High-resolution TEM (HRTEM) was carried out on a JEOL 4000EX (400 kV) with a point-to-point resolution of 1.7 Å.

Table 1: Sample Identification

ID	Annealing	I_c (A)
Sample 1	75 h (total), multi steps (fully processed)	44
Sample 2	<50 h, 1 step (1st annealing)	9
Sample 3	200 h, 1 step	20

6.2 Results

The superconducting Bi-2223 grains grow in so-called colonies. A colony is a stack of grains with a common *c*-axis, but twisted within the *ab*-plane ([001] twist boundaries between the BiO double layers) [15]. The *ab*-twist is seen as different grey levels in a TEM bright field image (Fig. 44). So-called colony and grain thicknesses are defined in Fig. 44 – they are measured along the *c*-axis direction. Colonies can be connected by two types of *c*-tilt grain boundaries [15]: small-angle *c*-axis tilt (SCTILT) boundaries (Fig. 44) and edge-on *c*-axis tilt (ECTILT) boundaries (Fig. 45).

6.2.1 Grain and colony thickness

For each sample, we have determined the grain and colony thickness in many different areas. The results are shown in Fig. 46 and Table 2. The average grain thickness for sample 1 is 30.5 ± 1.3 unit-cells. The peak maximum is at 25–28 unit-cells. In sample 2 the average grain thickness is 20.7 ± 1.1 unit-cells, while the peak maximum is at 13–24 unit-cells. Hence, the grains in the fully processed tape are on the average 50% thicker than after 1st annealing. The grains in sample 3 are found to be thicker than in sample 2. In sample 3 the average grain thickness is 27.9 ± 1.3 unit-cells. The distribution of the grain thickness for sample 3 shows a larger variation of the grain thicknesses. The histogram has a peak maximum at the same thicknesses as sample 2 plus lower peaks at higher grain thicknesses. Hence, the average value of grain thickness for sample 1 and 3 are similar but the distributions are not.

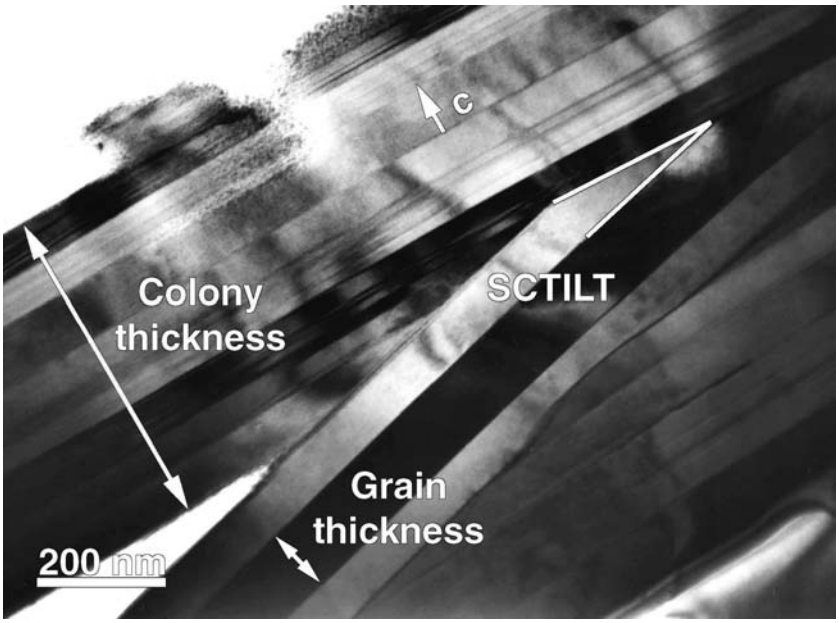

Figure 44: TEM bright field image showing two colonies forming a small-angle c-axis tilt (SCTILT) boundary. The different grey levels correspond to grains separated by ab-plane twist boundaries.

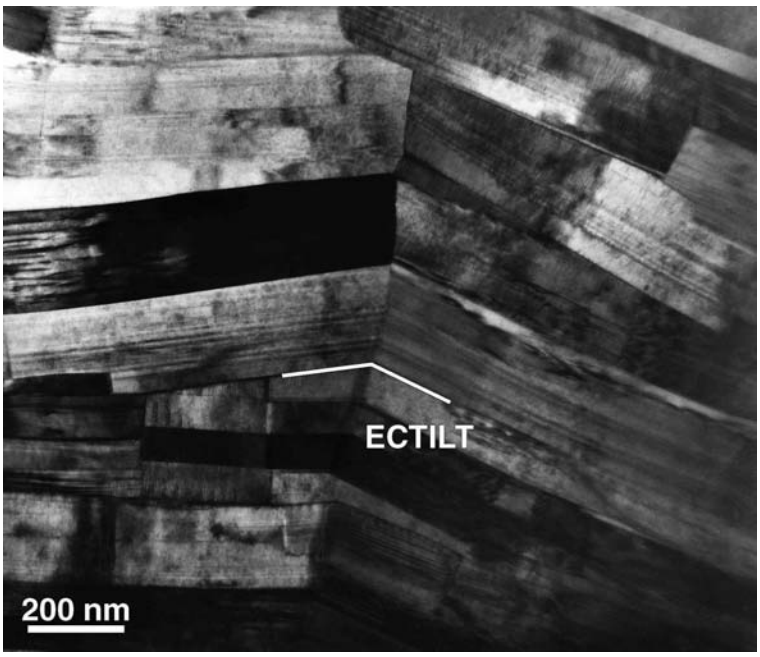

Figure 45: TEM bright field image showing edge-on c-axis tilt (ECTILT) boundaries.

Besides the grain thickness the colony thickness is also important for the current path. The minimum, maximum and average values of the colony thickness are shown in Table 2 for the three samples. The fully processed tape (sample 1) has thicker colonies than the tape after the 1st annealing (sample 2). Sample 3, which has been annealed

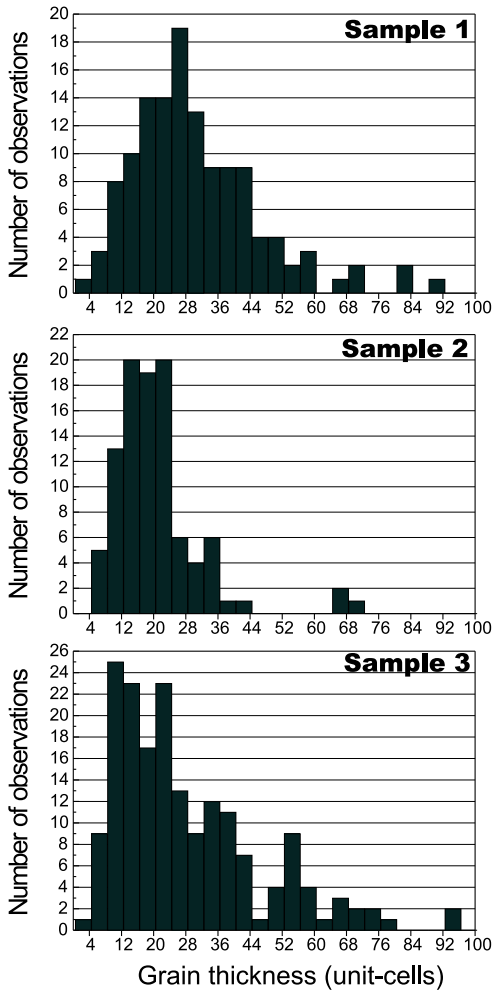

Figure 46: Histograms showing the distributions of grain thicknesses (in the c-axis direction). The number of observations is 128, 98 and 179 grains for sample 1–3, respectively.

for a longer time than sample 2, also has thicker colonies. The colony thickness of sample 1 and sample 3 are similar. Furthermore, the average number of grains per colony is calculated (Table 2). Within the statistical uncertainty this number is the same for each sample. These results indicate that the grain growth and colony growth are correlated.

6.2.2 Angles of c-axis tilt

The grain boundaries have been examined both in longitudinal cross-sections and in transversal cross-sections. We find the distribution of c-tilt angles to be the same in the two directions. Furthermore, the two types of c-tilt angles (SCTILT and ECTILT) have also the same distribution. Therefore, all the c-tilt angles are plotted in the same graph (Fig. 47). The average c-tilt angle is found to be $14.4° \pm 1.3°$ in sample 1. The peak maximum is at 7°–9°. The highest observed angle is 41°. Sample 2 has a

Table 2: The minimum, maximum and average values of the colony thickness for sample 1–3. The average values of grain thickness, number of grains per colony and c-tilt angle are also listed.

	Colony thickness			Average grain thickness	Number of grains per colony	Average c-tilt angle (°)
ID	Min (μm)	Max (μm)	Average (μm)	(unit-cells)		
1	0.4	1.2	0.73 ± 0.09	30.5 ± 1.3	6.5 ± 1.1	14.4 ± 1.3
2	0.1	0.8	0.40 ± 0.03	20.7 ± 1.1	5.2 ± 0.7	26.0 ± 1.7
3	0.2	1.7	0.69 ± 0.09	27.9 ± 1.3	6.7 ± 1.2	18.6 ± 1.7

wider distribution with a lot of large-angle c-tilt boundaries up to 90° besides similar small angles as in sample 1. The average c-tilt angle is found to be 26.0° ± 1.7°. A comparison between sample 1 and 2 indicates that the pressing and further annealing removes the highest c-tilt angles from the tape. In sample 3 the average c-tilt angle is found to be 18.6° ± 1.7°. The peak maximum is at 7°–12°. If the four observations with highest c-tilt values are removed the average value becomes 16.1° ± 1.2°. The distribution for sample 3 is within the statistical uncertainty similar to the distribution for sample 1. This suggests that further annealing without pressing in between should also provide grain boundaries with lower c-tilt values. For comparison these numbers are also listed in Table 2.

6.2.3 Intergrowth

The Bi-2223 grains mainly consist of pure Bi-2223 ($n = 3$) unit-cells, but intergrowth of half unit-cells of other periodicities e.g. Bi-2212 ($n = 2$) and Bi-2234 ($n = 4$) is observed. The intergrowth content and distribution can be investigated easily by high-resolution TEM (HRTEM). Fig. 48 shows an example of intergrowth near a twist boundary. The distribution of half unit-cells (building units) in sample 1 and in sample 2 is summarized in Table 3. The intergrowth varied from 3% to 39% at different places in the sample. We have seen both small and high content of intergrowth near twist, SCTILT and ECTILT boundaries. It was often observed that there is intergrowth just next to a grain boundary. The total intergrowth in the fully processed tape (sample 1) as well as in sample 2 is about 15%. About 70% of the intergrowth in both tapes is Bi-2212 ($n = 2$). Almost all of the grain boundaries are free of non-superconducting phases. Only at one twist boundary in sample 2 we have found an intermediate amorphous phase.

6.3 Comparison of texture results based on TEM and hard X-ray diffraction

The synchrotron texture results and the TEM angle of c-axis tilt results are not directly comparable. By the synchrotron X-ray technique we determine the FWHM of the distribution of mis-alignment angle between the c-axis of the grains and the tape normal. The TEM results are average values of a projection of the c-axis tilt angles

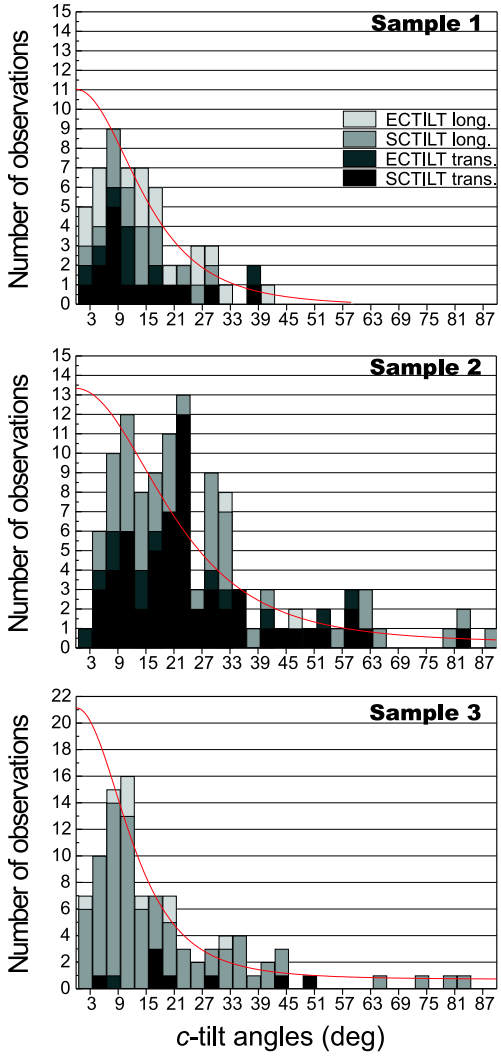

Figure 47: Histograms showing the distributions of *c*-tilt angles of SCTILT and ECTILT boundaries. 'long.' and 'trans.' refer to the longitudinal cross-section direction and the transversal cross-section direction, respectively. The number of observations is 55, 115 and 96 angles for sample 1–3, respectively. The line is a squared Lorentz fit with the midpoint fixed to zero to the data set truncated by the first two columns (cf. section 6.3).

between two connected colonies. If we assume that the colonies grow independently of each other we could in principle relate these two ways of expressing the texture mathematically. However, this has not been done.

By fitting the distributions of *c*-tilt angles (section 6.2.2 Fig. 47) to a squared Lorentz distribution with the midpoint fixed to zero we can compare the trend of the results obtained by TEM and the synchrotron. The fitting results are shown in Fig. 47. The data set has been truncated by the first two columns since these numbers of observations could be too low because boundaries with angles lower than 6° will not be observed at images recorded at low magnifications. The fit of especially sample 2

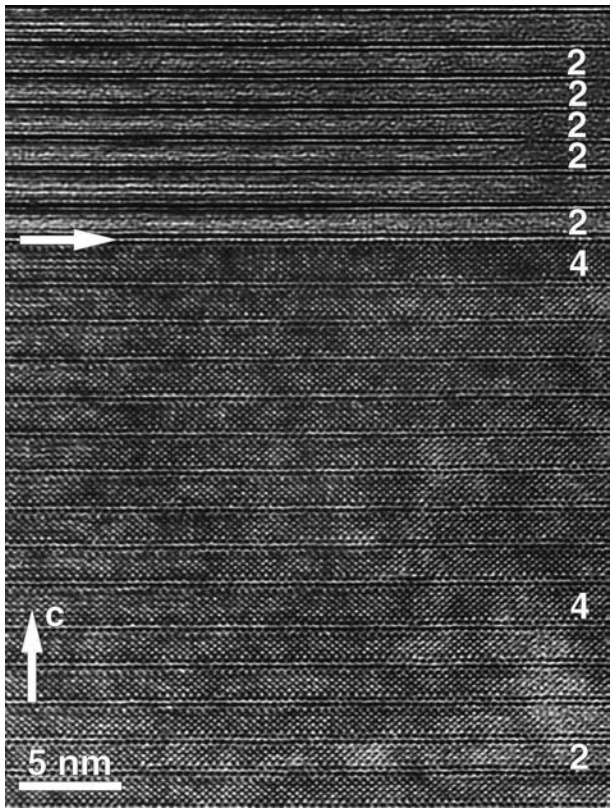

Figure 48: A section of a high-resolution TEM image of sample 2 showing two grains separated a twist boundaries (marked by an arrow). The lower grain is orientated along the [110] direction. The numbers indicate intergrowth of Bi-2212 (2) and Bi-2234 (4).

Table 3: The percentage of intergrowth in sample 1 and 2

$(Bi,Pb)_2Sr_2Ca_{n-1}Cu_nO_x$	Sample 1		Sample 2	
	Number of half unit-cells	%	Number of half unit-cells	%
$n = 3$	389		315	
Intergrowth				
$n = 2$	50	11	45	12
$n = 4$	17	4	20	5
$n = 5$	1	0.2	0	0
Total intergrowth		15		17

does not look good, but it is mainly due to binning of the data. The FWHM results of the squared Lorentz curves are listed together with the synchrotron FWHM results in Table 4. By comparing the results we observe a similar trend in the data. The factor of ∼2 between the synchrotron and TEM results seems reasonable, since we expect a value between 1 and 2. In the case of the two connecting grains lying 'around a plane

parallel to the tape plane' the angle in the 2D plane measured by TEM is equal to the sum of the two angles measured by the synchrotron.

ID	Synchrotron $\Delta\alpha$ (deg)	TEM FWHM (deg)
Sample 1	15.2	29.7
Sample 2	18.8	41.9
Sample 3	13.7	24.3

Table 4: Comparison of hard X-ray and TEM results for the tape texture.

It is worth noting that due to the variation of the texture throughout the filament [52] it is necessary to investigate a large number of grain boundaries by TEM to ensure a representative data set. This problem does not exist in relation to the synchrotron results since these are obtained from averaging over the tape width.

6.4 Discussion

The microstructural parameters in the present study yield information on the effects of annealing time and intermediate pressing. Longer annealing times result in thicker grains and smaller c-tilt angles. On the other hand, the effect of intermediate pressing on the average values of these structural parameters is relatively small. However variations of grain and colony thickness as well as of c-tilt angle are larger for sample 3 than for sample 1, indicating that the intermediate pressing has an effect of narrowing these distributions. Our observations also show that the content and distribution of the intergrowth is quite independent of the annealing time and pressing.

From Table 1 it is clear that both the extra annealing time and the intermediate pressing have a large effect on I_c. The longer annealing time of sample 3 as compared to sample 2 results in an increase of I_c by a factor of 2. A combination of longer annealing time and intermediate pressing increases I_c by a factor of 5 (comparing sample 1 to 2). In these two cases the improvement of I_c can be related, at least partly, to the increase in grain and colony thickness and the decrease in the c-tilt angle. It is worth noting however that these parameters are not the only ones related to I_c. The I_c values of sample 1 and 3 are 44 A and 20 A, respectively, even though the two samples have similar average values of grain thickness and c-tilt angle. Hence, other parameters such as grain connectivity and density are also important current limiting factors. Obviously, the intermediate pressing densifies the structure efficiently.

The present finding that the average number of grains per colony is nearly identical for all three tapes indicates that the grain growth and colony growth are correlated. The grains in sample 3 are thicker than the grains in sample 2. It means that further three-dimensional grain growth takes place after the conversion into Bi-2223. As discussed in section 3.1, it is possible that the nucleation process can be repeated for the Bi-2223 grains during further annealing. Differences in stoichiometry and grain size are then the driving force for re-melting of Bi-2223 grains and appearance of new and larger grains with a different stoichiometry. Furthermore, the fact that the average value of the angle of c-axis tilt is better in the tape annealed for 200 h than in the tape annealed < 50 h suggests that the texture evolution is determined by continued

nucleation and two-dimensional grain growth in the confined volume given by the filament thickness. This is confirmed by the observations from the 3DXRD experiment (cf. section 5), indicating a dynamic behavior, where the individual grains crystallize again and transform at different times.

Zhu *et al.* [14] have investigated the misorientation angle distributions for large-angle grain boundaries in Bi-2212 and Bi-2223 tapes. They have found that the grain boundary angles are randomly distributed for Bi-2223, while for Bi-2212 certain angles, in accordance with the 'Coincidence Site Lattice (CSL) theory' [59], are preferred. In agreement with the work of Zhu *et al.* we have found the distribution diagrams of the *c*-tilt angles to be smooth. The *ab*-plane twist ([001] twist boundary) of the grains inside a colony is also investigated in Ref. [14]. In that paper only angles higher than 10° are presented. They have observed *ab*-tilt angles from 10° to 90° with an almost random distribution, except for the angle of 90° ($\Sigma 1$), which has been observed several times. The *ab*-twist angles observed in the present study are as small as 0.1° and most of the observed angles are smaller than 10°.

Bi-2212 has $T_c = 85$ K (compared to $T_c = 110$ K for Bi-2223). This value of T_c is close to 77 K, therefore it is possible that the intergrowth will lower the critical current density J_c. However, in this particular case, since the intergrowth content and distribution are the same in sample 1 and sample 2, the intergrowth is not responsible for the lower J_c value in sample 2.

From the hard X-ray diffraction work presented in section 3, as well as neutron diffraction [55] and Cu K_α XRD [60, 61] studies elsewhere, the fraction of Bi-2223 in fully processed tapes is estimated to be as high as 98% [20]. All these techniques do not take intergrowth into account because the intergrowth domains are too small to be detected. The presented intergrowth results show that the content of intergrowth in the fully processed tape is 15%. This result is obtained near grain boundaries, but because the thickness of the grains is only 30 unit-cells, our result is general and the conversion into Bi-2223 is only about 83%.

7 SUMMARY OF MICROSTRUCTURAL DYNAMICS

In this section we summarize our hard X-ray diffraction and TEM results, describing the structural evolution from the green tape to the fully processed one.

In the green tape the Bi-2212 grains exhibit a weak texture, while they are heavily strained (to a level of $\varepsilon = 1.7 \times 10^{-2}$). During ramp up the strains are relieved continuously as result of a crystallization/grain growth process. Depending on the calcination process of the powder prior to tape processing a number of other reactions may take place during ramp up. In particular, if the 3221 phase is present it will dissociate at temperatures around 750 °C (depending on ramp rate).

Between 700 °C and 840 °C the $(Ca,Sr)_2PbO_4$ phase decomposes. Simultaneously the Bi-2212 lattice contracts in all directions by up to 0.2% and the integrated intensity of the (115) reflection increases by ∼20%. The sign and magnitude of these effects are consistent with an incorporation of Pb and possibly Ca in the structure. Furthermore, the amount of liquid rises, cf. Fig. 36. These results therefore supports a model where

the Bi-2212 and $(Ca,Sr)_2PbO_4$ react to form Ca and Pb enriched Bi-2212 plus liquid. The large temperature span over which this reaction takes place is not due to sluggish kinetics, cf. the results of section 4. Instead it is an intrinsic effect of a temperature dependent solubility limit for the Pb and Ca incorporation, in accordance with the work by Majewski *et al.* [62].

Our results for the structural dynamics at temperatures around the operation temperature are consistent with (at least) two types of reactions appearing simultaneously. Firstly, there is a temperature dependent equilibrium between Bi-2212 and the liquid plus one alkaline-earth cuprate. For annealing in air the alkaline-earth cuprate is shown to be (Ca,Sr)2CuO3. For annealing in 8% O_2 we have circumstantial evidence from quenched tapes that it is the 14:24 phase. Upon increasing temperature, the liquid content rises almost linearly, while the Pb and/or Ca content of Bi-2212 is steadily decreasing. The stoichiometry of $(Ca,Sr)_2CuO_3$ is also very temperature dependent. From the temperature cycles presented in section 4, we conclude that the reaction between the phases is fast (within a few minutes at the temperatures studied) and reversible with respect to the liquid/Bi-2212 concentrations. The $(Ca,Sr)_2CuO_3$ kinetics is slower, most likely due to the formation of large grains. At temperatures above 850 °C in air, Bi-2223 also reacts with the melt. The Bi-2223/liquid equilibrium is associated with similar effects, such as the Pb content of Bi-2223 being reduced at higher temperatures. (In other studies we have gone to even higher temperatures, where all the Bi phases were melted. Upon slow cooling large Bi-2212 grains precipitated.)

The second reaction taking place at or around the operation temperature is the formation of Bi-2223. This is a much slower process, with material being supplied by Bi-2212, the liquid and the alkaline-earth compound. The Bi-2212 reflections show no sign of strain or finite-size broadening during the process, implying that the dissociation/transformation of each Bi-2212 grain must be fast. The Bi-2223 grains form in colonies, with approximately 5 grains having a common c-axis. Avrami plots suggest that the reaction is the same throughout the 1st annealing. The transformation mechanism is discussed at length in section 3.1. In short, the data points to a nucleation-and-growth mechanism, whereby the Bi-2223 grains form on top of the existing Bi-type grains. However, the diffusion constants must be very temperature dependent as the amount of liquid varies. Hence, at low T, small liquid drops is thought to travel over the Bi-2212 platelets, while at sufficiently high T only small amounts of Bi-2212 is left and the grains will be nearly submerged in the liquid.

The 3DXRD study provides direct evidence that the Bi-2212 and Bi-2223 grains, once formed, will exist for a while, to be dissociated again. Likewise, TEM studies show that the grain and colony thickness of the Bi-2223 grains continue to increase after the conversion is completed, while the number of grains per colony remains constant. This result suggests that new grains/colonies are formed. It appears that local differences in stoichiometry and grain size are the driving force for a dynamic behavior, where the grains 're-crystallize' at different times. This scenario also describes the structural dynamics taking place during the last annealing. As the volume percentage of material undergoing reactions steadily decrease no change was observed in the average concentration or stoichiometry. But the grain and colony thickness increased by 50% and the texture improved by 2°.

The intermediate deformation steps help to densify the structure. According to the TEM results this seems to provide more homogeneous final distributions, while the average values for grain alignment and grain dimensions stay constant. The deformation steps also change the local grain configurations, enabling renewed grain growth.

The intergrowth content was revealed by HRTEM to be 15%, distributed between Bi-2212 and Bi-2234 in a ratio of 2.5:1. These numbers, which are the same after the first and last annealing, suggests further studies of the influence of intergrowth on the superconducting properties. In contrast, almost all the grain boundaries investigated by HRTEM were free of foreign phase contamination.

With respect to grain orientations the interesting property is the distribution of the c-axis tilt angle between the neighboring grains. As verified by the comparison between TEM and hard X-ray diffraction, macroscopic textures are a useful approximation. Within experimental uncertainty, for all tapes investigated the Bi-2223 grains exhibited an ideal fiber texture.

The major improvement in the c-axis alignment of the grains takes place during the initial ramp up for the green tape, as a consequence of the Bi-2212 grain growth. Two mechanisms are identified. Firstly, in the vicinity of the HTSC:Ag interface the ceramic grains will tend to align with the interface. Secondly, in bulk the alignment is an effect of the plate-like growth of the Bi-phases within the constrained geometry of the filament. As the geometry of the Bi-2212 and Bi-2223 grains is nearly the same, it is not surprising that the final c-axis alignment of the two phases is found to be the same. In addition, as discussed above, there is evidence of a transformation mechanism by which the Bi-2223 grains inherit the orientation of the Bi-2212 grains.

Comparing the results obtained in 8% O_2 and in air we observe a faster transformation in the case of 8% O_2. Furthermore, the lower oxygen partial pressure results in a higher Pb solubility of Bi-2212. Multi-filamentary tapes are found to transform faster and exhibit a better c-axis alignment than mono-filamentary tapes (best cases: $\Delta\alpha = 14^\circ$ and $\Delta\alpha = 21^\circ$). These properties are natural consequences of the geometry, in particular the proximity to the silver and the confinement constraints.

In outlook, we suggest to continue the reference type of studies presented here with emphasis on 3DXRD, TEM studies of tapes quenched at different times during the first annealing, and the coupling between structure and local superconducting properties as revealed by magneto-optics [63, 64].

Acknowledgements

In Denmark the optimizing of the Bi-2223 tapes takes place in a collaboration between Nordic Superconductor Technologies A/S (NST), Risø National Laboratory (RISØ) and the Technical University of Denmark (DTU). Support is provided by the Danish Energy Agency and the companies ELSAM and ELKRAFT. The synchrotron experiments took place within the framework provided by Dansync. L. Gottschalck Andersen was supported by the Engineering Science Center for Structural Characterization and Modeling of Materials (IVC). The TEM work has partially been performed within the framework IUAP 4/10. We gratefully thank our colleagues who participated in the synchrotron related research: N.H. Andersen, T. Frello, A. Abrahamsen, B.H. Larsen, B.A. Jacobsen, S. Garbe, all RISØ, M.D. Bentzon, NST, M. von Zimmermann, J. Süssenbach and

T. Tschentscher, HASYLAB, U. Lienert, ESRF, as well as in the TEM related research: S. Bals and G. Van Tendeloo, EMAT. In addition, we thank J.-C. Grivel, W.G. Wang, P. Morgan, Y.-L. Liu, and B. Kindl for fruitful discussions, and A. Hammersley and N.C. Krieger Lassen for help with software.

References

[1] K. Heine, J. Tenbrink, and M. Thoner, Appl. Phys. lett. **55**, 2441 (1989).

[2] M. D. Bentzon, Z. Han, L. O. Andersen, J. Goul, P. Bodin, and P. Vase, IEEE Trans. Appl. Supercond. **7**, 1411 (1997).

[3] P. Majewski, Supercond. Sci. Technol. **10**, 453 (1997).

[4] P. Majewski, A. Aubele, and F. Aldinger, Physica C **341**, 517 (2000).

[5] W. Wong-Ng, L. P. Cook, W. Greenwood, and A. Kearsley, J. Mater. Res. **15**, 296 (2000).

[6] H.-R. Wenk, D. Chateigner, M. Pernet, J. Bingert, E. Hellström, and B. Ouladdiaf, Physica C **272**, 1 (1996).

[7] T. R. Thurston, U. Wildgruber, N. Jisrawi, P. Haldar, M. Suenaga, and Y. L. Wang, J. Appl. Phys. **79**, 3122 (1996).

[8] T. R. Thurston, P. Haldar, Y. L. Wang, M. Suenaga, N. M. Jisrawi, and U. Wildgruber, J. Mater. Res. **12**, 891 (1997).

[9] H. F. Poulsen, T. Frello, N. H. Andersen, M. D. Bentzon, R. F. Jensen, J. Süssenbach, and D. Novikov, HASYLAB Jahresbericht, 1995.

[10] H. F. Poulsen, S. Garbe, T. Lorentzen, D. J. Jensen, F. W. Poulsen, N. H. Andersen, T. Frello, R. Feidenhans'l, and H. Graafsma, J. Synchrotron Rad. **4**, 147 (1997).

[11] D. J. Jensen, Å. Kvick, E. M. Lauridsen, U. Lienert, L. Margulies, S. F. Nielsen, and H. F. Poulsen, Mat. Res. Soc. Symp. Proc. **590**, 227 (2000).

[12] E. M. Lauridsen, D. J. Jensen, H. F. Poulsen, and U. Lienert, Scripta Mater. 43 **6**, 561 (2000).

[13] D. P. Grindatto, *Transmission Electron Microscopic Study of (Bi,Pb)$_2$Sr$_2$Ca$_2$Cu$_3$O$_x$ Silver-Sheathed Tapes*, Ph.D. thesis, Swiss Federal Institute of Technology Zurich, 1997.

[14] Y. Zhu, M. Suenaga, and R. L. Sabatini, Appl. Phys. Lett. **65**, 1832 (1994).

[15] B. Hensel, G. Grasso, and R. Flükiger, Phys. Rev. B **51**, 15456 (1995).

[16] H. F. Poulsen, T. Frello, N. H. Andersen, M. D. Bentzon, and M. von Zimmermann, Physica C **298**, 265 (1998).

[17] T. Frello, H. F. Poulsen, L. G. Andersen, N. H. Andersen, M. D. Bentzon, and J. Schmidberger, Supercond. Sci. Technol. **12**, 293 (1999).

[18] H. F. Poulsen, L. G. Andersen, T. Frello, S. Pratontep, N. H. Andersen, S. Garbe, J. Madsen, A. Abrahamsen, M. D. Bentzon, and M. von Zimmermann, Physica C **315**, 254 (1999).

[19] L. G. Andersen, S. Bals, G. van Tendeloo, H. F. Poulsen, and Y. L. Liu, Physica C (2001).

[20] Y. L. Liu, W. G. Wang, H. F. Poulsen, and P. Vase, Supercond. Sci. Technol. **12**, 376 (1999).

[21] Y. L. Liu, J.-C. Grivel, W. G. Wang, and H. F. Poulsen, Submitted to Supercond. Sci. Technol. (2001).

[22] O. V. Mishin, E. M. Lauridsen, N. C. K. Lassen, G. Brückner, T. Tschentscher, B. Bay, D. J. Jensen, and H. F. Poulsen, J. Appl. Cryst. **33**, 364 (2000).

[23] R. Bouchard, D. Hupfeld, T. Lippmann, J. Neuefeind, H. B. Neumann, H. F. Poulsen, U. Rütt, T. Schmidt, J. R. Schneider, J. Süssenbach, and M. von Zimmermann, J. Synchrotron Rad. **5**, 90 (1998).

[24] S. Keitel, C. C. Retsch, T. Niemöller, J. R. Schneider, S. N. Rossolenko, and H. Riemann, Nucl. Instrum. Methods A **414**, 427 (1998).

[25] M. Hatherly and W. B. Hutchinson, *An Introduction to Textures in Metals*, The Institution of Metallurgists, Monograph No. 5.

[26] L. G. Andersen, *Structural Properties of Superconducting Bi-2223/Ag Tapes*, Ph.D. thesis, The Technical University of Denmark, 2001.

[27] A. D. Rollett *et al.*, Textures and Microstructures **14-18**, 355 (1991).

[28] W. Lo, R. Stevens, R. Doyle, A. M. Campbell, and W. Y. Liang, J. Mater. Res. **10**, 2433 (1995).

[29] J. M. Yoo and K. Mukherjee, J. Mater. Science **29**, 4306 (1994).

[30] A. P. Hammersley, S. O. Svensson, M. Hanfland, A. N. Fitch, and D. Husermann, High Pressure Research **14**, 235 (1996).

[31] J. Als-Nielsen, N. H. Andersen, C. Broholm, K. N. Clausen, B. Lebech, M. Nielsen, and H. F. Poulsen, IEEE Trans. on Magnetics **25**, 2254 (1989).

[32] L. G. Andersen, H. F. Poulsen, T. Frello, N. H. Andersen, and M. von Zimmermann, IEEE Trans. Appl. Supercond. **9**, 2758 (1999).

[33] Y. Gao, P. Lee, P. Coppens, M. A. Subramanian, and A. W. Sleight, Science **24**, 954 (1988).

[34] C. L. Teske and H. Mller-Buschbaum, Z. Anorg. Allg. Chemie **379**, 234 (1970).

[35] Y. Ikeda, H. Ito, S. Shimomura, Z. Hiroi, M. Takano, Y. Bando, J. Takada, K. Oda, H. Kitaguchi, Y. Miura, Y. Takeda, and T. Takada, Physica C **190**, 18 (1991).

[36] J.-C. Grivel, A. Jeremie, B. Hensel, and R. Flükiger, Supercond. Sci. Technol. **6**, 725 (1993).

[37] A. Jeremie, K. Alami-Yadri, J.-C. Grivel, and R. Flükiger, Supercond. Sci. Technol. **6**, 730 (1993).

[38] G. S. Grader, E. M. Gyorgy, P. K. Gallagher, H. N. O'Bryan, D. W. Johnson, S. Sunshine, S. M. Zahurak, S. Jin, and R. C. Sherwood, Phys. Rev. B **38**, 757 (1988).

[39] T. Kanai, T. Kamo, and S. P. Matsuda, Jpn. J. Appl. Phys. **28**, L2188 (1989).

[40] I. Matsubara, R. Funahashi, T. Ogura, H. Yamashita, Y. Uzawa, K. Tanizoe, and T. Kawai, Physica C **218**, 181 (1993).

[41] S. F. Hulbert, J. Br. Ceram. Soc. **6**, 11 (1969).

[42] W. Bian, Y. Yhu, Y. L. Wang, and M. Suenaga, Physica C **248**, 119 (1995).

[43] P. E. D. Morgan, R. M. Housley, J. R. Porter, and J. J. Ratto, Physica C **176**, 279 (1991).

[44] Z. X. Cai, Z. Y, and D. O. Welch, Phys. Rev. B **52**, 13035 (1995).

[45] Y. L. Wang, W. Bian, Y. Zhu, Z.-X. Cai, D. O. Welch, R. L. Sabatini, M. Suenaga, and T. H. Thurston, Appl. Phys. Lett. **69**, 580 (1996).

[46] H. Nobumasa, K. Shimizu, Y. Kitano, and T. Kawai, Jpn. J. Appl. Phys. **27**, L846 (1988).

[47] N. Kijama, H. Endo, J. Tsuchiya, A. Sumiyama, M. Mizuno, and Y. Oguri, Jpn. J. Appl. Phys. **27**, L1852 (1988).

[48] J.-C. Grivel and R. Flükiger, Supercond. Sci. Technol. **9**, 555 (1996).

[49] J.-C. Grivel, D. P. Grindatto, G. Grasso, and R. Flükiger, Supercond. Sci. Technol. **11**, 110 (1998).

[50] T. Fahr, H.-P. Trinks, R. Schneider, and C. Fischer, Conf. Proc. on Applied Superconductivity Conference 2000 .

[51] F. Yi, Y. E. High, D. C. Larbalestier, Y. S. Sung, and E. E. Hellstrom, Appl. Phys. Lett. **62**, 1553 (1993).

[52] Y. Yamada, J. Q. Xu, J. Kessler, E. Seibt, W. Goldacker, W. Jahn, and R. Flükiger, Physica C **185**, 2483 (1991).

[53] Y. Iwai, Y. Hoshi, H. Saito, and M. Takata, Physica C **170**, 319 (1990).

[54] W. G. Wang, B. Seifi, Y.-L. Liu, M. Eriksen, P. Skov-Hansen, J. Grivel, and P. Vase, Conf. Proc. on Applied Superconductivity Conference 2000 .

[55] E. Giannini, E. Bellingeri, R. Passerini, and R. Flükiger, Physica C **315**, 185 (1999).

[56] J.-C. Grivel, R. E. Gladyshevskii, E. Walker, and R. Flükiger, Physcia C **274**, 66 (1997).

[57] J.-C. Grivel, A. Jeremie, B. Hensel, and R. Flükiger, in: J. Etourneau, J.B. Torrence and H. Yamauchi (Eds.), Proc. ICMAS-93, Paris 1993, I.I.T.T., 1993, pp. 359–364 .

[58] E. M. Lauridsen, S. Schmidt, R. M. Suter, and H. F. Poulsen, Submitted to J. Appl. Cryst. (2001).

[59] H. Grimmer and D. H. Warrington, Acta Cryst. **A43**, 232 (1987).

[60] S. X. Dou, R. Zeng, X. K. Fu, Y. C. Guo, J. Horvat, H. K. Liu, T.Beales, and M. Apperley, IEEE Trans. Appl. Supercond. **9**, 2436 (1999).

[61] B. Lehndorff, P. Hardenbicker, M. Hortig, and H. Piel, Physica C **312**, 105 (1999).

[62] P. Majewski, H.-L. Su, and F. Aldinger, J. Mater. Sci. **31**, 2035 (1996).

[63] M. R. Koblischka, T. H. Johansen, B. H. Larsen, N. H. Andersen, H. Wu, P. Skov-hansen, M. Bentzon, and P. Vase, Physica C **341-348**, 2583 (2000).

[64] M. R. Koblischka, W. G. Wang, B. Seifi, P. Skov-Hansen, P. Vase, B. H. Larsen, and N. H. Andersen, Conf. Proc. on Applied Superconductivity Conference 2000 .

A15

Journal of
Applied Crystallography
ISSN 0021-8898

Received 12 June 2002
Accepted 27 January 2003

Structural refinements of the individual grains within polycrystals and powders

S. Schmidt,[a]* H. F. Poulsen[a] and G. B. M. Vaughan[b]

[a]Center for Fundamental Research: Metal Structures in Four Dimensions, Risø National Laboratory, DK-4000 Roskilde, Denmark, and [b]European Synchrotron Radiation Facility, BP 220, F-38043 Grenoble Cedex, France. Correspondence e-mail: soeren.schmidt@risoe.dk

A method is presented for simultaneous structural refinement of up to several hundred grains inside powders or polycrystals. The method is based on the use of hard X-rays and the indexing program *GRAINDEX*, where grain orientations are found by scanning in Euler space. Conventional experimental setups and refinement programs for single-crystal work can be applied. The method is validated by a study of a sintered plate of α-Al_2O_3, containing of the order of 1500 grains in the gauge volume. 57 of the largest grains were refined with respect to the Al z and O x positions as well as the isotropic atomic displacement parameters. The $R1$ values were 3.4% and 3.8% for the grain average and the best grain, respectively. A discussion of the potential of the method is presented, as well as the main limitation: grain size and overlap of diffraction spots.

1. Introduction

In spite of the great recent progress in structure solution and refinement from powder diffraction data (McCusker *et al.* 1999; Harris *et al.*, 2001; Young, 1995; David *et al.*, 2002, and references within), it is clear that data obtained from single-crystalline samples will always be preferable, due to both the accuracy of the peak intensities thereby obtained and the greater quantity of statistically independent data (reflections) which can be measured. Single-crystal data give a greater number of both unambiguously independent unique reflections and multiple symmetry-equivalent reflections, leading to significantly more robust data with respect to systematic errors.

Although there is no universally accepted standard for the number of independent observations in a powder diffraction pattern (McCusker *et al.*, 1999) it is clearly lower than the corresponding number in a single-crystal data set by a factor of three at least (Altomare *et al.*, 1995). It is this data to parameter ratio as well as the much poorer signal to noise ratio present in a powder diffraction pattern that limits the scope of both structure refinement and solution from powder samples.

Recently, Wessels *et al.* (Wessels, Baerlocher, McCusker & Creyghton, 1999; Wessels, Baerlocher & McCusker, 1999) have used textured powder samples to solve and refine (isotropically equivalent to $\sim$350 structural parameters) a structure with 117 atoms in the asymmetric unit, a rather significant increase over the roughly $\leq$20 atoms from a 'typical' structure solved from powder diffraction data. This appears to be the most complex structure yet solved from powder data. On the other hand, structures with $\sim$5000 parameters can be solved and refined from even very small twinned single crystals with a large mosaic spread (*e.g.* compound 7 in the work of Saalfrank *et al.*, 2002).

However, in many cases single-crystal data cannot be obtained, for example during studies involving extreme environments, samples undergoing first-order phase transitions, studies of precious samples and in the many cases in which suitable single-crystalline samples simply cannot be grown. In such cases structural refinement may be impossible.

Another characteristic of powder diffraction is that it probes the average properties. However, in materials science it is often essential to characterize the heterogeneity, *e.g.* the distribution of grains as a function of a parameter such as stoichiometry, and the response of such a distribution to processing, heating, chemical potential, *etc*. While it is possible to derive mean quantities from powder diffraction data, it is practically impossible to derive information about the forms of such distributions. In principle, information about these distributions could be derived by selecting a representative set of grains and performing a diffraction study on each of them, but this procedure would be tedious and exclude studies of the dynamics. Likewise, the correlation between neighbouring grains is lost. Hence, there is a lack of a tool for local *in situ* crystallographic studies of the microstructure and its dynamics.

In a collaboration between Risø and the ESRF, we have recently developed several methods for non-destructive structural characterization of the individual grains inside bulk materials (Poulsen *et al.*, 1997; Lienert *et al.*, 1999; Nielsen, Wolf *et al.*, 2000; Juul Jensen & Poulsen, 2000). These are based on indexing algorithms such as *GRAINDEX* (Lauridsen *et al.*, 2001) and *GRAINSWEEPER* (Schmidt *et al.*, 2003). While the algorithms are universal, the typical applications have involved high-energy X-rays ($E \geq 50$ keV), enabling

Table 1
Values of structural parameters from the refinements.

First the weighted mean and the median of the values obtained from the 57 independent refinements are listed, then values from the best grain, followed by values arising from merging all data from the 17 largest grains into a single data set, and the result of a conventional Rietveld refinement. The last three rows contain single-crystal reference values from the literature.

	Al z	O x	Al u (Å^2)	O u (Å^2)
Grain median	0.35221	0.30527	0.0032	0.0010
Grain weighted mean	0.35203 (11)	0.3071 (6)	0.0048 (7)	0.0046 (5)
Best grain	0.35197 (13)	0.3072 (11)	0.0041 (8)	0.0048 (13)
Full data set	0.35220 (29)	0.3060 (15)	0.0038 (10)	0.0012 (17)
Treated as powder	0.35060 (40)	0.3094 (13)	0.057 (12)	0.052 (21)
Brown *et al.* (1993)	0.35215 (1)	0.30624 (5)	0.0035 (2)	0.0039 (3)
Maslen *et al.* (1993)	0.35223 (4)	0.30622 (17)	0.0027 (1)	0.0029 (1)
Sawada (1994)	0.35217 (2)	0.30618 (8)	0.0032 (1)	0.0028 (1)

three-dimensional studies within specimens of millimetre-to-centimetre thickness. As a result, under favourable conditions a fast and complete description can be given with respect to grain position, orientation, and the elastic and plastic strain of each grain (Poulsen *et al.*, 2001). Furthermore, for coarse-grained materials the topology of the grain boundaries can be mapped (Nielsen, Ludwig *et al.*, 2000; Poulsen *et al.*, 2001). These methods have been used *e.g.* to study the simultaneous growth of individual grains during recrystallization of aluminium (Lauridsen *et al.*, 2000) and the simultaneous plastic response of grains during tensile deformation (Margulies *et al.*, 2001; Winther *et al.*, 2000).

As an extension of these efforts we present here a method for performing single-crystal refinements on the individual grains embedded within a polycrystalline sample. The aim is to be able to derive single-crystal-quality data from powders or sintered pellets. The method separates the indexing part, namely sorting reflections with respect to grain of origin and calculating the orientation matrix of each grain, and the refinement part, such that any existing single-crystal refinement program can be used. Furthermore, many grains from a single sample can be refined either separately, enabling reasonable grain statistics, or, in the case of structurally identical grains, simultaneously, allowing highly complete and redundant data to be acquired with only a small sample rotation. This allows the rapid acquisition of complete data sets, enabling measurements of kinetics, highly radiation sensitive samples, *etc.*

To verify the technique we have performed a room-temperature study of a sintered plate of α-Al_2O_3 (Corundum). Refinements of the individual grains are compared with known average properties. The main limitation of the method is anticipated to be spot overlap. To study the effect of this limitation the number of grains within the gauge volume is chosen to be so large (of the order of 1500) that the majority of spots will overlap to some extent.

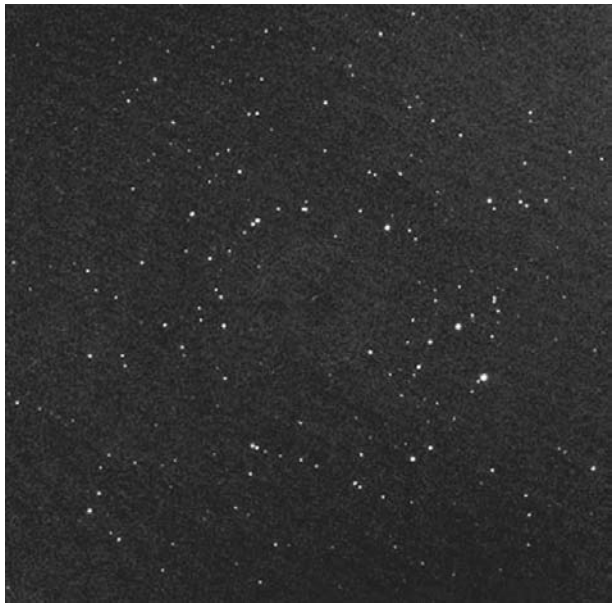

Figure 1
Example of raw data represented by rotation photograph number 306, *i.e.* pattern recorded in the φ range 30.55–30.65°.

2. Experimental

The specimen was a sintered plate of pure Al_2O_3, which had been annealed at 1773 K for 24 h to produce a material with virtually no texture, an average grain diameter of 20 µm, as determined by SEM, and a mosaic spread of the reflections of the order of 0.2°. The plate was 180 µm thick.

The experiment was performed similarly to a conventional single-crystal refinement study with a monochromatic beam and a two-dimensional detector. It was performed with a Bruker Smart 6500 fibre-optic-coupled CCD detector at the κ diffractometer at beamline ID11 at the ESRF. Using a double-bounce Si(111) monochromator, we obtained a homogeneous beam of 50 keV X-rays over an area of 250 × 250 µm^2. The instrumental resolution with this setup is approximately 0.4° in 2θ on the detector face. Oscillation images were taken at room temperature over a φ range of 90° and in 0.1° φ steps. One of these photographs is shown in Fig. 1. The exposure time was 1 s per frame. The detector distance and the beam zero point were calibrated using a silicon powder standard.

3. Rietveld refinement

In order to characterize the global data quality, a pseudo-powder pattern was generated by summing together all of the rotation images. The pixel by pixel median values were then subtracted; this procedure serves to remove the background (mostly air scattering) from the pattern, as the median image contains only the ubiquitous part of the data, eliminating outliers (diffraction spots). This difference image was then azimuthially integrated, and ten parameters (two lattice parameters, two atomic coordinates, two isotropic atomic displacement parameters, three peak shape parameters and a scale factor) were refined against the resulting powder pattern using *Fullprof* (Rodriguez-Carvajal, 1996). The results of the Rietveld refinement are given in Table 1.

The refinement is reasonable, considering the nature of the data used. All of the parameters are within an acceptable

range, except for the atomic displacement parameters, which are much too high. This is due to a poor signal to noise ratio at high Bragg angles, leading to underestimates of the peak intensities.

4. Multicrystal refinement

4.1. Indexing

The diffraction spots from the multiple crystal data were integrated and the reflections sorted with respect to grain of origin by the indexing program *GRAINDEX* (Lauridsen *et al.*, 2001), which had been modified for the κ geometry. Essentially this program scans through the non-redundant part of Euler space (orientation space). At each step it determines whether the diffraction pattern is compatible with one or more grains of the given orientation. If more grains seem to be present, a fitting routine is applied. The program needs as input the space group, the lattice parameters and the ratio of the pixel size to the distance between the sample centre of rotation and the detector. The latter were determined by the powder refinement.

By analysing nine {*hkl*} families, well separated from other families in the images, a total of 100680 diffraction spots were identified by the program. Most of these diffraction spots were not relevant for the further analysis for one of two reasons. Firstly, the gauge volume will change as function of the φ rotation. While grains near the centre of rotation will remain fully embedded in the beam throughout, other grains will at times be partly illuminated and possibly for some φ settings be positioned completely outside the illuminated volume. Secondly, the reflections from the smallest grains will be associated with the worst signal to noise ratios.

To discriminate against such spots, *GRAINDEX* imposed two thresholds: one on the completeness factor and an *ad hoc* one on intensity. The completeness factor is the fraction of predicted diffraction spots that are actually found in the images. This was set to 0.7. As a result *GRAINDEX* indexed 57 grains associated with approximately 35 reflections per grain. At this point the crystallographic orientations of the 57 grains are well determined. In order to increase the number of reflections associated with each grain, the search for reflections was extended to include {*hkl*} families which are not well separated, yielding 100–150 reflections per grain.

The integrated intensities of the reflections were determined by summing and subtracting a local background. For each of the pixel positions in a spot, the background was calculated as the median of the same pixel in a set of neighbouring images.

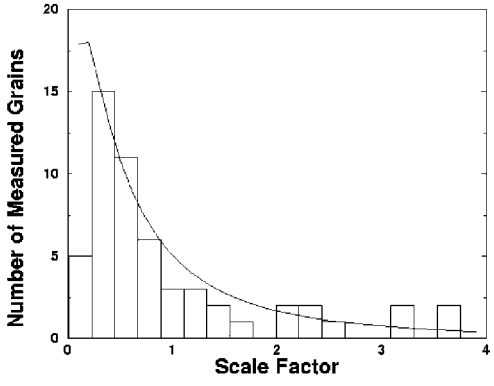

Figure 2
Distribution of scale factors of the 57 indexed grains. Superimposed is a log-normal curve to illustrate the assumed grain size distribution. The data are cut at the low-scale-factor end as a result of intensity cut-offs incorporated during the analysis.

4.2. Filtering and sorting

The integrated intensities obtained were filtered and scaled by methods similar to those commonly used for single-crystal data (*e.g.* Blessing, 1997, and references within). As we discuss below, the main aim of the filtering procedure is to detect and eliminate those peaks with intensities that are corrupted by weak reflections from smaller unindexed grains.

Explicitly, the process to merge, filter and scale the data is as follows.

Step 1. Integrated intensities (I) are adjusted for detector gain (G), Lorentz (L) and polarization (P) factors to obtain a list of $k|F|^2 = I/GLP$. The parameter k is the crystal scale factor, proportional to grain volume.

(a) The Lorentz factor for this configuration is $1/\sin(2\theta)|\sin(\eta)|$, where η is the azimuthal angle measured in the plane of the image with respect to the rotation axis (Lauridsen *et al.*, 2001).

(b) The polarization factor is $\frac{1}{2}\{[1 + \cos^2(2\theta) - P\cos(2\eta')\sin^2(2\theta)]$, where P is the degree of horizontal polarization, here taken as 1.0, and η' is the azimuthal angle with respect to the horizontal plane (Kahn *et al.*, 1982).

(c) Standard errors, σ, are propagated and convoluted with a 'machine error': $\sigma^2_{k|F|} = (I + \sigma_m^2 I^2)^{1/2}/GLP$. The machine error σ_m was set to 0.025. This factor is meant to take into account analog–digital noise, phosphor linearity and de-excitation, re-absorption, *etc*.

Step 2. For each grain and each group of symmetry-related equivalent reflections, the reflections are filtered against the mean of the group. Reflections more than $x\sigma$ from the mean are rejected and merging statistics are generated (for the data discussed subsequently, $x = 6$).

Step 3. The crystal scale factors are derived in two steps. First the mean value is calculated for each group of reflections and for each grain. Only reflections/groups satisfying certain criteria are used in the scaling (although at this point rejected reflections are kept for subsequent operations).

(a) Reject reflections with $I/\sigma < x$ ($x = 30$)

(b) Reject groups with less than x members ($x = 2$)

(c) Reject groups with variance/$\sigma_{\rm mean} > x$ ($x = 6$).

Step 4. Next the scale factor for each grain is determined as the weighted mean of the group scale factors. Gaussian weights are used: $\langle x\rangle = \sum x_i/\sigma_i^2 \big/ \sum 1/\sigma_i^2$; $\langle\sigma_i\rangle^2 = \sum 1 \big/ \sum 1/\sigma_i^2$. This implies the assumption of a Gaussian distribution of peak intensities, which according to Wilson statistics is a rather good estimate (Shmueli & Weiss, 1995).

Table 2
Probability of two or more peaks overlapping within an {*hkl*} family with a multiplicity of 12.

N is the number of grains in the gauge volume, *w* is the mosaic spread and I/I_0 is a measure of the texture ($I/I_0 = 1$ implies a random distribution of grain orientations).

	$w = 0.1°$, $I/I_0 = 1$	$w = 1°$, $I/I_0 = 1$	$w = 0.1°$, $I/I_0 = 10$	$w = 1°$, $I/I_0 = 10$
$N = 10$	0.00033	0.032	0.0033	0.306
$N = 100$	0.0036	0.319	0.036	0.996
$N = 1000$	0.036	0.995	0.32	1

Step 5. Reflections for the final merge are accepted if they are within $x\sigma$ from the scaled/merged group mean values ($x = 5$).

Following this filtering, the 57 grains were associated with 5576 reflections. The distribution of scale factors, proportional to grain volumes, is shown in Fig. 2. Also shown is a fit to a log-normal. The correspondence is reasonable, with the measured distribution being cut-off at the low end due to the intensity threshold. The intention with the fit is not to prove that the size distribution is log-normal, but to provide a test of the derived scale factors which is independent of crystallography.

As the main cause of error affects mainly the weakest data, the grains with scale factors less than 0.7 of the mean were rejected. The complete filtering and sorting process was repeated, resulting in a total of 17 indexed grains associated with 510 reflections.

4.3. Structure refinements

The data sets for each of the 57 grains as well as the fully merged data of the 17 grains were refined (Sheldrick, 1997) *versus* the known structure of Al_2O_3. As there were only $\leq$35 unique reflections for each grain, the anisotropic displacement parameters were not refined, leaving five parameters: Al *z*, O *x*, isotropic atomic displacement parameters, and a scale factor. Results from these refinements are shown in Table 1.

A very large distribution of *R*1 (Sheldrick, 1997) factors were found from the individual grain refinements ($0.038 < R1 < 0.5$). The best values represent excellent refinements, whereas the high values indicated seriously corrupted data. The value of *R*1 is highly correlated with the scale factor. This unsurprising result indicates that intense reflections are much less sensitive to the various factors (discussed below) which may compromise the integrated intensities, particularly during integration by straight summation.

The grain which gave the best refinement (as measured by the value of *R*1) also had the best $R_{\rm merge}$ (Weiss, 2001) and one of the highest redundancies. However, there is not a strong correlation in general between the final values of *R*1 and $R_{\rm merge}$ for the various grains. Thus $R_{\rm merge}$ alone is not a good indicator of data quality. This is not surprising, since all filtering operations discussed above will, by construction, improve it. Neither did the various other data quality factors such as $R_{\rm rim}$, $R_{\rm pim}$, and PCV (Weiss, 2001) seem to be highly correlated with the final refinement quality.

The best *R*1 value for a single grain was 0.038. The *R*1 for the merged set of the 17 grains was 0.034, but with much higher redundancy (14.5 as opposed to 3.6) and presumably better accuracy (within the assumption that the all grains are structurally identical). As can be seen in Table 1, the structural parameters derived from either the best grain, the various averages from the independent grain refinements, or the fully merged data are in good agreement with recent single-crystal studies. The merged data set may have slightly better atomic displacement parameters. The treatment of the current data as a powder by averaging the raw data produces much worse results.

5. Discussion

5.1. Systematic errors

There are several possible sources of systematic errors in the peak intensities, as described in the following subsections.

5.1.1. Absorption and extinction. In the multi-grain case, it may be feasible to carry out an empirical absorption correction (*e.g.* Blessing, 1995) for grains with sufficient redundancy. To correct accurately for the inter-granular secondary extinction will be difficult. In principle, the necessary information on the relative positions of the grains is obtainable (Nielsen, Ludwig *et al.*, 2000; Poulsen, Nielsen *et al.*, 2001), but the spatial resolution required and the complexity of the problem will in general be prohibitive. Hence, for the present study the effects of both absorption and extinction are reduced to negligible levels by carrying out the experiment at a sufficiently short wavelength.

Note that if present, both absorption and extinction would produce randomly reduced peak intensities (negative outliers).

5.1.2. Integration problems. These are the same sorts of problems that affect data integration on single crystals using two-dimensional detectors, namely poorly determined background or orientation matrices, inappropriate size of integration box, mis-indexed reflections, *etc*. The quantity of reflections mis-indexed as a different peak from the same grain will be rather small for all but very large low-symmetry structures. However, as opposed to a single-crystal integration, there will be a non-negligible quantity of reflections which are assigned to the wrong grain.

All of these effects will produce peak intensities which are randomly too low or too high, and thus will lead to a decrease in the statistical quality of the data, rather than to systematic errors.

5.1.3. Grains which rotate out of the beam. One is able to identify grains that fall into this category by the variation in structure factors *versus* the φ rotation angle. In principle one should be able to use data from the ranges where the grains are fully illuminated in the analysis. Presently all reflections from grains which have a large variation of $|F|_i/|F|_{n,i}$ *versus* φ, where $|F|_i$ is the structure factor of the reflection and $|F|_n$ is that of the group of symmetry-equivalent peaks to which it belongs, are simply eliminated.

5.1.4. The spot overlaps a spot from another grain. In Appendix *A* we give an estimate of the fraction of overlapping spots in a data set. It is a steep function of the mosaic spread, while linear in the number of diffraction spots (as given by the number of illuminated grains, the multiplicity and the texture). For illustration, numbers are provided in Table 2. It is seen that under favourable conditions a few thousand grains can be indexed simultaneously.

Inserting the present case into the equations, the chance of peak overlap is found to be close to one. Hence, many of the diffraction spots of the 57 indexed (large) grains are situated on top of minor spots from the unindexed grains. As this background from the small grains is rapidly varying, automatic removal of such spots is prohibited. This leads to non-random errors in the affected peak intensities, which uniformly will be too high.

It appears that spot overlap is the largest source of error. This is corroborated by the plots of $|F|_i^2/|F|_{n,i}^2$ shown in Fig. 3, where most of the extreme outliers are seen to be high in intensity. Furthermore, the outliers are more prominent for the smaller grains.

It is remarkable that high-quality refinements are derived despite the fact that the spot overlap was almost complete. There are two reasons for this. Firstly, the combination of a log-normal distribution of grain sizes and the fact that intensities are proportional to the grain size in the third power implies that the intensities of the strongest peaks are relatively robust. Secondly, the reflections most affected were removed from the final data set by the filtering operations above and therefore did not compromise the final data quality.

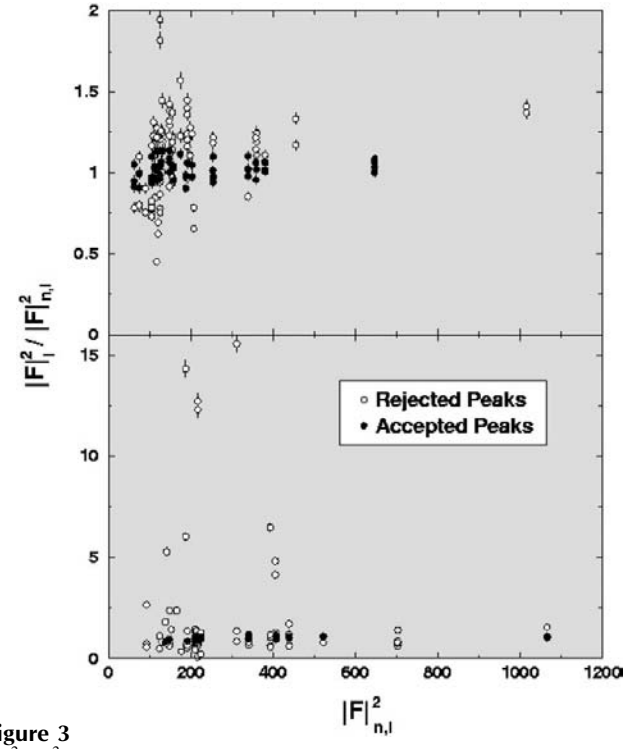

Figure 3
$|F|_i^2/|F|_{n,i}^2$ for a large grain (above) and a small grain (below) within the final set of 17 indexed grains. The distribution of outliers is asymmetrically weighted toward high values, particularly in the smaller grain. Filled circles indicate the data retained in the final merge; empty circles indicate those eliminated by the filtering procedure.

5.2. Outlook and possible improvements

Spot overlap is a main limitation of the method. Provided that samples are sufficiently thin, this can be avoided by focusing the beam. In addition, the presented methodology can be modified in a number of ways to reduce the number of overlapping spots or increase the fraction of usable spots in other ways.

Firstly, the indexing was based solely on the directions of the reflections as the diffraction geometry (detector resolution *versus* gauge volume dimensions) did not allow discrimination based on spatial information. In the case of the reverse situation, the detector resolution being smaller than the size of the gauge volume, the tracking method can be applied (Lauridsen *et al.*, 2001). This implies that the experiment is repeated with several sample–detector distances and the diffraction spots traced through such a virtual three-dimensional detector. In this way one can directly determine which spots are overlapping. Also in this case a more powerful indexing routine can be applied: the *GRAINSWEEPER* (Schmidt *et al.*, 2003).

Secondly, a conical slit can be introduced between the sample and the detector (Nielsen, Wolf *et al.*, 2000). The conical slit defines an interior gauge volume, centred at the rotation axis. All spots arising from this 'volume of interest' will reach the detector, while stray reflections from grains positioned along the beam path but outside the 'volume of interest' will be absorbed in the slit. Hence, the spot overlap can be substantially reduced. An example of the use of a conical slit for texture characterization is given by Winther *et al.* (2000).

Thirdly, the one-dimensional φ scan can be substituted by a two-dimensional scan by combining it with a translation of the sample perpendicular to the direction of the beam and to the axis of rotation. In this way, more grains are characterized and a uniform sampling is provided (all grains are probed). An example of such a use for texture characterization is given by Poulsen, Jensen *et al.* (2001).

As discussed in §1, the capability of powder diffraction to solve structures has increased greatly over the past couple of decades thanks to the development of new methodologies (see, for example, Harris *et al.*, 2001; David *et al.*, 2002, and references therein) and to extensions to direct-methods techniques (*e.g.* Altomare *et al.*, 1999).

Nevertheless, solution of even moderately complex structures (some tens of atoms) from powder diffraction data remains non-routine, generally requiring excellent data and substantial effort. In contrast, order of magnitude more complex structures may be solved without particular difficulty from average single-crystal data; this gap is never likely to be closed. It is interesting that what appears to be the most complex structure solved from 'powder' data (Wessels, Baerlocher, McCusker & Creyghton, 1999; Wessels, Baerlocher & McCusker, 1999), relied on inducing texture in the sample,

which is making it more single-crystal like. We have aimed to show that, in at least some cases, it is possible to extend this idea to its limit and treat the grains of a 'powder' sample as individual crystals.

Furthermore, although there have been marked advances in structure solution techniques, there has been no equivalent innovation in structure refinement methodology since the advent of the Rietveld method (Rietveld, 1969). The largest improvements have stemmed from the quality of the powder diffraction data that may be obtained from laboratory, neutron and synchrotron sources. Certainly, there have been structural refinements of very complicated systems (for example, von Dreele, 1999; von Dreele, *et al.* 2000), but such refinements rely on utilizing a huge array of soft constraints in order to bring the data to parameter ratio to an acceptable level. Powder refinements are, in addition, very susceptible to systematic errors, leading to chemically nonsensical bond lengths, *etc*.

The current example (Al_2O_3) is of trivial structural complexity; we have studied it in some detail in order to verify the proposed method. The real interest of the technique will be its use to solve and/or refine more complicated structures. In principle, one can isolate an appropriate number of grains in any crystalline powder by making the sample and/or the incident beam sufficiently small. The problem of spot overlap can equally be overcome if one has detectors of sufficient size and resolution; the size of the unit cell that may be treated effectively scales with the detector size and sample–detector distance. Currently available beam and detector sizes lead us to conclude that even rather complicated cases should be amenable to this technique. Such work is underway.

6. Conclusion

A multi-grain refinement procedure is presented. The potential is clear: as long as the majority of the diffraction spots do not overlap with other spots, any traditional single-crystal refinement program can be applied and the results will be of the same quality. Hence, even solutions and refinements of complicated structures should be feasible. Furthermore, the method is independent of the size of the unit cell and, since many grains from the same sample are merged together, complete data sets may be collected by sampling only a small angular range, making the method well adapted for time-resolved studies or radiation-sensitive samples. Furthermore, we have demonstrated that the fact that grain distributions typically are log-normal can be utilized to derive quality refinements even in the case where spot overlap is severe.

APPENDIX *A*
Fraction of overlapping spots in a data set

On occasion, the reflections arising from two grains will overlap. However, unless the orientations are nearly identical, this situation can only appear for a small sub-set of the reflections. Hence, the overlap can essentially be seen as a stochastic process.

The amount of spot overlap depends on the number of grains within the gauge volume, the detector resolution, the texture of the material, the symmetry of the sample and the mosaic spread of the grains. Noticeably, it does not depend on the cell volume, as long as the Debye–Scherrer rings can be separated.

Consider an $\{hkl\}$ family with a multiplicity of m, and N fully illuminated grains. What is the chance $P(k)$ of k or more reflections overlapping? Assume the mosaic spread of all reflections to be contained within a steric angle of πw^2. Assume further that the azimuthal resolution and the rotation step, for the κ geometry $\Delta\varphi$, are both smaller than w. Then for random orientations,

$$p = 2mw^2,$$

$$f(k) = \binom{N}{k} p^k (1-p)^{N-k}$$

and

$$P(k) = \frac{kf(k) + (k+1)f(k+1) + \ldots}{f(1) + 2f(2) + 3f(3) + \ldots}.$$

For $Np \ll 1$ we have

$$P(2) \simeq Np; \qquad P(3) \simeq (Np)^2/2.$$

In the case of a textured material, it is customary to plot the orientation distribution as pole figures with contour lines I/I_0, where I_0 is the average intensity. For reflections pointing in a specific direction, we can keep the formalism above provided that we set

$$p = [\pi(2w)^2/2\pi] m\, I/I_0.$$

We thank A. Götz, A. Terry, P. B. Olesen and J. Lindbo for technical support, L. Margulies for help in data analysis, and S. Larsen, B. Lebech, D. Juul Jensen and B. Kindl for scientific discussions. We acknowledge the Danish National Research Foundation for supporting the Centre for Fundamental Research: Metal Structures in Four Dimensions. The Danish Research Council SNF provided additional support *via* Dansync. Beamtime was provided by the European Synchrotron Radiation Facility.

References

Altomare, A., Cascarano, G., Giacovazzo, C., Guagliardi, A., Moliterni, G. G., Burla, M. C. & Polidori, G. (1995). *J. Appl. Cryst.* **28**, 738–744.

Altomare, A., Burla, M. C., Camalli, M., Carrozzini, B., Cascarano, G., Giacovazzo, C., Guagliardi, A. & Moliterni, G. G. (1999). *J. Appl. Cryst.* **32**, 339–340.

Blessing, R. H. (1995). *Acta Cryst.* A**51** 33–38.

Blessing, R. H. (1997). *J. Appl. Cryst.* **30**, 421–426.

Brown, A. S., Spackman, M. A. & Hill, R. J. (1993). *Acta Cryst.* A**49**, 513–527.

David, W. I. F., Shankland, K., McCusker, L. B. & Baerlocher, Ch. (2002). Editors. *Structure Determination from Powder Diffraction Data*. Oxford University Press.

Harris, K. D. M., Tremayne, M. & Kariuki, B. M. (2001). *Angew. Chem. Int. Ed. Engl.* **40**, 1626–1651.

Juul Jensen, D. & Poulsen, H. F. (2000). *Proceedings of the 21st Risø International Symposium on Materials Science, Roskilde, Denmark,* edited by N. Hansen, X. Huang, D. Juul Jensen, E. M. Lauridsen, T. Leffers, W. Pantleon, T. J. Sabin & J. A. Wert, pp. 103–124. Roskilde: Risø National Laboratory.

Kahn, R., Fourme, R., Gadet, A., Janin, J., Dumas, C. & André, D. (1982). *J. Appl. Cryst.* **15**, 330–337.

Lauridsen, E. M., Juul Jensen, D., Poulsen, H. F. & Lienert U. (2000). *Scr. Mater.* **43**, 561–566.

Lauridsen, E. M., Schmidt, S., Suter, R. M. & Poulsen, H. F. (2001). *J. Appl. Cryst.* **34**, 744–750.

Lienert, U., Poulsen, H. F. & Kvick, Å. (1999). *Proceedings of the 40th Conference of AIAA on Structures, Structural Dynamics and Materials, St. Louis, USA,* pp. 2067–2075. American Institute of Aeronautics and Astronautics.

McCusker, L. B., Von Dreele, R. B., Cox, D. E., Louër, D. & Scardi, P. (1999). *J. Appl. Cryst.* **32** 36–50.

Margulies, L., Winther, G. & Poulsen, H. F. (2001). *Science*, **291**, 2392–2394.

Maslen, E. N., Streltsov, V. A., Streltsova, N. R., Ishizawa, N. & Satow, Y. (1993). *Acta Cryst.* B**49**, 973–980.

Nielsen, S. F., Ludwig, W., Bellet, D., Lauridsen, E. M., Poulsen, H. F. & Juul Jensen, D. (2000). *Proceedings of the 21st Risø International Symposium on Materials Science, Roskilde, Denmark,* edited by N. Hansen, X. Huang, D. Juul Jensen, E. M. Lauridsen, T. Leffers, W. Pantleon, T. J. Sabin & J. A. Wert, pp. 473–478. Roskilde: Risø National Laboratory.

Nielsen, S. F., Wolf, A., Poulsen, H. F., Ohler, M., Lienert, U. & Owen, R. A. (2000). *J. Synchrotron Rad.* **7**, 103–109.

Poulsen, H. F., Garbe, S., Lorentzen, T., Juul Jensen, D., Poulsen, F. W., Andersen, N. H., Frello, T., Feidenhans'l, R. & Graafsma, H. (1997). *J. Synchrotron Rad.* **4**, 147–154.

Poulsen, H. F., Juul Jensen, D., Tschentscher, T., Wcislak, L., Lauridsen, E. M., Margulies, L. & Schmidt, S. (2001). *Textures Microstruct.* **35**, 39–54.

Poulsen, H. F., Nielsen, S. F., Lauridsen, E. M., Schmidt, S., Suter, R. M., Lienert, U., Margulies, L., Lorentzen, T. & Juul Jensen, D. (2001). *J. Appl. Cryst.* **34**, 751–756.

Rietveld, H. M. (1969). *J. Appl. Cryst.* **2**, 65.

Rodriguez-Carvajal, J. (1996). *Reference Guide for the Computer Program Fullprof.* Laboratoire Léon Brillouin, CEA-CNRS, Saclay, France.

Sawada, H. (1994). *Mater. Res. Bull.* **29**, 2, 127–133.

Saalfrank, R. W., Glaser, H., Demleitner, B., Hampel, F., Chowdhry, M. M., Schünement, V., Trautwein, A. X., Vaughan, G. B. M., Yeh, R., Davis, A. V. & Raymond, K. N. (2002). *Chem. Eur. J.* **8**, 493–497.

Schmidt, S., Poulsen, H. F. & Suter, R. M. (2003). In preparation.

Sheldrick, G. M. (1997). *SHELXTL97*. University of Göttingen, Germany.

Shmueli, U. & Weiss, G. H. (1995). *Introduction to Crystallographic Statistics*. Oxford University Press.

Von Dreele, R. B. (1999). *J. Appl. Cryst.* **32**, 1084–1089.

Von Dreele, R. B., Stephens, P. W., Smith, G. D. & Blessing, R. H. (2000). *Acta Cryst.* D**56**, 1549–1553.

Weiss, M. S. (2001). *J. Appl. Cryst.* **34**, 130–135.

Wessels, T., Baerlocher, Ch., McCusker, L. B. & Creyghton, E. J. (1999). *J. Am. Chem. Soc.* **121**, 6242–6247.

Wessels, T., Baerlocher, Ch. & McCusker, L. B. (1999). *Science*, **284**, 477–479.

Winther, G., Margulies, L. Poulsen, H. F., Schmidt, S., Larsen A. W., Lauridsen, E. M., Nielsen, S. F. & Terry, A. (2000). *Proceddings of ICOTOM 13, Seoul, August 2002.* In preparation.

Young, R. A. (1995). Editor. *The Rietveld Method*. Oxford University Press.